

AD-A094 912

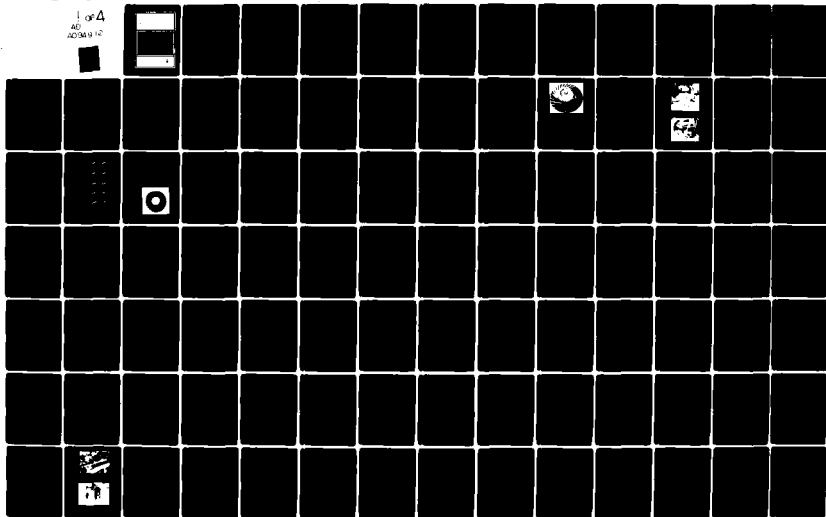
ADVISORY GROUP FOR AEROSPACE RESEARCH AND DEVELOPMENT--ETC F/6 21/5
CENTRIFUGAL COMPRESSORS, FLOW PHENOMENA AND PERFORMANCE.(U)
NOV 80

UNCLASSIFIED

AGARD-CP-282

NL

1 of 4
AD
A094 912



CP 282

CENTRIFUGAL COMPRESSORS, FLOW PHENOMENA
AND PERFORMANCE

D-CP-282

AD A004012

LEVEL

①

AGARD-CP-282

AGARD

ADVISORY GROUP FOR AEROSPACE RESEARCH & DEVELOPMENT

7 RUE ANCELLE 92200 NEUILLY SUR SEINE FRANCE

AGARD CONFERENCE PROCEEDINGS No. 282

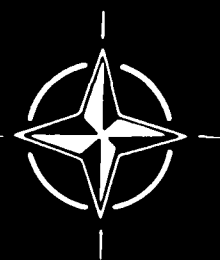
Centrifugal Compressors, Flow Phenomena and Performance

DISTRIBUTION STATEMENT A

Approved for public release;
Distribution Unlimited

DTIC
FEB 12 1981

NORTH ATLANTIC TREATY ORGANIZATION



DISTRIBUTION AND AVAILABILITY
ON BACK COVER

81 2 11 226

DDC FILE COPY

PEP

NORTH ATLANTIC TREATY ORGANIZATION
ADVISORY GROUP FOR AEROSPACE RESEARCH AND DEVELOPMENT
(ORGANISATION DU TRAITE DE L'ATLANTIQUE NORD)

AGARD Conference Proceedings No.282

CENTRIFUGAL COMPRESSORS, FLOW PHENOMENA
AND PERFORMANCE

DISTRIBUTION STATEMENT A

Papers presented at the 55th (B) Specialists' Meeting of the Propulsion and Energetics Panel of
AGARD held at the Royal Library, Brussels, Belgium, on 7-9 May 1980.

THE MISSION OF AGARD

The mission of AGARD is to bring together the leading personalities of the NATO nations in the fields of science and technology relating to aerospace for the following purposes:

- Exchanging of scientific and technical information;
- Continuously stimulating advances in the aerospace sciences relevant to strengthening the common defence posture;
- Improving the co-operation among member nations in aerospace research and development;
- Providing scientific and technical advice and assistance to the North Atlantic Military Committee in the field of aerospace research and development;
- Rendering scientific and technical assistance, as requested, to other NATO bodies and to member nations in connection with research and development problems in the aerospace field;
- Providing assistance to member nations for the purpose of increasing their scientific and technical potential;
- Recommending effective ways for the member nations to use their research and development capabilities for the common benefit of the NATO community.

The highest authority within AGARD is the National Delegates Board consisting of officially appointed senior representatives from each member nation. The mission of AGARD is carried out through the Panels which are composed of experts appointed by the National Delegates, the Consultant and Exchange Programme and the Aerospace Applications Studies Programme. The results of AGARD work are reported to the member nations and the NATO Authorities through the AGARD series of publications of which this is one.

Participation in AGARD activities is by invitation only and is normally limited to citizens of the NATO nations.

The content of this publication has been reproduced directly from material supplied by AGARD or the authors.

Accession For	
NTIS GRA&I	<input checked="checked" type="checkbox"/>
DTIC TAB	<input type="checkbox"/>
Unannounced	<input type="checkbox"/>
Justification	
By _____	
Distribution/	
Availability	
Dist _____	

A

Published November 1980

Copyright © AGARD 1980

All Rights Reserved

ISBN 92-835-0271-X



Printed by Technical Editing and Reproduction Ltd
Harford House, 7-9 Charlotte St, London, W1P 1HD

PROPULSION AND ENERGETICS PANEL

CHAIRMAN: Dr J.Dunham
National Gas Turbine
Establishment
Pyestock
Farnborough
Hants GU14 OLS
UK

DEPUTY CHAIRMAN: Professor E.E.Covert
Dept. of Aeronautics and
Astronautics
Massachusetts Institute of
Technology
Cambridge, Mass 02139
USA

PROGRAM COMMITTEE

M.J.Fabri (Chairman)
ONERA
29 Avenue de la Division Leclerc
92320 Châtillon
France

Dr J.Dunham
National Gas Turbine Establishment
Pyestock
Farnborough, Hants GU14 OLS
UK

Mr J.Acurio
Director, Propulsion Laboratory
US Army Research and Technology
Laboratories (AVRADCOM)
21000 Brookpark Road
Cleveland, Ohio 44135
USA

M. le Professeur Ch. Hirsch
Vrije Universiteit Brussel
Dienst Stromingsmechanica
Pleinlaan 2
1050 Brussel
Belgie

Professor D.Dini
Università degli Studi
Istituto di Macchine
Via Diotisalvi 3
56100 Pisa
Italy

Dr R.B.Whyte
Fuels and Lubricants Laboratory
Division of Mechanical Engineering
National Research Council
Ottawa
Ontario K1A 0R6
Canada

Professor Dr-Ing. G.Winterfeld
DFVLR
Institut für Antriebstechnik
Postfach 90 60 58
5000 Köln 90
Germany

HOST NATION COORDINATOR

M. le Professeur Ch. Hirsch
Vrije Universiteit Brussel
Dienst Stromingsmechanica
Pleinlaan 2
1050 Brussel
Belgie

LOCAL COORDINATOR

Major D'Aviation A.Cuffez
Etat Major Force Aérienne
Quartier Reine Elisabeth
1040 Bruxelles
Belgique

PANEL EXECUTIVE

Dr-Ing. E.Riester
AGARD-NATO
7 rue Ancelle
92200 Neuilly sur Seine,
France

ACKNOWLEDGEMENT

The Propulsion and Energetics Panel wishes to express its thanks to the Belgian National Delegates to AGARD for the invitation to hold its 55th Meeting in Brussels, and for the personnel and facilities made available for this meeting.

CONTENTS

	Page
PROPULSION AND ENERGETICS PANEL	iii
TECHNICAL EVALUATION REPORT by M.J.Hartmann	vi
DISCUSSION FOLLOWING TECHNICAL EVALUATION	x
	Reference
<u>SESSION I – EXPERIMENTAL INVESTIGATIONS ON FLOW IN IMPELLERS AND DIFFUSERS</u>	
EXPERIMENTAL AND THEORETICAL INVESTIGATIONS ON THE INTERNAL FLOW IN A CENTRIFUGAL COMPRESSOR DIFFUSER by H.Krain	1
FLOW IN CENTRIFUGAL COMPRESSOR IMPELLERS – A THEORETICAL AND EXPERIMENTAL STUDY by A.Goulas	2
ANALYSE EXPERIMENTALE DE L'ECOULEMENT DANS UN ETAGE DE MACHINE CENTRIFUGE par G.Bois, A.Vouillarmet, J.M.Duchemin et K.D.Papailiou	3
INLET FLOW DISTORTIONS ON INDUSTRIAL CENTRIFUGAL COMPRESSOR STAGES. EXPERIMENTAL INVESTIGATIONS AND EVALUATION OF EFFECTS ON PERFORMANCE by E.Benvenuti, L.Bonciani and U.Corradini	4
<u>SESSION II – THEORETICAL CALCULATIONS OF FLOWS IN IMPELLERS</u>	
CALCUL DE L'ECOULEMENT TRANSSONIQUE DANS UN COMPRESSEUR CENTRIFUGE PAR UNE METHODE PSEUDO-STATIONNAIRE par R.Sovrano	5
NUMERICAL ANALYSIS OF THE THREE DIMENSIONAL VISCOUS FLOW FIELD IN A CENTRIFUGAL IMPELLER by L.Walitt	6
THREE DIMENSIONAL INVISCID CALCULATIONS IN CENTRIFUGAL COMPRESSORS by Ch.Hirsch, Ch.Lacor and G.Warzee	7
TRANSONIC FLOW CALCULATION IN CENTRIFUGAL COMPRESSORS BY A TIME DEPENDENT METHOD OF CHARACTERISTICS by C.Osnaghi, A.Perdichizzi and F.Bassi	8
THREE-DIMENSIONAL, VISCOUS FLOW CALCULATIONS FOR ASSESSING THE THERMODYNAMIC PERFORMANCE OF CENTRIFUGAL COMPRESSORS – STUDY OF THE ECKARDT COMPRESSOR by J.Moore and J.G.Moore	9
COMPUTATION OF THREE DIMENSIONAL FLOW THROUGH THE ECKARDT COMPRESSOR IMPELLER by C.Bosman	10
<u>SESSION III – INTERACTION BETWEEN IMPELLER AND DIFFUSER</u>	
COMPUTATION OF FLOW IN RADIAL- AND MIXED-FLOW CASCADES BY AN INVISCID-VISCOUS INTERACTION METHOD by G.K.Serovy and E.C.Hansen	11

Reference

ROTATING NON UNIFORM FLOW IN RADIAL COMPRESSORS
by R.A. Van den Braembussche, P.Frigne and M.Roustan 12

THE INFLUENCE OF DIFFUSER INLET PRESSURE FIELDS ON THE RANGE AND
DURABILITY OF CENTRIFUGAL COMPRESSOR STAGES
by D.Japikse 13

INFLUENCE DE L'HETEROGENEITE DE L'ECOULEMENT A LA SORTIE DU ROTOR
SUR LES PERFORMANCES DU DIFFUSEUR D'UN COMPRESSEUR CENTRIFUGE
par H.Hus et C.Fradin 14

SESSION IV – DESIGN EXPERIENCE AND PERFORMANCE OF ADVANCED CENTRIFUGAL COMPRESSORS (PART I)

DESIGN AND EXPERIMENTAL PERFORMANCE OF SOME HIGH PRESSURE RATIO
CENTRIFUGAL COMPRESSORS
by P.M.Came and M.V.Herbert 15

A PROCEDURE FOR THE COMPUTER-AIDED CONSTRUCTION OF RADIAL COMPRESSOR
IMPELLERS WITH HIGH FLOW COEFFICIENT
by W.Fister and J.Eikermann 16

ROUE DE COMPRESSEUR CENTRIFUGE SANS FLEXION DANS LES AILES
par J.Poulain et G.Janssens 17

Paper 18 is cancelled

IMPROVEMENTS IN SURGE MARGIN FOR CENTRIFUGAL COMPRESSORS
by W.Jansen, A.F.Carter and M.C.Swarden 19

SESSION V – DESIGN EXPERIENCE AND PERFORMANCE OF ADVANCED CENTRIFUGAL COMPRESSORS (PART II)

MODEL 250-C30/C28B COMPRESSOR DEVELOPMENT
by D.C.Chapman 20

CENTRIFUGAL COMPRESSORS FOR SMALL AERO AND AUTOMOTIVE GAS TURBINE
ENGINES
by R.W.Chevis and R.J.Varley 21

EFFICIENCY OF CENTRIFUGAL COMPRESSOR IMPELLERS
by C.Rodgers 22

TECHNICAL EVALUATION REPORT

by

M.J.Hartmann
NASA
Lewis Research Center
Cleveland, Ohio, USA

1. INTRODUCTION

The 55th (B) Meeting of the Propulsion and Energetics Panel Specialists on Centrifugal Compressors, Flow Phenomena and Performance was convened at the Bibliotheque Royal (Albertim Royal Library), Mont des Arts in Brussels, Belgium on May 7-9, 1980. The purpose of the meeting was to provide to both the research scientist and the development engineer new knowledge gained by theoretical flow field calculations and by new experimental investigations. The following sessions include 21 papers and the related discussions:

- I Experimental Investigation of Flow in Impellers
- II Theoretical Calculations of Flow in Impellers
- III Interaction Between Impeller and Diffuser
- IV Design Experience and Performance of Advanced Centrifugal Compressors (Part I)
- V Design Experience and Performance of Advanced Centrifugal Compressors (Part II)

2. SUMMARY AND COMMENTARY

The meeting was arranged with the general theme and perhaps the expectation that advanced flow calculation procedures and advanced flow measuring systems which have evolved over the past several years may be used to provide centrifugal compressors with substantial performance improvements. The expected improvements to be achieved by providing designers and developers of centrifugal compressors with the ability to extend stable operating range. The meeting theme addresses the need for exchanging information between the analysts developing new analytical flow calculational methods and experimental engineers presently engaged in advancing technology through contemporary methods. In addition, considerable information was brought forth on the present design and development methods and the high levels of performance being achieved in centrifugal compressors. The meeting provided an excellent information exchange through the paper presentations and the related discussion periods. The papers were generally of very high quality and the meeting arrangements were excellent.

Rapid advances are being made in the area of flow analysis in centrifugal compressors. Several numerical analysis methods have been developed, programmed and some computations have been made, generally by the authors of the methods. The laser based and other methods of obtaining detail flow distributions with minimal or without intruding into the flow stream have been applied to compressors of moderate speed and pressure ratio. The authors of the numerical methods are attempting to validate the calculated flow and determine the necessary complexities and the input and boundary conditions required to properly model the observed flow in these machines. Partial agreement between calculation and experiment has been achieved. It is also noted that differences between the various theoretical analysis methods have not been totally resolved. Considerable experience and research are necessary to establish the level of confidence in the numerical methods to establish them as the basis for the design of high pressure centrifugal compressors.

Present design and development methods are being utilized to continue the advancement of centrifugal compressor technology. High levels of performance, and broad stable operating flow range, and other requirements have been achieved through extensive development efforts. In some cases, novel concepts have been evolved to provide desired improvements.

There is no doubt that these analytical methods will be utilized and are necessary to support the advancement of high pressure centrifugal compressors. The exact manner in which this support will evolve cannot be determined at this time. However, a strong dependence on contemporary design and development methods will be required for the foreseeable future.

3. RECOMMENDATIONS

The advancement of centrifugal compressor technology will be strongly dependent on continued research and the discrimination of information in a number of key areas. The key areas identified as a result of the subject meeting and recommended for additional consideration during the next five years are the following:

- Instrumentation and measurement systems that provide detail flow information in high pressure ratio centrifugal compressors (6:1 or greater).
- The use of numerical methods in the flow analysis and design of centrifugal compressors of moderate pressure ratio.
- Analytical and experimental studies of the structural design and aerodynamic-structural interaction in high speed centrifugal compressors.
- Flow phenomena and performance of high pressure ratio centrifugal compressors (6:1 or greater).

4. DISCUSSION

The general outline of the meeting provided first a discussion of the detail flow experimentally observed in centrifugal compressors. Secondly, the status and some new developments in theoretical flow computations in impellers was presented. The third session was primarily devoted to diffuser flows and diffuser impeller interactions. Finally, the last two sessions dealt with contemporary performance and the design/analysis/development approaches utilized to advance performance levels. The comprehensive review and information exchange afforded by the five sessions will be discussed in the following paragraphs.

Session I – Experimental Flows in Impellers and Diffusers

The four papers in this session dealt with the complex flow conditions which must be considered in a meaningful theoretical analysis of centrifugal compressor flows. Particular difficulty exists at the exit of the impeller and the entrance to the diffuser where the flow is highly spacially distorted and subject to severe unsteady conditions. Diffuser performance, however, is remarkably high at part speeds and in compressors designed for modest pressure ratios. These poor flow conditions do result in high losses and limit stable operating range of high pressure, high speed compressors. In analyzing the flow in centrifugal compressor components, both experimental and theoretical researchers have observed a variety of flow distributions. The reason for these differences may result in part because the analytical methods are still being developed; each method has unique capability and is subject to the interpretation of the researchers. It may also be that substantially different flow distributions do occur in centrifugal compressors. This probably should be expected in compressors since a number of interacting flow phenomena occur simultaneously. The observed flow configuration then is dependent on the particular phenomena controlling or dominating the flow process for the particular design or operating condition under study. Thus, in some cases what appear to be small design changes can result in considerable change in the detail flow configuration. Somewhat different secondary flows have been observed in impellers utilizing a front cover as compared to one that has no front cover. The fourth paper very neatly points out that in multistage centrifugal units the vaned duct returning the flow to the following impeller inlet contains a substantial velocity distortion. These velocity distortions like other flow defects in moderate pressure ratio machines can be empirically accounted for in the design in such a manner as to minimize the performance defect. To be successful and useful, advanced theoretical flow analysis methods must observe and suitably account for a wide variety of real flow phenomena shown to exist in moderate pressure ratio centrifugal compressors.

Session II – Theoretical Calculations of Flows in Impellers

The five presentations in this session indicated several advanced analytical methods that are in various stages of development. It is also known that numerous other theoretical methods employing analytical and numerical methods are under study. The streamline curvature, two-dimensional and quasi-three-dimensional methods have been continuously improved for many years. Analysts have included larger numbers of stations both radially and circumferentially. Some accounting for secondary flow effects and three-dimensional boundary layers have been included. Substantial improvement in computational time have been achieved through the applications of large computers and improved computation methods. Substantial progress has also been achieved in the adoption of numerical methods which can provide complete three-dimensional viscous flow simulation to the analysis of centrifugal compressors. The methods that provide solutions for the complete Navier-Stokes equations have generally been characterized as requiring excessive computational time. The advanced scientific computers and improved coding may reduce this substantially but the extent of the computational time reduction must still be determined. Improved algorithms providing for the modeling of three-dimensional inviscid and viscous flows in impellers that result in relatively short computational time are in various stages of development. Some of these methods are being examined by the authors and compared to available experimentally determined flows. Besides investigating the numerical performance of these codes, the authors are investigating such factors as the effect of inlet vorticity, inlet boundary layer, and impeller clearances to determine the impact these factors have on the general flow configuration. Whereas some general agreement between calculations and experiment has been achieved, notable exceptions in flow configuration and particularly in magnitude are also noted. Comparison between theoretical methods is presently not well in hand. Because the theoretical analysis methods are in various stages of development, it

is difficult at this time to draw overall conclusions concerning the relative merits of the methods, the degree of complexity necessary to suitably model the flow, or the manner in which these methods can best be applied. Substantial research of the theoretical flow analysis methods is still required to fully describe the flow at the near design (high efficiency) operation and even more effort will be required to extend the analysis to the off design and to the advanced levels of performance now expected of centrifugal compressors.

Session III – Interaction Between Impellers and Diffusers

Flow conditions in the diffuser component and the interaction of the diffuser flow with the impeller are not well understood. Advanced analytical methods apparently have not yet been devised that adequately describe the adverse, time unsteady, flow conditions in the diffuser. Available analytical studies do indicate that the geometries and flow conditions in the region of the diffuser are very sensitive to small changes in effective flow areas. Thus, what are generally thought to be small boundary layer or blockage effects can result in substantial changes in velocity gradients. Generally, empirical data and experimental development studies are coupled with the design process to achieve the best performance of inducer impeller combinations.

Shock and unsteady flows result in detrimental interactions between the diffuser and impeller flows particularly when high flow velocities occur at the entrance to the diffuser vanes. Poor flow and/or structural damage have been observed. Detail flow measurements in the region of the diffuser indicate that rotating nonuniformities (rotating stall) may be observed at certain operating conditions. The last paper in this session provides an interesting experimental approach to determine the diffuser performance defects associated with the unsteady and the steady diffusion. Continuation of this or related developments could lead to a more rational and less empirical design method for diffusers. The discussion presented in this session indicated that the diffuser performance and the interaction of the diffuser and impeller flows are probably the least understood and most difficult problem associated with the centrifugal compressor.

Sessions IV and V – Design Experience and Performance of Advanced Centrifugal Compressor (Part I and Part II)

The presentations of these two sessions delineated a number of very important points in considering the methods to continue advancing centrifugal compressor technology. Present analytical/empirical design methods have been computerized so that centrifugal compressors can be optimized for a given application. These overall flow design/analysis systems have been developed in a consistent manner and are backed by an extensive experimental base. These optimization approaches generally include directly or indirectly stress and aerostructural computations and evaluations. In some cases, impeller blading is adapted to particular computer controlled or automatic machining processes as well as providing an optimum performance potential indicated by the data base. Extensive background also exists to "trim" or optimize the design through an experimental development program. These experimental development programs have in some cases been long and costly but they generally have resulted in centrifugal compressors of very high levels of performance. In the course of developing advanced compressors, "novel" concepts have often been utilized. These concepts include various approaches and are the "stock and trade" of the development engineer. The extent that a design system can be "stretched" with dependence on these novel concepts must be based on experience with the particular design system. How these or similar concepts can be exploited in the analytical/design process is not yet known.

Flow conditions that control the surge line of a high performance compressor continue to be relatively unknown. It should be noted that compressor flow components contribute to surge through energy addition and/or loss, and their dynamic stability characteristics such as rotating stall. These flow components determine the compressor dynamic performance characteristics, which along with those of the system, determine the likelihood of surge. Thus, a discussion of surge is not meaningful when considered only from the standpoint of compressor design. It has also been observed (and should come as no surprise) that compressors operating in different systems exhibit changes in the surge lines. The compressor technologist should be concerned primarily with the energy addition and/or loss characteristics and the stalling characteristics of the flow components of the compressor. These are the areas he has available to extend the capability of the compressor to operate surge free. No suitable analytical method yet exists for dynamically matching of the flow components of a centrifugal compressor. Until this is achieved, it must remain the task of the empiricist (by correlations or experimental) to extend and predict by whatever available means the performance characteristics and in particular, the stalling characteristics (and thus the surge margin) of advanced centrifugal compressors.

5. CONCLUSIONS

The 55th (B) Meeting of the Propulsion and Energetics Specialists on Centrifugal Compressors, Flow Phenomena and Performance provided a good interchange of information between analytical and experimental researchers. Contemporary as well as advanced design/analysis/development methods were discussed and a reasonable indication of the level of technology achieved in centrifugal compressors was displayed. The meeting provided an opportunity to consider the evolutionary nature of centrifugal compressor technology and specifically pointed out the following:

- Substantial progress has been made in the development of several new flow analysis methods. It is quite probable that over the next several years the authors of these methods will have demonstrated the capability of calculating the flow field characteristics which have presently been measured in centrifugal compressor impellers of moderate pressure ratio. These flow analysis methods can be an effective and necessary design/analysis tool in improving

performance and delaying flow conditions leading to stall of moderate pressure ratio compressors in the near future. Detail flow measurements in a broad range of centrifugal compressor impellers will be necessary to verify and develop a high degree of confidence in the flow analysis methods.

The application of the advanced flow analysis methods to design very high pressure ratio centrifugal compressors (6:1 or greater) will require considerable research. It is necessary to examine a number of analysis methods to determine the type of analysis required to predict the more extreme flow conditions. It is quite possible that several analytical methods will be necessary over the range of flow conditions usually encountered. The research will require a substantial number of detail flow measurements in centrifugal compressors. It will be necessary to extend the instrumentation and measurement systems to be capable of obtaining the detail flow data in high pressure ratio compressors.

It is not evident that present numerical analytical methods being evolved will totally model the severe flow conditions encountered in the diffuser element of centrifugal compressors. It is desirable to reduce the diffuser flow Mach number through increased impeller backsweep. This requires higher rotational speeds to achieve a given pressure ratio, and structural difficulties may result. The unsteady flow interactions between the diffuser and impeller increase these difficulties. The unsteady aerodynamic forces have been observed to excite a wide range of structured modes resulting in impeller or diffuser cracking and failure.

The advanced flow analysis methods will not in the foreseeable future replace the experimental development approaches presently employed to achieve advanced levels of performance in centrifugal compressors. The analysis methods will be used in conjunction with advanced experimental development methods. The exact manner in which the flow analysis will be utilized cannot be predicted at the present time. The levels of performance and technology achieved will depend even more, than with present methods, on the skill and ability of the researchers to interpret the available analytical and experimental information.

DISCUSSION FOLLOWING TECHNICAL EVALUATION

by

M.J.Hartmann

Opening the discussion Mr Jansen (NREC) asked whether the suggestions and recommendations that had been generated by the meeting would be followed up by AGARD. He particularly wanted to know whether AGARD was able to provide any financial assistance in order to ensure that the more important recommendations for further research were properly followed up. Dr Dunham (Chairman of the Propulsion Panel) explained that AGARD is an organisation which has no funds of its own for sponsoring research; funds are provided in order to organise conferences and for certain consultative missions. The technical recommendations of AGARD meetings are really addressed to managers of research in commercial or university research organisations. It is really for them to take the initiative and to follow up the recommendations. Dr Dunham hoped, however, that the existence of a recommendation from an AGARD Panel may be sufficient to convince those who control the funding in research organisations which topics are worthwhile and that research support would bring benefits. Dr Dunham then went on to say that he had noted from the discussions and from the papers presented at the conference that many flow field calculations had been described, covering a great range of complexity. He enquired as to whether there was any consensus as to how complicated a method is required to represent the viscous and other important effects in a centrifugal impeller. Is it necessary, he asked, to make a big advance in order to improve one's modelling of the flow?

Mr Hartman replied that, as he saw it, the situation in the centrifugal compressor is very analogous to the situation in the axial compressor. For machines of reasonably easy duties then the simpler methods are sufficient to give the designer a knowledge of the flow within the machine but for compressors which are attempting duties of an advanced nature, or for compressors for which speeds and Mach numbers are high, then it is necessary to employ a more complicated flow model, probably including viscous effects.

Dr Japikse said that, in his view, history had shown that good turbomachines had been designed with comparatively simple analytical tools, but he wondered how long this pattern is likely to continue. He said that the analytical worker should keep the design objectives in mind and that dialogues are required between the analytical researchers and the compressor designer so that the more advanced analytical tools can become effective. This dialogue had been absent from the present conference. Mr Hartmann agreed. There seemed to be a missing link due to the fact that analysts who are presently working on advanced methods would in future go on to work on other advanced methods rather than assist the designer in benefitting from the advancements. The kind of man that is missing, he said, is a designer with an analytical viewpoint.

Prof. E.Covert (MIT) said that he could see that there was a difference between design and analysis problems. The designer has to solve the inverse problem, that is to say he would like to specify the performance of a compressor or a blade and have the analytical tool to design the shape for his required duty. Most of the analytical methods that had been described in the conference could not be reversed in the way that the designer would prefer.

Dr Cumpsty (Cambridge University) said that, as far as he could see, calculation methods, no matter how sophisticated, have no use unless they are properly verified against good experimental results so what are needed badly are good definitive test results. The results of Eckardt, however, are the only examples of well-categorised comprehensive measurements in a centrifugal impeller. This seemed to be, said Dr Cumpsty, an indictment of the research programmes that we are pursuing. In order to make a correct assessment of analytical methods each one should be examined with reference to the same set of experimental results. In mentioning the overall results for compressor stages presented at the conference, Dr Cumpsty continued by saying that there was a need to provide measurements and complete geometry for the whole compression system before one could make definitive statements, particularly about range and surge margin. He therefore asked that investigators should provide all the necessary information when reporting overall compressor rig measurements.

Professor Serovy (Iowa State University) very much agreed with Dr Cumpsty. He said that Working Group 12 of the PEP had recently been examining the subject of throughflow in turbomachinery but so far they had managed to ignore the problem of centrifugal compressors, in spite of making reasonably good progress in axial compressors. In the light of the progress of Working Group 12, Professor Serovy confirmed that what are needed are good test data obtained from carefully defined geometry.

Dr Eckardt (MTU, Munich) stated that his compressor test results which have been so widely used by other investigators have only recently been made fully available by the German industrial concerns who funded the experiments.

However, in the recent ASME Conference (New Orleans, 1980) further details of the geometry of the radially-bladed impeller had been released and also laser anemometer measurements on a swept-back impeller had been described. Dr Eckardt stated that any researcher who required further details of either the measurements or the geometry of both of these impellers could contact him and there would be no difficulty in providing full information on these machines. He supplemented this by saying that much of the aerodynamic data which had been gathered had not been reported even in summary form and there was very much more data available than had been mentioned in the literature.

Dr Japikse added to this the information that the Creare centrifugal compressor of pressure ratio 8 had also been extensively tested and that full information on the measurements and geometry were available on application to Creare. He added that measurements did not, of course, include detailed information about the flow within the impeller as in the case of the Eckardt compressor.

Mr Langdon (Holset Engineering) said that others were following Eckardt's lead; Holset, in collaboration with Cranfield Institute of Technology, have been conducting a programme of laser anemometry measurements in a centrifugal impeller for 2 years. Unfortunately it was not possible to produce the information obtained which was considered to be of a proprietary nature.

Dr Moore (Virginia Polytechnic Institute) said that, as early as 1861, a pump of 68 per cent efficiency had been constructed and that, in his opinion, the progress made since then had been great. We are now struggling to obtain the last remaining available deficits in efficiency. He hoped, however, that 3-dimensional viscous methods will be able to assist the designer in improving efficiency by small amounts and that these methods would be indeed used by compressor designers. He pointed out that his method and the method of Dodge in the USA are already being used by turbine designers for the design of turbine nozzle vanes with some success. In this context he emphasised the importance of 3-dimensional flow, particularly the effect of secondary flow. Dr Moore said that 2-dimensional or quasi 3-dimensional blade-to-blade methods such as that recently developed by Serovy and Hansen which include some viscous effects are extremely useful but only in a limited range of near 2-dimensional situations. Three-dimensional methods will bring important light to bear on many turbomachinery flow situations.

EXPERIMENTAL AND THEORETICAL INVESTIGATIONS ON THE INTERNAL FLOW IN A CENTRIFUGAL COMPRESSOR DIFFUSER

by

H. Krain

DFVLR-Institut für Antriebstechnik
Linder Höhe, 5 Köln 90, W. Germany

SUMMARY

Based on empirical flat diffuser performance maps a two-dimensional straight diffuser has been designed and tested. First experimental results concerning overall diffuser recovery, diffuser inlet conditions and diffuser performance development are presented. A two-dimensional finite difference blade-to-blade calculation method has been developed taking into account diffuser losses and sidewall blockage.

NOMENCLATURE

A	area
AR	diffuser area ratio
AS	diffuser aspect ratio
B	boundary layer blockage $B = 1 - A_{\text{eff}}/A_{\text{geo}}$
b	meridional diffuser height (Fig.3)
c	absolute velocity
c_p	diffuser recovery coefficient $c_p = (p - p_{\text{ref}})/(p_{\text{tref}} - p_{\text{ref}})$
HU	hub
h	diffuser width (Fig.3)
h_t	total enthalpy
l/h	diffuser length/width ratio (Fig.3)
M	Mach number
\dot{m}	mass flow rate
n	shaft speed
\vec{n}	unit streamsurface normal vector
PS	pressure side
p	static pressure
p_t	total pressure
R	gas constant
r	radial coordinate
rpm	rotations/minute
SH	shroud
SS	suction side
s	entropy
T	temperature
x	cartesian coordinate
y	cartesian coordinate
y/t	relative blade spacing
z/b	relative diffuser height (Fig.3)
z_d	diffuser blade number
z_R	impeller blade number
α	absolute flow angle (Fig.17)
$\Delta\alpha_{31}$	diffuser incidence
δ_1	displacement thickness
2ϵ	diffuser passage divergence angle
η	efficiency
κ	specific heat ratio
Π_t	total pressure ratio
ρ	density

ψ stream function

SUBSCRIPTS

0	compressor inlet
1	inducer leading edge
2	impeller tip
2*	jet/wake mixing out
3	vaned diffuser inlet
4	vaned diffuser discharge
c	absolute
D	diffuser
eff	effective
geo	geometrical
max	maximum
red	corrected to standard conditions
rel	relative
s	isentropic
s-t	total/static (efficiency)
th	throat
t-t	total/total (efficiency)

INTRODUCTION

Small gas turbines utilizing centrifugal compressor stages are predominantly used as helicopter engines and are increasingly tested for vehicular applications. Especially in regenerative gas turbines compressor efficiency influences specific fuel consumption considerably [1, 2, 3]. Requirements for small and efficient engines necessitate high pressure ratio centrifugal compressors with relatively high stage efficiencies. Today's total to static isentropic peak efficiencies of centrifugal compressor stages are about 84 %. This level is generally only reached by centrifugal compressors equipped with vaned diffusers, since vaned diffusers typically have higher recovery compared with vaneless diffusers.

Although diffusers are much less restricted by mechanical limitations than impellers, they are very often the critical flow elements which govern both surge and efficiency of centrifugal compressor stages. Their difficult fluid dynamic task is the conversion of kinetic energy into static pressure. At the design point impeller discharge Mach numbers range from 0.9 to 1.2. Consequently transonic flows connected with shocks - which may extend into the impeller - occur. Due to the highly distorted impeller discharge conditions (Jet/Wake) the flow is significantly unsteady in both the absolute and relative frame [4]. On the other hand it has to be expected that diffuser vanes will affect the three-dimensional unsteady flow within centrifugal compressor impellers. In order to contribute to the enlightenment of this complex flow situation, a flat straight-channel diffuser has been designed and employed at the DFVLR centrifugal compressor test rig. This paper deals with the design procedure and the experimental and theoretical results gained during the first period of this research program.

DIFFUSER DESIGN PROCEDURE

Precise diffuser recovery prediction is a still unsolved task in centrifugal compressor fluid dynamics. Inviscid, steady flow theories connected with boundary layer calculations may reveal an impression of diffuser performance development but in most cases fail quantitatively in the impeller exit/diffuser entry region, since usually they do not take care of the highly distorted impeller discharge flow [6]. Therefore the designer of centrifugal compressor diffusers generally is forced to refer to empirical data available in the open literature. Most extensive experimental data concerning flat diffuser performance has been published by Runstadler, Dolan and Dean [5]. Fig. 1, which has been reproduced from Runstadler's Diffuser Data Book, shows typical flat diffuser performance maps. Diffuser recovery c_p , dependent on geometry and boundary layer blockage B, is plotted. Runstadler's experiments revealed that besides the geometrical parameters boundary layer blockage has a strong influence on diffuser recovery (Fig. 2). Maximum recovery is obviously obtained for aspect ratios $AS \approx 1$, divergence angles $7^\circ < 2\alpha \leq 10^\circ$ and length/width ratios about $16 \leq l/h_3 \leq 20$. It is this material which generally is the basis of today's diffuser design methods, although it is well known that the transmission of these data to real machine applications is affected with several uncertainties. This is predominantly due to our limited knowledge about

- boundary layer development from impeller discharge to diffuser throat,
- shock wave boundary layer interactions in case of supersonic impeller discharge Mach numbers,

- impeller/diffuser interactions especially in the transonic flow case.

Despite these uncertainties the diffuser data presented by Runstadler, Dolan and Dean are today's most effective design tool for flat centrifugal compressor diffusers.

Runstadler's performance maps are presented for diffuser aspect ratios of $AS = 0.25$, 1.0 and 5.0 (Fig.1). Unfortunately, due to imposed geometrical constraints, the designer is often forced to deviate considerably from the available diffuser performance maps. If an appropriate diffuser has to be designed for an existing impeller, diffuser entrance/impeller exit radius ratio r_3/r_2 , the meridional diffuser depth b_3 and the absolute flow angle α_3 at diffuser leading edge are largely fixed (Fig.3). Since maximum diffuser recovery is always desirable the designer will be intended to select a diffuser with aspect ratio $AS = 1$. Especially for high specific speed centrifugal compressors this procedure may reveal inconvenient overall compressor dimensions. Fig.4 shows such an example for a 4 : 1 radial discharge compressor. Maximum admitted diffuser exit/impeller discharge radius ratio is $r_4/r_2 = 2$. For $AS = 1$ and maximum diffuser recovery the resulting radius ratio r_4/r_2 is about 3.0 and exceeds the permissible radius ratio of $(r_4/r_2)_{max} \approx 2$ considerably. In order to realize the geometrical conditions two possibilities may be taken into account

1. passing over to a diffuser design with $AS > 1$, which according to Fig.2 - especially for $B > 0.08$ - results in a significant recovery deficiency,
2. deviation from optimum length/width ratio l/h_3 , which - depending on the degree of deviation - also results in a recovery deficiency. Fig.5 indicates the chosen deviation from optimum l/h_3 , which delivered the dotted line of Fig.4.

Sometimes both procedures have to be performed simultaneously since otherwise the corresponding blade number becomes too large (see Fig.4). In these cases an interpolation between the plotted diffuser maps has to be carried out, not knowing, whether such an interpolation - as indicated in Fig.2 - is tolerable. Fig.6 shows the estimated compressor and diffuser performance for both the maximum recovery and small dimension design. Because the admitted deviation from maximum recovery has been small, performance deficiency seems to be acceptable. Nevertheless, significant reduction of overall compressor dimensions is to be recognized (Fig.4).

Table I displays the final diffuser geometry obtained by the indicated empirical approach.

TABLE I

diffuser parameter	description
$r_3/r_2 = 1.1$	radius ratio diffuser leading edge/impeller discharge
$r_4/r_2 = 1.905$	radius ratio diffuser discharge/impeller discharge
$AS = 1.6$	throat aspect ratio
$l/h_{3th} = 11.46$	length/width ratio of channel diffuser
$2\epsilon = 7.54^\circ$	divergence angle
$z_d = 27$	diffuser blade number

THEORETICAL APPROACH

The empirical design procedure previously described permits the selection of a geometrically appropriate diffuser and an estimation of the diffuser recovery to be expected. However, it yields no information about the flow field development ahead of and within the diffuser passages, which would be of prime interest, especially if the designer has to deviate from the published diffuser performance maps. Unfortunately, no convenient flow theory - taking care of the previously mentioned flow phenomena - is available. Most existing theories are based on a steady, inviscid approach - although sometimes they take into account entropy gradients [8] - but mostly don't take into consideration such significant effects as boundary layer growth and secondary flows [7 - 13]. Present advanced analysis is mainly based on Wu's fundamental work [14], who splitted the steady, adiabatic, inviscid three-dimensional flow equations into two sets of equations. The introduction of prescribed S_1 and S_2 stream surfaces permits to deal with the actually three-dimensional problem in a mathematically two-dimensional manner. Although it is well known that this concept, applied to centrifugal compressor diffuser flow, might fail quantitatively, it nevertheless may yield valuable insight into the flow development to be expected ahead of and within the diffuser blade passages. Preliminary information concerning blade loading and flow deceleration for an empirically selected high-performance centrifugal compressor diffuser may be extracted.

A blade-to-blade calculation - based on Wu's streamsurface method - has been developed. For a flat, straight channel diffuser the corresponding S_1 stream surface is plane. A steady, adiabatic flow and a gas of constant specific heats have been assumed. The principal equations for these assumptions are:

Continuity:

$$\nabla \cdot (\rho \vec{c}) = 0 \quad (1)$$

Motion:

$$-\vec{c} \cdot (\nabla \times \vec{c}) = -\nabla h_t + T \nabla s \quad (2)$$

Energy:

$$\nabla h_t = 0 \quad (3)$$

State of gas:

$$\rho/\rho_0 = (T/T_0)^{\frac{1}{\kappa-1}} \cdot e^{-\frac{s-s_0}{R}} \quad (4)$$

Geometric condition:

$$\vec{n} \cdot \vec{c} = 0 \quad (5)$$

If a streamfunction ψ is introduced into equations (1 - 5) a governing second order, elliptic partial differential equation is obtained, restricting the calculation method to subsonic flows:

Streamfunction:

$$\frac{\partial \psi}{\partial x} = -B \rho c_y \quad (6)$$

$$B = \frac{b - \delta_1}{b}$$

$$\frac{\partial \psi}{\partial y} = B \rho c_x \quad (7)$$

Fundamental equation (cartesian coordinates):

$$\frac{\partial^2 \psi}{\partial y^2} + \frac{\partial^2 \psi}{\partial x^2} = \frac{\partial \ln \rho B}{\partial y} \frac{\partial \psi}{\partial y} + \frac{\partial \ln \rho B}{\partial x} \frac{\partial \psi}{\partial x} - (B \rho)^2 T \frac{\partial s}{\partial y} / \frac{\partial \psi}{\partial y} \quad (8)$$

These basic equations are solved by using a finite difference scheme described in detail in references [7, 12]. Due to equation (3) a constant flow property distribution at impeller discharge has been postulated, an assumption certainly doubtful for a station before jet/wake mixing out [4]. Along the suction and pressure side of the blades the stream function has been taken constant. For simplicity the flow boundaries in the vaneless diffuser part have been assumed as logarithmic spirals (constant swirl).

Fig.8 illustrates a typical result of the approach described. Isobarics are plotted for the impeller exit/diffuser entry region. A strong pressure gradient connected with an abrupt raise of the isobarics is observed upstream of the diffuser throat, whereas a nearly one-dimensional flow occurs downstream of the throat. This predicted flow pattern agrees qualitatively with measurements [1, 15, 16, 17] and indicates a significant pressure rise in the prediffuser region, which has to be overcome by the hub and shroud side-wall boundary layers, resulting in a considerable throat blockage, which - according to Runstadler's diffuser data - is a dominating variable governing channel diffuser recovery (Fig.2).

Throat blockage prediction is mostly based on an empirical approach which necessitates knowledge about the pressure rise from impeller discharge to diffuser throat. Fig.9 shows such a correlation suggested by Dean [1]. Utilization of these data requires a flow field prediction in the impeller discharge/diffuser entry region unless compiled empirical data, derived from previous experiments, are available.

TEST RIG AND INSTRUMENTATION

A detailed description of the DFVLR centrifugal compressor test rig is given in references [4, 19]. The rig has been equipped with a radial discharge impeller of 400 mm outer diameter and the flat straight channel diffuser of Fig.7.

The first experimental investigations have been mainly concerned with diffuser flow analysis in the impeller exit/diffuser entrance region. Consequently most measurement systems have been located in this area. Fig.10 shows the corresponding measurement system arrangement from impeller discharge to diffuser exit. In reality - due to space limitations - the static pressure taps as well as the combined time averaging total pressure/flow angle probes had to be distributed circumferentially assuming periodic flow in this region. However, the distribution has been carried out in such a way that the pressure taps and probes kept their relative position to the diffuser blades as indicated in Fig.10. 6 combined total pressure/flow angle probes, spacing one diffuser pitch, have

been employed at a radius ratio $r/r_2 = 1.075$. Measurements have been performed at 9 equidistant axial positions. A similar arrangement has been employed at a radius ratio $r/r_2 = 1.975$ situated near diffuser exit/collector entrance. Total temperature measurements have been performed at the compressor inlet and exit plenum. Mass flow has been measured by means of a venturi nozzle situated within the inlet pipe. Fig.11 and 12 show the test rig equipped with the described measurement systems. The compressor is driven by a Ward-Leonard regulation of 1 500 KW maximum power input.

RESULTS AND DISCUSSION

Fig.13 displays the measured compressor performance map up to 18 000 rpm. Maximum achieved total to static isentropic efficiency at measurement plane 4 ($r/r_2 = 1.975$) is 83 %. Flow range at 18 000 rpm is about 17 %. Nearly constant maximum overall compressor efficiency occurs up to 16 000 rpm, whereas at 18 000 rpm a remarkable efficiency-drop is to be observed, which seems to be due to Mach number influences. Fig.14 reveals the mean Mach number level at inducer tip, diffuser entrance ($r/r_2 = 1.075$) and exit ($r/r_2 = 1.975$). The approach Mach numbers for the impeller and diffuser are approximately equal and vary - dependent on rotational speed - between $0.6 \leq M \leq 0.9$, whereas the Mach number distribution at diffuser exit is mostly independent of compressor speed and varies between $0.15 \leq M_{c4} \leq 0.3$. The Mach number levels at inducer tip and diffuser entrance for 18 000 rpm indicate that Mach number effects caused the mentioned efficiency drop at this rotational speed. Fig.15 illustrates the measured overall diffuser recovery c_{pD34} . Maximum recovery is obtained for all speed lines near rotating stall, whereas diffuser recovery drops rapidly for constant impeller speed and increasing mass flow, resulting in a considerable overall stage pressure-drop indicated in Fig.13. Maximum achieved recovery is largely independent of entrance Mach number corresponding with Rundstadler's flat diffuser performance measurements. Therefore the observed stage efficiency-drop at 18 000 rpm is obviously caused by the impeller and not by the diffuser.

Diffuser inlet conditions for $n = 14\ 000$ rpm and $\dot{m} = 5.3$ kg/s are displayed in Fig.16 - Fig.19. Fig.16 shows the measured total pressure distribution 5 mm ahead of a diffuser channel. The total pressure is smooth circumferentially and raises gradually from shroud to hub. The corresponding absolute flow angle and radial velocity distribution are illustrated in Fig.17 and 18, which reveal a much more disturbed pattern in both the circumferential and axial direction. A mass flow concentration is to be observed in the hub region, indicating that jet/wake mixing out has not yet finished up to this measurement area. The circumferential flow angle distribution is obviously a result of the diffuser blades which react upstream causing impeller/diffuser interaction. For 5 axial cross sections Fig.19 shows the absolute velocity direction in reference to the diffuser blades near diffuser leading edge. In the shroud region the flow is directed towards the pressure side and near the hub towards the suction side of the diffuser blades, resulting in a considerable incidence distribution across the relatively small diffuser height. Despite these non-uniform inlet conditions the diffuser reveals a good overall recovery (see Fig.15), which seems to be due to enhanced high-intensity mixing at diffuser inlet, which is known to increase diffuser recovery considerably [20].

A comparison between the measured and calculated static pressure development along the diffuser blades and along the diffuser passage mean centerline is presented in Fig.20. The calculation has been performed assuming a constant polytropic efficiency and constant mean boundary conditions at impeller discharge ($r/r_2 = 1$), which have been derived from measurements. Good coincidence is obtained in the passage diffuser region ($r/r_2 > 1.15$), whereas - due to the theoretically assumed two-dimensional, steady, inviscid blade-to-blade flow - expected deviations between measurement and calculation occur in the vaneless and prediffuser region ($r/r_2 < 1.15$).

Fig.21 is a photography of the shroud wall after compressor dismantling. Pronounced separated flow patterns - caused by air pollution - are to be observed at the blade suction sides in the vaned diffuser exit area and behind the blade trailing edges.

CONCLUSIONS

The investigations described in this paper revealed a highly distorted flow pattern at the vaned diffuser entrance. A comparison with calculated data proves that the simplified steady, inviscid blade-to-blade calculation is not capable to predict the flow field in the diffuser entrance region sufficiently. More detailed experimental investigations - especially concerning the unsteady flow character at the diffuser entrance - are necessary to improve today's calculation methods continuously with respect to reliable flow field predictions in this area.

REFERENCES

- [1] Dean, R.C., Jr. "The Fluid Dynamic Design of Advanced Centrifugal Compressors. Create, TN-185, July 1974, p.76.
- [2] Köhler, M.,
Walzer, P. "Influences on the Fuel Economy of an Automotive Gas Turbine". ASME-Paper, 77-GT-92, p.8
- [3] Heilmann, W.,
Hagemeister, K. "Small Regenerative Gas Turbine Design and Development at MTU". ASME-Paper, 77-GT-103, p.19.
- [4] Eckardt, D. "Detailed Flow Investigations Within a High-Speed Centrifugal Compressor Impeller", Journal of Fluids Engineering. Trans.ASME (1976), pp.390-402.
- [5] Japikse, D. "REVIEW-Progress in Numerical Turbomachinery Analysis". Journal of Fluids Engineering, Trans.ASME (1976), pp.592-606.
- [6] Rundstadler, P.W., Jr.
Dolan, F.X.,
Dean, R.C., Jr. "Diffuser Data Book". Create, TN-186 (1975), p.88.
- [7] Krain, H.,
Eckardt, D. "The Flow Field in a High-Speed Centrifugal Impeller. A Comparison of Experimental and Theoretical Results". Proc.First International Conference on Centrifugal Compressor Technology, February 1978, B1-25, Madras.
- [8] Marsh, H. "A Digital Computer Program for the Through-Flow Fluid Mechanics in an Arbitrary Turbomachine Using a Matrix Method". Her Majesty's Stationary Office Reports and Memoranda No.3509 (1968), p.32.
- [9] Bosman, C.,
El-Shaarawi, M.A.I. "Quasi-Three-Dimensional Numerical Solution of Flow in Turbo-machines". Journal of Fluids Engineering, Trans.ASME (1977), pp.132-140.
- [10] Hirsch, Ch.,
Warzee, G. "A Finite Element Method for Through-Flow Calculations in Turbomachines". ASME-Paper, 76-FE-12.
- [11] Howard, J.H.G.,
Osborne, C. "A Centrifugal Compressor Flow Analysis Employing a Jet-Wake Passage Flow Model". Journal of Fluids Engineering, Trans.ASME (1977), pp.141-147.
- [12] Krain, H. "Contribution to the Quasi-Three-Dimensional Calculation within Centrifugal Compressor Impellers" (in German). Thesis TH Aachen (1975), p.185.
- [13] Eckardt, D.,
Krain, H. "Secondary Flow Studies in High-Speed Centrifugal Compressor Impellers". AGARD-Conference "Secondary Flows in Turbomachines". Den Haag, in AGARD CP 214 (1977), p.18/1-18/13.
- [14] Wu, C.H. "A General Theory of Three-Dimensional Flow in Subsonic and Supersonic Turbomachines of Axial, Radial and Mixed-Flow Types". NACA TN-2604 (1952), p.92.
- [15] Verdonk, G. "Vaned Diffuser Inlet Flow Conditions for a High Pressure Ratio Centrifugal Compressor". ASME-Paper, 78-GT-50, p.16.
- [16] Baghdadi, S. "A Study of Vaned Radial Diffusers using Swirling Transonic Flow Produced by a Vortex Nozzle". Thesis Purdue University (1973), p.280.
- [17] Reeves, G.B. "Estimation of Centrifugal Compressor Stability with Diffuser Loss-Range System". Symposium on Centrifugal Compressor and Pump Stability Stall and Surge, ASME (1976), pp.107-119.
- [18] Kenny, D.P. "A Comparison of the Predicted and Measured Performance of High Pressure Ratio Centrifugal Compressor Diffusers". ASME-Paper, 72-GT-54.
- [19] Eckardt, D. "Instantaneous Measurements in the Jet-Wake Discharge Flow of a Centrifugal Compressor Impeller". Journal of Engineering for Power, TRANS.ASME, Series A, Vol.97, No.3, July 1975, pp.337-346.
- [20] Waitman, B.A.,
Reneau, L.R.,
Kline, S.J. "Effects of Inlet Conditions on Performance of Two-Dimensional Subsonic Diffusers". Journal of Basic Engineering. TRANS.ASME, Ser.D. (Sept.1961), pp.349-360.

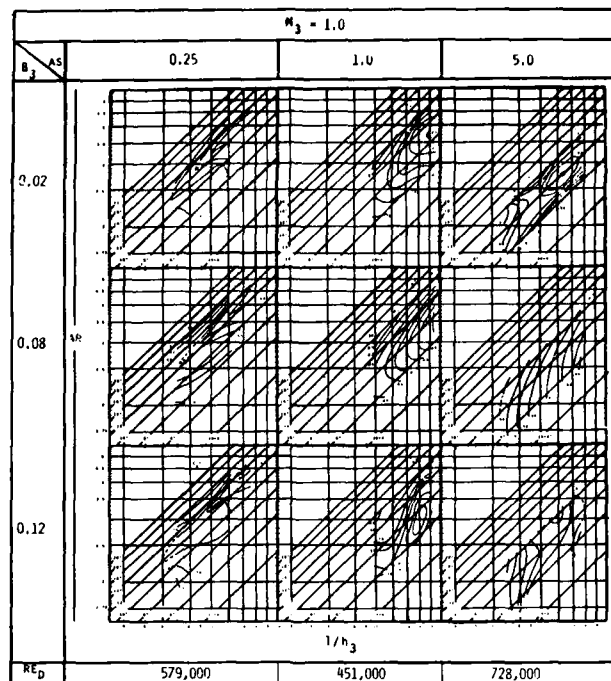


Fig.1 Straight channel two-dimensional diffuser performance maps (Runstadler, Dolan, Dean, ref.[6])

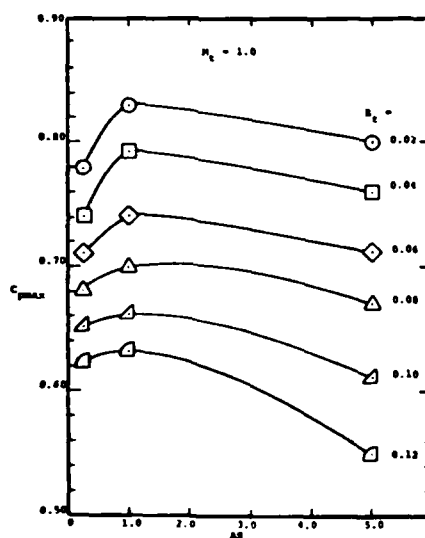


Fig.2 Maximum pressure recovery of straight channel two-dimensional diffusers, depending on aspect ratio AS and boundary layer blockage B_t (Runstadler, Dolan, Dean, ref.[6])

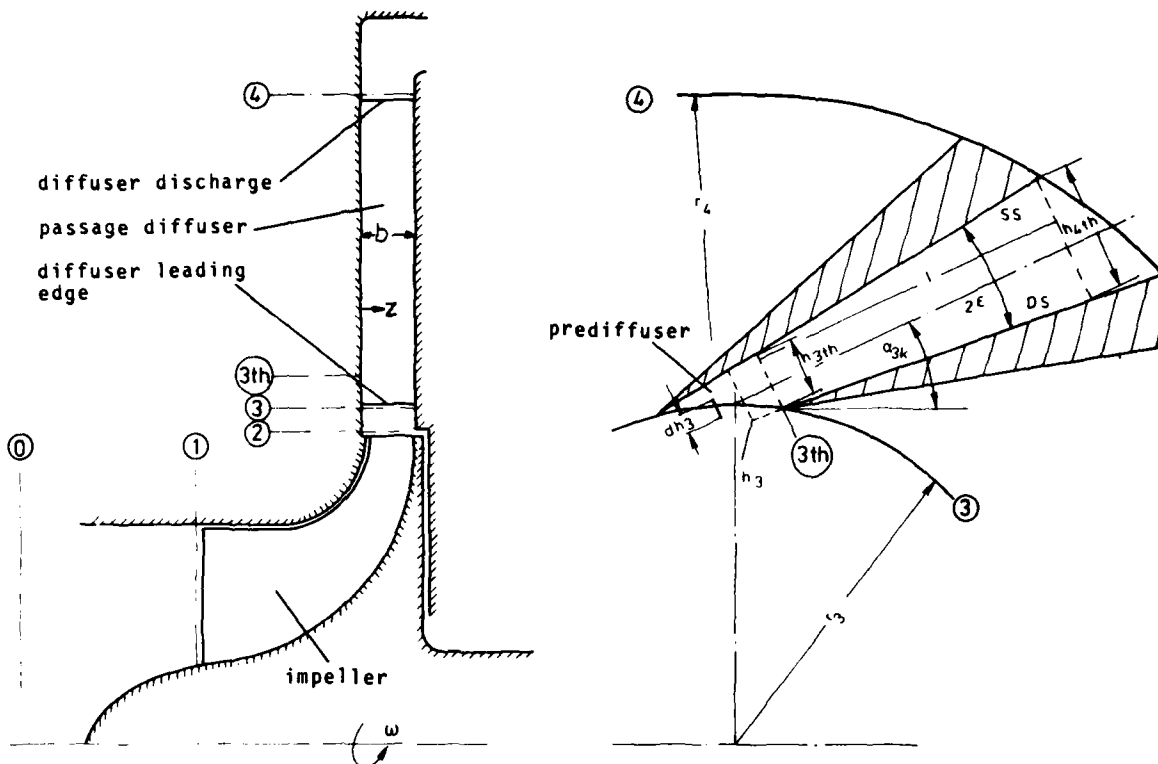


Fig. 3 Cross-sections of the centrifugal compressor stage and station designation

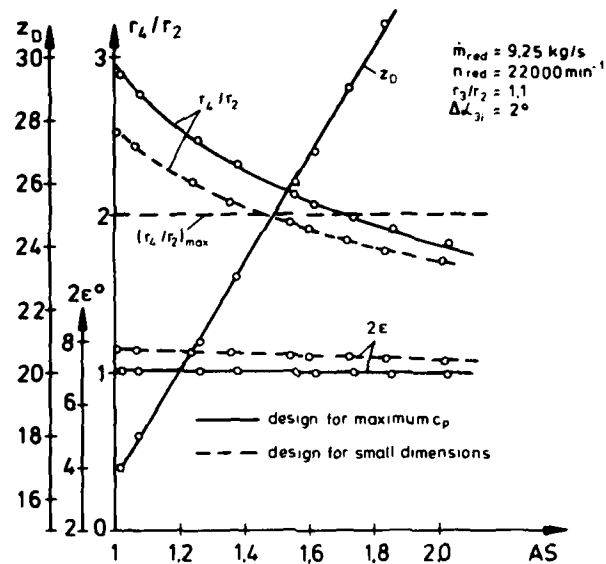


Fig. 4 Calculated diffuser discharge/impeller exit radius ratio r_4/r_2 , diffuser blade number z_D and diffuser divergence angle 2ϵ for maximum recovery and small dimension design, depending on aspect ratio AS

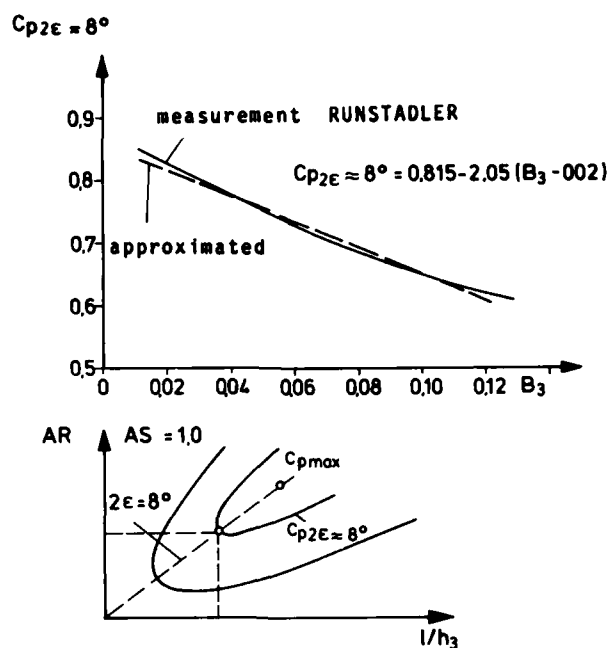


Fig.5 Deviation from optimum length/width ratio to obtain small diffuser dimensions

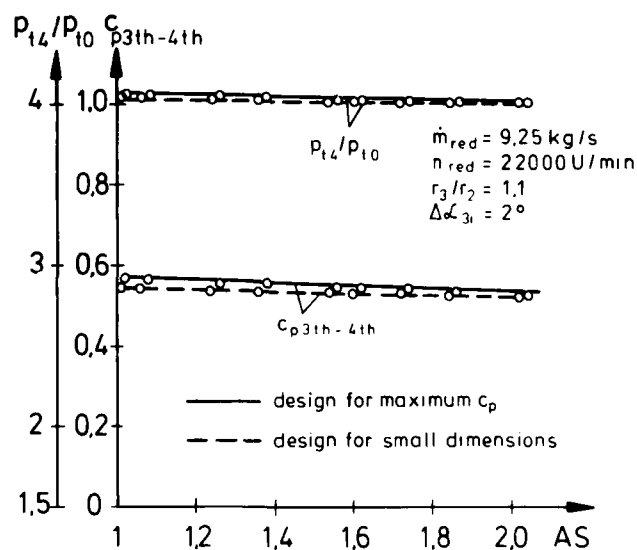


Fig.6 Estimated compressor and diffuser performance for maximum diffuser recovery and small dimension design, depending on diffuser aspect ratio AS

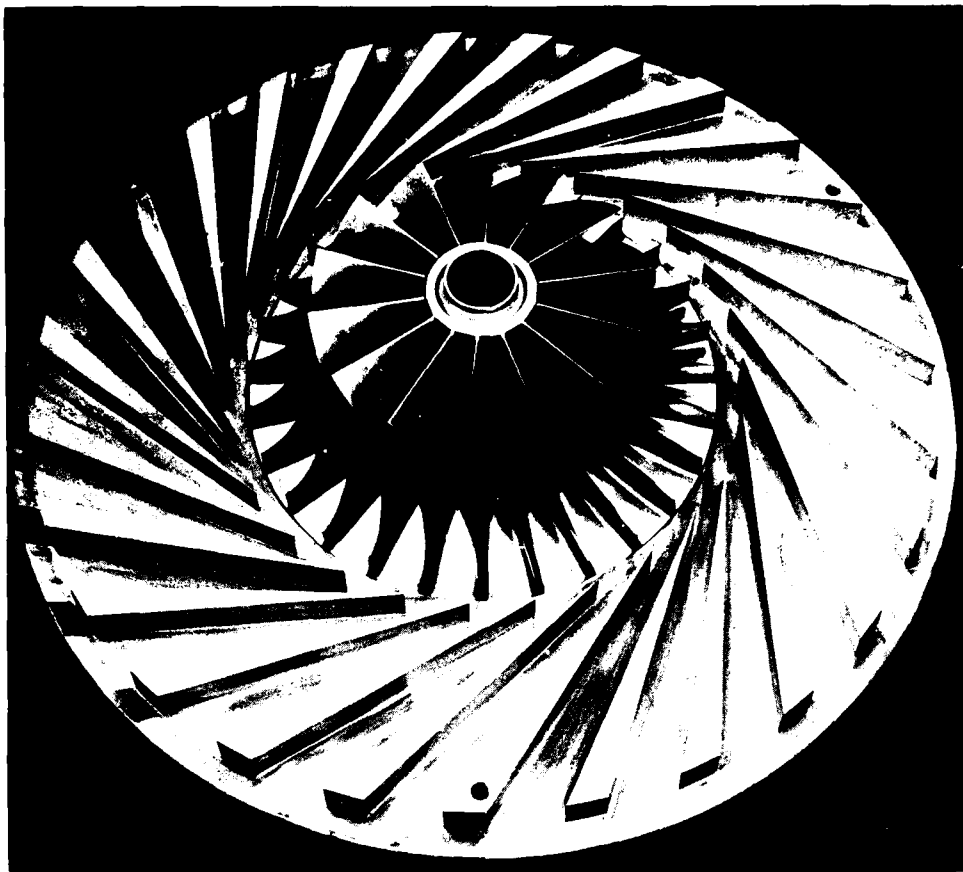


Fig.7 Final design of the flat straight channel diffuser

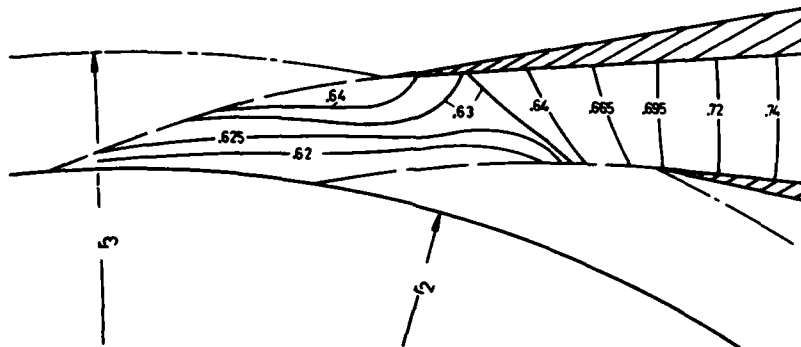


Fig.8 Calculated isobarics for the impeller discharge/
diffuser entry region,
 $\dot{m}_{red} = 6,73 \text{ kg/s}$, $n_{red} = 17\,600 \text{ min}^{-1}$

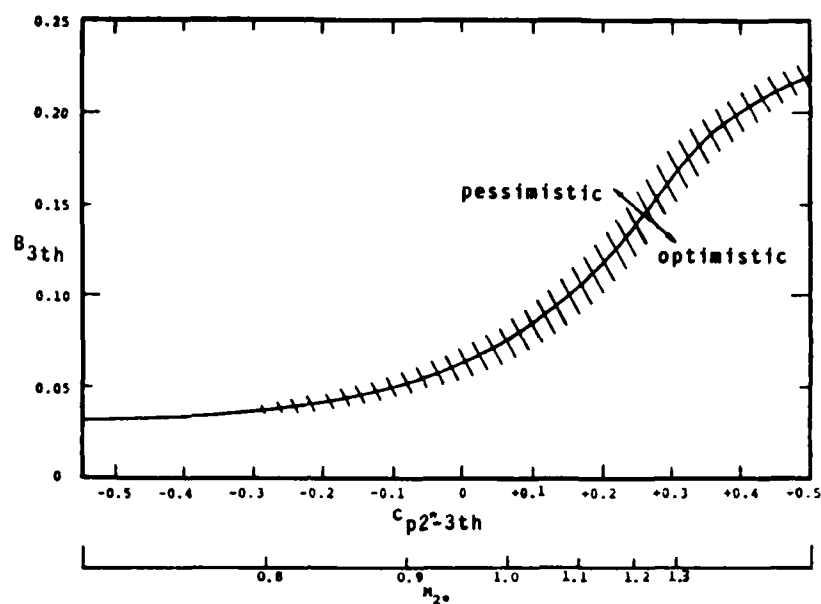


Fig.9 Diffuser throat blockage dependent on pressure rise coefficient (ref. [1], [18])

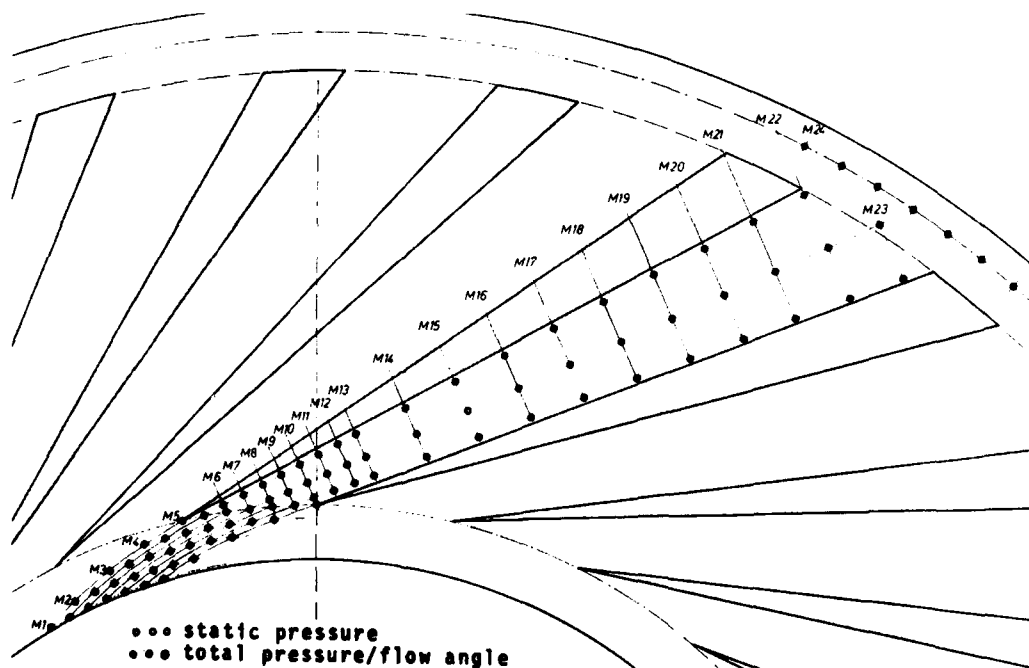


Fig.10 Arrangement of static pressure taps and combined total pressure/flow angle probes from impeller discharge to diffuser exit

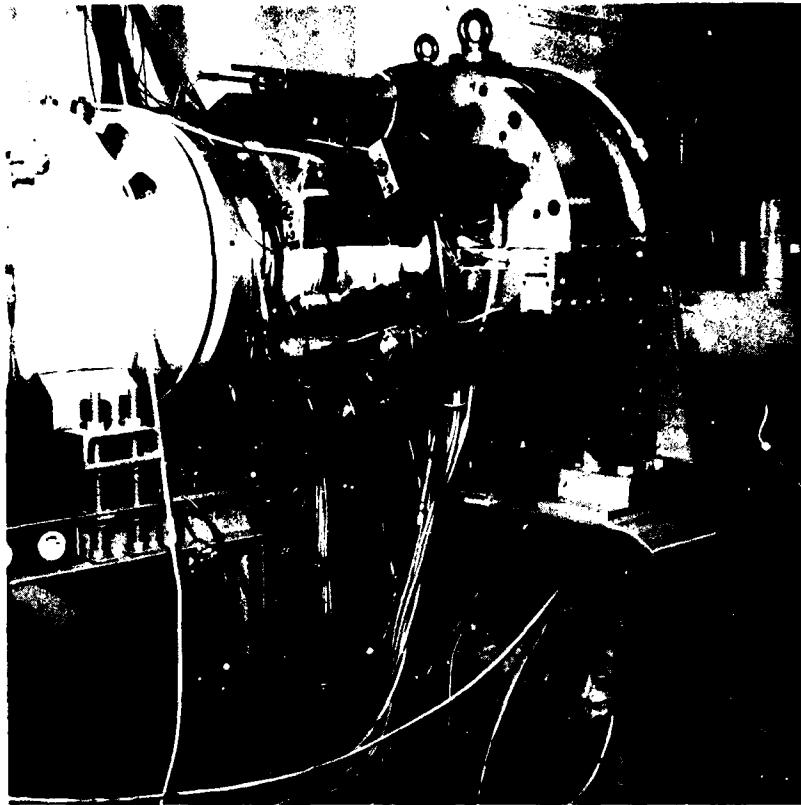


Fig.11 Test rig equipped with movable combined total pressure/flow angle probes



Fig.12 Test rig and distribution of static pressure taps in the diffuser region

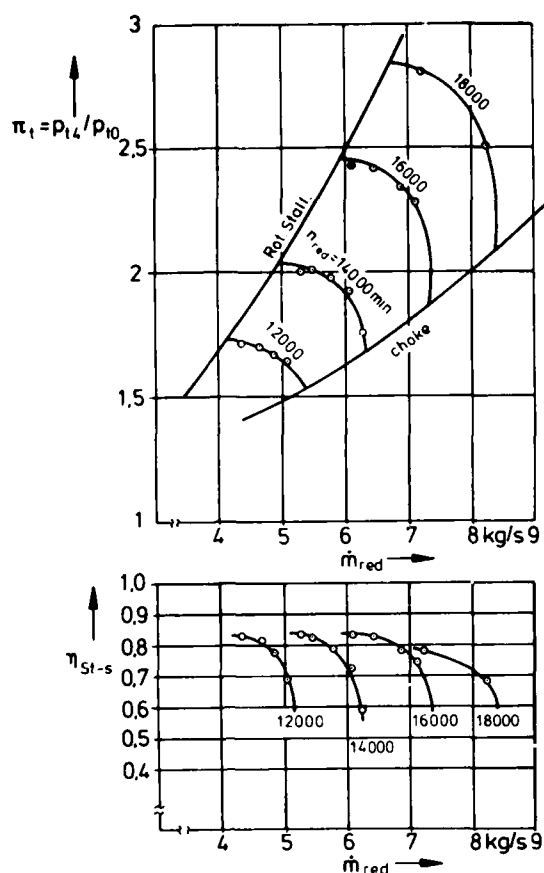


Fig.13 Centrifugal compressor performance map

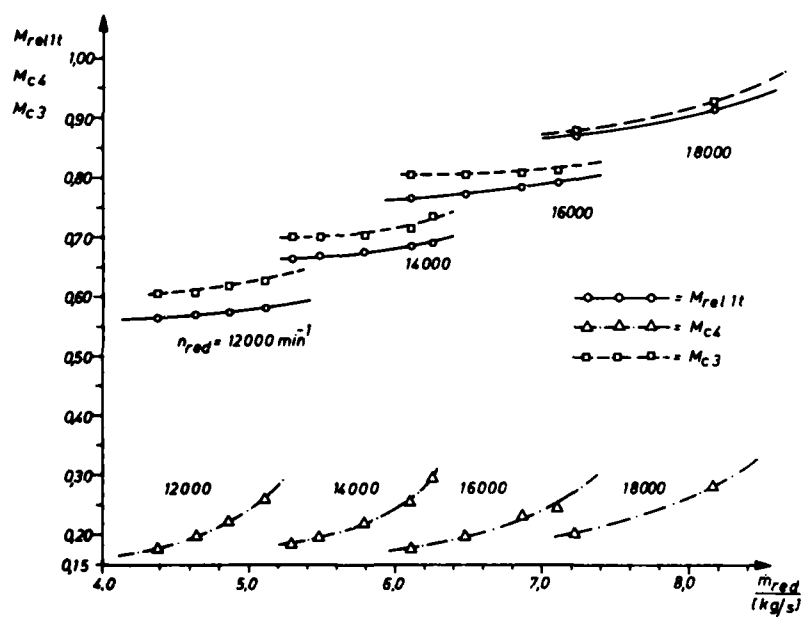


Fig.14 Mean Mach number at inducer tip ($M_{rel\,it}$), vaned diffuser inlet (M_{c3}) and diffuser exit (M_{c4})

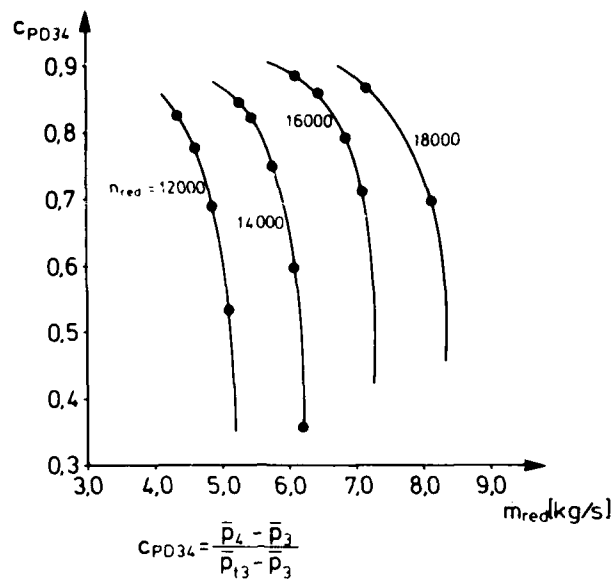


Fig.15 Overall diffuser recovery c_{PD34}

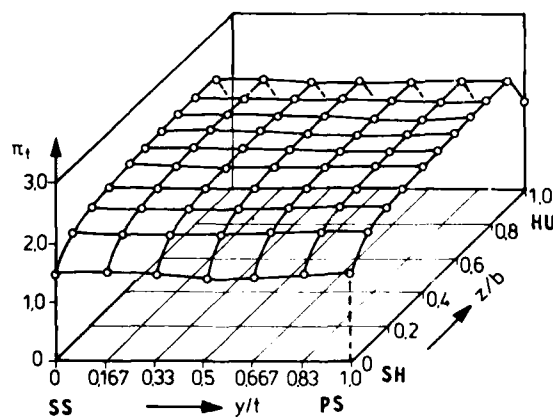


Fig.16 Total pressure distribution 5 mm ahead of a vaned diffuser passage, $n_{red} = 5.3 \text{ kg/s}$, $n_{red} = 14\,000 \text{ min}^{-1}$, $r/r_2 = 1.075$

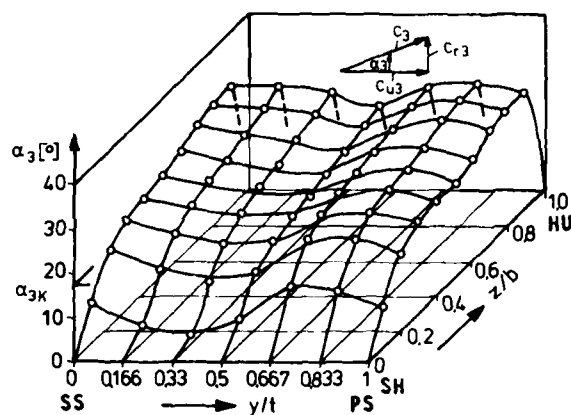


Fig. 17 Absolute flow angle distribution
5 mm ahead of a vaned diffuser
passage,
 $\dot{m}_{red} = 5.3 \text{ kg/s}$, $n_{red} = 14\,000 \text{ min}^{-1}$,
 $r/r_2 = 1.075$

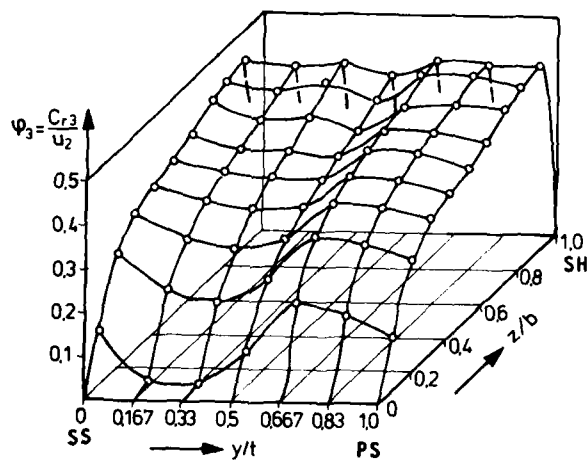


Fig. 18 Distribution of the radial ve-
locity component 5 mm ahead of
a vaned diffuser passage,
 $\dot{m}_{red} = 5.3 \text{ kg/s}$, $n_{red} = 14\,000 \text{ min}^{-1}$
 $r/r_2 = 1.075$

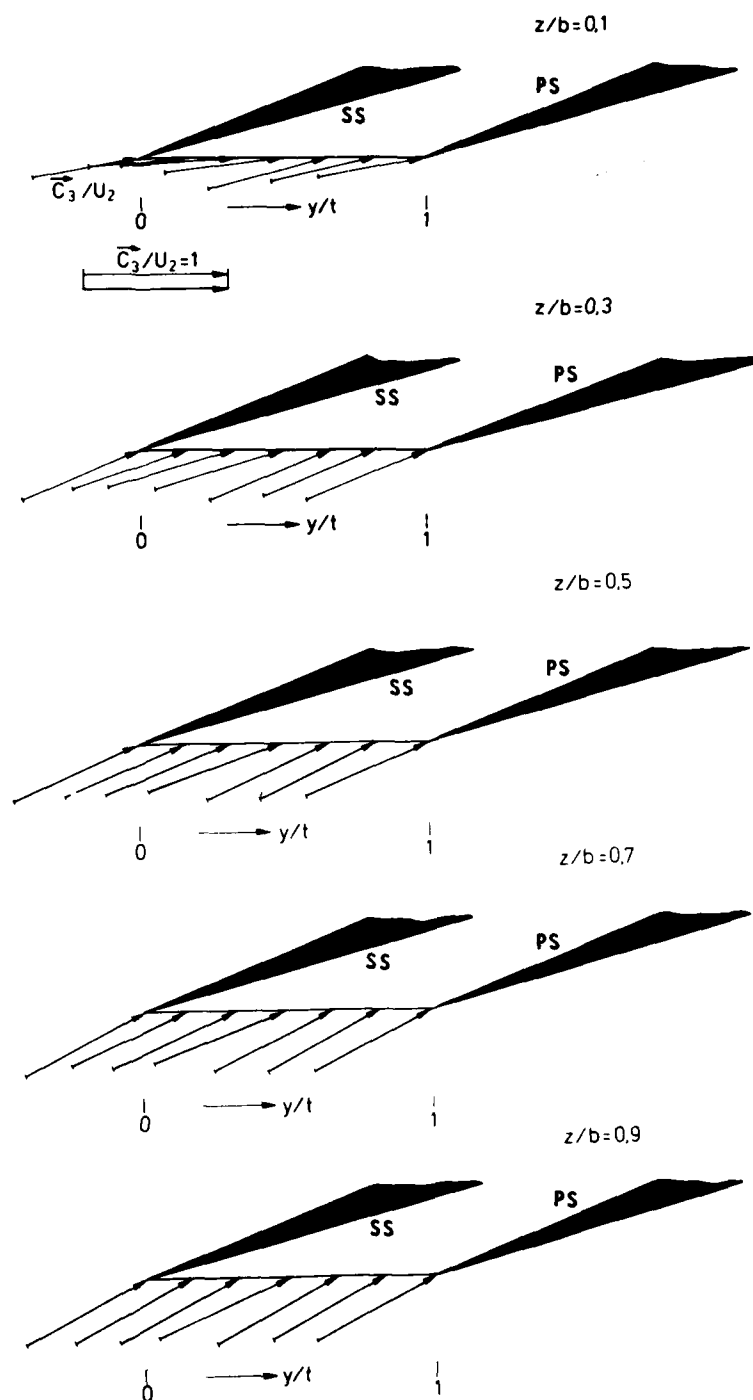


Fig.19 Absolute velocity direction in reference to the diffuser blades for 5 relative axial positions, $\dot{m}_{red} = 5.3 \text{ kg/s}$, $n_{red} = 14\,000 \text{ min}^{-1}$, $r/r_2 = 1.075$

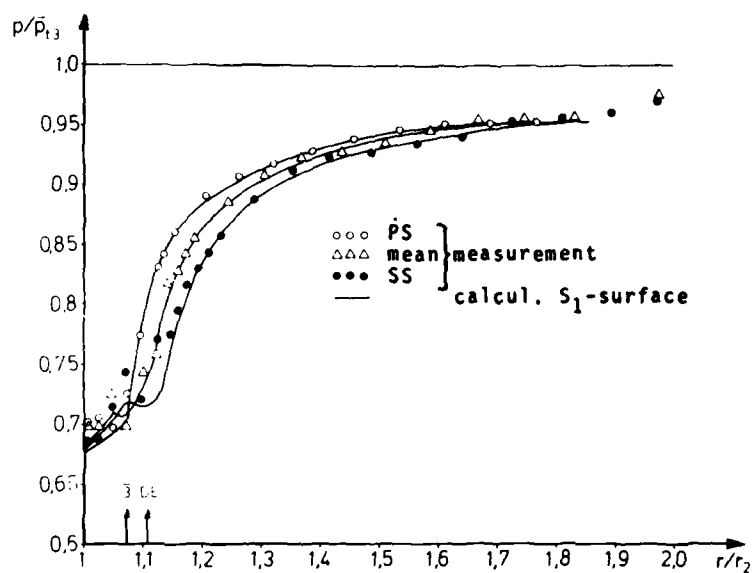


Fig.20 Comparison of the measured and calculated static pressure development along the diffuser blades and along the diffuser passage mean centerline, $\dot{m}_{red} = 5.3 \text{ kg/s}$, $n_{red} = 14\,000 \text{ min}^{-1}$

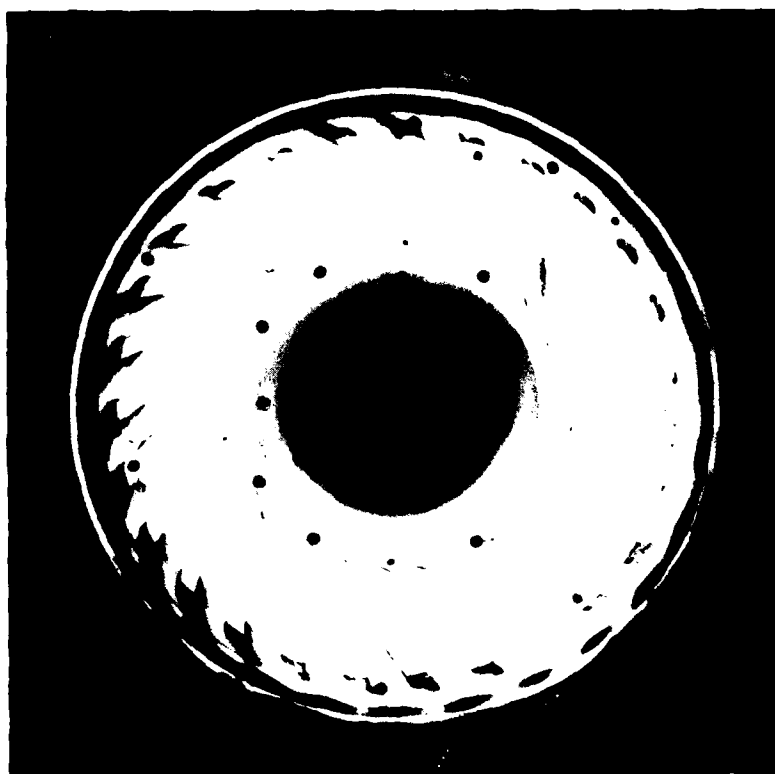


Fig.21 Diffuser shroud wall after compressor dismantling

DISCUSSION

P.M.Came, NGTE, UK

In the calculation by Wu's S1 method, how was the value of polytropic efficiency chosen? Also, please could the author explain how the boundary layer blockage value was selected.

Author's Reply

Both values were taken from measurements of the corresponding parameters.

T.Yoshinaka, Pratt & Whitney Aircraft, Ca

According to the calculation results shown in Figure 8 an aerodynamic loading appears (at the upstream end of the vaneless diffuser) which causes a static pressure discontinuity in the circumferential direction inside the vaneless space. Would the author please explain this phenomenon.

Author's Reply

According to the assumed boundary condition in the vaneless space a streamline curvature occurs at the impeller discharge. Due to this curvature a static pressure gradient in the circumferential direction has to be taken into account by this calculation method.

Y.Ribaud, ONERA, Fr

I cannot see the difference between your theoretical calculation and Katsanis' method which also takes account of blockage and polytropic efficiency.

Author's Reply

The author is not familiar enough with Katsanis' calculation method to answer your question in detail. However, the presented results have been obtained by using our own calculation method developed at DFVLR. This method is not based on a computer program published by Katsanis.

D.Eckardt, MTU, Munich, Ge

Looking at Figure 10, it is obvious that at least three out of seven probes at diffuser discharge are within the diffuser blade wake region. Would the author please comment on firstly, the applied averaging procedure in this plane; secondly, the relevance of wake probe readings with respect to the overall compressor exit state.

Author's Reply

The averaging procedure at the diffuser exit was actually the same as in the measurement area near diffuser leading edge. The mean total pressure is an integral mean value of the measured total pressure distribution; the mean static pressure is an arithmetical mean value across the diffuser pitch. The indicated total pressure in the separated flow area behind the diffuser leading edge coincides with the corresponding static pressure.

FLOW IN CENTRIFUGAL COMPRESSOR IMPELLERS
A THEORETICAL & EXPERIMENTAL STUDY

by

A. GOULAS *

Senior Research Fellow
 Fluid Engineering Unit
 Cranfield Institute of Technology
 Cranfield
 Bedford

Summary

The flow field in various centrifugal compressor impellers is studied both theoretically and experimentally, the aim being:

- (i) To improve the understanding of the flow phenomena involved, and
- (ii) To develop numerical methods capable of predicting the complex viscous and turbulent flow field.

The circumferential and radial components of velocity and the rms of the corresponding fluctuations in the impeller of a centrifugal compressor have been obtained using a Laser Doppler anemometer. The results indicate a two unequal vortex arrangement with opposite direction of rotation and with the smaller vortex immediately behind the suction side of each blade. The radial velocity profiles indicate a weak wake at the centre of the passage near the shroud as for curvature dominated flows.

The study of the published experimental data points to the vorticity being a dominant feature of the flow inside the impeller.

Numerical integration of the vorticity equations shows that the production of streamwise vorticity is affected by:

- (i) the diffusion achieved in the inducer, and
- (ii) the length of the radial part of the impeller, both major design parameters.

The prediction method is a finite difference scheme based on the matrix through flow analysis as has been modified to incorporate the effect of viscosity and turbulence on the flow field.

The results obtained for a low speed compressor are compared with data given by Mizuki. Furthermore, results for a high speed compressor impeller are presented and quantitative agreement with experimental data is shown. Finally the problems of turbulence modelling in centrifugal compressor is discussed in the light of the experimental data obtained and the turbulence models available.

Nomenclature

B	Integration factor
C_1, C_2, C_u	Constants in turbulence model
D	Dissipation force per unit mass
F	Body force
G	Generation term defined by Equation
h_0	Stagnation enthalpy
h	Enthalpy
I	Rothalpy ($I = h_0 - \omega r V_u$)
N	Normal to the stream line
n	Normal to the stream surface
r	Radius
S	Streamwise direction
s	Entropy
T	Temperature
V	Absolute velocity
W	Relative velocity

* Seconded to BHRA Fluid Engineering, Cranfield, Bedford

x_i	Cartesian space coordinates (S, N, n)
z	Axial direction

Greek

ϵ	Rate of dissipation of turbulence
κ	Kinetic energy of turbulence
λ, ν	Angles of stream surface
μ_t	Turbulence viscosity
ρ	Density
τ	Stress Tensor
θ	Angle
ψ	Stream function
ω, Ω	Angular velocity

Subscripts

b	Basic
e	Inlet
h	Hub
p	Perturbation
r	Radial direction
s	Shroud
u	Circumferential direction
z	Axial direction

1. Introduction

The calculation of the flow in impellers plays an important role in the theoretical research and design of centrifugal compressors. As the three-dimensional turbulent flow within the impeller is too complicated to allow a full numerical solution, several methods are developed assuming steady and inviscid flow. The calculations usually involve a combination of the flow field obtained by solving the governing equations for different stream surfaces. Such solutions are described by Stanitz (1), Katsanis (2), and recently by Krimmerman et al (3). Comparisons of the above solution with the experimental results of Eckardt (4), Adler et al (5) and Johnson et al (6) reveal significant differences in the velocity profiles which can be due to the effects of viscosity and turbulence on the main flow. Better predictions, therefore, of the flow inside centrifugal compressor impellers can only be obtained when viscosity and turbulence are taken into account.

Furthermore, examination of the experimental results of Eckardt (4) and Adler et al (5), obtained using laser anemometry and Johnson et al (6) using pressure probes, shows significant differences between each other although the phenomena involved are basically the same. Thus the need for further experimental information which will allow a better understanding of the flow inside centrifugal compressor impellers. In addition, in the above reports, there is no information of the turbulence characteristics and since they are often responsible for the mean flow characteristics and aid to the understanding of the phenomena involved, their determination is very desirable.

An experimental investigation was carried out in order to improve the understanding of the flow phenomena inside centrifugal compressor impeller passage. It made use of laser-Doppler anemometry, which allowed the measurement of the centrifugal and radial components of velocity and the corresponding normal stresses, and an Air Research compressor which was rotated at 11,800 rpm. The flow configuration and instrumentation are described briefly in the next section detail and can be found in reference 7 and is followed by the presentation and discussion of the experimental results.

An outline of the theoretical method follows and the results of calculations of the flow field are presented and discussed. Finally the problems of turbulence modelling are discussed in the light of the experimental data obtained and the turbulence models available.

2. Flow Configuration and Instrumentation

The centrifugal compressor is part of an Air Research T04B turbocharger. The impeller had 16 blades with tip and eye radii of 0.035m and 0.022m and had a nominal design speed of 80,000 rpm. For the present work, it was driven at 11,800 rpm by the turbine of the turbo-charger unit which was supplied with compressed air. A 90 degree segment of the shroud was removed and replaced by a plexiglass

insert which allowed optical access over the 90 degree sector and from a radius of 0.028m to 0.035m. The surfaces of the plexiglass insert were polished.

The rotational speed of the impeller and the location within a blade passage was determined by the optical tachometer of ref. (8).

The laser doppler anemometer comprised an optical transmission arrangement and a data acquisition and signal processing unit.

The optical transmission arrangement contained an Argon laser, a water filled Bragg cell, focussing lens, a back scatter light collecting arrangement and a photomultiplier.

The signal from the photomultiplier was input to a frequency analyser which was controlled by a micro-processor. The microprocessor arranged for the signal to be swept with a 300 kHz bandwidth filter and Doppler bursts were observed above a preset amplitude of 5mV and their frequency recorded on magnetic tape. The sweep rate corresponded to steps of 1 MHz and a velocity of 1.478 m/s. An analogue signal was provided by the spectrum analyser and had a voltage level, proportional to the Doppler frequency, which changed with each recognised Doppler burst of new frequency. A typical signal is indicated diagrammatically on figure 1 which also presents the basis for its analysis.

As indicated on figure 1, the signal was differentiated, amplified, rectified and Schmidt triggered to produce TTL-compatible pulse which represent the time at which the particle crossed the measuring volume. The output from the tachometer provided a pulse for each blade and splitter, as indicated on figure 2, and a counter reduced these pulses to one per revolution. The resulting pulse triggered a pulse generator which produced a sequence of equispaced pulses which, with analogue to digital conversion resulted in a ramp. The time between pulses indicated the circumferential position and could be preset to provide a desired spatial resolution and the duration of the enable gate which allowed the measured frequency to be recorded on a magnetic tape.

The present results were obtained with 64 pulses within a blade passage of 22 degrees and correspond to a circumferential spatial resolution of 0.3 degrees. When a particle crossed the measuring volume and the enable gate is high, a pair of pulses instructed the system to store the value of the Doppler frequency and the instantaneous position in a buffer. On completion of 1024 pulses, the stored information was written on the magnetic tape which was analysed subsequently on a CDC6400 computer. Each value of velocity and normal stress was determined from between 60 and 200 individual frequency values.

The error associated with the measurements was analysed and the results of this analysis are as follows:

The radial and axial positions of measurement were known to better than ± 0.0001 m and introduce no significant error as does the evaluation of circumferential position. Similarly, gradient broadening was calculated and found to be insignificant as was the effect of the bandwidth of the spectrum analyser filter. The sweep rate of the analyser precluded the interpretation of an individual velocity within ± 0.739 m/s and was probably the largest single source of uncertainty. Bias errors may have been introduced by the method of averaging but, in view of the low turbulence intensities, would have an insignificant influence on the results. In general, it can be expected that the measured mean and rms values were within $\pm 2.5\%$ and $\pm 10\%$, respectively of the maximum measured values.

3. Results and Discussion of the Experimental Study

The measured distributions of mean and rms radial and circumferential velocities are presented in figures 3 and 4 respectively. One of the features of these profiles is that they are different for the two channels formed between blade-splitter and splitter-blade surfaces. This is a particular characteristic of the impeller under consideration and has been observed by Goulas (9) at the exit of the same impeller using hot-wire anemometry. The difference is probably due to the geometry of the leading edge of the splitter which is usually matched with the blade leading edge to produce similar profiles when the compressor operates at the design point. For operation at an off-design point, as here, differences tend to be magnified.

The radial velocity profiles for the two channels share common features. They indicate an area near the pressure side with $\partial V_r / \partial \theta < 0$, a low velocity area near the centre of the channel, and finally an area of high velocity with $\partial V_r / \partial \theta > 0$ near the suction side of the blades.

The circumferential velocity profiles indicate the presence of two vortices, a large one covering most of the channel and a smaller one behind the blade at the suction side. This system of vortices produces positive velocities in the region near the shroud (positive being flow towards the suction side) for the large vortex and negative velocities for the small one as is the case here.

The core of the small vortex is established near the suction-side-shroud corner of the passage where it is fed with air by the tip leakage flow. The radial velocity profiles do not show a wake in the suction side-shroud corner where an isentropic flow is established since the gradient of the radial velocity $\partial V_r / \partial \theta$, is almost equal to 2ω . Thus the present measurements indicate a weak wake near the centre of the channel. The measurements of Adler et al (5) show similar radial velocity profiles at the centre of the closed channel, which correspond to the shroud area for the unshrouded impeller.

The rms values of the radial component of velocity, figure 5, has maxima at the suction side of the splitter and at some distance away from the suction side of the blade. These maxima suggest that small scale vortices are shed into the flow from the region of separation formed near the leading edge. This region of separation is largely the result of the negative angle of incidence (-15°) associated with the present impeller and its rotational speed. As the length of the blade is greater than the length of the splitter, the vortices formed at the blade leading edge have time to be convected into the main flow. As a result, the two maxima lie in different circumferential positions, relative to the suction sides of the blade and splitter. The rms value of the circumferential component of velocity, figure 6, near the pressure side of the blade or the splitter is of the same order of magnitude as the radial one, suggesting near-isotropic turbulence in this region. Near the suction side of the blades, the rms value of the circumferential component is almost half its radial counterpart and suggests suppression of turbulence in this direction due to the stabilizing effect of the Coriolis force, see Johnston et al (10) in their investigation of flow in rotating diffusers.

4. Theoretical Investigation

The three-dimensional flow field in a centrifugal compressor impeller can be predicted by solving the following equations:

1. continuity (1)
2. motion (3)
3. energy (1)
4. state (1)

These six equations are sufficient to determine the mean components of velocity and the mean fluid properties, provided enough information is given about the turbulence correlations in the form of a turbulence model. A straight numerical solution of the above system of partial differential equations though, requires a prohibitive amount of computer storage and time, instigating thus the need for a method to reduce at least the necessary computer core.

The method used here is based on Wu's (11) general theory as was improved by Bosman et al (12) and Goulas (13) and consisted of a combination of hub-to-shroud and blade-to-blade solutions of the viscous and turbulent flow field. Details of the method can be found in reference 14. Here only the basic points will be presented.

4.1 The 3-D Prediction Method

The solution procedure starts by obtaining a solution of the flow field on a hub-to-shroud stream surface having geometry similar to the blade camber surface.

The resulting streamlines can then be used to generate several axisymmetric blade-to-blade stream surfaces. The solution of the flow field on each individual stream surface will provide the geometry and integration factor distribution on "basic" hub-to-shroud stream-surfaces. The solution will proceed into solving the flow field on each one of the hub-to-shroud stream-surfaces starting from the surface nearest to the pressure side and "marching" towards the suction side of the passage. During solution the geometry of each stream surface is allowed to deviate from the geometry of the basic stream-surface in order to satisfy the relation,

$$\bar{W} \cdot \bar{n} = 0 \quad (1)$$

4.2 Flow on a Stream-Surface

Expressed in a curvilinear orthogonal system of coordinates with axes S along and N across a streamline on the stream-surface and a third axis n normal to the surface, the equations governing the flow on a stream-surface are:

- (i) Continuity
- (ii) Equation of motion for the N-direction:

$$\bar{N} \cdot \bar{W}_x (\bar{V}_x \bar{V}) = \bar{N} \cdot (\bar{V} \bar{I} - T \bar{V}_S) \quad (2)$$

- (iii) Equation of motion for the S-direction:

$$T \frac{D_S}{Dt} = - \bar{W} \cdot \bar{D} \quad (3)$$

- (iv) Equation of motion in the n-direction.
- (v) The energy equation for steady flow:

$$\frac{DI}{Dt} = 0 \quad (4)$$

- (vi) and the equation of state.

For the flow on stream-surfaces Wu introduced special derivatives in order to reduce the number of independent variables from three to two. Thus when $r-\theta$ are the two variables the special derivatives are defined as:

$$\frac{\partial}{\partial x_1} = \frac{\partial}{\partial x_1} - \frac{n_1}{n_z} \frac{\partial}{\partial z}$$

For the $z-\theta$ variables the special derivatives are:

$$\frac{\partial}{\partial x_1} = \frac{\partial}{\partial x_1} - \frac{n_1}{n_r} \frac{\partial}{\partial r}$$

Finally for the $r-z$ variables the special derivatives are:

$$\frac{\partial}{\partial x_1} = \frac{\partial}{\partial x_1} - \frac{n_1}{rn_u} \frac{\partial}{\partial \theta}$$

A stream function Ψ can then be defined for each individual pair of coordinates such as to satisfy the continuity equation. At the same time an integration factor B must be introduced which is equal to the thickness of the stream surface. The N equation of motion then can be modified to produce a Poisson type equation from which Ψ can be calculated.

The definition of Ψ for each pair of coordinates together with the resulting equation for Ψ are given below:

For the $r-\theta$ variables:

$$\frac{\partial \Psi}{\partial r} = -B\rho W_u$$

$$\frac{1}{r} \frac{\partial \Psi}{\partial \theta} = B\rho W_r \quad (5)$$

$$\frac{\partial^2 \Psi}{\partial r^2} + \frac{1}{r^2} \frac{\partial^2 \Psi}{\partial \theta^2} = W_r \frac{1}{r} \frac{\partial}{\partial \theta} (B\rho) - W_u \frac{\partial}{\partial r} (B\rho) + (B\rho)^2 \frac{dI}{d\Psi} +$$

(6)

$$+ \frac{TB\rho}{W^2} \left[\frac{\partial s}{\partial r} (W_u - W_z \tan \mu) - \frac{1}{r} \frac{\partial s}{\partial \theta} (W_r - W_z \tan \lambda) \right] +$$

$$+ \left[\tan \lambda \frac{1}{r} \frac{\partial W_z}{\partial \theta} - \tan \mu \frac{\partial W_z}{\partial r} \right] \rho B + \left(\frac{W_u}{r} + 2\omega \right) B\rho$$

For the $z-\theta$ variables:

$$\frac{\partial \Psi}{\partial z} = -B\rho W_u$$

(7)

$$\frac{1}{r} \frac{\partial \Psi}{\partial \theta} = B\rho W_z$$

$$\begin{aligned}
\frac{1}{r^2} \frac{\partial^2 \psi}{\partial \theta^2} + \frac{\partial^2 \psi}{\partial z^2} = W_z \frac{1}{r} \frac{\partial}{\partial \theta} (B\rho) - W_u \frac{\partial}{\partial z} (B\rho) + (\rho B)^2 \frac{dI}{d\psi} - \\
- \frac{TB\rho}{W^2} \left[\frac{1}{r} \frac{\partial s}{\partial \theta} (W_z - W_r \tan \lambda) - \frac{\partial s}{\partial z} (W_u - W_r \tan \mu) \right] + \\
+ B\rho \left[\frac{1}{r} \frac{\partial W_r}{\partial \theta} \tan \lambda - \frac{\partial W_r}{\partial z} \tan \mu \right] - B\rho \left[\frac{W_u}{r} + 2\omega \right] \tan \lambda
\end{aligned} \quad (8)$$

For the r-z variables:

$$\begin{aligned}
\frac{\partial \psi}{\partial r} &= \rho B r V_z \\
\frac{\partial \psi}{\partial z} &= -\rho B r V_r
\end{aligned} \quad (9)$$

$$\begin{aligned}
\frac{\partial^2 \psi}{\partial r^2} + \frac{\partial^2 \psi}{\partial z^2} = V_z \frac{\partial}{\partial r} (\rho B r) - V_r \frac{\partial}{\partial z} (\rho B r) + (\rho B r)^2 \frac{dI}{d\psi} - \\
- \frac{\rho B r T}{W^2} \left[\frac{\partial s}{\partial r} (V_z - W_u \tan \mu) - \frac{\partial s}{\partial z} (V_r - W_u \tan \lambda) \right] + \\
+ \rho B \left[\tan \mu \frac{\partial}{\partial r} (r V_u) - \tan \lambda \frac{\partial}{\partial z} (r V_u) \right]
\end{aligned} \quad (10)$$

The angles λ and μ define the local geometry of the stream-surface. For example in the case of the r-z coordinates λ and μ are given as:

$$\tan \lambda = \frac{n_r}{n_u}, \quad \tan \mu = \frac{n_z}{n_u} \quad (11)$$

During the third stage of the calculation, calculation of the flow field on various hub-to-shroud stream-surfaces, the circumferential component of the relative velocity is split into two parts. One part W_{up} is dictated by the geometry of the "basic" stream-surface; the other one is a perturbation circumferential velocity W_{up} , so:

$$W_{up} = W_u - W_{ub} \quad (12)$$

This perturbation is considered to be the result of the stresses which arise due to circumferential gradients of velocity. If the flow is isentropic, the viscosity is zero and, thus, W_{up} will be zero. Therefore:

$$W_u \Big|_{\text{isentropic}} = W_{ub} \quad (13)$$

and the flow will follow the stream-surface.

For non-isentropic cases, the geometry of the stream surface will change in order to take account of the different circumferential component of velocity. Therefore, the integration factor B, has to be changed accordingly.

An equation for the "perturbation" of the circumferential component of velocity can be obtained from the θ -equation of motion. The final expression is:

$$\frac{D}{Dt} (r w_{u_p}) = r (D_{u_s}' - D_{u_b}') - \frac{\mu_t}{\rho r} w_{u_p} = Q_u \quad (14)$$

where:

$$\rho (D_{u_i}') = \left[\frac{1}{r} \frac{\partial v_r}{\partial \theta} \left(\frac{\partial \mu_t}{\partial r} - \mu_t \frac{\partial \rho}{\partial r} \right) + \frac{1}{r^2} \frac{\partial w_u}{\partial \theta} \left(\frac{\partial \mu_t}{\partial \theta} - \mu_t \frac{\partial \rho}{\partial \theta} \right) + \frac{1}{r} \frac{\partial v_z}{\partial \theta} \left(\frac{\partial \mu_t}{\partial z} - \mu_t \frac{\partial \rho}{\partial z} \right) + 3 \frac{\mu_t}{r^2} \frac{\partial v_r}{\partial \theta} \right]_i \quad (15)$$

where i stands for either s or b.

The term $(D_{u_b}')_b$ is obtained from the previous step, the solution of the flow field on the blade-to-blade stream surfaces.

The change in the geometry of the stream surface requires changes in the integration factor B.

An equation for B again can be derived as:

$$\frac{D}{Dt} (B - B_b) = - \frac{B}{r} \left(w_r \frac{\partial}{\partial \theta} (\tan \lambda) + w_z \frac{\partial}{\partial \theta} (\tan \lambda) \right) \quad (16)$$

The above two expressions for w_{u_p} and B were derived assuming that the deviation of the geometry of the stream surface from the "basic" one is small and circumferential gradients of w_{u_p} are negligible.

The solution of the flow field on any stream surface is obtained by solving equation (6), (7) or (10) according to the system of coordinates appropriate to the geometry of the stream surface simultaneously with the streamwise equation of motion, eq. (3).

The dissipation force which appears in (3) is shown by Goulas and Baker (13) to be:

$$\bar{D} = \frac{1}{\rho} (\nabla \cdot \tau) \quad (17)$$

For turbulent flows a turbulence model has to be used to obtain the stress tensor. Throughout the present work, the κ - ϵ turbulence model, as described by Launder and Spalding (15), is used. The stresses in this model are given by the equation:

$$\tau_{ij} = - \rho \overline{u_i u_j} = \mu_t \left(\frac{\partial w_i}{\partial x_j} + \frac{\partial w_j}{\partial x_i} \right) - \frac{2}{3} \rho \delta_{ij} \kappa \quad (18)$$

The scalar turbulent viscosity, μ_t is given as:

$$\mu_t = c_\mu \rho \kappa^2 / \epsilon \quad (19)$$

The kinetic energy κ and the rate of dissipation ϵ of turbulence are obtained by solving the following system of differential equations:

$$\frac{D\kappa}{Dt} = \frac{1}{\rho} \frac{\partial}{\partial x_k} \left(\frac{\mu_t}{\sigma_k} \frac{\partial \kappa}{\partial x_k} \right) + G - \epsilon \quad (20)$$

$$\frac{D\epsilon}{Dt} = \frac{1}{\rho} \frac{\partial}{\partial x_k} \left(\frac{\mu_t}{\sigma_\epsilon} \frac{\partial \epsilon}{\partial x_k} \right) + \frac{c_\epsilon}{\kappa} G - c_2 \frac{\epsilon^2}{\kappa} \quad (21)$$

The generation term G is given by the following relation:

$$G = \frac{\mu_t}{\rho} \left(\frac{\partial W_i}{\partial x_k} + \frac{\partial W_k}{\partial x_i} \right) \frac{\partial W_i}{\partial x_k} \quad (22)$$

The constants involved are given as:

$$c_\mu = 0.09, \quad c_1 = 1.44, \quad c_2 = 1.92$$

$$\sigma_k = 1, \quad \sigma_\epsilon = 1.3$$

4.3 The Vorticity Equations

The production of vorticity has been recognized as an important factor in the development of the flow field within the impeller passage (see ref. 6 and 16).

Relative vorticity defined as :

$$\zeta = \nabla \times W$$

is produced by the interaction between velocity gradients in the axial direction and/or density gradients with Ω and by the interaction of normal components of vorticity with curvature.

The transport equations for the streamwise and normal components of vorticity on stream surfaces are given as (see ref. 16) :

$$\frac{\partial}{\partial s} \left(\frac{\zeta_s}{\rho W} \right) = \frac{2\zeta_N}{\rho W R} + 2\Omega_s \frac{W}{\rho} \frac{\partial \rho}{\partial s} + \frac{2\Omega \cdot (\nabla W)}{\rho W^2} \quad (23)$$

for the streamwise component, and

$$\frac{\partial}{\partial s} (\zeta_N W) = - \frac{W}{a_n} \frac{\partial a_n}{\partial s} (\zeta_N + 2\Omega_N) - 2\Omega_N \frac{\partial W}{\partial s} + 2 \frac{\Omega_s W}{R} \quad (24)$$

for the normal to the streamline component of vorticity. Equations (23) and (24) can be integrated along streamlines on stream surfaces to obtain the secondary vorticity components.

4.4 Numerical Solution

The numerical solution of the flow on a stream surface involves the simultaneous solution of eq. (1), (3), (21), (22) and during the final stage of the calculation eq. (14) and (16), together with one of the eq. (6), (8) or (10) according to the system of coordinates used.

The finite difference scheme used is derived from Taylor's series expansion. The lattice for each point extends over four grid lines in both directions. This ensures accuracy of the finite difference of the

$$O \left| \frac{\partial^4 \psi}{\partial x^4} \right|$$

In the last stage 'marching stage' and for the circumferential gradients, a backward finite difference scheme is used.

The solution procedure to obtain the flow field on a stream surface is an iterative one. Each iteration starts with an initial distribution of the stream function ψ on the stream surface. Differentiation of the ψ will give two components of velocity with the third calculated through eq. (1). The next step is to solve eq. (10) and (23) for the kinetic energy and the rate of dissipation of turbulence. With the turbulence viscosity μ_t then known the stresses can be obtained through eq. (18) and finally the dissipation force from eq. (17).

Eq. (3), (14), and (16) can then be integrated along streamlines to obtain the distribution of entropy s , perturbation velocity W_u , and integration factor B . The integration is possible because the distribution of the stream function is assumed to be known. With velocity, rothalpy and entropy known, the density can be obtained from the equation of state.

Finally, with velocity, entropy and density known, the right hand side of eq. (6) or (8) or (10) can be calculated, a banded matrix can be set up, so the system of linear equations can be solved.

The resulting distribution of ψ has to be compared with the initial one and the whole procedure repeated until a convergence criterion defined as :

$$\left| \frac{\psi_{\text{new}} - \psi_{\text{old}}}{\psi_{\text{old}}} \right| < 0.001$$

is satisfied at each point of the stream surface.

The boundary conditions necessary are as follows :

The distribution of the stream function at the inlet is calculated from the given initial distribution of velocity at the inlet, by integrating eq. (5a) for the blade-to-blade stream surface or eq. (9a) for the hub-to-shroud one;

The stream function is constant along solid walls;

The exit conditions are : for a hub-to-shroud stream surface $\frac{\partial \psi}{\partial x} = 0$, where x is the grid line direction parallel to the solid walls; for the blade-to-blade stream surface the Kutta condition was used;

Solid walls are streamlines thus ψ is constant along walls.

The boundary conditions for the stresses at the walls and the values of the kinetic energy and the rate of dissipation of turbulence at the nearest internal point of the flow field are obtained using the logarithmic law of the wall. Details about the relations involved can be found in Launder and Spalding (15).

The logarithmic law of the wall is also used to calculate the tangential velocity gradients near the pressure and suction sides of the channel.

For the vorticity calculations the initial boundary conditions are :

$$\zeta_z = 2\omega$$

i.e. the absolute vorticity is zero.

5. Results of the Theoretical Study

Two types of centrifugal compressor impellers were studied using the above described method.

The first is a typical high speed centrifugal compressor used for turbocharger applications. Fig. 7 gives the meridional cross section and the camber line of the blade. The calculations were carried out for a tip speed of 228 m/s, rotational speed 60000 RPM, and for the corresponding mass flow of 0.14 kg/s. More details of the results can be found in ref. (16) and (17).

Fig. 8 gives the pattern of streamlines for isentropic flow and the prediction obtained using the $k-\epsilon$ turbulence model. The growth of the boundary layers can be seen as a displacement of the streamlines away from the walls for the $k-\epsilon$ turbulence model.

Fig. 9 shows the meridional velocity at the grid points nearest to the shroud along the shroud for the same impeller, but with or without shroud. There are differences at the inducer and the radial part. In the curved region connecting those two parts, there are no changes since the curvature effects, which are the same for both shrouded and unshrouded impeller, dominate the flow in this region. The relatively small effect of the presence of the shroud on the flow, indicated by Fig. 9, is in agreement with the experimental results obtained by Howard and Kittmer (19). They obtained velocity profiles within a radial impeller with backward curved blades. They found that the primary velocity profiles were basically unaltered despite the considerable change in the secondary flow patterns thought to result from the tip leakage. Such effects, however, have been ignored in the present calculations.

In Fig. 10a the streamwise component of vorticity along the hub and in Fig. 10b along the shroud for a mid-passage hub-to-shroud stream surface is presented.

Along the hub, ζ_s is the same for both cases of shrouded and unshrouded impellers; negative and increasing in strength.

Along the shroud, the streamwise component is different. For the shrouded impeller, the streamwise vorticity is increasing in strength. For the unshrouded impeller, the vorticity is reduced in strength along the shroud. This is due to different circumferential velocity gradients in the two cases as the primary flow on the stream surface remains almost unchanged.

Fig. 11 gives the normal component of vorticity along the hub and shroud. There is no difference between shrouded and unshrouded impeller as ζ_n is not affected by velocity gradients. In real terms, there will be differences introduced by the binormal component of vorticity ζ_n and the radius of torsion r which are different for shrouded and unshrouded impellers.

In the case of the unshrouded impeller the initial rise in streamwise vorticity is followed by a reduction in strength and as a result the vorticity may even change sign. In this case the secondary flow is expected to change drastically. The factors affecting this change are the length of the radial part and the maximum value of streamwise vorticity produced within the inducer, which in turn depends on the diffusion within the inducer.

As for the length of the radial part, experience has shown that there is an optimum ratio of eye to tip diameter either side of which efficiency for the same otherwise design drops.

As for the importance of the diffusion within the inducer, Dean (18) suggests that most of the diffusion within an impeller is obtained in the inducer.

The flow field within the low speed centrifugal compressor impeller used by Mizuki et al. (21), (20) is predicted also using the method described in Section 4.

The calculations were carried out for the C-type impeller with a tip diameter of 270 mm, rotational speed 6000 RPM and for a flow coefficient $\phi = 0.50$.

Fig. 12 shows the measurements by Mizuki and fig. 13 shows the predicted velocity profiles. Although direct comparison is impossible because of the scales of fig. 12, the relative trends are correct.

Fig. 14 shows the velocity distribution near the hub at the inlet to the radial part of the impeller. The comparison with the experimental data is satisfactory.

Fig. 15 shows the pressure distribution along the pressure and suction sides at mid-height and for the nearest calculation point. There is some disagreement with the experimental results at the suction side in region of the inlet of the radial part. This may be attributed to the fact that due to curvature, pressure gradients may exist which will make direct comparison of the results difficult.

6. Conclusions

The experimental results obtained using laser anemometry do not show a large wake area as it was experienced by Eckardt and Johnson and are in agreement with the results obtained by Adler. The present and Adler's measurements were taken in impellers without an inlet pipe. Eckardt and Johnson's measurements, on the other hand, had a long inlet pipe. This may indicate that inlet boundary layers are responsible, to a certain degree, for the secondary flows experienced in centrifugal compressor impellers. Theoretical studies show that vorticity plays an important role in the development of the flow field in a centrifugal compressor impeller.

The experimental results of the RMS show also a suppression of turbulence near the suction side, similar to that experienced by Johnston et al. (10). This effect cannot be predicted by the usual turbulence models, i.e. $k-\epsilon$ model, without introducing empirical corrections.

The prediction method discussed was used to calculate the flow field in two impellers : a high speed impeller and a low speed one. The results show satisfactory agreement with the experimental data available.

7. Acknowledgments

Most of the work reported here was carried out under contract with the Ministry of Defence (Procurement Executive). The author would like to thank Professor R. C. Baker and Mr. P. Came for their help, advice and encouragement in carrying out this project.

REFERENCES

1. Stanitz, J.D. "Some theoretical aerodynamic investigations of impellers in radial and mixed flow centrifugal compressors".
Trans. ASME 74, p. 473, 1952.
2. Katsanis, T.H. "Computer program for calculating velocities and streamlines on a blade-to-blade stream surface of a turbomachine".
NASA-TN-D-4225, 1968.
3. Krimmerman, Y. and Adler, D. "The complete three-dimensional calculation of the compressible flow field in turbo impellers".
J. Mech. Eng. Science, 20, p. 149, 1978.
4. Eckardt, D. "Detailed flow investigation within a high speed centrifugal compressor impeller".
ASME J. Fluid Eng., 98, 390, 1976.
5. Adler, D. and Levy, Y. "Laser Doppler flow investigation inside a back-swept closed centrifugal compressor impeller".
J. Mech. Eng. Science, 21, 1, 1979.
6. Johnson, M.W., Moore, J. "The Development of wake flow in a centrifugal compressor".
ASME, 79-GT-152, 1979.
7. Goulas, A., Duraõ D.F.G., Whitelaw, J. "Measured velocity characteristics of the flow in the impeller of a centrifugal compressor".
ASME 79-HT-32, 1979.
8. Goulas, A. and Baker, R.C. "An optical tachometer for turbo-charger research".
Int. Journal of Mech. Eng. Education, 5, 159, 1977.
9. Goulas, A. "On the internal flow in centrifugal compressor impellers".
University of London, Ph.D. Thesis, 1977.
10. Johnston, J.P., Halleen, R.M. and Lesius, D.K. "Spanwise rotation of turbulent channel flow".
J. Fluid Mech., 56, 533, 1972.
11. Wu, C.H. "A general theory of three-dimensional flow in subsonic and supersonic turbomachines of axial, radial and mixed flow types".
NACA-TN-2604, 1952.
12. Bosman, C. and Marsh, H. "An improved method for calculating flow in turbomachines including a consistent loss model".
J. Mech. Eng. Science, 16, p. 25, 1974.
13. Goulas, A. and Baker, R.C. "Through flow analysis of viscous and turbulent flows".
ARC CP1382, 1977.
14. Goulas A. "The prediction of the 3-D flow field in centrifugal compressor impellers".
Submitted for publication.
15. Launder, B. and Spalding, D.B. "The numerical computation of turbulent flow".
Computer Methods in Applied Mechanics and Eng., 3, p. 269, 1974.
16. Goulas A. "The production of vorticity and its effects on the flow in centrifugal compressor impellers".
ASME 79-GT-113, 1979.
17. Goulas A., and Baker, R.C. "Through flow analysis of centrifugal compressors".
ASME GT-78-110, 1978.
18. Dean, R.C.Jr. "The fluid dynamic design of advanced centrifugal compressors".
VKI lecture notes 1974.
19. Howard, J.H.G., Kittmer, C.W. "Measured passage velocities in a radial impeller with shrouded and unshrouded configurations".
ASME J. of Eng. for Power 97, p. 207, 1975.
20. Mizuki, S., Ariga, I., Watanabe, I. "A study of the flow mechanism within centrifugal impeller channels".
ASME 75-GT-14, 1975.
21. Mizuki, S., Ariga, I., Watanabe, I. "Investigation concerning the blade loading of centrifugal impellers".
ASME 74-GT-143, 1974.

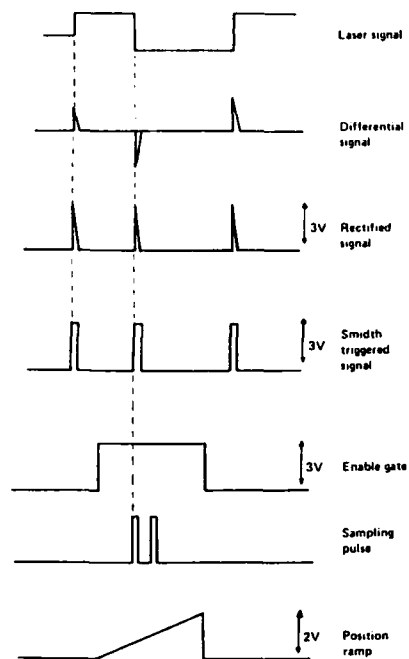


Fig. 1 Sampling pulse production

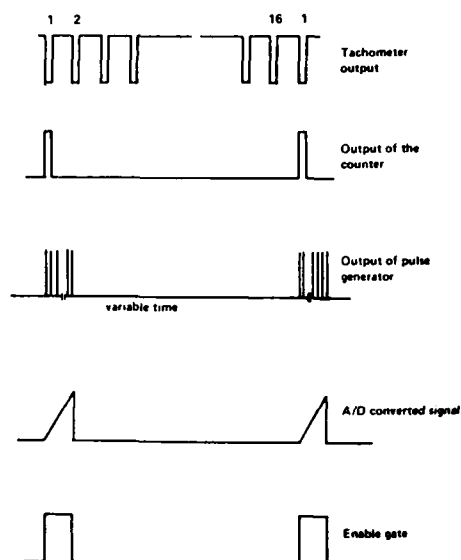


Fig. 2 Position ramp production

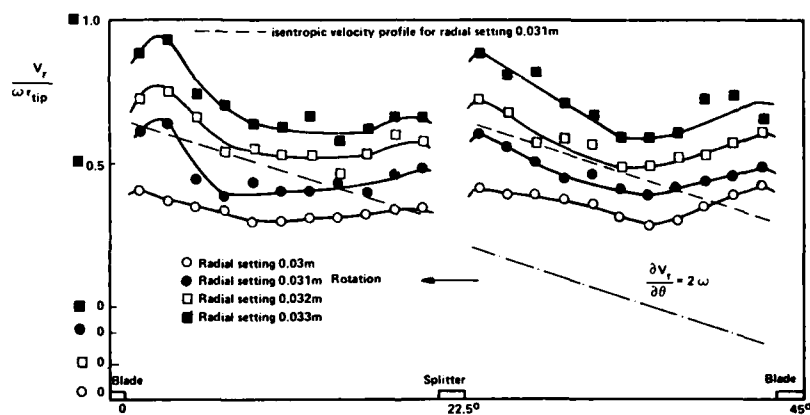


Fig. 3 Mean radial velocity profiles

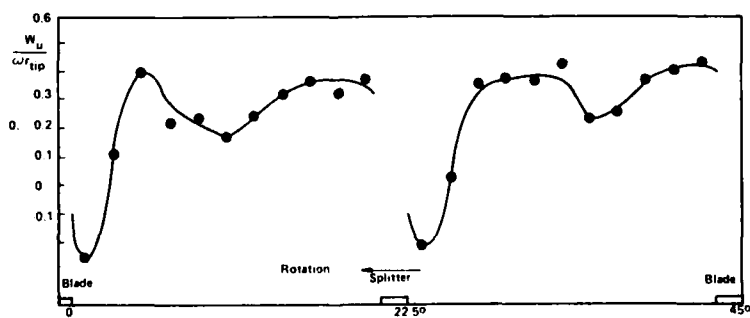


Fig. 4 Mean circumferential velocity profiles

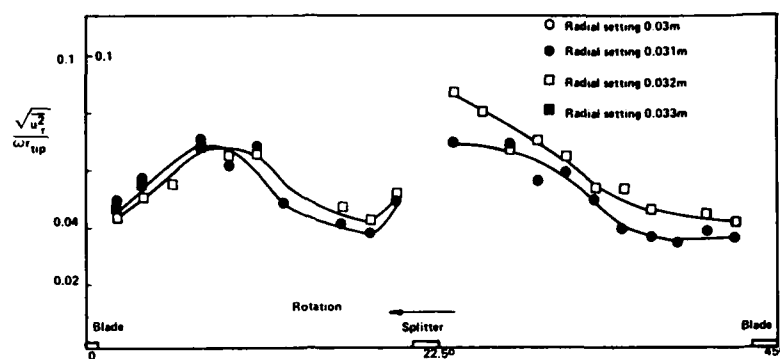


Fig. 5 RMS of the radial velocity component

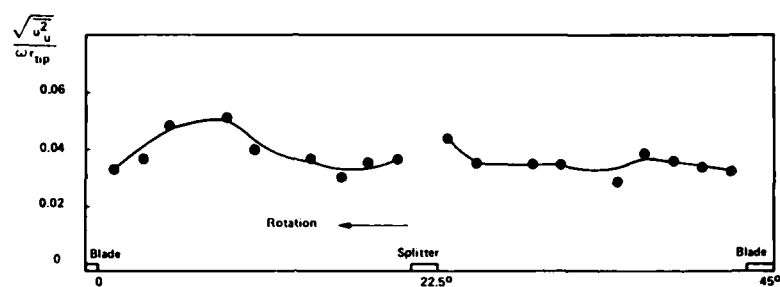


Fig. 6 RMS of the circumferential velocity component

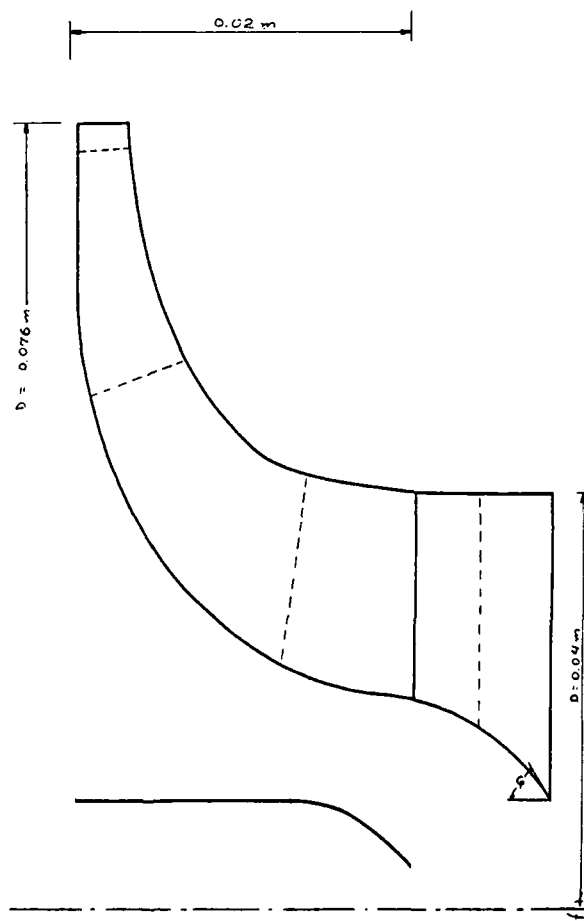


Figure 7. Meridional profile of the centrifugal compressor.

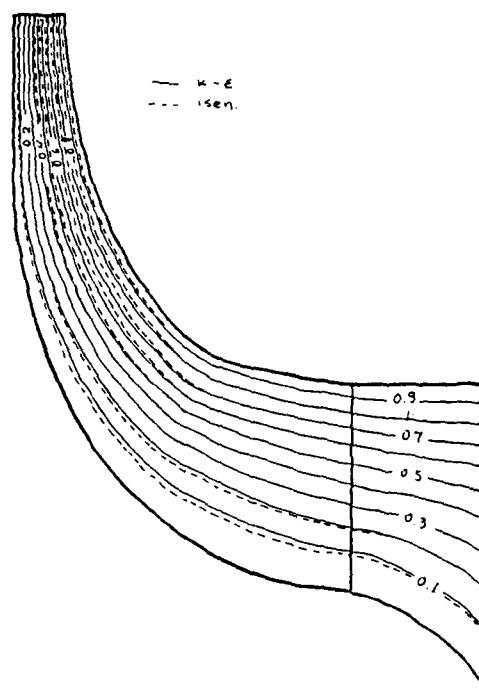


Figure 8. Streamline patterns for isentropic flow and predictions using the $k-\epsilon$ turbulence model.

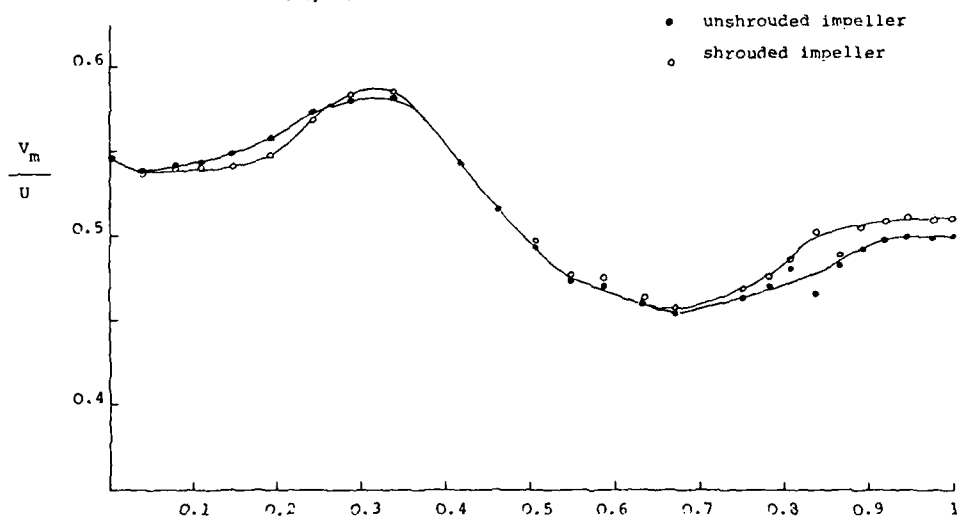


Fig. 9 Meridional velocity along the shroud

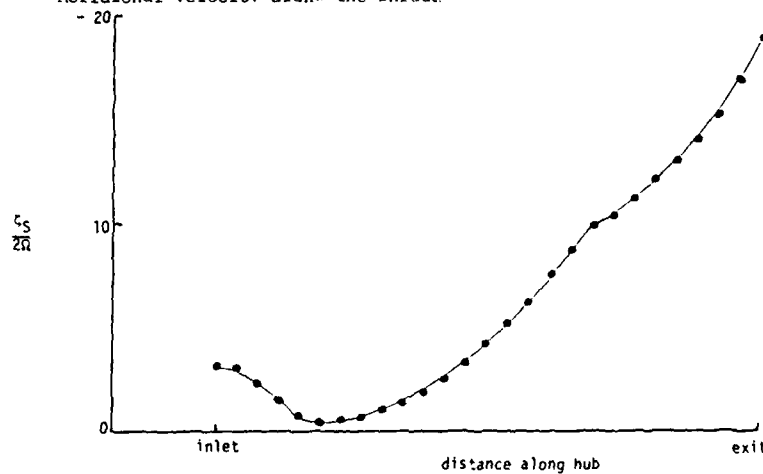


Fig. 10a Streamwise component of vorticity along the hub

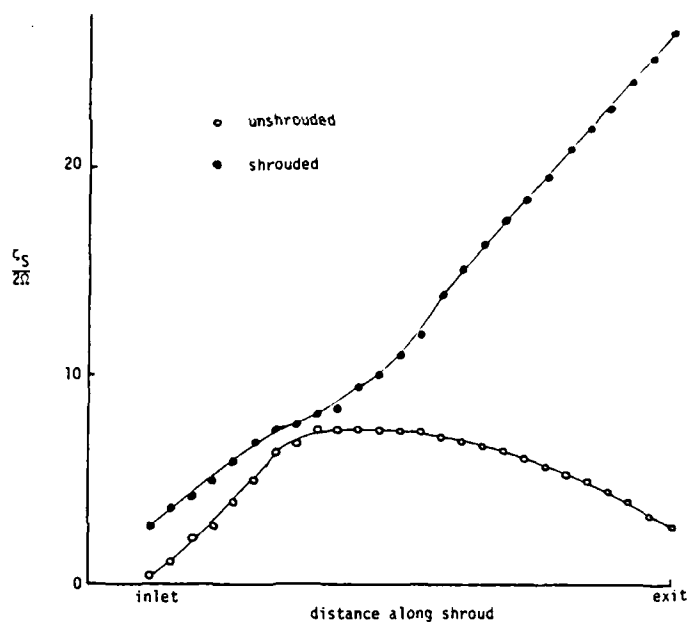


Fig. 10b Streamwise component of vorticity along the shroud

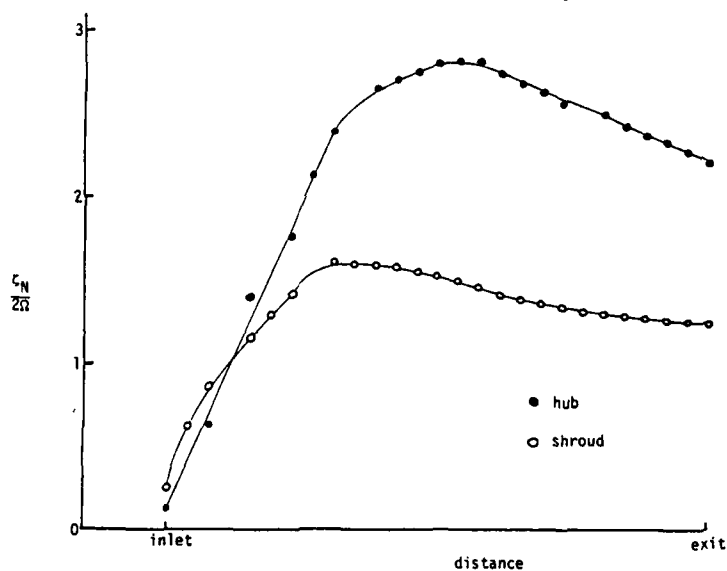
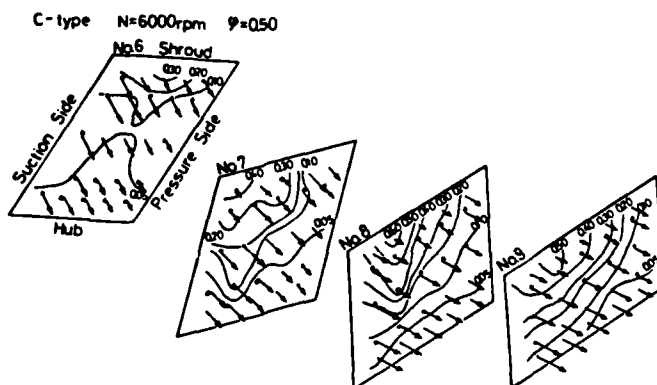


Fig. 11 Normal component of vorticity along the hub and shroud

Fig. 12 Three-dimensional flow patterns within impeller channel (C-type, $\varphi=0.50$)

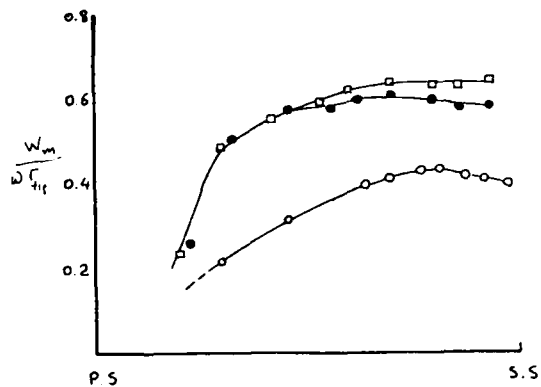


Fig. 13a Velocity profiles at station 6.

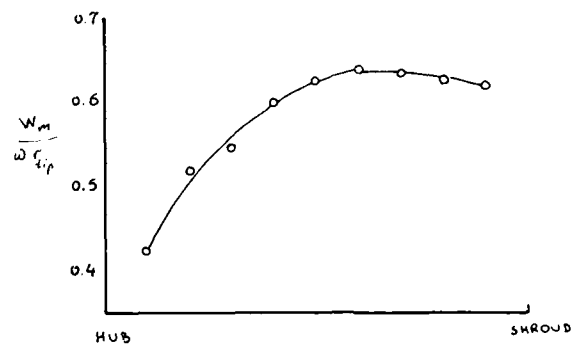


Fig. 13b Velocity profile at mid-channel station 6.

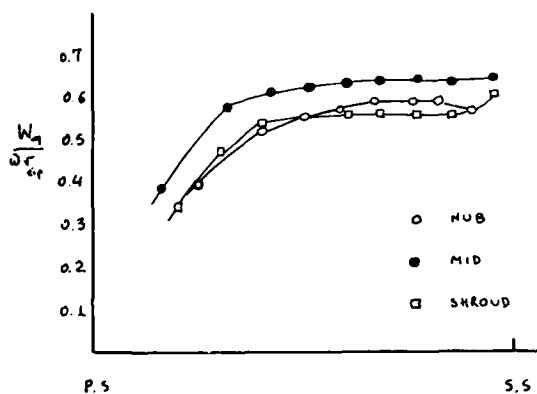


Fig. 13c Velocity profiles at station 9.

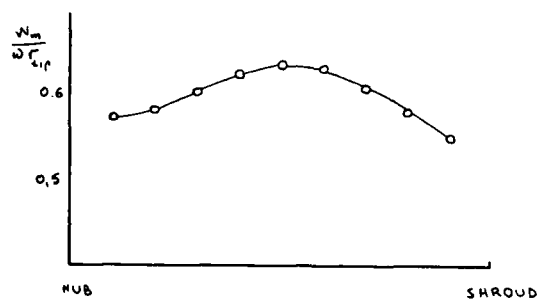


Fig. 13d Velocity profile at mid-channel station 9.

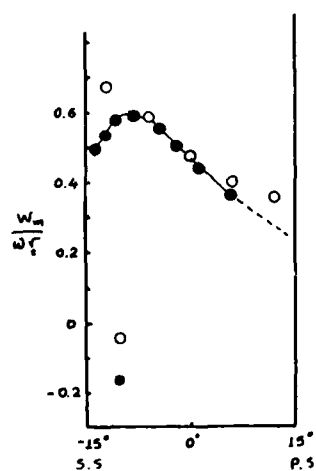


Fig. 14 Velocity distribution near the hub station 8.

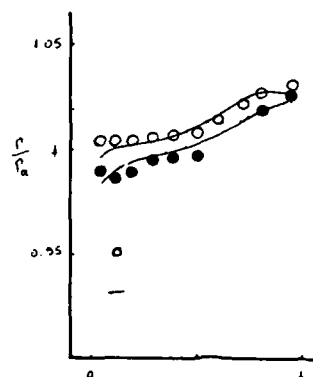


Fig. 15 Pressure distribution along the pressure and suction sides.

DISCUSSION

H. Weyer, DFVLR, Cologne, Ge

Could the author please comment on what kind of seeding was used in the experiments. Does the author realize that particles should not exceed 0.3 microns in order to avoid errors due to particles following the flow badly?

Author's Reply

It is well known that particle size control is necessary to avoid errors in laser doppler signal interpretation. It is also known that the largest size of particles which can be tolerated is a function of the maximum velocity encountered within the flow field.

In this application silicon oil was used for seeding with a mean droplet diameter of 2 μm . This was considered acceptable as the maximum velocity encountered was only 50 m/s.

ANALYSE EXPERIMENTALE DE L'ÉCOULEMENT DANS UN ÉTAGE DE MACHINE CENTRIFUGE

G. BOIS INGENIEUR
METRAFLU SARL
24 bis Chemin des Mouilles
69 130 Ecully, France

J.M. DUCHEMIN INGENIEUR
Société CREUSOT-LOIRE
B.P. 31 Cedex 71 208 Le Creusot, France

A. VOUILLARMET ASSISTANT
Ecole Centrale de Lyon
36 Route de Dardilly
69 130 Ecully, France

K.D. PAPAILIOU PROFESSEUR
Dept of Thermal Turbomachinery
National Technical University of Athens
Faculty of Mechanical Engineering
42 October 28th Street
Athens, Grèce

RESUME

On présente des résultats expérimentaux obtenus à la sortie des rouets et dans des diffuseurs lisses de deux compresseurs centrifuges avec et sans couvercle.

Deux méthodes de mesure sont ainsi comparées, l'une conventionnelle qui utilise des sondes de pression directionnelles, l'autre qui fait intervenir l'utilisation d'un système Laser.

A partir des résultats obtenus, une tentative d'analyse des écoulements secondaires est faite en prenant pour base les résultats d'un calcul méridien quasi-tridimensionnel. L'approche "écoulement secondaire" exploite les résultats déjà acquis pour le cas des machines axiales avec une prise en compte plus complète des termes supplémentaires qui interviennent dans la formulation.

ABSTRACT

EXPERIMENTAL FLOW ANALYSIS IN A STAGE OF CENTRIFUGAL MACHINERY

Experimental results obtained at the exit of the impellers and in the vaneless diffusers of two centrifugal compressors, with and without a cover plate, are presented.

Two measurement methods are compared : one is conventional and uses directional pressure probes ; the other rests on the use of a Laser system.

Based on the results obtained, an attempt is made at analyzing secondary flows, using the results of a quasi-three dimensional meridional calculation. The "secondary flow" approach uses the results already acquired for axial machines, taking fuller account of the additional terms appearing in the formulation.

I INTRODUCTION

Les deux dernières décennies ont vu un progrès considérable dans le domaine des compresseurs centrifuges, longtemps abandonnés au profit des compresseurs axiaux.

Afin d'améliorer les performances de ce type de machines, une clarification des idées a été rendue nécessaire devant l'impossibilité d'appliquer directement les modèles issus des expériences acquises dans le domaine des machines axiales. Le développement des moyens de mesure stationnaires, instantanés et embarqués a contribué en grande partie à cette clarification [1 à 10].*

De nombreux résultats d'essais ont ainsi permis une meilleure connaissance de l'écoulement et une meilleure compréhension des phénomènes. Cependant, ces essais s'appliquent en grande majorité soit à des compresseurs d'école basse vitesse, soit à des prototypes de haut de gamme. Par contre, le domaine des compresseurs centrifuges de type "process" dans lequel peut être classé le compresseur utilisé pour cette étude est relativement inexploré. Ce type de machines utilisé pour des applications terrestres se trouve, par sa gamme de fonctionnement, à mi-chemin des différentes machines précitées.

Les analyses expérimentales qui ont été menées visent deux objectifs. Le premier consiste à améliorer la prédiction du champ de caractéristiques de ce type de machines. Le second objectif qui se situe à plus long terme, est d'aborder les problèmes qui restent sans réponse en ce qui concerne le développement des écoulements visqueux, et les mécanismes de production des pertes dans les rouets de telles machines.

Pour mener ces études, la Société Creusot-Loire a développé et construit un étage de compresseur centrifuge correspondant à sa gamme de fabrication. Ce compresseur a été muni des équipements spécifiques nécessaires à une investigation détaillée de l'écoulement. Deux versions de la roue mobile ont été réalisées, l'une étant munie d'un couvercle et l'autre version n'en possédant pas.

Les mesures ont été effectuées sur le banc d'essais installé au laboratoire de Mécanique des Fluides de l'Ecole Centrale de Lyon.

* Les chiffres entre crochets correspondent aux références.

II OBJECTIFS DE L'ETUDE

Pour répondre à l'objectif concernant la prédiction du champ de caractéristiques nous nous sommes inspirés des travaux qui traitent le problème sous un aspect monodimensionnel. Ces travaux peuvent être décomposés en deux catégories : ceux qui traitent du niveau d'énergie transféré de la roue au fluide, et ceux qui s'intéressent à la manière dont s'effectue ce transfert c'est-à-dire à la qualité de l'énergie absorbée par le fluide. Pour ce qui est du premier point il nécessite la modélisation du coefficient de glissement pour lequel on peut citer les travaux de WIESNER [11], LIVSHITS [12], BALJE [13]. Quant au second, il prend en compte les divers modèles de pertes parmi lesquels on peut mentionner ceux de COPPAGE [14], JANSEN [15], et VAVRA [16].

Une comparaison de ces différents critères disponibles a été effectuée, et un choix a été opéré. Un effort particulier a porté sur l'analyse des caractéristiques en dehors du point nominal. Enfin, une évaluation des caractéristiques de l'étage sera également présentée en utilisant une analyse globale de l'écoulement dans le diffuseur lisse.

L'idée contenue dans l'objectif à long terme est de réaliser des progrès tangibles dans la conception des compresseurs centrifuges. Pour cela nous avons pensé qu'il était intéressant d'explorer la possibilité offerte par les modèles de calcul et les expériences effectuées dans le domaine des compresseurs axiaux. La formulation théorique qui a été développée jusqu'à maintenant à l'E.C.L. [17, 18] a notamment fait ressortir certains aspects originaux de l'écoulement visqueux dans une machine axiale, et a abouti à une méthode de calcul intégral-différentielle des écoulements secondaires à l'intérieur d'une grille d'aubes. Quelques résultats illustrant les performances de cette méthode seront présentés ici. Bien que nous soyons conscients de certaines limitations quant à la modélisation utilisée, nous avons décidé de nous en inspirer pour développer une méthode spécifiquement adaptée à une machine centrifuge.

La démarche ainsi suivie nous a conduit à mettre en oeuvre un calcul quasi-tridimensionnel de l'écoulement dit "sain", dont quelques résultats seront présentés. Les résultats de ce calcul doivent servir de base au développement théorique concernant l'écoulement visqueux, dont nous avons déjà tenté une première formulation [19].

Cependant, il faut conserver à l'esprit le fait qu'un calcul complet reste actuellement hors de portée de l'ingénieur, et que la seule possibilité qui nous reste est le développement de modèles de calcul utilisant plus ou moins de données semi-empiriques tirées de l'expérience. En effet, notre connaissance sur les écoulements visqueux fortement tridimensionnels, tels qu'ils se présentent dans une machine radiale, reste encore incomplète malgré les efforts qui ont été effectués en ce domaine notamment par JONHSON et MOORE [20]. Notre savoir concernant un écoulement stationnaire dans un repère fixe est déjà très limité. La présence de la force de Coriolis pour le cas tournant complique les choses de façon sérieuse comme le montrent les travaux de BRADSHAW [21, 22], JONHSON [23], PAPAILIOU [24], et BERTOGLIO et AL [25]. De plus, il semble que le caractère instationnaire de l'écoulement joue un rôle suffisamment important pour qu'un calcul stationnaire visqueux même complet ne donne pas une représentation de l'écoulement conforme à la réalité. Cet effet a notamment été mis en évidence par DEAN [26].

Ceci met l'accent sur la nécessité du développement de procédés de mesure donnant notamment accès à des informations sur le comportement de l'écoulement à l'intérieur du canal tournant de la roue mobile. Il faut de plus souligner la haute précision demandée aux mesures destinées à préciser quantitativement les caractéristiques d'un écoulement visqueux. Ce fait a été mis en évidence par l'équipe de turbomachines de l'Ecole Centrale de Lyon [27] lors de mesures effectuées sur un compresseur axial. Ces deux remarques apportent sa justification à l'utilisation de moyens de mesure sophistiqués telle l'anémométrie Laser.

Dans le cadre des objectifs précités, on présente après une description de l'installation et des moyens de mesure les résultats d'une analyse unidimensionnelle pour les deux versions du compresseur. Les essais détaillés qui ont permis cette analyse globale seront ensuite comparés à des résultats locaux obtenus par l'anémométrie LASER à la sortie de la roue mobile.

Ces résultats seront ensuite comparés avec des méthodes de prédiction quasi 3-D de l'écoulement qui constituent la base du développement d'une formulation des écoulements secondaires dans les compresseurs centrifuges.

III DESCRIPTION DE L'INSTALLATION ET DES MOYENS DE MESURE.

III.1-Le banc d'essai de compresseurs.

Le compresseur étudié a été monté sur le banc d'essais de compresseurs du laboratoire de Mécanique des Fluides de l'Ecole Centrale de Lyon. Ce banc a une puissance installée de 630 kw. Il se compose d'un moteur électrique à courant continu auquel sont adjoints deux multiplicateurs en série permettant d'obtenir une vitesse de rotation maximum d'environ 14000 tours/mn. Le circuit de décharge est constitué par une vanne de réglage, une vanne anti-pompage, et un venturi servant à la mesure du débit. La salle dans laquelle est implantée le compresseur servant de caisson d'alimentation, les conditions amont correspondent donc aux conditions atmosphériques.

L'ensemble des manoeuvres et de l'acquisition des données s'effectue par l'intermédiaire d'un ordinateur Hewlett Packard installé dans une salle de contrôle séparée.

III.2-Le compresseur centrifuge.

Comme nous l'avons déjà signalé les caractéristiques du compresseur d'essai de la Société Creusot-Loire, dont on trouvera une représentation schématique figure (1), correspondent aux gammes de fabrication généralement utilisées par le constructeur. Nous allons les énumérer brièvement ci-dessous.

- a) Le taux de compression de l'étage s'étale de 1.25 à 1.75.
- b) L'entrée de l'étage est axiale afin d'assurer des conditions aérodynamiques initiales correctes.
- c) Un pavillon d'entrée relativement long a cependant été placé afin d'obtenir des épaisseurs de couches limites pariétales suffisamment importantes à l'entrée de la roue mobile, telles qu'on les rencontre dans une machine multi-étagée.
- d) Le rouet réalisé répond à des critères industriels : encombrement axial faible, aubes du type "couchées en arrière" générées par des surfaces simples, et présence d'un couvercle.
- e) L'évolution de la largeur du canal permet de maintenir la section de passage sensiblement constante.
- f) La largeur de veine du diffuseur lisse purement radial est suffisamment importante pour permettre une exploration détaillée.
- g) La volute est du type industriel et permet d'étudier les éventuelles distorsions azimutales qui en résultent.
- h) Afin de mettre en évidence l'effet de jeu, et de permettre la réalisation de mesures par anémométrie laser un rouet sans couvercle a également été réalisé et étudié. Pour cette seconde version de la roue, seul un anneau a été conservé dans la partie axiale pour des impératifs de tenue mécanique des pales en rotation.
- i) Les principales caractéristiques géométriques et aérodynamiques de la machine sont présentées dans le tableau ci-après :

$\frac{b_1}{R_1}$ (-)	0,059
β_1 (deg)	63
N (tr/mn)	8000
Q (Kg/s)	6,5
Π (-)	1,75

Signalons enfin que pour permettre les essais Laser, le carter a été muni d'une fenêtre en verre disposée le long de sa génératrice verticale.

III.3 - Description et implantation de l'instrumentation.

a) Détermination des plans de mesure.

Les sections choisies pour effectuer les mesures de pression statique pariétale et réaliser les explorations de l'écoulement sont respectivement présentées figures (2) et (3). Le grand nombre de sections qui a été défini a permis d'obtenir le maximum d'informations à l'amont de la roue mobile et surtout dans le diffuseur lisse. Les prises de pression statique y sont réparties suivant le rayon et la circonférence et ce sur les deux flasques de ce diffuseur. Les explorations ne sont, elles, effectuées que pour une position azimutale.

b) Le choix des sondes d'exploration.

La grande précision de mesure nécessaire aux explorations des zones pariétales des machines axiales que nous avons précédemment réalisées [27] nous a donné une certaine expérience dans ce domaine. A la lueur de cet acquis nous avons utilisé deux types de sondes pour réaliser ces mesures. Celles-ci sont présentées figure (4). Il s'agit de sondes de pression directionnelles qui permettent de déterminer les valeurs de la pression totale et les caractéristiques du vecteur vitesse dans un plan, moyennant un étalonnage angulaire préalable pour plusieurs valeurs du nombre de Mach. Une perle de thermocouple insérée dans ces sondes donne également accès à la mesure de la température totale connaissant le coefficient de récupération.

La forme géométrique des deux sondes a été déterminée afin de pouvoir s'approcher au plus près des parois. La sonde cylindrique dite "droite" pouvant entrer à l'intérieur de son bossage permet la réalisation de mesures jusqu'au droit de la paroi extérieure de la veine. La sonde type "crochet" permet par contre d'approcher la paroi opposée au bossage. Cette dernière possède en outre une prise de pression qui peut être assimilée à une statique, et les résultats obtenus par son intermédiaire seront discutés. Notons que pour un même plan de sondage, il est possible d'obtenir une zone de recoupement des informations recueillies par les deux sondes. Ceci va nous permettre de minimiser les risques d'erreur de mesure.

Cependant la présence même de la sonde dans l'écoulement va induire un certain nombre d'erreurs de mesure dues à des effets de déplacement, de gradient et de blocage. Il est néanmoins possible par une analyse complète des résultats de restituer la cohérence des mesures, et de pouvoir faire confiance à la mesure au moins en ce qui concerne certains paramètres. Ce point particulier fait ressortir l'intérêt de posséder un moyen d'investigation tel que l'anémométrie Laser.

c) Le système d'anémométrie Laser.

La vélocimétrie Laser ne présente pas les inconvénients précités. Elle n'est notamment pas limitée par la vitesse de l'écoulement, et surtout elle n'y procure aucune perturbation. Outre qu'elle ne donne pas accès aux mesures de la pression et de la température,

il ne faut cependant pas non plus minimiser les problèmes nouveaux qu'elle soulève. Parmi ceux-ci nous pouvons citer la nécessité d'ensemencer l'écoulement et le coût relativement élevé des installations. La vélocimétrie Laser reste cependant un moyen d'investigation puissant, et le seul à permettre des mesures à l'intérieur de la roue mobile de compresseurs haute-vitesse, la solution consistant à embarquer des moyens conventionnels [10, 25] s'avérant très difficile à mettre en oeuvre lorsque la vitesse de rotation de la machine excède 3000 tours/mn.

La taille réduite du canal inter-aubes ou de la veine dans le diffuseur lisse des compresseurs radiaux, et la volonté d'obtenir des informations sur l'écoulement jusque dans les zones visqueuses pariétales nous ont fait opter pour un type de vélocimètre laser à temps de vol (TFV). En effet, si des mesures ont déjà été effectuées avec succès dans des compresseurs à grande vitesse avec des vélocimètres laser-Doppler (LDV) [28, 29], elles ont mis en lumière l'extrême difficulté qu'il y avait à s'approcher à une distance de moins de 10mm d'une paroi opaque. Si l'on excepte les quelques tentatives faites pour adapter la vélocimétrie LDV à la mesure dans de petites machines [30], la vélocimétrie TFV dont les bases ont été jetées par THOMSON [31] et TANNER [32] semble être la seule à permettre des mesures très près des parois (moins de 2mm) comme l'ont montrées les expériences effectuées au DFVLR [33], [34] et [35], ce que nous confirmons ici.

Il est de plus apparu que dans un souci technique et financier il n'était pas souhaitable d'acquérir une version commercialisée d'anémomètre, mais que nous devions en redessiner un. En effet, il devait s'adapter d'une part à la géométrie des compresseurs radiaux et du banc d'essais en notre possession, et utiliser au mieux les moyens d'acquisition déjà à notre disposition afin de diminuer le coût de l'installation, montrant de ce fait qu'il était possible, avec des moyens financiers raisonnables, de se doter d'un outil puissant aux performances acceptables.

L'anémomètre laser que nous avons réalisé est schématisé figure (5). La chaîne optique a été dessinée afin de répondre aux diverses contraintes géométriques, et a obtenir les caractéristiques désirées du volume de mesure. L'optimisation de ces caractéristiques prend en compte un certain nombre de paramètres qui sont énumérées ref [36].

Les caractéristiques retenues sont les suivantes : une distance entre les taches de convergence de 0.5 mm, une longueur axiale d'environ 0.4 mm, un demi-angle de convergence des faisceaux laser de 5 degrés et un diamètre de focalisation d'environ 15 μ m. La distance entre ce volume de mesure et la lentille frontale de l'anémomètre est d'environ 210 mm.

Le support sur lequel repose l'ensemble du vélocimètre est en granit ce qui lui assure une grande inertie thermique et une meilleure rigidité qu'un support en acier pour un poids trois fois moins important. Le positionnement du point de mesure s'effectue par déplacement de tout cet ensemble.

La source lumineuse est constituée d'un laser Argon qui peut fournir 2.4 Watts sur la raie verte à $\lambda = 5145\text{\AA}$. Cette puissance donne une marge de sécurité importante par rapport à la centaine de milliwatts nécessaire à l'expérience.

Un schéma synoptique de l'électronique est donné sur la figure (6). Les signaux issus des deux photomultiplicateurs sont, après amplification, envoyés respectivement sur les entrées START et STOP d'un compteur qui travaille en mesure d'intervalle de temps entre deux entrées. Les données sont ensuite stockées puis traitées à l'aide du calculateur Hewlett-Packard déjà mentionné.

Afin d'ensemencer l'écoulement deux générateurs de particules ont été utilisés. Le premier utilise la dispersion de poudre de dioxyde de silicium à partir d'un lit fluidisé, et le second permet la production de fumée par combustion lente d'huile de type vaseline.

L'anémomètre laser a été préalablement testé sur une configuration de jet pariétal bidimensionnel dont la section de sortie était de 80x4mm. Les résultats présentés figures (7) et (8) démontrent sa bonne résolution longitudinale ce qui permet d'une part d'effectuer des mesures dans des veines de faible dimension en présence de gradients importants et d'autre part de pouvoir approcher les parois à un millimètre au moins. De plus, la précision de mesure est encore acceptable dans des écoulements fortement turbulents (intensité de turbulence dépassant 30 %).

IV PRESENTATION DES RESULTATS ET ANALYSE

De manière à couvrir le maximum du champ de caractéristiques, 8 points de fonctionnement ont été choisis pour effectuer les explorations détaillées par l'intermédiaire des sondes. Ces points, portés figure (9), ont été retenus pour les deux versions du compresseur avec et sans la présence du couvercle.

Nous présenterons principalement les résultats des sondages concernant le diffuseur lisse pour lequel les 2 versions seront systématiquement comparées. A titre informatif, la figure (10) présente l'évolution de la vitesse méridienne en amont de la roue mobile.

Les résultats des sondages en sortie de roue mobile pour la version sans couvercle seront ensuite comparés à ceux obtenus à l'aide de l'anémométrie LASER. Cette comparaison portera sur le point nominal de fonctionnement.

IV.1 - Les caractéristiques aérodynamiques dans le diffuseur lisse.

Les caractéristiques moyennes de l'écoulement sont déduites des quantités locales telles que les distributions de pression totale P_0 , température totale T_0 et angle absolu α respectivement présentées figures (11), (12) et (13). On notera les possibilités de recouplement des valeurs obtenues par les 2 types de sonde et la cohérence des résultats.

a - L'évolution des caractéristiques moyennes dans le diffuseur lisse
Pour les 2 versions du compresseur, on présente fig (14) les évolutions des pres-

sions totales, de l'angle absolu et de RV_0 pour un point de fonctionnement. Le premier plan de sondage après le plan de sortie de la roue mobile est situé à un rapport de rayon $\frac{R}{R_2} = 1.068$. Ceci veut dire que l'on ne pourra obtenir les caractéristiques dans le plan de sortie du rouet qu'à l'aide d'une extrapolation. Le cas de la quantité PV_0 peut alors être examiné car il doit satisfaire à l'équation d'énergie et recouper le niveau de température totale mesuré.

Les écarts les plus importants enregistrés après dépouillement sont de l'ordre de 1% comme on peut le voir sur la figure (15) en considérant bien entendu la zone "saine" de l'écoulement dans le diffuseur lisse pour $\frac{R}{R_2} = 1.068$.

b) Le choix des pressions statiques

On connaît les difficultés qui surgissent lorsque l'on veut mesurer une pression statique surtout dans des écoulements délivrés par la roue mobile d'un compresseur centrifuge.

La tendance consiste à prendre en compte des pressions statiques pariétales et généralement une distribution linéaire est adoptée entre les 2 flasques du diffuseur. Cette hypothèse donne effectivement de meilleurs recoupements du débit dans notre cas, comme on peut le voir figure (16). Il est d'ailleurs nécessaire, pour un recoupement correct, de prendre en compte les éventuelles distorsions enregistrées fig (17). Cette hypothèse de distribution linéaire de pression statique a pu être également vérifiée par un calcul d'équilibre d'écoulement. Ce calcul prend en compte les distributions mesurées de pression totale, température totale et angle absolu. Les courbures sont négligées. La convergence s'effectue sur le débit imposé et on en déduit les pressions statiques locales. Le recoupement est très bon avec les mesures des pressions pariétales comme on peut le voir figure (18).

Cela confirme, enfin, la confiance que l'on peut avoir dans les mesures de P_0 , T_0 et α . La mesure des pressions statiques obtenues par les sondes reste donc un problème. Il faut cependant noter que ces mêmes sondes ont donné des résultats très satisfaisants dans le cas de veines axiales plus larges [27].

IV.2 - Analyse des résultats.

IV 2.1 - L'aspect mono-dimensionnel.

a) Transfert d'énergie

Etant donné la possibilité que nous avons de comparer les performances d'une même machine avec et sans la présence d'un jeu, le choix des critères de pertes proposés dans la littérature ouverte s'est porté sur les auteurs qui avaient tentés une classification des pertes roue mobile comme JANSEN [15] ou VAVRA [16] en particulier. Notons ici l'importance des termes qui prennent en compte, dans ces formulations, la décélération relative de l'écoulement. Ceci met l'accent sur la bonne connaissance du coefficient de blocage nécessaire pour ce type de prédiction.

Le calcul du diffuseur lisse prend en compte les effets d'éclatement brusque à la sortie de la roue mobile et le calcul des effets du "jet-sillage" proposé par DEAN et SENOO [37] étendu à un écoulement compressible [38] et [39]. Les modélisations de la largeur de la zone de sillage et du rapport de débit ont été introduites d'après les travaux de GREGG [40] présentés fig (19) et (20).

b) Les caractéristiques en dehors du point nominal.

L'essentiel porte sur la bonne détermination de l'évolution du coefficient de glissement. D'après les travaux de GREGG [40], il est possible de déduire une courbe empirique présentée fig (21). Les résultats expérimentaux confirment la tendance observée. L'analyse qui consiste à faire l'hypothèse d'un angle relatif constant en sortie de roue mobile quelque soit le point de fonctionnement donne de bons résultats pour le cas analysé fig (21).

c) Les prédictions des caractéristiques moyennes.

On présente figure (22) la comparaison du champ de caractéristiques sortie roue mobile mesuré et calculé pour les deux versions du compresseur étudié. En ce qui concerne l'étage (plan de sortie du diffuseur lisse) les résultats sont présentés figure (23). On peut estimer que la prédiction est correcte surtout si l'on considère que les critères ont été fixés uniquement au point nominal de fonctionnement.

L'analyse des résultats dans le diffuseur lisse conduit à déterminer un coefficient de frottement C_f différent pour les 2 versions comme le montre la figure (14). Les travaux de SENOO [41] et [42] ont déjà montré l'importance de l'écoulement délivré par la roue mobile sur le fonctionnement du diffuseur lisse, et l'approche proposée par SENOO confirme le caractère trop global d'une analyse qui ne prend en compte qu'un coefficient de frottement moyen.

IV 2.2 - Les caractéristiques locales de l'écoulement délivré par la roue mobile. Comparaison avec les mesures LASER.

Pour des raisons de simplification, cette analyse portera sur le point nominal de fonctionnement des 2 versions étudiées.

a) Le résultat des sondages

Dans le plan de mesure le plus proche du plan de sortie du rouet on constate des différences notables sur les distributions des pressions et des températures totales entre les 2 versions du même compresseur fig (24). Il reste cependant que les distributions de l'angle absolu α et du rendement isentropique sont comparables du moins dans une zone où

les effets visqueux sont négligeables fig (25). Les différences que l'on constate dans les zones pariétales, en particulier l'augmentation de la vitesse tangentielle liée aux variations de l'angle α dans le cas de la roue sans couvercle, confirment l'analyse de SENOO et al (43) sur l'augmentation du coefficient de glissement. Nous avons tiré de la réf (43) une courbe fig (26) où nous figurons le cas du compresseur testé. Le rendement, par contre est plus faible pour le cas sans couvercle étant donné la présence du jeu. On peut remarquer que la corrélation proposée par GREGG (40) présentée figure (27) est satisfaisante.

b) Les essais laser

Trois sections de mesure ont été explorées pour les rapports de rayon $R/R_2 = 1.018, 1.059$ et 1.107 .

Les histogrammes de probabilité de l'angle absolu de l'écoulement à la sortie du rouet, présentés figures (28) et (29), montrent une fluctuation très importante de cet angle (plus de 40° pour le cas le plus défavorable). Ce phénomène peut s'expliquer en grande partie par la très grande inhomogénéité circumférentielle présentée par l'écoulement à la sortie du rouet dans le repère relatif aux aubages. Cette inhomogénéité est en générale d'autant plus marquée que l'on se situe à proximité de la sortie de la roue d'une part, et du couvercle d'autre part [20] ce qui doit se traduire dans le repère absolu par une fluctuation de vitesse et d'angle équivalente. Cette explication semble être valable car les fluctuations d'angle enregistrées sont effectivement d'autant plus importantes que l'on se rapproche d'une part de la sortie du rouet et d'autre part du couvercle, même si les effets du jeu dans cette zone sont également très importants. Seule une mesure synchronisée avec la rotation de la machine permettrait de confirmer définitivement cette hypothèse.

En ce qui concerne les répartitions d'angles moyens, présentées figure (30), nous pouvons faire plusieurs remarques. Tout d'abord les valeurs des angles pour les deux sections sont à peu près identiques, au demi degré près, ce qui est en accord avec la physique de l'écoulement. La seconde remarque concerne la comparaison, présentée pour $R/R_2 = 1.059$, des mesures laser avec des mesures provenant d'une sonde directionnelle de pression. L'allure générale des deux courbes est tout à fait comparable, mais on enregistre entre les deux un décalage d'environ quatre degrés. Ce décalage systématique ne peut s'expliquer que par un mauvais repérage angulaire initial du volume de mesure par rapport à la machine.

Les répartitions de vitesses absolues et leur comparaison avec les mesures par sonde de pression, présentées figure (31), sont elles tout à fait satisfaisantes. L'écart maximum enregistré est voisin du pour cent, et les courbes sont comparables jusqu'à une distance d'un millimètre des deux parois. Notons cependant qu'aucun sondage avec une sonde de pression n'ayant été effectué dans le plan le plus proche de la roue, les valeurs portées sur la figure (31) ont été extrapolées sur chaque ligne de courant ce qui introduit une certaine imprécision dans des zones pariétales. Cette extrapolation donne cependant une idée des niveaux de vitesse et peut être considérée comme assez précise, au moins dans la zone médiane.

Les répartitions de fluctuations de vitesse, présentées figure (32), n'ont pas été comparées à celles obtenues avec des moyens conventionnels. Les évolutions enregistrées semblent cependant correctes. On assiste en effet à une légère augmentation de la fluctuation avec le rayon (effet de gradient de pression), et le relèvement de cette fluctuation dans les zones pariétales est en accord avec l'épaississement enregistré de la couche visqueuse.

V ANALYSE THEORIQUE

V.1 - Le calcul de l'écoulement "sain" par la méthode des éléments finis.

Un programme de calcul méridien a été développé dans le laboratoire pour obtenir les caractéristiques de l'écoulement "sain" dans un compresseur centrifuge [44] et [45]. Les résultats du calcul du compresseur ont été comparés avec ceux d'un programme déjà mis en place à CREUSOT-LOIRE (méthode de courbure des lignes de courant), et dont on peut voir un exemple de résultat figure (33). Les blocages dus aux couches limites pariétales ont été introduits ainsi qu'une distribution de glissement et de perte sur la largeur du canal de sortie afin d'obtenir un réseau de lignes de courant qui est le point de départ de l'approche "écoulement secondaire".

Les distributions de vitesse sur les aubages déduites de ces deux calculs quasi-tridimensionnels ont été comparées avec celles obtenues avec une méthode matricielle développée par KATSANIS [46]. Cette comparaison est présentée figure (34) pour deux lignes de courant caractéristiques au moyeu et au carter.

V.2 - La prédiction des caractéristiques relatives de l'écoulement sain.

Cette prédiction porte sur les valeurs de l'angle relatif et de la pression totale relative en sortie de roue.

a) L'angle relatif

La prédiction de l'angle relatif β_r , pour chaque ligne de courant déduite du calcul méridien, utilise le calcul circumférentiel de KATSANIS [46] et les travaux de MILLER [47]. Les résultats sont présentés figure (35), et on remarque une très bonne concordance de la distribution d'angle β_r dans l'écoulement sain obtenu par ce type d'analyse, avec les mesures.

b) La pression totale relative fig (36)

A partir de la répartition de vitesse déduite des analyses précédentes il est pos-

sible de calculer les caractéristiques des couches limites se développant sur les aubes à l'aide d'un calcul intégral prenant en compte les effets de courbure et de CORIOLIS [24]. Les résultats ne sont pas encore disponibles mais les premiers calculs tentés donnent des résultats très encourageants.

V.3 - Formulation théorique de la prédiction des écoulements secondaires dans un compresseur radial.

Une formulation théorique concernant l'écoulement visqueux qui se développe dans les zones pariétales d'une grille d'aubes a été développée, incluant au système d'équations final le cadre semi-empirique nécessaire à la fermeture du problème [17]. Cette formulation a été testée de manière satisfaisante en présence d'un jeu [18]. Cette méthode a également été appliquée telle quelle au cas d'un compresseur axial transsonique avec la présence d'un jeu [19]. Quoique non conçue pour cela, et malgré les nombreuses approximations qui ont dû être faites afin de l'appliquer à un cas compressible sur machine, elle a donné des résultats très encourageants fig (37).

C'est cette méthode que nous avons essayé d'étendre à l'écoulement compressible spécifique d'un compresseur centrifuge [36] et que nous présentons brièvement ici.

a) Modèle des trois zones

L'hypothèse consistant à diviser l'écoulement dans le compresseur en trois zones distinctes (modèle dit "des trois zones") a été retenue pour cette formulation, bien que nous ne rejetions pas l'éventualité de machines ne s'y adaptant pas. Des mesures effectuées en sortie du compresseur Creusot-Loire fig (36) tendent cependant à confirmer la validité de ce modèle, au moins en dehors du passage aubé et pour cette gamme de machines même en présence d'un jeu.

b) Equations utilisées.

Nous avons fait usage pour la résolution du problème des équations intégrales de quantité de mouvement moyennées dans la direction circonférentielle, d'une équation régissant le développement de la composante longitudinale moyenne de vorticit   dite secondaire et de l'équation d'entraînement de HEAD. Ces équations sont développées dans les systèmes de coordonnées orthogonales curvilignes adaptés à la géométrie de la machine fig (38). Les équations de HEAD et de quantité de mouvement sont à caractère parabolique et régissent l'évolution de la couche limite dans son ensemble (forme intégrale) dans la direction longitudinale. L'équation de vorticit   aborde elle le problème dans la direction transversale sous une forme différentielle, et restitue au problème son caractère elliptique. Ces équations sont présentées en Annexe 1.

c) Cadre semi-empirique

L'information semi-empirique nécessaire à la fermeture du problème peut   tre divis  e en six points :

- . le profil longitudinal de vitesse moyenne.
 - . le raccordement à la paroi du profil transversal de vitesse moyenne.
 - . la loi de frottement à la paroi
 - . l'information relative à l'équation d'entraînement
 - . la relation régissant la variation de la masse volumique
 - . l'estimation des termes additionnels provenant d'une part des intégrations successives et d'autre part du degré supérieur d'approximation utilisé dans cette formulation.
- Ce cadre semi-empirique est pour le moment issu de l'expérience accumulée dans le domaine de la grille d'aubes. Seules des mesures précises, que nous comptons obtenir à l'aide de l'an  mom  trie laser, dans la roue mobile d'un compresseur radial nous permettront de contr  ler la validit   de ces relations, et de les modifier si besoin est. Nous pouvons cependant d  j  , à la lueur des r  sultats exp  rimentaux obtenus, faire quelques remarques.

En ce qui concerne le profil longitudinal de vitesse moyenne, une famille de profils bidimensionnelle à deux param  tres a   t   retenue. Cette famille propos  e par KUHN et NIELSEN [49] d  crit de fa  on acceptable le profil mesur   juste en aval du rouet du compresseur test   fig (39), et ce r  sultat est encourageant m  me s'il n  cessite une confirmation à l'int  rieur du passage interaubes.

En ce qui concerne les termes additionnels explicit  s en Annexe 1, ce sont les composantes ΔD_{1u} et ΔD_{1m} du d  ficit de force d      la variation de la force d'aubage à l'int  rieur de la couche visqueuse, les composantes ΔD_{2u} et ΔD_{2m} de la variation des fluctuations circonf  rentielles des param  tres de l'  coulement, la quantit   ΔD_{3m} qui r  sulte de la variation de la pression statique dans la direction normale à la paroi et les composantes ΔD_{4u} et ΔD_{4m} qui sont issues du d  gr   sup  rieur d'approximation utilis   dans cette formulation.

Une relation liant les deux composantes du d  ficit de force mise en   vidence par PAPAILIOU et al [50] nous permet de les   liminer de la formulation.

Le terme de d  ficit de pression statique a   t   n  glig  , hypoth  se qui a   t   v  rifi  e en grille et sur compresseur axial transsonique. Notons qu'une v  rification sur machine radiale est rendue extr  mement difficile car les mesures de pression statique dans les veines de petites dimensions telle qu'on les rencontre dans ce type de machine s'av  rent tr  s d  licates.

Aucune mod  lisation n'existe actuellement concernant les termes de fluctuations, bien que leur importance reste tr  s controvers  e. La compr  hension de ph  nom  nes complexes parmi lesquels nous pouvons citer la migration du fluide à basse   nergie du disque vers le couvercle dans les zones proches des aubes et la structure jet-sillage est indispensable avant de pouvoir esp  rer mod  liser correctement ces termes.

Quant aux termes supplémentaires apparaissant dans notre formulation et qui prennent notamment en compte les gradients normaux de vitesse de l'écoulement sain, les courbures des lignes de courant de ce même écoulement et la présence de la force de CORIOLIS, ils ne constituent pas des inconnues supplémentaires du problème. Ils sont en effet parfaitement déterminés lorsque les deux profils de vitesse sont connus, et seront injectés avec un pas de retard dans la procédure itérative de calcul. Nous avons évalué ces termes pour le cas du compresseur Creusot-Loire. Nous avons pour cela utilisé, d'une part les résultats d'un calcul méridien de l'écoulement sain, et d'autre part ceux d'un calcul des couches visqueuses pariétales simplifié, tel qu'il a été développé pour une grille d'aubes. Les deux termes additionnels $\Delta D_{v,u}$ et $\Delta D_{v,w}$ ont été calculés à partir de ces données. Leurs évolutions à travers le passage inter-aubes sont données figure (40).

Enfin nous présentons figure (41) une comparaison entre les valeurs mesurées des écarts de β dans les couches visqueuses pariétales par rapport à l'écoulement sain, et celles obtenues par un calcul simplifié (incompressible et sans termes supplémentaires $\Delta D_{v,u}$). La concordance est bonne dans ce cas précis. Notons cependant que l'existence du profil transversal de vitesse lié à cette variation de β dans ce cas est en majeure partie explicable par le changement de repère à l'entrée du rouet.

VI - CONCLUSIONS

Des mesures détaillées des caractéristiques de l'écoulement délivré par la roue mobile d'un compresseur centrifuge ont été effectuées. Ces essais ont porté sur des configurations de rouet possédant et ne possédant pas de couvercle. Les tentatives de restitution du champ de caractéristiques de l'ensemble de l'étage (roue et diffuseur lisse) ont donné de bons résultats en utilisant des critères globaux de pertes et de glissement y compris pour les zones de fonctionnement hors adaptation.

Les résultats obtenus en sortie de roue mobile par des moyens conventionnels de mesure ainsi que par une technique d'anémométrie LASER dans le cas de la roue sans couvercle, nous confortent dans l'idée, qu'au moins pour ce type de machines, l'analyse de l'écoulement peut s'appuyer sur le modèle dit des "trois zones" tel qu'il est développé dans le cas des machines axiales.

La prévision des caractéristiques de l'écoulement sain a été abordée en utilisant un programme de calcul quasi 3-D qui utilise la méthode des éléments finis. L'évaluation des écoulements secondaires, même si elle fait encore appel à des simplifications a donné des résultats encourageants.

Une formulation plus complète a alors été tentée pour le cas de machines radiales. Ceci devrait permettre, en s'appuyant sur des mesures LASER à l'intérieur du passage inter-aubes de telles machines, d'en tester l'extension possible pour une plus large gamme de machines.

- 1 ACOSTA A.J.
"An experimental and theoretical investigation of two dimensionnal centrifugal pump impellers" trans. ASME july 1954
- 2 ACOSTA A.J & BOWERMAN R.D.
"An experimental study of centrifugal pump impellers" Trans. ASME - November 1957
- 3 FOWLER H.S.
"The distribution and stability of flows in a rotating channel" Trans. ASME J. of Eng for Power - July 1968
- 4 FOWLER H.S.
"Some measurements of the flow pattern in a centrifugal compressor impeller" ASME Paper 65 WA/GTP 7 April 1965.
- 5 MOORE J.
"Effects of Coriolis on turbulent flow in rotating rectangular channels" Gas Turbine Laboratory M.I.T. Report nb 89 January 1967.
- 6 MOORE J.
"A wake and an Eddy in a rotating radial-flow passage".
Part I : "Experimental observations"
Trans ASME - J. of Eng for Power. July 1973.
- 7 HOWARD J.H.G. & LENNEMANN E.
"Measured and predicted secondary flows in a centrifugal impeller".
Trans ASME J. of Eng for Power . January 1971.
- 8 HOWARD J.H.G. & KITTNER C.W.
"Measured passage velocities in a radial impeller with shrouded and unshrouded configurations"
Trans ASME J.of Eng for Power . April 1975.
- 9 MIZUKI S., ARIGA I & WATANABE I.
"Investigation concerning the blade loading of centrifugal impellers"
ASME Publication nb 74-GT-143-1974
- 10 MISUKI S, ARIGA I & WATANABE I.
"A study on the flow mechanism within centrifugal impeller channels".
ASME Publication nb. 75-GT-14-1975.
- 11 WIESNER F.J.
"A review of slip factors for centrifugal impellers".
Trans ASME Oct 1967 pages 558-569
- 12 LIVSHITS & P."The circulation factor for centrifugal compressor wheel".
Teploenergetika 1955.
- 13 BALJE O.E. "A contribution to the problem of designing radial turbomachines".
Trans ASME May 1952.
- 14 COPPAGE ET al. "Study of supersonic radial compressors for refrigeration and pressurization systems". WADC Report n°55. 257 Dec 1956.
- 15 JANSEN W. "A method for calculating the flow in a centrifugal impeller when entropy gradients are present". Inst Mec. Eng. Int Aerodynamics
- 16 VAVRA M.H. "Advanced compressors"
AGARD LS39 -1970-
- 17 COMTE A. "Calcul des écoulements secondaires à l'intérieur du canal d'une grille d'aubes".
Thèse de Docteur Ingénieur LYON I juillet 1978
- 18 OHAYON G. "Contribution à l'étude des écoulements secondaires dans les compresseurs axiaux, avec effets du jeu radial".
Thèse de Doctorat 3è cycle. LYON I. juillet 1979.
- 19 PAPAILIOU K.D. "Viscous Flows in centrifugal compressors VKI LS 95 Industrial centrifugal compressors February 21-25 1977.
- 20 JOHNSON M.W. & MOORE J.
"The development of wake Flow in a centrifugal Impeller".
ASME Publication. 79.G.T. 152.
- 21 BRADSHAW P.
"The analogy between streamline curvature and Boyancy in turbulent shear flow".
J. of Fluid Mech. Vol 36 part 1 -1969-
- 22 BRADSHAW P.
"Effects of streamline curvature on turbulent flow".
AGARD ograph nb 169 August 1973.

- 23 JONSTON J.P.
"The suppression of shear turbulence in rotating systems. Turbulent shear flow".
AGARD CP 93 71.
- 24 PAPAILIOU K.D.
"The coriolis force influence when we calculate Turbulent boundary layers. in
centrifugal compressors" Conference presented at International conf. on
Gas Turbines HAIFA ISRAEL juillet 1979.
- 25 BERTOGLIO J.P. , CHARNAY G. & MATHIEU J.
"Effets de la rotation sur un champ turbulent cisailé : application au cas
des turbomachines". Journal de Mécanique Appliquée 1980.
- 26 DEAN R.C.
" On the necessity of unsteady flow in fluid machines" Trans ASME
J. of Basic Eng March 1959.
- 27 BOIS G., LEBOEUF F., COMTE A. & PAPAILIOU K.D.
"Experimental study of the behaviour of secondary flows in a transsonic compressor"
AGARD CP 214 September 1977.
- 28 WEYER H.
"Pressure measurements in fluctuating turbomachinery flows". VKI LS 78 April 1975.
- 29 ECKARDT D. "Instantaneous measurements in the jet-wake discharge flow of a
centrifugal compressor impeller". Trans ASME j. of Eng for Power July 1975.
- 30 RUNSTADLER P.Q & DOLAN F.X.
"Design, development and test of a Laser velocimeter for high speed turbomachinery"
Proceedings of the LDA symposium. Copenhagen 1975.
- 31 TANNER L.H.
"A particle timing Laser velocity meter"
Optics and Laser Technology June 1973.
- 32 THOMPSON D.H.
"A tracer-particule fluid velocity meter incorporating a Laser".
j. of Scientific Inst. j. of Ph. E series 2 vol 1 1968.
- 33 SCHODL R. "A laser dual focus velocimeter for Turbomachines applications"
VKI LS 78 April 1975.
- 34 SCHODL R. " Laser two focus velocimetry (L2F) for use in aeroengines "
AGARD LS nb 90 - September 1977
- 35 ECKARDT D.
"Detailed flow Investigations within a high speed centrifugal compressor impeller "
76 FE 13. 1976.
- 36 VOUILLARMET A.
"Contribution à l'étude et à la compréhension de l'écoulement visqueux dans un
compresseur centrifuge" Thèse de Docteur Ingénieur - Lyon I Oct 1979
- 37 DEAN R.C. & SENOO Y. "Rotating wakes in Vaneless diffusors".
Trans ASME j. of Basic Eng Sep 1960 pages 563-574.
- 38 VAN DEN BRAEMBUSSCHE R.
"Flow modelling and aerodynamic design technique for centrifugal compressors".
VKI - LS 95 On Industrial Centrifugal compressors". February 1977.
- 39 PAPAILIOU K.D., VOUILLARMET A. & BOIS G.
"Analyse monodimensionnelle d'un étage de compresseur centrifuge".
Contrat Creusot-Loire/Metraflu n° 06/530 908 C 57 Oct 1975.
- 40 GREGG P.G. "On prediction of the performance of centrifugal compressors" VKI PR
70 . 272 (1970).
- 41 SENOO Y. KINOSHITA Y. & ISHIDA M.
"Asymmetric flow in vaneless diffusors of centrifugal Blowers" 1976
joint gas turbine and Fluid Engineering Division conference.
- 42 SENOO Y. & KINOSHITA Y. "Influence of Inlet Flow conditions and geometries of
centrifugal Vaneless Diffuser on critical Flow angle for Reverse flow" 1976
joint gas turbine and Fluid Engineering Division conference.
- 43 SENOO Y., MARUYAMA S., KOIZUMI T. & NAKASE Y.
"Viscous effects on slip factor of centrifugal Blowers" Journal Eng Power
January 1974. pages 59-65

- 44 HONG TUAN HA A.
"Développement d'un programme de calcul de l'écoulement dans le plan méridien d'une turbomachine radiale par la méthode des éléments finis."
Rapport de DEA ECL 1977.
- 45 HONG TUAN HA A.
"Application de la théorie des éléments finis à l'analyse de l'écoulement moyen dans une turbomachine radiale".
Thèse de Docteur Ingénieur LYON I Juillet 1979.
- 46 KATSANIS Th & Mc NALLY W.D.
"Fortran Program for calculating velocities and streamlines on a Blade-to-Blade stream surface of a tandem Blade turbomachine" NA-SA TND 5044.
- 47 MILLER M.J.
"Estimations of deviation angle axial flow compressor Blade Sections using inviscid flow solutions" NASA TND 7549 1974.
- 48 LEBOEUF F., COMTE A. & PAPAILIOU K.D.
"Calculations concerning the secondary flows in compressor bladings. Secondary flows in turbomachines". AGARD CP 214 March 1977.
- 49 KUHN GD & NIELSEN J.N.
"Prédiction of turbulent separated boundary layers".
AIAA 6th fluid and plasma dynamics conference July 1973.
- 50 PAPAILIOU K.D., FLOT R. & MATHIEU J.
"Secondary flows in compressor bladings" ASME PAPER 76 GT 57 1976
- 51 TAILLAND A.
"Contribution à l'étude d'un jet plan dirigé tangentiellement à une paroi plane"
Thèse de Docteur ès Sciences - LYON I - 1970.

REMERCIEMENTS

Nous tenons à remercier la Société Creusot-Loire et la Délégation Générale de la Recherche Scientifique et Technique (DGRST), qui ont financé ces travaux.

ANNEXE 1

Nous présentons ci-dessous les diverses équations qui servent de base au calcul des écoulements secondaires.

a) Les deux équations intégrales de quantité de mouvement dans les directions circonférentielle u et méridionale m sont les suivantes :

$$\begin{aligned} \frac{1}{b_i R_i} \frac{\partial}{\partial m} \left[\rho_i b_i R_i W_{m_i}^2 \theta_{mu} \right] + \rho_i W_{m_i} \frac{\partial W_{u_0}}{\partial m} S_m^* + \Delta D_{4u} \\ = \Delta D_{1u} + \Delta D_{2u} + (z_{un} - z_{une})_i + \frac{b_o R_o}{b_i R_i} (z_{une} - z_{un})_o \\ \frac{1}{b_i R_i} \frac{\partial}{\partial m} \left[\rho_i b_i R_i W_{m_i}^2 \theta_{mm} \right] + \rho_i W_{m_i} \frac{\partial W_{m_0}}{\partial m} S_m^* + \Delta D_{4m} \\ = \Delta D_{1m} + \Delta D_{2m} + \Delta D_{3m} + (z_{mn} - z_{mne})_i \\ + \frac{b_o R_o}{b_i R_i} (z_{mne} - z_{mn})_o \end{aligned}$$

où δ_m^* est l'épaisseur de déplacement dans la direction m.

θ_{mm} et θ_{mu} sont des épaisseurs de quantité de mouvement.

Les quantités indicées i sont relatives à la paroi, et indicées 0 relatives à l'extérieur de la zone visqueuse. L'indice e indique que la valeur s'applique à l'écoulement sain de référence.

Les termes ΔD_{1u} et ΔD_{1m} expriment le déficit de la force d'aubage à l'intérieur de la

couche visqueuse pariétale, les termes ΔD_{2u} et ΔD_{2m} sont les termes de fluctuation et ΔP_m prend en compte la différence entre la pression statique imposée par l'écoulement sain dans la couche visqueuse et celle qui existe réellement.

Les termes ΔD_{4u} et ΔD_{4m} qui sont issus du degré supérieur d'approximation utilisé dans cette formulation s'expriment ainsi :

$$\begin{aligned} \Delta D_{4u} = & \frac{1}{b_i R_i} \frac{\partial}{\partial m} b_i R_i \int_{n_i}^{n_o} \rho \frac{b}{b_i} R W_m (W_{u_o} - W_{u_e}) d\left(\frac{n}{R_i}\right) - \int_{n_i}^{n_o} \rho \frac{b}{b_i} R W_{m_e} \frac{\partial}{\partial m} (W_{u_o} - W_{u_e}) d\left(\frac{n}{R_i}\right) \\ & + \int_{n_i}^{n_o} \rho \frac{b}{b_i} \frac{R}{R_i} R_i K_n W_m (W_{u_o} - W_{u_e}) d\left(\frac{n}{R_i}\right) \\ & + \int_{n_i}^{n_o} \frac{b}{b_i} \left(\rho_e W_{u_e} W_{m_e} - \rho W_u W_m \right) \sin \phi d\left(\frac{n}{R_i}\right) + \int_{n_i}^{n_o} 2 \omega R \frac{b}{b_i} \left(\rho_e W_{m_e} - \rho W_m \right) \sin \phi d\left(\frac{n}{R_i}\right) \\ & + \int_{n_i}^{n_o} \rho \frac{b}{b_i} W_n \left[\frac{R}{R_i} R_i K_m W_{u_o} - W_{u_e} \cos \phi - 2 \omega R \cos \phi - \frac{R}{R_i} R_i K_n W_u \right] d\left(\frac{n}{R_i}\right) \\ & + \frac{1}{b_i R_i} \frac{\partial}{\partial m} b_i R_i \int_{n_i}^{n_o} \frac{b}{b_i} R \left(\rho_e W_{m_e} - \rho_e W_{m_e i} \right) (W_{u_e} - W_u) d\left(\frac{n}{R_i}\right) \\ & - \int_{n_i}^{n_o} \frac{b}{b_i} (Z_{mu_e} - Z_{mu}) \sin \phi d\left(\frac{n}{R_i}\right) - \int_{n_i}^{n_o} \frac{b}{b_i} (Z_{nu_e} - Z_{nu}) \cos \phi d\left(\frac{n}{R_i}\right) \end{aligned}$$

$$\begin{aligned} \Delta D_{4m} = & \frac{1}{b_i R_i} \frac{\partial}{\partial m} b_i R_i \int_{n_i}^{n_o} \rho \frac{b}{b_i} R W_m (W_{m_o} - W_{m_e}) d\left(\frac{n}{R_i}\right) - \int_{n_i}^{n_o} \rho \frac{b}{b_i} R W_{m_e} \frac{\partial}{\partial m} (W_{m_o} - W_{m_e}) d\left(\frac{n}{R_i}\right) \\ & + \int_{n_i}^{n_o} \rho \frac{b}{b_i} \frac{R}{R_i} R_i K_n W_m (W_{m_o} - W_{m_e}) d\left(\frac{n}{R_i}\right) \\ & - \int_{n_i}^{n_o} \frac{b}{b_i} \left(\rho_e W_{u_e}^2 - \rho W_u^2 \right) \sin \phi d\left(\frac{n}{R_i}\right) - \int_{n_i}^{n_o} 2 \omega R \frac{b}{b_i} \left(\rho_e W_{u_e} - \rho W_u \right) \sin \phi d\left(\frac{n}{R_i}\right) \\ & + \int_{n_i}^{n_o} \rho \frac{b}{b_i} W_n \left[\frac{R}{R_i} R_i K_m W_{m_o} - 2 \frac{R}{R_i} R_i K_m W_m + \frac{R}{R_i} R_i K_n W_n \right] d\left(\frac{n}{R_i}\right) \\ & + \frac{1}{b_i R_i} \frac{\partial}{\partial m} b_i R_i \int_{n_i}^{n_o} \frac{b}{b_i} R \left(\rho_e W_{m_e} - \rho_e W_{m_e i} \right) (W_{m_e} - W_m) d\left(\frac{n}{R_i}\right) - \int_{n_i}^{n_o} (\omega R)^2 \frac{b}{b_i} \left(\rho_e - \rho \right) \sin \phi d\left(\frac{n}{R_i}\right) \end{aligned}$$

b) L'équation d'entraînement de HEAD se formule ainsi :

$$\frac{\partial}{\partial m} \left[\rho_e b_i R_i W_{s_{e i}} \left(H_e \theta_{ss} (\cos \beta_e)_{m y} + S_N^* (\sin \beta_e)_{m y} - \int_{n_i}^{n_o} R \frac{b}{b_i} \left(1 - \frac{\rho_e W_{s_e}}{\rho_e W_{s_{e i}}} \right) \cos \beta_e d\left(\frac{n}{R_i}\right) \right) \right] + D_5 = \rho_o R_o b_o W_{s_{e o}} E$$

avec

$$D_5 = \int_{n_i}^{n_o} \rho b R \left[(W_s \cos \beta_e - W_n \sin \beta_e) K_n + W_n K_m \right] dn$$

$$H_e = (S - S_s^*) / \theta_{ss}$$

$$E = (W_{m_o} \cdot \frac{dn_o}{dm} - W_{n_o}) / W_{s_{e o}}$$

où : H_e est le facteur de forme de HEAD, et E le facteur d'entraînement.

S_{ss}^* est l'épaisseur le déplacement dans la direction transversale, et θ_{ss} l'épaisseur de quantité de mouvement dans la direction longitudinale.

c) L'équation régissant le développement de la composante longitudinale de vorticit  dite secondaire.

Cette  quation exprime l' volution de la composante longitudinale moyenne de vorticit  qui est responsable du profil transversal de vitesse et s' crit dans le rep re in-

trinsèque (N,S,n) sous la forme suivante :

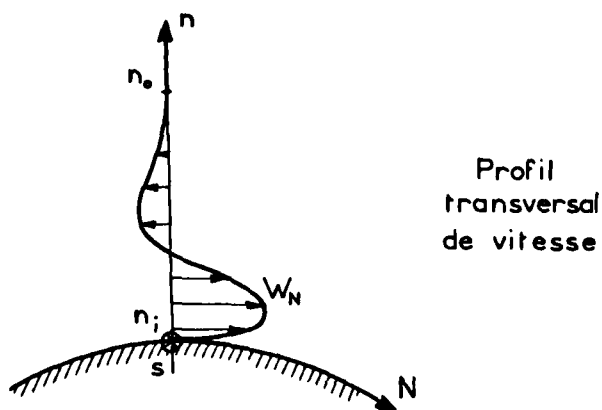
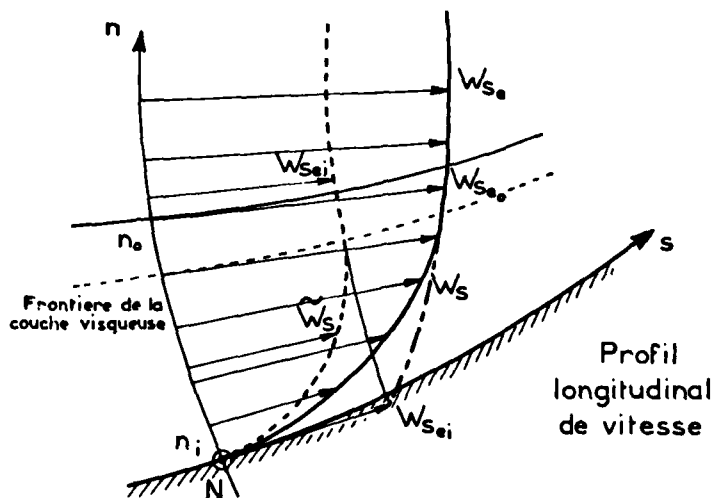
$$d_s \left(\frac{\Omega_s}{\rho W_s} \right) = 2 \frac{\Omega_N}{\rho W_s} d\beta + \frac{2W}{\rho W_s^2} \left[\cos \varphi \left(\cos \beta_c \frac{\partial W_s}{\partial s} - \sin \beta_c \frac{\partial W_s}{\partial n} \right) + \sin \varphi \frac{\partial W_s}{\partial n} \right]$$

Dans cette équation $d\beta$ représente la déflexion de l'écoulement sur la surface aube-à-aube.

La composante longitudinale moyenne de vorticit  Ω_s ainsi obtenue, induit un champ de vitesse que nous appellerons secondaire sur une surface normale aux lignes de courant. Ce champ de vitesse est d termin  par la fonction de courant ψ , qui s'obtient   partir de l' quation suivante :

$$\frac{\partial^2 \psi}{\partial n^2} + \frac{\partial^2 \psi}{\partial N^2} = - \frac{1}{h_N} \frac{\partial}{\partial n} \left(\frac{h_N}{\rho} \right) \rho \frac{\partial \psi}{\partial n} - \frac{1}{h_n} \frac{\partial}{\partial N} \left(\frac{h_n}{\rho} \right) \rho \frac{\partial \psi}{\partial N} + \rho \Omega_s$$

o  h_n et h_N sont les m triques du syst me de coordonn es intrins ques.



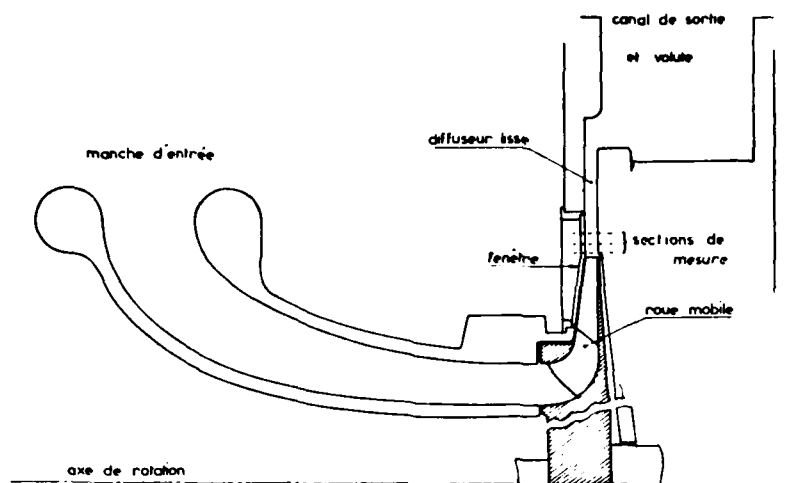
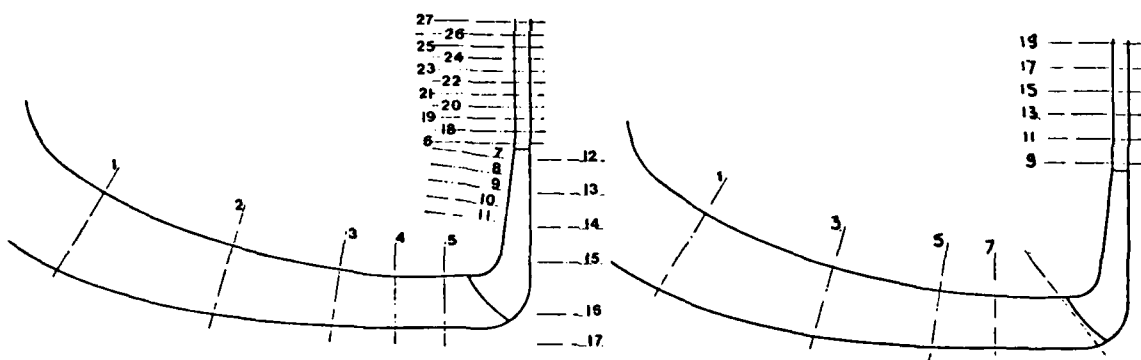


Figure 1 - Schéma du compresseur CREUSOT-LOIRE

Prises de pression statique

Plans de sondages



	Plans de mesures	Nombre par plan
Pavillon d'aspiration	1-2-3-4	8
Entrée roue	5	8
Sortie roue	6	32
Face externe couvercle	7-8-9-10-11	1
Face externe moyeu	12-13-14-15-16-17	1
Diffuseur	18-19-20-21-22-23 24-25-26-27	32

Figure 2 - Implantation des prises de pression statique

	Plans de sondages
Pavillon d'aspiration	1-2-3-4
Entrée roue	5
Sortie roue	6
Diffuseur	8-7-8-9-10-11

Figure 3 - Positionnement des plans de sondage.

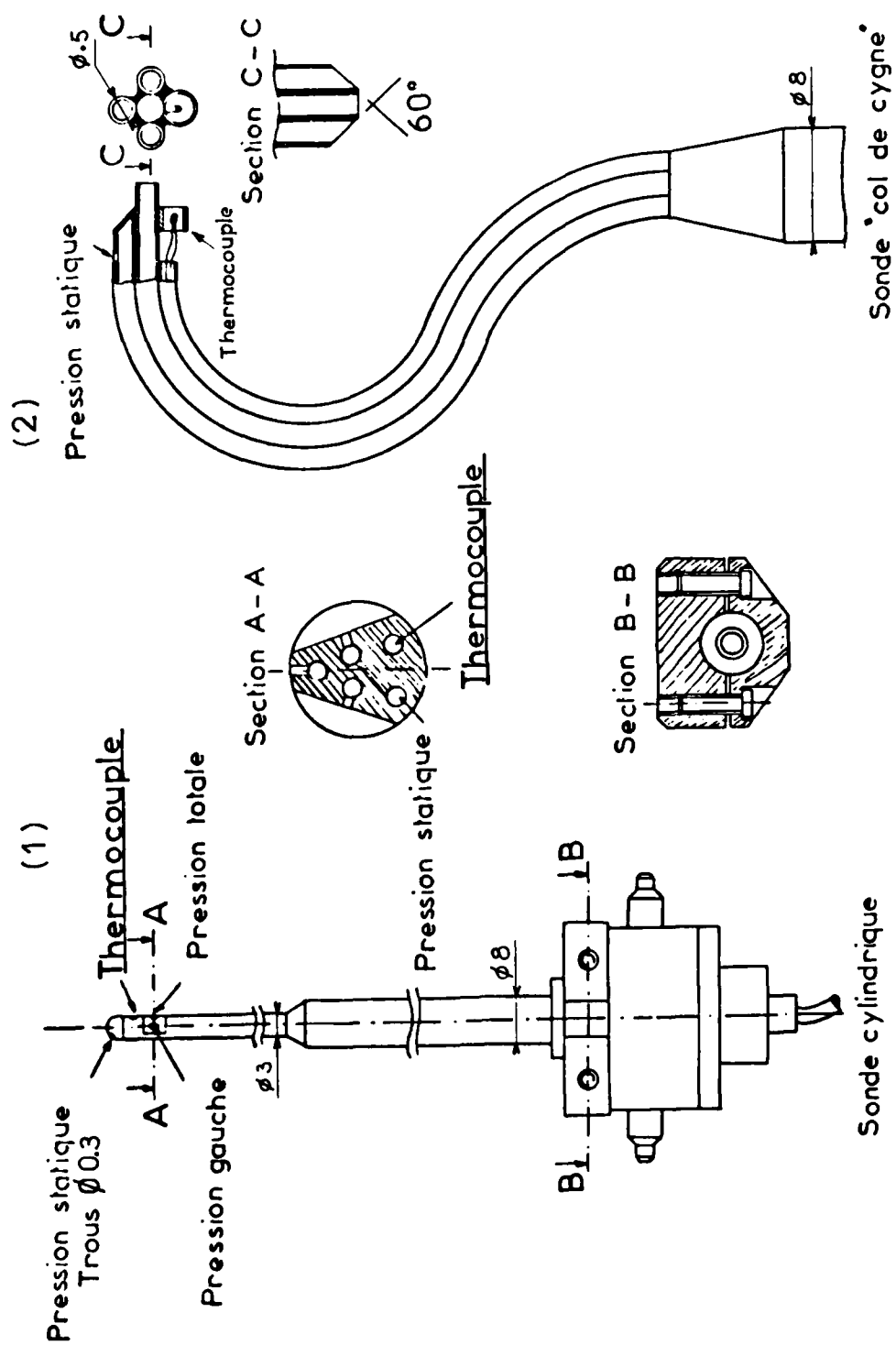


Figure 4 - Schéma des sondes d'exploration.

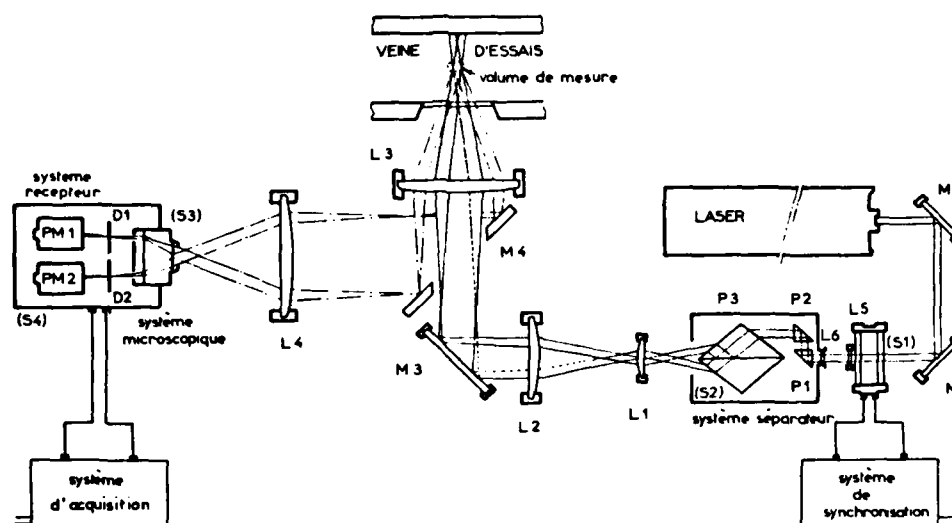


Figure 5 - Schéma de l'anémomètre Laser.

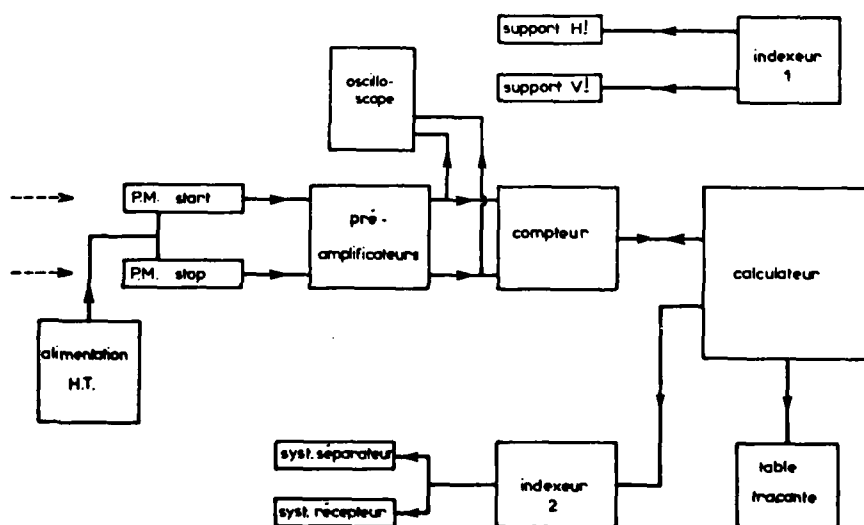


Figure 6 - Schéma synoptique de l'électronique

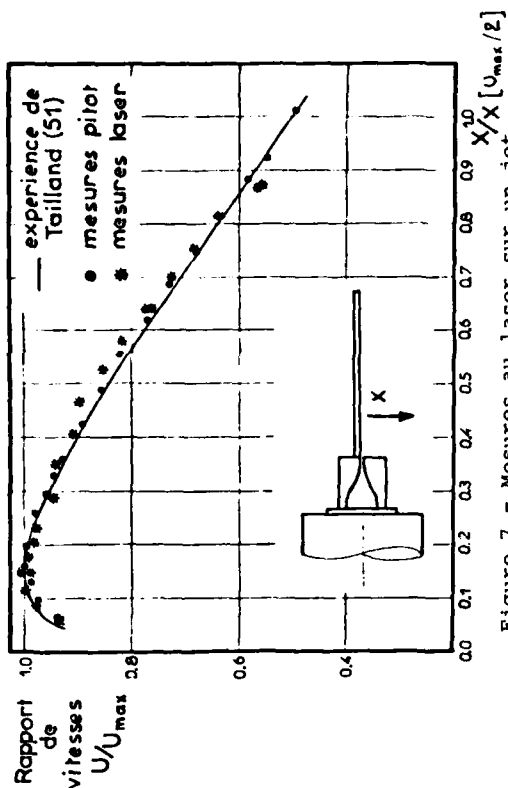


Figure 7 - Mesures au laser sur un jet pariétal bidimensionnel : vitesses moyennes.

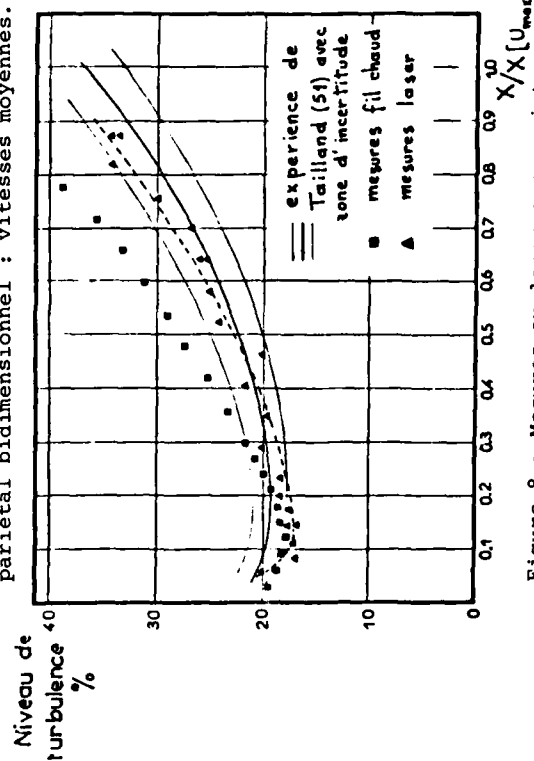


Figure 8 - Mesures au laser sur un jet pariétal bidimensionnel : niveaux de Turbulence

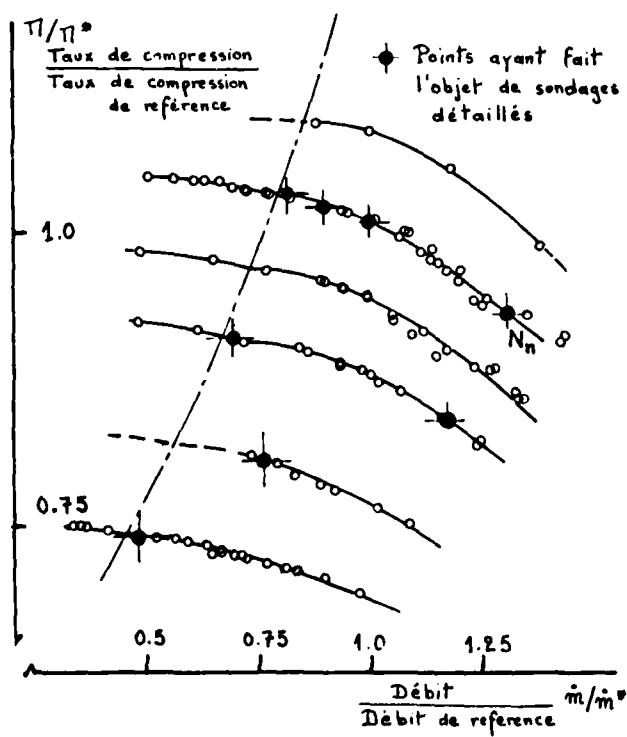


Figure 9 - Définition des points de caractérisation.

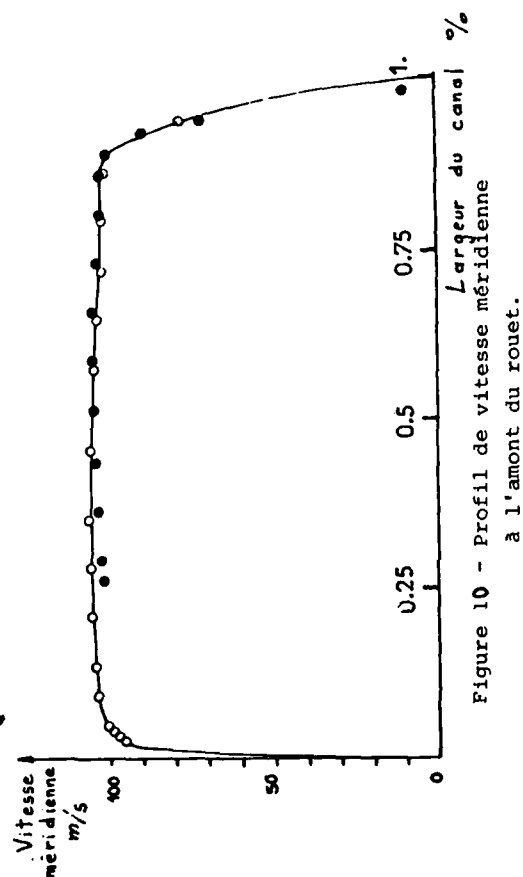


Figure 10 - Profil de vitesse méridienne à l'amont du rouet.

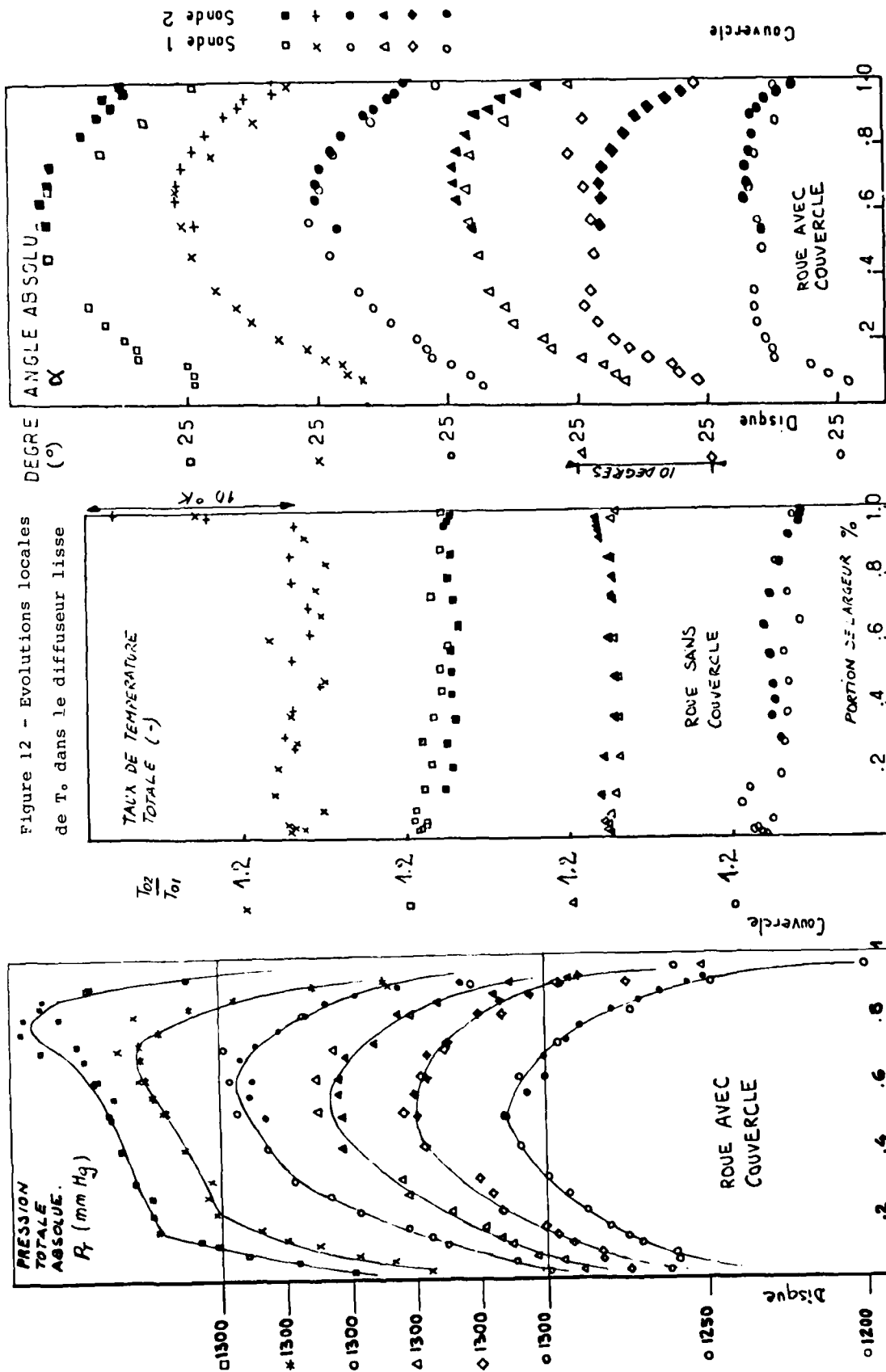


Figure 13 - Evolutions locales de α dans le diffuseur lisse

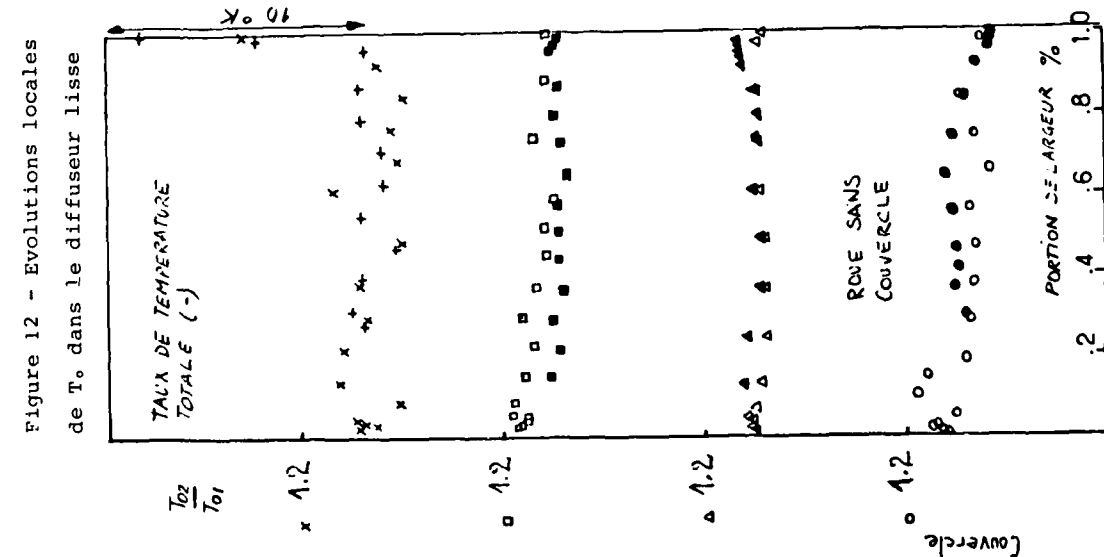
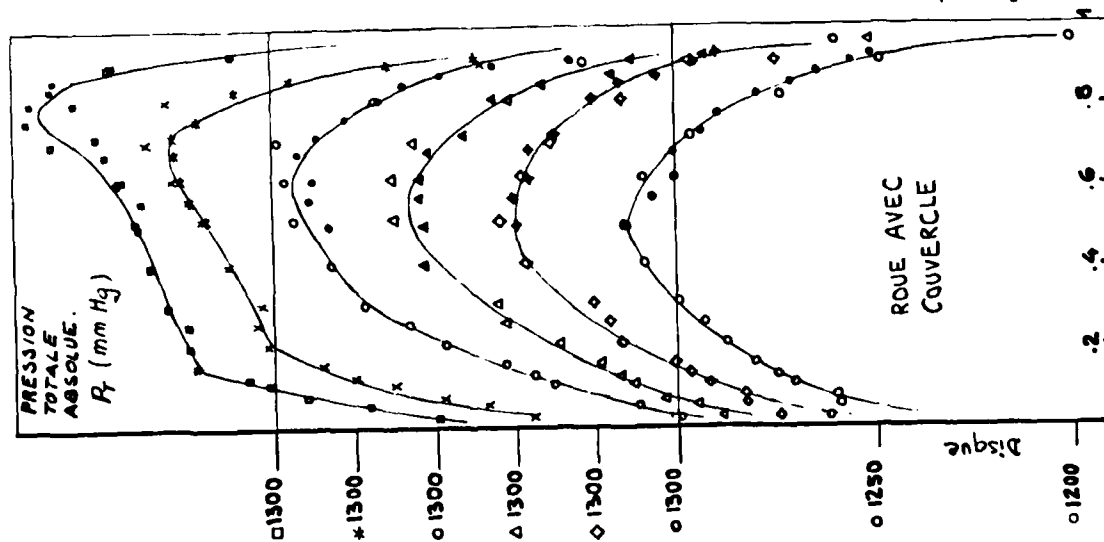


Figure 14 - Evolutions locales de β dans le diffuseur lisse



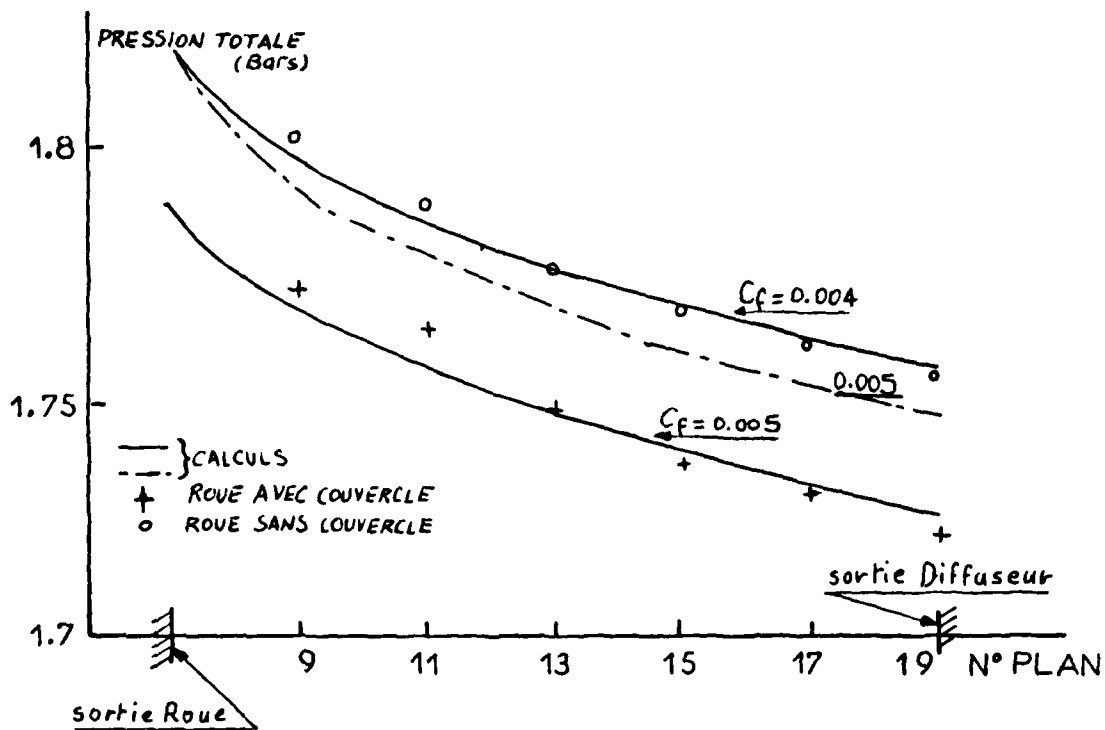
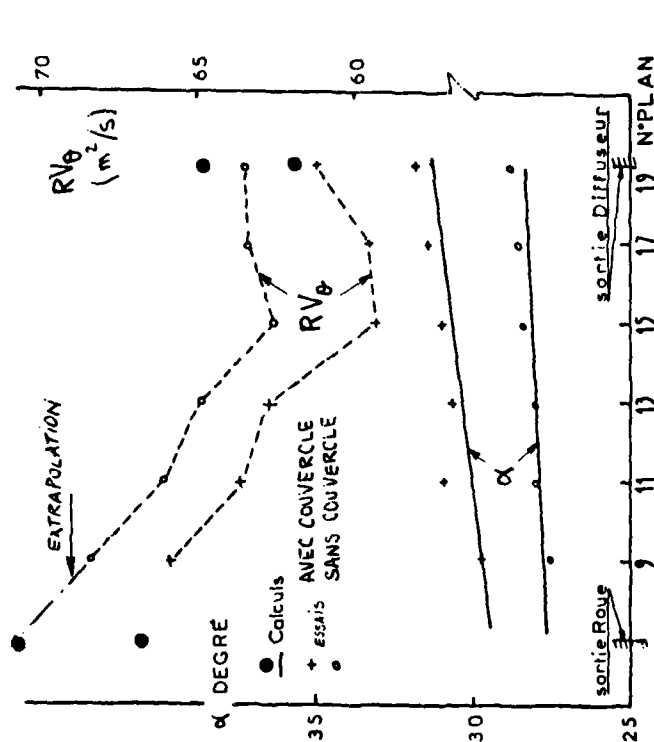
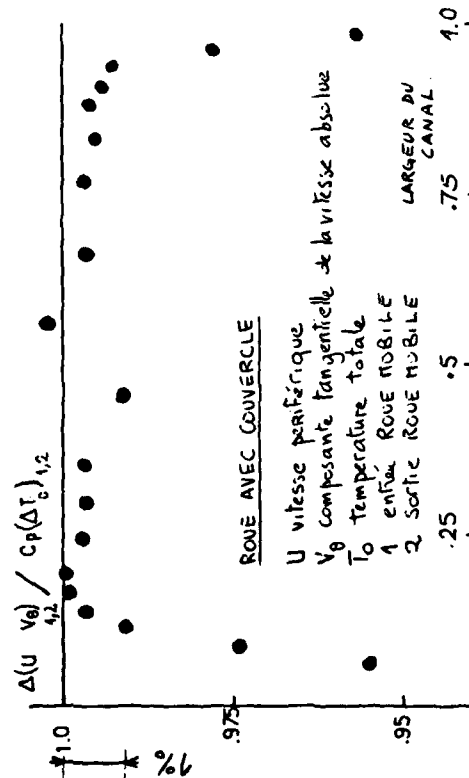
Fig 14 a - Evolutions moyennes de P_0 dans le diffuseur lisse.Fig 14 b - Evolutions moyennes de α et RV_0 dans le diffuseur lisse.

Fig 15 - Vérification de la relation d'EULER

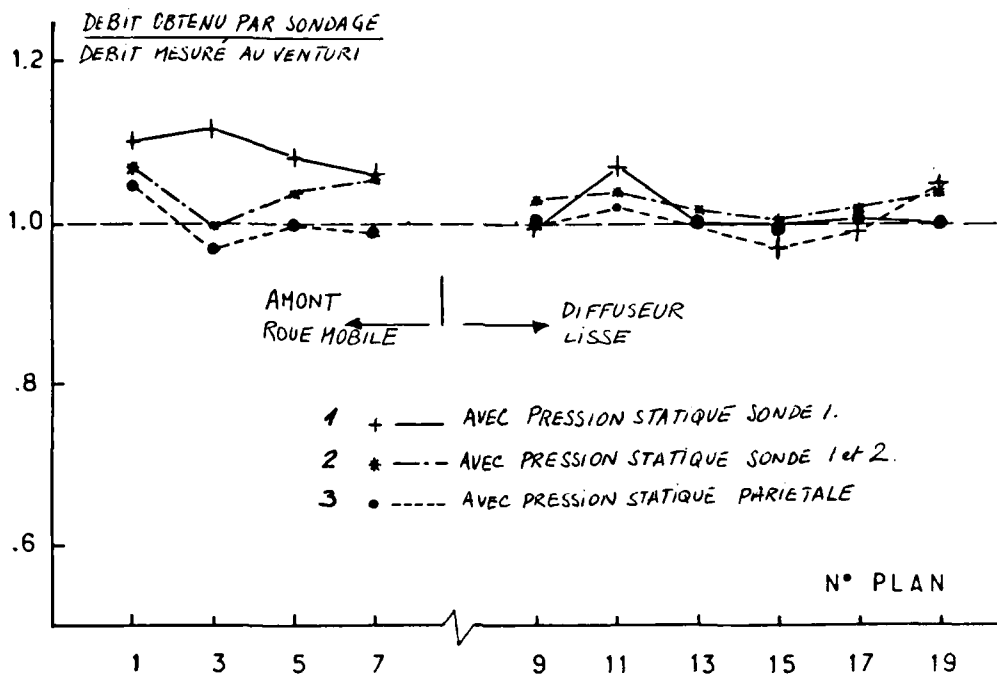


Figure 16 - Recouplement du débit dans les différents plans de mesure du diffuseur lisse.

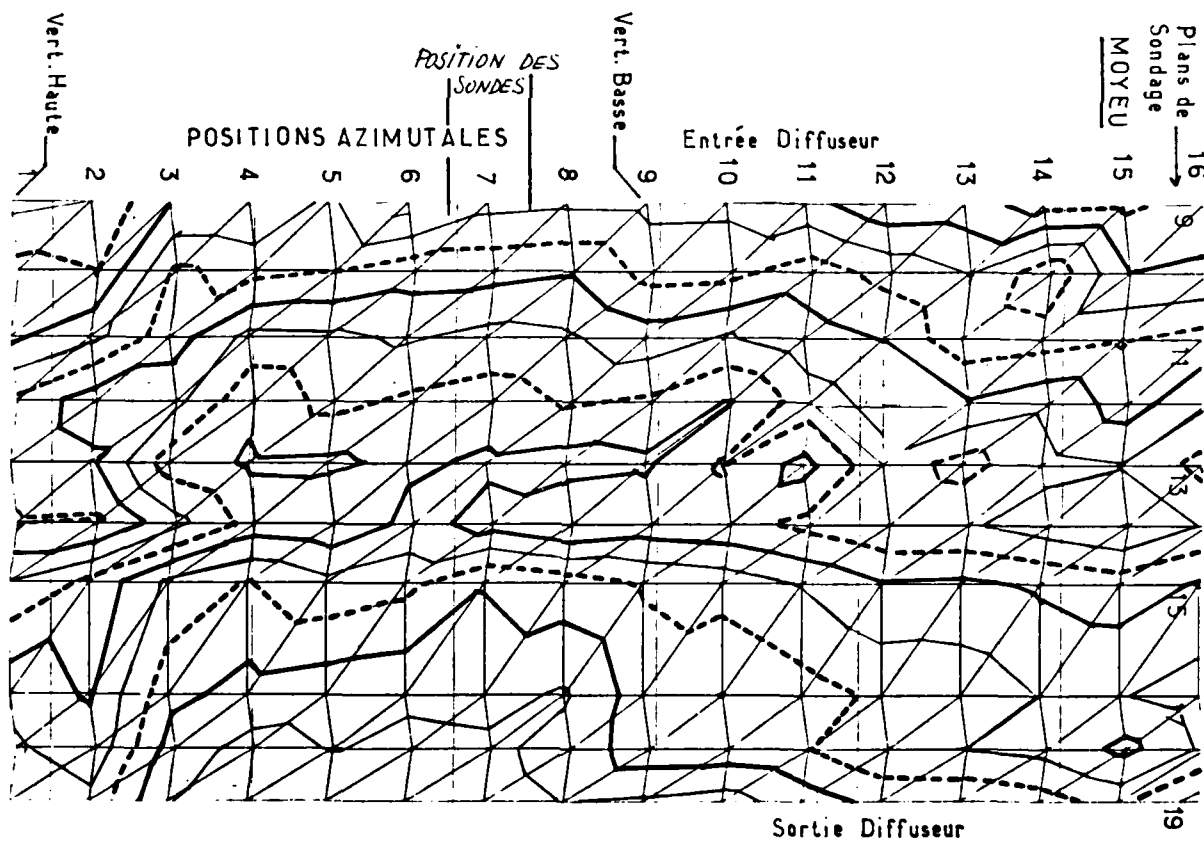


Figure 17 - Distributions azimuthales des pressions statiques pariétales dans le diffuseur lisse.

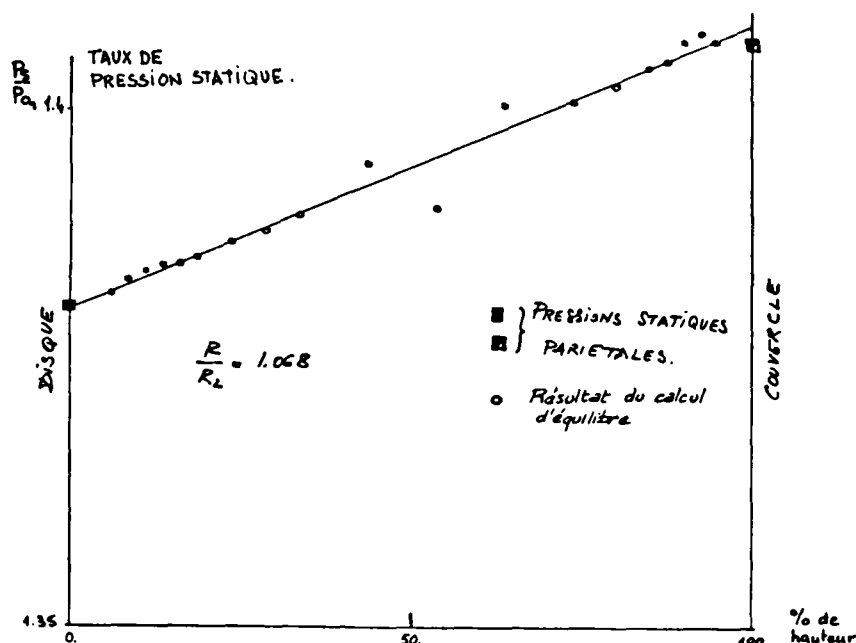


Fig 18 - Pressions statiques obtenues par un calcul d'équilibre de l'écoulement.

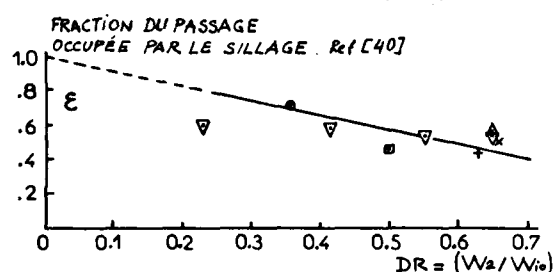


Fig 19 - Evolution de la largeur du sillage en fonction du facteur de deceleration.

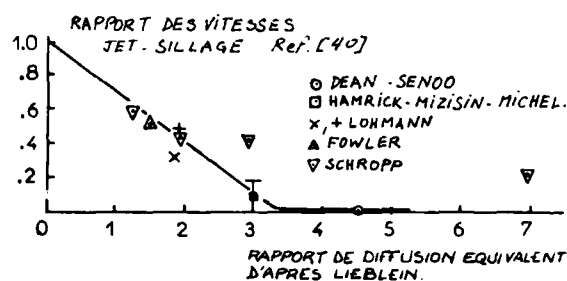


Fig 20 - Evolution du rapport des vitesses dans le sillage et le jet selon un critère de charge.

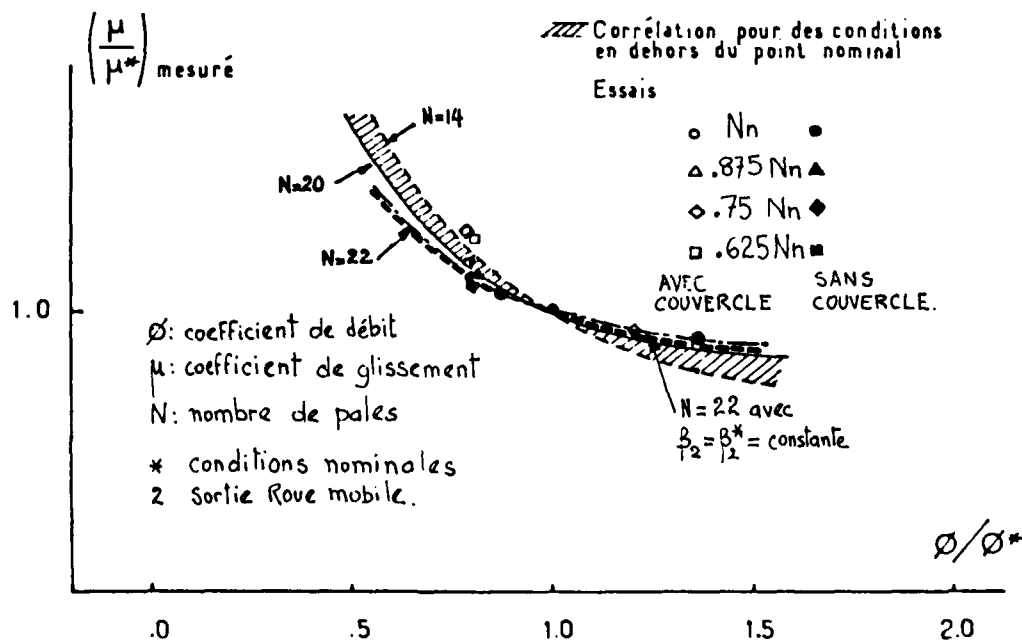


Figure 21 - Evolution du coefficient de glissement en dehors du point nominal.

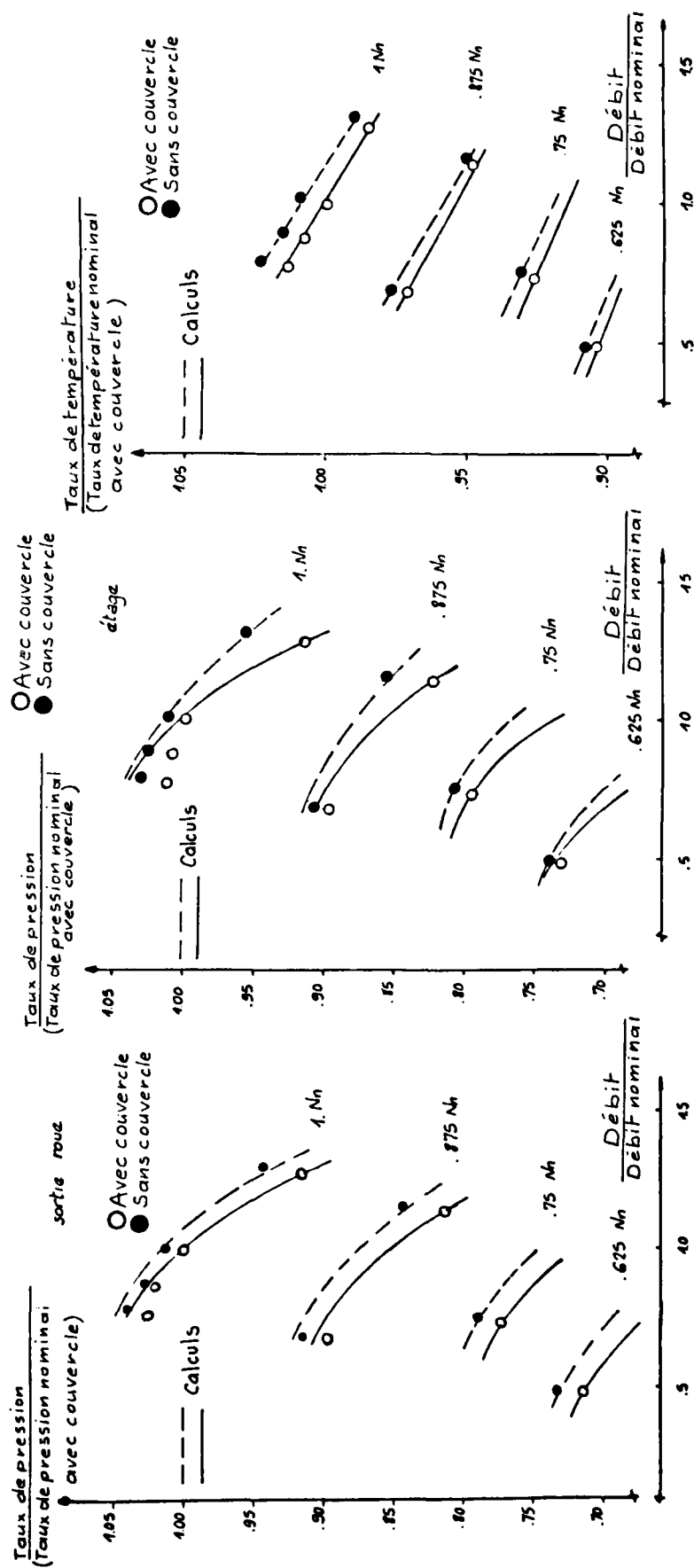


Figure 22 - Champ de caractéristiques en sortie de roue.

Figure 23 a - Champ de caractéristiques en sortie d'étage : taux de pression.

Figure 23 b - Champ de caractéristiques en sortie d'étage : taux de température.

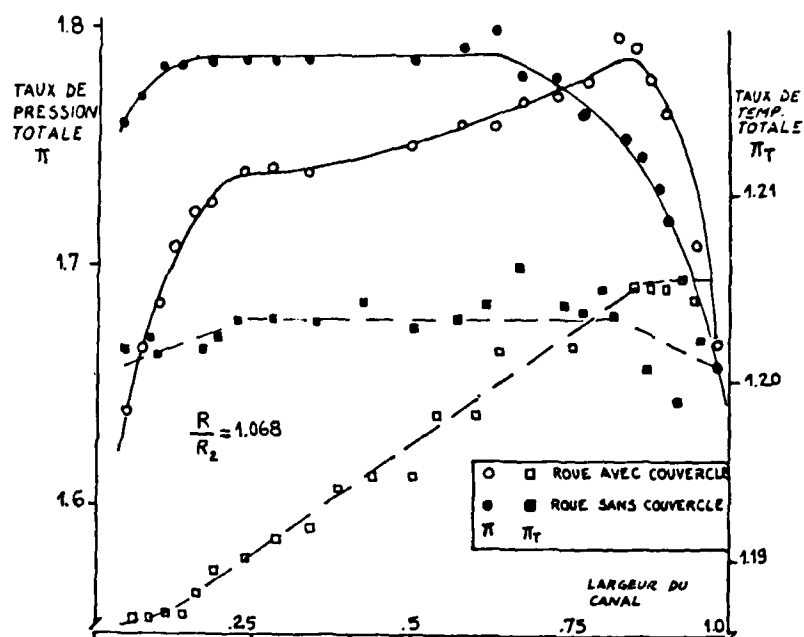


Figure 24 - Evolutions des taux de pression et de température totale en sortie de roue mobile.

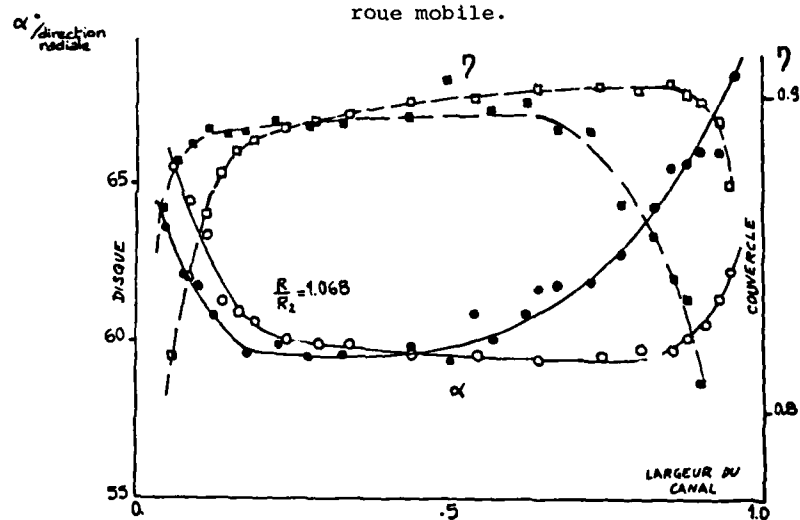
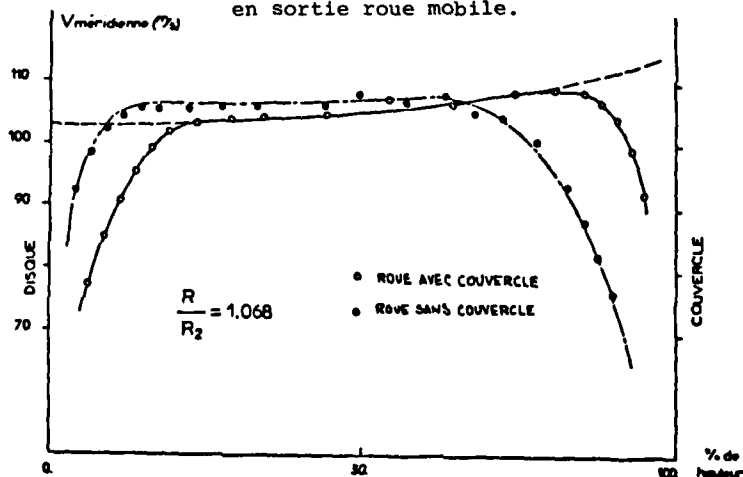


Figure 25 - Evolutions de l'angle absolu et du rendement isentropique en sortie de roue mobile.



Profil de vitesse méridienne en aval du rouet

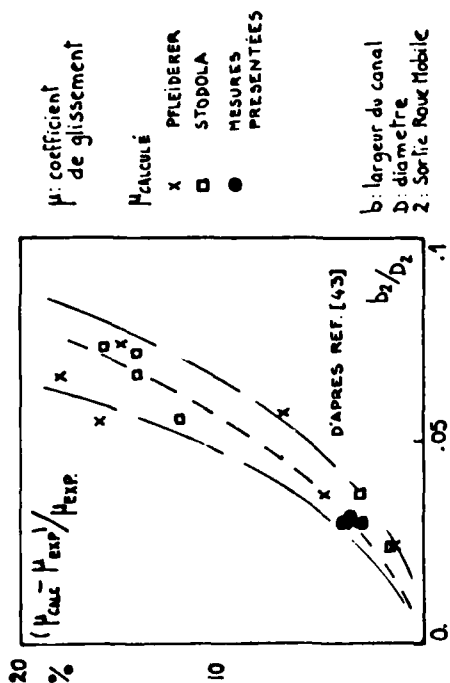


Figure 26 - Variation du coefficient de glissement due à la présence d'un jeu.

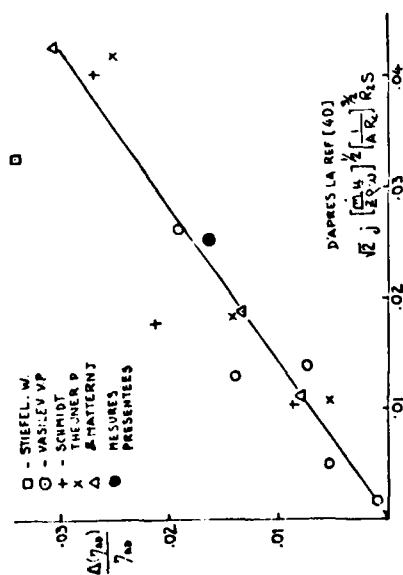


Figure 27 - Variation du rendement isentropique due à la présence d'un jeu.

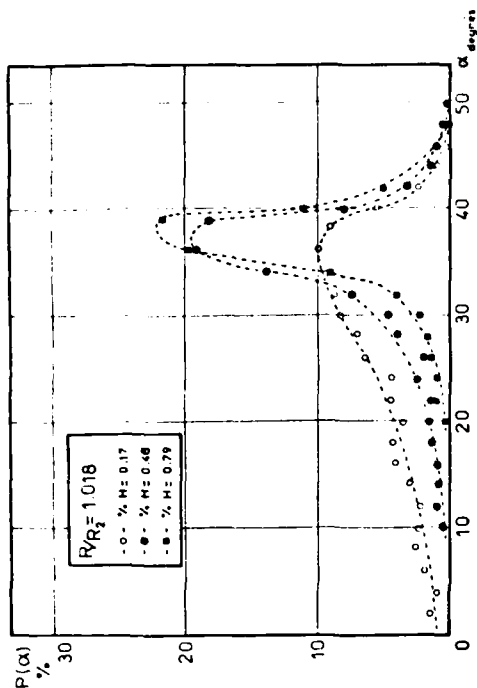


Figure 28 - Mesures laser en aval du rouet. Histogramme de probabilité de l'angle absolu pour $R/R_2 = 1.018$.

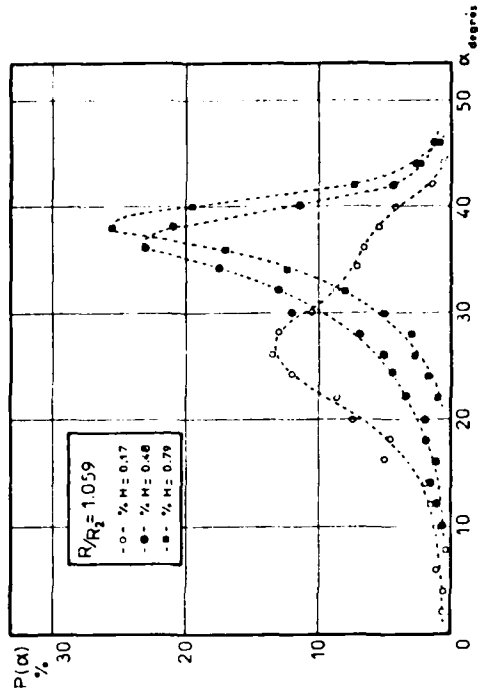


Figure 29 - Mesures laser en aval du rouet. Histogramme de probabilité de l'angle absolu pour $R/R_2 = 1.059$.

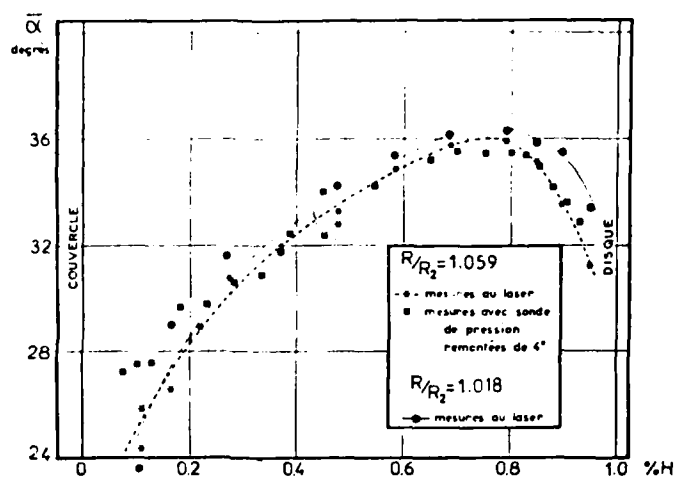


Figure 30 - Mesures laser : angle absolu du vecteur vitesse en aval du rouet.

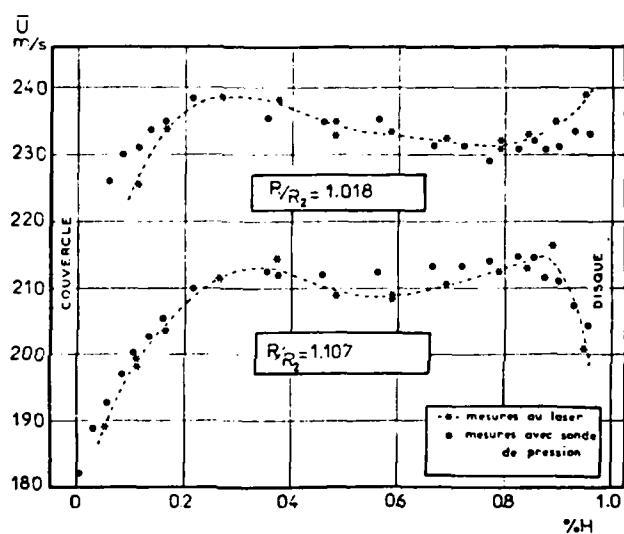


Figure 31 - Mesures laser : module de la vitesse absolue en aval du rouet.

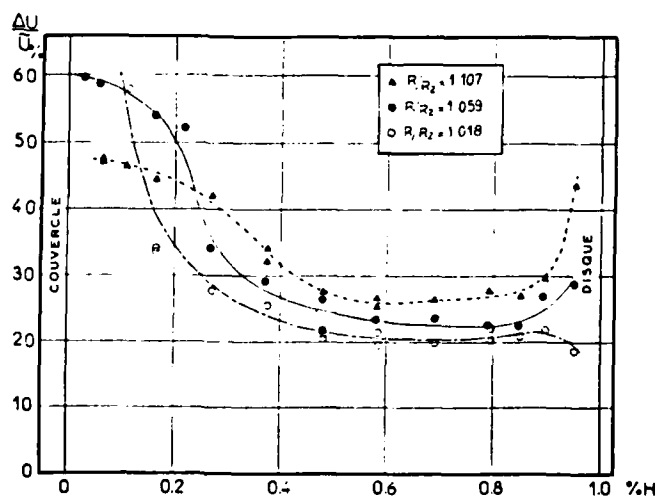


Figure 32 - Mesures laser : fluctuation longitudinale de vitesse en aval du rouet.

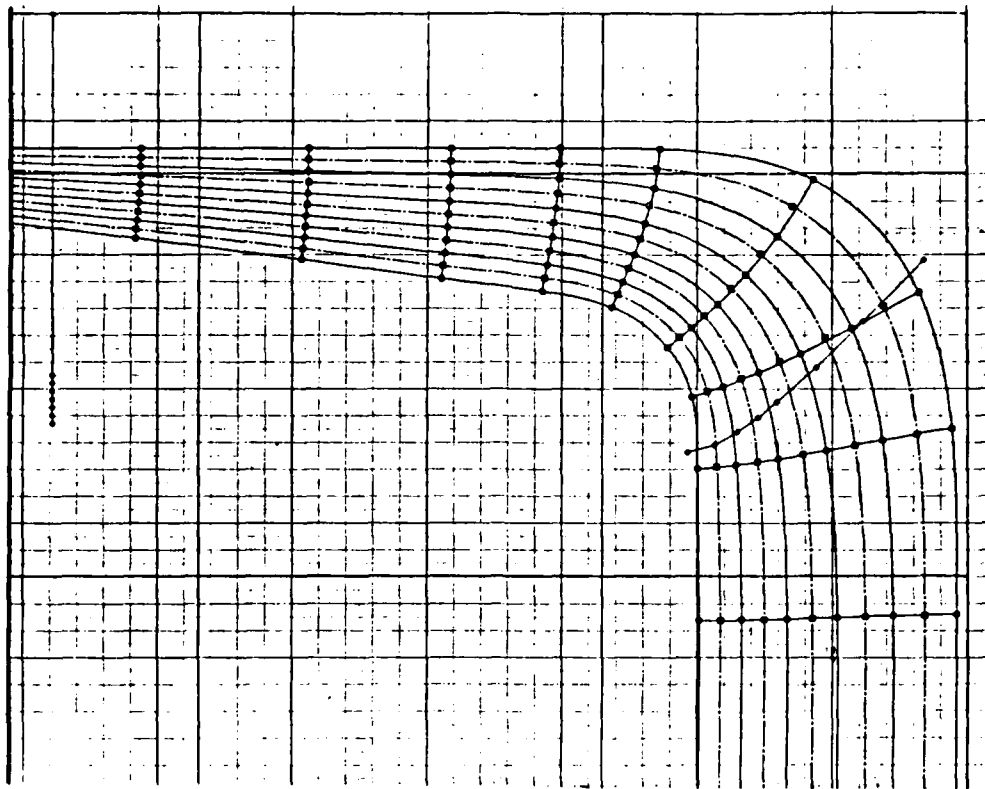


Figure 33 - Calcul Creusot-Loire par la méthode de courbure des lignes de courant.

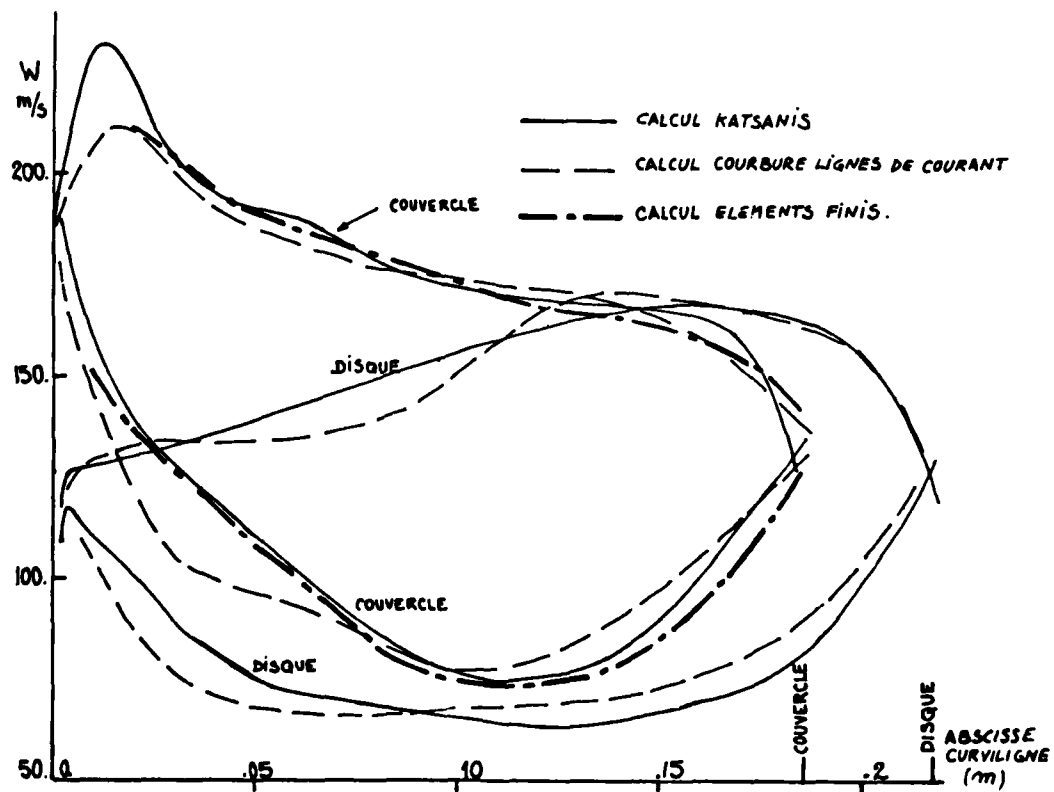


Figure 34 - Distributions de vitesse calculées par différentes méthodes.

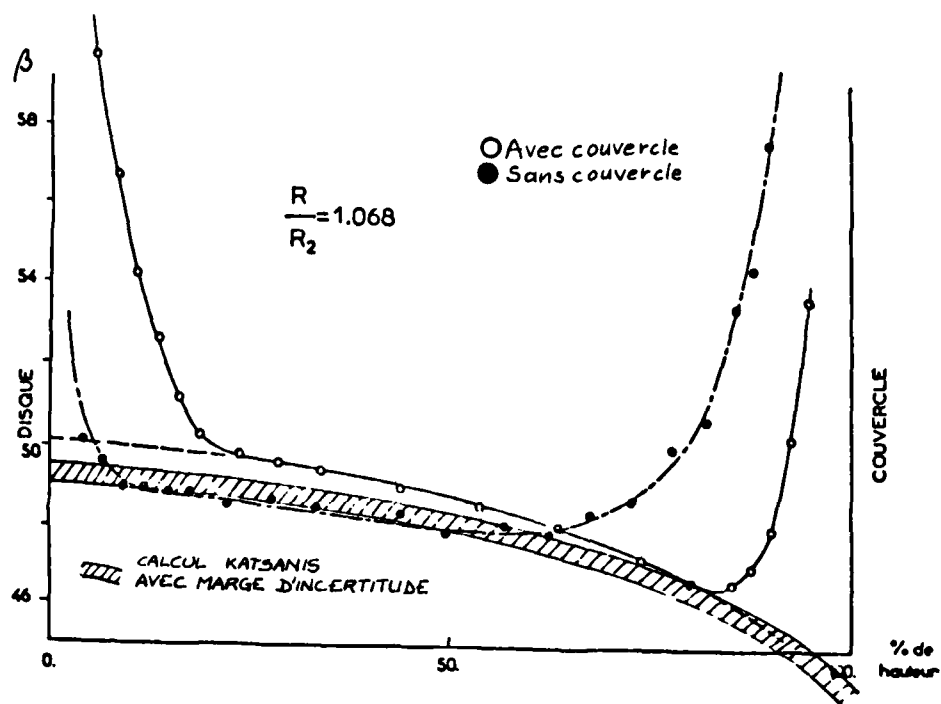


Figure 35 - Evolution de l'angle relatif : comparaison théorie-expérience.

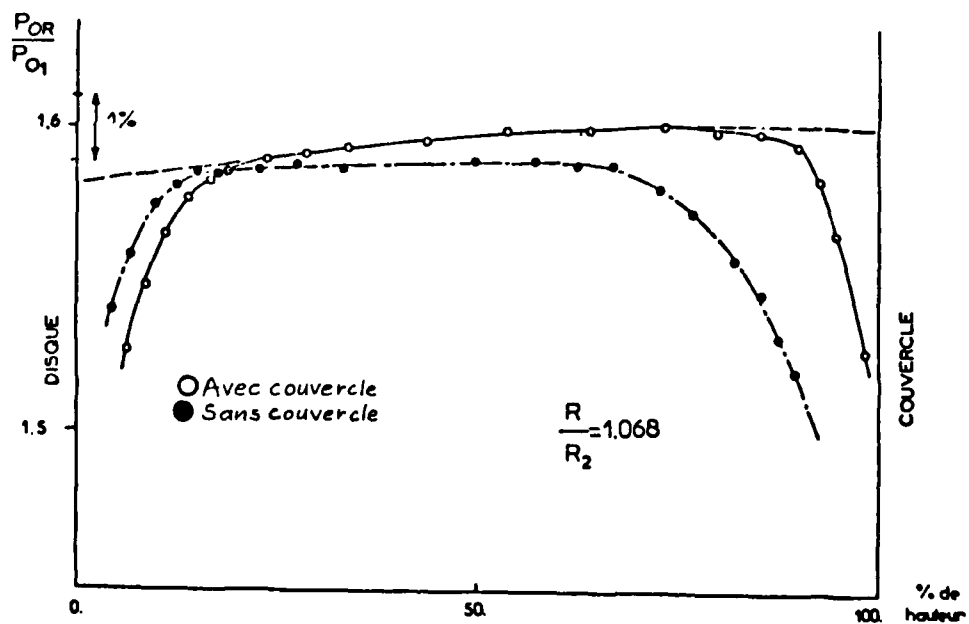
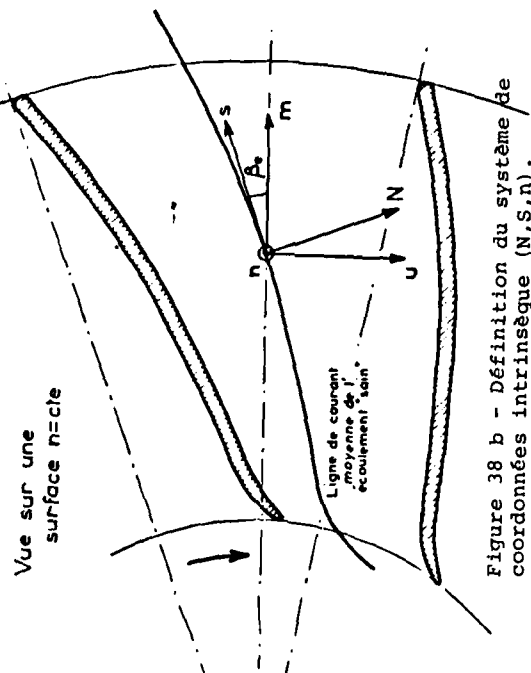
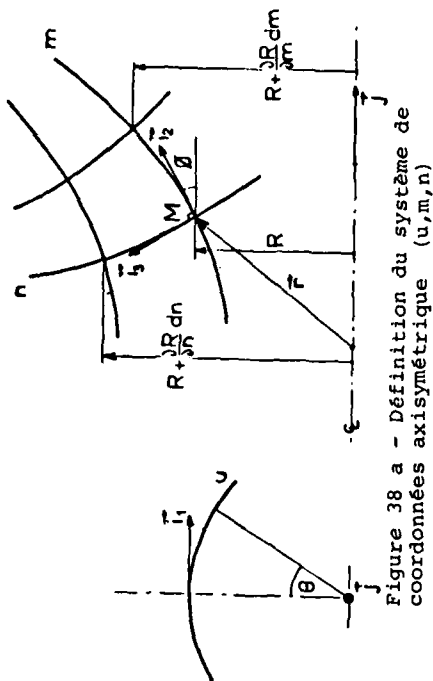
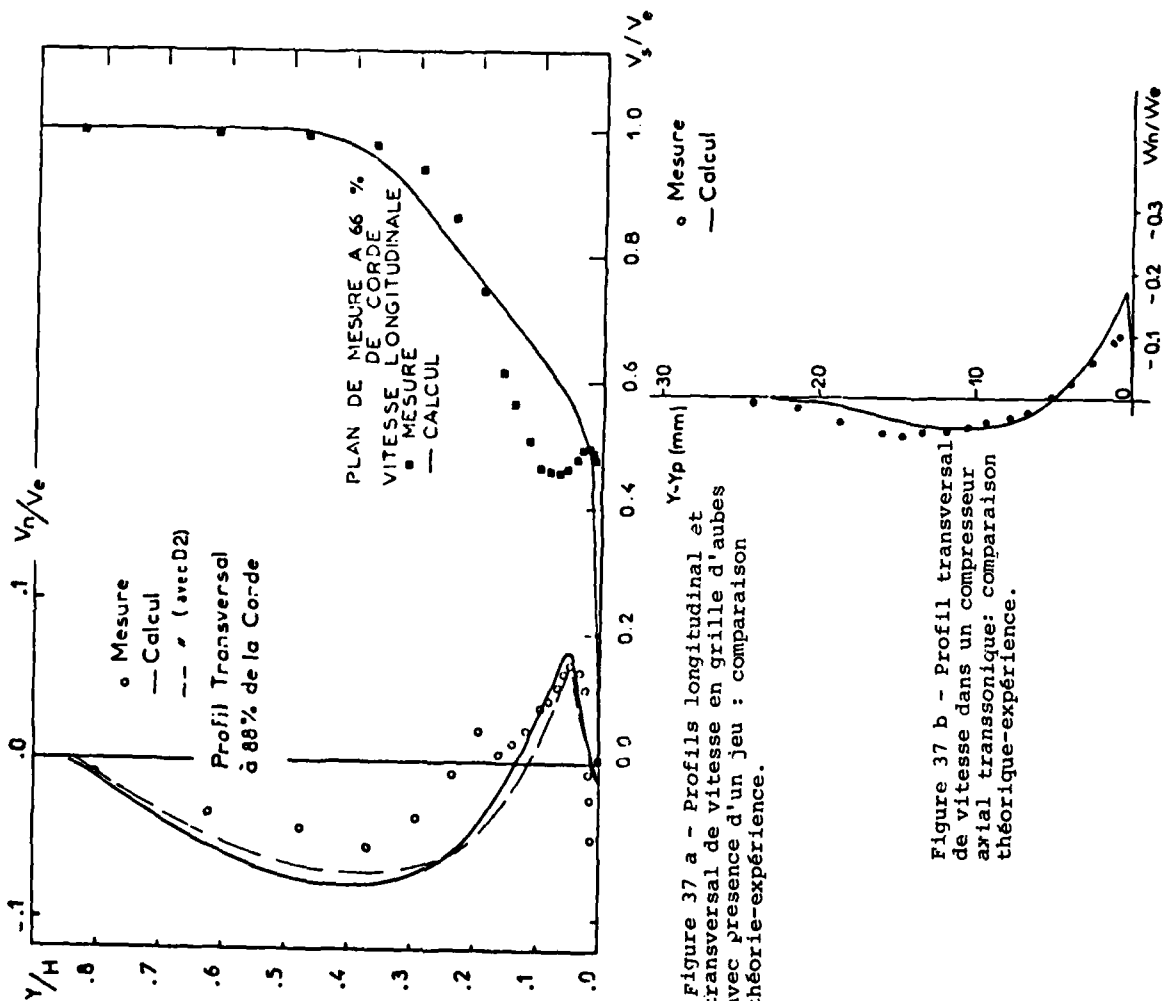


Figure 36 - Evolution mesurée de la pression totale relative.



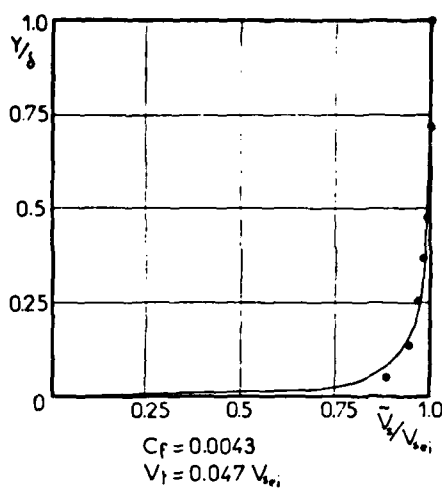


Figure 39 a - Profil moyen de vitesse longitudinal en sortie roue côté couvercle

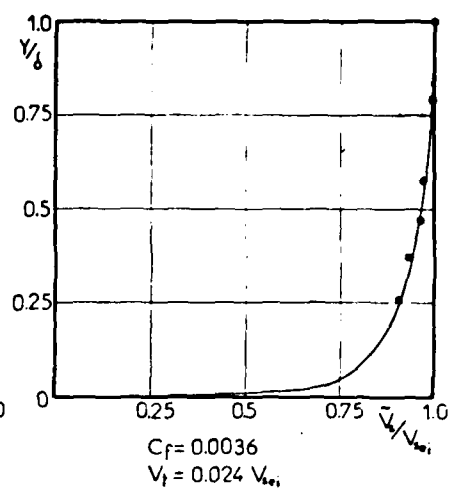


Figure 39 b - Profil moyen de vitesse longitudinal en sortie roue côté disque.

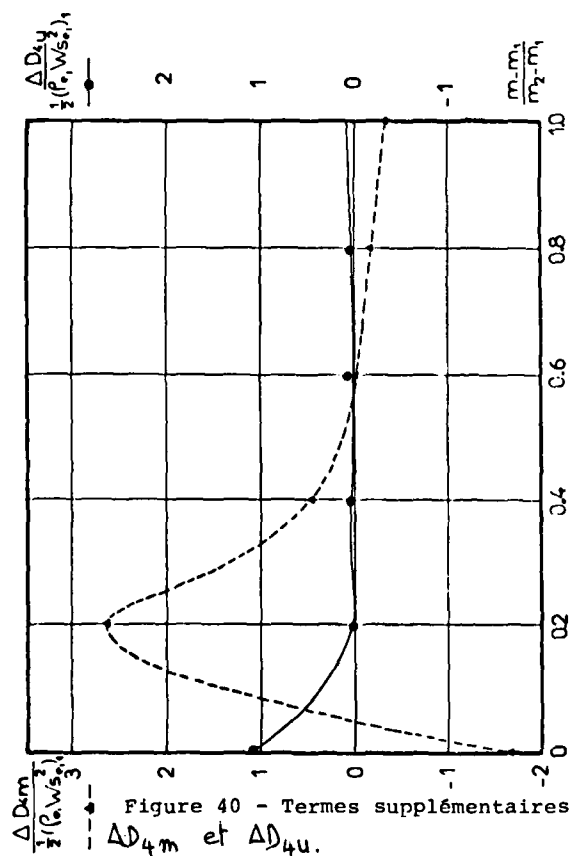


Figure 40 - Termes supplémentaires ΔD_{4m} et ΔD_{4u} .

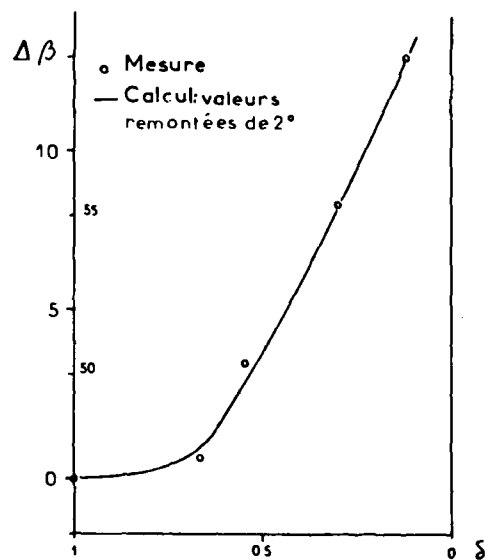


Figure 41 - Ecart de l'angle relatif entre les écoulements sain et visqueux au couvercle : comparaison théorie-expérience.

DISCUSSION

H.Weyer, DFVLR, Cologne, Ge

I was surprised by the good agreement between the laser anemometer data and the probe data for velocity measurement. At the beginning of your presentation you referred to differences in measurements between the various types of probe. What probe was used for the velocity measurement?

Author's Reply

A cobra probe and a straight probe were used for the velocity measurement. We were able to obtain good velocity measurements using the information given by the cobra probe in the region opposite the fixing lug and by the straight probe in the other region. Both probes give the *same* information in the intermediate region. The information from the 2 probes we took into account are:

- total pressure
- total temperature
- absolute angle

The static pressure is given by the wall pressure.

The two probes were calibrated in yaw and pitch angles over a range of $\pm 10^\circ$ and a Mach number range from 0.2 to 0.8. A calibration was also done for the temperature recovery factor for the same conditions.

C.Rodgers, Solar, US

Would the authors care to generalise concerning the efficiency which is obtainable firstly from shrouded, and secondly unshrouded impellers?

Author's Reply

The authors are unable to comment in a general way on efficiencies obtainable from shrouded and unshrouded impellers.

K.D.Papailiou, University of Athens, Gr

The authors should like to thank Dr Schodl of DFVLR for his most valuable assistance in helping us to interpret our laser anemometer measurements.

INLET FLOW DISTORTIONS
ON INDUSTRIAL CENTRIFUGAL COMPRESSOR STAGES
EXPERIMENTAL INVESTIGATIONS AND EVALUATION
OF EFFECTS ON PERFORMANCE

by
E. Benvenuti¹⁾, L. Bonciani²⁾, U. Corradini³⁾
Nuovo Pignone S.p.A.
Via F. Matteucci, 2 - 50127 Firenze, Italy

Abstract

In the manufacture of process centrifugal compressors use is made of standardized stages, whose performance must be individually known and experimentally evaluated in the same fluid-dynamic environment present on the multistage configuration. This latter usually implies the presence of a return channel with high-turning de-swirl vanes upstream of the impeller, and associated circumferential and radial flow distortions. Results are presented of tests carried out on a stage equipped with three different inlet configurations, two of which with, respectively, curved de-swirl vanes and straight vanes, and one with no vanes. Test results show the presence of high intensity wakes downstream of both the curved and straight vanes, that are not completely mixed-out along the path towards the impeller. Wake mixing is associated with a total pressure loss, whose magnitude can be well evaluated from the measurements. Stage efficiency is decreased by the presence of both straight and curved vanes, the decrease being almost the same despite the different wake amplitudes produced by the two types of vanes; the strong wakes from the curved de-swirl vanes decrease the impeller's head coefficient somewhat at high flows. The good repetitiveness and consistency of test results are indications of the reliability of the procedures selected for investigating complex flow-fields of this kind and assessing their effect on stage performance.

Introduction

In process centrifugal compressors a relatively high number of stages must be assembled inside a single compressor casing. This can be achieved if stage geometries having reduced axial pitch are available insofar as manufacturing and operating requirements allow.

Fig. 1 shows the horizontally split diaphragms and rotor of a multistage process compressor; as can be seen, 180° U-bends at the impeller inlet and between the diffuser outlet and de-swirl vanes are necessary for achieving stage axial compactness.

On its way through the U-bends and interstage de-swirl vanes strong deflections that produce highly complex and sometimes irregular flow-fields, whose existence is clearly shown by testing carried out on this type of configuration (Refs. 1 and 2). Generally speaking it is virtually impossible to predict flow-fields of this kind exclusively by means of the available analytical methods.

This paper describes test procedures and related data reduction methods set up and calibrated within an extensive and continuing process centrifugal compressor stage testing program. The purpose of this detailed testing program was to investigate the structure of the radial circumferential flow distortions existing at the impeller inlet and the related effect on performance. In fact, distortions are normally of prime importance in determining stage performance and flow range, especially during operation at the high Mach numbers required for achieving high pressure ratios per stage.

Testing standardized stages

Combining a number of standardized stages, i.e. stages each having given and fixed geometrical configurations, may represent a design procedure for multistage process centrifugal compressors (Ref. 2). To predict the performance of compressors set-up with standardized stages, it is essential that the single stage performance curves be available. These can be obtained experimentally from stage test configurations that reproduce as closely as possible the flow conditions existing during operation of the same stage inside the complete compressor. The flow-field at impeller inlet, one of the essential conditions, can be reproduced by assembling the components present in the compressor right on the test set-up. Specifically, in the case of an intermediate stage of a multistage compressor, a return channel with de-swirl vanes must be installed upstream of the impeller in order to simulate the presence of the preceding stage.

1) Manager, Design Computing System Development, R&D Dept.

2) Senior Design Engineer, Turbocompressor and Steam Turbine Division

3) Specialist, Radial Turbomachine Aerodynamics, R&D Dept.

Fig. 2 shows an overall view of a test rig of this kind used for routine testing of industrial centrifugal compressor stages. The components are shown clamped to special devices specifically designed for quick set-up of the test configuration.

A typical cross-section of a stage set-up on the test rig is shown in Fig. 3. A thorough investigation into the flow field at impeller inlet on configurations of this kind is imperative for two major reasons:

- a - the average total pressure at the de-swirl vane outlet has to be accurately determined in order to evaluate stage performance parameters (pressure ratio and efficiency).
- b - since the impeller geometry does not usually allow direct measurement of the flow parameters at the blade leading edge, accurate knowledge of these parameters for an upstream section is very helpful when used in conjunction with appropriate analytical methods for checking the flow conditions at the blade leading edge, thus allowing correct evaluation of the incidence angles.

In order to achieve these objectives, particular test procedures were set-up and special devices were designed, as will be shown below.

Measuring flow distortions at impeller inlet

Fig. 3 shows the special device designed for investigating non-uniform flow fields at impeller inlets. Its purpose is to allow aerodynamic probes to be traversed in two fundamental flow-path sections: the de-swirl vane outlet (corresponding to the inlet of the stage being tested) and the impeller eye (the section closest to the blade leading edge that is accessible without particularly complex devices). The device consists of a shaped hub (A) which reproduces a portion of the inlet channel and can be turned 360° around an axis coincident with the impeller's centerline. A rake of kiel probes (B) located close to the de-swirl vane trailing edge and a three-hole cobra directional probe (C) that can be radially traversed across the impeller eye are installed on the hub. Miniature pistons moved by high pressure oil rotate the hub and actuate traversing of the cobra probe. Accurate positioning is pre-programmed and operated by a minicomputer which handles all data acquisition. The combined movement of hub rotation and cobra probe traversing allows complete maps of total pressures and flow angles at the impeller eye to be drawn. The kiel-probe rake in turns provides a complete map of the total pressures just downstream of the de-swirl vanes. As the flow's circumferential distribution is repetitive, exploration is normally limited to a circumference sector that includes a minimum of two de-swirl vanes. Exploration takes a relatively short time as the device is automatically operated by the minicomputer.

It has been proven by the long-term testing of a large number of stages that detailed knowledge of the flow-field structure at impeller inlet is essential for correctly calculating the average values to be used in evaluating stage performance. Repeatability of the measurements is achieved through the use of the previously-described procedure, which, however, must be properly suited to routine testing by keeping the number of measuring positions within limits representing an acceptable compromise between accuracy and time requested. This result is also achieved by availability of present-generation computer-controlled data acquisition systems capable of handling, analyzing, and synthesizing the huge mass of data resulting from each individual test.

Test data reduction

The kiel-probe total pressure readings require no correction since they are valid over a flow angle range of $\pm 60^\circ$. On the other hand, the total pressure measurements of the non-rotated cobra probe have to be corrected versus pitch and yaw angles, by means of calibration curves (Fig. 4). Moreover, the local static pressure is evaluated as an average of the P_2 and P_3 cobra-probe side pressures, and corrected for yaw and pitch angles, by means of other calibration curves (not shown in Fig. 4). Since the static pressure measured by means of cobra probes is generally speaking not wholly reliable, a correction is performed by integrating the mass flow on the probe's measuring section and comparing it with the flow measured by means of the calibrated orifice installed in the piping at the test rig outlet. The static pressures measured with the probe are then corrected until the measured mass flow is coincident with the flow integrated on the measurement section.

For weight-averaging the total pressures measured by the kiel-probe rake, static pressures are measured on the two opposite channel walls, and linearly interpolated inbetween. Local dynamic pressures can then be estimated, allowing the weight-averaging of the total pressures on the whole section to be established with sufficient accuracy. After a preliminary data reduction that allows the local values of the flow parameters (total pressure, static pressure, and flow angles) to be known, first the circumferential weighted averages and then the radial ones, are calculated. This is followed by calculation of the average total pressure at the de-swirl vane outlet and at the impeller eye for determining the performance of respectively the whole stage and the impeller alone. It is worth noting that the average total pressure at the stage outlet used to calculate overall performance is measured in the same way as that at suction, i.e. by means of a rotating device fitted with a multiple probe (detail D in Fig. 3).

Characteristics of the flow-field at the impeller inlet

A number of results from measurements made at the impeller inlet of a typical standard stage using the equipment and procedure described above are shown below. The impeller specific speed

$$N_s = \frac{n\sqrt{Q}}{(H_{ad})^{3/4}} \quad (1)$$

was equal to 38 (with n expressed in rpm, Q in m^3/sec and H_{ad} in meters). This corresponds to a value midway among those typical of impellers commonly used in process compressors. The impeller blades were 30° backward-leaning at the outlet..

The results shown refer to the three different stage inlet section configurations tested. The first (shown in Fig. 3) is typical of a multistage compressor intermediate stage with a return channel and vanes for removing the flow swirl coming from the preceding stage. The second was identical to the first, with the exception of the inlet duct that was fitted with straight vanes in place of the curved de-swirl vanes. This configuration was examined for estimating the effect on performance of wakes having not as great an amplitude as those coming from strongly curved de-swirl vanes. Furthermore, straight vanes are sometimes used upstream of the first stage on a multistage configuration to remove any swirl coming from the inlet scroll.

Lastly, a series of tests were also carried out with an inlet configuration typical of the front end of a multistage compressor (Fig. 5). No vanes were fitted for this test, which was aimed at determining the performance of the stage fitted with an inlet duct without any obstacles; the results were used as reference for evaluating the net performance loss associated with the presence of upstream vanes (curved and straight).

Figs. 6a and 6b show velocity distributions at the curved de-swirl vane outlet. These were evaluated by making use of the total pressures measured by the kiel probes and the wall static pressures. Of note is the substantial circumferential repetitiveness of the flow field for all capacities and the considerable magnitude of the wakes filling the whole sector included between two consecutive vanes.

Wake mixing that reduces wake size occurs along the path between the de-swirl vane outlet and the impeller eye. Fig. 7 shows the circumferential velocity distributions at the impeller eye corresponding to the cobra probe's six radial positions for maximum capacity. Although the wakes are still well-defined and easily distinguishable in the vicinity of the hub and shroud, they are flatter at the mean radius and also have lost their repetitiveness. Nonetheless, in all positions, wake sizes are appreciably smaller than those existing at the de-swirl vane outlet.

Variations in wake magnitude for various stage capacities are shown in Figs. 8a and 8b for the streamlines adjacent to the shroud (8a) and hub (8b). While wake size drastically decreases as capacity decreases at the shroud, this fails to occur at the hub; this fact can be seen quantitatively in Fig. 9. For each circumference sector between two consecutive de-swirl vanes, the following parameter was evaluated:

$$\frac{V_{max} - V_{min}}{V_{average}}$$

Its average was evaluated at the de-swirl vane outlet and the impeller eye respectively for the four sectors investigated. The ratios between the two averages for various capacities representing wake size reduction at shroud and hub appear in Fig. 9.

Figs. 10a and 10b show the velocity distributions measured at the exit of the straight

vanes near the shroud and hub respectively.

The smaller size of the wakes is of special note. This is due to the presence of vanes without aerodynamic loading in place of de-swirl vanes providing a 65° deflection. The decay of the wakes at the impeller's eye is equivalent to that observed on the configuration with curved vanes, and is not shown here. There is a drop in total pressure in conjunction with the decay of the wakes. Using the weighted averages of the total pressures measured, the wake mixing loss coefficient for each test point was calculated:

$$\omega_{\text{mix}} = \frac{P_{r, \text{vane exit}} - P_{r, \text{imp. eye}}}{(P_r - P_s)_{\text{imp. eye}}} \quad (2)$$

The ω_{mix} coefficients are shown in Fig. 11; it is evident that the loss coefficient is only 37% that of curved vanes as a consequence of the minor initial intensity of the wakes.

Fig. 12 shows the radial meridional velocity profiles at the impeller eye. They were obtained by circumferentially averaging the velocities measured on the configuration with curved de-swirl vanes. The velocities were referred to the weight-averaged velocity corresponding to maximum efficiency capacity. A substantial consistency of the meridional velocity distribution can be observed despite the differences in wake magnitude at shroud and hub shown above.

The same figure also shows meridional velocity profiles calculated using a potential streamline curvature flow analysis method for maximum and minimum test mass-flow rates respectively. Measured calculated velocities mostly agree over two-thirds of the section span. The divergence observed near the hub may be attributed to local thickening of the boundary layer due to deceleration along the hub contour (not present along the shroud). The boundary layer actually shifts the streamlines, producing curvatures different from those considered by the potential calculation justifying the difference in velocities.

In the configuration with curved de-swirl vanes, the flow at impeller inlet shows whirl due to the deviation of the flow with respect to the geometric angle at the vane outlet. Fig. 13 shows the radial distribution of the whirl angles, circumferentially averaged, for different flows.

Stage performance

The performance parameters of the different stage configurations were made non-dimensional with respect to the corresponding values measured at the maximum efficiency flow stage with free inlet (Fig. 5).

The performance trends shown here refer only to the impeller design speed, since practically identical behavior was observed at other test speeds.

Figs. 14 and 15 show the overall stage polytropic efficiency and the head coefficient based on total temperature increase:

$$\text{Head coeff.} = \frac{g C_p \Delta T_{\text{tot}}}{U_2^2} \quad (3)$$

Since, as previously described, there is a certain amount of flow whirl at the impeller inlet in the configuration with curved de-swirl vanes, the head coefficients were corrected by the addition of the corresponding inlet angular momentum to make them comparable to those measured on the other configurations:

$$\text{Head coeff. (corrected)} = \frac{g C_p \Delta T_{\text{tot}}}{U_2^2} + \frac{V_{u1} r_1}{U_2 r_2} \quad (4)$$

where U_2 is the impeller tip speed, r_1 the mean impeller eye radius, and r_2 the impeller outer radius; the corrected head coefficients correspond to curve 4 in Fig. 15. Likewise, in Fig. 14, the efficiencies measured on the configuration with curved de-swirl vanes were referred to flows corrected as a function of the average flow whirl angle at the impeller eye (curve 4). The corrected flows correspond to those required in the absence of flow whirl to obtain average incidence angles at the blade leading edge equal to those actually existing in test conditions.

Fig. 15 shows that the head coefficients relating to an inlet fitted with straight vanes and a free inlet do not appreciably differ at flows below maximum; at maximum flow, some residual wake from the vanes reduces the work output to a certain extent. Efficiencies with straight vanes average 1.3% lower than those with free inlets.

At first glance, the performance curves with de-swirl vanes reveal a shift in the flow capacities toward lower values as an effect of the positive impeller inlet whirl. Comparisons of the head coefficients and stage polytropic efficiencies with the equivalents of the other two configurations are possible by using the curves corrected for pre-whirl as previously described (curves 4 in Figs. 14 and 15). Efficiency is not apparently reduced with respect to the straight vane configuration if the shift in capacities due to whirl is removed.

As far as head coefficients are concerned, adding the flow angular momentums due to the de-swirl vanes brings them back to values measured on the straight vane configuration, with the exception of high flow points where a 2 - 3% decrease is observed. This fact is an indication of the possible existence of residual wakes at the blade leading edge which prevent the impeller from providing more work; in fact, incomplete mixing of wakes, especially on the shroud streamline, was previously noted at the impeller eye for high capacities.

From the two above illustrations, it can be concluded that the stage performance is only slightly affected by the pressure of upstream vanes, either straight or curved, and different associated wake amplitudes. This fact, in turn, can be considered a good indication of a fair inlet duct system capability for handling and damping circumferential inlet flow distortions.

Conclusions

The experimental results described and analyzed above offer a number of useful indications for determining the effect of inlet distortions on performance, as well as establishing the validity of the test procedures set up for executing fluid-dynamic measurements within flow fields of this kind. This latter aspect is of great importance when considering that a relatively high number of stages must be tested and reliable performance data must be provided for predicting overall performance of multistage compressors designed by suitably combining these stages. Also, a sufficient amount of detailed information about the structure of the flow field is required for improving the design and related analytical tools.

With regards to the aspects mentioned above, the main conclusions that can be drawn are:

- at the de-swirl vane outlet, total pressure gradients are of such great magnitude that it is unadvisable to take measurements by keeping the kiel-probe rake in a fixed position where the local average total pressure corresponds to the circumferentially weight-averaged value. No matter how greatly test times are decreased this way, the reliability of the measurements would still be appreciably reduced.

The regularity of the meridional velocity profiles and flow angles at the impeller eye and the repetitiveness of the mixing loss coefficients downstream of the de-swirl vanes make it possible to decrease the number of radial traverses with the moving probe. However, this can only be done after the non-variable parameters of the configuration being tested have been identified by means of a series of preliminary measurements.

Despite the great intensity of the wakes at the curved de-swirl vane outlet, the meridional velocity profiles circumferentially averaged at the impeller eye are still not far from those predicted using axi-symmetric streamline curvature potential analysis methods. This is also a sign that the inlet duct geometry is able to handle, and even reduce, the circumferential distortions, without producing considerable meridional flow separations.

- The presence of both straight and curved vanes upstream of the impeller causes a variation in performance (polytropic efficiency and head coefficient) which is relatively limited compared to the corresponding performance obtained with the free inlet. This limited effect represents still further confirmation of the quality of the design of the inlet configuration which successfully minimizes the effects of wakes even when they are of great intensity.
- Similar testing performed on stage configurations differing from the one described in this paper has shown that, despite the repetitiveness of certain phenomena and flow field parameters, the stage performance may be accurately known only by direct testing on the actual configuration itself. This depends upon the degree of variable pre-whirl at the outlets of different de-swirl vane configurations and upon the different degree of wake damping provided by the inlet duct configurations which at first glance would seem to differ only slightly.

References

1. Benvenuti, E. - Aerodynamic Development of Stages for Industrial Centrifugal Compressors. Part. 1: Testing Requirements and Equipment - Immediate Experimental Evidence. ASME paper 89 - GT - 4.
2. Benvenuti, E. - Aerodynamic Development of Stages for Industrial Centrifugal Compressors. Part. 2: Test Data Analysis, Correlation and Use. ASME paper 78 - GT - 5.

Acknowledgements

The authors wish to thank Nuovo Pignone S.p.A. for releasing publication of the information presented herein.

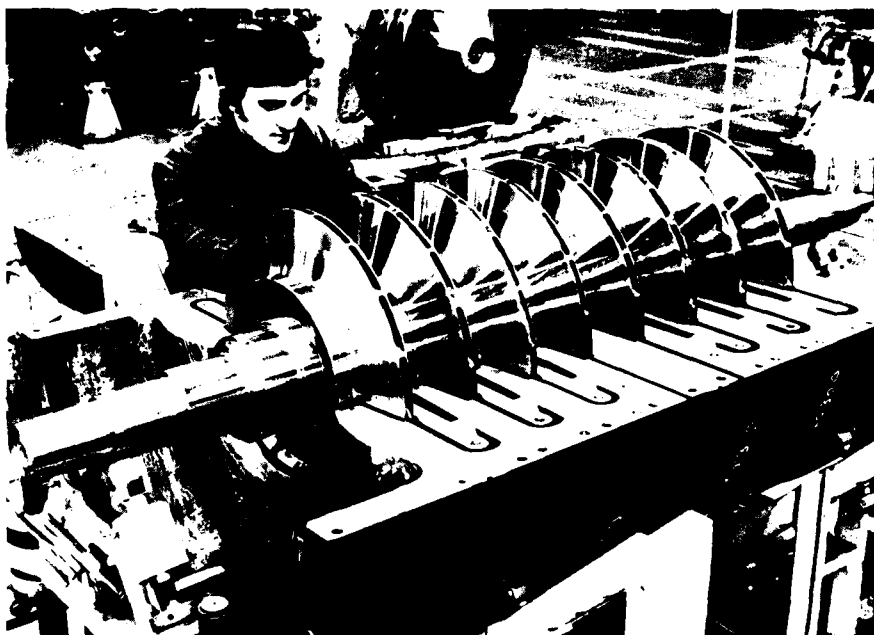


Fig. 1. Typical multistage process centrifugal compressor showing the flow-path layout.



Fig. 2. Test rig for individual process compressor stage aerodynamic testing.

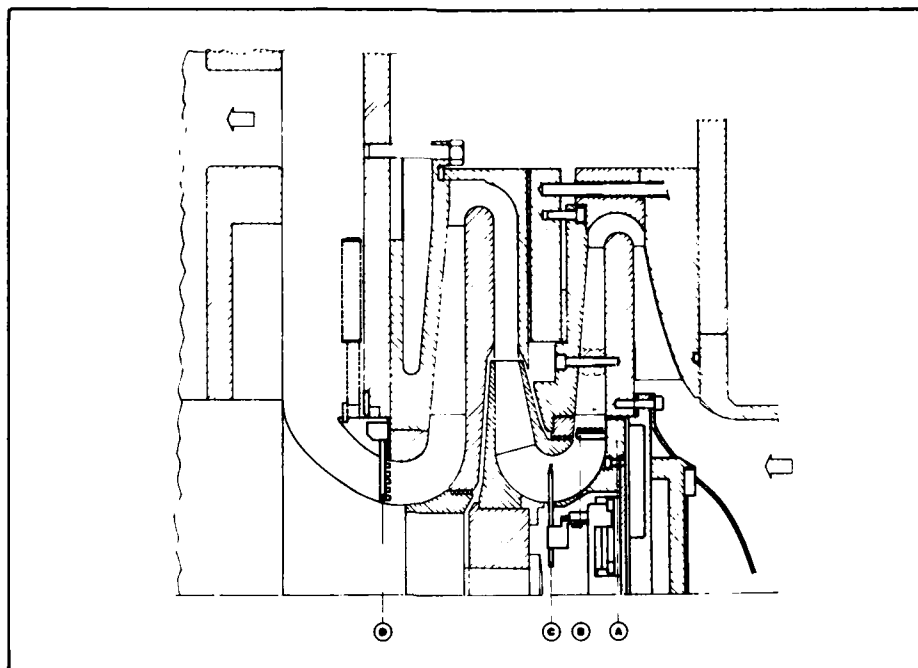
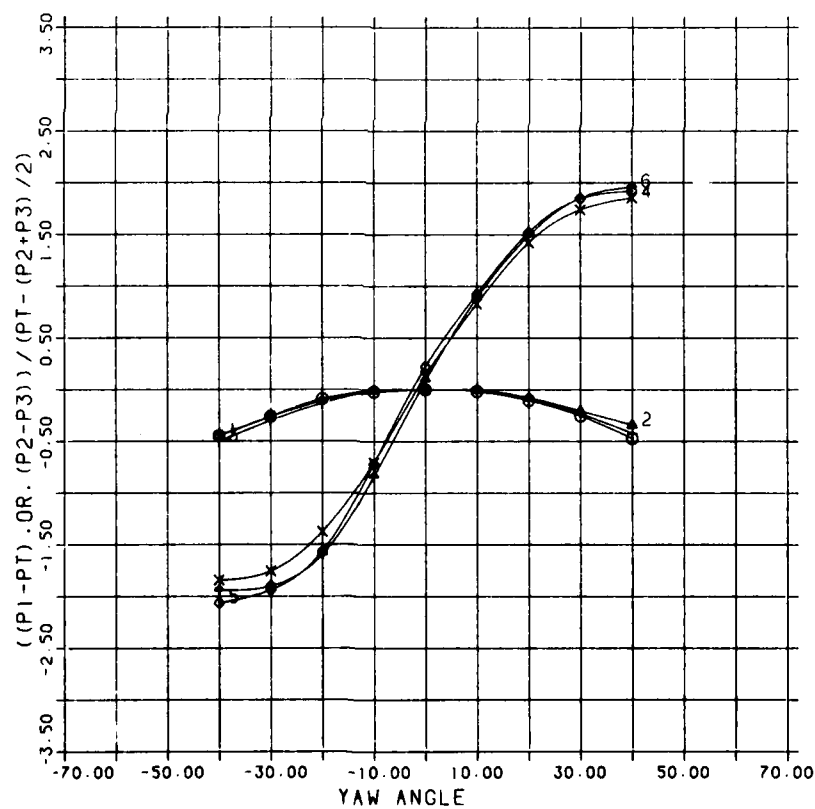


Fig. 3. Stage test set-up assembly - Upstream return channel installed.



1 (○) .	PITCH ANG. = 0	2 (△) .	PITCH ANG. = 0
3 (+) .	PITCH ANG. = +10	4 (X) .	PITCH ANG. = +10
5 (◇) .	PITCH ANG. = -10	6 (∗) .	PITCH ANG. = -10

FIG. 4 CALIBRATION CURVES OF A NON-ROTATED COBRA TYPE PROBE

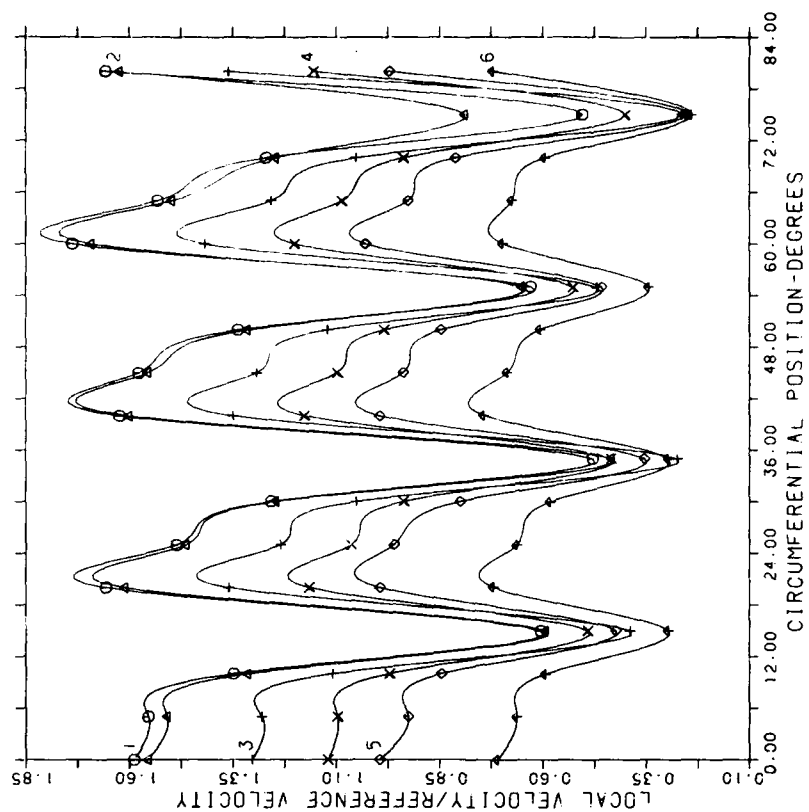


FIG. 6A VELOCITY DISTRIBUTIONS AT THE DE-SWIRL VANES EXIT-SHROUD SIDE

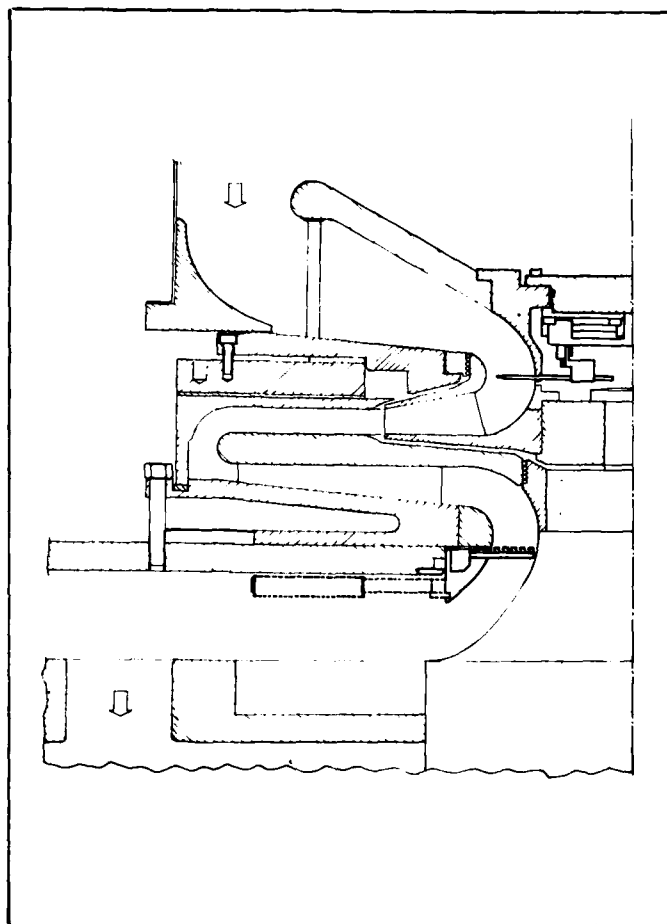


Fig. 5. Stage test set-up assembly - Inlet duct without vanes.

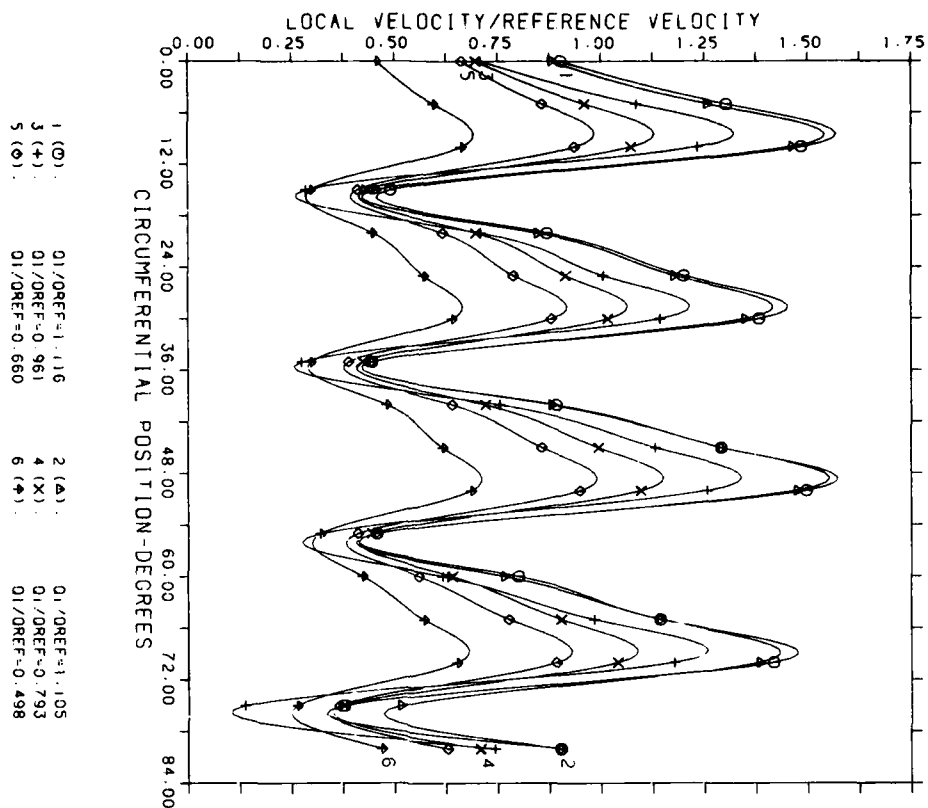


FIG. 6B VELOCITY DISTRIBUTIONS AT THE DE-SWIRL VANE EXIT-HUB SIDE

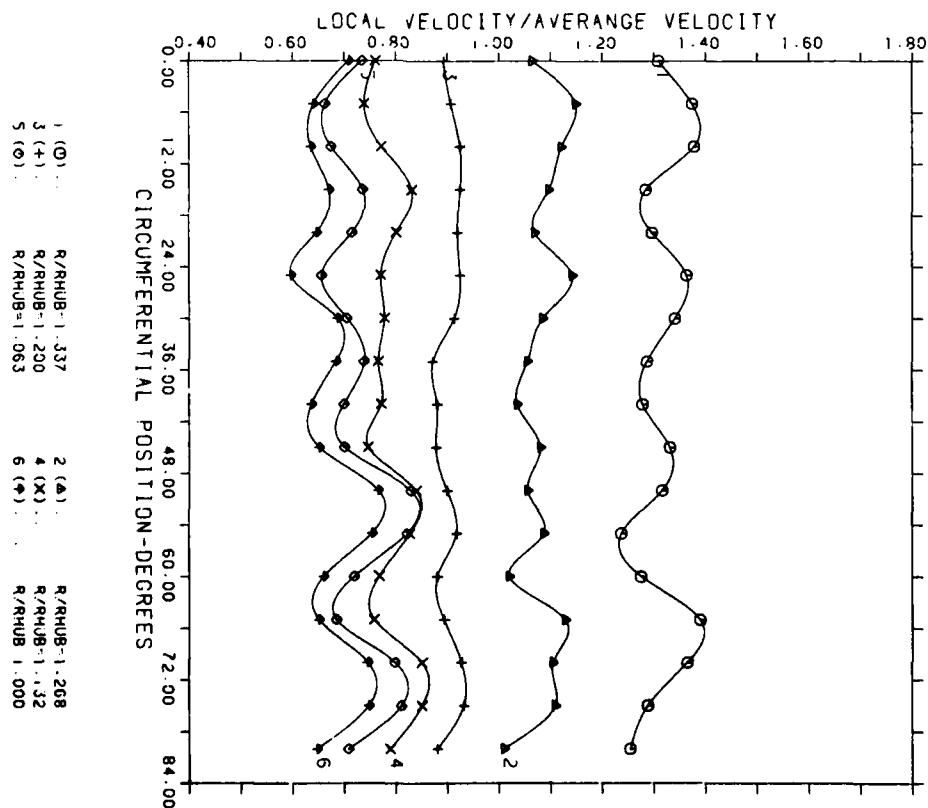


FIG. 7 VELOCITY DISTRIBUTIONS AT THE IMPELLER EYE WITH DE-SWIRL VANE MAXIMUM INLET FLOW

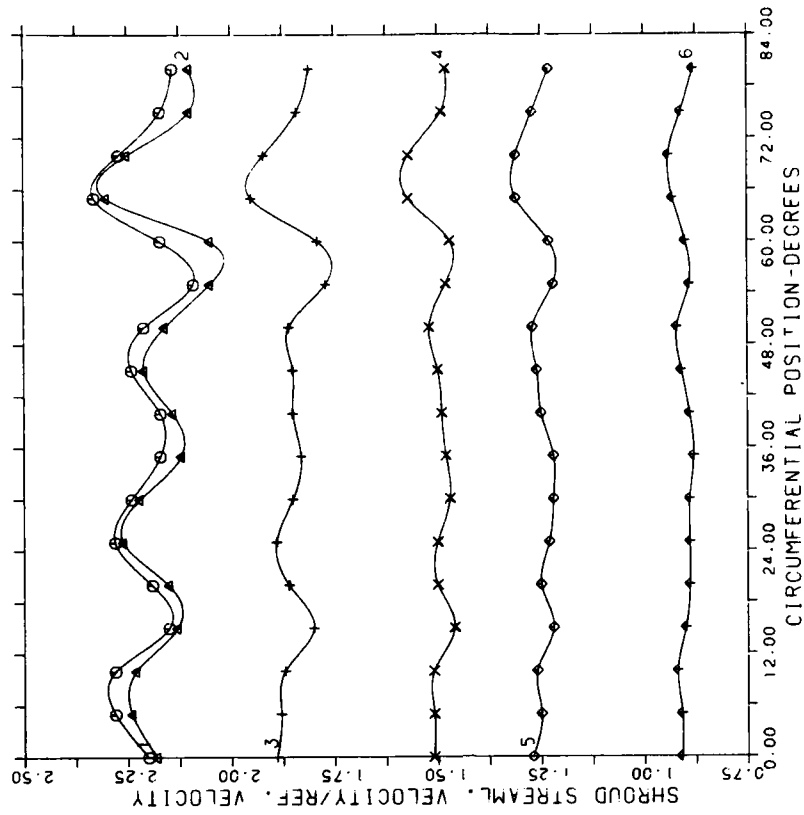


FIG. 8A VELOCITY DISTRIBUTIONS AT THE IMPELLER EYE
FOR VARYING CAPACITY AND WITH DE-SWIRL VANES.
SHROUD STREAMLINE

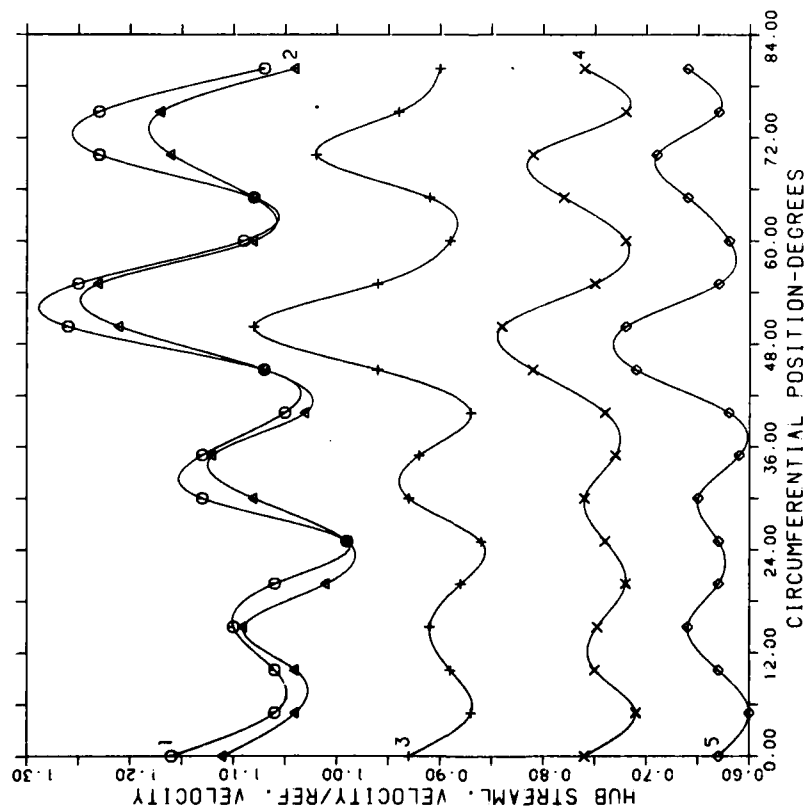


FIG. 8B VELOCITY DISTRIBUTIONS AT THE IMPELLER EYE
FOR VARYING CAPACITY AND WITH DE-SWIRL VANES.
HUB STREAMLINE

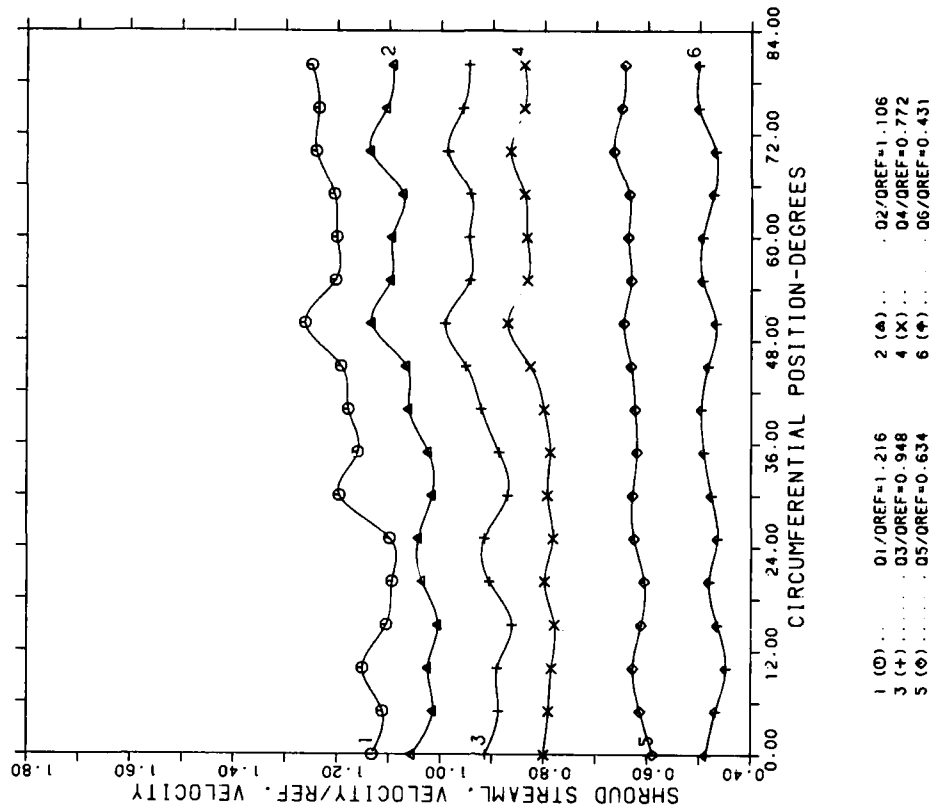


FIG. 10A AVELOCITY DISTRIBUTIONS AT THE STRAIGHT VANE EXIT-SHROUD SIDE

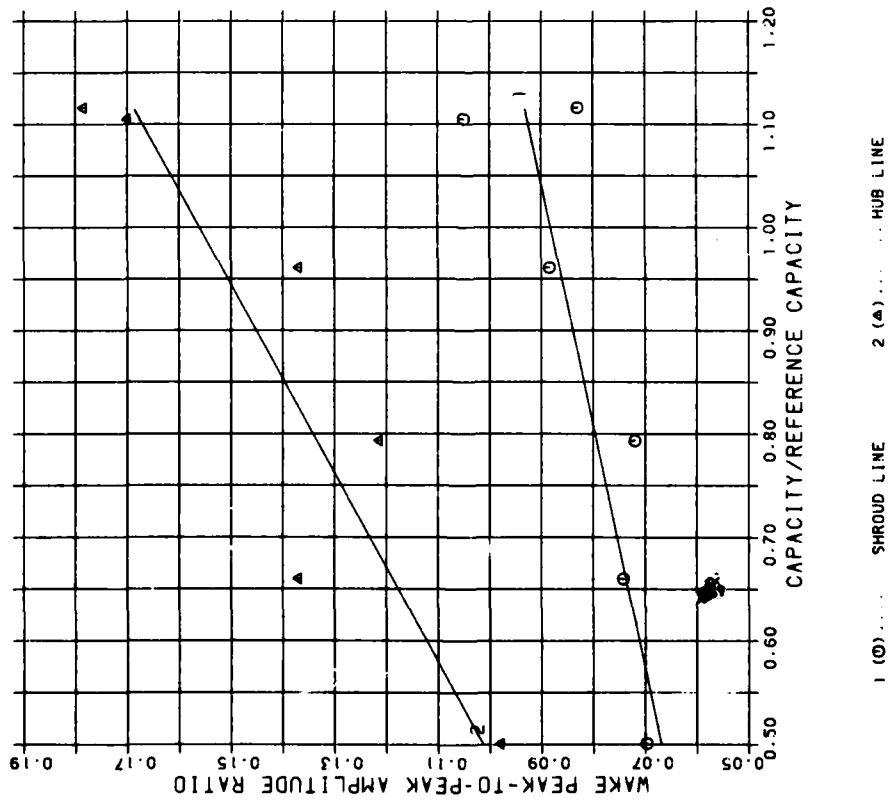


FIG. 9 WAKE PEAK AMPLITUDE DECREASE FROM DE-SWIRL VANE EXIT TO IMPELLER EYE FOR VARYING CAPACITY

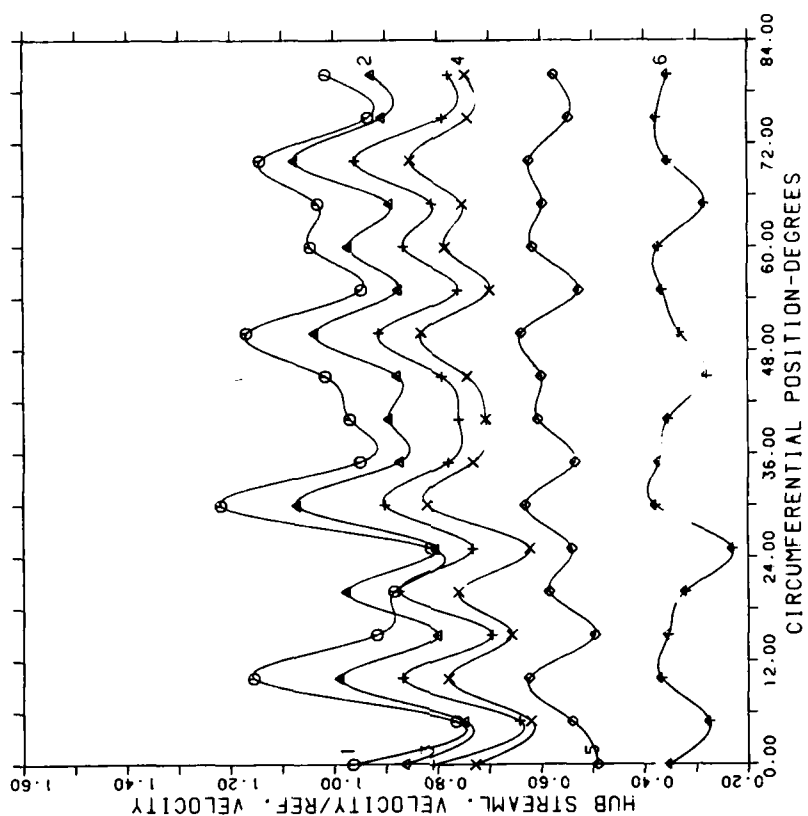


FIG. 10B VELOCITY DISTRIBUTIONS AT THE STRAIGHT VANE EXIT - HUB SIDE

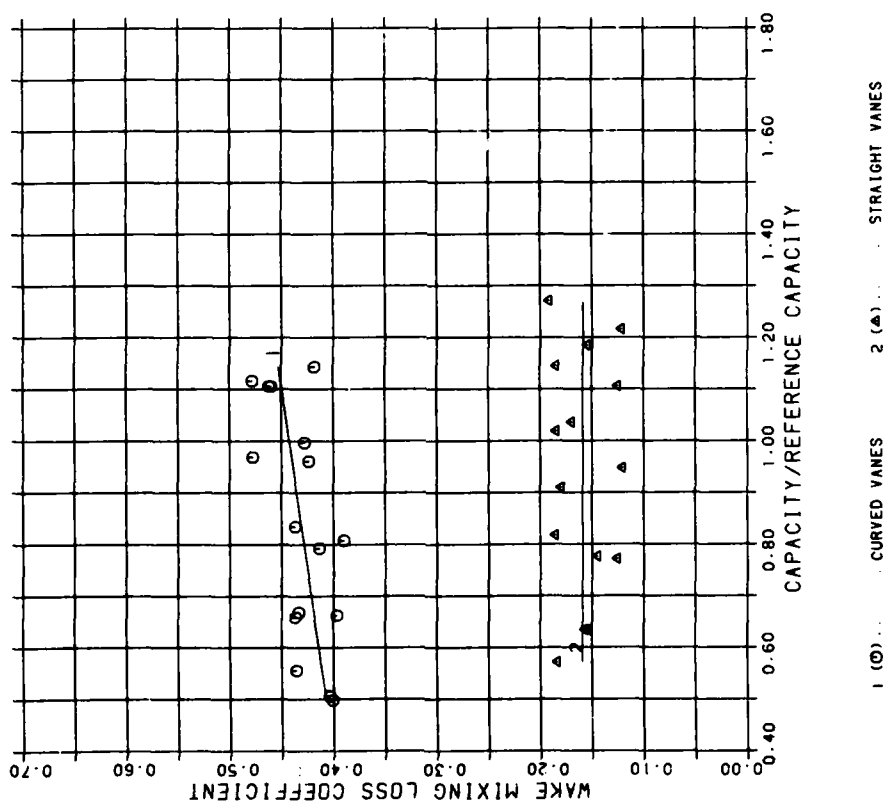


FIG. 11 WAKE MIXING LOSS COEFFICIENTS FOR CURVED AND STRAIGHT VANES (SPEED/DES. SPEED = 0.8, 1.0, 1.15)

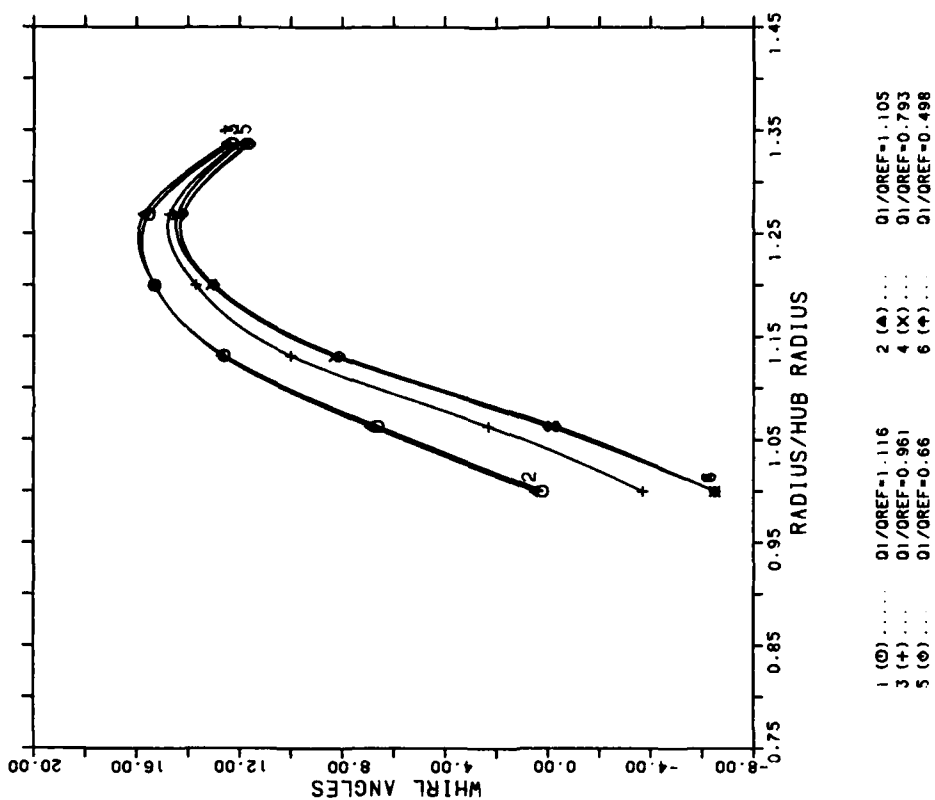


FIG. 12 NON-DIMENSIONAL MERIDIONAL VELOCITY PROFILES AT THE IMPELLER EYE WITH DE-SWIRL VANES

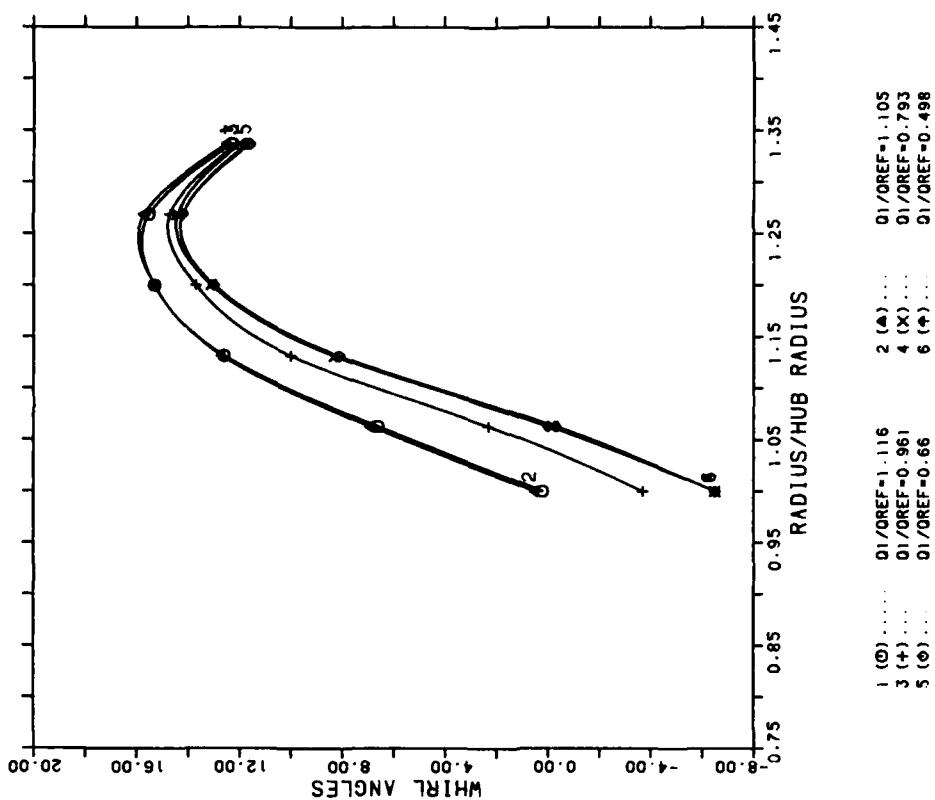


FIG. 13 WHIRL ANGLES AT THE IMPELLER EYE WITH CURVED VANES

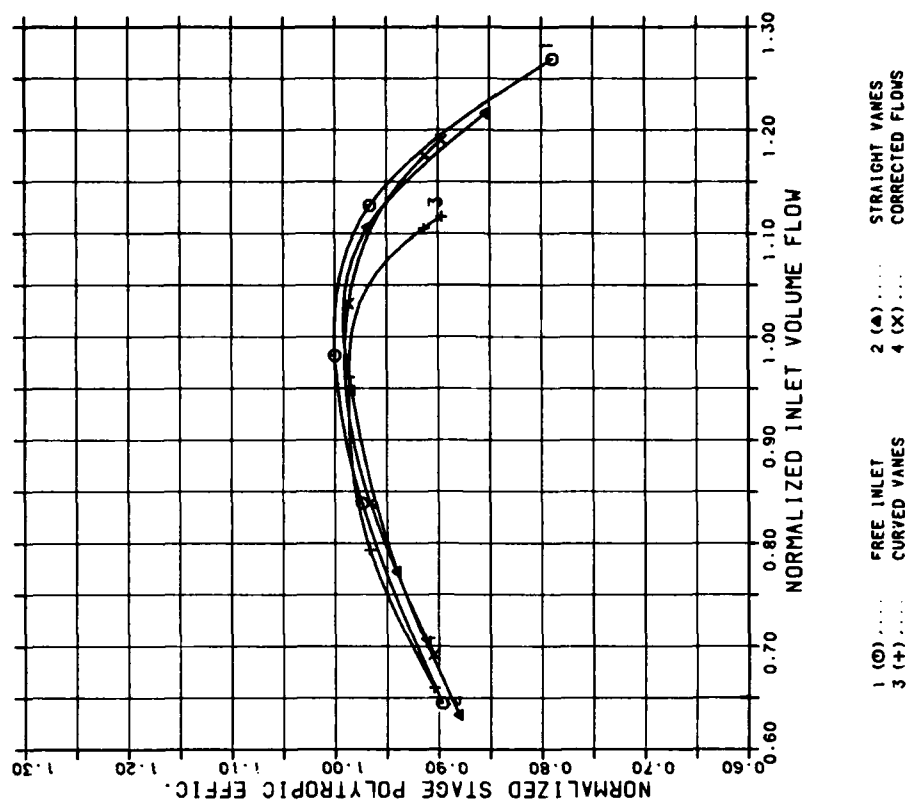


FIG. 14. NORMALIZED STAGE POLYTROPIC EFFICIENCY CURVES FOR THE THREE CONFIGURATIONS TESTED

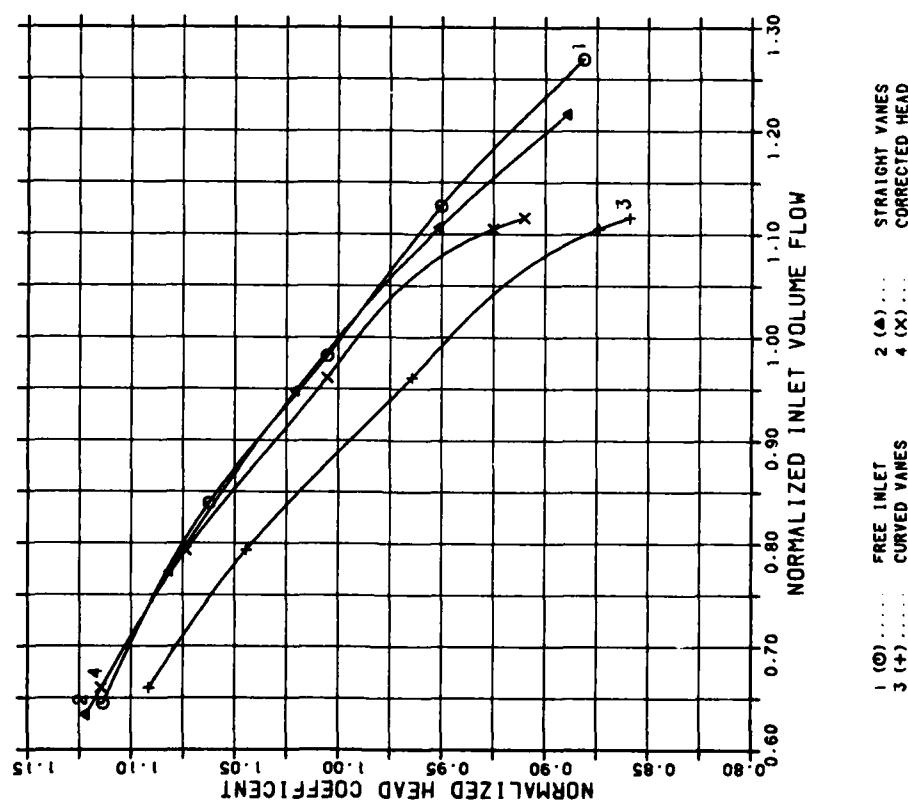


FIG. 15. NORMALIZED STAGE HEAD COEFFICIENT CURVES FOR THE THREE CONFIGURATIONS TESTED

DISCUSSION

H.E.Gallus, Technical University of Aachen, Ge

The results of your paper depend on the profiles of the return channel vanes. The figures of your paper give no information on this topic. Could the author say where such information can be found?

Author's Reply

An indication of the type of shapes used for deswirl vanes can be found in Part 1 of the paper cited in the reference list of the present paper. The profiles used are of types specifically designed for this application and experimentally developed especially to match the flow conditions existing at the exit of the crossover bend. For more details of the flow behaviour within the deswirl vanes the authors refer you to the above cited paper.

C.Rodgers, Solar, US

In matching the inlet meridional profile to the impeller blading, what radial variation of impeller incidence is prescribed?

Author's Reply

In two-dimensional impellers which are dealt with in this paper, with moderate specific speeds, the blades used are simple with constant angles at the same radii (non-twisted blades). The inlet blade angle variation from hub to shroud is obtained by inclination of leading edge in the meridional plane. This procedure may not allow one to have optimum incidences over the entire leading edge. In these cases incidence is minimised at the shroud (design point incidence is kept equal or close to zero) allowing for a few degrees of incidence at the hub where the relative Mach number is a minimum. For impellers operating at higher overall Mach numbers (e.g. for operation with heavy gases) the design is usually changed by making use of three dimensional (or twisted blades) with an inducer section that protrudes forward into the inlet channel. In this case more freedom is available for selecting incidence angles, and more use is made of criteria coming from axial compressor technology and from design of high speed, high pressure ratio, inducer-type impellers with axial inlets.

T.Yoshinaka, Pratt & Whitney Aircraft, Ca

Could the author please tell us how many points in efficiency would be lost if the severe vane wakes were kept at the impeller inlet.

Author's Reply

From the experience gained in the testing of a large number of industrial pressure stages we may predict a loss of efficiency of two to three per cent in the presence of wakes of considerable amplitude at the leading edge with respect to situations with little or no wakes. This figure should however be kept as an indication, referred to medium specific speed, medium Mach number impellers with conventional blades. Considerable scatter in efficiency variation for operation at high Mach numbers is possible. Also, specific speed, inlet configuration, and blade shape, can give substantial changes to the quoted figure. It should also be kept in mind that severe inlet flow distortions can affect surge limit considerably especially in high Mach number, high specific speed impellers. In several cases, improvement of the impeller inlet flow field was pursued in order to achieve a better surge margin as primary goal that usually also led to improvements in efficiency levels.

CALCUL DE L'ÉCOULEMENT TRANSSONIQUE DANS UN COMPRESSEUR CENTRIFUGE PAR UNE MÉTHODE PSEUDO-STATIONNAIRE

par Roland SOVRANO

*Office National d'Etudes et de Recherches Aéronautiques (ONERA)
92320 Châtillon (France)*

RESUME

Une étude de l'écoulement de fluide parfait à travers un compresseur centrifuge est effectuée. Un accent particulier est mis sur la méthode de calcul de l'écoulement relatif à des surfaces de courant de révolution en régime transsonique. Basé sur la résolution des équations d'Euler - sauf l'équation de l'énergie qui est remplacée par l'équation de Bernoulli stationnaire -, le calcul vise l'obtention de la solution permanente de l'écoulement à travers la grille étudiée. Cette approche, qui comprend la discrétion explicite des équations suivant la technique prédictor-correcteur, conduit, en définitive, à une méthode conservative dont la mise en oeuvre ne pose pas de difficultés particulières. Les résultats, que fournit ce calcul, constituent une étape importante dans l'établissement de projets de turbomachines à performances élevées.

SUMMARY

A study of perfect fluid flow through a centrifugal compressor is presented here. The calculation of a transonic flow on a blade-to-blade stream surface is emphasized. Based upon the solution of the time dependent Euler equations, -except the energy one which is replaced by the Bernoulli steady equation-, the study is directed towards the obtaining of the steady flow through the blade row. The numerical scheme is a time marching method derived from the Mac Cormack model, extended at ONERA. This approach, combining an explicit discretization of the equations according to the well-known predictor-corrector technique, corresponds to a conservative method the writing of which is not too difficult. The numerical results are very useful for designing high performance turbomachines.

1 - INTRODUCTION

Parmi les nombreuses approches des écoulements tridimensionnels dans les turbomachines, celle qui est décrite ici est semblable à celle préconisée par Wu [1]. Elle consiste à représenter l'écoulement complet par deux écoulements fictifs bidimensionnels relatifs à deux surfaces de courant dénommées S_1 et S_2 par Wu. Les premières (S_1), supposées de révolution autour de l'axe de rotation de la machine, sont déterminées par un calcul d'écoulement axisymétrique, désigné encore sous le nom d'écoulement moyen, tandis que les secondes (S_2) sont assimilées aux surfaces-squelettes des aubes et ce dans l'hypothèse d'un nombre d'aubes très élevé.

La définition géométrique des surfaces S_1 , dans les compresseurs axiaux ou centrifuges, est actuellement largement répandue [2], [3], [4], [5], [6]. A l'ONERA, une méthode matricielle a servi à l'obtention de ces surfaces de courant de révolution [7]. Son domaine d'application recouvre les écoulements compressibles subsoniques, mais lorsque localement apparaissent des écoulements transsoniques, il reste légitime de supposer qu'en l'absence de phénomènes perturbateurs intenses (décollements de couches limites, ondes de chocs, phénomènes secondaires), les géométries des tubes de courant ne varient pas de façon trop sensible, de sorte que celles qui sont obtenues dans la gamme des écoulements hautement subsoniques peuvent être conservées pour les écoulements transsoniques. Dans les compresseurs centrifuges, les domaines transsoniques se trouvent essentiellement en tête de pale à l'entrée du rouet (en mouvement relatif) et en aval de la roue (en mouvement absolu) lorsque les machines délivrent des taux de pression élevés.

C'est le calcul "d'aube à aube" de ces écoulements transsoniques sur les surfaces de courant ainsi définies qui sera décrit et réalisé grâce à une méthode pseudo-stationnaire, dérivée d'un schéma préconisé par Mac Cormack [8] et développée à l'ONERA par Viviani et Veuillot [9].

Les applications aux roues mobiles et diffuseurs de compresseurs centrifuges seront illustrées par un exemple.

2 - EQUATIONS GENERALES

Pour un écoulement de fluide compressible non visqueux, les équations générales de continuité, de mouvement et d'énergie s'écrivent :

$$(1) \quad \frac{\partial \rho}{\partial t} + \operatorname{div}(\rho \vec{w}) = 0$$

$$(2) \quad \frac{D\vec{w}}{Dt} + 2\vec{\omega} \times \vec{w} - \omega^2 \vec{r} = -\frac{1}{\rho} \operatorname{grad} p$$

$$(3) \quad \frac{D\varepsilon}{Dt} + p \frac{D(1/\rho)}{Dt} = Q$$

Ce travail a été effectué sous contrat DRET.

avec
$$\frac{D}{Dt} = \frac{\partial}{\partial t} + (\vec{w} \cdot \text{grad})$$

t , temps,

ρ , masse volumique du fluide,

\vec{w} , vitesse relative à la roue considérée (absolue dans les grilles fixes et relative dans les roues mobiles),

ω , vitesse angulaire de rotation (supposée constante dans les rotors et nulle dans les grilles fixes),

r , position radiale du point considéré.

p , pression locale,

E , énergie interne du fluide,

Q , quantité de chaleur échangée avec l'extérieur,

A ces équations, il faut associer l'équation d'état :

$$(4) \quad p = \rho R T$$

où R désigne la constante massique du gaz,

et T la température.

D'après le premier principe de la thermodynamique l'équation de l'énergie en régime permanent peut encore s'écrire sous la forme :

$$(5) \quad T ds = dh - \frac{dp}{\rho}$$

où s et h représentent respectivement l'entropie et l'enthalpie massiques du fluide, avec $h = E + \frac{p}{\rho}$

L'introduction pour un écoulement adiabatique ($Q = 0$) de la rothalpie \mathcal{I} en mouvement relatif ou de l'enthalpie d'arrêt H en mouvement absolu

$$(6) \quad \mathcal{I} = h + \frac{w^2 - \omega^2 r^2}{2}$$

$$(7) \quad H = h + \frac{v^2}{2}$$

où ωr est la vitesse d'entraînement et v la vitesse absolue,

conduit à modifier l'équation du mouvement (2) qui devient :

$$(8) \quad \frac{\partial \vec{w}}{\partial t} + (\vec{w} \cdot \text{grad} \vec{w} + \vec{\omega} \times \vec{w}) = - \text{grad } \mathcal{I} + T \text{grad } s$$

Le passage de l'écoulement relatif à l'écoulement absolu se fait simplement par la mise à zéro de ω et l'identification de \vec{w} et \vec{v} , donc de \mathcal{I} et H .

3 - ECOULEMENTS SUR LES SURFACES S_1 ET S_2

3.1 - Ecoulement axisymétrique - définition des surfaces S_1

Dans un repère de coordonnées cylindriques (r, θ, z) , lié à la grille étudiée, le traitement des équations générales a lieu, moyennant les hypothèses suivantes :

- l'écoulement est considéré comme permanent dans le repère choisi ($\partial/\partial t = 0$), ce qui revient à négliger les influences des "sillages" des aubes sur les grilles situées plus en aval,
- le nombre d'aubes est supposé très élevé, de sorte qu'en première approximation les diverses grandeurs aérodynamiques ne dépendent que des coordonnées axiale et radiale (z et r),
- dans les grilles, la vitesse est supposée tangente à une ligne moyenne fixée à l'avance, déduite des squelettes des aubes, mais pouvant être corrigée éventuellement pour tenir compte du "glissement" du fluide.

L'introduction d'une fonction de courant, satisfaisant à l'équation de continuité (1), permet de transformer l'équation du mouvement (8), et conduit à une équation différentielle non linéaire du second ordre aux dérivées partielles, suivant les directions axiale et radiale, de cette fonction de courant.

Sa résolution, effectuée dans un maillage épousant au mieux la géométrie de la machine, nécessite une discrétisation des dérivées partielles qui sont approchées par un développement limité au second ordre. Les conditions aux limites sont de type mixte, soit de type Dirichlet et de type Neumann.

Le procédé itératif employé, associé à une technique de relaxation, permet une rapide convergence du calcul, de sorte que, après obtention de la solution, il est aisé de déterminer, par interpolation, la géométrie des tubes de courant de révolution, dont la "trace moyenne" constitue la surface S_1 .

3.2 - Écoulement sur les surfaces S_1 - Écoulement d'aube à aube

Le passage du calcul de l'écoulement axisymétrique, réalisé dans le système de coordonnées (r, z) , au calcul dans un tube de courant d'épaisseur locale δ , mesurée normalement à la surface de courant S_1 définie ci-dessus, conduit à utiliser un repère (m, θ) , où m représente l'abscisse curviligne méridienne.

La figure 1 représente schématiquement la géométrie de tels tubes de courant dans un plan méridien et leur développée dans le repère (m, θ) , limitée à deux lignes de courant distantes d'un pas des aubes.

Les équations instationnaires s'écrivent, avec l'équation de mouvement projetée suivant les directions m et θ :

$$(9) \quad \frac{\partial(\delta p)}{\partial t} + \frac{\partial(\delta r \rho u)}{\partial m} + \frac{\partial(\delta p v)}{\partial \theta} = 0$$

$$(10) \quad \frac{\partial(\delta r \rho u)}{\partial t} + \frac{\partial[\delta r (\rho + \rho u^2)]}{\partial m} + \frac{\partial(\delta p r u)}{\partial \theta} = \rho \frac{d(\delta r)}{dm} + \delta p (v + \omega r)^2 \frac{dr}{dm}$$

$$(11) \quad \frac{\partial(\delta r \rho v)}{\partial t} + \frac{\partial(\delta r \rho u v)}{\partial m} + \frac{\partial[\delta r (\rho + \rho v^2)]}{\partial \theta} = -\delta p u (v + \omega r) \frac{dr}{dm}$$

$$(12) \quad \frac{\partial[\delta r (\rho T - p)]}{\partial t} + \frac{\partial(\delta r \rho u T)}{\partial m} + \frac{\partial(\delta p r T)}{\partial \theta} = 0$$

où u et v désignent les composantes de \vec{w} suivant m et θ .

Dans l'écriture de ces équations, il est admis implicitement que les variations locales, suivant la normale à S_1 , sur l'épaisseur δ du tube de courant, sont négligeables, ce qui suppose que les hauteurs du tube étudié restent modérées. De plus, l'absence de source ou puits se traduit par un second membre nul dans l'équation de continuité (9). Dans un écoulement adiabatique (cas généralement réalisé pour les compresseurs), l'équation de l'énergie (12) peut être prise sous sa forme intégrée stationnaire (6) ou (7), ce qui entraîne que le système d'équations (de (9) à (12)) n'est plus entièrement instationnaire, d'où la dénomination de pseudo-instationnaire.

Cette modification implique une diminution du nombre d'inconnues, réduit à 3 ($\delta p, \delta r \rho u, \delta r \rho v$) et se traduit par un gain de temps de calcul. En revanche, lors du déroulement du calcul itératif, les résultats intermédiaires n'ont pas de signification physique.

Si les itérations convergent vers une solution unique, c'est elle qui représentera l'écoulement stationnaire de fluide parfait dans le tube de courant étudié.

4 - TECHNIQUE NUMERIQUE

La résolution numérique des équations (9) à (11), compte tenu de (6), est effectuée dans le domaine de calcul tel que celui représenté sur la figure 1b, dans le cas de l'étude d'une roue mobile. La discrétisation des équations et le choix des conditions aux limites sont faits en fonction de la géométrie de ce domaine.

4.1 - Domaine de calcul

Dans le repère (m, θ) le domaine de calcul comprend, outre la grille proprement dite, des zones amont et aval, dans lesquelles un écoulement non uniforme peut s'établir par suite des variations de rayon (donc de m) et de la présence d'ondes de choc (près des bords d'attaque notamment).

Le maillage du champ est constitué de lignes épousant globalement la forme des lignes de courant et de colonnes qui sont quasi-normales à ces lignes (figure 2), ce qui a pour effet l'obtention de mailles quasi-rectangulaires. Le temps de progression du calcul est lié aux dimensions de l'ellipse inscrite dans de telles mailles ; comme pour les mailles "rectangulaires", cette ellipse est proche d'un cercle, on remarque que le maillage choisi se prête à nombre de points de calcul donné, aux pas de temps les plus grands.

4.2 - Schéma de calcul

La méthode de Mac Cormack [8], utilisée pour résoudre le système d'équations hyperboliques pseudo-instationnaires, consiste à prendre en chaque point, pour le passage du temps t^n au temps $t^{n+1} = t^n + \Delta t$, un schéma prédictor-correcteur ; au cours de chacune des phases, les dérivées, représentées par des différences, sont décentrées (avancées à l'étape prédictor et retardées à l'étape correcteur).

Partant de l'équation matricielle :

$$(13) \quad \frac{\partial U}{\partial t} + \frac{\partial F(U)}{\partial m} + \frac{\partial G(U)}{\partial \theta} = H$$

AD-A094 912

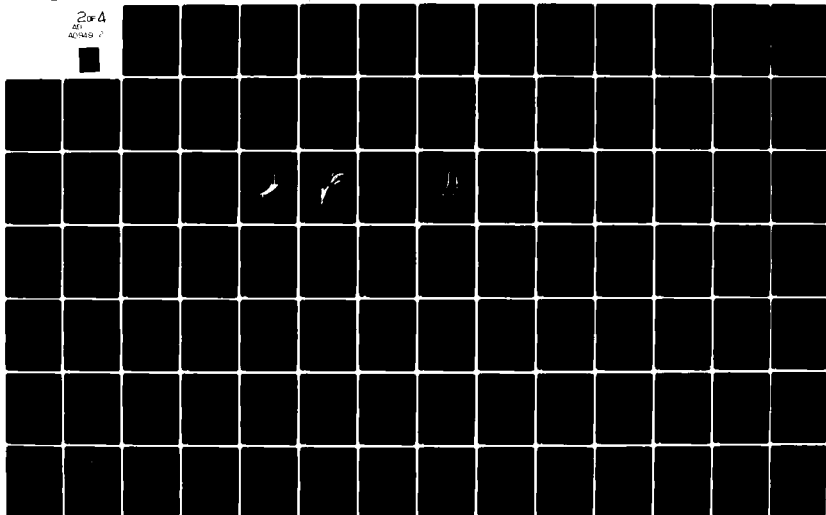
ADVISORY GROUP FOR AEROSPACE RESEARCH AND DEVELOPMENT--ETC F/6 21/5
CENTRIFUGAL COMPRESSORS: FLOW PHENOMENA AND PERFORMANCE.(U)
NOV 80

UNCLASSIFIED

AGARD-CP-282

NL

2 of 4
SERIAL
ACQUISITION



représentant le système d'équations de (9) à (11)

où

$$\begin{aligned} U &= (brp, brpu, brpv) \\ F &= (brpu, br(p+pu^2), brpuv) \\ G &= (brpv, brpuv, br(p+pv^2)) \\ H &= (0, p \frac{d(brp)}{dt} + brp(v+\omega r)^2 \frac{dr}{dt}, -brpu(v+\omega r) \frac{d\theta}{dt}) \end{aligned}$$

la décomposition du calcul comprend, pour le point courant $M(i,j)$, telle que le représente la figure 3, les trois phases suivantes que l'on suivra facilement sur cette figure.

1ère phase : prédicteur

$$(14) \quad U_{i,j}^{\tilde{n+1}} = U_{i,j}^n - \Delta t \left[\left(\frac{\partial F}{\partial m} \right)_{i,j}^n + \left(\frac{\partial G}{\partial \theta} \right)_{i,j}^n - H_{i,j}^n \right]$$

où les dérivées spatiales (avancées) sont obtenues simplement par un développement limité au premier ordre, en considérant les points P et N, voisins de M, soit pour la fonction F par exemple :

$$(15) \quad \begin{cases} F_P = F_M + \left(\frac{\partial F}{\partial m} \right)_M (m_P - m_M) + \left(\frac{\partial F}{\partial \theta} \right)_M (\theta_P - \theta_M) + \dots \\ F_N = F_M + \left(\frac{\partial F}{\partial m} \right)_M (m_N - m_M) + \left(\frac{\partial F}{\partial \theta} \right)_M (\theta_N - \theta_M) + \dots \end{cases}$$

De ces relations il est aisé de déduire les dérivées partielles par rapport à m et à θ .

A partir de $U_{i,j}^{\tilde{n+1}}$ de l'équation d'état et de l'équation de l'énergie que nous avons pris stationnaire, on peut calculer les $F_{i,j}^{\tilde{n+1}}$, $G_{i,j}^{\tilde{n+1}}$, $H_{i,j}^{\tilde{n+1}}$.

2ème phase : correcteur

$$(16) \quad U_{i,j}^{n+1} = \frac{1}{2} \left\{ U_{i,j}^n + U_{i,j}^{\tilde{n+1}} - \Delta t \left[\left(\frac{\partial F}{\partial m} \right)_{i,j}^{\tilde{n+1}} + \left(\frac{\partial G}{\partial \theta} \right)_{i,j}^{\tilde{n+1}} - H_{i,j}^{\tilde{n+1}} \right] \right\}$$

où, cette fois, les points considérés autour du point M sont Q et R, et les différences seront retardées.

3ème phase : introduction d'une viscosité artificielle

Afin d'assurer une meilleure stabilité aux calculs, notamment dans les régions à forts gradients, il est nécessaire d'introduire un terme dissipatif, appelé "viscosité artificielle", dont le rôle est de corriger les résultats obtenus dans la phase 2.

Durant chacune des principales phases (prédicteur et correcteur), sont calculées les conditions imposées sur les frontières.

4.3 - Conditions initiales et conditions aux limites

4.3.1 - Conditions initiales

Jusqu'à présent, nous n'avons défini que la géométrie de la machine. La définition de l'écoulement nécessite de plus la connaissance des caractéristiques de l'écoulement : vitesse de rotation, débit, pression et température génératrices. Au moyen de ces données, il est possible en principe d'initialiser, au temps $t = 0$, les inconnues dans tout le champ, en effectuant par exemple une approximation par tranches planes. Ces conditions de départ peuvent être assez éloignées du résultat final, cependant, on a tout avantage à partir d'une solution initiale qui ne soit pas trop éloignée de la solution stationnaire finale, de façon à réduire les temps de calcul.

4.3.2 - Conditions aux limites

Le traitement des conditions aux limites a été décrit de façon détaillée en [9]. On peut le résumer ainsi. Comme le schéma de Mac Cormack ne peut s'appliquer tel quel sur les frontières, par suite du manque de "points voisins", il est nécessaire de calculer les dérivées spatiales à l'aide d'opérateurs aux différences décentrées. De plus, il semble intéressant de pouvoir traiter toutes les frontières (solides ou non) par un même mode de calcul, tout en assurant des conditions spécifiques à chaque frontière.

En considérant un système d'axes local, lié à la frontière (figure 4), on peut réécrire l'équation (13) sous la forme :

$$(17) \quad \frac{\partial U}{\partial t} + [A] \frac{\partial U}{\partial \xi} + [B] \frac{\partial U}{\partial \eta} = H$$

où $[A]$, $[B]$ désignent les matrices de passage dépendant de U seulement. La théorie des caractéristiques montre qu'on peut obtenir une combinaison linéaire (ou relation de compatibilité) des équations (17) où n'interviennent que les dérivées suivant deux directions dans un plan caractéristique (qui sera choisi ici comme celui dont la trace dans un plan $t = \text{cte}$ sera parallèle à la frontière, c'est-à-dire à l'axe $M\eta$).

Dans ces conditions, si les dérivées partielles par rapport à \mathfrak{y} sont connues ainsi que la matrice unicolonne H , il suffit de chercher dans le plan $(\mathfrak{f}, \mathfrak{t})$ les directions caractéristiques (ou valeurs propres de la matrice $[A]$), $\frac{d\mathfrak{f}}{dt} = \lambda$ ainsi que les relations de compatibilité associées au système

$$(18) \quad \frac{\partial U}{\partial t} + [A] \frac{\partial U}{\partial \mathfrak{f}} = P$$

$$\text{avec} \quad P = H - [B] \frac{\partial U}{\partial \mathfrak{y}}$$

Comme U a trois composantes $(b_1 p, b_2 p u_f, b_3 p u_y)$, où u_f et u_y sont les composantes de la vitesse \vec{w} suivant \mathfrak{f} et \mathfrak{y} , on peut obtenir aisément les valeurs propres de $[A]$:

$$(19) \quad \begin{cases} \lambda^{(1)} = u_f \\ \lambda^{(2)} = \frac{\gamma+1}{2\gamma} u_f + \left[\frac{a^2}{\gamma} + \left(\frac{\gamma-1}{2\gamma} u_f \right)^2 \right]^{1/2} \\ \lambda^{(3)} = \frac{\gamma+1}{2\gamma} u_f - \left[\frac{a^2}{\gamma} + \left(\frac{\gamma-1}{2\gamma} u_f \right)^2 \right]^{1/2} \end{cases} \quad \text{où} \quad a^2 = \left(\frac{\partial p}{\partial \rho} \right)_s = \gamma \frac{p}{\rho}$$

à ces valeurs propres, on associe les vecteurs propres α , solution du système :

$$(20) \quad \alpha \cdot ([A] - \lambda [I]) = 0 \quad \text{où } [I] \text{ est la matrice unité,}$$

soit

$$(21) \quad \begin{cases} \alpha_1 = \left(\frac{\gamma+1}{\gamma} u_f - \lambda \right) (u_f - \lambda) + \frac{\gamma-1}{\gamma} u_y^2 \\ \alpha_2 = \lambda - u_f \\ \alpha_3 = - \frac{\gamma-1}{\gamma} u_y \end{cases}$$

ce qui conduit à :

$$(22) \quad \alpha_1^n \bar{U}_1 + \alpha_2^n \bar{U}_2 + \alpha_3^n \bar{U}_3 = \alpha^n \cdot \bar{R}$$

où $\bar{U}_1 = b_1 p$, $\bar{U}_2 = b_2 p u_f$, $\bar{U}_3 = b_3 p u_y$ (au prédicteur comme au correcteur), tandis que \bar{R} aura pour expression, déduite du schéma numérique :

$$(23a) \quad \bar{R} = U^n + \Delta t [H^n - [A] \left(\frac{\partial U}{\partial \mathfrak{f}} \right)^n - [B] \left(\frac{\partial U}{\partial \mathfrak{y}} \right)^n]$$

au prédicteur, et

$$(23b) \quad \bar{R} = \frac{1}{2} \left\{ U^n + U^{n+1} + \Delta t [H^{n+1/2} - [A] \left(\frac{\partial U}{\partial \mathfrak{f}} \right)^{n+1/2} - [B] \left(\frac{\partial U}{\partial \mathfrak{y}} \right)^{n+1/2}] \right\}$$

au correcteur.

- Conditions de glissement

Le long des profils, considérés comme paroi imperméable, la condition de glissement s'écrit simplement par $u_y = 0$ (ou vitesse normale nulle), donc le module de la vitesse sera donné par u_f , et partant des valeurs propres négatives ou nulles (ou directions caractéristiques sortant du domaine), on aura les deux relations du type (22) :

$$(24) \quad \begin{cases} \alpha_1^{(1)n} \bar{U}_1 + \alpha_3^{(1)n} \bar{U}_3 = \alpha^{(1)n} \cdot \bar{R} \\ \alpha_1^{(3)n} \bar{U}_1 + \alpha_3^{(3)n} \bar{U}_3 = \alpha^{(3)n} \cdot \bar{R} \end{cases}$$

où les vecteurs propres $\alpha^{(1)}$ et $\alpha^{(3)}$ sont associés aux valeurs propres $\lambda^{(1)} = 0$ et $\lambda^{(3)} = -a/\gamma$

Du système (24), on calcule \bar{U}_1 (ou p) et \bar{U}_3 (ou $p u_y$) donc, le module de la vitesse.

- Conditions amont et aval

Le nombre de conditions à imposer aux "infinis" amont et aval dépend de la nature subsonique ou supersonique de l'écoulement dans ces régions, c'est-à-dire de la grandeur de la vitesse M_∞ normale à ces frontières. Ce nombre est égal à celui des directions caractéristiques Λ entrant dans le domaine de calcul, donc $2 > 0$

Si la normale à une frontière est dirigée vers l'intérieur du domaine de calcul, alors les vitesses normales en amont sont positives, tandis que celles en aval sont négatives, alors le signe des valeurs propres s'en déduit immédiatement par (19).

Un tableau peut résumer le nombre de ces conditions :

Frontières	Amont	Aval
Supersonique	3	0
Subsonique	2	1

Frontière amont

Dans le cas d'un écoulement supersonique à l'entrée du domaine, trois conditions sont imposées, à savoir, la pression génératrice, la direction et le module de la vitesse.

Pour un écoulement subsonique, c'est encore la pression génératrice que l'on imposera et on lui adjoint soit la direction de l'écoulement, soit le nombre de Mach, le schéma numérique par une relation de compatibilité calcule la grandeur inconnue.

Frontière aval

Les cas les plus fréquemment rencontrés dans la pratique des compresseurs centrifuges concernent ceux où l'écoulement sortant du domaine est subsonique. Comme on doit imposer une condition, naturellement on pense à la pression statique qui joue le rôle de contrepression, ce qui, ajouté aux relations de compatibilité associées aux valeurs propres λ_1 et λ_2 , fournit un système linéaire de trois équations à trois inconnues, dont la résolution ne pose pas de difficultés de principe.

5 - APPLICATIONS

La méthode pseudo-instationnaire de calcul d'écoulement, décrite ci-dessus, a été appliquée à divers problèmes d'écoulement stationnaire de fluide parfait, tels que ceux rencontrés dans les grilles d'aubes [10], [11], dans les entrées d'air supersoniques avec un couplage à un calcul basé sur la méthode des caractéristiques.

Pour le calcul de l'écoulement dans les compresseurs à taux de pression élevé (compresseurs centrifuges notamment), une extension du programme de calcul relatif à des configurations fixes (tuyères, grilles d'aubes bidimensionnelles) a été réalisée.

5.1 - Cas d'une roue mobile

Afin de valider l'étude précédente, une comparaison des résultats obtenus par cette méthode et celle développée par Katsanis [12] à la NASA a été effectuée dans le cas d'un écoulement subsonique sur une surface de courant de révolution. Le bon accord entre les deux calculs a servi de base à l'extension de la méthode pseudo-instationnaire vers les domaines transsoniques. Les résultats de calcul présentés ici correspondent au cas d'un compresseur centrifuge. Nous ne montrerons que les résultats obtenus pour un tube de courant qui présente une convergence de 3,33 et un rapport de rayon de 1,98 entre l'aval et l'amont.

L'écoulement d'entrée est à Mach subsonique très élevé ($M = 0,927$). Les profils sont de faible épaisseur et constituent des pales couchées en arrière. La figure 5a montre la variation le long du profil ($\pi = \pi$ rapportée à la corde projetée sur l'axe) de l'angle de cet aubage. Le calcul a permis de représenter le nombre de Mach le long de l'aube (figure 5b). On peut constater la faible charge dans la partie de captation de la roue ; elle est vraisemblablement due à la géométrie locale du profil, associée aux effets d'incidence qui sont importants. Dans le cas considéré, les phénomènes transsoniques sont limités au voisinage du bord d'attaque. Un calcul relatif à un compresseur dont les profils sont épais et le pas relatif assez faible a donné les résultats portés sur la figure 6.

5.2 - Cas d'un diffuseur

Le diffuseur est généralement constitué par une grille bidimensionnelle, placée en aval de la roue mobile ; sa réalisation ne pose pas de gros problèmes d'ordre mécanique. Sur le plan aérodynamique, le diffuseur est chargé de récupérer de la pression par ralentissement de la vitesse absolue du fluide. Placé dans de difficiles conditions de captation (le fluide issu de la roue mobile présente des hétérogénéités tant axiales qu'azimutales, le diffuseur a un comportement qui est fortement influencé par son écoulement incident.

Cependant, dans une première étape, on n'a pris en compte le voisinage immédiat de la roue mobile que par la simulation de l'écoulement issu de cette grille par une source tourbillon d'intensité connue.

Pour valider le calcul, les aubes du diffuseur ont été assimilées à des lignes sans épaisseur, équivalentes aux lignes de courant de l'écoulement source-tourbillon donné.

Les résultats numériques sont portés sur la figure 7, sur laquelle les répartitions de nombres de Mach le long des lignes moyennes sont comparées à celles que donne l'écoulement de source-tourbillon. Deux cas ont été traités, l'un concerne un écoulement subsonique et l'autre un écoulement transsonique.

Le bon accord obtenu entre la méthode numérique et le calcul théorique laisse augurer un avenir intéressant pour des applications à des diffuseurs réels.

6 - CONCLUSION

L'approche théorique présentée ci-dessus des calculs d'écoulement transsonique dans les turbomachines et notamment les compresseurs centrifuges offre des avantages indéniables mais possèdent des inconvénients certains.

Parmi les avantages, on peut citer la relative commodité de mise en oeuvre de tels programmes de calcul, le faible encombrement mémoire dans les ordinateurs, l'intérêt des résultats pour le calcul de projet de compresseurs.

En contrepartie, le temps relativement long des calculs pseudo-instationnaires ainsi que l'hypothèse de géométrie axisymétrique pour les tubes de courant limitent la portée de ces méthodes. Cependant, tant que d'autres méthodes, notamment tridimensionnelles, n'auront pas été mises au point, la méthode de calcul présentée ci-dessus, qui permet d'étudier le comportement de grilles d'aubes placées dans des écoulements transsoniques, continue à être d'une grande utilité pour les motoristes.

REFERENCES

- [1] - C.H. WU
"A general theory of three-dimensional flow in subsonic and supersonic turbomachines of axial, radial, and mixed-flow types"
Trans. of the ASME - pp. 1363-1380 - nov. 1952.
- [2] - R.A. NOVAK and R.M. HEARSEY
"A nearly three-dimensional interblade computing system for turbomachinery"
Parts I and II, ASME 76-FE-19 et 76-FE-20 - 1976.
- [3] - H. MARSH
"A digital computer program for the through-flow fluid mechanics in an arbitrary turbomachine using a matrix method"
N.G.T.E. Report n° R.282.
- [4] - J.D. STANITZ
"Some theoretical aerodynamic investigations of impellers in radial - and mixed - flow centrifugal compressors".
Trans. of the ASME - pp. 473-497 - May 1952.
- [5] - Th. KATSANIS
"Use of arbitrary quasi-orthogonals for calculating flow distribution in the meridional plane of a turbomachine"
NASA TN-D-2546 (1964).
- [6] - M.R. VANCO
"Fortran program for calculating velocity in the meridional plane of a turbomachine"
NASA TN D-6701 (Mars 1972).
- [7] - R. SOVRANO et Y. RIBAUD
"Approche des écoulements compressibles dans les turbomachines par une méthode de calcul axisymétrique".
A.T.M.A. (Session 1979).
- [8] - R.W. Mac CORMACK
"The effect of viscosity on hypervelocity impact cratering".
AIAA Paper n° 69-354 (1969)
- [9] - H. VIVIAND et J.P. VEUILLLOT
"Méthodes pseudo-instationnaires pour le calcul d'écoulements transsoniques".
ONERA Public. n° 1978-4.
- [10] - J.P. VEUILLLOT
"Calcul numérique de l'écoulement transsonique d'un fluide parfait dans une grille d'aubes".
La Recherche Aérospatiale n° 1975-6 - pp. 327-338.
- [11] - J.P. VEUILLLOT
"Calculation of the quasi three-dimensional flow in a turbomachine blade row."
ASME Paper n° 76-GT-56 (1976).
- [12] - Th. KATSANIS et W.D. Mc NALLY
"Revised Fortran program for calculating velocities and streamlines on a blade-to-blade stream surface of a turbomachine".
NASA TM X-1764 -(1969).

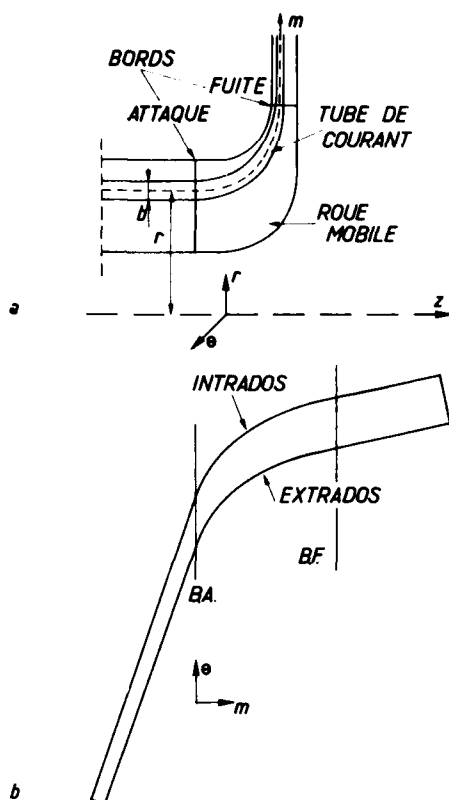


Fig. 1 - Schéma des domaines de calcul.
a) Écoulement axisymétrique (S2)
b) Écoulement sur la surface (S1).

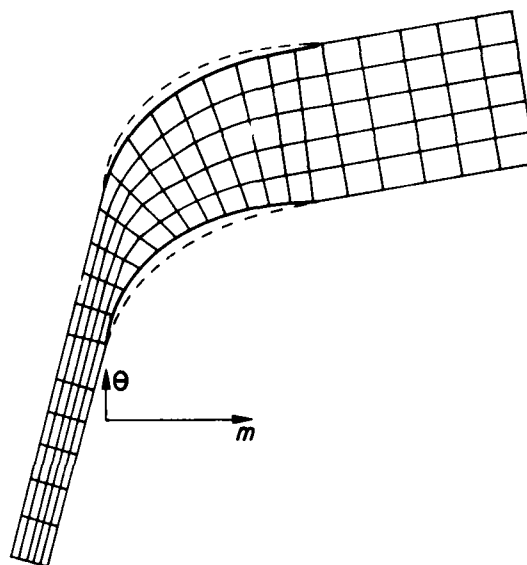


Fig. 2 - Vue schématique du maillage dans le repère (m, θ) .

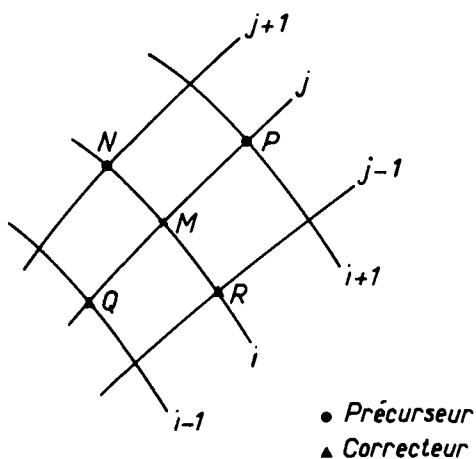


Fig. 3 - Maille autour du point courant M .

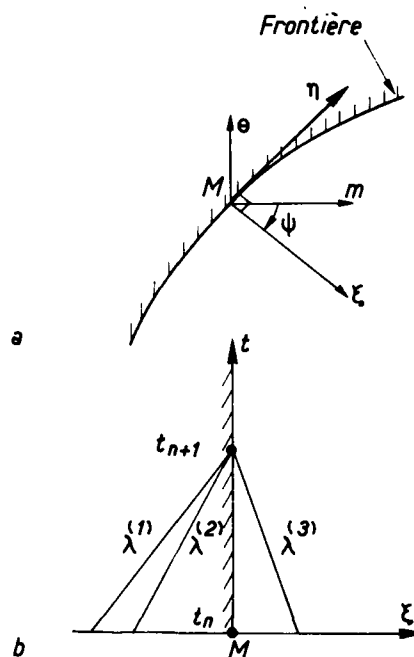


Fig. 4 - Représentation locale des configurations sur les frontières pour application des relations de compatibilité.

a) Coordonnées locales (ξ, η)

b) Plan (ξ, t) $(\lambda = \frac{d\xi}{dt})$

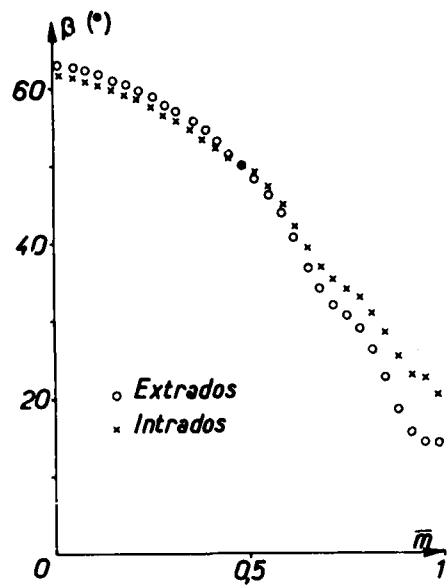


Fig. 5a — Angle géométrique du profil.

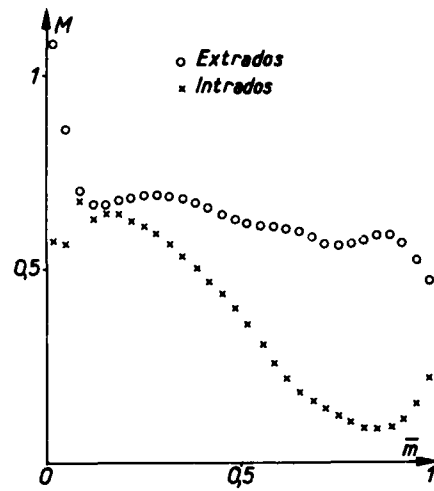


Fig. 5b — Répartition du nombre de Mach le long de l'aubage.

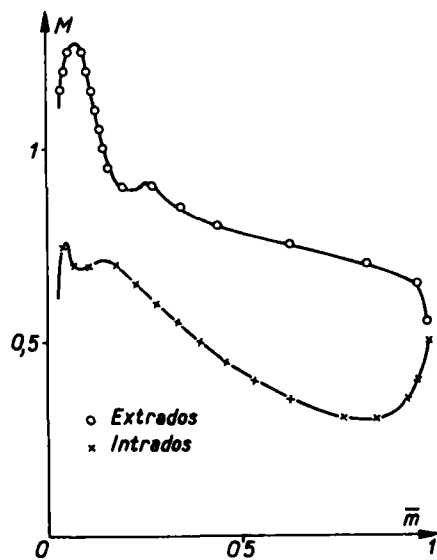


Fig. 6 — Répartition du nombre de Mach sur le profil dans le cas d'un compresseur non bloqué.

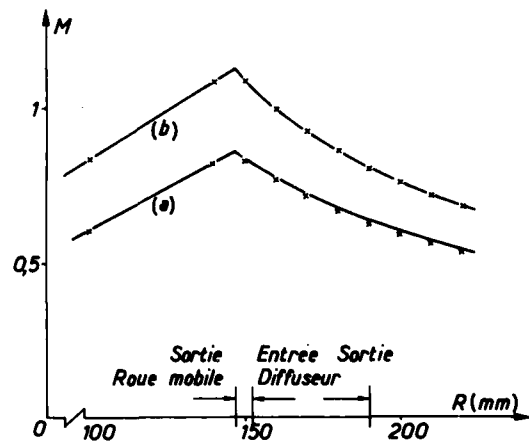


Fig. 7 — Répartition radiale du nombre de Mach absolu en subsonique (a) et transsonique (b).

x Points de calcul (méthode présente)
 — Ecoulement de source-tourbillon

DISCUSSION

P.M.Came, NGTE, UK

In your application of the S1 surface calculation to a vaned diffuser you mentioned the introduction, in the future, of irreversibilities. Could the author please comment on how he would include the effects of irreversibility in the calculation. Would it be by the use of a viscous/inviscid interaction method or would the viscous terms be included in the equations of motion?

Author's Reply

In the future, the introduction of irreversibilities in the flow calculation to a vaned diffuser will include the viscous terms in the equations of motion. This calculation will be realised by means of two steps:

- in the near future, a two-dimensional calculation will be developed,
- and later, the three-dimensional type will be treated, once the flow pattern at the rotor outlet is known.

P.Ramette, CEP, Saclay, Fr

Is the term artificial viscosity necessary in all calculation cases? This term helps to ensure the stability of the calculation but does it not risk the increase of calculating times in certain cases? Is the value of this term optimised perhaps?

Author's Reply

The term artificial viscosity is introduced essentially to ensure convergence of the calculation especially where strong gradients exist, for example in the presence of shock waves. Depending on what type of flow is being calculated, this term is applied and it works best as a function of pressure ratio. It is true that some time is lost because of the extra calculation caused by this term but in general the artificial viscosity stabilises the calculations and in particular one obtains a gain in time because of the improvements in the convergence obtained. At present, it is difficult to give an optimised value for such a parameter when a general non-square mesh is used in a two-dimensional flow calculation. In fact, this term is compounded of the product of a constant coefficient multiplying the second derivative and the absolute value of the gradient of each variable, and that in the two directions m and θ .

NUMERICAL ANALYSIS OF THE THREE DIMENSIONAL VISCOUS FLOW FIELD IN A CENTRIFUGAL IMPELLER

Leonard Walitt

Numerical Continuum Mechanics, Inc.
6269 Variel Ave., Suite 200
Woodland Hills, California 91367

SUMMARY

The steady three-dimensional Reynolds averaged Navier-Stokes equations have been solved numerically via a successive approximation method. The method is applicable to centrifugal impellers, axial rotors, turbines and stator cascades.

Viscous flow fields have been calculated in a radial impeller, two backswept centrifugal impellers, one with a splitter vane, and an axial supersonic compressor cascade. The radial impeller field contained a significant separation region near the trailing edge of the suction surface, while the backswept fields showed significant leading edge separation and some trailing edge separation near the shroud. Kulite recordings of the shroud pressure variation between the blades in the inducer region and in the radial portion of the backswept impeller with the splitter vane, generally agreed with corresponding calculations. Pressure measurements on the blades of the supersonic compressor cascade agreed with corresponding computations.

This paper reviews numerical methods for turbomachines, describes the successive approximation method employed in this study, and presents results of its application.

SYMBOLS

A	small area in (x,y) plane contained within the region bounded by the closed curve C
a	local sound speed
C	perimeter of curve in (x,y) plane
(h_x, h_y, h_z)	metrics of transformation in the (x,y,z) directions, respectively
$(\underline{i}, \underline{j}, \underline{k})$	unit basis vectors for (x,y,z) curvilinear coordinates
l	$\int h_x dx$
m	$\int h_y dy$
\underline{n}	unit normal to surface
p	pressure
p_t	total pressure
S_x	mesh point coordinate velocity in x-direction
S_y	mesh point coordinate velocity in y-direction
t	time-like-coordinate
U_z	marching velocity of computational surface
(u,v,w)	curvilinear velocity components in x,y,z directions, respectively
w_s	streamwise component of velocity
w_{cr}	critical velocity
w^1	z-direction velocity perturbation ($w^1 = w - U_z$)
(x_1, x_2, x_3)	cartesian rotating coordinates
(x,y,\bar{z})	rotating curvilinear coordinates ($z = U_z t$)
ρ	density
$(\sigma_{xx}, \tau_{yx}, \tau_{zx})$	stress tensor components associated with x-direction
$(\sigma_{yy}, \tau_{xy}, \tau_{zy})$	stress tensor components associated with y-direction
σ_{zz}	normal stress in z-direction
ω	angular frequency

INTRODUCTION

Based on advanced experimental means and quasi-three-dimensional numerical methods, such as those of Katsanis and McNally (1) and Hearsey (2), significant advances in the design of centrifugal compressors have been made. Dean (3) indicates that state-of-the-art stage efficiency varies from 85% at a stage pressure ratio of 3 to 75% at a stage pressure ratio of 10. Resolution of the detailed viscous fluid mechanics of the centrifugal compressor can lead to ultimate stage efficiencies of 90% (3).

Dodge (4,5) has developed a technique for analyzing viscous flow in turbomachines. The basis for this technique lies in the substitution of a potential gradient plus a viscous perturbation for the velocity vector. A steady partial differential equation is developed for the potential function comprised of terms on the right hand side having to do with the viscous perturbation. All terms on the right-hand side of the potential equation are presumed known. Furthermore, an additional equation is developed by Dodge for the viscous potential itself. The relaxation method of Murman and Cole (6) was modified to numerically solve the potential equation. The viscous perturbation equation is solved by marching in the streamwise direction. The Dodge code can handle up to 10,000 mesh points and requires a few minutes on the CDC 7600 to solve a problem. The method appears useful for turbo-machines whose blade passages are filled with potential flow and attached boundary layers. However, a strong, three-dimensional vortical flow

in a separated region adjacent to the blade surface of a turbomachine is beyond the scope of this technique (see Supersonic Compressor Cascade example).

A solution of the unsteady, 3-D Reynolds-averaged Navier Stokes equations is clearly the most viable way to account for the complex flow field in the passage of a centrifugal impeller. However, unsteady, 3-D viscous numerical solutions are impractical on present day computers such as the CDC 7600. To properly account for 3-D and viscous effects (such as separations and boundary layers) in the complicated impeller flow field, finite difference meshes of the order of 100,000 points are required. Current 3-D time-dependent implicit methods overrun core memory on the CDC 7600 computer somewhere between 10,000 and 20,000 mesh points. Explicit 3-D techniques require a core memory near 30,000 mesh points.

Pulliam and Steger (7) have developed a 3-D, time-dependent, viscous code using the implicit method of Beam and Warming. Their technique is second order and can be run at high Courant numbers, i.e., $Cr = 400$. The flow field was calculated over a sphere-cylinder body at a Mach number of .90, a Reynolds number based on cylinder diameter of 212,500 and at 5° angle of attack. The finite difference mesh employed was comprised of 30 axial points, 30 radial points and 18 angular points, i.e., 16,200 points. Spacing of axial points was too coarse to resolve the leeward separation at the sphere-cylinder junction. Experimentally separation was recorded; however, numerically attached flow was determined. A large discrepancy in calculated and measured leeward surface pressure resulted.

Kutler (8) developed a propeller code using the Beam and Warming method. This computer program was set up to solve either an inviscid or viscous propeller problem. The code was applied to compute the inviscid flow field about a turbofan operating at Mach .80. A finite difference mesh was used, which was comprised of 18 points along the chord of the propeller airfoil section, 11 points along the span of the propeller and 45 points normal to the propeller surface, i.e., 10,000 mesh points. The numerical solution had oscillations in it, and had to be smoothed artificially, i.e., through the use of smoothing functions. The detailed flow field numerical results were therefore of dubious value. However, overall performance predictions based on these results may have some value.

Thompkins (9,10) solves the 3-D, time-dependent Euler equations using the Mac-Cormack time-splitting method. For an axial rotor the finite difference mesh is composed of 18 radial points, 17 tangential points and 100 axial points, i.e., 30,600 mesh points. Inviscid solutions have been obtained on four rotors. A recent calculation, performed by Haymann-Haber (11), was on a transonic axial compressor of tip mach number 1.2 and inlet hub to tip ratio of .5. Comparisons were made between the computations and the fluorescent density measurements of Epstein (12) taken on various blade-to-blade sections of constant radius. The computed solution agreed qualitatively with the measurements as long as data on these blade-to-blade sections far from either blade surface were considered. Important differences occurred in the shock position and in the size of the low density region in the blading passage. The most difficult effect to resolve in these comparisons was viscosity. The Thompkins solution did not contain viscous effects while the measurements did.

Due to the impracticality of unsteady, viscous, 3-D computations, a solution of the steady, Reynolds-averaged, 3-D Navier Stokes equations appears to be the most viable alternative for the rotor problem.

*

A set of computer codes, called VANS was developed to embody the successive approximation numerical method. The numerical method is best termed an Alternating-Direction Explicit technique, i.e., ADE. A set of finite difference analogs of the full three-dimensional, compressible Reynolds averaged Navier-Stokes equations is solved explicitly in the blading passage of a rotor. In addition to three-dimensionality and compressibility, the following effects are included:

1. Centrifugal and Coriolis forces
2. Transition and turbulence
3. Arbitrary geometry
4. Blade tip clearance

This paper formulates the numerical method for a radial impeller, describes the VANS computer codes and gives four numerical examples to show the results that can be obtained with VANS.

1. Calculations of the flow field in the blading passage of a radial impeller operating at 38600 r.p.m.
2. Calculations of the flow field in the blading channel of a backswept impeller operating at 75000 r.p.m.
3. Calculations of the flow field in the blading passage of a backswept impeller, with splitter vanes, operating at a pressure ratio of 3.
4. Calculations of a supersonic compressor cascade with splitter vanes.

*

The letters VANS stand for Vectorized Asymmetric Navier Stokes codes.

FORMULATION OF NUMERICAL METHOD

The successive approximation VANS numerical method has been described in detail previously (13), and the integral equations which are numerically solved have been cited (13). It is the purpose of this section to briefly review the method.

For illustrative purposes we start with a schematic of a radial impeller for a centrifugal compressor shown in Fig. 1. The machine is rotating clock-wise about the system's axis. Let us consider the darkened blading passage. The blade surface labelled "pressure surface" is like the windward side of an airfoil, while the blade surface, labelled "suction surface" is like the leeward side of an airfoil.

In the blade-to-blade mode of marching, the computation takes place on a blade-to-blade surface which is normal to the meridional planes of the machine, extends from inducer to the discharge, and moves from the hub to the shroud. The darkened surface of Fig. 1 is the hub blade-to-blade surface. The blade-to-blade method of marching is illustrated in the blade passage schematic shown in Fig. 2. The x_1, x_2 , and x_3 coordinates of Fig. 2 represent a left handed, rotating, Cartesian coordinate system and coordinates (x, y, z) represent a left-handed, rotating, orthogonal, curvilinear coordinate system. The z -direction is the marching direction with the calculation taking place in the (x, y) blade-to-blade surfaces. The (x, y) blade-to-blade surfaces move from the hub to the shroud of the impeller. As the surface moves from hub to shroud, elliptic terms of the finite difference equations are evaluated from the zeroth approximation, i.e., the solution of Katsanis and McNally (1), while parabolic terms are evaluated directly from data within the blade-to-blade surface. Elliptic terms have to do with hub to shroud derivatives, with respect to z , and all other terms are considered parabolic terms.

In the cross-sectional mode of marching we move down the channel, from the inducer to discharge, in cross-sectional surfaces normal to the hub and shroud of the system. A schematic of the blade passage with the cross-sectional surface indicated is presented in Fig. 3. The z -direction is now normal to the (x, y) cross-sectional surface of Fig. 3. The (x, y) cross-sectional surfaces move from the inducer to the discharge of the impeller. The elliptic and parabolic terms in the cross-sectional mode of marching are the reverse of what they were previously in the blade-to-blade mode. Now streamwise derivatives become elliptic terms, since z moves in the streamwise direction, and hub-shroud derivatives are parabolic terms. This permutation of elliptic and parabolic terms, resulting from alternating the direction of marching, produces rapid adjustment of the field in a few passes through the system.

The blade-to-blade march accounts for blade separations and upstream influence effects, while the cross-sectional march accounts for shroud scrubbing, blade leakage, hub effects and channel corner vortices. The cross-sectional mode of computation integrates the blade fluid mechanics with the effects of the shroud, hub and leakage.

To illustrate the elliptic source terms and parabolic terms of the equations of motion, the equation for y -momentum conservation on a zone of the blade-to-blade surface (Fig. 2) is presented below.

y-direction momentum

$$\begin{aligned} \frac{\partial}{\partial t} \int_A \rho v h \frac{h}{x y} dA + \int_C \rho v (q_s - q_s) \cdot \underline{n} dC + \int_A h h h \frac{h}{x y z y} dA - \frac{1}{U_z} \int_C v w' q_s \cdot \underline{n} dC \\ = - \frac{1}{U_z} \frac{\partial}{\partial t} \int_A \tilde{v} \tilde{w}' h \frac{h}{x y} dA + \frac{1}{U_z} \frac{\partial}{\partial t} \int_A h h \frac{h}{x y z y} dA - \frac{1}{U_z} \int_C \tau_{zy} q_s \cdot \underline{n} dC \\ + \int_A h_x h_y h_z \pi_y dA + \int_C \bar{\sigma}_p \cdot \underline{n} dC \end{aligned} \quad (1)$$

where

$$q = u h \frac{h}{y z} + v h \frac{h}{x z}$$

$$q_s = S h \frac{h}{x x y} + S h \frac{h}{y y x}$$

$$\bar{\sigma}_p = h h \frac{\tau}{y z} \frac{1}{x y} + h h \frac{\sigma}{x z} \frac{1}{y y}$$

$$\pi_y = \frac{\tau_{yz}}{h h} \frac{\partial h}{\partial z} + \frac{\tau_{xy}}{h h} \frac{\partial h}{\partial x} - \frac{\sigma_{zz}}{h h} \frac{\partial h}{\partial y} - \frac{\sigma_{xx}}{h h} \frac{\partial h}{\partial y}$$

$$\begin{aligned}
 A_y = & \frac{\rho v}{h} \left\{ \frac{u}{h} \frac{\partial h}{\partial x} + \frac{v}{h} \frac{\partial h}{\partial y} + \frac{w}{h} \frac{\partial h}{\partial z} \right\} - \frac{\rho}{h} \left\{ \frac{2}{h} \frac{\partial h}{\partial y} + \frac{2}{h} \frac{\partial h}{\partial y} + \frac{2}{h} \frac{\partial h}{\partial y} \right\} \\
 & + 2\rho\omega \left(\frac{u}{h} \frac{\partial x}{\partial z} - \frac{w}{h} \frac{\partial x}{\partial x} \right) - \frac{\rho\omega^2}{h} \left(x_1 \frac{\partial x}{\partial y} + x_2 \frac{\partial x}{\partial y} \right)
 \end{aligned}$$

Equation 1 represents the conservation of momentum in the y-curvilinear direction in terms of area integrals for a zone in the (x,y) plane and line integrals on a curve C representing the zone perimeter in the (x,y) plane. Curvilinear effects are accounted for by the metrics h_y, h_x, h_z and their derivatives. The term on the right-hand-side of Equation (1) is an elliptic source term and must be evaluated from flow field properties of the zeroth approximation; the (\sim) symbol indicates a property from the zeroth approximation. The second term on the left-hand-side of Equation 1 is a parabolic term which is evaluated directly. The third term on the left-hand-side of Equation 1 accounts for centrifugal and coriolis forces. Term 4 on the left-hand-side of Equation 1 is associated with grid motion and the elliptic source term on the right-hand-side. Terms 2 and 3 on the right-hand-side are associated with forces due to the shear stress τ_{zy} , while Term 4 on the right-hand-side accounts for the metric derivatives and the stresses. Finally, the last term on the right-hand-side is the force balance in the y-direction on the perimeter of a zone in the (x,y) plane.

THE VANS COMPUTER CODES

Under sponsorship of the Research and Technology Laboratory, Aviation Research and Development Command, and under contract to NASA Lewis Research Center through the U.S. Army Propulsion Laboratory, the VANS computer codes were developed. These codes, which solve the steady, Reynolds averaged Navier-Stokes equations in rotating coordinates fixed with respect to the rotor, are applicable to impellers, rotors of axial stages, turbines and cascades.

The VANS codes are applied in modular form to generate the successive approximation solution. In the first module the quasi-three-dimensional technique of Katsanis and McNally (1) is used to generate the zeroth approximation. Based on the zeroth approximation, we employ the blade-to-blade module to march from the hub to the shroud of the system; Fig. 2 illustrates the blade-to-blade mode of marching. In this way the first viscous approximation is developed. The second viscous approximation is generated from the first through the cross-sectional module, which moves through the blading passage; Fig. 3 illustrates the cross-sectional mode of marching. This alternating-direction method permits computation of blade separations, secondary flows, shroud scrubbing, shroud separation and leakage effects (13). Turbulence is computed from an eddy viscosity model based on Prandtl's mixing length theory (13).

At present there exist two VANS computer codes; namely, 1. a blade-to-blade version designated "VANS/BB," and 2. a cross-sectional version, designated "VANS/CS." The principal differences between the two codes are in the boundary conditions and the implementation of the turbulence model. For computational efficiency, both versions of VANS were vector-coded to take advantage of CDC 7600 hardware (14,15). A brief description of the numerical method embodied in VANS follows as well as a discussion of the VANS/BB and VANS/CS computer codes.

Finite difference analogs to the continuity, momenta, and internal energy relations of Reference (13) are integrated in the z marching direction by an explicit first order method based on the work of Trulio (16). The principal attribute of the scheme is that the difference equations maintain their self-consistency property; that is, the finite difference equations for continuity, momenta, and internal energy imply exact satisfaction of the consistently differenced equation for total energy. This means that the total energy, which is not a directly calculable dependent variable, is computed to the same degree of accuracy as the directly calculable variables. To the knowledge of the author, this is the only numerical scheme known which maintains self-consistency of the finite difference equations of motion.*

The VANS/BB code computes the field on (x,y) blade-to-blade surfaces which move from the hub to the shroud of the system and distort as the blade surfaces distort. This version of VANS has a subroutine which automatically develops the finite difference mesh in accordance with the blade geometry. Identical boundary conditions are prescribed for all blade-to-blade surfaces. Let us consider the blade-to-blade surface of Fig. 2. The boundary conditions are as follows:

1. No slip flow is imposed on the blades.
2. Periodic conditions are imposed on the lateral boundaries upstream of and downstream of the blades.
3. Zeroth approximation properties are specified at the upstream boundary.

*This self-consistency property is a valuable tool for debugging the VANS codes.

4. The static pressure is varied along the downstream boundary of each blade-to-blade surface to maintain the integrated passage mass flux.

A mixing length turbulence model was incorporated into the VANS/BB code (13). The formulation considered only the components of velocity in a given blade-to-blade surface, and included the turbulent boundary layers growing on both the suction and pressure blade surfaces. At a given point in the blade-to-blade surface, normals were constructed to the pressure and suction blade surfaces. The shortest normal distance defined the turbulent boundary layer, either on the suction or pressure surface, from which the eddy viscosity was computed.

The VANS/CS code computes the field on (x,y) cross-sectional surfaces which move from inducer to discharge and distort as the blade surfaces distort. Due to the nearly rectangular cross-sectional surface geometry, specification of the mesh points in (x,y) space was relatively simple. The boundary conditions for the cross-sectional computational surface of Fig. 3 are as follows:

1. No slip flow enforced along the hub upstream of the blade trailing edge and on the blades of the system.
2. Periodic flow is enforced at the lateral boundaries upstream of and downstream of the blades.
3. An angular component of velocity equal to the product of the local radius and the angular frequency, i.e., $u_\theta = r\omega$ is imposed on the shroud of the system and the system's hub aft of the discharge.

A mixing length turbulence model was incorporated into the VANS/CS code (13). The formulation considers all components of velocity, as well as streamwise boundary layers along the blades and hub of the system. A cross-sectional boundary layer grows on the shroud of the system due to the angular motion of the shroud relative to the blades. The eddy viscosity coefficient at any point in the cross-section is determined by the nearest wall turbulent boundary layer. The nearest wall is defined by the shortest normal distance from the point to all the walls.

NUMERICAL EXAMPLES - RADIAL CENTRIFUGAL IMPELLER

To test the numerical method, blade-to-blade calculations were made for a radial impeller operating at 38,600 r.p.m. (17).^{*} The design pressure ratio = 1.55; the tip diameter = .152m; and the tip speed = 304.8 m/s. The Reynolds number, based on arc length along the hub, was set to 5000. This was done to permit relatively coarse finite difference meshes in the blade-to-blade surfaces of computation. The geometry of the hub and shroud lines are shown in Fig. 4. In the remainder of this section the finite difference mesh is discussed, the zeroth approximation to the impeller field is presented, and the numerical results are shown.

The hub blade-to-blade finite difference mesh is shown in Fig. 5. This mesh is comprised of 20 streamline-like-lines and 39 potential-like-lines for a total of 780 points. Mesh point spacing is finer near the blades and coarser in the center of the passage.

Based on the velocity gradient method of Katsanis and McNally (1), the zeroth approximation field was generated. First the relative velocity field was calculated on the mean hub-to-shroud surface of the impeller, and suction surface and pressure surface velocities computed. A linear variation of relative velocity with angle produced the velocity field. Density and specific internal energy were computed from the relative velocity field using the constant rothalpy principle and the isentropic relations. Fig. 6 shows a relative velocity vector plot on the hub blade-to-blade surface from the inviscid solution. These vectors have magnitudes proportional to the particle velocities in the (x,y) plane with their tails emanating from the mesh points of Fig. 5. Velocities are seen to increase as one moves from the pressure to the suction blade surface.

The radial impeller problem was run through 750 cycles** on the CDC 7600 computer. After 750 cycles the blade-to-blade surface moved to approximately 37% of the distance between hub and shroud at discharge. The computation required 23 minutes on the CDC 7600 computer.

The viscous solution is depicted in the relative velocity vector plot shown in Fig. 7. This figure corresponds to a blade-to-blade surface located 31% of the distance between hub and shroud at discharge. The meridional trace of this surface is seen in Fig. 4. At the trailing edge of the suction surface a large separated region is indicated. This region, which is caused by blade loading, initially forms just aft of the trailing edge and then moves into the channel. Suction blade velocities upstream of the vortex adjust to the vortex and accelerate around it due to the reduced flow area. The VANS blade-to-blade computer code has duplicated, at least qualitatively, viscous flow phenomena that have been observed in the radial portion of an impeller (3).

^{*} This work was monitored by the National Aeronautics and Space Administration Lewis Research Center under Contract No. NAS3-18016.

^{**}A cycle of computation consists of updating all the dependent variables of motion on one blade-to-blade surface.

BACKSWEEP CENTRIFUGAL IMPELLER

An advanced backswept impeller, developed by CREAKE, Inc. served as the second turbomachinery application of the VANS computer codes. In this study both blade-to-blade (13,17) and cross-sectional approximations (13)* were completed for the backswept impeller operating at 75000 r.p.m. The design pressure ratio = 8; the tip diameter = .1595m; and the tip speed = 626.36 m/s. The Reynolds number, based on an average inviscid relative velocity along the hub and distance along the hub, was 1.43×10^6 . This Reynolds number produced transition from laminar to turbulent flow in the blading channel.

To adequately describe this calculation five topics are covered; namely,

1. geometry and mapping
2. meshes
3. zeroth approximation
4. blade-to-blade numerical results
5. cross-sectional numerical results

The geometry of the backswept impeller hub and shroud lines is shown in a meridional plane in Fig. 8. In addition, Fig. 8 presents two families of orthogonal lines, the first family coincides with the hub and shroud lines and the second family is orthogonal to the first. Let us consider the point $P(x_1, x_2, x_3)$ of Fig. 8 as a function of the rotating Cartesian coordinates (x_1, x_2, x_3) . The mapping of the point $P(x_1, x_2, x_3)$ to curvilinear space $P(x, y, z)$ is defined as follows. The streamline-like-line passing through P is rotated about the system's axis. This surface of revolution defines the coordinate z . The potential-like-line passing through P is also rotated about the system's axis. This orthogonal surface of revolution defines the curvilinear coordinate y . Finally the angle the meridional plane passing through P makes with some reference meridional plane defines the curvilinear coordinate x . Thus, the point $P(x_1, x_2, x_3)$ is uniquely related to the point $P(x, y, z)$. The metrics and their derivatives for this axisymmetric, orthogonal curvilinear transformation have been developed by Vavra (18). The above defines the mapping for the blade-to-blade mode of marching; a permutation of the y and z coordinates defines the mapping for the cross-sectional mode of marching.

The hub finite difference mesh is shown in Fig. 9. This mesh is comprised of 30 streamline-like-lines and 101 potential-like-lines, i.e., 3030 points. Streamline-like-lines are spaced finely close to the blade and coarsely in the center of the passage. About five points are present in the boundary layer at the suction surface trailing edge.

The MERIDL computer code, developed by Katsanis and McNally (1), was employed to generate the zeroth approximation. This code determined the inviscid velocity field. The density and specific internal energy fields were then computed as functions of the velocity field by invoking constant rothalpy and isentropic flow assumptions. Fig. 10 shows the inviscid velocity field on the hub blade-to-blade surface. The velocity increases from the pressure surface to the suction surface.

The procedure for generating the blade-to-blade solution with the VANS/BB code, starts by first attempting to stabilize the flow field near the hub. This is done by moving the blade-to-blade surface slowly near the hub. After stabilization has occurred, i.e., the hub field changes little with continued computation, the blade-to-blade surface is moved more rapidly until it coincides with the shroud. To complete this procedure required 8073 cycles of calculation, which took 4.5 hours on the CDC 7600 computer.

The viscous field is shown in the velocity vector plots of Figs. 11 and 12, on a blade-to-blade surface located 19% of the distance between hub and shroud at discharge. Fig. 11 shows a leading edge separation on the suction blade and a boundary layer growing along the pressure surface. Due to the backswept geometry, the blade-loading is reduced at discharge and flow separation is prevented there (Fig. 12).

The cross-sectional approximation integrates the blade-to-blade field, which principally gives the effects of the blades on the flow, with the effects of shroud scrubbing, blade leakage and hub effects. Based on the blade-to-blade field on a three-dimensional mesh of 106,000 points as the previous approximation, the VANS/CS computer code was run through 6300 cycles of calculation. A single cycle of calculation consists of updating all the variables of motion on one cross-sectional surface comprised of 1050 mesh points. The solution required 2.3 hours on the CDC 7600 computer.

On cross-sectional surfaces just aft of the blade leading edge, the leading edge suction surface separation was re-computed. This separation extends from hub to tip along suction blade. Through alternating the direction of marching a vortex was computed in cross-sectional surfaces which did not contain the vortex. This points out one of the principal advantages of the ADE numerical method.

The cross-sectional flow field contained two other fluid mechanical phenomena that could be identified and understood; namely,

1. A vortical secondary cross-flow
2. Flow separation along the shroud at discharge.

*This work was monitored by the National Aeronautics and Space Administration Lewis Research Center under Contracts NAS3-18016 and NAS3-20032.

Secondary impeller cross-flows are depicted in velocity vector plots in cross-sectional surfaces tipped nearly normal to the camber surface of the blading (Figs. 13 and 14). Fig. 13 shows a velocity vector plot in the inducer region of the impeller. A cross-sectional vortex is clearly seen in the figure. It is believed that this vortex is caused by the relative motion between the shroud and impeller blades. At the discharge of the system the vortical cross-sectional flow disappears. This is shown in the velocity vector plot of Fig. 14 at the discharge. In addition, Fig. 14 shows the effect of shroud scrubbing on the fluid.

Flow separation along the shroud at discharge is depicted in a contour plot of the ratio of the streamwise component of velocity to the local critical velocity, i.e., W_{zs}/W_{cr} . Fig. 15 shows contours of W_{zs}/W_{cr} plotted on a cross-sectional surface near the discharge. At the intersection of the pressure blade and shroud, a contour labelled $W_{zs}/W_{cr} = 0$ encloses a contour labelled $W_{zs}/W_{cr} = -.03$. Since a great amount of impeller pumping has taken place W_{cr} is high; thus, the negative streamwise flow is substantial.

BACKSWEEP CENTRIFUGAL IMPELLER WITH SPLITTER VANES

An advanced backswept impeller with a splitter vane, developed by General Electric Company (19), is the third turbomachine application of the VANS computer codes. The blade-to-blade field has been generated by the VANS/BB code, and the VANS/CS computer code is in the process of computing the cross-sectional field.* The impeller has a design pressure ratio of 3 and a tip speed of 420 m/sec. The Reynolds number, based on an average inviscid velocity along the hub and distance along the hub, was 1.0196×10^6 .

The general flow field structure computed by the VANS/BB code, contained three elements, 1) a separation in the vicinity of the suction surface leading edge, 2) strong boundary layer flows along both blade surfaces and 3) a small separation at the suction surface trailing edge. The suction surface separation did not occur at the leading edge itself; hence, the shape of the camber line may be the cause of this vortical flow. Due to the leading edge suction surface separation more mass flux passed between the splitter suction surface and main blade pressure surface than in the passage between the splitter pressure surface and main blade suction surface.

Three comparisons of blade-to-blade numerical computations were made with experimental data; namely,

1. Measured averaged shroud pressures were compared with calculations.
2. Calculated shroud pressure variations with angle, at two stations along the shroud, were compared with Kulite measurements.
3. Measured impeller stage efficiency and slip factor were compared to corresponding computed values.

At the blade leading edge and in the radial portion of the impeller, calculated shroud average pressures agreed with measurements. In the inducer region the calculated pressures were a little lower. The calculated shroud pressure variation with angle in the inducer region and radial portion of the impeller in general agreed with corresponding Kulite measurements. Differences were recorded across the blade tip and splitter vane tip. The calculated impeller stage efficiency and slip factor were slightly higher than corresponding measured values.

The three comparisons with data qualitatively described above, tended to verify the blade-to-blade field computed by VANS/BB. Since this field does not include shroud scrubbing, impeller tip blade leakage, secondary flows and hub effects, the above areas of difference are to be expected. The cross-sectional approximation, which includes these effects, should bring the computational results in closer accord with measurements.

AXIAL COMPRESSOR CASCADE

The cascade flow field was computed through blade-to-blade and cross-sectional approximations (20)** at a freestream Mach number of 1.46, at a freestream Reynolds number (based on chord) of 1.36×10^6 , and at a pressure ratio of 1.883. To describe this calculation five items are discussed; namely, 1) geometry and mapping, 2) meshes, 3) zeroth approximation, 4) blade-to-blade numerical results and 5) cross-sectional numerical results.

The geometry of the cascade is shown in Fig. 16 in terms of traces of the contoured sidewalls and symmetry plane in a fictitious meridional plane. A radius of 254m was added to the ordinates of this geometry to provide an axis from which the axisymmetric, orthogonal, curvilinear coordinates (x,y,z) were determined. In a manner similar to that described for the backswept impeller, the curvilinear coordinates x,y,z were numerically generated.

The finite difference mesh in the (x,y) plane, corresponding to the lower contoured wall blade-to-blade surface (Fig. 16), is shown in Fig. 17. The main blade and splitter

*This work funded by General Electric Co. under Purchase Order Numbers 201SL4829323 (1978) and 201SL4908656 (1979).

**This work was sponsored by the U.S. Air Force Aero Propulsion Laboratory under Contract No. F33615-76-C2011.

geometries are indicated in figure. The blade leading edge occurs at $y = .000416$ radians, the trailing edge occurs at $y = .0006167$ radians and the main blade chord is $.0762m$. There are 42 streamline-like-lines and 80 potential-like-lines, i.e., 3360 points. Streamline-like-lines are spaced finely near the blade surfaces and splitter vane are coarsely elsewhere.

The zeroth approximation was generated by the Air Force Aero Propulsion Laboratory Program UDO300 (2). The inviscid UDO300 velocity field was employed to compute the corresponding density and specific internal energy fields through invoking constant stagnation enthalpy and under the assumption of isentropic flow.

The VANS/BB computer code was applied to solve for the cascade flow field by marching in blade-to-blade surfaces. The blade-to-blade surface was moved from the lower contoured wall of Fig. 16 to the symmetry plane. This calculation required 5300 cycles and took 3.68 hours on the CDC 7600 computer.

Fig. 18 shows a velocity vector plot of the cascade flow field on a blade-to-blade surface 62% of the distance between contoured wall and symmetry plane of the system. A large separation region is indicated on the suction surface starting approximately 14 percent of a chord aft of the suction surface leading edge and terminating at about 60 percent of a chord. In addition separated flow is indicated along the pressure surface of the splitter vane.

Fig. 19 presents a velocity vector plot of the inducer region of the cascade flow field on a blade-to-blade surface 80% of the distance between the lower contoured wall and symmetry plane. A curved bow shock wave emanates from the pressure surface leading edge and causes the suction surface boundary layer to separate. This strong suction surface separated region distorted the cascade flow field downstream and resulted in high system losses, particularly in the passage between the pressure surface of the splitter vane and main cascade blade suction surface.

Based on the blade-to-blade field on a 3-D finite difference mesh of 63840 points as the previous approximation, the cross-sectional calculation was carried through 2216 cycles. In 2216 cycles the cross-section, which is comprised of 1200 mesh points, moved from the upstream boundary of the system (Fig. 16) to the cascade exit. The cascade cross-sectional approximation required 53 minutes in the CDC 7600 computer. In order to run this iterate, the boundary conditions described previously for the VANS/CS code were revised for the cascade (20).

The flow field structure is depicted in contour plots of the ratio of the streamwise component of velocity W_{zs} to the local sound speed a on cross-sectional planes tipped nearly normal to the blading. Fig. 20 presents such a contour plot on a cross-sectional surface located at an axial distance ratio x/r of $.206$ of the total axial distance from the leading to trailing edges of the blades. This cross-section is located in the region of suction surface separation computed earlier in the blade-to-blade approximation (Fig. 19). Upstream of the blading $W_{zs}/a = 1.46$, while in the tipped cross-section of Fig. 20 velocity ratios less than one appear. Therefore, the shock wave pattern upstream of the cascade entrance is sufficient to produce subsonic conditions. Boundary layers are clearly indicated on the hub and pressure surface of the main cascade blade.

A contour level of $W_{zs}/a = -.20$ exists in the vicinity of the suction blade surface (Fig. 20). The negative ratio indicates the presence of a separated region. The separated region starts at an ordinate m of about $.04$ and takes up about a third of the cross-section. The shock wave emanating from the leading edge of the pressure surface of the main cascade blade interacts with the turbulent boundary layer flowing along the suction surface to produce the separation. This separated region reduces the effective flow area of the cross-sectional surface; thus, markedly disturbing the flow pattern there.

The suction surface separated region shown in Fig. 20 is in accord with the suction surface separated region of Fig. 19, computed in the blade-to-blade approximation. Thus, two successive approximations produced nearly the same separated flow. Furthermore, as in the case of the backswept impeller, through alternating the direction of marching a vortex was computed in cross-sectional surfaces which did not contain the vortex.

A comparison of calculated and measured static pressures along the main blade and splitter vane are shown in Figs. 21 and 22, respectively. These data are taken at the symmetry plane of the system. The solid line indicates VANS calculated results, the dashed line indicates results from the Dodge code (5), and these data points represent measurements of Holtman, McClure and Sinnet (21).

On the main suction blade (Fig. 21) the VANS computed pressures are generally in accord with these data. The Dodge computed pressures indicate good correlation with measurement along the suction surface to about the 65 percent chord station. At this point the numerical results tend to drop off and then gradually build up to the proper level at the trailing edge of the system. Previously (Fig. 18), it was indicated that re-attachment of the suction surface separated flow takes place at about the 60 percent chord station. Thus, it appears that the re-attachment process was not properly computed by the Dodge code.

Comparisons on the main blade pressure surface (Fig. 21) of VANS computed pressures and pressure data are generally good. The VANS surface pressure distribution has a leading edge compression, followed by a rapid expansion to the 5 percent chord station, and then a more gradual compression. The Dodge curve has the same general shape; however, the expansion minimum occurs at about the 38 percent chord station. Aft of the 40 percent chord station the VANS and Dodge results are in accord with the data.

Numerical and experimental static pressures at the symmetry plane are shown in Fig. 22 for the cascade splitter vane. The calculated pressures along the splitter suction surface are in excellent agreement with corresponding data for both the VANS and Dodge numerical methods. Near the trailing edge of the splitter suction surface the VANS pressures are higher than the Dodge predictions. More data are required to evaluate these results. The initial drop in VANS predicted pressure on the splitter pressure surface is due to separation. It appears from Fig. 22 that the VANS calculated initial pressure drop is over-estimated; thus, the extent of the separated region may be over-estimated. The Dodge pressures on the splitter pressure surface are in excellent agreement with these data. After reattachment has taken place the VANS numerical and experimental pressures are in accord on the splitter pressure surface.

SUMMARY AND CONCLUSIONS

An alternating direction explicit numerical method has been developed to solve the steady, 3-D Navier-Stokes equations for impellers, turbines and cascades of airfoils. The method is based on successive approximations, which start from a quasi-three-dimensional solution to generate a flow field on blade-to-blade surfaces of the turbomachine or cascade. The blade-to-blade field is then employed to develop the flow field on cross-sectional surfaces in the blading passage.

The VANS computer codes, which embody the ADE method, were applied to solve for the flow fields within the blading passages of a radial impeller, two backswept impellers, and an axial cascade. Detailed viscous fluid mechanical phenomena were calculated, such as trailing edge suction blade separation for the radial impeller, leading suction blade separation and shroud separation for the backswept impellers, and a strong shock-wave boundary interaction for the axial cascade. Information of this type is essential to the development of significant improvements in the performance of blading for impellers, turbines and cascades.

The impeller and cascade computations indicate that the ADE numerical method can produce a useful engineering solution to complex turbo-machinery problems within two iterations. Future computations of turbo-machinery problems, involving more than two iterations, are required to demonstrate convergence of the method and quantitatively define its accuracy.

The VANS/BB and VANS/CS explicit computer codes are presently being converted to run on the CRAY-1 computer. Shang and Hankey (22) determined the speed of their 3-D, explicit Navier-Stokes code on the CRAY-1 computer. It was found that the vectorized CRAY-1 version outperformed the scalar CDC 7600 version by a factor of 24.5. Thus, it is not unreasonable to assume that the VANS CDC 7600 codes can be sped-up by a factor of 10 on the CRAY-1 computer. Therefore, on the CRAY-1 computer the VANS codes will run turbo-machinery type problems in 40 minutes. In addition, the real time to solve a problem will diminish from 2½ months on the CDC 7600 computer to four days on the CRAY-1 computer.

It is further pointed out that in the area of computational efficiency great strides may yet be made. It may be possible to speed-up the VANS codes by an additional factor of ten. The VANS finite difference equations can be upgraded to second order accuracy and high computational efficiency through implicit computation. In implicit computation the marching increments may be increased markedly from the CFL marching increment. For example, on an implicit basis we may be able to affect the cross-sectional mode of marching in 200 cycles of computation, where the present explicit cross-sectional code of marching requires 8000 cycles. A cycle of computation is defined as updating the dependent variables on all the mesh points of one blade-to-blade or cross-sectional surface. Therefore, it seems very possible that the VANS codes can become a design tool, requiring a few minutes on a CRAY-1 computer.

ACKNOWLEDGEMENT

The author is pleased to acknowledge the contributions of Dr. Theodore Katsanis of NASA Lewis Research Center, Dr. Arthur J. Wennerstrom of the Air Force Aero Propulsion Laboratory and Capt. William A. Buzzell of the Air Force Aero Propulsion Laboratory to the work reported herein. Dr. Katsanis developed the inviscid backswept impeller flow field, which served as the zeroth approximation for the impeller calculation, and provided many helpful suggestions and discussions in the course of the impeller work. Dr. Wennerstrom provided many helpful suggestions and discussions in the process of solving for the cascade flow field. Capt. Buzzell developed the inviscid cascade solution, which served as the zeroth approximation for the cascade problem.

Acknowledgement is given to Mr. Lawrence W. Blair and Dr. Carol J. Russo of the Centrifugal Aero Design Group of General Electric Co. in Lynn, Massachusetts. Dr. Russo developed the inviscid backswept impeller flow field, which served as the zeroth approximation for the impeller calculation, and provided many helpful discussions in the course of the work. Mr. Blair provided many helpful suggestions and discussions in the development of the blade-to-blade solution.

REFERENCES

1. Katsanis, T., and McNally, W.D., "Revised FORTRAN Program for Calculating Velocities and Streamlines on the Hub-Shroud Mid-Channel Stream Surface of an Axial, Radial, or Mixed Flow Turbo-Machine or Annular Duct," II Programmers Manual, NASA TN D-8431, July 1977.
2. Hearsey, R.M., "A Revised Computer Program for Axial Compressor Design," ARL TR 75-0001, Vol. I, January 1975.
3. Dean, Jr., R.C., "On the Unresolved Fluid Dynamics of the Centrifugal Compressor," Advanced Centrifugal Compressors, ASME Publication, New York, 1971.
4. Dodge, P.R., "Transonic Two-Dimensional Flow Analysis of Compressor Cascade with Splitter Vanes," AFAPL-TR-75-110, December 1975.
5. Dodge, P.R., and Lieber, L.S. "Transonic 3-D Flow Analysis of Compressor Cascade with Splitter Vanes," AFAPL-TR-78-23, May 1978.
6. Murman, E.M., and Cole, J.D., "Calculation of Plane Steady Transonic Flows," AIAA Paper 70-188, 1970.
7. Pulliam, T.H., and Steger, J.L., "On Implicit Finite Difference Simulations of Three-Dimensional Flow," AIAA 16th Aerospace Sciences Meeting, Huntsville, Alabama, AIAA Paper No. 78-10, Jan. 16-18, 1978.
8. Kutler, P., "Transonic Propeller Computations," NASA CP-2092, Proceedings of Conference held at NASA Lewis Research Center, Cleveland, Ohio, 15-16 May 1979, pp. 193,194.
9. Thompkins, W.T., "Axial Fan Computations," NASA CP-2092, Proceedings and Conference held at NASA Lewis Research Center, Cleveland, Ohio, 15-16 May 1979, pp. 194.
10. Thompkins, W.T., and Epstein, A.H., A Comparison of the Computed and Experimental Three-Dimensional Flow in a Transonic Compressor Rotor, AIAA Paper 76-368, July 1976.
11. Haymann-Haber, G., "A Computational Study of the Flow in a Transonic Axial Compressor Using an Inviscid Three-Dimensional Finite Difference," GT & PDL Report No. 145, May 1979.
12. Epstein, A.H., Kerrebrock, J.L., and Thompkins, W.T., Jr., "Shock Structure in Transonic Compressor Rotors," AIAA Journal, Vol. 17, No. 4, April 1979, pp. 375-379.
13. Walitt, L., Liu, C.Y., and Harp, J.L., "An Alternating Direction Explicit Method for Computing Three-Dimensional Viscous Flow Fields in Turbomachines," SAE Paper No. 781001, Vol. 87 of the 1978 SAE Transactions, pp. 3829-3854.
14. King, L.S., Walitt, L., and Enos, J.A., "An Investigation of Computational Time Reduction Methods for Solving the Navier-Stokes Equations," NASA TMX-73, 102, October 1975.
15. Walitt, L., and Liu, C.Y., "Computation of Viscous Transonic Flow about a Lifting Airfoil," NASA CR-151999, Nov. 1976; also, AIAA Paper No. 77-679, AIAA 10th Fluid and Plasmadynamics Conference, Albuquerque, New Mexico, June 27-29, 1977.
16. Trulio, J.G., "Theory and Structure of the AFTON Codes," Air Force Weapons Laboratory, AFWL-TR-66-19, 1966.
17. Walitt, L., Harp, J.L., and Liu, C.Y., "Numerical Calculation of the Internal Flow Field in a Centrifugal Compressor Impeller, NASA CR 134984, December 1975.
18. Vavra, M.H., "Aero-Thermodynamics and Flow in Turbomachines," Wiley, pp. 499-508, 1960.
19. Private communication from L. Blair and C. Russo of the General Electric Co. Centrifugal Aero Design Group at Lynn, Massachusetts.
20. Walitt, L., and Liu, C.Y., "Numerical Calculations of the Viscous Flows in a Supersonic Compressor Cascade with Splitter Vanes," AFAPL-TR-78-2, February 1978.
21. Holtman, R.L., McClure, R.D., and Sinnet, G.T., "Test of Supersonic Compressor Cascade with Splitter Vanes," Aerospace Research Laboratories Report ARL 73-0142, pp. 257-265, December 1973.
22. Shang, J.S., Buning, P.G., Hankey, W.L., and Wirth, M.C., "The Performance of a Vectorized 3-D Navier-Stokes Code on the CRAY-1 Computer," AIAA Paper No. 79-1948, pp. 27-35, Computation Fluid Mechanics Conference Proceedings, Williamsburg, Maryland, 1979.

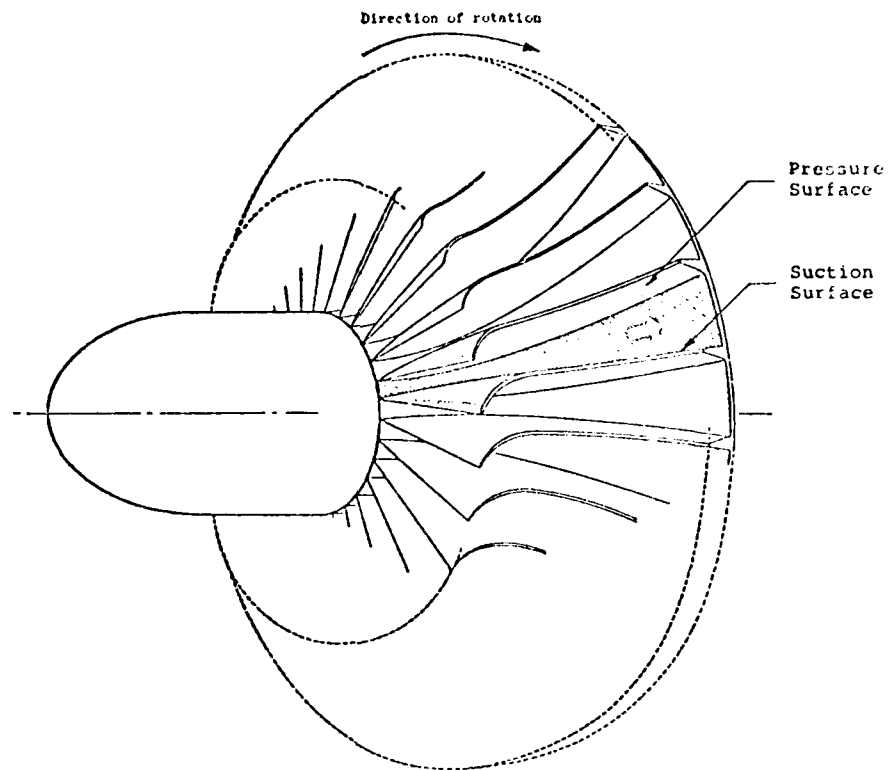


Fig. 1 Passage between blades in impeller of typical centrifugal compressor

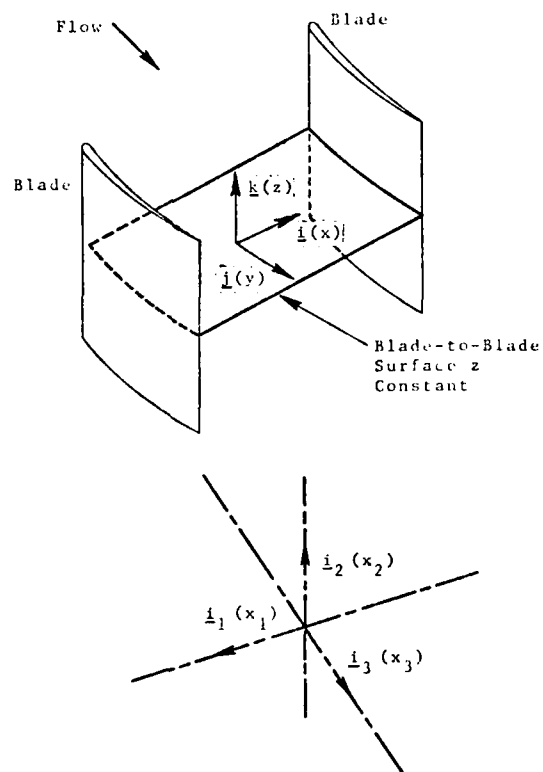


Fig. 2 Schematic of rotor blading passage illustrating the blade-to-blade mode of marching

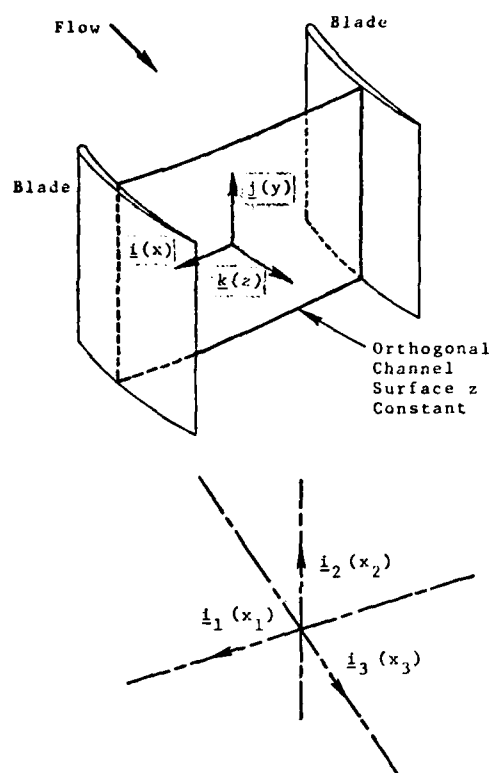


Fig. 3 Schematic of rotor blading passage illustrating cross-sectional mode of marching

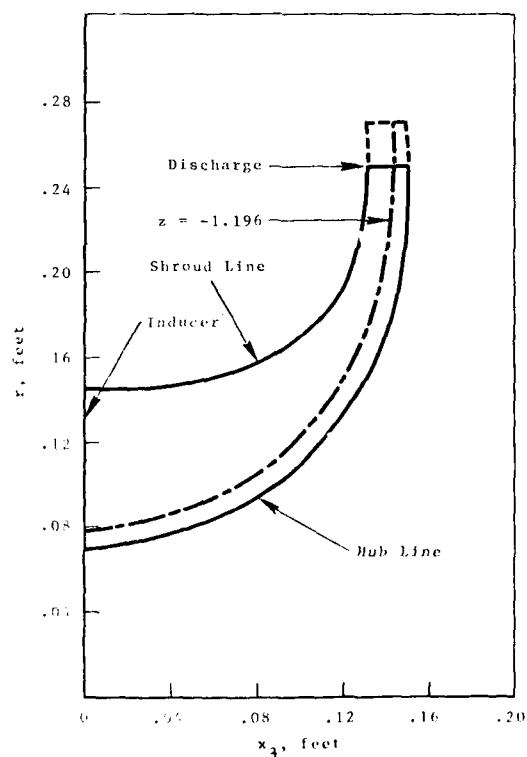


Fig. 4 Radial and axial coordinates of the hub and shroud, solid lines indicate actual geometry; dashed line indicates blade-to-blade surface 33% of total hub to shroud distance at discharge

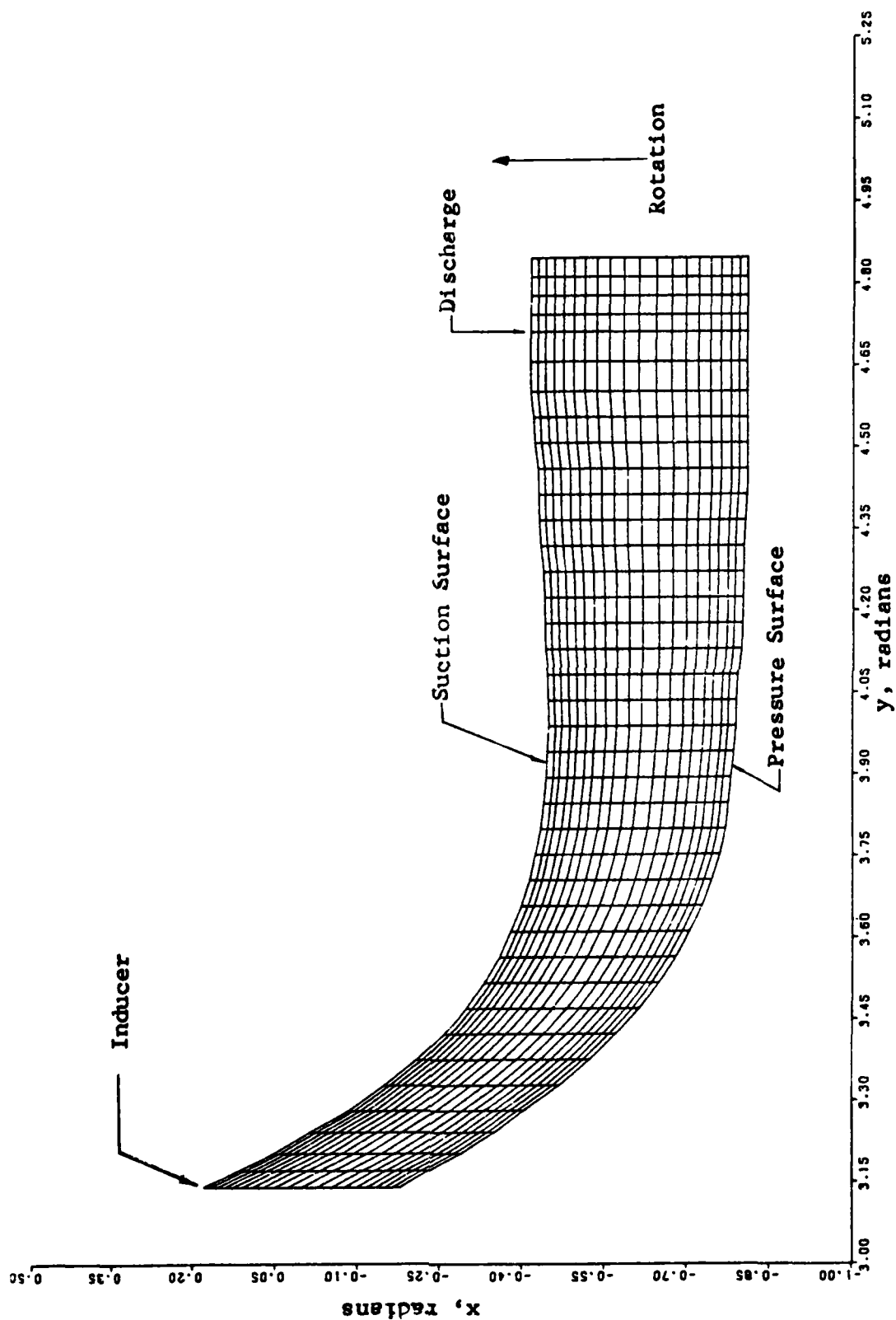


Fig. 5 Finite difference mesh for the impeller hub blade-to-blade surface of calculation;
 $z = -1.22524$ radians; mesh is composed of 20×39 points

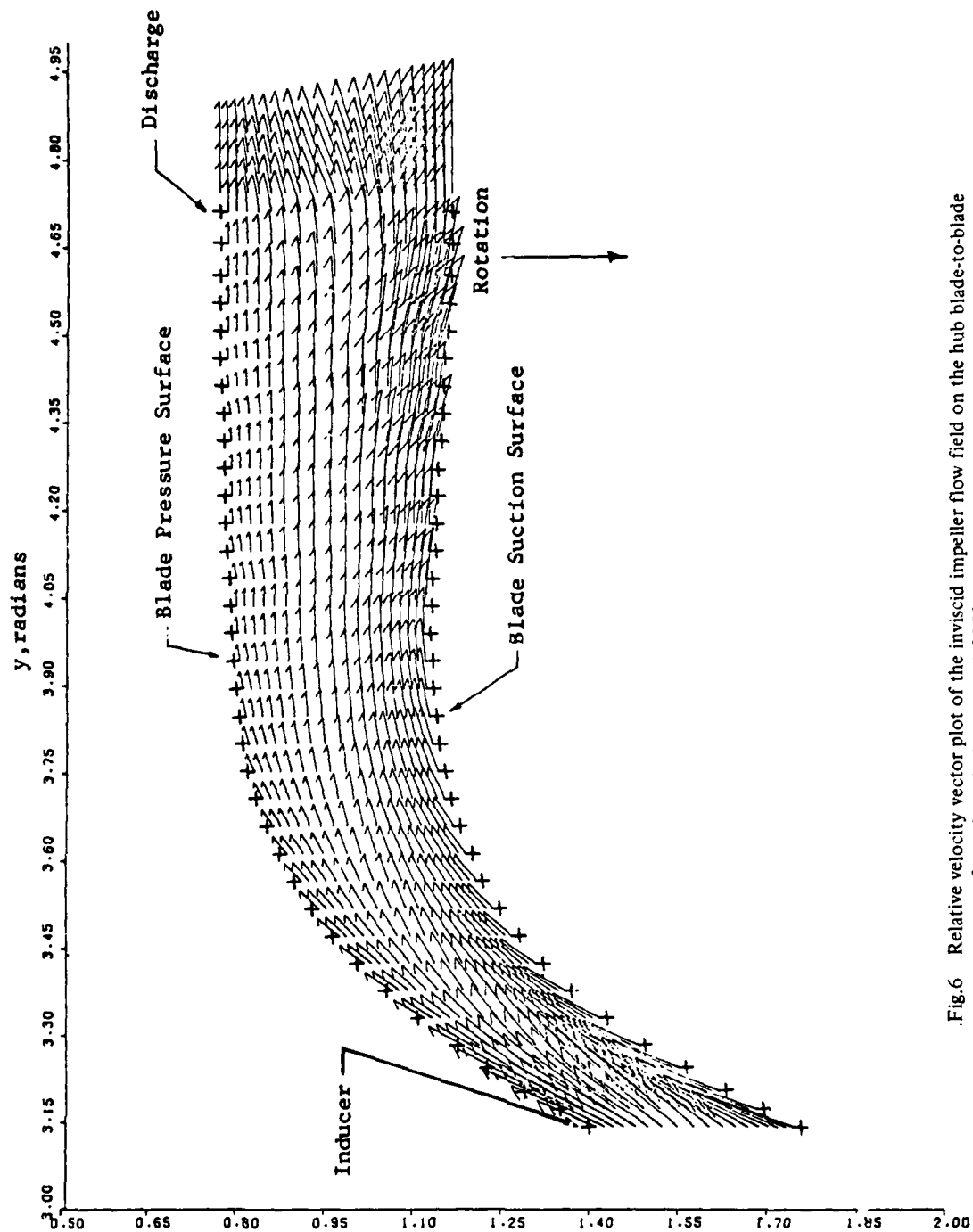


Fig.6 Relative velocity vector plot of the inviscid impeller flow field on the hub blade-to-blade surface of revolution, $z = -1.22524$ radians; + symbols indicate the pressure and suction blade surfaces

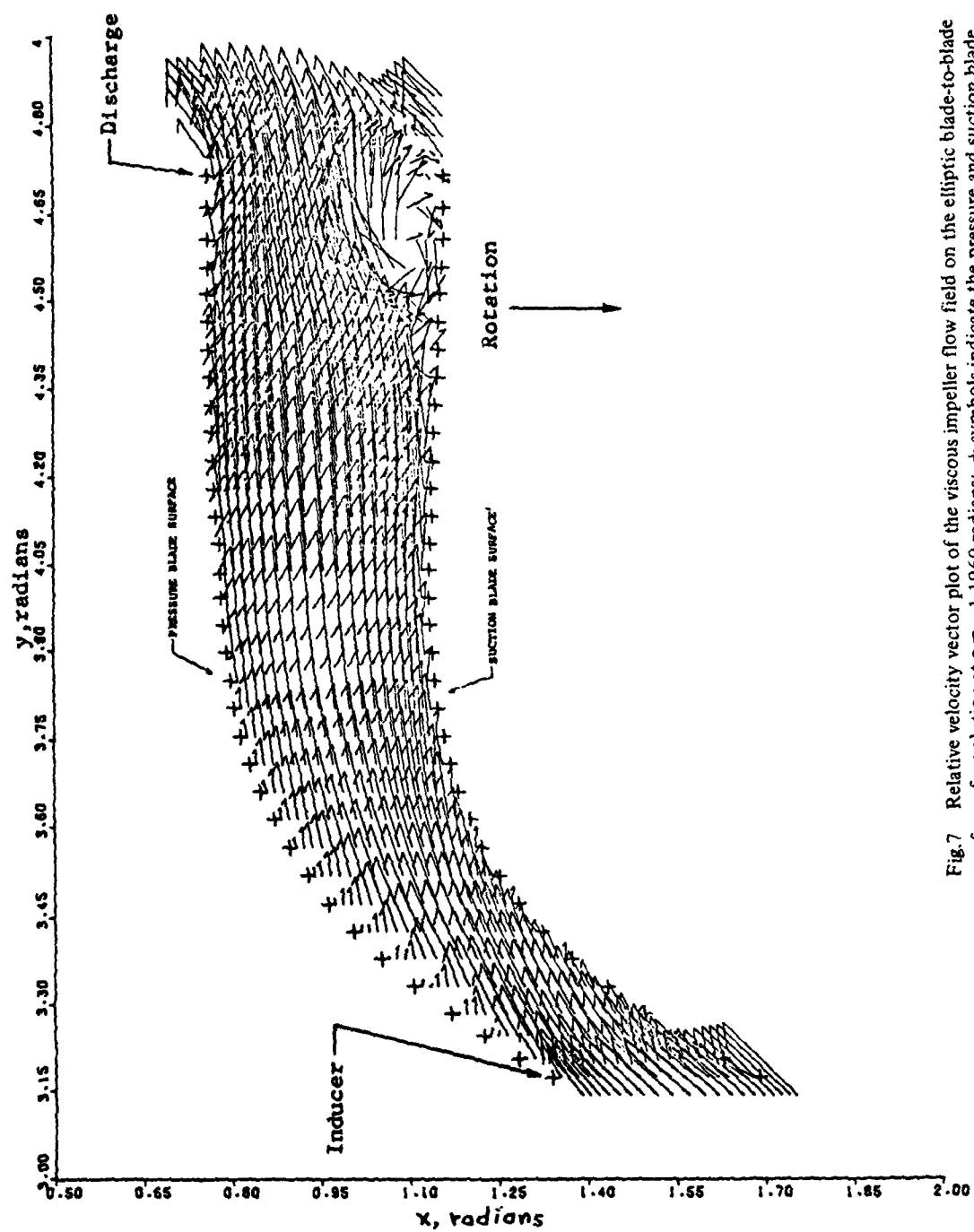


Fig. 7 Relative velocity vector plot of the viscous impeller flow field on the elliptic blade-to-blade surface of revolution at $z = -1.1960$ radians; + symbols indicate the pressure and suction blade surfaces; blade-to-blade surface moved 31% of distance between hub and shroud at discharge

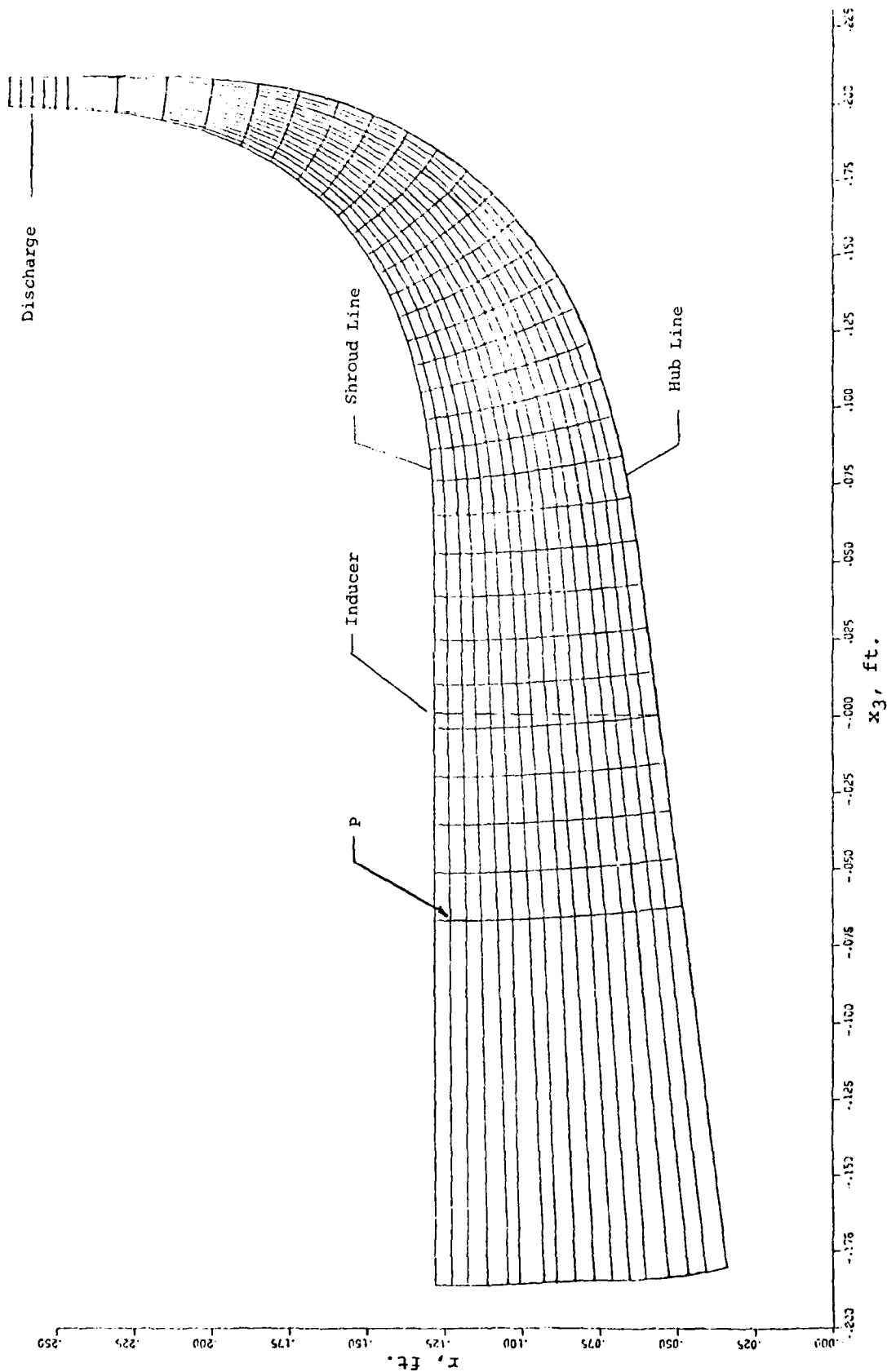


Fig.8 Meridional traces of hub and shroud lines for CREARE backswept centrifugal impeller; orthogonal coordinate system also shown

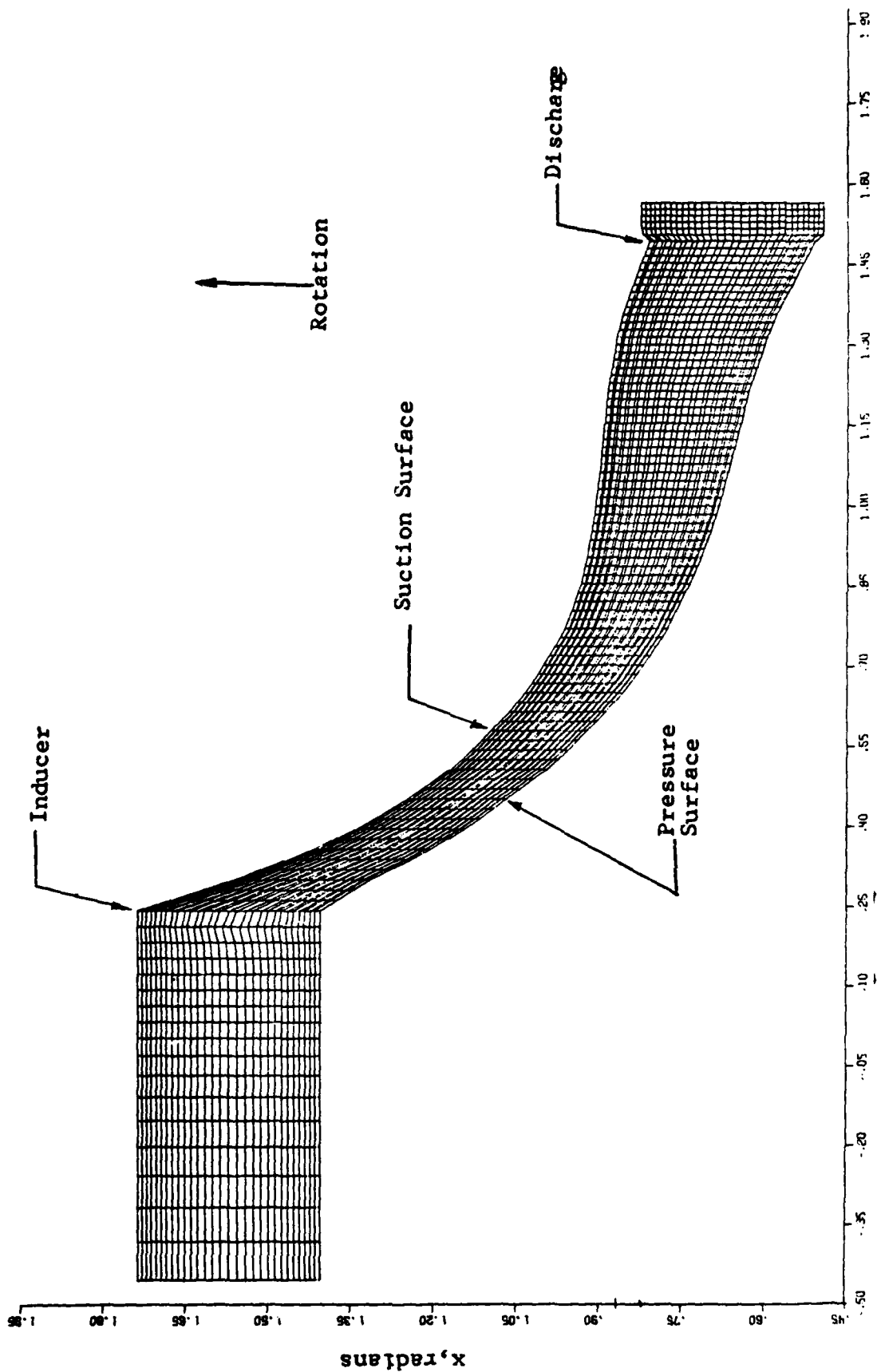


Fig.9 Finite difference mesh for the impeller hub blade-to-blade surface of calculation;
 $z = 0$; mesh composed of (30 x 101) points

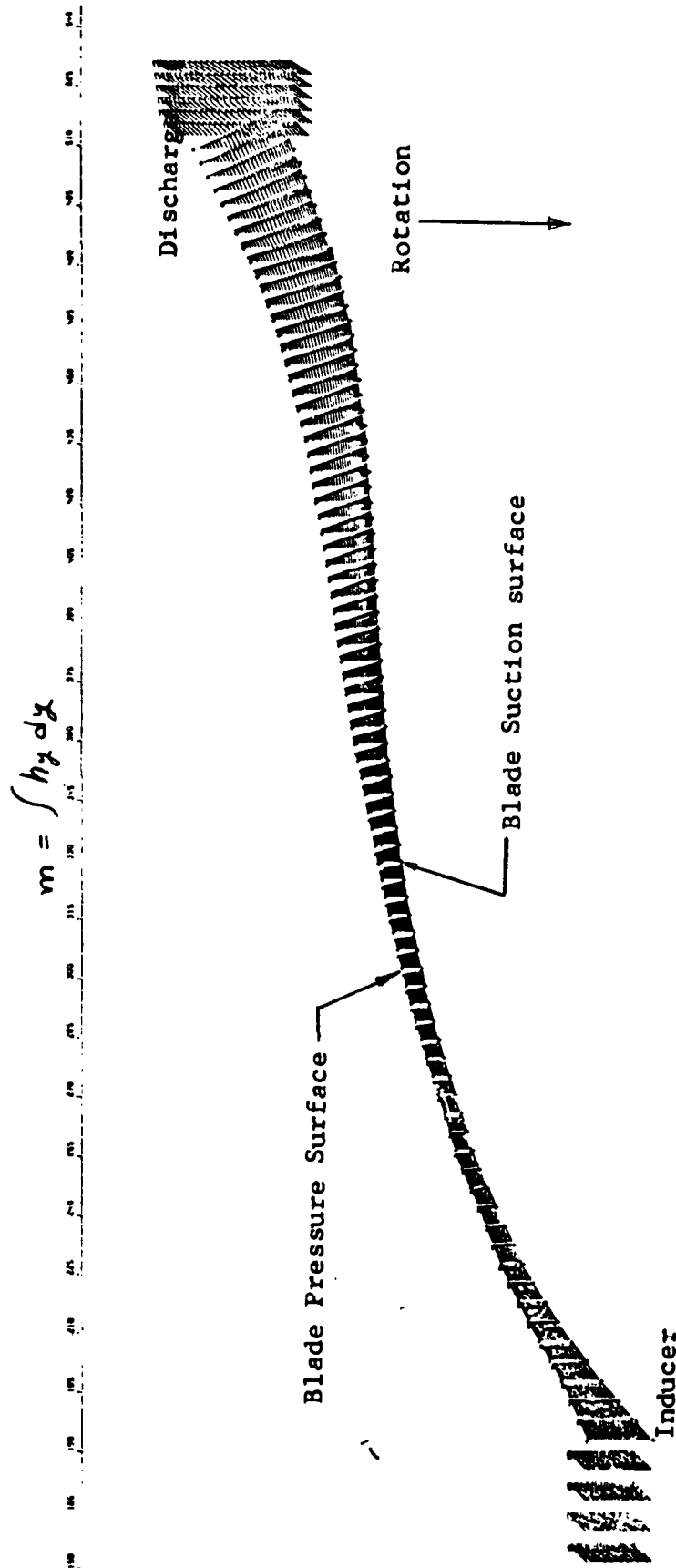


Fig. 10 Relative velocity vector plot of the inviscid impeller flow field on the hub blade-to-blade surface of calculation; $z = 0$; + symbols indicate the pressure and suction blade surfaces

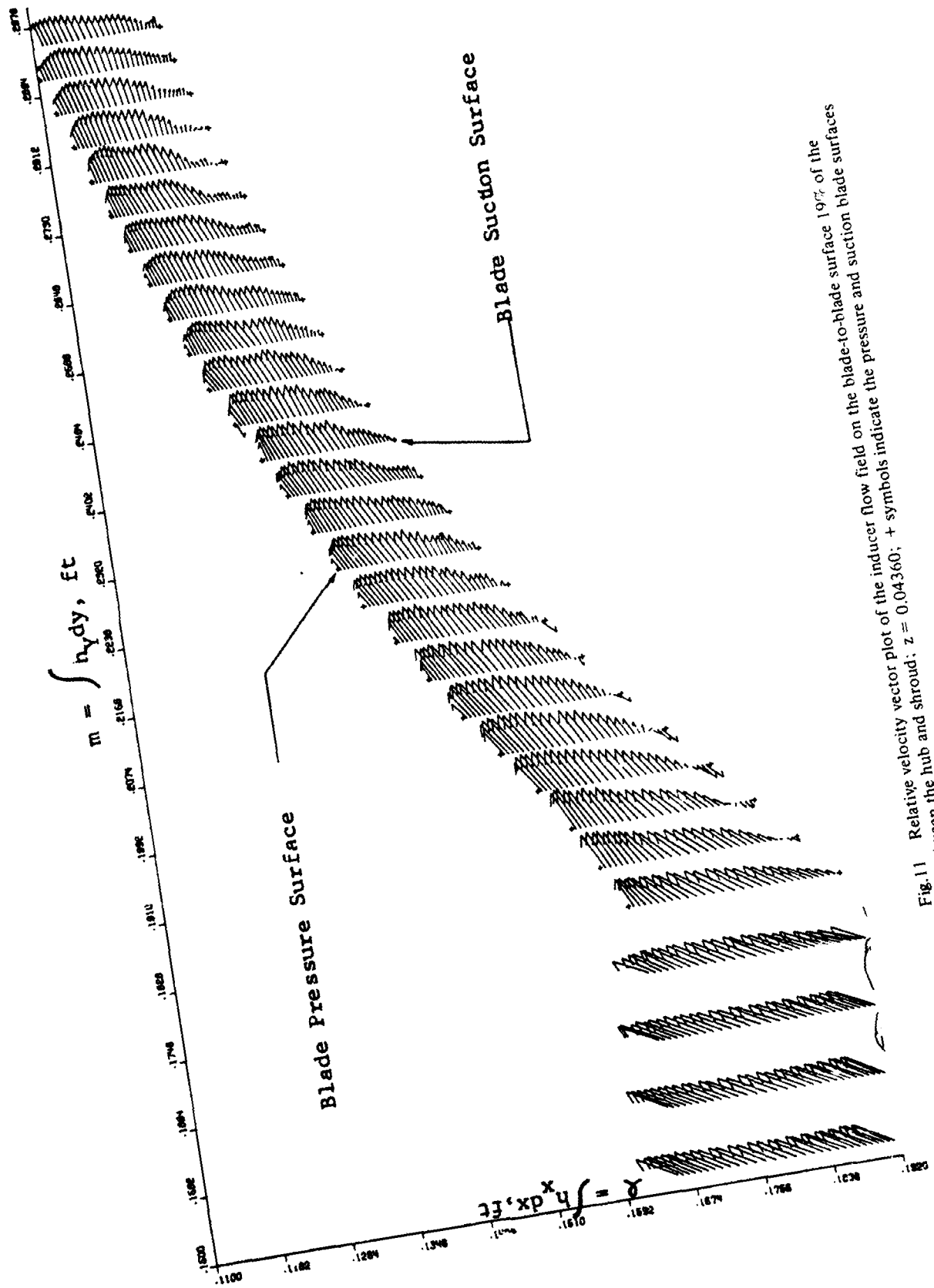


Fig. 11 Relative velocity vector plot of the inducer flow field on the blade-to-blade surface 19% of the distance between the hub and shroud; $z = 0.04360$; + symbols indicate the pressure and suction blade surfaces

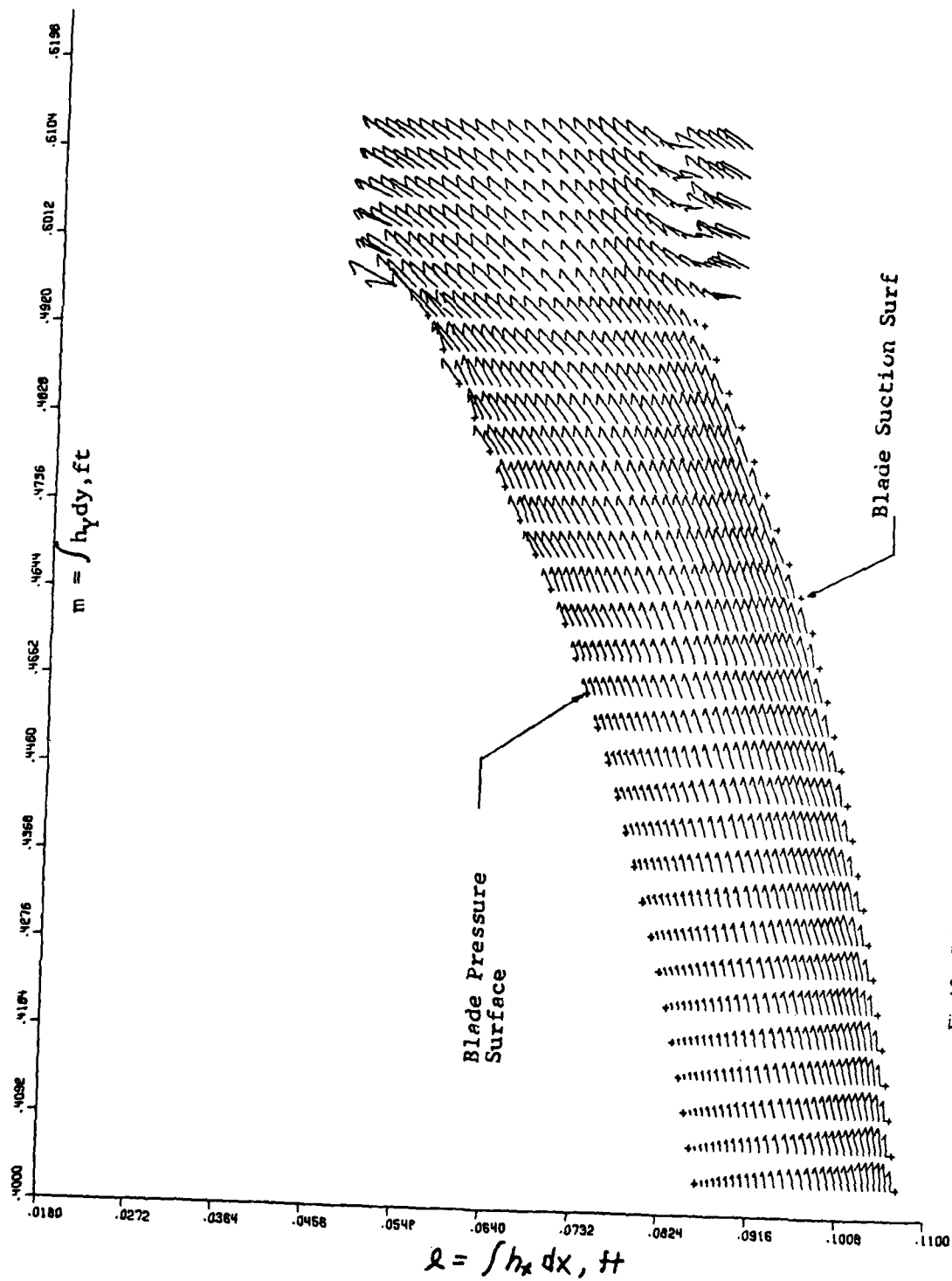


Fig. 12 Relative velocity vector plot of the discharge flow field on the blade-to-blade surface 19% of the distance between the hub and the shroud;
 $z = 0$; -4360; + symbols indicate the pressure and suction blade surfaces

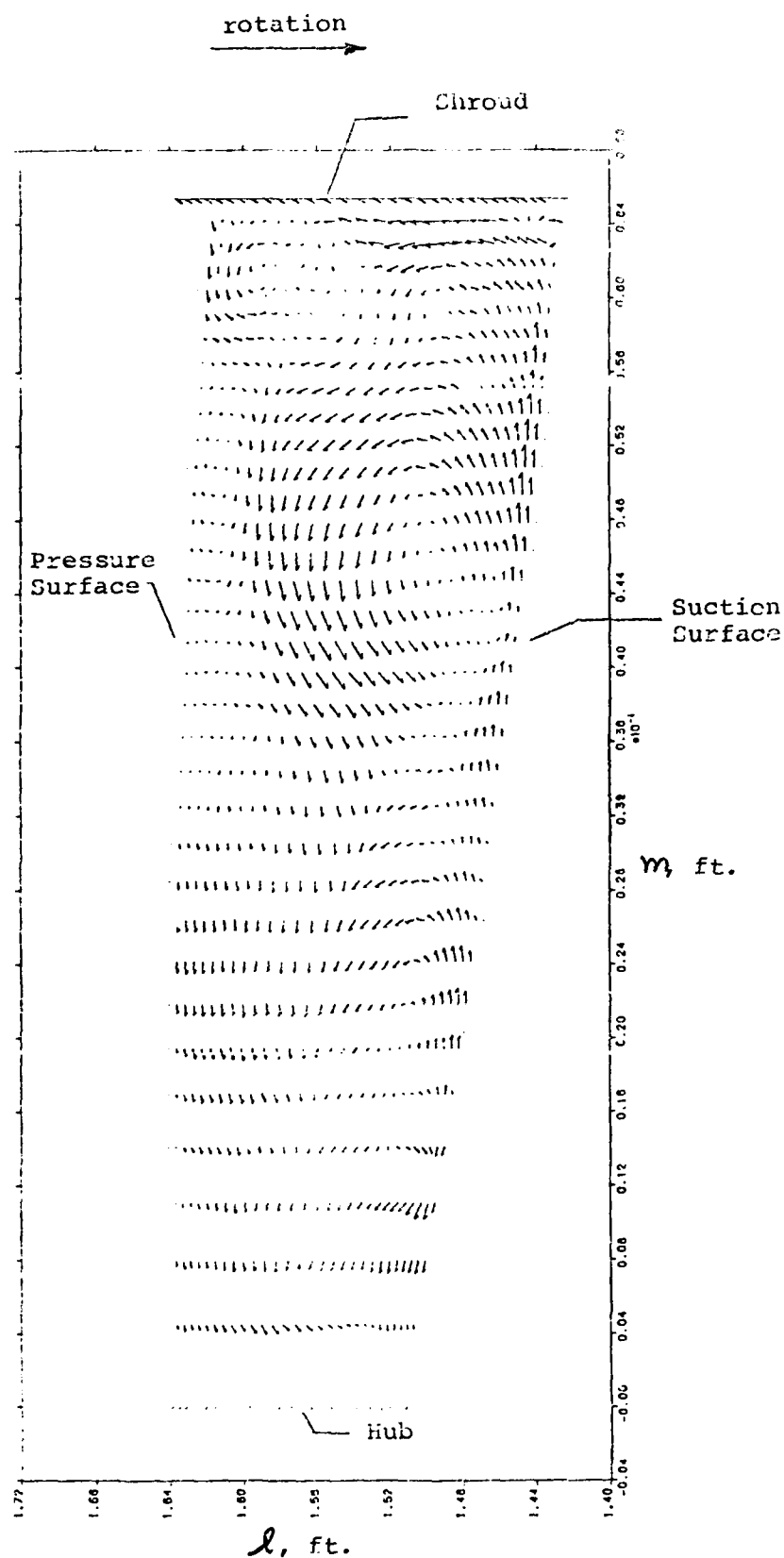


Fig.13 Velocity vector plot of the cross-sectional flow field; cross-section corresponds to 18% of total hub distance between leading and trailing edges of blades;

$$m = \frac{1}{10} \int h_y dy \quad l = \frac{1}{10} \int h_x dx$$

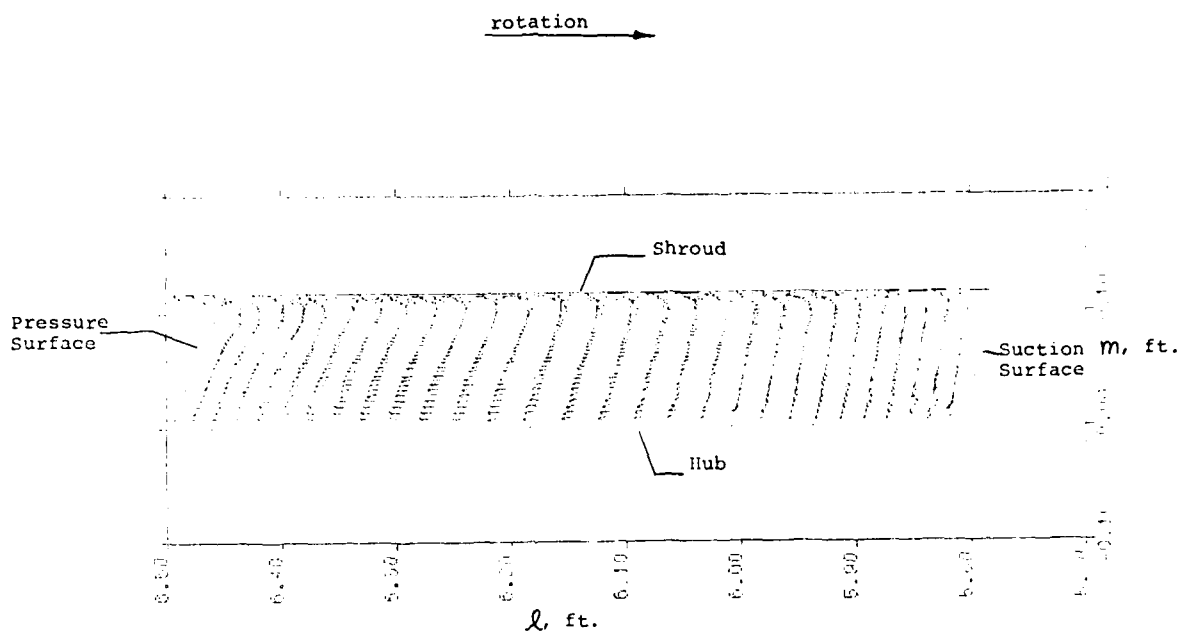


Fig.14 Velocity vector plot of the cross-sectional flow field; cross-section corresponds to 97% of total hub distance between leading and trailing edges of blades;

$$l = \frac{1}{10} \int h_x dx \quad m = \frac{1}{10} \int h_y dy,$$

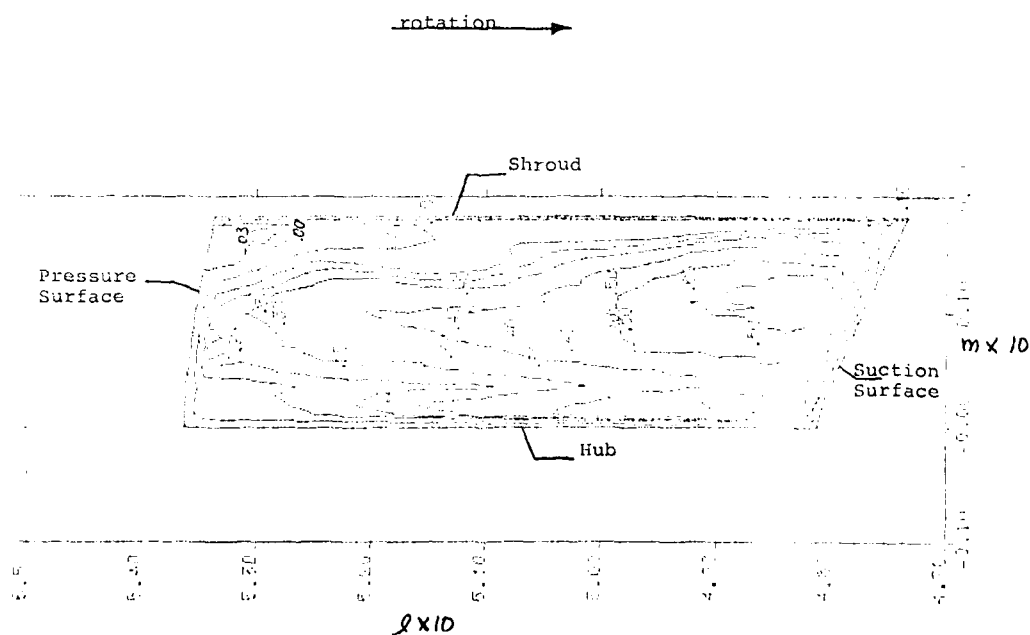


Fig.15 Contour plot of the streamwise component of relative velocity to the critical velocity; cross-section corresponds to 85% of total hub distance between leading and trailing edges of blades

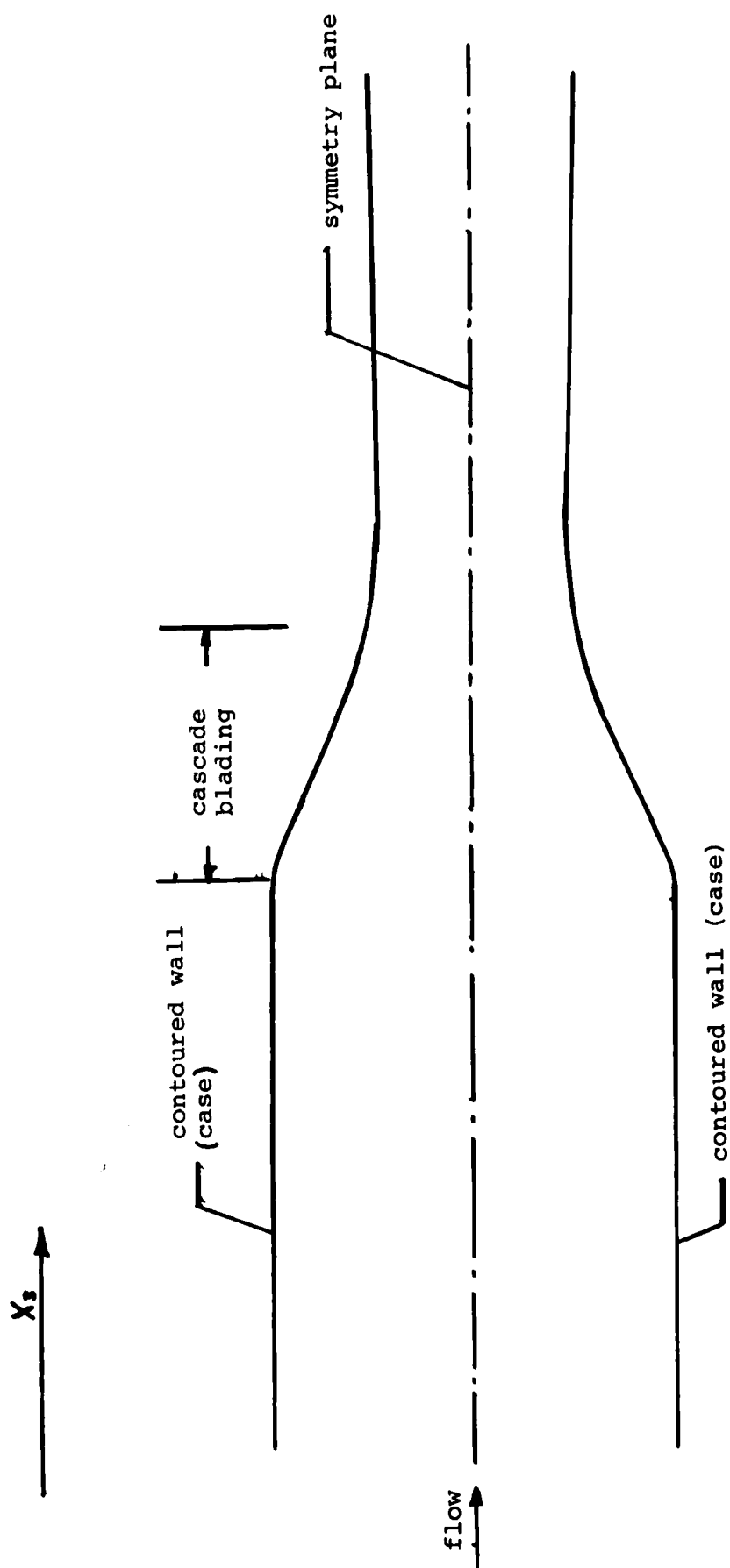


Fig. 16 Contoured sidewalls and symmetry plane of cascade

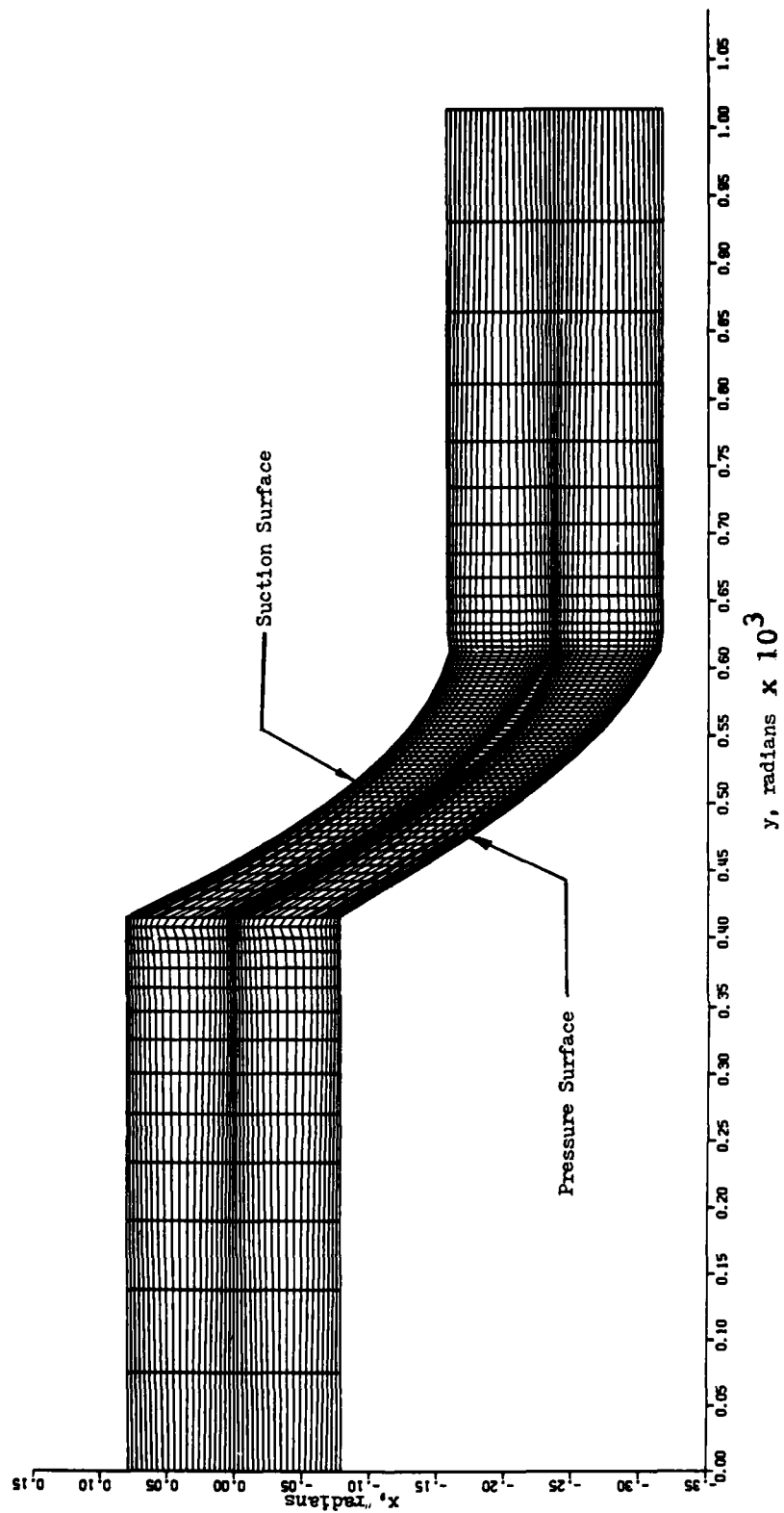


Fig. 17 Finite difference mesh on the hub blade-to-blade surface, $z = 0$; the parameters x and y correspond to curvilinear coordinates on this surface; the mesh is comprised of 42 streamline-like-lines and 80 potential-like-lines

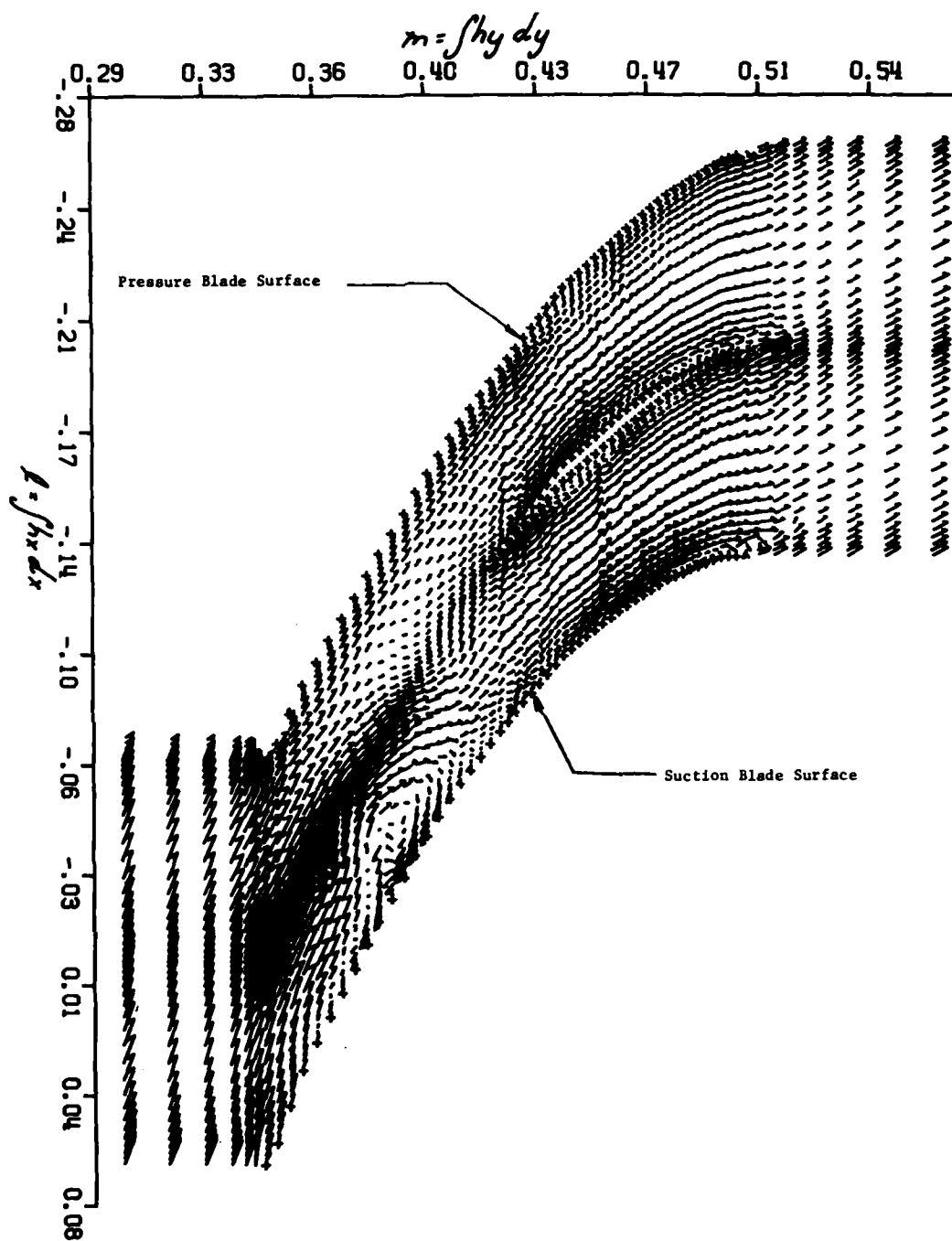


Fig.18 Velocity vector plot of the cascade flow field on a blade-to-blade surface 62% of the distance between the hub and symmetry plane; $z = .1787 \times 10^{-3}$

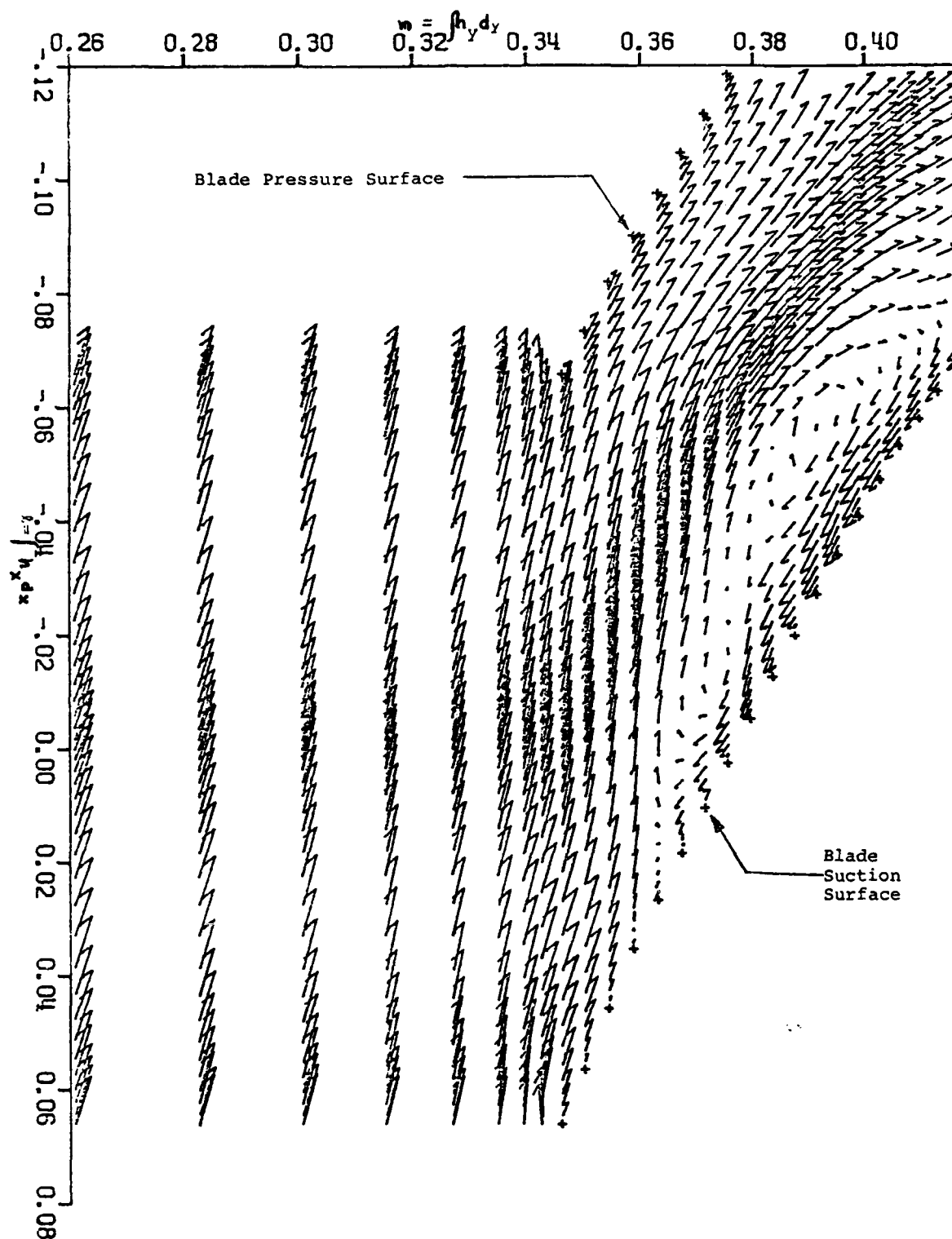


Fig.19 Velocity vector plot of the inducer flow field on a blade-to-blade surface 80% of the distance between the hub and symmetry plane; $z = .2278 \times 10^{-3}$

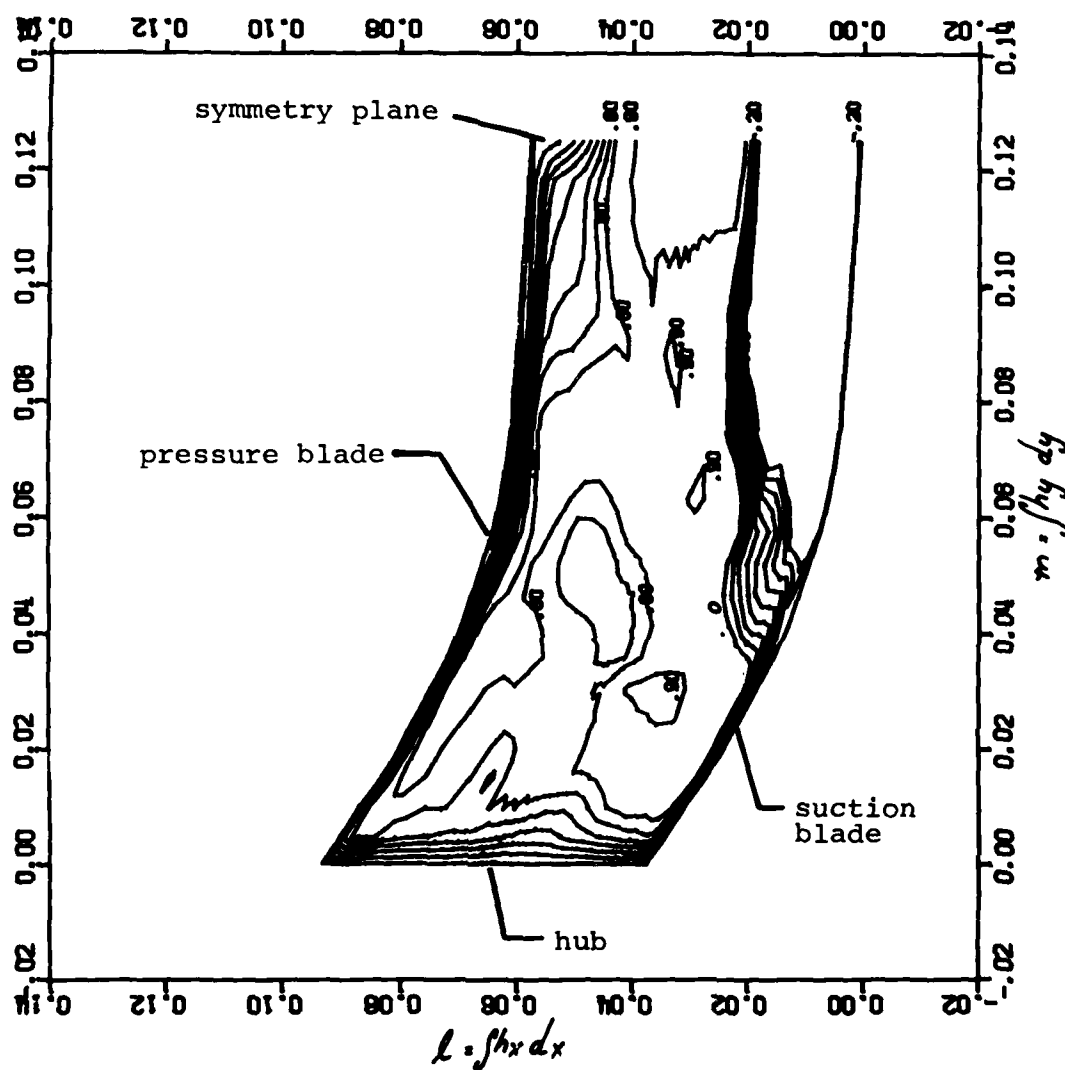
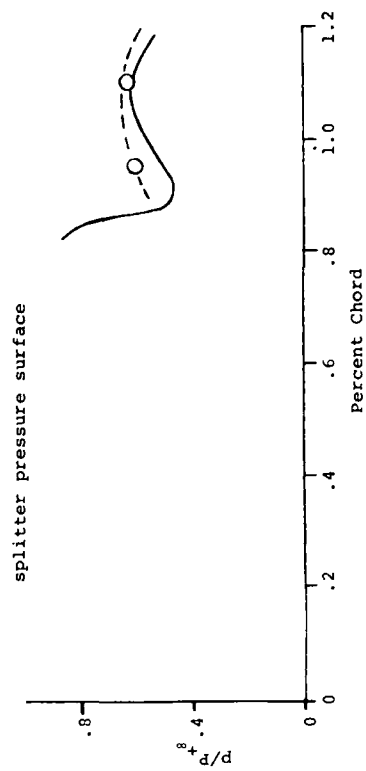
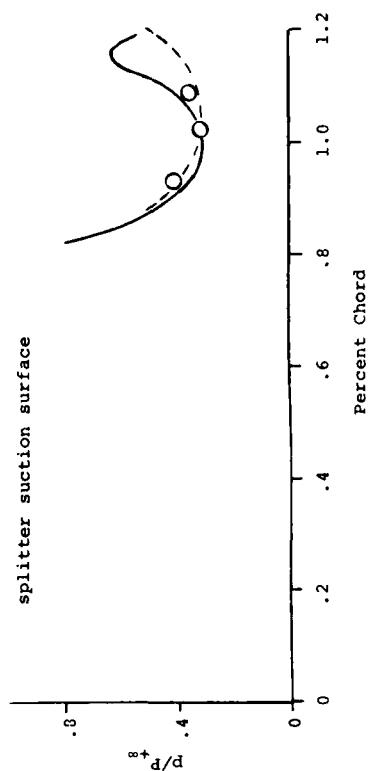


Fig.20 Contour plot of the streamwise velocity component on a cross-sectional surface located at an axial distance ratio l_r of .206

○ experimental data
(Ref. 21)
— numerical result
- - - Dodge result



○ experimental data
(Ref. 21)
— numerical result
- - - Dodge result

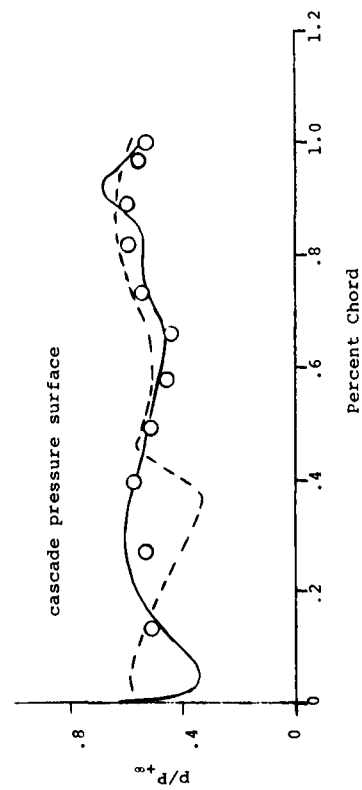
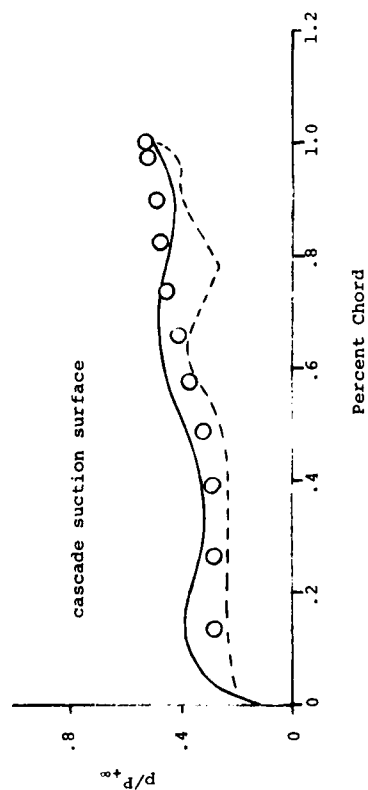


Fig.21 Comparison of numerical and experimental results on cascade main blade; $M_\infty = 1.46$, $Re_\infty = 1.36 \times 10^6$

Fig.22 Comparison of numerical and experimental results on cascade splitter vane; $M_\infty = 1.46$, $Re_\infty = 1.36 \times 10^6$

DISCUSSION

T.Yoshinaka, Pratt & Whitney, Ca

Your calculated results must be affected by the loss model used.

Author's Reply

There is no loss model used in the calculations. The appearance of loss arises simply from the viscous terms in the flow equations as governed by the turbulence model. There is however a degree of empiricism in the calculation of the tip clearance loss and the eddy viscosity.

G.Serovy, Iowa State University, US

Could the author please describe in more detail the nature of the blade-to-blade calculating surfaces which are defined by the grid. Are these specifically stream surfaces?

Author's Reply

The calculations are carried out on a set of blade-to-blade calculating grids but these are not stream surfaces because there is no assumption made that flow cannot pass through these surfaces. They are simply surfaces defined by grid points and there is complete freedom of movement of flow across them.

K.Papailiou, University of Athens, Gr

I would like to congratulate the author of this paper on an excellent piece of work. I would also like to ask him if the effects of Coriolis and curvature are dealt with in the turbulence model.

Author's Reply

The Coriolis and curvature effects are not contained in the turbulence model and so the method is deficient in this respect.

J.W.Railly, Birmingham University, UK

In the example of the calculation of flow through an axial cascade the author referred to the calculation of flow in the presence of supersonic inlet Mach numbers at incidence. Please could the author explain how the elliptic calculation copes with this situation. The only steady method of which I am aware which can account for this situation is the method of Spalding, which uses pressure-marching terms in the blade-to-blade plane.

Author's Reply

Professor Railly addresses an important problem, that of development of an upstream boundary condition. We prescribe the velocity components along the upstream boundary and the inlet mass flux. The computer code computes the density and pressure at the upstream boundary. Provided that the upstream boundary is located a few chords upstream of the cascade, disturbances emanating from the cascade are small at the upstream boundary. However, it is clear that a boundary condition is required which permits the upstream boundary to be located close to the cascade.

THREE DIMENSIONAL INVISCID CALCULATIONS IN CENTRIFUGAL COMPRESSORS

by

Ch. Hirsch and Ch. Lacor
Vrije Universiteit Brussel
Dept. Fluid Mechanics
Pleinlaan, 2, 1050 Brussels

G. Warzee
Université Libre de Bruxelles
Dept. Continuum Mechanics
Av. Fr. Roosevelt, 50, 1050 Brussels

SUMMARY

An inviscid, rotational, three-dimensional flow model in centrifugal compressors is presented. The 3D flow is separated into a potential flow part and a rotational part described by a simple additional function. The solution of the potential flow part is described in this paper and applied to several centrifugal compressors. Results are compared to experimental data as well as to results of a quasi-3D calculation procedure.

INTRODUCTION

Recent attempts to model the complex three-dimensional flow in centrifugal compressors range from full viscous calculations to various quasi three-dimensional calculation techniques as illustrated in a recent ASME symposium on Performance Prediction in centrifugal compressors [1]. The viscous calculation methods besides the larger computer times they require, are presently limited to 'parabolic marching' approximations [2], [3], valid only in absence of back flow and hence do not yet handle properly strongly separated regions such as the wake flow occurring frequently in the shroud-section side corner of radial compressors. On the other hand the quasi three-dimensional calculations (Q3D) combine various two-dimensional flows in an interactive way (through-flow and blade-to-blade stream surfaces) based on inviscid calculations with superimposed loss models and eventually 2D boundary layer calculations. With the exception of the Adler and Krimmerman calculation [4], these methods are all based on axisymmetric blade-to-blade stream surfaces and hence do not consider properly the secondary flow components.

All these methods require some level of empirical input. The viscous calculations need information with regard to the turbulence and as shown in [3] lead to results which are quite sensitive to the intensity of the turbulent eddy viscosity introduced in the model. The Q3D calculations are based on the existence of an inviscid core flow and require either empirical input with regard to loss levels and slip factors or empirical input with regard to three-dimensional effects when 2D boundary layer calculations are coupled to the basic inviscid model.

If one accepts a boundary layer type approximation, eventually with an adapted calculation for the separated region, an intermediate model between the viscous calculation and the interactive Q3D calculation is provided by an inviscid rotational three-dimensional model. Methods based on this model can be quite fast on present day computers since they require a smaller number of mesh point and less operations per point than the viscous calculations. Hence, the question arises to define under which conditions such a model would be acceptable as an intermediate level of approximation. The present paper is an initial step in an attempt to answer this question.

The first step in such a calculation is provided by a potential flow model, the second step consisting in adding a rotational component to the basic potential flow. This procedure will be described in the first section and the second section presents the basic method and the Finite Element procedure for the potential flow part.

Results are obtained for this irrotational component for the A, B and C impellers of Mizuki & al [5], [6] and are compared with experimental data and with previous results based on a quasi-3D calculation [7].

1. General equations

We consider the 3D steady flow of a non-viscous, compressible fluid through a blade row, which might be fixed or rotating at constant angular velocity Ω . The basic equations are written as follows, assuming steady relative flow

$$\text{continuity equation} \quad \vec{\nabla} \cdot (\rho \vec{V}) = 0 \quad (1)$$

$$\text{Euler equation} \quad \vec{\nabla} \cdot (\vec{V} \otimes \vec{V}) = -\vec{\nabla} I - \tau \vec{\nabla} S \quad (2)$$

$$\text{conservation of energy} \quad \vec{\nabla} \cdot \vec{V} I = 0 \quad (3)$$

When the blade row is of the stator type we have

$$\vec{U} = \vec{\Omega} \wedge \vec{r} = \vec{0}$$

and I, \vec{W} become respectively H, \vec{V} in equation (1) to (3).

From (2) and (3) follows the entropy equation, in absence of any drag force,

$$\vec{\nabla} \cdot \vec{V} S = 0 \quad (4)$$

As appears from eq. (2), the general flow is rotational when the rothalpy I and the entropy S are not constant in the whole flow field.

If one considers inlet flow conditions without tangential distortion and more particularly an inlet flow field of the form

$$\vec{V} = \vec{V}(r) \quad (5)$$

and initial profile of I and S with only radial gradient, that is

$$I = I(r) \text{ and } S = S(r) \quad (6)$$

than one has the property that

$$\vec{\omega} \vec{V} I = \vec{\omega} \vec{V} S = 0 \quad (7)$$

where $\vec{\omega}$ is the absolute vorticity vector

$$\vec{\omega} = \vec{\nabla} \wedge \vec{V} \quad (8)$$

Eq.(7) together with eqs.(3) and (4) will be compatible with eq.(6) if the inlet flow field satisfies the condition

$$V_r = 0 \quad (9)$$

that is, the inlet flow has no radial velocity components.

This situation is likely to occur in most of the practical inlets to radial compressors, or can be simulated in a model by an appropriate inlet region. The interest of relations (7) lies in the fact that it allows to reduce the number of unknown functions from three to two.

The general representation of a rotational flow field can be written as (the so called Clebsch representation)

$$\vec{V} = \vec{\nabla} \phi + \psi_1 \vec{\nabla} S + \psi_2 \vec{\nabla} I \quad (10)$$

the three unknown functions ϕ , ψ_1 and ψ_2 correspond to the three unknown velocity components.

With (3), (4) and (6), one has

$$\vec{\nabla} I = \frac{dI}{dS} \vec{\nabla} S \quad (11)$$

leading to a representation of the form

$$\vec{V} = \vec{\nabla} \phi + \psi \vec{\nabla} S \quad (12)$$

or

$$\vec{V} = \nabla \phi + \psi \vec{\nabla} I \quad (13)$$

Since, from (12)

$$\vec{\nabla} \wedge \vec{V} = \vec{\nabla} \psi \wedge \vec{\nabla} S \quad (14)$$

eq. (2) leads to the equation for ψ

$$\vec{\nabla} \vec{\nabla} \psi = \tau - \frac{dI}{dS} \quad (15)$$

Similarly, the representation (13) leads to

$$\vec{\nabla} \vec{\nabla} \psi = \tau \frac{dS}{dI} - 1 \quad (16)$$

Therefore, introducing the representation (12) in the continuity equation one obtains

$$\vec{\nabla} \rho \vec{\nabla} \phi = -\vec{\nabla} \rho \psi \vec{\nabla} S + \vec{U} \vec{\nabla} \rho \quad (17)$$

which can be solved interactively together with eq.(15) for the unknowns ϕ and ψ .

The importance of this family of flows comes from the property shown by Cazal[8] that if (7) is satisfied at a given instant, it will be satisfied always.

In ref. [8] an equivalent representation is used, namely

$$\vec{V} = \vec{\nabla} \phi + S \vec{\nabla} \psi$$

leading to an equation for ψ identical to (15) but with a reverse sign.

The function ϕ is the potential function and describes the irrotational flow field. The ψ function will therefore describe the rotational components of the flow if initial gradient of I or (and) S are present.

It appears from (17), that the basic equation does not differ fundamentally from the potential flow equation and that the same basic computational method can be adopted.

The first step is therefore to develop a calculation method for the potential flow component and this step is described in the present paper.

Assuming

$$\vec{\nabla} I = \vec{\nabla} S = 0 \quad (18)$$

eq.(2) reduces to the irrotationality condition for the absolute flow

$$\vec{\nabla} \wedge \vec{V} = 0 \quad (19)$$

and with the introduction of the potential function

$$\vec{V} = \vec{\nabla} \phi \quad (20)$$

the continuity equation leads to

$$\vec{\nabla} \rho \vec{\nabla} \phi = \vec{U} \vec{\nabla} \rho \quad (21)$$

which is the equation to be solved for the 3D potential flow.

As is well known, the condition $I = H - UV = \frac{c^2}{2}$ in the flow field, with $H = \frac{c^2}{2}$ in the in- and outlet regions, implies that (rV_θ) remains constant in the in- and outlet regions.

2. Finite Element Solution for Potential Flow

The Finite Element method is applied to solve the basic three-dimensional potential flow field, through a standard Galerkin method applied to eq.(21), leading to

$$\int_V \rho \nabla W_i \cdot \nabla \phi \, dV = - \int_V \vec{U} \cdot \nabla \rho W_i \, dV + \oint_S \rho \frac{\partial \phi}{\partial n} \cdot W_i \, dS \quad (22)$$

where V is the volume taken by the whole flow domain
 S is the surface, enclosing V
 W_i is a weighted function.

The flow region is discretized with finite elements :

$$\phi = \sum_i \phi_i N_i \quad (23)$$

where N_i are the shape functions, and using the shape functions as weight function, (23) becomes :

$$\sum_j \int_V \rho \cdot \nabla N_i \cdot \nabla N_j \, dV = - \int_V \vec{U} \cdot \nabla \rho N_i \, dV + \oint_S \rho \frac{\partial \phi}{\partial n} \cdot N_i \, dS \quad (24)$$

The boundary conditions are defined as follows :

Along the inlet and outlet surfaces, the normal derivatives

$$\rho \frac{\partial \phi}{\partial n} = \rho V_n$$

are imposed where V_n will generally be the meridional velocity taken usually as uniform if the planes are sufficiently far downstream and upstream of the blade row.

Along the blade surfaces, one has

$$\frac{\partial \phi}{\partial n} = + \vec{U} \cdot \vec{n}$$

expressing that the relative normal velocity component is zero.

Along the boundaries limiting the domain in the pitchwise direction upstream and downstream of the blade row, periodicity conditions are imposed - fig. 5.

$$\phi_Q - \phi_P = \phi_B - \phi_A = (sV_\theta)_{in}$$

$$\phi_{Q'} - \phi_{P'} = \phi_{B'} - \phi_{A'} = (sV_\theta)_{out}$$

where B and A are periodic points.

At inlet, V_θ is known while at outlet V_θ is obtained through a slip factor or a Kutta-Joukowski condition.

The present computational procedure is an extension of the two-dimensional methods developed for subsonic blade-to-blade flows [9]. Finite element computations of the 3D potential flows have also been performed by Worster [10] for incompressible flows in pumps and by Laskaris [11] for the compressible subsonic case.

Application to radial compressors

The finite element code for potential flows has been developed with cubic trilinear elements (8 nodes per three-dimensional element) and applied to the three compressors A, B, C tested by Mizuki & al. [5], [6]. Figures 1 to 3 give a three-dimensional view of the flow domain between two blades, for respectively compressors A, B, C, the numbers of the different stations being indicated on the figures. For the sake of clarity, not all of the grid points are shown on these figures.

In order to obtain a solution which satisfies accurately the boundary conditions, a higher density of grid-points near the blades, hub and shroud is required. Figures 4, 5 show the distribution of the grid points in respectively a meridional and blade-to-blade surface of compressor C. As can be seen 9 blade-to-blade and 11 meridional surfaces are used. Using 3 stations upstream and downstream of the blade row, the total number of gridpoints is 2178. Figure 6 shows the evolution of the calculated velocities in the meridional surfaces, going from suction towards pressure side, for compressor B and $\phi = 0.5$. The first surface is the suction side of the blade and the last one the pressure surface of the next blade.

Figure 7 shows the velocities in some points on the hub side of compressor A for $\phi = 0.5$. Figure 8 represents the streamlines in the same case, as obtained by the quasi-3D method [7] and in figure 9 the measured results by Mizuki et al. [6] are shown. On the three figures it is seen that, halfway the passage, the streamlines slightly bend from pressure toward suction side. At the outlet of the blade row there is a slip tendency from suction toward pressure side.

In figures 10 to 15 the blade static pressure distributions in the hub and shroud surfaces are represented along the suction and pressure sides. The points show the experimental results obtained by Mizuki et al. [5]. The continuous line represents the calculated three-dimensional inviscid results, while the dashed line shows the results as obtained by Adler and Krimerman with their 3D calculation method [12]. The mass flow is in all cases $\phi = 0.5$.

In the case of compressor A, fig. 10, a local acceleration is found at the suction side near the shroud, in a point approximately 30% downstream from the impeller inlet, i.e. at exit of the inducer. This decrease might be caused by the shocked inlet conditions at the reducer, according to Mizuki et al. [5]. Due to the large gradient of static pressure along the shroud-suction surface streamline, the flow will separate in this corner. As the present model is non-viscous, the obtained results disagree rather strongly with the experimental data. Near the hub the flow is not separated, due to the concave wall and better agreement between measurements and prediction is obtained, fig. 11.

Compressor B also shows a decrease of pressure at inducer outlet, at the suction side near the shroud. The decrease is smaller than for the A-type and therefore the flow is not separated. In consequence the predicted results follow the measurements quite closely, fig. 12 and 13. The third line on the figures 12 and 13 shows the results obtained with a quasi-3D method [7] with axisymmetric blade-to-blade surfaces. It is to be noted that the measured data correspond to the 7/8 streamline of ref [5] while the calculated data were taken along the shroud. The results obtained from the calculation show indeed a less marked drop in pressure along the corresponding stream surface, although the local acceleration is still stronger than in the measured data and stronger than the calculated distributions by Adler and Krimerman.

In the case of compressor C, fig. 14 and 15, the measurements show a pressure reversal near the shroud, i.e. the pressure on the suction side becomes higher than the pressure on the pressure side. This reversal is not found theoretically; it can be attributed to secondary and shroud clearance effects as well as eventually to flow instabilities induced by the convex wall boundary layers. Only a slight decrease of the pressure at inducer outlet occurs and again there will be no separation. The predicted and measured results agree quite well with the data and with the calculation from [12], with the exception of the mentioned reversal effect. Figures 16 to 18 show the pitch-averaged pressure along the shroud for the three compressors. Again the continuous line represents the results obtained with the present 3D potential program while the dashed line shows the prediction of Adler, Krimerman [12]. In all cases, ϕ is set to 0.5. The sudden pressure decrease at inducer outlet for type A compressor, indicating a flow separation, is noticed again, fig. 16. After the point of separation the predicted results differ rather strongly from the measurements, as already mentioned earlier. Better agreement is obtained for the B and C compressors, fig. 17 and 18, although the calculated isentropic pressure rise is stronger than the measured one in both cases. In figures 19, 20 the secondary flow pattern in station number 9 of compressor B is represented, for $\phi = 0.5$. Figure 19 shows the results obtained by the 3D potential program, while fig. 20 shows the measured flow pattern as obtained by Mizuki et al. [6].

As can be seen on fig. 20, the real flow yields a clockwise rotation, i.e. a rotation in the sense of $\vec{\Omega}$, in station number 9. As mentioned in [6] a part of this rotation can be derived from the potential flow theory (fig. 19).

Hence, the inherent secondary flow components in station 9 could be obtained by subtracting the velocity-vector, from the 3D potential flow calculation, from the real measured velocity-vector.

The same results, predicted and measured, for compressor C, $\phi = 0.5$, are represented in respectively figures 21 and 22, and the similar potential flow rotation is seen.

Figure 23 shows a comparison between measured and calculated meridional velocity distributions from the pressure side to the suction side along station number 13 for the hub blade-to-blade surface. The full line is obtained from the present method while the dashed line is from a quasi-3D calculation of [6]. As noted also by Adler and Krimerman [12], the fully potential flow calculation predicts a slope which is closer to the measured data, although the level is underpredicted, due probably to blockage effects of the wall boundary layers.

CONCLUSION

A three-dimensional potential flow calculation method has been developed and applied to the three compressors tested by Mizuki et al. The calculated data show that a potential flow model can be used with an acceptable prediction capability, if no separation occurs as in compressors B and C. Secondary flow effects are not predicted by the present calculation and their inclusion, together with the addition of hub and shroud boundary layers should improve further the reliability of the 3D computations in absence of strong separation.

REFERENCES

- [1] S. Gopalakrishnan, P. Cooper, C. Grennan, J. Switzer, Ed. "Performance Prediction of Centrifugal Pumps and Compressors"; ASME Symposium, 22nd Annual Gas Turbine Conference, New Orleans, March 1980.

- [2] J. Moore and J.G. Moore ; "Calculations of Three-Dimensional, Viscous Flow and Wake Development in a Centrifugal Impeller" ; ASME ref [1] pp. 61-67.
- [3] M.R. Malin, H.I. Rosten, D.G. Tatchell ; "Three- Dimensional Computations of Flows in Centrifugal Pumps and Compressors" ; ref ASME [1], pp 33-45.
- [4] D. Adler, Y. Krimmerman ; "The Complete Three-Dimensional Calculation of the Compressible Flow Field in Turbo Impellers" ; Journal of Mechanical Engineering Science, Vol.20, 1978, pp.149-159.
- [5] S. Mizuki, I. Ariga, I. Watanabe ; "Investigation Concerning the Blade Loading of Centrifugal Impellers" ; ASME paper 74-GT-143, 1974.
- [6] S. Mizuki, I. Ariga, I. Watanabe ; "A study on the Flow Mechanism within Centrifugal Impeller channels" ; ASME paper 75-GT-14, 1975.
- [7] Ch. Hirsch, G. Warzee ; "Quasi 3D Finite Element Computation of Flows in Centrifugal Compressors" ; ref ASME [1], pp. 69-75.
- [8] P. Cazal ; "Principes Variationnels en Fluide Compressible et en Magnétohydrodynamique des Fluides" ; Journal de Mécanique , Vol. 5, N°2, pp. 149-161, 1966.
- [9] Ch. Hirsch, G. Warzee ; "An Integrated 3D Finite Element Calculation Program for Turbomachinery Flows" ; ASME paper, 78-GT-56 ; Journal of Engineering for Power, 101, pp. 141-148, 1979.
- [10] D.M. Worster ; "The Calculation of Fully Three-Dimensional Flows in Impellers Using a Finite Element Method" ; Report from Department of Mechanical Engineering at Heriot-Watt University ; Edinburgh, 1973.
- [11] T.E. Laskaris ; "Finite-Element Analysis of Three-Dimensional Potential Flow in Turbomachines" ; AIAA Journal, Vol.16, N°7 pp. 717-722, July 1978.
- [12] D. Adler, Y. Krimmerman ; "Comparison between the Calculated Subsonic Inviscid Three-Dimensional Flow in a Centrifugal Impeller and Measurements" ; ASME ref [1], pp. 19-31.

NOMENCLATURE

H	total enthalpy
I	rotalphy ; $I = H - U V_\theta$
\bar{r}	radius
S	entropy
s	pitch
T	static temperature
\vec{U}	wheel speed vector = $\Omega r \vec{I}_\theta$
\vec{V}	absolute flow vector
\vec{W}	relative flow vector
ρ	specific mass
ϕ	potential function; mass flow coefficient= mean outlet radial velocity / outlet wheel speed
ψ	unknown function in the expression for \vec{V}
Ω	rotor angular velocity
$\vec{\omega}$	curl of the absolute velocity vector.

SUBSCRIPTS

n	normal component
r	radial component
θ	tangential component

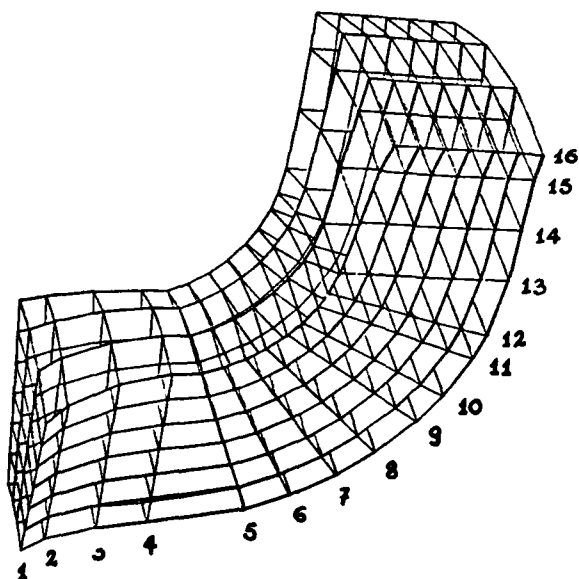


Figure 1. 3-D view of A-type compressor with part of the finite element mesh .

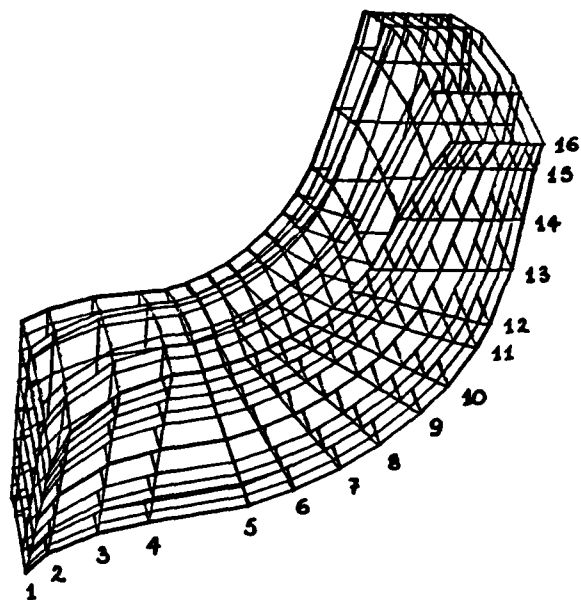


Figure 2. 3-D view of B-type compressor with part of the finite element mesh .

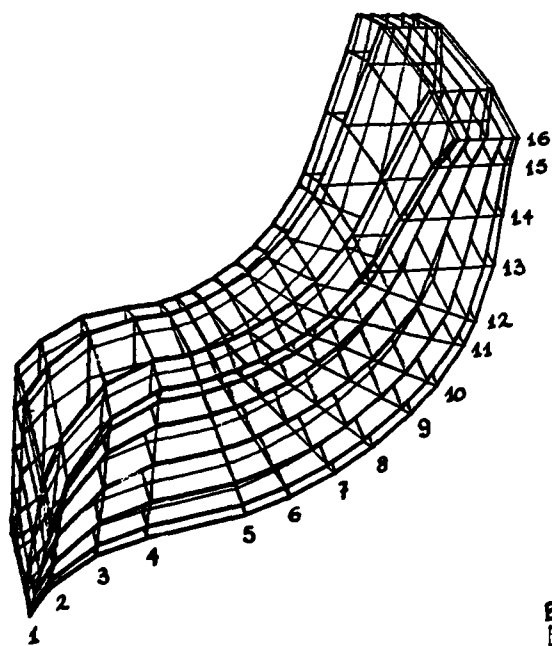


Figure 3 .3-D view of C-type compressor with part of the finite element mesh .

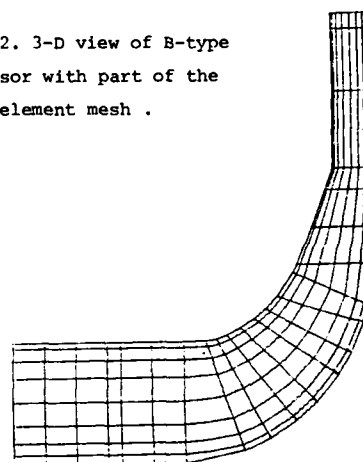


Figure 4. Meridional finite element mesh of compressor C.

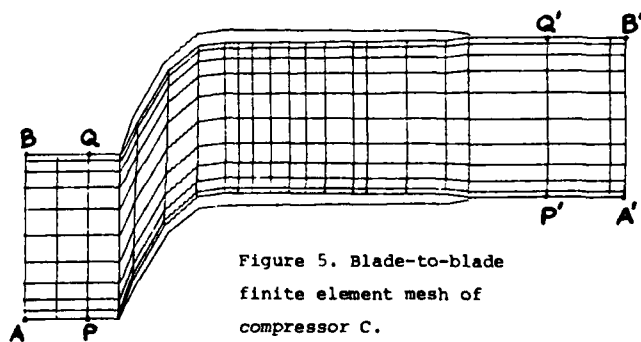


Figure 5. Blade-to-blade finite element mesh of compressor C.

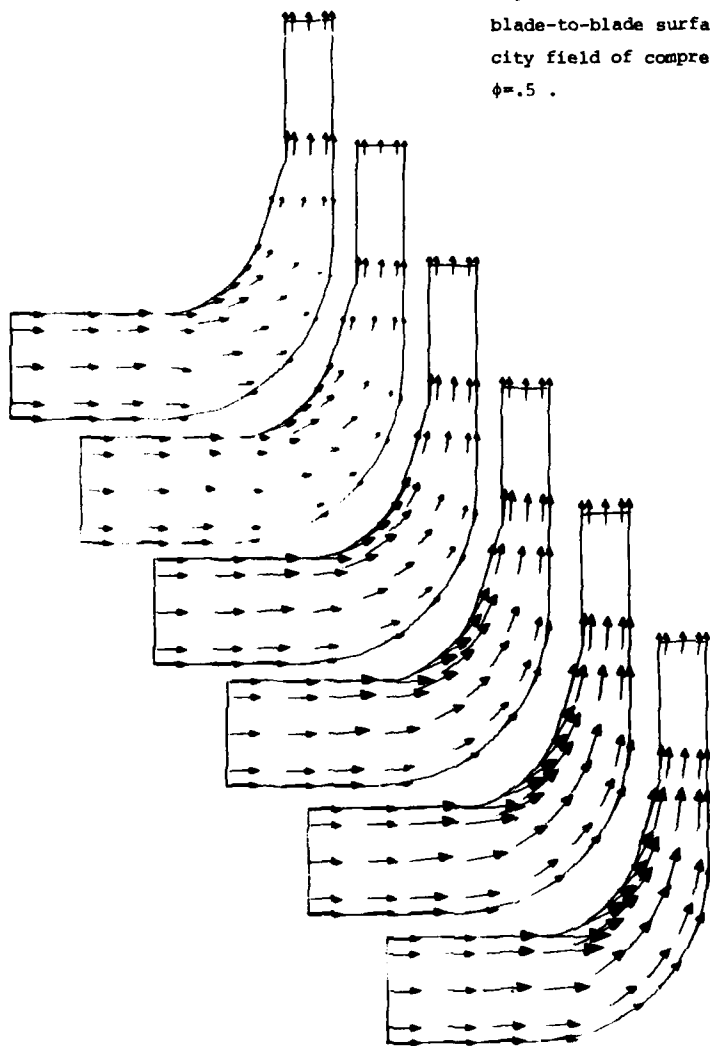


Figure 6. Calculated velocity field in the various meridional surfaces from pressure side to suction side of B compressor at $\phi=.5$.

Figure 9. Measured hub blade-to-blade surface velocity field of compressor A at $\phi=.5$.

Figure 7. 3-D calculated hub blade-to-blade surface velocity field of compressor A at $\phi=.5$.

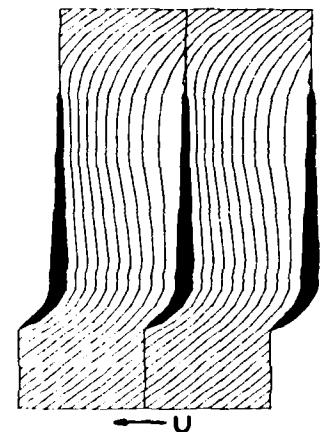
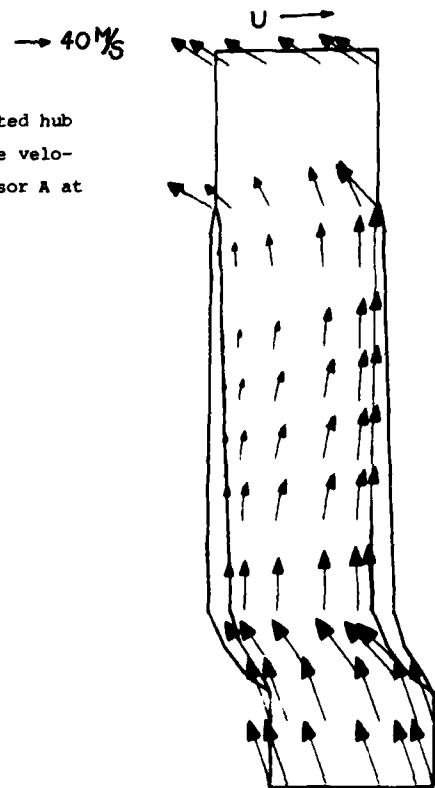
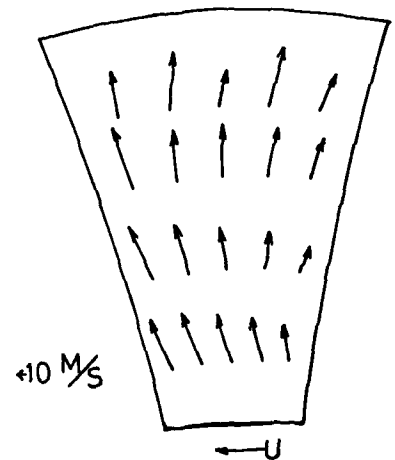


Figure 8. Calculated streamline pattern along the hub blade-to-blade surface with the Q3-D approach [7]. (A-type, $\phi=.5$)



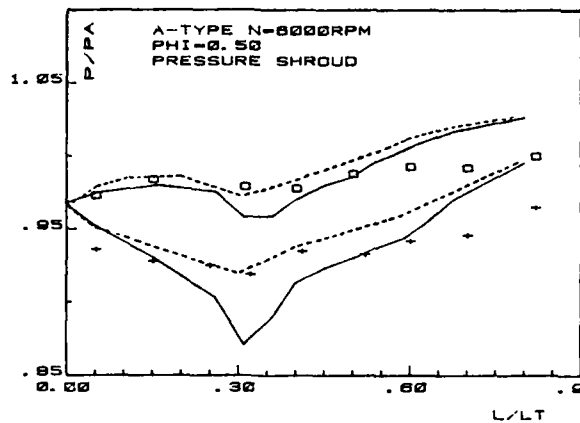


Figure 10. Blade static pressure distribution on shroud surface of A-type impeller at $\phi=0.5$.

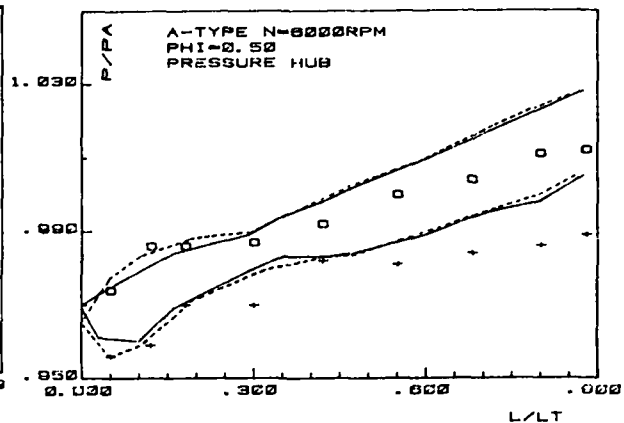


Figure 11. Blade static pressure distribution on hub surface of A-type impeller at $\phi=0.5$.

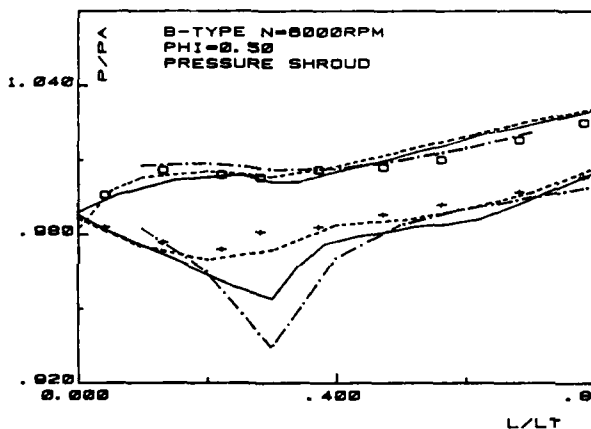


Figure 12. Blade static pressure distribution on shroud surface of B-type impeller at $\phi=0.5$.

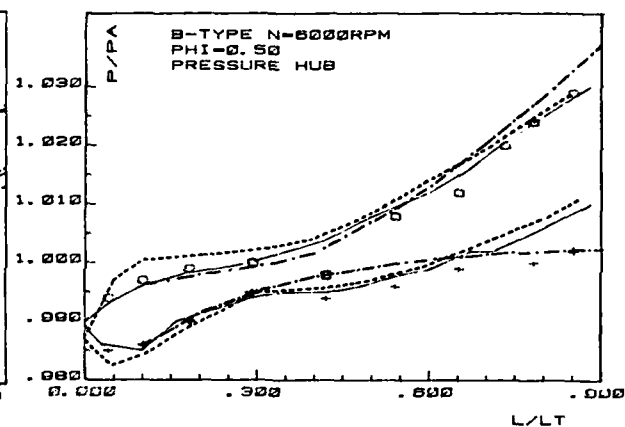


Figure 13. Blade static pressure distribution on hub surface of B-type impeller at $\phi=0.5$.

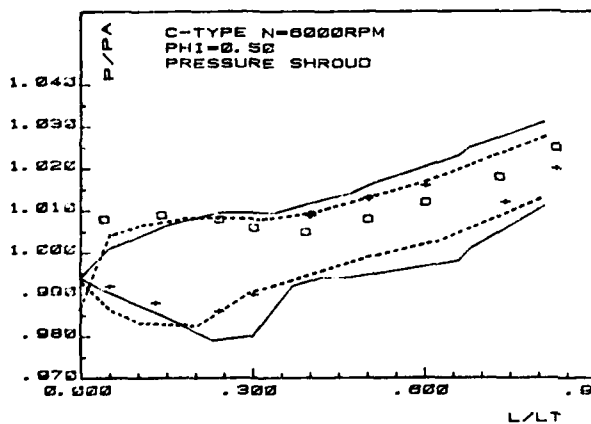


Figure 14. Blade static pressure distribution on shroud surface of C-type impeller at $\phi=0.5$.

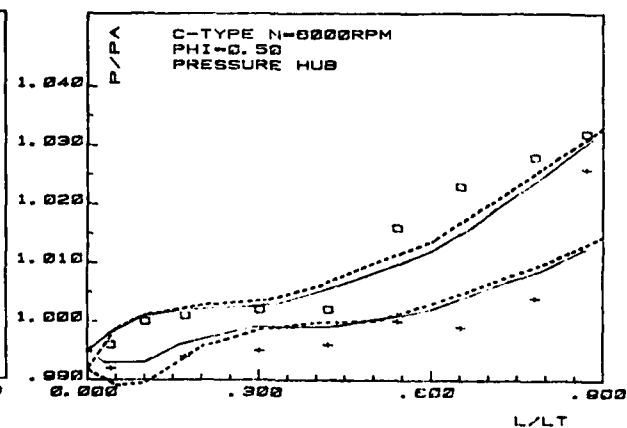


Figure 15. Blade static pressure distribution on hub surface of C-type impeller at $\phi=0.5$.

— present 3D results - - - 3D results of ref. [12] - · - Q3D results of ref. [7]

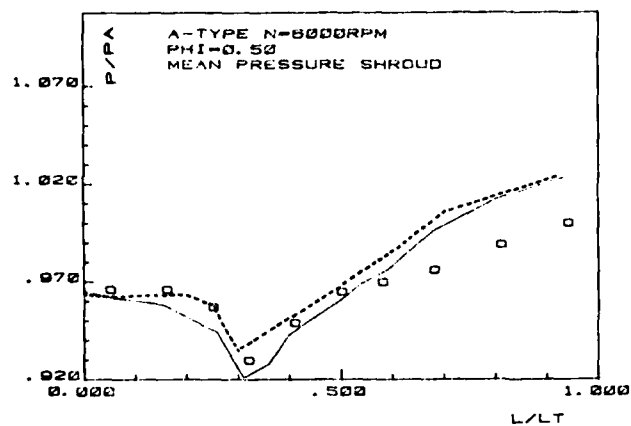


Figure 16. Pitch-averaged static pressure distribution on shroud surface of A-type impeller at $\phi=0.5$.

Figure 17. Pitch-averaged static pressure distribution on shroud surface of B-type impeller at $\phi=0.5$.

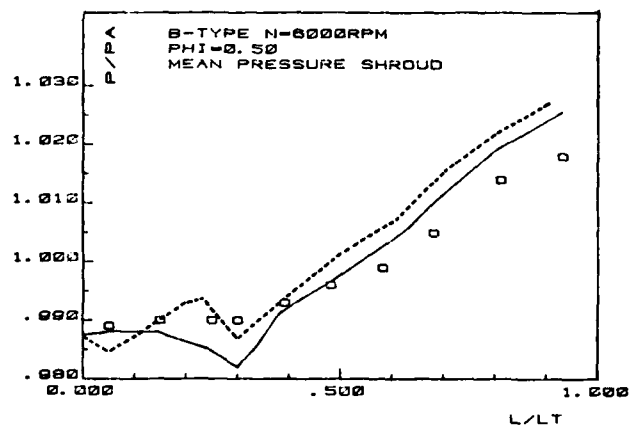


Figure 18. Pitch-averaged static pressure distribution on shroud surface of C-type impeller at $\phi=0.5$.

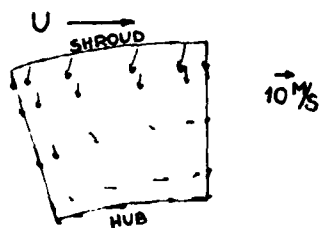
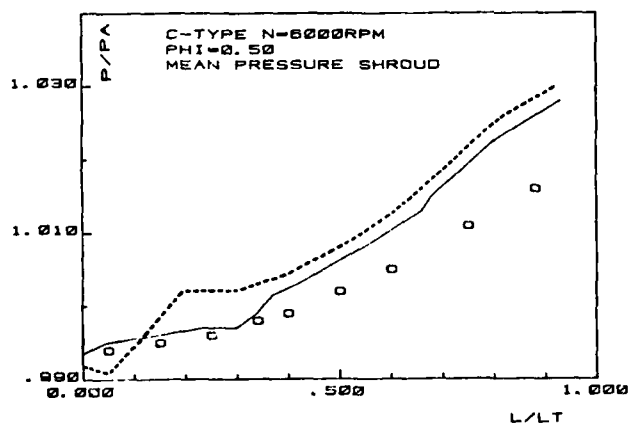


Figure 19. Projection of calculated flow field on station No.9 of B-type impeller at $\phi=0.5$.

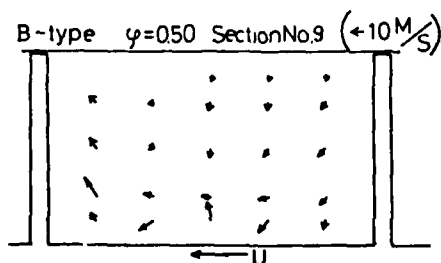


Figure 20. Measured flow pattern in station No.9 of B-type impeller at $\phi=0.5$.

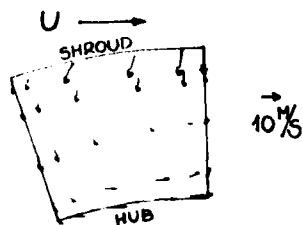


Figure 21. Projection of calculated flow field on station No.9 of C-type impeller at $\phi=.5$.

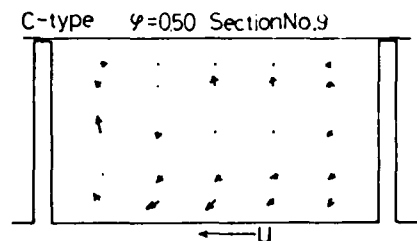


Figure 22. Measured flow pattern in station No.9 of C-type impeller at $\phi=.5$.

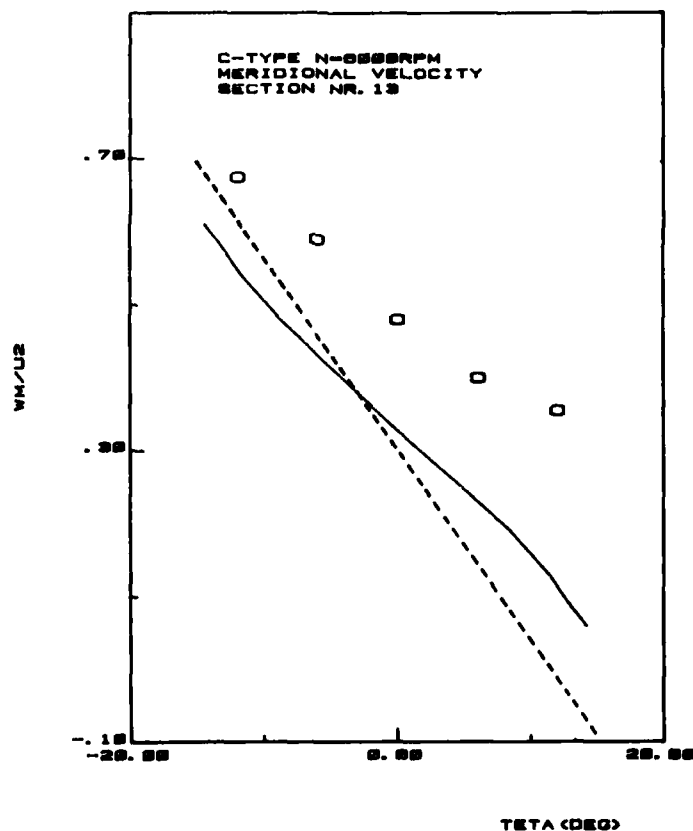


Figure 23. Blade-to-blade measured and calculated meridional velocity distributions on the hub surface of impeller C. (station No.13 at $\phi=.5$)

— present 3D results - - - - Q3D results of ref.[6]

DISCUSSION

D.Japikse, CREARE, US

I would like to ask the author if he has calculated the secondary flow for Case 'A' of Mizuki which was published at the ASME conference earlier this year. I would also like to ask the author if he feels that the wake structure in the impeller is predictable using inviscid methods only.

Author's Reply

The calculation of the secondary flow is not possible with the potential function alone. The addition of the non-viscous rotational component will allow that calculation which is underway for various compressors and in particular for the case 'A' of Mizuki. However these results are not yet available at the present time.

As is well known the calculation of a separated region is not possible with non-viscous methods. However, we feel that a rotational, non-viscous calculation would be able to detect the tendency towards separation, since one can consider, in a "boundary layer sense", that the non-viscous flow determines the tendency towards separation and "triggers" the viscous separation. However this should be confirmed by explicit calculations.

Y.Ribaud, ONERA, Fr

I would like to comment that two types of vortex flow seemed to appear in a centrifugal rotor where the flow is assumed to be non-viscous.

- (1) For low flows there appear true vortices on the pressure surface. These are shown by flow visualisation using smoke.
- (2) In the cases where there are strong gradients of stagnation pressure upstream of the impeller where, if the work varies spanwise, there will be downstream of the leading-edge a vortex sheet which one must take into account in the calculation. The use of the velocity potential will help to simulate this effect.

Author's Reply

The shed trailing edge vortices, appearing from the deviations from free vortex flow, can be described by the present method and will automatically be included in the solution when the rotational components are added to the potential flow solution.

TRANSONIC FLOW CALCULATION IN CENTRIFUGAL COMPRESSORS
BY A TIME DEPENDENT METHOD OF CHARACTERISTICS

by

CARLO OSNAGHI
Lecturer of Turbomachinery- Politecnico of Milan

ANTONIO PERDICHIZZI
Research Engineer

FRANCESCO BASSI
Assistant Professor

ISTITUTO DI MACCHINE - POLITECNICO DI MILANO
Piazza Leonardo da Vinci, 32 - 20133 Milano - Italy

SUMMARY

Difficulties in the numerical solution of the flow in advanced centrifugal compressors arise from the transonic nature of the flow. In order to solve this problem a time dependent method of characteristics, which takes into account shock waves, boundary layer and wakes, is presented. Separated flow is simulated by simplified models. Such a program is proposed for centrifugal compressors both for impellers and diffusers. Extension of the method to unsteady phenomena is discussed. Results are discussed, and they demonstrate the possibilities of the method at the present state-of-the-art.

LIST OF SYMBOLS

a speed of sound
b channel width
h enthalpy
h channel height (see Fig.1)
m meridional coordinate (see Fig.1)
 \dot{m} mass flow rate
M Mach number
n normal coordinate (see Fig. 1)
p pressure
r radius
S entropy
t time
 t_{in} time for impeller acceleration
U peripheral velocity
V absolute velocity
W relative velocity
x,y,z auxiliary transformed coordinates (see appendix A1)
 x_1, y_1 natural coordinates
X,Y rectangular working coordinates
 α, β functions defined by Eqs. (5)
 ϵ angle of m-lines in the meridional plan (see Fig.1)
 θ angle between W and meridional coordinate m
 ρ density
 ϕ angular coordinate (see Fig.1)
 ω angular velocity
E, η , ζ rotated coordinates for the blade nose definition (see App.A1)

SUBSCRIPTS

in inlet
J in the jet
out outlet
P at the pressure side of the blade
R total values in relative motion
S at the suction side of the blade or shear layer between jet and wake
sep at separation point
t at blade tip (shroud)
T total values in absolute motion
W in the wake
O at infinity upstream
1 at blade inlet
2 at blade outlet

1) INTRODUCTION

In the last 20 years great emphasis has been placed in designing centrifugal compressors with very large pressure ratio and rotating speed. For this purpose transonic calculation methods have been developed in order to deal with very heavy flow conditions with particular regard to viscous and 3-dimensional phenomena, e.g. rotating boundary layers and wakes. Moreover, many authors pointed out that the energy exchange in the mixing process downstream of the rotor are fundamentally unsteady. Different approaches are proposed for this goal.

In the present paper a time dependent method is described, which has been applied successfully in turbine and compressor cascades. Such method seems to include many of the required features even if the present time its extension to 3-dimensional cases is unrealistic.

2) METHOD OF ANALYSIS

2a) Equation of Motion

The equations of motion for adiabatic and inviscid flows, neglecting gravity forces, from the point of view of a relative observer, who turns together with the turbomachine rotor at a quasi-constant angular speed, are:

$$1) \text{ continuity equation } \frac{\partial \rho}{\partial t} + \nabla \cdot (\rho \vec{W}) = 0 \quad (1)$$

$$2) \text{ momentum equation } \frac{\partial \vec{W}}{\partial t} - \vec{W} \times (\nabla \times \vec{W} + 2\vec{\omega}) + \nabla \left(\frac{W^2}{2} - \frac{\omega^2 r^2}{2} \right) + \frac{1}{\rho} \nabla p = 0 \quad (2)$$

$$3) \text{ energy equation } d' h_R = \frac{\partial}{\partial t} \left(\frac{W^2}{2} \right) dt \quad (3)$$

The equation (3) is written along the particle path, the symbol (d') being defined by $(d') = \vec{W} \cdot \nabla () dt$.

We introduced the total enthalpy in relative motion $h_R = h + \frac{W^2}{2} - \frac{(\omega r)^2}{2}$.

Of course the equation of state should be added, $\rho = \rho(h, p)$.

A blade-to-blade surface, with arbitrary radii and channel heights, in the usual hypothesis of stream surfaces coincident with surfaces of revolution (1) is considered and the equations 1-3 are written in (m, φ) coordinates (2).

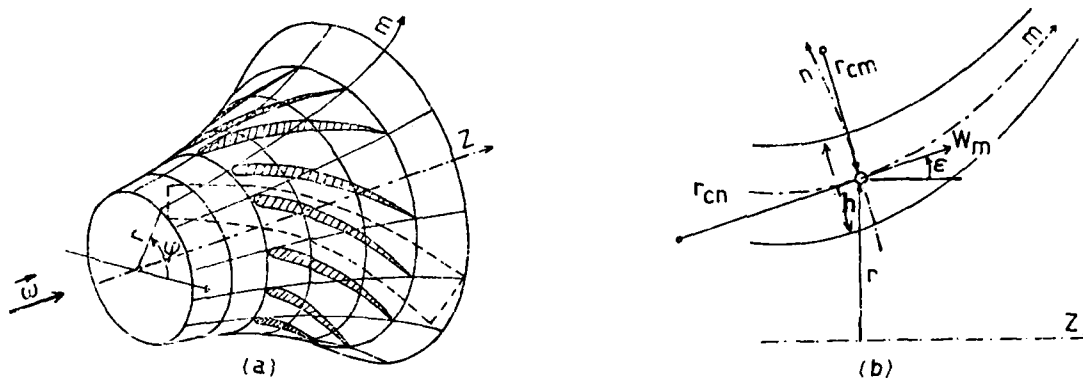


Fig. 1) Blade-to-blade surface of revolution (a) and meridional channel (b).

According to Carriere and Capelier (3) the equations on this blade-to-blade surface are derived for a natural coordinate system (x_1, y_1) defined by

$$dx_1 = \cos \vartheta dm + r \sin \vartheta d\varphi \quad dy_1 = r \cos \vartheta d\varphi - \sin \vartheta dm \quad (4)$$

Finally the system (x_1, y_1) is normalized by introducing two functions α and β defined by $dx_1 = \alpha dx$ and $dy_1 = \beta dy$ so as to obtain a new system (X, Y) where X is parallel to the velocity and Y is perpendicular, which is cartesian and rectangular if α and β (considered as functions of X, Y, t) satisfy the conditions:

$$\frac{\partial \alpha}{\partial Y} + \beta \frac{\partial \vartheta}{\partial X} = -\alpha \beta \frac{\sin \vartheta}{r} \sin \epsilon \quad \frac{\partial \beta}{\partial X} - \alpha \frac{\partial \vartheta}{\partial Y} = \alpha \beta \frac{\cos \vartheta}{r} \sin \epsilon \quad (5)$$

which are the integrability conditions for the system:

$$dm = \alpha \cos \vartheta dX - \beta \sin \vartheta dY \quad d\varphi = \alpha \frac{\sin \vartheta}{r} dX + \beta \frac{\cos \vartheta}{r} dY \quad \text{equivalent}$$

to Eqs. (4). If Eqs. (5) are valid we have a correspondence between the systems (m, φ) and (X, Y) . We can work in the rectangular system (X, Y) where streamlines are lines $Y = \text{const}$. By making use of the equations of motion it is possible to develop Eqs. (5) so as to obtain the relations:

$$\begin{cases} \frac{\partial}{\partial Y} \ln(\alpha W) = \frac{1}{W^2} \left(\frac{\partial h_R}{\partial Y} - T \frac{\partial}{\partial Y} \right) + \frac{\beta}{W} (2\omega \sin \epsilon - \frac{\partial \vartheta}{\partial t}) \\ \frac{\partial}{\partial X} \ln(\beta \rho W h) = -\frac{\alpha}{W \rho} \frac{\partial \rho}{\partial t} \end{cases} \quad (\text{for } h, \text{ see Fig. 1}) \quad (6)$$

If the insteady phase is not too rapid, according to the physical transient phenomenon, only the term $\frac{\beta}{W} (2\omega \sin \epsilon)$ is important to the right side of Eqs. (6). It is important to note, from Eqs. (6), that α can be assigned on an arbitrary streamline and β on a X constant arbitrary line (normal).

The blade-to-blade equations, in (X, Y) coordinates, become:

$$\frac{1}{\rho a} \frac{\partial p}{\partial t} + \frac{a}{\alpha} \frac{\partial W}{\partial X} + \frac{W}{\rho a \alpha} \frac{\partial p}{\partial X} + \frac{W a}{\beta} \frac{\partial \theta}{\partial Y} = C_1 \quad (7)$$

$$\frac{\partial W}{\partial t} + \frac{W}{\alpha} \frac{\partial W}{\partial X} + \frac{1}{\rho a} \frac{\partial p}{\partial X} = C_2 \quad (8)$$

$$W \frac{\partial \theta}{\partial t} + \frac{W^2}{\alpha} \frac{\partial \theta}{\partial X} + \frac{1}{\rho \beta} \frac{\partial p}{\partial X} = C_3 \quad (9)$$

where

$$C_1 = -aW \cos \theta (k_n + \frac{\sin \epsilon}{r})$$

$$C_2 = \omega^2 r \cos \theta \sin \epsilon$$

$$C_3 = -\sin \epsilon (\omega^2 \sin \theta + \frac{W^2}{r} \sin \theta + 2\omega W)$$

$$k_n = \frac{1}{h} \frac{\partial h}{\partial m} \quad \text{and} \quad \epsilon = \sin^{-1} \frac{\partial x}{\partial m} \quad \text{are defined in Fig. (1)}$$

The functions α and β are to be recalculated for all time-steps. In appendix 1 practical expressions for α and β are derived from Eqs. (6-9).

2b Equation of characteristics

Being the equations to be solved hyperbolic in the time coordinate, a characteristic surface is found to exist at any point M at time t. This surface is a conoid, having M as a vertex, which cuts X,Y plane at time $t_0 = t - dt$ along a pseudo-ellipse having $(a/\alpha)dt$ and $(a/\beta)dt$ as main axes. Furthermore, also the trajectory O-M has the properties peculiar to characteristic, being the point O the position of the physical particle M at time t_0 .

According to the classical theory, it is possible to write the equations (7-9) on this surface or even, on particular lines of it, but in this case it is not possible to eliminate all partial derivatives. If we choose the four lines (bicharacteristics) passing through the intersections of the ellipse with its main axes (see Fig. 2), the derivatives along the bicharacteristics are predominant. If the symbol $\frac{d}{dt}$ indicates derivatives along the line considered, we obtain the Eqs. (10), (11), (12), (13).

The energy equation can also be written in a discrete way along the trajectory; anyway, if the irreversible effects due to shock waves are explicitly accounted for by means of the Hugoniot relations, the energy equation can be simply written as $S_M = S_0$ for all the points not crossing the shock waves.

Combining the four equations (10-13), which are not independent, we obtain W_M, θ_M, p_M starting from the points A, B, C, D at time t_0 : ρ_M and h_M can be calculated from p_M and S_M by the equation of state. To calculate the points lying along the boundaries some of the Eqs (10-13) can be substituted by imposition of proper boundary conditions.

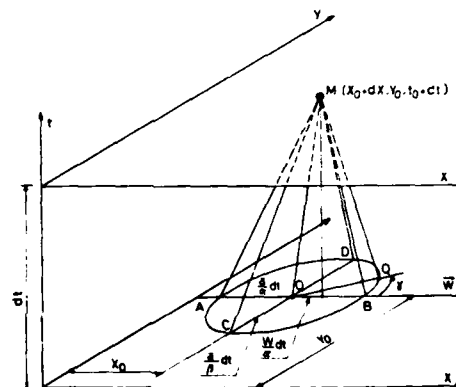


Fig. 2) Characteristic cone passing through the point M.

line	line equation	(d/dt) line	compatibility equation	
AM	$\frac{dX}{dt} = \frac{W+a}{\alpha}, \frac{dY}{dt} = 0$	$\frac{\partial}{\partial t} + \frac{W+a}{\alpha} \frac{\partial}{\partial X}$	$\frac{1}{\rho a} \frac{dp}{dt} + \frac{dW}{dt} = C_1 + C_2 - \frac{aW}{\beta} \frac{\partial \theta}{\partial Y}$	(10)
BM	$\frac{dX}{dt} = \frac{W-a}{\alpha}, \frac{dY}{dt} = 0$	$\frac{\partial}{\partial t} + \frac{W-a}{\alpha} \frac{\partial}{\partial X}$	$\frac{1}{\rho a} \frac{dp}{dt} - \frac{dW}{dt} = C_1 - C_2 - \frac{aW}{\beta} \frac{\partial \theta}{\partial Y}$	(11)
CM	$\frac{dX}{dt} = \frac{W}{\alpha}, \frac{dY}{dt} = + \frac{a}{\beta}$	$\frac{\partial}{\partial t} + \frac{W}{\alpha} \frac{\partial}{\partial X} + \frac{a}{\beta} \frac{\partial}{\partial Y}$	$\frac{1}{\rho a} \frac{dp}{dt} + W \frac{d\theta}{dt} = C_1 + C_3 - \frac{a}{\alpha} \frac{\partial W}{\partial X}$	(12)
DM	$\frac{dX}{dt} = \frac{W}{\alpha}, \frac{dY}{dt} = - \frac{a}{\beta}$	$\frac{\partial}{\partial t} + \frac{W}{\alpha} \frac{\partial}{\partial X} - \frac{a}{\beta} \frac{\partial}{\partial Y}$	$\frac{1}{\rho a} \frac{dp}{dt} - W \frac{d\theta}{dt} = C_1 - C_3 - \frac{a}{\alpha} \frac{\partial W}{\partial X}$	(13)

Table 1 Total derivatives with respect to time and compatibility equations.

3) BOUNDARY CONDITIONS AND SPECIAL POINTS CALCULATION

The possible situations which can occur on the characteristic surface at various boundaries (inlet and outlet: subsonic and supersonic, boundary profile, free jet, slip-lines periodic boundaries, etc.) have already been described in details in (4). In particular as to the study of blade or wing profiles, it must be remembered that the first and the last streamline are copied one pitch to the left and to the right respectively, to obtain periodicity conditions between upstream and downstream boundaries; this allows to calculate the points on periodic boundaries as internal points. In this case the profile is put inside the flow field.

To solve the flow in steady or rotating turbomachine blades, with radii and meridional channel height variations, regarding boundary layer, separated flow, and finite thickness wake including possible energy exchange with the main flow, the following possibilities have been necessarily introduced into the calculation program.

- 1) Possibility of imposing different inlet and outlet boundary conditions for supersonic flows discriminating between $Ma \geq 1$, as in the Table 2.

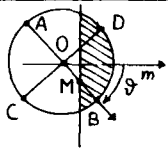
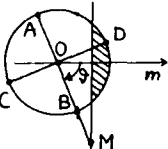
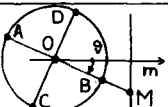
		UPSTREAM	DOWNSTREAM
$M < 1$		1 equation from point B p or W } are given arbitrarily ϑ and S } Note: Point D is not considered	W is calculated from point A ϑ is calculated from points C and D S is calculated from O p is given arbitrarily
$M > 1$ $Ma < 1$		1 equation from point D (C if $\vartheta > 0$) p or ϑ } are given arbitrarily W and S } Note: if D is outside it is extrapolated from inside	W is calculated from points A and B ϑ is calculated from point C (D if $\vartheta > 0$) S is calculated from O p is given arbitrarily
$Ma > 1$		p, W, ϑ, S are given arbitrarily	p, W, ϑ, S are calculated from A, B, C, D, O

Table 2. Conditions at inlet and outlet boundaries for different Mach numbers.

- 2) Possibility of a strict leading-edge subsonic flow solution that is necessary for the two following reasons:
- the leading-edge solution gets singularities in velocity, angle, α - β auxiliary functions and partial derivatives at the right of Eq.s (10-13), nevertheless such quantities must be obtained in the internal points of the calculation network. Since the usual interpolations become invalid in the region near the leading-edge and cause calculation instability, it is necessary to resort to interpolations respecting the function singularities at the leading edge and derived from the analytical solution of the flow. Being impossible to deal with the leading-edge region by increasing the meshes number of the calculation network not to exceed in the calculation time, rough solutions, as for example the one of the incompressible flow at a corner, are to be excluded because inadequately approaching the blade profile in the first mesh, and because neglecting the circulating flow due to the blade lift;
 - it is necessary to follow properly the evolution of the stagnation point along the blade profile at the changing of the velocity circulation during the unsteady calculation period, not to cause an inconsistent velocity distribution deriving from the trailing-edge closure condition.
- Because of the previous reasons it has been approached the blade profile in the leading edge region in order to obtain an adequate analytical approximation and a good flow solution in such a region, even if very large meshes are employed. Such a method in its fundamental lines is referred in appendix A 2.
- 3) Possibility of modifying the blade profile in order to simulate the boundary-layer displacement thickness, calculated in several times during the calculation, by means of classical steady methods. The separation point is therefore determined in different times. Anyway, in this paper, very simple empirical separation criteria have been employed, because of the great difficulty of this problem in the radial turbomachines wheels.
- 4) Possibility of dealing with separated flows in a simple way up to the trailing-edge and imposing complex closure conditions, fit for finite thickness trailing-edge and wake.
- 5) Possibility of treating wake points downstream the trailing-edge by means of a generalization of a double slip-line point calculation, so that it is possible to consider, besides velocity discontinuities, transversal wake pressure gradients and different directions (connected with the thickness wake variation) between right and left wake flow, at the boundary with the jet-flow.
- 6) Possibility of accelerating the wheel by varying its angular speed ω up to the final value. The flow model satisfying the points 3-5 is referred in appendix A 2 and derives from the jet-wake classical model (5), (6), (7). It provides the matching of the non-viscous, quasi-bidimensional mainflow (jet), with a zero or small flowrate flow (wake) in which most of the losses accumulate, and which is therefore at an initial energy level very inferior to the jet one.

4) FLOW CALCULATION IN A CENTRIFUGAL COMPRESSOR

The computer code requires the initial flow conditions. The flow field at the subsequent instant is calculated as follows: definition of upstream and downstream boundary conditions; boundary-layer calculation and blade profile correction; pressure imposition into the possible separated region; evaluation of the wake quantities; calculation of all the points inside the inviscid flow by means of the characteristics method; imposition of the periodicity condition; calculation of α and β functions; determination of the physical network (m, φ). After increasing the time by a Δt , the code again calculates the flow field following the previous scheme up to steadiness of the flow, or assigned end time.

This computer code was used for the flow calculation of the centrifugal compressor wheel 1611 VL 1 developed by the Northern Research and Engineering Corp.. The calculation was made in cooperation with Franco Tosi s.p.a., (Italy).

The main data of this machine are:

rotational speed = 39,000 rpm
 total pressure vaneless diffuser exit/total inlet pressure = 7.15
 relative Mach number at impeller inlet: hub = 0.611; casing = 1.303
 absolute Mach number at impeller exit = 1.259
 blade speed at impeller exit (fps) = 1726.9

For the time being, calculations are available for the hub profile blade; the application of the computer code to the tip profile blade, where relative Mach number exceeds unity, does not present any problem: indeed the same code was already used without difficulties in supersonic axial compressor calculations. Because of operating reasons it was necessary to remove the "splitter" blade from the channel. Therefore the results cannot be compared with the available data.

The meridional channel profile was calculated for a flow rate equal to 1/10 of the total, having arbitrarily assumed the meridional velocity profile, since this is out of the purpose of this paper. The initial flow configuration was obtained by means of a classical blade-to-blade method (10) for angular speed and mass flow rate equal to half of the design values and assuming that no flow separation exists under such conditions. Whether the above position is true or not is not relevant because the final solution is not affected by the initial approximation.

The network calculation is made by 11 streamlines and 30 normal lines, 19 of which are inside the blades. The transient conditions consist of rotational speed acceleration and contemporary static pressure increase at the downstream boundary, while the total pressure and absolute inlet angle are kept constant. Actually the counter-pressure is a flow rate function; however it was imposed by means of a different law because of computer costs: indeed, being the channel inlet very small, the time step (proportional to the minimum width of the numerical meshes) is strongly limited. This makes impossible to extend the transient period to more than 200-300 time steps. Under these circumstances, perturbations propagate too slowly. Finally the downstream pressure increase was anticipated, so that it could propagate in due time inside the rotor. This makes phenomenon history less realistic.

Two types of calculations were made: the first one in the hypothesis that no separation exists; the second one in which flow separation is progressively accounted for starting from the initial solution. In this second case the ratio v wake velocity over separation velocity was arbitrarily assumed equal to 0.2; the variation law of wake thickness downstream the trailing edge was imposed although this can easily be computed (see appendix A2).

5) RESULT ANALYSIS

Though in this calculation the shock waves are not taken explicitly into account, they are correctly predicted in an isentropic flow calculation; consequently, the thermodynamics quantities are affected from error; particularly the continuity equation is not satisfied and the pressure discontinuity is over estimated. The flow solution at half of the design rpm, from which the time dependent calculation starts, is referred in Figs. (3a-3b).

A stability test was conducted with no condition change. It was possible to verify that the solution was very stable after 300 time steps. Particularly the obtained slip-factor value was equal to the one imposed to the solution deriving from (10).

The basic time period t_{in} is assumed equal to the time in which the rotating speed reaches the final value. Consequently to the acceleration of the rotating speed, the mass flow rate increases correctly. The flow shows an excessive trend to accelerate (see Fig. 4 at time = $2t_{in}$) if the downstream boundary pressure increasing is not sufficiently rapid. The large transversal gradient of the velocity shows that steady state is not yet reached.

The flow is choked at time $t = 2.5 t_{in}$. The counter-pressure goes upstream into the blade channel and at time $t = 5 t_{in}$ a very strong shock wave reaches the final position at the end of the inducer.

The flow is sufficiently steady in time and satisfactorily uniform (see Fig. 9A). The pressure at the impeller outlet is very high ($p/p_{in} = 4$). The calculation made with a counter pressure less than the previous one shows (Fig. 6) large Mach numbers, and an unsteady situation at $t = 4 t_{in}$; this demonstrates the importance of the outlet law in function of time.

Meaningful results are obtained in the case of separated flow (Fig. 8, 9) even if a simplified model was used. The flow separation leads to a large variation at the outlet; nevertheless at $t = 4.5 t_{in}$ there is an opposite trend, and the variation is still large. The Mach number at the boundary between jet and wake is not constant because the total relative enthalpy is not yet constant either as well. In such a condition it is impossible to distinguish clearly the jet-wake energy exchange, but some interesting information on the variations of the main quantities is available (Fig. 10).

For Figs. (3-9) a conformal mapping is used:

$$\varphi, X = X_{in} + \int \frac{dm}{r} \quad \text{for the inducer,} \quad \varphi, R = R_{in} e^{\int \frac{dm}{r}} \quad \text{for the impeller.}$$

6) CONCLUSIONS

The proposed method is interesting for the following reasons:

- possibility of taking into account transonic flows without any difficulty even with very different upstream and downstream conditions;
- possibility of dealing with very sophisticated conditions along particular streamlines in a simple way, due to the use of a natural calculation network;
- possibility of dealing with inlet variable conditions, as distortions, rotor-stator interactions, etc..

In author's opinion it is very interesting to use this method for the study of rotors and transonic diffusers, moreover, in the case of unsteady conditions. It could be very useful in dealing with intrinsically unsteady problems as the reversible energy exchange into the mixing process downstream the centrifugal compressor wheel.

REFERENCES

1. Wu, C.H. "A General Theory of Three-Dimensional Flow in Subsonic and Supersonic Turbo-machines of Axial, Radial and Mixed-Flow Types", Transactions of the ASME, November 1952.
2. Osnaghi C. and Macchi E., "A Method for Calculating Unsteady Transonic Flow in Turbo-machinery Cascades", XXXIII Congresso ATI - Ancona (Italy), 5/8/1978.
3. Carriere P. and Capelier C., "Application de la methode des caracteristiques instationnaires au calcul numerique d'un ecoulement permanent compressible" AGARD-CP-35, 1968.
4. Osnaghi C. and Macchi E., "On the Application of a Time-Dependent Technique in Transonic Double Flow Nozzle Solutions" AGARD-CP-91, pp. 27-1-27A 2-3.
5. Dean R. & Senoo Y., "Rotating wakes in vaneless diffusers" ASME Transact., Series D: J. Basic Engrg, Vol. 82, 1960, pp. 563-570.
6. Senoo Y. & Kinoshita Y., "Limits of rotating stall and stall in vaneless diffuser of centrifugal compressors" ASME P 78 GT 19.
7. Frigne P. and Van den Braembussche R., "One dimensional Design of Centrifugal Compressors taking into account flow Separation in the Impeller" V.K.I. TN129 - June 1979.
8. Sarmiento A., "One dimensional design and analysis of centrifugal compressors", VKI PR 1977-12, June 1977.
9. Dean R., "The fluid dynamic design of advanced centrifugal compressors in advanced radial compressors", VKI LS 66, March 1974.
10. Katsanis T. and McNally N.D., "Fortran Program for Calculating Velocities and Streamlines on a Blade-to-Blade Stream Surface of a Tandem Blade Turbomachine", NASA TN-D. 5044, 1969.

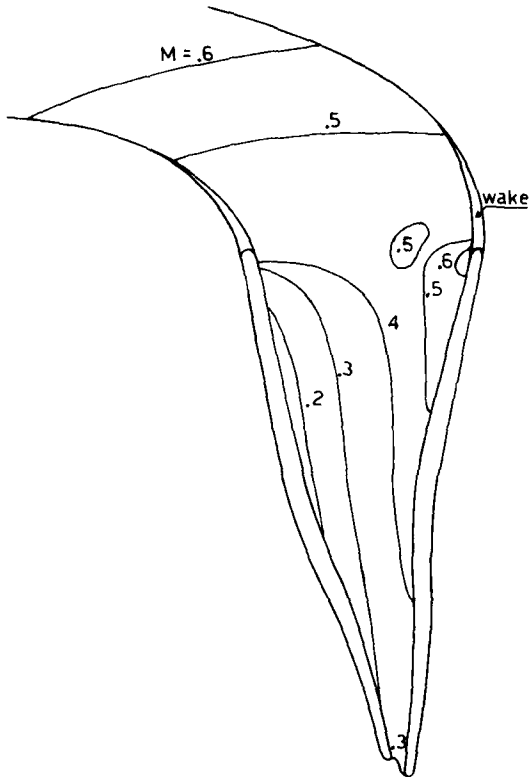


Fig 3a) CONSTANT RELATIVE MACH NUMBER LINES
(IMPELLER)
 $t/t_{in} = 0$

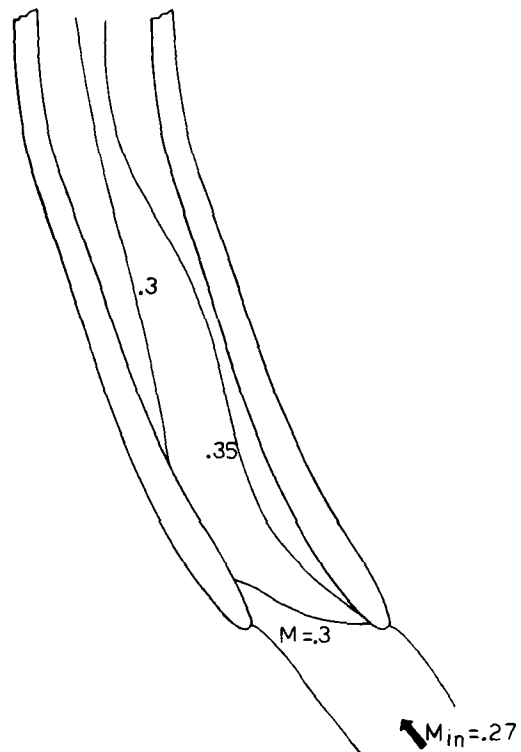


Fig 3b) CONSTANT RELATIVE MACH NUMBER LINES
(INDUCER)
 $t/t_{in} = 0$

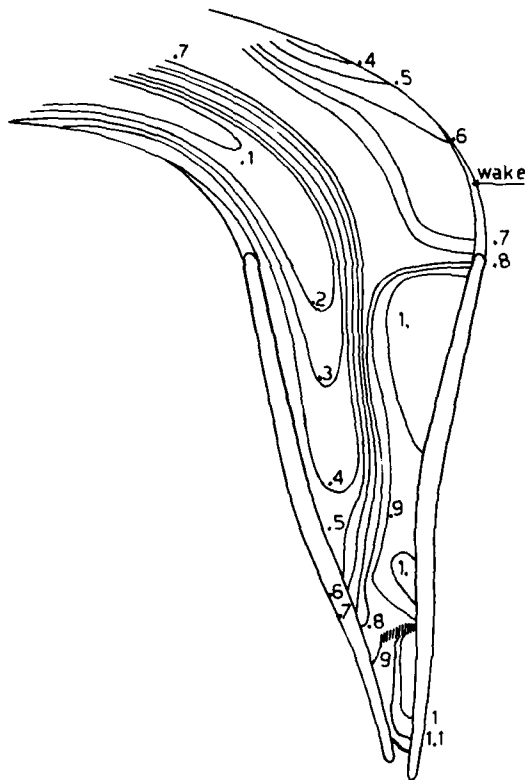


Fig 4a) CONSTANT RELATIVE MACH NUMBER LINES
(IMPELLER)
 $P_{out}/P_{Tin} = 8$ $t/t_{in} = 2$

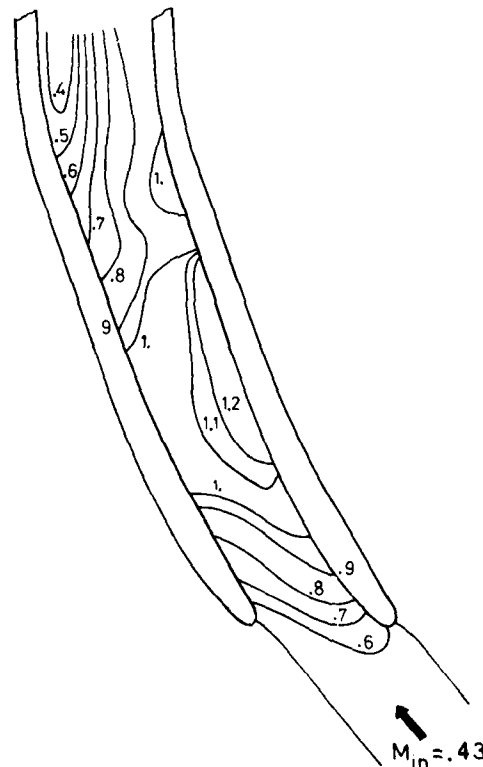


Fig 4b) CONSTANT RELATIVE MACH NUMBER LINES
(INDUCER)
 $P_{out}/P_{Tin} = 8$ $t/t_{in} = 2$

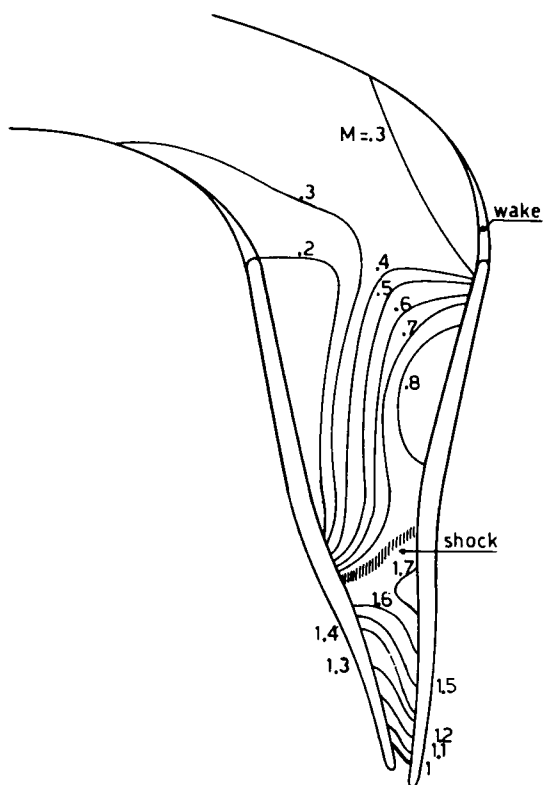


Fig 5a) CONSTANT RELATIVE MACH NUMBER LINES
(IMPELLER)
 $P_{out}/P_{Tin}=8$ $t/t_{in}=5$

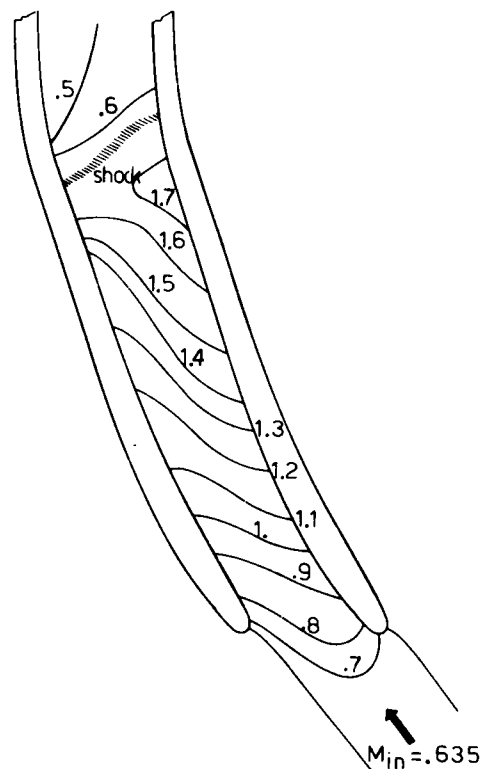


Fig.5b) CONSTANT RELATIVE MACH NUMBER LINES
(INDUCER)
 $P_{out}/P_{Tin}=8$ $t/t_{in}=5$

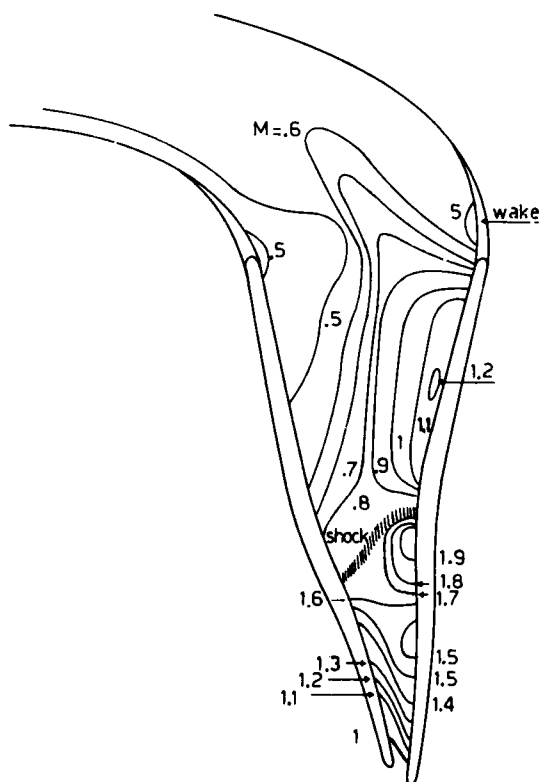


Fig 6) CONSTANT RELATIVE MACH NUMBER LINES
(IMPELLER)
 $P_{out}/P_{Tin}=7$ $t/t_{in}=4$

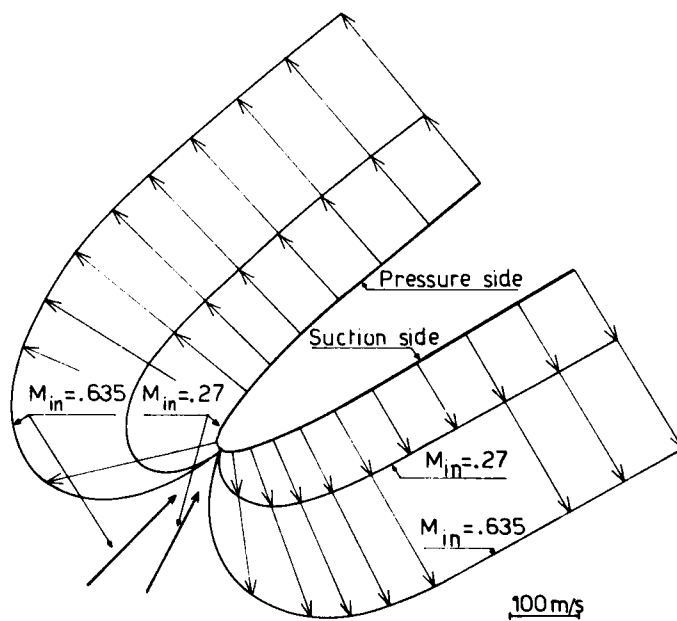


Fig 7) VELOCITY PROFILES IN THE L.E. REGION

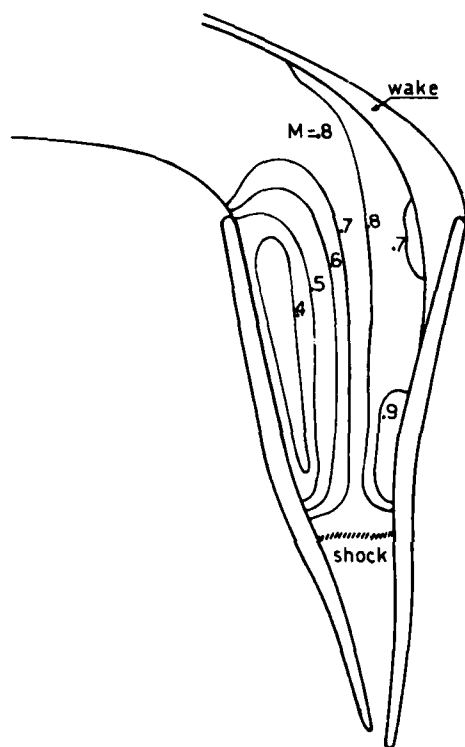


Fig. 8 CONSTANT RELATIVE MACH NUMBER LINES
(IMPELLER)

$$P_{out}/P_{Tin} = 4 \quad t/t_{in} = 2$$

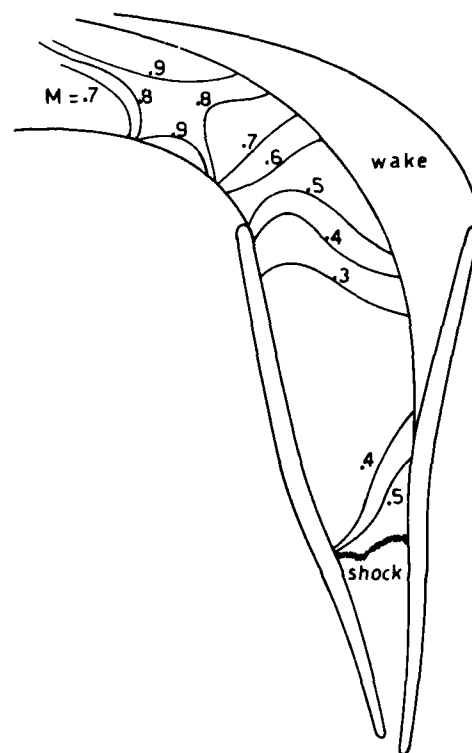


Fig. 9 CONSTANT RELATIVE MACH NUMBER LINES
(IMPELLER)

$$P_{out}/P_{Tin} = 4 \quad t/t_{in} = 4$$

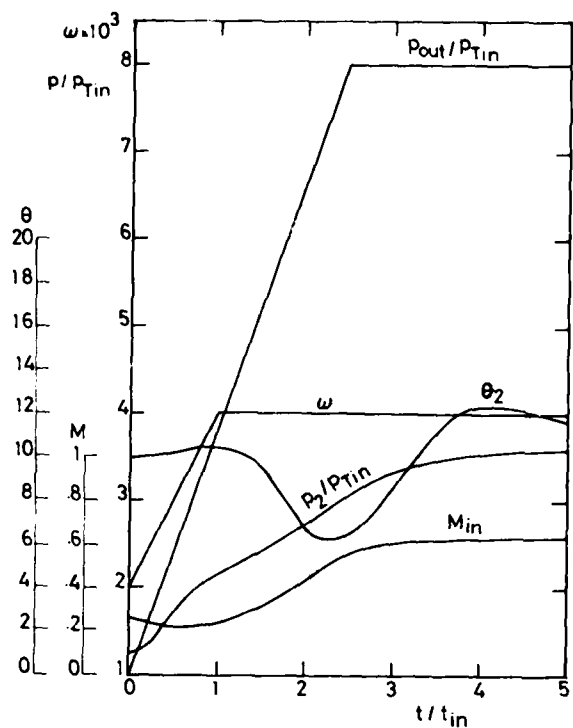


Fig 10a

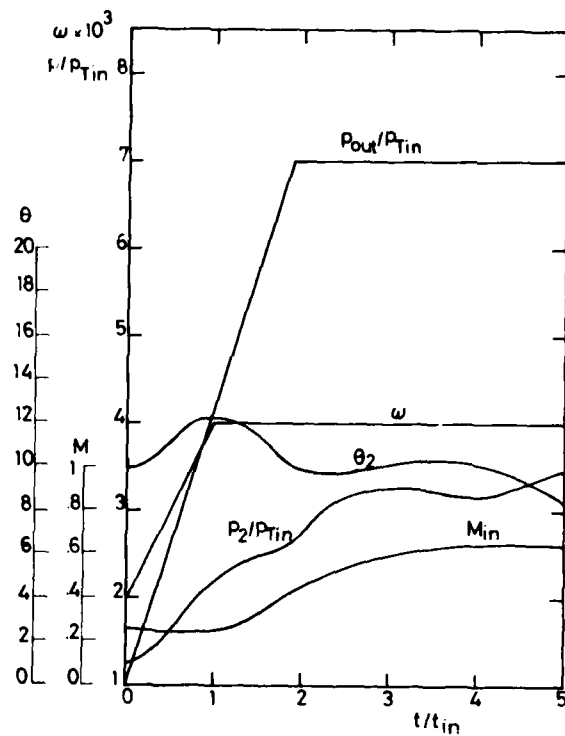


Fig. 10 b

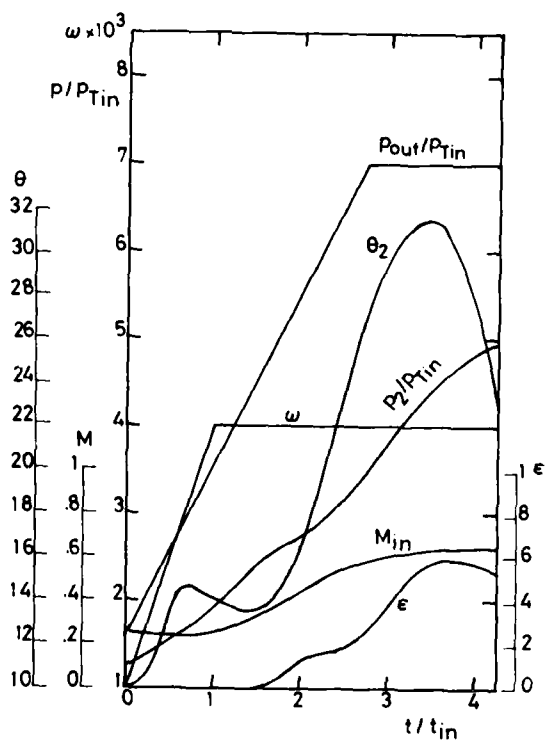


Fig. 10c

Fig. 10) Main quantities versus time: rotational speed; downstream pressure/inlet total pressure; inlet Mach number; impeller outlet pressure/inlet total pressure; impeller outlet angle.

a), b) unseparated flow ; c) separated flow

APPENDIX 1

LEADING EDGE CALCULATION

The initial blade profile, upstream the two former meshes 1D, 1V, is approximated by a pseudo-ellipse. This was obtained by transforming a unit radius circle, centered at the origin of an auxiliary plane $z = x + iy$, in the physical plane $\zeta = \xi + i\eta$ by means of the following conformal transformation: $\zeta = h + k/(z - z_0)$ where $z_0 = iy_0$. For $y_0 = 0$ an ellipse is obtained, whose half-axes are $a = (h + k)$, $b = (h - k)$. For $y_0 \neq 0$ the ellipse is distorted in the ordinate and is transformed into a simple line, representing the blade nose even in the case of small thickness blades. The parameter y_0 is automatically determined in order to make the line to pass through the given point (01V).

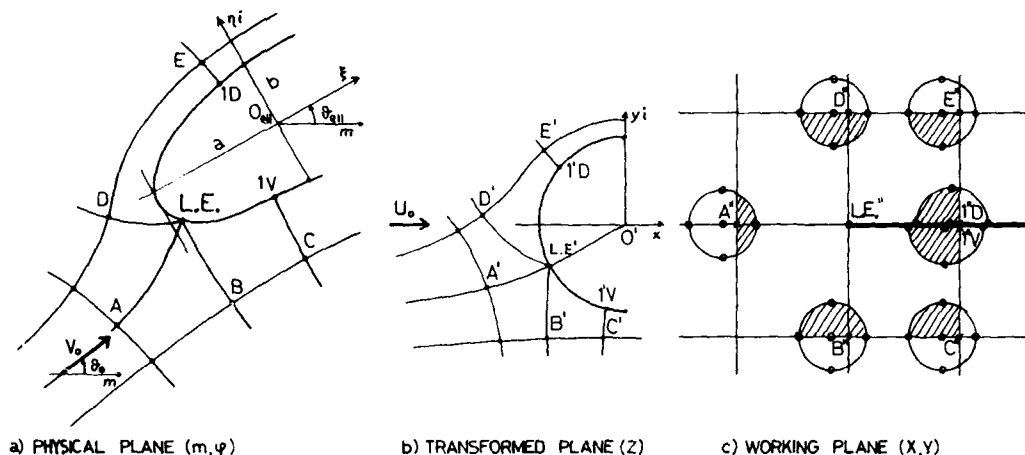


Fig. A1-1) Leading Edge Model

Obviously, the center and the half-axes of the pseudo-ellipse are necessarily given.

The flow in the leading edge region is calculated by means of conformal transformation of the translo-circulating flow around the circle in the z plane, which at the upstream infinite has velocity $U_0 = V_0 h$, and angle $\alpha = \theta - \theta_{ell}$, being V_0 and θ_0 obtained by averaging the inlet flow of the blade to be calculated.

The ratio V_0/V_{1V} determines the velocity circulation Γ ; then all the quantities close around the leading edge can be computed. Classical corrections can be done to the incompressible solution for taking into account large Mach number flows. In the calculation of the points A, B, C, D, E, F, G (see fig. A1-a for the physical plane and fig. A1-c for the work plane) part of the dependence domain is into the region near the leading edge; therefore the points of the bicharacteristics are interpolated by the use of the analytical solution which must be matched with the time dependent one. The flow near the trailing edge is quasi-potential and the work coordinates (X, Y) are proportional to the functions Φ and Ψ obtained from analytical solution: in fact it is $d\Phi/dx_1 = V = \cos\alpha$; $d\Psi/dy_1 = W = \cos\beta$. The X, Y definitions and the previous relations give $d\Phi = aWdx$, $d\Psi = \beta Wdy$. From the Eqs. (5), (6), it is possible to demonstrate that for $W \neq 0$ aW and βW can be taken constant.

APPENDIX 2

JET AND WAKE MODEL

Referring to the classical jet and wake scheme (see Dean (5) and Senoo (6)), an inviscid jet flow and a wake one, in which all losses are supposed to be concentrated, can be discriminated. The general calculation principle is based on the fact that the method is unsteady and, consequently, a flow solution at a previous time is always available. This allows to evaluate the side boundary evolution, in order to account for the following quantities: boundary layer from the leading-edge up to the separation point S_1 , free jet from S_1 to S_2 and wake downstream the trailing-edge. At the initial time the calculation generally starts from an inviscid solution; in such a case the boundary layer and separated flow introduction is made gradually in time to avoid calculation discontinuities.

Boundary layer - It is possible to use an approximate method in order to evaluate the boundary layer displacement thickness (8).

Separation point - To determine the separation point on the suction side of the blade the value of $DR = W_{1t}/W_{sep,t}$ at the tip is taken from (9). Actually, the knowledge of the meridional plane velocity is required, but the distribution of such a velocity was assumed without check, being its evaluation beyond the aim of the present work. Once the separation point is determined by means of the time dependent computing code, it is possible to evaluate $h_{J,sep}$, $h_{RJ,sep}$.

Separated flow - According to Van den Braembussche (7) the jet Mach number at the boundary with the separated region is assumed to be constant. This is equivalent to supposed that there is no diffusion in the jet downstream the separation point and the pressure is to be conditioned only by the centrifugal potential. This is true only for zero or very small wake velocities. Furthermore, $h_{RJ,S}$ is assumed constant in the hypothesis

that the wake evolution has to proceed slowly (quasi-steady) compared to the rotating speed and flow rate variations. Along the boundary (S) it is: $h_{J,S} = h_{RJ,S} + U^2/2 - W_{J,S}^2/2$, i.e.

$$h_{J,S} = h_{RJ,sep} + \frac{U^2}{2} - \frac{a_{J,S}^2}{2} M_{J,sep}^2 \quad (A2-1)$$

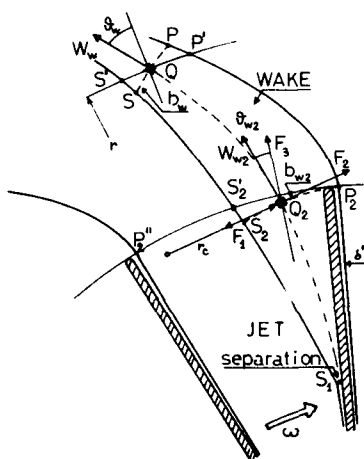
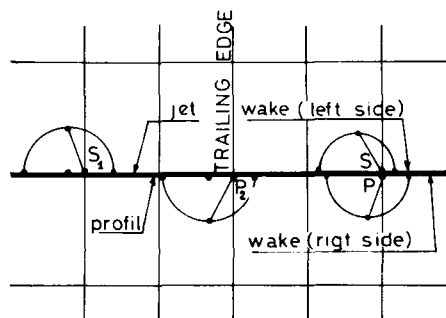
where the sound velocity $a_{J,S}$ is a function of the enthalpy $h_{J,S}$ and entropy S_J assumed constant in the jet. Finally, it is possible also to determine $p_{J,S}$ from the state equation. The wake flow is evaluated from the separation point. For the jet it is

$$h_{J,S} - h_{sep} = \frac{W_{sep}^2 - W_J^2}{2} + \frac{U^2 - U_{sep}^2}{2} \approx \frac{U^2 - U_{sep}^2}{2}, \quad \bar{h}_W - h_{sep} = \frac{W_{sep}^2 - \bar{W}_W^2}{2} + \frac{U^2 - U_{sep}^2}{2}$$

If \bar{W}_W , \bar{h}_W , $\bar{\rho}_W$, \bar{p}_W are the averaged values inside the wake, being the ratio $v = \bar{W}_W/W_J$, $\bar{S}_W = \bar{W}_W/W_{J,sep}$ assigned, at the impeller outlet it is

$$\bar{h}_{W,2} \approx h_{J,S_2} + (1-v^2) \frac{W_{J,sep}^2}{2} \quad (A2-2)$$

than, being the pressures at 2 and (sep) known, it is possible to evaluate the average pressure $\bar{p}_{W,2} = 1/2 (p_{J,p_2} + p_{J,S_2})$ from which $\bar{\rho}_{W,2} = f(\bar{p}_{W,2}, \bar{h}_{W,2})$

a) PHYSICAL PLANE (m, φ)

b) WORKING PLANE

Fig.A2-1) Jet and Wake Model

The pressure computed at the previous time is sufficiently precise to calculate \bar{p}_W . Since the ideal flow calculation network is made along streamlines and normal lines, it is useful to assume as separated flow final section the normal arc $b_{w,2}$. This is automatically defined by the streamline S_2 and determines also the wake pitch portion $\epsilon = S_2 p / p_S$ at the impeller outlet and the mass flow ratio (wake to total) $\lambda = \dot{m}_W / (\dot{m}_W + \dot{m}_J)$.

The last quantity to be defined is the trasversal pressure difference $q = (p_S - p_P)$. In contrast with what was assumed for the density and enthalpy, the pressure must be taken variable in the wake, following, for example, a linear law. The previous difference must balance the following terms: the Coriolis force F_1 directed normally to the flow and in opposition to the rotating speed, the force F_2 due to the flow curvature in the wake (generally in opposition to F_1 , if $r_c > 0$) and the component of the centrifugal force F_{3n} normal to the flow. It follows

$$q = b_W \bar{\rho}_{W,2} \left(2\omega \bar{W}_{W,2} - \frac{W_{W,2}^2}{r_c} - \omega | \omega | r \sin \beta_{W,2} \right) \quad (A3-3)$$

usually the first term is preponderant; if necessary, the curvatures radius must be assigned.

Trailing-edge condition - Being $(p_{sep} - p_S)$ and $(p_S - p_P)$ known, the closure condition of the blade requires the contemporary calculation of the points sep and P by means of six bicharacteristics (only four are independent) and by imposing the two profile angles and pressure difference $(p_{sep} - p_P)$. There is one redundant condition to determine the two velocities and the two pressures: such a condition defines the blade profile circulation, which usually is assigned by means of the downstream flow angle (slip-factor).

Jet and wake mixing process - Let $q = p_S - p_P$. Suppose that the wake pressure tangential distribution is linear (at the same radius) and neglect the forces due to the wall diffuser and jet-wake drag in order to evidence the reversible energy exchange. \bar{p}_W , $\bar{\rho}_W$, \bar{W}_W are the wake averaged quantities, the wake motion equations are (7):

continuity $\dot{m} = b_W h \bar{\rho}_W \bar{w}_W = b_{W,2} h_{2} \bar{\rho}_{W,2} \bar{w}_{W,2}$ (A2-4)

tangential momentum $\bar{\rho}_W \frac{b_W}{r} \bar{w}_W \frac{d}{dr} \left| r^2 \omega + r \bar{w}_W \sin \bar{\theta}_W \right| = q$ (A2-5)

radial momentum $\bar{\rho}_W \bar{w}_W \frac{d}{dr} \left| \bar{w}_W \cos \bar{\theta}_W \right| + \frac{b_W}{\cos \bar{\theta}_W} \frac{d \bar{p}_W}{dr} - \bar{\rho}_W \frac{b_W}{r \cos \bar{\theta}_W} (r \omega + \bar{w}_W \sin \bar{\theta}_W)^2 = q \tan \bar{\theta}_W$ (A2-6)

Removing q from the previous equations, only one differential equation in \bar{w}_W is found:

$$(\sin^2 \bar{\theta}_W - \cos^2 \bar{\theta}_W) \frac{d \bar{w}_W}{dr} = \frac{1}{\bar{\rho}_W \bar{w}_W} \frac{d \bar{p}_W}{dr} - 2 \bar{w}_W \sin \bar{\theta}_W \cos \bar{\theta}_W \frac{d \bar{\theta}_W}{dr} - 4 \omega \sin \bar{\theta}_W - \frac{\bar{w}_W}{r} \sin^2 \bar{\theta}_W - \frac{\omega^2 r}{\bar{w}_W}$$

\bar{p}_W and $\bar{\theta}_W$ varying with the radius can be obtained with a good agreement by the time dependent calculation at the previous time. The density $\bar{\rho}_W$ is found from the enthalpy calculated by means of the following energy equation:

$$\bar{h}_{TJ} \dot{m}_J + \bar{h}_{TW} \dot{m}_W = \bar{h}_{TJ,2} \dot{m}_J + \bar{h}_{TW,2} \dot{m}_W$$

from which

$$\left(\bar{h}_W + \frac{\bar{v}_W^2}{2} \right) \lambda + \bar{h}_{TJ} (1-\lambda) = \left(\bar{h}_{W,2} + \frac{\bar{v}_{W,2}^2}{2} \right) \lambda + \bar{h}_{J,2} (1-\lambda) \quad (A2-7)$$

The absolute wake velocity \bar{v}_W is obtained from ω, \bar{w}_W and $\bar{\theta}_W$.

Once the equation (A2-6) has been solved by means of standard methods, it is possible to evaluate q from Eq. (A2-5), and $\epsilon = b_W / (\Delta \varphi r \cos \bar{\theta}_W)$ from Eq. (A2-4). Therefore it is possible to compute the transversal pressure difference $\Delta p_W = (p_S - p_P)$ and the angle difference $\Delta \theta_W$, which constitute the input quantities for the inviscid jet calculation by means of the time dependent method. For this reason six bicharacteristic (four independent equations) and the two path lines are used to evaluate $w_S, w_P, p_{SP}, \theta_{SP}$. Imposing Δp_W and $\Delta \theta_W$, $p_S, p_P, \theta_S, \theta_P$ can be determined. The points S and P in the (X, Y) plane become a unique point.

If $m_W \neq 0$ it is possible to take into account the decrease of the jet flow rate in a simple way by a fictitious increase of the meridional channel height.

DISCUSSION

R.Sovrano, ONERA, Fr

Could the authors please discuss the problems of convergence of their calculation method?

Author's Reply

The authors have conducted stability tests and the method was found to be extremely stable in the compressor case. It was also found to be stable in the case of a turbine blade.

THREE-DIMENSIONAL, VISCOUS FLOW CALCULATIONS
FOR ASSESSING
THE THERMODYNAMIC PERFORMANCE OF CENTRIFUGAL COMPRESSORS
- STUDY OF THE ECKARDT COMPRESSOR

John Moore and Joan G. Moore
Mechanical Engineering Department
Virginia Polytechnic Institute
Blacksburg, Virginia 24061, USA

SUMMARY

A calculation procedure for partially-parabolic flow is used to calculate flow in the impeller and diffuser of the Eckardt centrifugal compressor. This is a general-geometry cascade-flow method including the effects of tip leakage and stationary walls.

The calculated and experimental results for three-dimensional viscous flow and overall thermodynamic performance are compared. Wake flow, resulting from boundary layer accumulation, causes blockage of the impeller passage. Calculated wake development, with and without flow leakage through the tip-clearance gap, is compared with measurements.

The thermodynamic process in the Eckardt compressor, at the maximum efficiency point at 14000 RPM, is represented on a temperature-entropy diagram. Calculated results of the development of mass-averaged temperature and entropy through the impeller and diffuser are presented. The work done, the pressure ratios and the efficiencies of the impeller and compressor are calculated to within 1 or 2 %. The influence of the boundary conditions on the compressor flow and performance is discussed.

NOMENCLATURE

c, C	absolute velocity	<u>Subscripts</u>	
c_p	specific heat capacity at constant pressure	t0, N	standard stagnation state at impeller inlet
H	rothalpy	inlet	flow inlet (Fig. 1)
H, P, S, S	hub, pressure, shroud, suction sides	r	reduced static
i, j, k	grid indices	r, θ , z	radial, tangential and axial components
\dot{m}	mass flow rate	t	absolute stagnation
p	pressure	0, 1, 3, t3 etc.	state points (Fig. 22)
r or R, θ , z	cylindrical coordinates	<u>Efficiency Subscripts</u>	
R_2	radius at impeller exit	D	diffuser
s	entropy	p	polytropic
T	temperature	s-s	static-to-static
u, U, W	relative velocity	t-s	total-to-static
u_1, u_2, u_3	calculated relative velocity components	t-t	total-to-total
u_{normal}	velocity component perpendicular to measurement or calculation plane	W	wheel
I - V	measurement planes in the impeller	<u>Superscripts</u>	
α, β	flow angles (Table 2)	*	rotary stagnation
ϵ	blockage factor (Table 2)	-	area-averaged
η	efficiency (Table 2)	-	mass-averaged
μ	viscosity; or slip factor (Table 2)		
ρ	density		
ϕ	flow coefficient (Table 2)		
ω, Ω	angular velocity of the impeller		

INTRODUCTION

In a recent paper [1], we presented a calculation procedure for partially-parabolic flow in general-geometry turbomachinery cascades. Incompressible flow through a shrouded centrifugal impeller [2] was calculated. In this paper, we report the further developments necessary to allow the method to handle compressible flow with tip leakage and a stationary shroud wall. We demonstrate the method by calculating flow through the centrifugal impeller and diffuser tested experimentally by Eckardt [3,4,5]. The calculated and experimental results for three-dimensional viscous flow and overall thermodynamic performance are compared, and the influence of the boundary conditions on the compressor flow and performance is discussed.

The main objectives of this study were

1. to calculate steady, three-dimensional, viscous, compressible flow in a centrifugal impeller and diffuser, allowing the development of secondary flows due to curvature and rotation [6,7] and due to tip leakage and stationary walls,
2. to calculate the accumulation of low-momentum, boundary layer fluid under the action of these secondary

- flows to form a wake flow at the impeller exit,
3. to calculate the subsequent mixing of the wake with the jet in the vaneless diffuser,
 4. to calculate the entropy production in the flow field particularly near the wall boundaries where three-dimensional flow is known to influence losses [8,9,10],
 5. to represent the thermodynamic process in Eckardt's centrifugal compressor on a temperature-entropy diagram [11],
 6. to compare the calculated flow development and thermodynamic efficiencies with the measurements of Eckardt.

The physics of the flow phenomena in a centrifugal compressor is, of course, contained in the conservation equations of mass, momentum and energy for turbulent flow. To meet the objectives of this paper, these equations are solved with appropriate boundary conditions using an appropriate non-uniform, finite-difference grid.

Five different boundary conditions were used in the present calculations:

1. an inviscid wall, for the inviscid flow calculations used to build up the pressure solution [9,10],
2. a viscous wall with zero relative velocity at the wall,
3. a stationary viscous wall with zero absolute velocity at the wall,
4. a circumferentially repeating boundary used upstream of the impeller leading edge and downstream of the impeller trailing edge,
5. a combined viscous wall and repeating boundary condition used for blade surfaces with tip leakage.

These boundary conditions together with the non-uniform grid spacing allow the calculation of

1. non-collateral wall boundary layers, in which significant transport of low-momentum, boundary layer fluid occurs,
2. tip leakage flow, with the associated unloading of the static pressure at the blade tips,
3. flow near the stationary shroud wall in the impeller and near the stationary hub and shroud walls in the diffuser,
4. gradients of rothalpy near the stationary walls,
5. shear stresses and entropy production near the walls,
6. mass-averaged temperature and entropy.

ECKARDT'S CENTRIFUGAL COMPRESSOR

The detailed investigations of the flow within a high-speed centrifugal compressor impeller and in the constant-area vaneless diffuser downstream, which Eckardt performed between 1970 and 1977 at the DFVLR, make this compressor flow one of the most carefully documented in the literature [3,4,5]. From the results of laser and hot wire anemometry and from instantaneous pressure measurements, relative velocity profiles are presented showing boundary layer accumulation leading to the development of a jet-wake flow pattern within the impeller, and then showing the mixing of the jet and the wake in the impeller discharge flow. Flow angle measurements indicate the magnitude and likely configuration of secondary flows, and static pressure measurements along the stationary shroud wall monitor the static pressure rise through the compressor. Sufficient information is also given by Eckardt from which to reconstruct the geometry of the impeller [12] and the overall thermodynamic performance of the compressor.

Flow Geometry

The geometry of Eckardt's impeller is quite closely described by equations [12] for an elliptical-arc camber line, and for circular-arc hub and shroud wall profiles. With the assumption that the blades have radial sections and with blade thickness information obtained from velocity profile figures, a reasonable representation of the impeller geometry can be obtained. Our reconstruction resulted in the geometry shown in Figures 1 and 2.

Figure 1 shows the flow domain used for the present study. The calculations start with axial flow upstream of the impeller inlet, march through the impeller to the radial exit at a radius R_2 of 0.2 m, and then proceed to station 4 in the constant-area vaneless diffuser at a radius ratio R/R_2 of 1.687. The flow is assumed to be steady relative to this rotating flow domain.

A meridional cross-section of the flow domain is shown in Figure 2. This shows clearly the locations of five of the measurement planes I-V on which Eckardt made detailed laser anemometry measurements within the impeller. These planes and the other intermediate planes shown were used in generating the finite-difference grid for the present calculations.

Thermodynamic Performance

In this paper, we consider the flow development at the maximum efficiency condition, test point M2, at a rotational speed of 14000 RPM and a mass flow rate of 5.31 kg/s. The overall thermodynamic performance of the compressor at this operating condition is described by the states shown on the temperature-entropy diagram of Figure 3.

The standard stagnation conditions at the impeller inlet, state t_0, n' , were 288.1 K and 1.0133 bar. The static conditions at the impeller inlet and the diffuser radii $R/R_2 = 1.017$ and 1.687 are states 1, 3 and 4 respectively, and the corresponding absolute stagnation conditions are points 0, t_3 and t_4 . State U [11] corresponds to the isentropic centrifugal pressure rise in the impeller, and state E3 is the relative stagnation condition at $R/R_2 = 1.017$.

The impeller tip speed at this test point was 293.2 m/s, the measured total-to-total pressure ratio was 2.094 and the measured total-total efficiency was 0.88. States 3, t_3 , 4 and t_4 on Figure 3 are based on pressure and efficiency data given by Eckardt; states 0, 1, U and E3 are based on estimated flow conditions in the inlet duct and an estimate of the change in rothalpy through the impeller. The pressures and temperatures at these state points are tabulated in Table 1. The remaining points derive from measurements in the vaneless diffuser; the triangles represent instantaneous pressure measurements and the circles represent conventional pressure measurements.

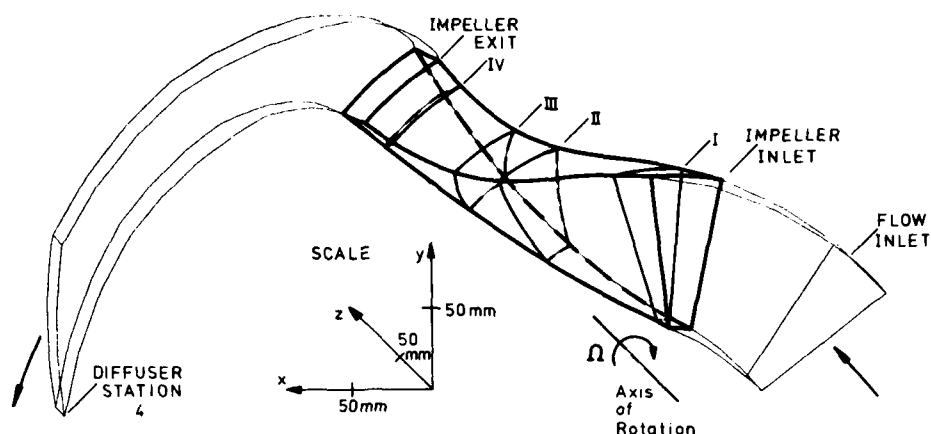


Figure 1. The domain for the flow calculations in the Eckardt centrifugal compressor. I - IV, measurement planes in the impeller.

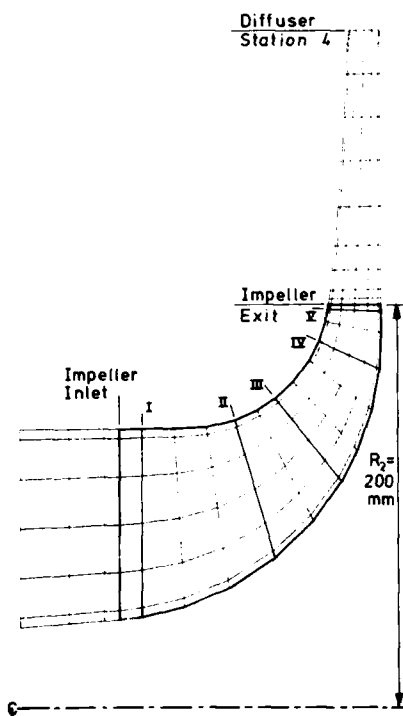


Figure 2. The calculation field for the Eckardt compressor in the meridional plane, showing grid lines appropriate for inviscid flow calculations with no tip leakage. I - V, measurement planes in the impeller.

THE FLOW MODEL

The Governing Equations

The equations are written for the steady flow of a perfect gas relative to a reference frame rotating with constant angular velocity, Ω . An isotropic viscosity μ is assumed and compressibility effects are neglected in the viscous terms. Viscous work associated with gradients of $\Omega \times R$ and with gradient of velocity in the streamwise direction are neglected. Energy conservation is written in terms of the rothalpy H , where

$$H = c_p T + \frac{1}{2}(\underline{u} \cdot \underline{u}) - \frac{1}{2}(\underline{\Omega} \times \underline{R} \cdot \underline{\Omega} \times \underline{R}).$$

Mass conservation:

$$\nabla \cdot \rho \underline{u} = 0.$$

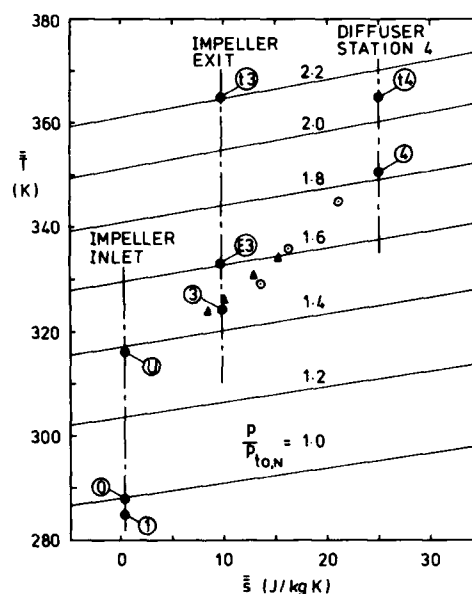


Figure 3. The thermodynamic performance of Eckardt's centrifugal compressor as derived from his measurements at test point M2 (14000.RPM and 5.31 kg/s). 1, 3, 4, Δ , \odot , static conditions; 0, t_3 , t_4 , absolute stagnation conditions; E3, relative stagnation; U, isentropic centrifugal pressure rise.

Momentum conservation:

$$(\nabla \cdot \rho \underline{u}) \underline{u} - (\nabla \cdot \mu \nabla) \underline{u} = \nabla \cdot \mu \nabla T - \nabla p - (2\Omega \times \underline{u} + \Omega \times (\Omega \times \underline{R})).$$

Energy conservation:

$$(\nabla \cdot \rho \underline{u}) H - (\nabla \cdot \mu \nabla) H = 0.$$

Here, c_p is the specific heat capacity of the gas; T , the static temperature; \underline{u} , the relative velocity vector; \underline{R} , the radius vector; ρ , the density; and p is the static pressure.

The effective viscosity is the sum of the laminar viscosity, μ_l , and a turbulent viscosity described by a mixing-length formulation

$$\mu = \mu_l + \rho L^2 "du/dy".$$

This model has been used with success in our earlier work [10,1]. Again the edges of boundary and shear layers are defined in terms of a gradient of local dimensionless stagnation pressure,

$$\Delta P_L^* = \frac{p^* - p_r}{p_{\max} - p_r}.$$

However, here we redefine the rotary stagnation pressure, p^* , and the reduced static pressure, p_r , for use with compressible flow, as described in the Appendix.

Solution Procedure and Rothalpy Boundary Condition

The finite-difference solution procedure used here is that appropriate for partially-parabolic flow in general cascade geometries and is described in Reference 1. The extensions required for the present calculations are the solution of the rothalpy equation, calculation of the density and the inclusion of alternative boundary conditions. The rothalpy equation has the same form as the momentum equations, i.e. $(\nabla \cdot \rho \underline{u} - \nabla \cdot \mu \nabla) \psi = B$. It is solved following each solution of the momentum equations. The density is recalculated after each adjustment of the pressure correction.

The boundary condition used for the rothalpy equation is an adiabatic wall; that is, the static temperature gradient normal to the wall is zero. The rothalpy gradient in the normal direction, n , is

$$\frac{\partial H}{\partial n} = c_p \frac{\partial T}{\partial n} + \underline{u} \cdot \frac{\partial \underline{u}}{\partial n} - \Omega \times \underline{R} \cdot \frac{\partial (\Omega \times \underline{R})}{\partial n}.$$

$\partial(\Omega \times \underline{R})/\partial n$ is negligible, therefore

$$\left(\frac{\partial H}{\partial n} \right)_{\text{wall}} = \left(\underline{u} \cdot \frac{\partial \underline{u}}{\partial n} \right)_{\text{wall}}$$

When the wall is stationary in the relative reference frame $(\partial H/\partial n)_{\text{wall}} = 0$ and rothalpy is conserved. When the wall is stationary in the absolute reference frame $(\partial H/\partial n)_{\text{wall}} = -\Omega \times \underline{R} \cdot \partial \underline{u}/\partial n$ and the rothalpy increases.

The Finite-Difference Grid

The finite-difference grid used for inviscid flow calculations is shown in the meridional plane in Figure 2. Seven points at relative spacings of 0., 0.05, 0.25, 0.5, 0.75, 0.95 and 1.0 span the hub-to-shroud (k) direction. Seven points at the same relative spacings also span the circumferential (blade-to-blade, j) direction.

At viscous walls more points are required to represent three-dimensional turbulent boundary layer flow. In these regions three more points, each a factor of five closer to the wall, were added giving points at relative spacings of 0.0004, 0.002, 0.01 and 0.99, 0.998, 0.9996. This distribution of points was chosen so that the near-wall point was sufficiently close to the wall that it was either in or near the edge of the laminar sublayer.

For the tip-leakage calculations a 1 % tip gap was used. Thus the blade tip was at a relative hub-to-shroud spacing of 0.99. To allow the equations sufficient freedom in determining the flow through the tip gap, a point near the blade tip is required in the tip gap. Therefore additional grid points at a relative hub-to-shroud spacing of 0.992 were used.

In the diffuser, where the additional points included for the calculation of tip leakage flow and boundary layer flow on the blade walls are not required, they are omitted. The additional points required for the calculation of the boundary layers on the diffuser walls are, of course, retained.

Calculation Details

Calculations of the flow in Eckardt's compressor were performed with three different viscous-wall boundary conditions:

1. no tip gap with a rotating shroud attached to the impeller;
2. a tip gap with a shroud rotating with the impeller and a rotating diffuser;
3. a tip gap with a stationary shroud and stationary diffuser walls.

Eckardt gives little information about the tip clearance of his impeller. For simplicity we assume a uniform relative gap size equal to 1 % of the hub-to-shroud distance. The tip gap for the calculations was then 0.95 mm at the impeller inlet decreasing to 0.26 mm at the exit.

The conditions specified at the flow inlet, shown in Figure 1, were uniform axial velocity in the free stream and turbulent boundary layers each with a thickness of 5 % of the hub-to-shroud distance on the walls. Here also, a uniform static pressure was prescribed.

RESULTS OF CALCULATIONS - THREE-DIMENSIONAL VISCOUS FLOW

PRESSURE DISTRIBUTIONS

The blade loading of Eckardt's impeller, calculated for the case of an attached rotating shroud, is

shown in Figure 4. The calculated reduced static pressures, p , in the four corners of the impeller passage are normalized with the inlet stagnation pressure $p_{t0,N}$. For isentropic flow from the inlet, the local value of p^* will equal $p_{t0,N}$ everywhere, and thus the pressure ratio $p_r/p_{t0,N}$ gives the local isentropic Mach number, as shown in the Appendix.

The inducer is lightly loaded almost to measurement station II. The loading at the shroud wall then increases to a maximum between stations III and IV (see Figures 1 and 2), before decreasing rapidly as the impeller exit is approached. At the hub, the loading is low until station III and the isentropic relative Mach number remains below 0.2 almost until station II. In the hub/pressure-side corner region the flow is close to stagnation, a Stanitz-eddy effect, until station IV quite close to the impeller exit.

The isentropic relative Mach number at the shroud wall in the inducer is approximately 0.6. In the shroud/suction-side corner region the local Mach number increases to 0.7 at station III, before rapidly decreasing to approximately 0.38 at the impeller exit. This steep pressure rise in the shroud/suction-side corner region of the impeller passage clearly influences the rapid growth of the wake flow which Eckardt observes at this location between stations III and V.

Figure 4 also shows the elliptic pressure variation upstream of the impeller leading edge. A rapid deceleration of the flow at the hub wall on the spinner upstream of the leading edge is seen. This elliptic influence is allowed in the present partially-parabolic flow model.

The calculation with the attached, rotating shroud wall allowed the blade loading in the shroud corners of the impeller passage to be obtained free from the influence of tip-leakage with its associated local blade unloading. The corresponding distribution of static pressure p on the shroud wall therefore also shows the blade loading through the impeller, as seen in Figure 5a. Here the static pressure is normalized with the static pressure, p_{inlet} , at the inlet to the flow domain. The long lightly-loaded inducer is clearly seen, together with the rise in pressure to a static pressure ratio of approximately 1.5 at the impeller exit and the subsequent pressure rise in the vaneless diffuser.

The shroud wall static pressure distribution, calculated for the case of a stationary shroud and a 1 % tip gap is shown in Figure 5b. Now the repeating boundary condition in the tip gap allows the static pressure distribution to repeat, and the calculated distribution of static pressure ratio agrees very closely with Eckardt's measurements shown in Figure 5c.

Figure 4. The reduced static pressures, $p_r/p_{t0,N}$, in the four corners of the Eckardt impeller passage, calculated for the case of an attached rotating shroud. i, impeller inlet; e, impeller exit.

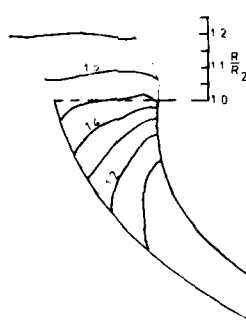
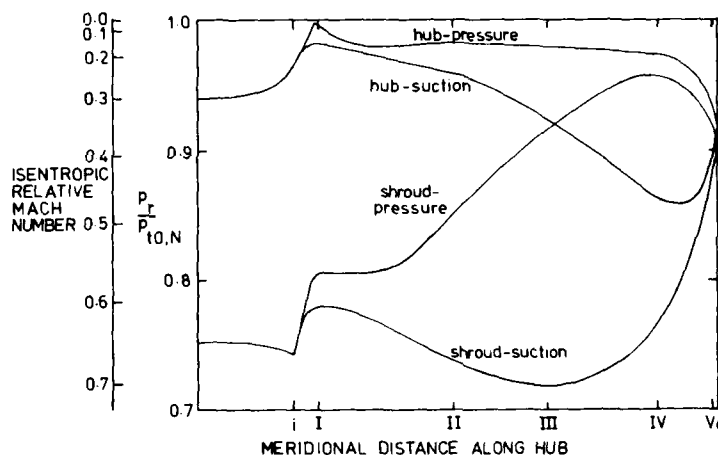


Fig. 5a

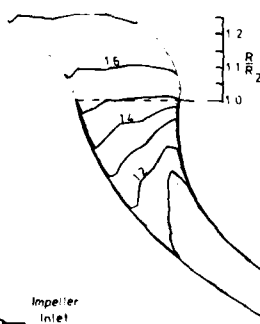


Fig. 5b

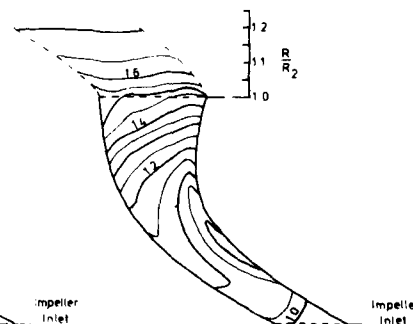


Fig. 5c

Figure 5. Contours of static pressure ratio, p/p_{inlet} , on the shroud surface in the impeller and diffuser. Fig. 5a. Calculated with no tip gap and rotating shroud and diffuser walls. Fig. 5b. Calculated with 1 % tip gap and stationary shroud and diffuser walls. Fig. 5c. Eckardt's measurements.

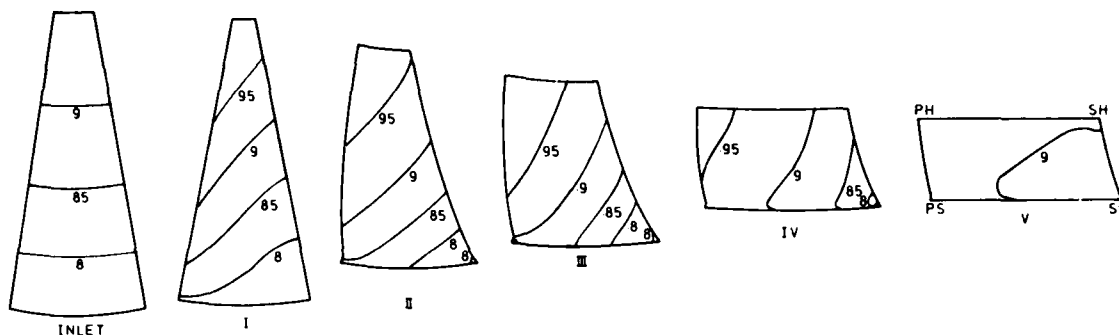


Figure 6. Contours of reduced static pressure ratio, $p_r/p_{0,N}$, at the flow inlet and five measurement planes in the impeller, calculated with a 1 % tip gap and a stationary shroud. SS, suction-shroud corner; PH, pressure-hub corner.

In three-dimensional flow calculations using pressure-correction methods, if the geometry is adequately described and if the three-dimensional pressure distribution is correctly building up, it only remains to improve the turbulence model and improve the solution procedure to get corresponding agreement from the velocity distributions. Thus this agreement between the measured and calculated pressure distribution is encouraging.

The calculated distribution of reduced static pressure p_r , again normalized with the inlet stagnation pressure, are shown in Figure 6 for the inlet plane and for Eckardt's five measurement planes, for this case of a stationary shroud and a 1 % tip gap. The gradient of p_r never becomes completely tangential, showing that the curvature of the impeller in the meridional plane is an important factor in the flow development. Indeed, even at stations IV and V, where the passage is nearly radial, the lowest reduced static pressure is still found in the shroud/suction-side corner. This is important, for it is gradients of reduced static pressure and not of static pressure itself which govern secondary flows in impellers. It is a most important contribution, in fact, in determining the location of wake flow in the impeller exit plane, for low-momentum boundary layer fluid tends to migrate towards the region of lowest reduced static pressure. In the shroud/suction-side corner region, wake fluid in Eckardt's impeller experiences an adverse gradient of reduced static pressure which causes it to slow down, increasing the blockage it causes in the flow. Clearly the blockage will be a maximum for wake fluid constrained to remain in this region. Flow adjacent to the middle of the shroud wall, for example, will experience virtually no adverse gradient of reduced static pressure in passing from station IV to station V.

VELOCITY DISTRIBUTIONS

Velocities Normal to Measurement Planes

Figure 7 shows the distribution of velocity normal to the five measurement planes, as measured by Eckardt. The results have been replotted from his perspective views to show contours of velocity normalized by the impeller tip speed, ωR_2 .

At all five stations, a large potential flow region can be recognized with a velocity gradient corresponding to the gradient of reduced static pressure described above. A near stagnation of the flow in the hub/pressure-side corner region is also evident.

At station III on the shroud wall, the first evidence of three-dimensional boundary layer accumulation is observed at $y/t \approx 0.6$. The wake flow then grows rapidly from these small beginnings to become a significant blockage in the flow at station IV. It is worth noting, as discussed above, that the wake grows in a region of adverse pressure gradient, and that it penetrates the flow until at station V it extends out to mid-way between the hub and shroud walls.

Eckardt uses a blockage factor $\epsilon_{k3}(c)$ to quantitatively describe the blockage caused by his wake. This parameter is defined as

$$\epsilon_{k3}(c) = 1 - \bar{c}_{r3k} / \bar{c}_{r3},$$

where, at the diffuser station $R/R_2 = 1.017$, \bar{c}_{r3k} is the area-averaged radial velocity and \bar{c}_{r3} is the mass-averaged radial velocity. At the test point M2 considered in this paper, this blockage parameter had a measured value of 0.183.

Figure 8 shows for comparison our results obtained with a 1 % tip gap and a rotating shroud wall. At stations I, II and III, we obtain remarkably good agreement with Eckardt's measured velocity contours indicating that we have the impeller geometry reasonably well described. We see signs of wake formation at station III in our calculation and the wake grows to present a significant blockage in the flow at station V. The normal velocity distribution at a radius ratio of 1.017 in the vaneless diffuser is shown in perspective view in Figure 10a. This calculated result gives a blockage factor $\epsilon_{k3}(c)$ of 0.119.

Our calculations with a 1 % tip gap and a stationary shroud wall gave the results shown in Figure 9. Again early in the passage the agreement is good, as expected. Now, however, with this combination of tip gap and boundary condition, the calculated wake flow is mixed out across the shroud wall and located centrally at a location where it does not experience an adverse pressure gradient between stations IV and V. Consequently it does not grow to form the large blockage observed in Figure 8 and especially in the measurements of Figure 7. At $R/R_2 = 1.017$ the calculated normal velocity distribution is as shown in Figure 10b and the blockage factor is 0.074.

Figure 10c completes the series of calculations with different boundary conditions by showing the results obtained with a rotating shroud wall and zero tip clearance. The location of the wake flow is reasonably well calculated in this case but the blockage is only 0.056.

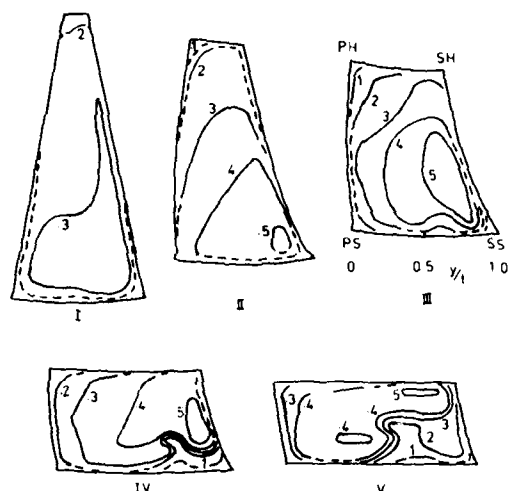


Figure 7. Eckardt's measured contours of $u_{normal}/\omega R_2$, the velocity component perpendicular to the five measurement planes, I - V in the impeller.

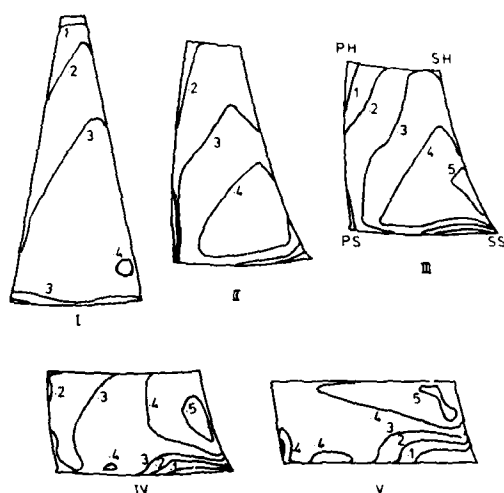


Figure 8. Contours of $u_{normal}/\omega R_2$, calculated for 1% tip gap and rotating shroud, at planes I - V in the impeller.

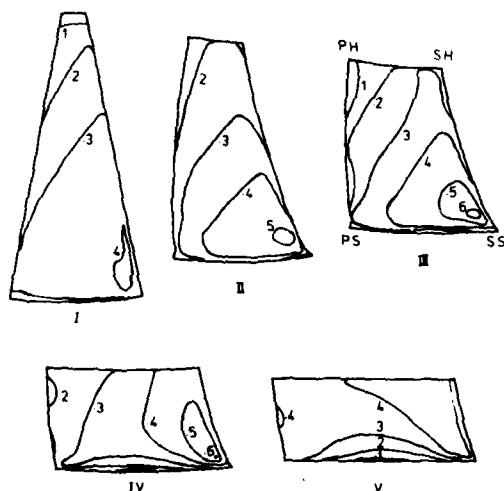


Figure 9. Contours of $u_{normal}/\omega R_2$, calculated for 1% tip gap and stationary shroud, at planes I - V in the impeller.

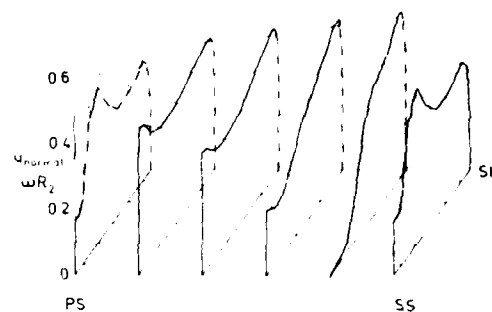


Fig. 10a

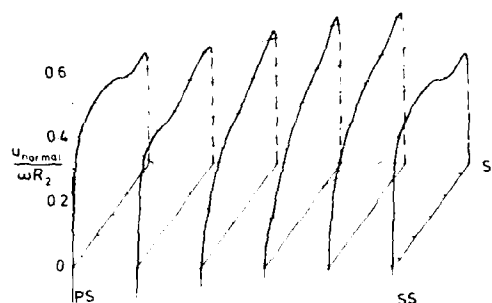


Fig. 10b

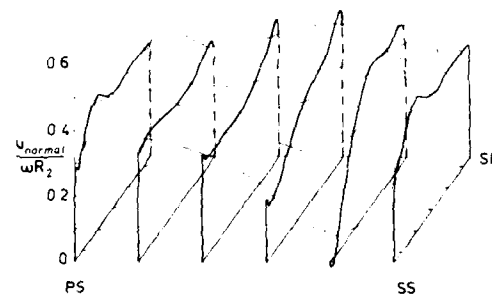


Fig. 10c

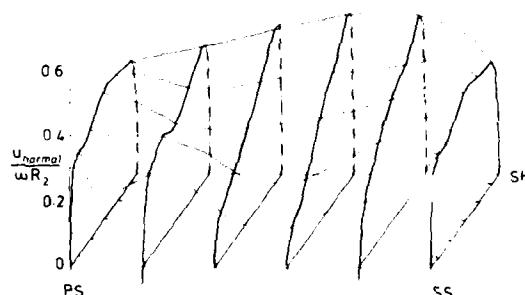


Fig. 10d

Figure 10. The calculated radial velocity distribution in the diffuser. Fig. 10a. $R/R_2=1.017$; 1% tip gap and rotating shroud. Fig. 10b. $R/R_2=1.017$; 1% tip gap and stationary shroud. Fig. 10c. $R/R_2=1.017$; zero tip gap and rotating shroud. Fig. 10d. $R/R_2=1.151$; 1% tip gap and stationary shroud.

A question of interest is how quickly the wake flow mixes out in the vaneless diffuser. Eckardt's measurements show it still causing significant flow non-uniformity at a radius ratio $R/R_2 = 1.151$. Our calculations confirm this, as shown in Figure 10d. This shows the development of the velocity profile in the vaneless diffuser for the case of the stationary shroud wall and the 1% tip gap in the impeller. Clearly the velocity profile has not become uniform at $R/R_2 = 1.151$, and there is a significant axial gradient of radial velocity from the shroud to the hub wall.

Secondary Flow Velocities

The secondary flow velocity components solved for in the present calculation procedure are u_2 and u_3 , normal to finite-difference grid surfaces of constant j and k respectively. These two components are not necessarily mutually orthogonal but they are both orthogonal to the u_1 velocity component in the bulk flow (i) direction.

Figures 11 and 12 show u_2 and u_3 velocity components calculated mid-way between blades and mid-way between the hub and shroud walls. Figure 11 gives the results for the case of a 1% tip gap and a stationary shroud wall, and Figure 12 shows the velocities from the calculation with no tip gap and a rotating shroud. The results are shown for measurement planes II - V in the impeller.

Immediately apparent from the comparison of the two figures is the effect of the different shroud-wall boundary conditions. No overturning of the flow, to give a velocity component from the pressure side to the suction side, occurs near the shroud wall in the calculation with the stationary shroud wall. This is contrary to the measurements presented by Eckardt at planes III and IV of his impeller. In contrast, Figure 12 shows that with the rotating shroud and no tip gap secondary flow velocities from the pressure to the suction side do occur near the shroud wall. Possibly our estimate of 1% tip clearance is too large.

Evidence of the influence of the relative eddy ($\nabla \times \mathbf{u} = -2\Omega$) on the secondary flow pattern in the free stream is seen in both calculations at planes II and III. This results in the clockwise secondary flow pattern observed in the figures. Curvature in the meridional plane, see Figure 2, gives rise to u_3 velocities along the blade surfaces in the hub-to-shroud direction. These play an important role in boundary layer transport at stations IV and V.

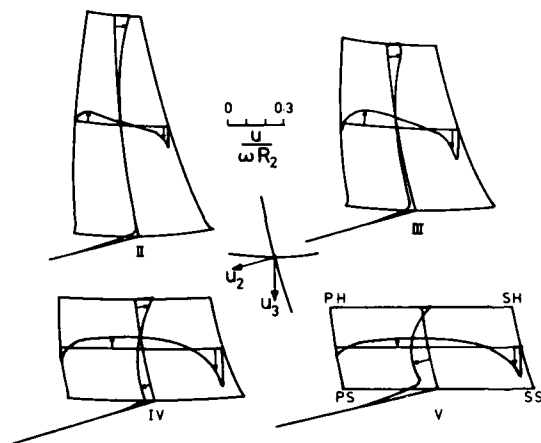


Figure 11. The cross flow velocity components at planes II - V in the impeller, calculated with 1% tip gap and a stationary shroud.

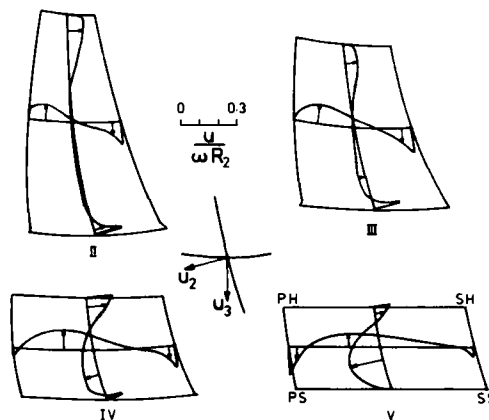


Figure 12. The cross velocity components at planes II - V in the impeller, calculated with no tip gap and a rotating shroud.

Tip-Leakage Flow

The tip-leakage flow velocities in the u_2 direction are shown in Figure 13 for the calculation with the stationary shroud wall. The velocity of the shroud wall relative to the blades imposes a harsh boundary condition on this pressure-driven flow. This flow is calculated with the distribution of grid points shown arrowed in the 1% tip-clearance gaps, which are shown to scale for the three measurement stations I, III and V.

The resulting cumulative mass flow rate through the impeller passage is presented in Figure 14 as a function of distance along the blade tip. Results from the two calculations with tip clearance are presented, one with the rotating shroud wall and the other with the stationary shroud wall. With the

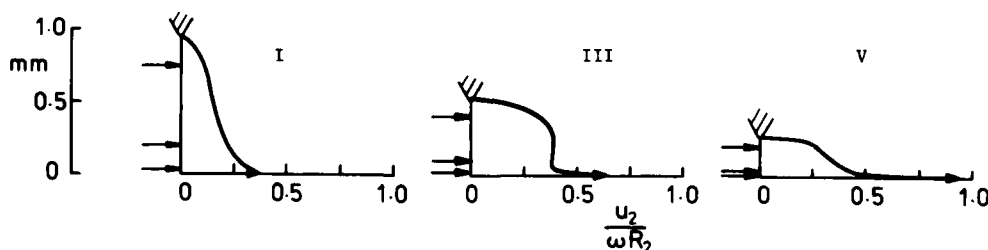


Figure 13. The calculated cross flow velocity through the tip gap versus distance from the shroud wall at planes I, III and V in the impeller. + location of grid points in the tip gap.

rotating shroud wall, 3.2 % of the flow through the passage passed through the tip gap, and with the stationary shroud wall this flow rate rose to 4.2 %. With the particular tip gap distribution used, one half of this leakage flow passed through the tip gap by station II. These tip-leakage flows are consistent with a discharge coefficient of approximately 0.5, based on the shroud tip loading calculated for flow with a rotating shroud and no tip clearance.

Polar Plot of Secondary Flow Velocities

An interesting question to be asked after considering the secondary flow velocities and the tip-leakage flow is whether the grid spacing need have been as non-uniform near the walls as was in fact chosen. One way to answer this question is by plotting the calculated relative tangential velocity against the velocity normal to the calculation plane, as in the polar plot of Figure 15. Here, for the calculation with a stationary shroud wall in the impeller and with stationary walls in the diffuser, we present two polar plots, one at station IV in the impeller and one at a radius ratio $R/R_2 = 1.017$ in the diffuser. Both plots are for velocities on a plane mid-way between the blade surfaces.

Marked on the plots are the points at which the flow angle differs by 5° from the angle of the limiting streamline at the wall. It is then found that the only wall on which there is considerable collateral flow, i.e. within 5° , is the hub wall in the diffuser. With this criterion, this calculated flow is collateral for 78 % of the distance to the opposite wall! The boundary layer at this point would give little trouble to the modeller.

The boundary layers at the other three locations exhibit different behaviour. To be at a location where the flow angle differs by less than 5° from the calculated limiting direction, the near-wall point should be approximately 0.003 of the hub-to-shroud distance from the wall and at these points the corresponding values of y^+ were approximately 50.

To be reasonably sure of the limiting flow direction, two grid points giving approximately the same flow direction are required. In the present calculation this condition was satisfied with points at 0.0004 and 0.002 relative spacing.

Impeller Exit Velocity Triangles

The mass-averaged normal and tangential velocities are also shown on Figure 15 for the two stations. At the diffuser station $R/R_2 = 1.017$, the normal velocity is close to the radial direction, thus the velocity triangle for the mass-averaged flow can be drawn as shown. This velocity triangle for the calculation with the stationary shroud wall and 1 % tip-leakage is compared with Eckardt's measured velocity triangle in Figure 16. As a result of the lower calculated wake blockage, 0.074 compared with the measured value of 0.183, the mass-averaged radial velocity at $R/R_2 = 1.017$ is 0.367 ωR_2 compared with the measured

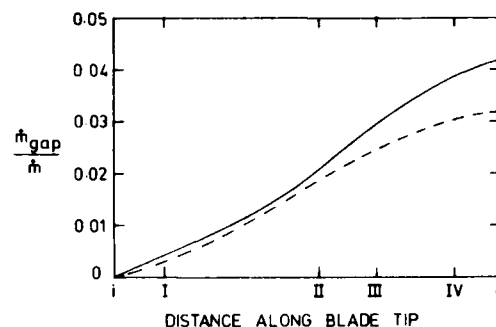


Figure 14. The cumulative fraction of the mass flow passing through the tip gap versus distance along the blade tip. - - - calculated for 1 % tip gap and rotating shroud. — calculated for 1 % tip gap and stationary shroud. i, impeller inlet; e, impeller exit.

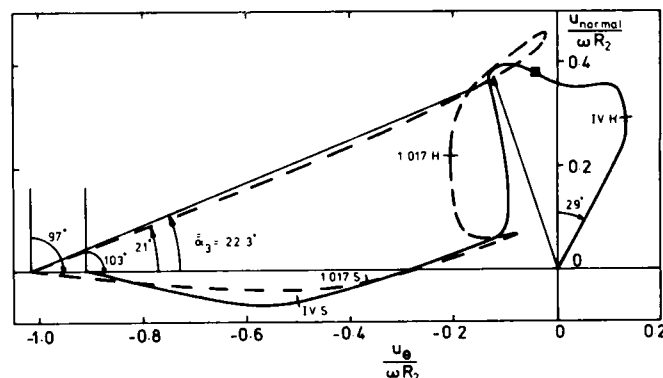
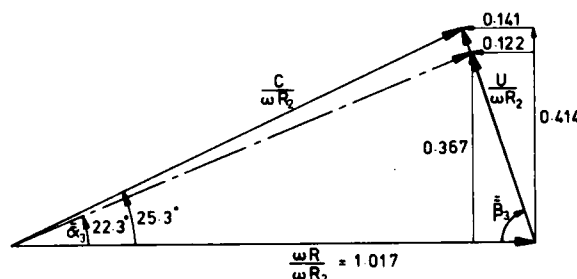


Figure 15. Polar plot of the normal and circumferential velocities calculated for 1 % tip gap with stationary shroud and diffuser walls.

— mid-way between the blade surfaces at impeller plane IV. ■ mass-averaged at impeller plane IV. - - - mid-way between the repeating boundaries at $R/R_2 = 1.017$. ▲ mass-averaged at 1.017.

Figure 16. Comparison of calculated and measured mass-averaged velocity vectors near the impeller exit ($R/R_2 = 1.017$). — measured; - - - calculated with 1 % tip gap and stationary shroud.



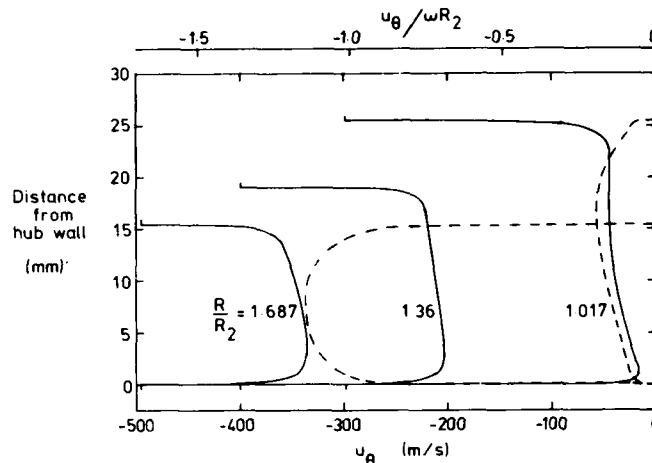
value of $0.414 \omega R_2$. The calculated relative flow angle $\bar{\alpha}_3$ of 71.6° agrees well with the measured value of 71.2° , but the calculated absolute flow angle α_3 of 22.3° is significantly smaller than the measured value of 25.3° .

Tangential Velocities in the Diffuser

Having calculated the flow in the impeller, it remains to calculate the shear stress distribution at the walls in the vaneless diffuser. The shear work associated with these stresses, in the rotating reference frame chosen for the calculations, constitutes a major source of loss production in the diffuser. Again the stationary-wall boundary condition provides a harsh test of the calculation procedure.

Figure 17 shows calculated relative tangential velocities, mass-averaged in the circumferential direction. The profiles are shown at radius ratios of 1.017, 1.36 and 1.687, and it can be seen that with the stationary diffuser walls the velocity gradient at the wall starts at a high level and gradually decreases at larger radii. Also shown are two profiles at radius ratios of 1.017 and 1.687 for the case of a rotating vaneless diffuser. In this case, in contrast, the shear at the wall due to tangential velocities is relatively very small initially, but it rises to very high values at large radii.

Figure 17. The calculated circumferential velocity component in the diffuser, mass-averaged in the circumferential direction. — 1 % impeller tip gap and stationary diffuser walls. - - - 1 % impeller tip gap and rotating diffuser walls.



RESULTS OF CALCULATIONS - THERMODYNAMIC PERFORMANCE

We have considered the influence of the boundary conditions on the three-dimensional flow in Eckardt's centrifugal compressor. Now let us consider how well the calculation procedure can model the overall thermodynamic performance and how important a contribution is made by the boundary conditions.

The calculated distributions of pressure, velocity and rothalpy provide all the information necessary to completely describe the thermodynamic performance of the compressor. Local distributions of pressure, temperature and entropy can be obtained and these can be mass-averaged at intermediate calculation planes throughout the compressor to define the compression process thermodynamically.

In this section, we present such results for the calculation with a stationary shroud wall and a 1 % tip clearance in the impeller, and with stationary walls in the vaneless diffuser.

Mass-Averaged Flow Properties

Figures 18-20 show the variation of mass-averaged properties with distance through the compressor. In the impeller, the distance is measured as the meridional distance along the hub wall, and in the vaneless diffuser radial distance is used. The five measurement planes in the impeller between the inlet and exit are shown, together with diffuser station 4 at a radius ratio $R/R_2 = 1.687$. Eckardt's data is shown for comparison in the vaneless diffuser.

The development of the static pressure ratio $\bar{p}/p_{t0,N}$ and the stagnation pressure ratio $\bar{p}_t/p_{t0,N}$ are shown in Figure 18. The agreement between the measured and the calculated static pressures is particularly good. In the vaneless diffuser at $R/R_2 = 1.017$ the measured static pressure ratio is 1.462 compared with the calculated value of 1.483, and at diffuser station 4 the measured value is 1.82 compared with 1.831. The stagnation pressure level in the diffuser is also calculated quite closely and the initial rate of decrease of stagnation pressure, mainly due to shear at the diffuser walls, is reasonably well modelled. At $R/R_2 = 1.017$, the measured stagnation pressure ratio was 2.207 compared with the calculated value of 2.235, and, at $R/R_2 = 1.687$, 2.094 was measured compared with 2.137.

Figure 19 gives a picture of the work done by the compressor, in terms of the stagnation temperature rise in the impeller, and the change in the absolute tangential velocity of the air. (The development of angular momentum rc_θ is not shown because of its similarity to the development of \bar{T}_t .) The tangential velocity c_θ is normalized by the impeller tip speed ωR_2 , thus giving the slip factor in the impeller exit plane. The measured slip factor (actually derived from the overall stagnation pressure ratio and the total-to-total efficiency) was 0.90, which is approximately 2 % lower than the calculated value of 0.916. This difference is consistent with the differences noted between the two velocity triangles in Figure 16. There, the difference in absolute tangential velocity was seen to be $\Delta c_\theta / \omega R_2 = 0.019$, and this was explained by reference to Figures 7 and 9, in which the measured wake blockage was found to be 0.183 compared with the calculated blockage of 0.074.

The calculated stagnation temperature \bar{T}_t in the adiabatic vaneless diffuser should remain constant at the calculated impeller exit value of 366.4 K. In fact numerical errors cause the calculated value first

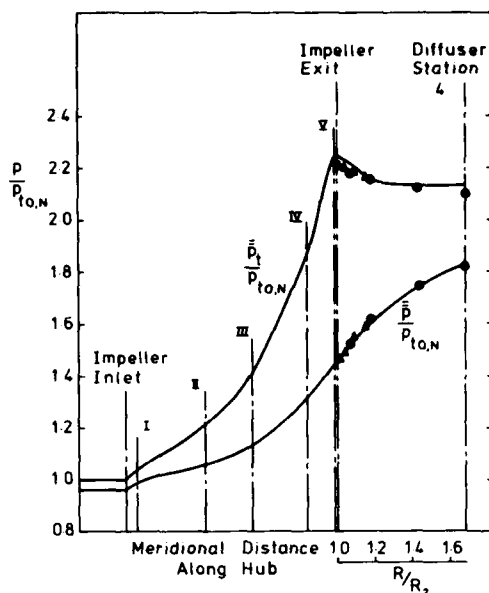


Figure 18. The variation of mass-averaged static and total pressures through the compressor. — calculated, 1 % tip gap and stationary shroud and diffuser walls. Δ , \bullet , Eckardt's measurements.

to fall below the measured value of 364.8 K and then to rise to 368.3 K at diffuser station 4. Some improvement in the numerical procedure in the vaneless diffuser is clearly possible, although in fairness it should be stated that this is a difficult flow to calculate, when the boundary conditions are stationary walls and when one boundary layer is near separation. The calculated rise in stagnation temperature in the impeller of 78.3 K is approximately 2 % higher than the measured rise of 76.7 K showing at least that the calculation is consistent in the impeller.

Finally, we present the mass-averaged static temperature \bar{T} and the mass-averaged entropy \bar{s} , the properties required for the thermodynamic representation of the compression process on a T-s diagram. Here we should note that the temperature and entropy data in the vaneless diffuser, shown in Figure 20, were obtained from instantaneous pressure measurements (the triangles) and from conventional pressure measurements (the circles), together with the assumption that the stagnation temperature remained constant in the adiabatic diffuser. The agreement between the measured and calculated entropies is especially encouraging early in the diffuser up to a radius ratio R/R_2 of 1.2, which in many machines would be the extent of the vaneless diffuser. At radius ratios larger than 1.2, the calculated entropy is higher than that derived from the measurements and this may be associated with the anomalous stagnation temperature variation shown in Figure 19.

The mass-averaged static temperatures appear to agree well throughout the diffuser and certainly they do agree well where we have noted before good agreement with static pressure and entropy. It is interesting to calculate, however, the change in entropy for a temperature change of 1.9 K such as is seen at diffuser station 4. $c_p \ln (352.4/350.5)$ gives an entropy change of 5.4 J/kg K, close to the difference between the calculated value and the data point. Further work is planned to attempt to improve our calculations of vaneless diffuser flow.

Temperature-Entropy Diagrams

The temperature-entropy diagram of Figure 3 is used as the basis for Figures 21 and 23. The data points, the compressor stations, the isobars and the nomenclature are retained. Calculated results are then superposed for comparison.

The temperature and entropy results shown on Figure 20 are replotted in Figure 21, together with the stagnation temperatures of Figure 19. Figure 21 therefore gives a comparison of the measured and calculated thermodynamic performance of Eckardt's compressor.

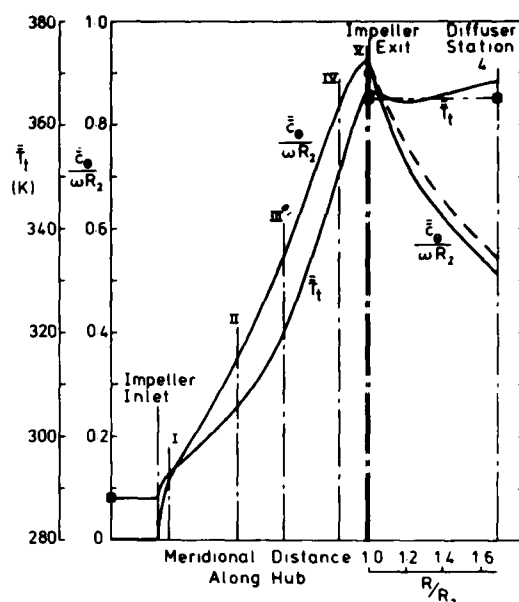


Figure 19. The variation of mass-averaged stagnation temperature and absolute circumferential velocity through the compressor. — calculated, 1 % tip gap and stationary diffuser walls. - - - $Rc_\theta = \text{constant}$. Δ , \bullet , Eckardt's measurements.

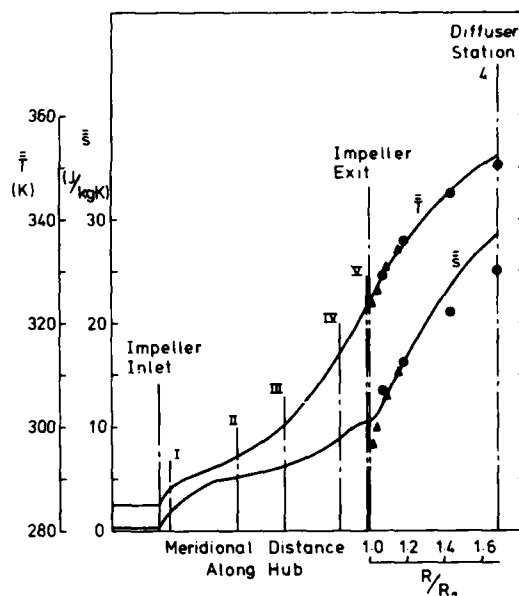


Figure 20. The variation of mass-averaged temperature and entropy through the compressor. — calculated with 1 % tip gap and stationary shroud and diffuser walls. Δ , \bullet , Eckardt's measurements.

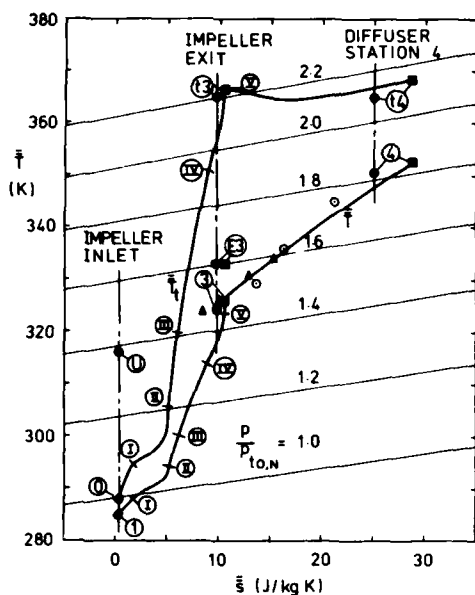


Figure 21. Comparison of the calculated and measured thermodynamic performance of the Eckardt compressor. \blacksquare calculated with 1 % tip gap and stationary shroud and diffuser walls. \bullet , \circ , Δ , from Eckardt's measurements.

TABLE 1

Pressures and temperatures for the state points shown on Figure 22. Comparison of states deduced from measurements and states calculated with a 1 % tip-clearance gap and a stationary shroud wall.

State	Deduced from measurements		Calculated	
	$\frac{\bar{p}}{P_{t0,N}}$	\bar{T} (K)	$\frac{\bar{p}}{P_{t0,N}}$	\bar{T} (K)
$t_{0,N}$	1.0	288.1	1.0	288.1
0	0.999 ⁽¹⁾	288.1	0.999	288.1
1	0.963 ⁽¹⁾	285.0 ⁽¹⁾	0.963	285.0
U	1.384	316.2	1.384	316.2
t_2'	2.282	364.8	2.320	366.4
3	1.462	324.3	1.483	325.9
$3'$	1.462	321.1	1.483	322.5
E1	1.657	332.9 ⁽²⁾	1.657	332.9
E3	1.602	332.9 ⁽²⁾	1.598	332.9
t_3	2.207	364.8	2.235	366.4
t_3'	2.207	361.3	2.235	362.6
4	1.82 ⁽³⁾	350.5	1.831	352.4
$4'$	1.82 ⁽³⁾	345.2	1.831	346.1
$4''$	1.82 ⁽³⁾	342.0	1.831	342.5
t_4	2.094	364.8	2.137	368.3
t_4'	2.094	355.9	2.137	358.0

(1) Based on estimated inlet flow conditions.

(2) Estimate based on calculated rothalpy increase through impeller equivalent to 0.6 K temperature rise.

(3) Extrapolation of static pressure data.

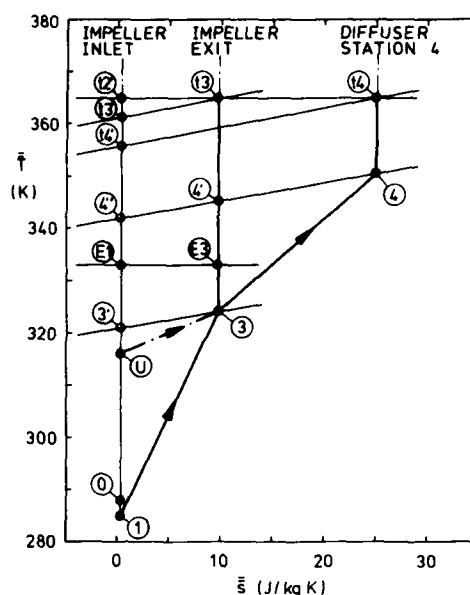


Figure 22. State points deduced from Eckardt's data and required for efficiency calculations. 1, 3, 4, static; 0, t_3 , t_4 , absolute stagnation; E3, relative stagnation; U, isentropic centrifugal pressure rise.

TABLE 2

Impeller and compressor efficiencies consistent with the data presented in Figure 22 and Table 1.

	Deduced from measurements	Calculated
$\bar{\phi}_3 = \bar{c}_{r3k}/\omega R_2$	0.338	0.340
$\bar{\alpha}_3 = \sin^{-1}(\bar{c}_{r3}/\bar{c}_3)$	25.3°	22.3°
$\bar{\beta}_3 = \sin^{-1}(\bar{c}_{r3}/\bar{w}_3)$	71.2°	71.6°
$\epsilon_{k3}(c) = 1 - \bar{c}_{r3k}/\bar{c}_{r3}$	0.183	0.074
$\eta_{s-s13} = \frac{T_3' - T_1}{T_3 - T_1}$	0.920	0.917
$\eta_{p13} = \ln \frac{T_3'}{T_1} / \ln \frac{T_3}{T_1}$	0.925	0.922
$\eta_{t-t03} = \frac{T_{t3}' - T_0}{T_{t3} - T_0}$	0.954	0.951
$\eta_{w13} = \frac{T_3' - T_U}{T_3 - T_U}$	0.605*	0.649
$\eta_{s-s14} = \frac{T_4'' - T_1}{T_4 - T_1}$	0.870*	0.853
$\eta_{t-s04} = \frac{T_4'' - T_0}{T_4 - T_0}$	0.864*	0.846
$\eta_{t-t04} = \frac{T_{t4}' - T_0}{T_{t4} - T_0}$	0.884*	0.872
$\eta_{D34} = \frac{T_4' - T_3}{T_4 - T_3}$	0.798*	0.762
$\mu = \frac{c_p(T_{t3} - T_0)}{\omega^2 R_2^2}$	0.897*	0.916

Note: the temperatures are all mass-averaged.

* The uncertainty in these efficiencies deduced from the measurements may be as much as ± 0.01 , the uncertainty in the slip factor, ± 0.02 .

As anticipated by the agreement of Figure 20, the calculated states in the vaneless diffuser at $R/R_2 = 1.017$ are in reasonably close agreement with the states deduced from the measured data. The calculated static and stagnation temperatures are 325.9 and 366.4 K respectively, compared with the corresponding measured temperatures of 324.3 and 364.8 K, and the calculated mass-averaged entropy is 10.6 J/kg K compared with 9.8 J/kg K. It is interesting, therefore, to see the calculated processes between states 1 and 3, and between states 0 and t3. The calculation shows that approximately one half of the entropy increase in the impeller occurs in the inducer up to station II, where less than one quarter of the work has been done on the air. The relatively long, lightly-loaded inducer appears to make a sizeable contribution to the losses. The increase in entropy in the rest of the impeller is then relatively small in comparison with the work done.

More than one half of the overall entropy rise occurs in the diffuser, and both the calculation and the data show the process between states 3 and 4 to be a nearly straight line on the T-s diagram. In fact, a straight line with a slope of approximately 1.4 kg/J, almost the same as calculated for the inducer, and four times as small as that calculated for the impeller between stations II and V.

The design philosophy behind the geometry of Eckardt's impeller is apparent from the figure. The pressure rise in the inducer up to station II is mostly due to a reduction in the relative kinetic energy of the flow. After station II, the impeller passage turns quickly to the radial direction and the pressure rise is mostly due to centrifugal compression.

Clearly the temperature-entropy diagram aids understanding of the compression processes, as was appreciated by Vavra [11]. We now, therefore, summarize the measured and calculated performance of Eckardt's impeller by presenting pressures and temperatures at the state points required for the calculation of the overall and component efficiencies.

Figure 22 shows the state points deduced from Eckardt's data and shown earlier in Figure 3. It also shows other states required for the calculation of thermodynamic efficiencies; these states are obtained by isothermal and isobaric processes as shown on the figure. Figure 22 therefore represents a complete thermodynamic representation of the overall compression process in Eckardt's compressor. Table 1 gives a comparison of the measured and calculated values of pressure and temperature for all the state points shown on the figure.

Efficiencies

The impeller and compressor efficiencies consistent with the data presented in Figure 22 and Table 1 are tabulated and defined in Table 2. Also presented are values of the flow coefficient, the impeller exit flow angles, the wake blockage factor and the slip factor.

The static-to-static, polytropic and total-to-total impeller efficiencies are all calculated to better than one half of one percent. The calculated static-to-static, total-to-static and total-to-total compressor efficiencies are 1-2 % below the measured values.

The wheel and diffuser efficiencies discussed by Vavra are also tabulated. The wheel efficiency gives a measure of the impeller performance with the centrifugal pressure rise removed and represents an efficiency of the diffusion process in the impeller. The calculated value of 0.65 agrees reasonably well with the value of 0.6 derived from the measurements, and both are much smaller than the other impeller efficiencies which are in excess of 91 %. The measured and calculated diffuser efficiencies are 0.8 and 0.76 respectively.

Influence of Boundary Conditions on Thermodynamic Performance

As we have seen, the present calculation procedure gives a thermodynamic compression process corresponding quite closely with the actual process. Furthermore it allows us to change the boundary conditions of the flow in order to delineate the individual contributions of effects such as tip leakage on the compressor performance.

Figure 23 presents the results of these computational investigations. The results of three different calculations of the impeller exit states 3 and t3 are shown in comparison to the measured states. These calculations were for the three sets of boundary conditions described above, and the temperature and entropy values for each of these states are given in Table 3.

The largest variation in the calculated impeller exit states is caused by the tip leakage. The calculation with zero tip gap gives an entropy s_3 of only 6.75 J/kg K compared with values of 10.56 and 10.22 J/kg K for the two cases with a 1 % tip gap. In fact, these two values with tip leakage are remarkably close considering that one calculation imposed a stationary shroud wall while the other used a rotating shroud wall. These calculations do not allow us to distinguish between the unresisted-expansion and mixing losses experienced by the tip-leakage flow and the loss due to increased viscous shear at the shroud wall, but with further calculations and consideration of results like those shown in Figure 13 this may be possible.

As expected, the closest agreement with the measured impeller exit state is given by the

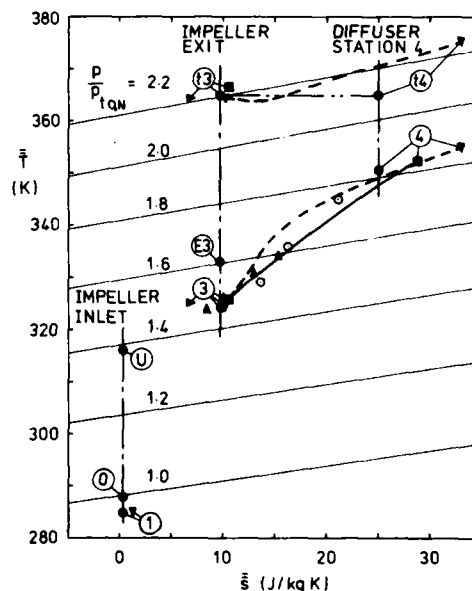


Figure 23. Influence of boundary conditions on calculated thermodynamic performance. ■—■ calculated with 1 % tip gap and stationary shroud and diffuser walls; ▽—▽ calculated with 1 % tip gap, and rotating shroud and diffuser walls; ▲, calculated with zero tip gap and rotating shroud; ●, ○, ▲, from Eckardt's measurements.

TABLE 3

Impeller exit states 3 and t3, measured, and calculated with three different sets of boundary conditions.

Description	\bar{T}_3 (K)	\bar{T}_{t3} (K)	\bar{s}_3 J/kg K	\bar{p}_3 $\bar{p}_{t0,N}$	\bar{p}_{t3} $\bar{p}_{t0,N}$	$\epsilon_{k3}(c)$	$\bar{\alpha}_3$
Deduced from measurements	324.3	364.8	9.77	1.462	2.207	0.183	25.3°
1 % tip gap - stationary shroud wall	325.9	366.4	10.56	1.483	2.235	0.074	22.3°
1 % tip gap - rotating shroud wall	324.6	364.3	10.22	1.465	2.197	0.119	23.6°
zero tip gap - rotating shroud wall	325.4	364.3	6.75	1.495	2.225	0.056	22.2°

calculation which most closely models the measured wake flow. This was obtained with the combination of a 1 % tip gap and a rotating shroud wall, as discussed above and as seen in Figures 7 and 8. In this case, the temperatures and pressures at the impeller exit agree particularly well with the measurements.

Rotating Vaneless Diffuser

The increase in entropy in the stationary vaneless diffuser arises mostly due to the high shear at the wall caused by the large tangential velocity of the flow. As discussed above and as shown in Figure 17, these shear stresses may be reduced, especially at small radius ratios, by rotating the walls of the diffuser.

Figure 23 shows the calculated diffuser performance for the case of a 1 % tip gap and a rotating shroud in the impeller, and with diffuser walls rotating at the rotational speed of the impeller. As can be seen, the rotating diffuser gives less loss and improved performance at small radius ratios, up to about $R/R_2=1.35$; thereafter, the shear stresses at the walls become larger than with the stationary diffuser walls, and the diffuser performance becomes progressively worse. The total-to-static and total-to-total efficiencies calculated for the compressor with the rotating vaneless diffuser were 0.828 and 0.861 respectively. Thus, apart from the increased work due to the shear in the diffuser and the higher pressure ratios of $p_4/p_{t0,N} = 1.85$ and $p_{t4}/p_{t0,N} = 2.25$, extending the rotating vaneless diffuser all the way to a radius ratio of 1.687 would not appear to offer a performance gain. A combination of a rotating diffuser to a radius ratio of 1.3 followed by a diffuser with a stationary wall might offer some improvement in compressor efficiency, but at the expense of mechanical complexity and weight.

COMMENTS ON THE FLOW MODEL

As described in the introduction to reference 1, it is fifteen years since we began studying various aspects of the fluid dynamics of centrifugal impeller flows. Now, finally, we have created a computational model which combines these effects and allows an assessment of the thermodynamic performance of compressors.

The key features of this model are:

1. the use of a general three-dimensional grid, without any orthogonality restrictions on the grid lines, so that flows in real turbomachinery cascades may be calculated and circumferentially repeating boundary conditions may be simply applied;
2. the handling of the equations in vector form, so that equations for three velocity components of local interest in the flow are relatively easy to formulate;
3. the choice of the three velocity components:
 - a. the u_1 velocity in the bulk-flow direction will, over most of the flow domain, be the largest of the velocity components;
 - b. the u_2 and u_3 velocities normal to the blade walls and normal to the hub and shroud walls respectively, so that the boundary values of the velocity normal to the wall may be specified without numerical interpolation problems;
4. the highly non-uniform grid spacing, which allows the location of grid points in regions of physical interest, for example near the walls, while using an economical number of grid points;
5. a sophisticated solution procedure for the pressure-correction equations, which combines the use of single and integrated strips of grid points to allow a rapid, accurate solution over highly non-uniform grid spacing;
6. a Prandtl mixing-length viscosity model with a Van Driest modification, which can be used in the laminar sublayer, in the logarithmic region of the boundary layer and throughout the entire flow domain, without any restrictions on the grid point locations;
7. the nearly-separated pressure correction, which is convenient to use over the general non-orthogonal grid and allows the pressure used in the density and total pressure calculations to be consistent with the pressure used in the bulk-flow velocity calculation. Since this is usually the largest velocity component, the nearly-separated pressure correction results in total pressure being conserved without a tight convergence of the three-dimensional pressure distribution.

The calculations are economical to perform, both in terms of computer storage and computer time. A calculation of the three-dimensional flow and thermodynamic performance of a centrifugal compressor at one operating point, such as described here, requires 440k bytes of memory and 45 minutes of CPU time on an IBM 3032 computer.

CONCLUDING REMARKS

- a. Unlike the Ghost centrifugal impeller which we studied earlier [1], the impeller used by Eckardt has a lightly-loaded inducer at the M2 test point. Thus the large leading-edge loss, with its associated large turbulence levels and unsteadiness, which were observed in the Ghost inducer near the shroud wall, are not expected in the Eckardt impeller and they were not observed. Since our partially-parabolic flow assumption neglects such leading edge effects, we expected it to more closely model Eckardt's impeller flow than it did the flow in the Ghost impeller. Indeed, the model is appropriate for present-day impellers with lightly loaded inducers.
- b. Further work should be undertaken to evaluate the relative importance of the loss mechanisms associated with tip-leakage flows and with flow near the stationary shroud wall in the impeller. The question as to the optimum tip-clearance gap still remains to be answered. The present method can be used to gain a better understanding of these effects.
- c. At its present stage of development, the calculation procedure gives the work done, the pressure ratios and the efficiencies of Eckardt's centrifugal compressor within 1 or 2 %. Considering the approximations made in estimating the impeller geometry, the tip-clearance gap and the inlet flow conditions, and considering the uncertainty in the measurements and their interpretation, this is perhaps more than could be expected.
- d. In more general terms, the model is applicable to steady, subsonic flows in stationary and rotating turbomachinery cascades, which have small leading-edge effects. The present calculations represent significant progress in handling steady relative flow with complex boundary conditions in passages of complex geometry. They offer hope for improved predictions from preliminary design studies and for reduced component development costs.

REFERENCES

1. Moore, J. and Moore, J.G., "Calculations of Three-Dimensional, Viscous Flow and Wake Development in a Centrifugal Impeller," in "Performance Prediction of Centrifugal Pumps and Compressors," ASME Publication, 1980.
2. Johnson, M.W. and Moore, J., "The Development of Wake Flow in a Centrifugal Impeller," ASME Paper No. 79-GT-152, to be published, ASME J. of Eng. for Power.
3. Eckardt, D., "Detailed Flow Investigations within a High-Speed Centrifugal Compressor Impeller," Trans. ASME, J. of Fluids Eng., Vol. 98, pp390-402, 1976.
4. Eckardt, D., "Instantaneous Measurements in the Jet-Wake Discharge Flow of a Centrifugal Compressor Impeller," Trans. ASME, J. of Eng. for Power, Vol. 97, No. 3, pp 337-346, July 1975.
5. Eckardt, D., "Untersuchung der Strahl/Totwasser-Stromung hinter einem hochbelasteten Radialverdichter-laufgrad," DFVLR Report, DLR-FB 77-32, 1977.
6. Smith, A.G., "On the Generation of the Streamwise Component of Vorticity for Flows in a Rotating Passage," Aeronautical Quarterly, Vol. 8, pp 369-383, 1957.
7. Hawthorne, W.R., "Secondary Vorticity in Stratified Compressible Fluids in Rotating Systems," C.U.E.D./A-Turbo/TR63/1974.
8. Stanitz, J.D., Osborne, W.M. and Mizisin, J., "An Experimental Investigation of Secondary Flow in an Accelerating, Rectangular Elbow with 90° of Turning," NACA TN 3015, Oct. 1953.
9. Moore, J. and Moore, J.G., "A Calculation Procedure for Three-Dimensional, Viscous, Compressible Duct Flow. Part I - Inviscid Flow Considerations," Trans ASME, J. of Fluids Eng., Vol 101, pp 415-422, Dec. 1979.
10. Moore, J. and Moore, J.G., "A Calculation Procedure for Three-Dimensional, Viscous, Compressible Duct Flow. Part II - Stagnation Pressure Losses in a Rectangular Elbow," Trans. ASME, J. of Fluids Eng., Vol. 101, pp 423-428, Dec. 1979.
11. Vavra, M.H., "Basic Elements for Advanced Design of Radial- Flow Compressors," AGARD Lecture Series No. 39 on "Advanced Compressors," 1970.

ACKNOWLEDGEMENTS

The authors wish to thank Professors J.B. Jones, H.L. Moses and W.F. O'Brien for their encouragement and for giving them the facilities and the opportunity to perform this study.

APPENDIX. Thermodynamic Representation of States in a Rotor.

Figure A1 shows the processes used to define auxiliary states for the representation of flow with static pressure p , static temperature T and relative velocity U at a point in a rotor at which the angular velocity is ωr . Three auxiliary states are marked; state Or is the relative stagnation point, state $*$ is the rotary stagnation point and state r is the reduced condition.

The relationships between the temperatures are

$$\begin{aligned} T_{Or} &= T + U^2/2c_p \\ \text{and} \quad T_{Or} &= T^* + \omega^2 r^2/2c_p, \\ \text{so that} \quad T^* &= T + (U^2 - \omega^2 r^2)/2c_p = H/c_p, \end{aligned}$$

where H is the rothalpy, and the equations are written for a perfect gas.

Four pressures are considered:

1. the static pressure p ,
2. the reduced static pressure p_r ,
3. the relative stagnation pressure p_{Or} ,
4. the rotary stagnation pressure p^* .

The relationships between these pressures are calculated using the relation for isentropic flow of a perfect gas. In particular,

$$\begin{aligned} \frac{p}{p^*} &= \left(\frac{T}{T^*} \right)^{\frac{\gamma}{\gamma-1}} \\ \text{or} \quad p^* &= p / \left[(T^* - \frac{U^2}{2c_p} + \frac{\omega^2 r^2}{2c_p}) / T^* \right]^{\frac{\gamma}{\gamma-1}} \\ \text{and} \quad \frac{p}{p_r} &= \left(\frac{T_{Or}}{T^*} \right)^{\frac{\gamma}{\gamma-1}} \\ \text{or} \quad p_r &= p / \left[(T^* + \frac{\omega^2 r^2}{2c_p}) / T^* \right]^{\frac{\gamma}{\gamma-1}}. \end{aligned}$$

The local relative Mach number M_{rel} may be found from the relation

$$\frac{p^*}{p_r} = \frac{p_{Or}}{p} = \left[1 + \frac{\gamma-1}{2} M_{rel}^2 \right]^{\frac{\gamma}{\gamma-1}}.$$

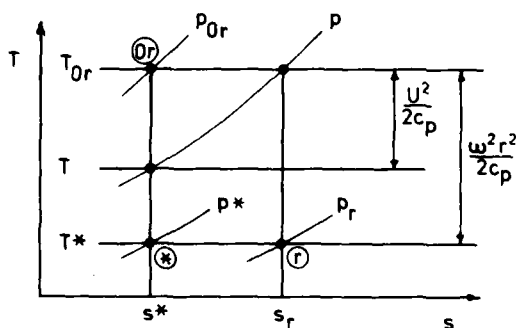


Figure A1. Definition of the reduced static (r), relative stagnation (Or) and rotary stagnation ($*$) state points.

DISCUSSION

H.B.Weyer, DFVLR, Cologne, Ge

Did you perform parametric studies -- using your code -- to demonstrate design features of separation free impellers? Is there a chance to do that?

Author's Reply

To date, our program development for centrifugal compressor flows has concentrated on reproducing the main features of the flow and performance of the compressor which Herr Dr Eckardt tested at the DFVLR. The data available for this compressor (Rotor 0) is the most comprehensive in the literature and should be considered by modellers before they embark on parametric studies. The results presented in this paper are being supplemented by calculations using different thicknesses of inlet boundary layer. In this way, we are studying the sensitivity of the wake development in Eckardt's compressor to inlet conditions.

In March this year, Herr Dr Eckardt reviewed the results presented in this paper and he pointed out that the 5% boundary layer thickness on the shroud wall at the impeller inlet was too small. We therefore repeated the calculations with a 15% shroud boundary layer and a 1% hub boundary layer at the inlet. The wake development at the impeller exit, $R/R_2 = 1.017$, was then calculated as shown in Figure 24, which can be compared with the development shown in Figure 10b.

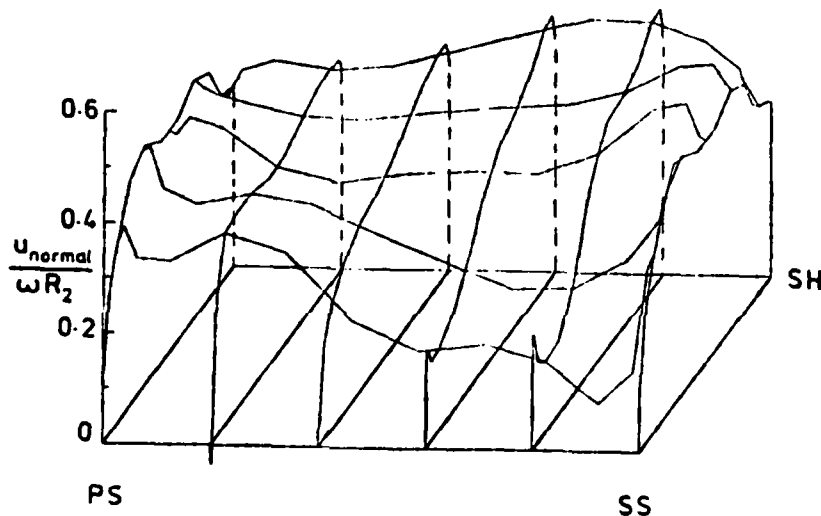


Fig.24 The calculated radial velocity distribution in the diffuser at $R/R_2 = 1.017$. Calculation with 1% tip gap, stationary shroud, 15% inlet shroud boundary layer, and 1% inlet hub boundary layer

The normal vorticity of the thicker shroud boundary layer at the inlet develops a strong streamwise component in the rotating impeller, and the secondary flow velocities, from the pressure side to the suction side near the shroud wall, are now sufficient to convect the wake fluid into the shroud/suction side corner region. Here, in the adverse pressure gradient caused by the blade unloading, the wake grows to give a blockage factor $\epsilon_{k3}(c)$ of 0.110.

Following our current study of the influence of inlet conditions on impeller flow and performance, we plan to perform calculations of flows in other compressors and parametric studies will also be possible.

R.A.Novak, G.E. Company, US

Why was Bosman seemingly able nearly to reproduce the Eckardt discharge velocity profile without an inlet shear layer, while Moore and Moore needed a 15% shear layer (as opposed to original 5% layer) to reproduce (nearly) the measured profile?

Author's Reply

The momentum equation for inviscid, compressible, steady flow in a rotating reference frame may be written¹³

$$-\underline{u} \times (\nabla \times \underline{u} + 2\underline{\Omega}) = T\nabla s - \nabla H.$$

For flow with

- (1) zero absolute vorticity at inlet, i.e. $\nabla \times \underline{u} + 2\underline{\Omega} = 0$,
- (2) uniform rothalpy, H ,
- (3) uniform entropy, s .

it can be shown¹⁴ that

$$\nabla \times \underline{u} = -2\underline{\Omega}$$

everywhere.

It would at first appear that these assumptions would apply to Bosman's calculation of the flow in Eckardt's impeller. If so, then one would expect no streamwise (\sim radial) component of vorticity at the impeller exit – the above equation shows that in the relative frame the vorticity is only in the axial direction. Correspondingly, however, one *would* expect a streamwise component of vorticity in the impeller inducer, since here the streamwise direction is partly in the axial direction.

From these observations and Bosman's fourth conclusion, "the 3-D calculation shows the development of a single passage relative vortex *commencing* in the inducer *exit*", one can conclude that Bosman did not start with the obvious inlet condition of uniform axial flow (in the absolute reference frame) upstream of the impeller. What absolute vorticity Bosman imposed at the flow inlet we do not know but again we can conclude that the inlet conditions are very important.

An alternative explanation is that gradients of entropy or rothalpy were introduced into Bosman's calculations by numerical approximations.

Further correspondence with Herr Dr Eckardt has revealed that the 15% boundary layer thickness was measured on the shroud wall near the inlet to Rotor 0, at 18000 RPM and 7.15 kg/s. A calculation of the flow at 14000 RPM and 5.31 kg/s, assuming this measured inlet boundary layer shape, produced secondary flow velocities at station IV in the impeller passage, which agreed well not with the measurements at 14000 RPM but with those at 18000 RMP! This suggests that the subtle differences in secondary flow patterns observed by Eckardt may be due to small differences in inlet flow conditions. These could be due to changes in Reynolds number for example.

Alternatively, changes in impeller Reynolds number or even changes in turbulence structure may also contribute. Ironically, it may be that turbulence modification, due to rotation and curvature, influences distributions of normal vorticity and that these in turn influence secondary flow patterns! If the latter is so, the agreement we obtain at 14000 RPM with measurements at 18000 RPM is fortuitous.

C.Rodgers, Solar, US

For a fixed clearance gap the dynamic distortion of the impeller will result in clearance flow varying with speed. This could cause the changes in exit flow distributions exhibited by the Eckardt Impeller.

J.W.Railly, Birmingham University, UK

With reference to the calculating planes that lie across the bulk mean flow direction, are these surfaces exactly normal to the blade surfaces; because it appears from the diagrams that there are no velocity components pointing across the boundaries of these calculating planes.

Author's Reply

The calculating planes are not normal to the blade surfaces. The u_2 and u_3 components of velocity shown in Figures 11 and 12 do not lie in the calculation planes (the planes shown), but are shown on them for convenience.

C.Bosman, U.M.I.S.T., Manchester, UK

I observe that the cross flow velocities illustrated in Figure 12, plane IV indicate a passage vortex having the opposite sense (i.e. contrary to the direction of rotation) to that observed by Eckardt and those presented in Paper No.10. Also the qualitative distribution is different from those observed by Eckardt in that the cross over point on the hub to shroud distribution is nearer to the hub while Figure 6, Paper No.10 shows it to be nearer to the shroud. As this secondary flow is regarded as vital to the correct determination of the boundary layer development and migration and consequently to the whole loss mechanism in the impeller, could the authors comment on this feature?

Author's Reply

As discussed above, the boundary layer on the shroud wall at the impeller inlet has a significant effect on the secondary flow pattern measured in the Eckardt impeller. Calculations omitting the vorticity associated with this thick shroud inlet boundary layer will not *correctly* represent the secondary flows.

ADDITIONAL REFERENCES

12. Moore, J. *Eckardt's Impeller -- a Ghost from Ages Past*, University of Cambridge, Dept. of Engineering, CUED/A -- Turbo/TR 83, 1976.
13. Wu, C.H. *A General Theory of Three Dimensional Flow in Subsonic and Supersonic Turbomachines of Axial, Radial and Mixed Flow Types*, N.A.C.A. TN 2604, 1952.
14. Hawthorne, W.R. Private Communication, 1968.

Computation of Three Dimensional Flow through the Eckardt Compressor Impeller

C. BOSMAN Lecturer, Dept. of Mech. Eng.,
U.M.I.S.T., Sackville Street, Manchester, U.K.

Summary

The inviscid flow through the Eckardt impeller reported to the ASME in 1976 has been computed using a time marching technique with primitive variables. Comparison is made at one operating point between the experimental results, computed quasi-three-dimensional (Q3D) inviscid results using stream surface techniques and the computed inviscid three-dimensional (3D) results. The computed 3D results exhibit the presence of a passage vortex, which is necessarily absent in the Q3D solution, and generally show improved agreement with experimental results. The presence of a jet/wake efflux pattern is evident in the 3D inviscid solution although its strength is less than that of the experimental result.

List of Symbols

b.l.	boundary layer.
q-o	quasi-orthogonal
s _m	meridional blade chord at shroud
x ^m	meridional distance measured from the L.E.
C _p	relative static pressure rise coefficient $\equiv 1 - \left(\frac{w_2}{w_1} \right)^2$
L.E.	leading edge.
M	relative Mach number
P.S.	blade pressure face.
S.S.	blade suction face.
U _t	blade tip speed
W	relative velocity
Δβ	departure of flow angle from blade angle $\equiv \beta - \beta_b$
β	flow angle measured to the meridional plane
β _b	blade angle measured to the meridional plane
I, II, III, IV, V	observation planes use by Eckardt

Introduction

Conventional design procedures in both axial and centrifugal turbomachines are aided by flow calculation based on well established prescribed streamsurface flow models. The primary, mean, hub-to-shroud flow is usually calculated by assuming a blade-like surface, with some allowance for slip or deviation, having a tangential thickness distribution equal to the tangential pitch between adjacent blade surfaces.⁽¹⁾ There are many examples of this type of calculation employing either a fixed grid as in Bosman⁽¹⁾, Marsh⁽²⁾, et al or streamline curvature as in Katsanis⁽³⁾, Stanitz⁽⁴⁾ et al. Estimates of blade surface property values have usually followed by the application of blade-to-blade streamsurface calculations which at their simplest estimate a single tangential property gradient from the mean flow above as in Stanitz and Prian⁽⁵⁾ or estimate the blade-to-blade flow detail assuming a streamsurface of revolution based on the streamlines calculated from the mean hub-to-shroud flow as by Smith and Frost⁽⁶⁾, Katsanis⁽⁷⁾, Stanitz and Ellis⁽⁸⁾, Hill⁽⁹⁾ et al. The application of these two dimensional calculation techniques when used in combination as by Bosman and El-Shaarawi⁽¹⁰⁾ is often referred to as quasi-three-dimensional (Q-3-D). Further developments as by Krimerman and Adler⁽¹¹⁾ have relaxed the constraint of the blade-to-blade streamsurfaces to being surfaces of revolution except at the hub and the shroud and employ multiple hub-to-shroud streamsurfaces. All these methods suffer the inadequacy of constraining the fluid particles which enter the blade passage at the corners formed by blade surfaces with hub or shroud, to remaining in their respective corners. The effect of this is to suppress the passage vortex which though weak and insignificant in much axial flow machinery, plays a vital role in the behaviour of most centrifugal impellers⁽¹²⁾ and appears to be even more important in radial turbines.⁽¹³⁾

The realisation of these inadequacies led Denton⁽¹⁴⁾ and Bosman⁽¹⁵⁾ to develop simultaneously three dimensional (3-D) calculation procedures which in no way suppresses the passage vortex phenomenon. In application to centrifugal machines it is becoming increasingly clear that the inviscid 3-D calculation procedure gives better qualitative and quantitative⁽¹³⁾ agreement with experimental results than the 2-D or Q-3-D procedures notwithstanding the lower numerical accuracy of the 3-D methods. It appears that even the suction - shroud corner wake efflux phenomenon in centrifugal impellers is not wholly of viscous origin. The current incorporation into the 3-D calculation at UMIST of a two equation turbulence flow model with wall slip and shroud in relative motion, may offer considerably greater accuracy of flow detail than hitherto.

Discussion

The object of the work presented is to make a detailed comparison of the results of a full three dimensional (3-D) flow calculation with the type of computed results normally used in design procedures which are of a two dimensional nature, being streamsheet flows, but which are often referred to as quasi-three dimensional (Q-3-D) and further to compare these with detailed experimental results. To this end it was found convenient to take the published results of Eckardt⁽¹⁶⁾ which contain not only extraordinarily good experimental details of the flow through a centrifugal impeller but also contains quasi-three dimensional computed results by the method of Stanitz⁽⁴⁾ and Stanitz and Prian⁽⁵⁾

The three dimensional computed results here presented have been obtained by the method which may be found in Bosman and Highton⁽¹⁵⁾ and Bosman⁽¹²⁾. This method which is for viscous adiabatic flow is used here in the inviscid mode and employs time marching with primitive variables applied to a three dimensional structure of cells whose corners are formed by the grid points of a three dimensional grid. A meridional projection of the grids 25 quasi-orthogonals (q-o's) may be seen in Fig 1, on which is superposed the 5

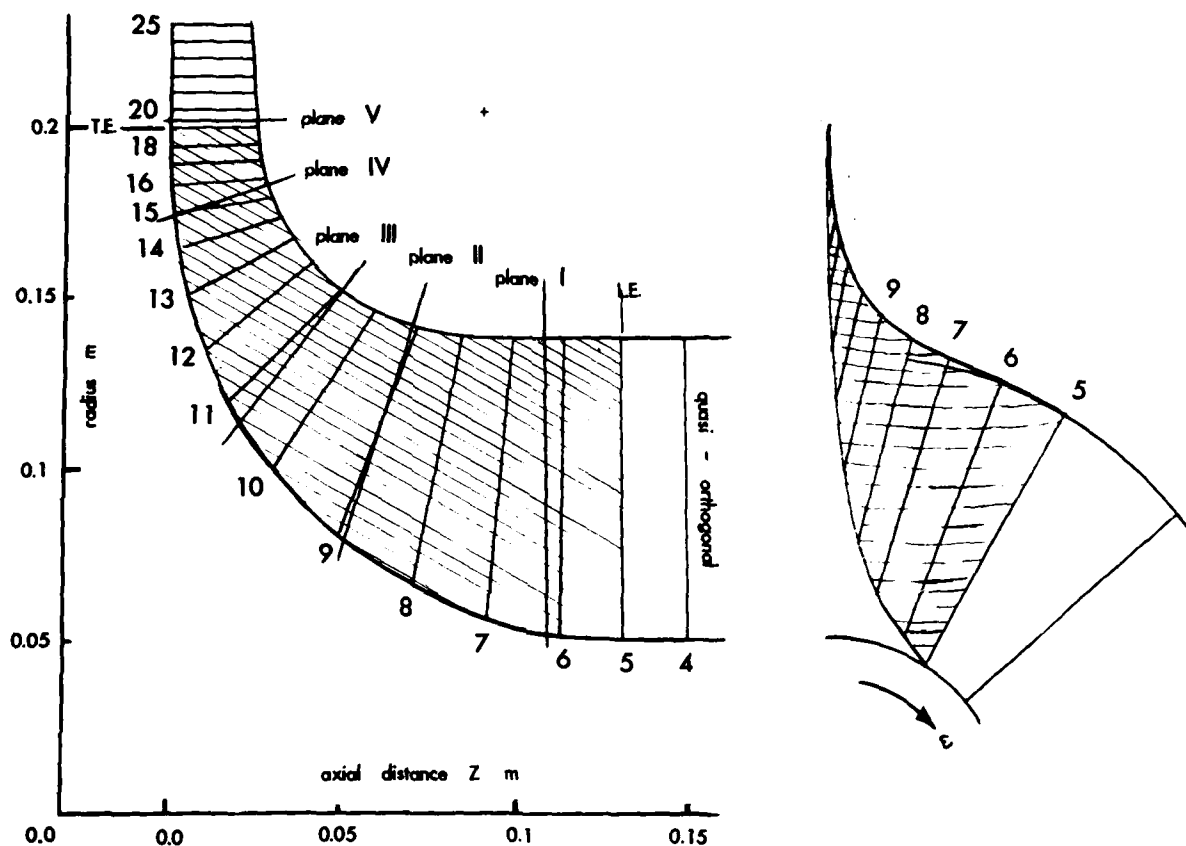


FIGURE 1 COMPRESSOR CONFIGURATION AND COMPUTATION GRID

observation planes designated I, II, III, IV, V as used by Eckardt⁽¹⁶⁾. The computation grid consisted of 7 points from hub to shroud, equally spaced along each q-o, and 7 points from blade-to-blade also equally spaced along each circular arc. The blade leading edge (L.E.) and trailing edge (T.E.) coincide with q-o's number 5 and 19 respectively. The impeller has 20 blades of a shape which may be seen in end view in Fig 1.

The results are for the single test point at rotational speed 14000 rev/min at a mass flow rate of 5.31 kg/s, the upstream conditions being approximately 9×10^4 N/m² pressure and 264 K temperature. The computed results have been obtained to a relative velocity convergence criterion of 3×10^{-5} with a time step of 5×10^{-6} s. In order to make comparisons simple, the computed results have been presented largely in the manner of Eckardt⁽¹⁶⁾.

Fig 2 shows the development of the hub-to-shroud relative velocity profiles non dimensionalised on tip speed, at mid-pitch and the similarly non-dimensionalised velocity profiles from blade-to-blade at the mid-channel height between hub and shroud. In general the 3-D results show a marked improvement over the Q-3-D results when compared to the experimental values. The 3-D results show a consistently high level of agreement at the channel centre point, the Q-3-D results being consistently low. The general character of the blade-to-blade results is in good agreement with experiment throughout the impeller, even after the appearance of the wake which is already in evidence at section III (see Eckardt⁽¹⁶⁾ Fig 9). The hub-to-shroud profiles show less good agreement in the early part of the meridional deflection at sections II and III but show marked improvement over the Q-3-D results in the later part of the meridional deflection at section IV and V. It seems to be a common feature of 2-D inviscid flow calculations that the hub-to-shroud velocity profile at impeller exit generally show the higher velocity at the shroud whereas experimental results and 3-D calculations⁽¹²⁾ show the reverse. Because of the existence of a substantial amount of wake flow at section IV (Eckardt⁽¹⁶⁾, Fig 10) in the shroud-suction corner, it might be argued that compared to the Q-3-D results the higher experimental flow velocities towards the hub and towards the pressure side, are a result of jet flow displacement by the developing wake. However the inviscid 3-D results display similar characteristics to the experimental ones, suggesting that even if contributory, the viscous wake explanation may only be partial.

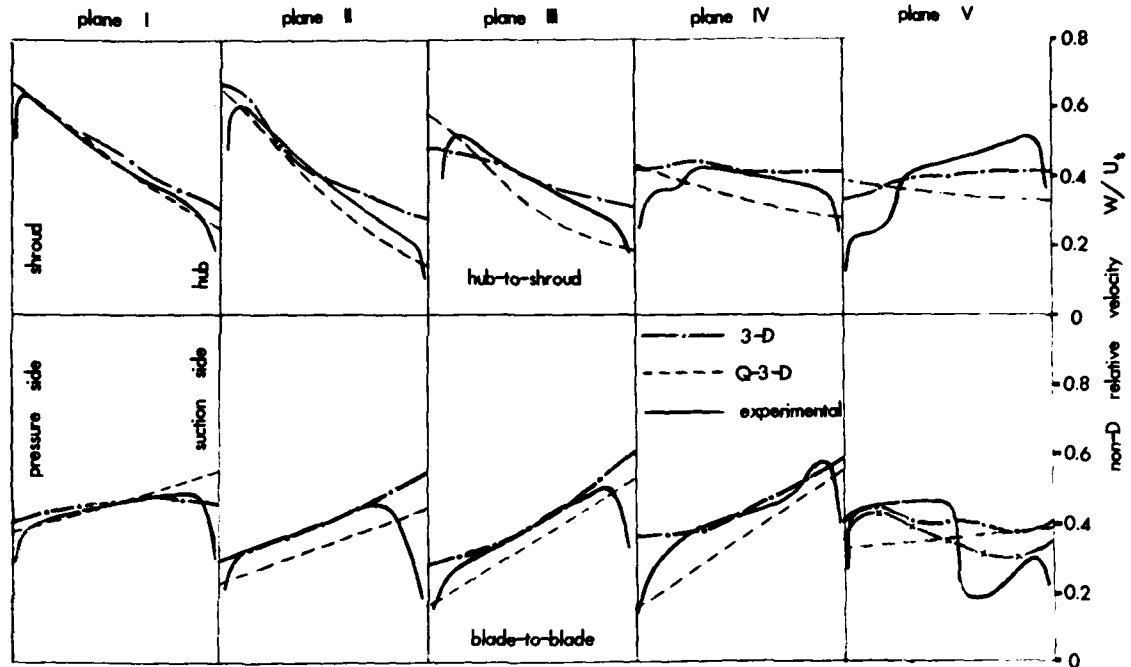


FIGURE 2 COMPARISON OF 3-D, Q-3-D AND EXPERIMENTAL
RELATIVE VELOCITY PROFILES AT MID-CHANNEL

Similar remarks may be made concerning the impeller discharge flow as observed by Bosman⁽¹²⁾. Fig 3 shows that the jet wake character of the experimental flow is clearly reflected in the inviscid 3-D flow

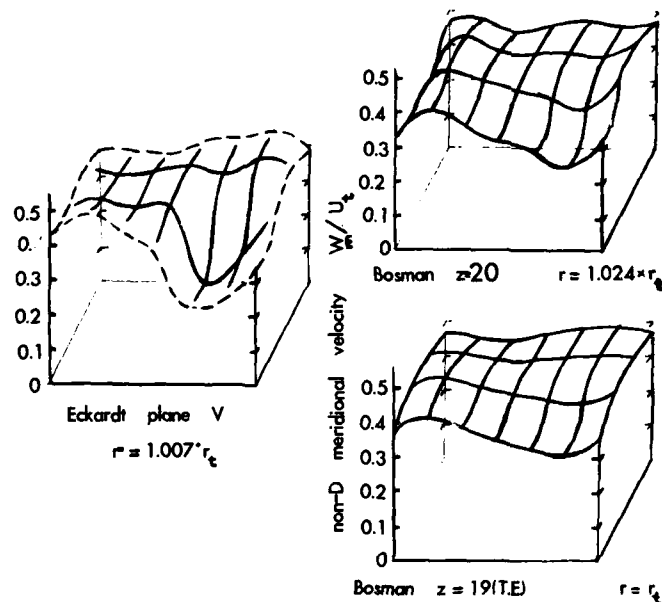


FIGURE 3 DISTRIBUTION OF NON-D MERIDIONAL
VELOCITY AT BLADE DISCHARGE

result, though naturally to a less marked degree. The very strong jet-wake discharge character of the 3-D inviscid results of Bosman⁽¹²⁾ were explained by the necessity to equalise the slip velocity at the discharge section on hub and shroud in order to satisfy irrotationality, being imposed on a shroud flow which was virtually unloaded by the passage vortex. The shroud flow had been unloaded as a consequence of a passage vortex, counter to blade rotation, causing suction-to-pressure face flow migration on the shroud. The strong diffusion in the suction-shroud corner caused by these effects resulted in a strong inviscid wake.

In the present case the situation is rather different as seen at Fig 9, in that there is no visible shroud flow migration up to plane III, after which a pressure-to-suction flow migration develops before being cancelled by the effects of slip at plane IV. In this case as is evident from Fig 4 there is substantial blade loading after the inducer section, yet the effects of slip still produce suction-shroud corner diffusion as discharge is approached. One is drawn to the conclusion that a sufficiently heavily loaded shroud section would eliminate the tendency to create an inviscid wake discharge but would inevitably induce a stronger wake by viscous separation.

Fig 5 illustrates the bulk mean relative Mach number distribution against shroud distance measured from blade L.E. The computed results which include both section area mean and section centre line values are compared to the experimental area mean values. All three distributions possess similar features of diffusion to about $(x/s_m) = 0.5$, followed by approximately zero diffusion to blade T.E. at $(x/s_m) = 1.0$. Since Eckardt's experimental results indicate (See Eckardt⁽¹⁶⁾, Fig's 9, 19) that the diffusion appears at $(x/s_m) = 0.5$ he argued that the subsequent zero diffusion was a result of the wake diffusion, implying that the diffusion would have persisted to the blade T.E. in the absence of the wake. The 3-D inviscid results suggest that in fact the zero diffusion feature for $(x/s_m) > 0.5$ is a characteristic of the flow.

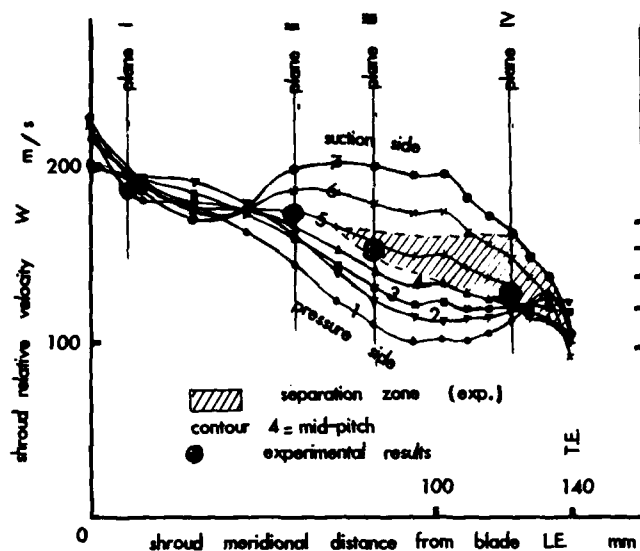


FIGURE 4 SHROUD DISTRIBUTION OF RELATIVE VELOCITY AND DIFFUSION

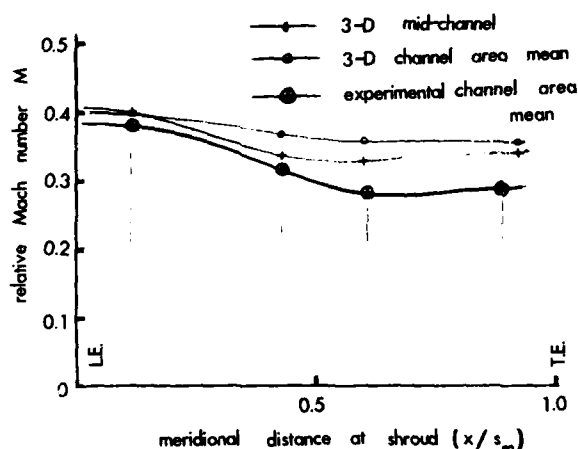


FIGURE 5 COMPARISON OF COMPUTED AND EXPERIMENTAL RELATIVE MACH NUMBER

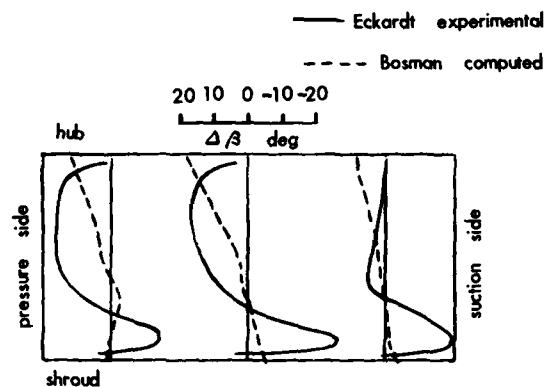


FIGURE 6 COMPARISON OF FLOW DEPARTURE ANGLE $\Delta\beta$ AT PLANE IV

vortex as indicated by the cross migrations is in the same sense as blade rotation however the axial component of circulation is counter to that of blade rotation as required by irrotationality because the shroud relative velocities are very much larger than those on the other three faces. It is interesting to observe that the impeller analysis reported in Bosman⁽¹²⁾ has a passage vortex whose migrations indicated an axial component in a sense counter to that of blade rotation in spite of having blade shape and hub and shroud profiles geometrically similar (though different in scale) to the present one. The sense of the passage vortex which plays a large part in distributing blade load from hub to shroud, appears to be dependent on details of hub, shroud and particularly blade profiles even where basic geometry is similar.

Fig 4 demonstrates the 3-D computed velocity distributions along grid lines on the shroud. The hatched area indicates the extent of the wake region on the shroud as determined by Eckardt's observations and the horizontal lines indicate the levels of ideal static pressure rise coefficient C_p (i.e. $C_p = 1 - w^2/w_{LE}^2$) based on the mean relative velocity of the L.E. flow. As can be seen in Fig 8, the shroud flow from blade L.E. to plane III is almost conformal with the blade shape (i.e. there is negligible blade-to-blade flow migration) hence, up to plane III the diffusion along relative streamlines is also the diffusion along grid lines so that the contours on Fig 4 may be interpreted as the diffusion experience of the free stream particles. Eckardt's experimentally observed velocities just outside the boundary layer, (b.l.) at mid-pitch are also shown on Fig 4 at planes I, II, III and IV and should be compared to contour 4 on the figure to assess the reliability of the calculated results. The experimental observations indicate incipient b.l. separation on contour 5 at a point where $C_p < 0.5$. This is a level of C_p at which we might not expect separation in a co-lateral b.l. but the shroud b.l. will be highly skewed on account of the relative tangential motion of the shroud. It has been suggested⁽¹⁶⁾ that the point of separation may be governed by the effects of rotation and flow curvature on the b.l. turbulence structure. If this were so one would anticipate from Fig 4 that separation would have occurred on the blade pressure face (contour 1) rather than contour 5 where it actually occurred, because the pressure side flow has

There is basic agreement between the computed 3-D inviscid secondary flow features and those observed experimentally. Fig 6 compares the departure $\Delta\beta$ of the flow angle β from the blade angle $\beta_{b,op}$ at plane IV. Approximately 70% of the flow nearest the hub shows suction-to-pressure face flow migration with departure angles $\Delta\beta$ both computed and experimental rising to nearly 20° near the hub. Such large angles could not be predicted by blade-to-blade stream surface calculations. The 30% flow near the shroud shows pressure-to-suction face flow migration, the stronger experimentally observed migration being influenced by the presence of the wake. These flow angle departures are indicative of a single passage vortex having counter clockwise sense as seen in the figure. Fig's 7, 8, 9 and 10 depict the streamlines on the hub, shroud, blade pressure and blade suction faces respectively, having been constructed by streak line synthesis, and confirm the presence of an inviscid passage vortex first becoming apparent at plane II. The axial component of this passage

experienced similar curvature history to contour 5, the flow at the inducer shroud being almost conformal with the blade (see Fig 8b), but has experienced a much more severe diffusion history. Indeed the pressure side flow has experienced a $C_p = 0.7$ and yet is still unseparated.

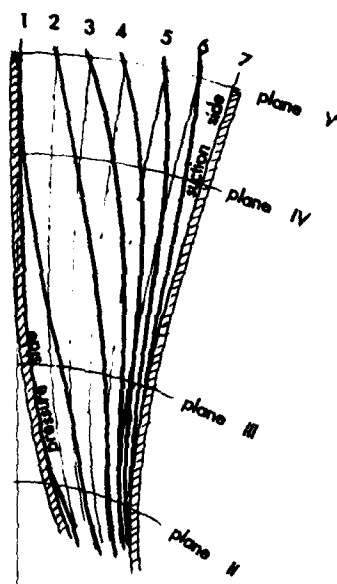


FIGURE 7 COMPUTED RELATIVE STREAMLINES ON THE HUB

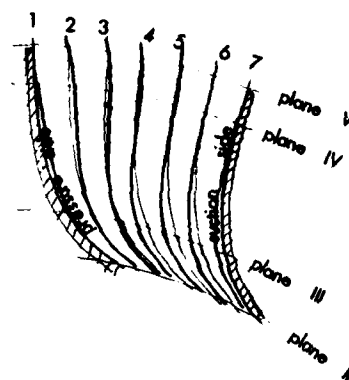


FIGURE 8a COMPUTED RELATIVE STREAMLINES ON THE SHROUD

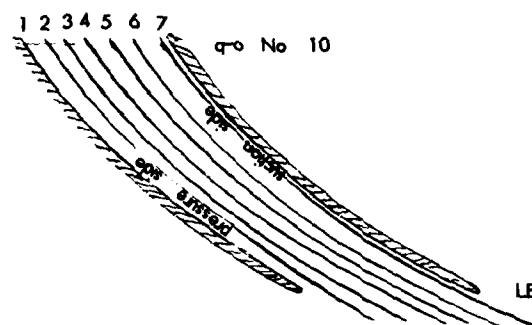


FIGURE 8b COMPUTED RELATIVE STREAMLINES ON THE INDUCER SHROUD

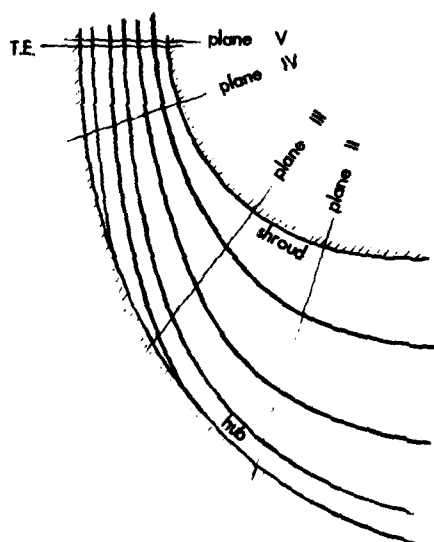


FIGURE 9 COMPUTED RELATIVE STREAMLINES ON THE BLADE PRESSURE FACE

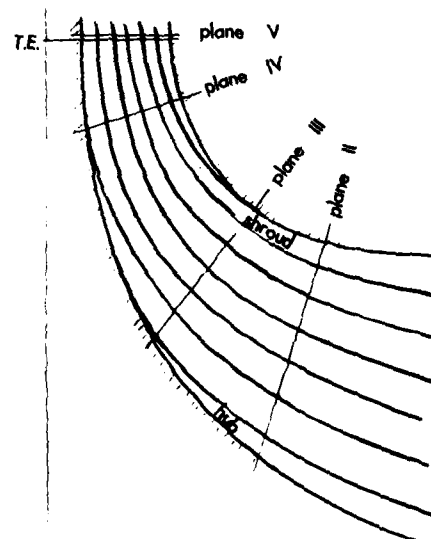


FIGURE 10 COMPUTED RELATIVE STREAMLINES ON THE BLADE SUCTION FACE

A plausible explanation of the occurrence of separation near mid-pitch on the shroud can be found by consideration of tip clearance and of the shroud boundary sub-layer migration as a result of the relative motion of the shroud and the fact that the shroud b.l., unlike the other b.l.'s., does not benefit from being energized by rotation. Consider the shroud boundary sub-layer not exceeding the tip clearance which is transported tangentially by the relative shroud motion. The effect of this transportation will be to transfer some low energy sub-layer from the blade pressure side, across the tip clearance, into regions of high free stream energy on the suction side. Also high energy sub-layer on the suction side of the passage will be transferred to regions of low free stream energy on the pressure side. The first of these processes will encourage separation on the suction side while the second will discourage separation on the pressure side. We would therefore anticipate large pressure side diffusions without separation, as occurs, and that separation will occur in a region where diffusion is less than one would have anticipated for separation in a co-lateral b.l., such as actually occurs, on the suction side of the channel.

Fig 11 has been drawn to illustrate and quantify the argument. Streaklines have been drawn, which are the vector mean of the shroud values of W and U , to represent the relative velocity somewhere on the Johnston diagram in the shroud boundary sub-layer. The streaklines have then been joined to form contours which represent the sub-layer particle trajectories relative to a blade. The sub-layer arriving at B has originated from A and has a higher energy than would be anticipated from the history of the free stream arriving at A by consideration of Fig's 8b and 4, which show that $C_{pA} = 0.7$. The sub-layer arriving at C through the tip clearance has originated from D which had a $C_{pD} = 0.6$ on leaving the blade pressure side and is now in a free stream $C_{pC} = 0.2$ and will sustain some considerable further diffusion before separation, which will however occur at a higher C_p than would have been anticipated for the co-lateral b.l. on account of the lower energy sub-layer. The argument leads to the conclusion that mid-channel separation is to be anticipated. The action of the pressure difference across the blade tip will be to assist the shroud in transporting the sub-layer in cases where the inducer shroud is positively loaded. This hypothesis suggests that reducing tip clearance will shift separation towards the shroud pressure side.

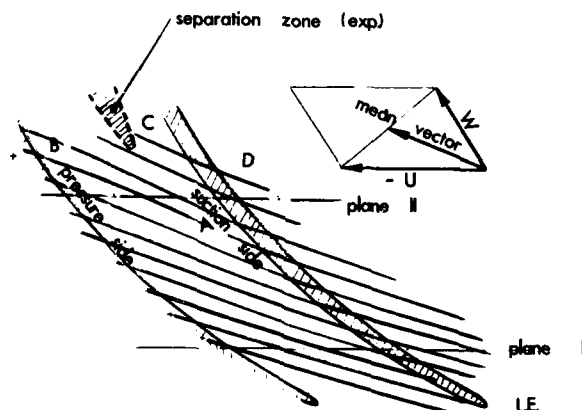


FIGURE 11 COMPUTED RELATIVE STREAMLINES
IN THE INDUCER SHROUD VISCOUS LAYER

Conclusions

It is shown that the 3-D inviscid flow calculation procedure reported by Bosman and Highton⁽¹³⁾ converges to a satisfactory solution for the experimental flow reported by Eckardt⁽¹⁶⁾.

As compared to Q-3-D calculations the results show considerable improvement in reflecting the experimental meridional profiles of velocity and particularly blade-to-blade profiles.

As reported by Bosman⁽¹²⁾ the unseparated, inviscid impeller discharge flow has a jet wake character similar to the experimental result, though naturally less pronounced.

Unlike the Q-3-D calculation, the 3-D calculation shows the development of a single passage relative vortex commencing in the inducer exit where meridional deflection commences. The sense of the vortex is the same as that of blade rotation and is confirmed by the experimental results.

Since in general Q-3-D calculations do not exhibit a jet-wake efflux characteristic it is assumed that this characteristic is in part related to the presence of the passage vortex.

In this impeller, the calculated passage vortex shows strong blade-to-blade flow migration on the hub and weak migration on the shroud in agreement with the experimental results.

It appears that the cessation of mean passage diffusion after the point of separation is not wholly explained by the wake growth and has some reflection in the inviscid flow.

A possible explanation is given of the occurrence of the onset of separation on the shroud at mid-channel in terms of the relative shroud motion and tip clearance which doesn't rely on boundary layer turbulence structure.

References

1. BOSMAN, C. The occurrence and removal of indeterminacy in flow calculations in turbomachines
ARC R & M No 3746. Feb. 1973.
2. MARSH, H. A digital computer program for the through fluid mechanics in an arbitrary turbomachine using a matrix method.
ARC R & M No. 3509
3. KATSANIS, T. Use of arbitrary quasi-orthogonals for calculating flow distribution in the meridional plane of a turbomachine.
NASA TN D-2546. 1964.
4. STANITZ, J.D. Two-dimensional compressible flow in turbomachines with conic flow surfaces.
NACA Rep 935. 1949.
5. STANITZ, J.D. and PRIAN, V.D. A rapid approximate method of determining velocity distribution on impeller blades of centrifugal compressors.
NACA TN 2421. July 1951.
6. SMITH, J.D.L. and FROST, D.H. Calculation of flow past turbomachinery blades.
I.Mech.E. Thermo-Fluid Mech. Conv. 1970. (Paper 27)
7. KATSANIS, T. Use of arbitrary quasi-orthogonals for calculating flow distribution on a blade to blade surface of a turbomachine.
NASA TN D-2909. 1965.
8. STANITZ, J.D. and ELLIS, G.D. Two-dimensional compressible flow in centrifugal compressors with straight blades.
NACA Rep. 954. 1950.
9. FILL, M. Numerical studies for mixed flow turbomachines.
Ph.D. Thesis, UMIST, Manchester, U.K. 1974.
10. BOSMAN, C. and EL-SHAARAWI, M.A.I. Quasi-three-dimensional numerical solution of flow in turbomachines.
ASME Paper No. 76-FE-23. 1976.
11. KRIMERMAN, Y. and ADLER, D. The complete three-dimensional calculation of the compressible flow field in turbo-impellers.
JMES Vol 20 No. 3 1978.
12. BOSMAN, C. An analysis of three-dimensional flow in a centrifugal compressor impeller.
ASME. Paper 79-GT-Isr-13.
13. BOSMAN, C. and HIGHTON, J. A calculation procedure for three-dimensional, time dependent, inviscid, compressible flow through turbomachine blades of any geometry.
JMES Vol 21 No. 1 1979.
14. DENTON, J.D. A time marching method for two and three dimensional blade-to-blade flow
ARC R & M No. 3775. 1975.
15. BOSMAN, C. and HIGHTON, J. The computation of three-dimensional, viscous, compressible flow.
Proc. of the First Int. Conf. on Num. Methods in Laminar and Turbulent Flow.
Univ. Coll. of Swansea, Wales, U.K. March 1978.
16. ECKARDT, D. Detailed flow investigations within a high-speed centrifugal compressor impeller
Trans ASME, Journ. of Eng. for Power, Series A, Vol. 98, No. 3, 1976.

DISCUSSION

R.A. Novak, G.E. Company, US

Why was the author seemingly able nearly to reproduce the Eckardt discharge velocity profile without an inlet shear layer, while Moore and Moore needed a 15% shear layer (as opposed to original 5% layer) to reproduce (nearly) the measured profile?

Author's Reply

The inviscid jet/wake efflux pattern appears to be related to the combination of the blade trailing edge unloading phenomenon in the neighbourhood of a passage vortex. This conclusion is based on computed results which show that if the radial part of the blade is long so that there is no passage vortex in the neighbourhood of the trailing edge then 3-D inviscid calculations show no jet/wake efflux pattern. On the other hand if the passage vortex is suppressed as in Q-3-D calculations which constrain particles to remaining in blade-hub-shroud corners, even where otherwise the stream surfaces are allowed to twist as in Krimerman and Adler¹¹, then no jet/wake efflux pattern is observed.

Bosman¹² suggests a mechanistic explanation for the wake in the case there presented but it is then related to the shroud section remaining unloaded in the trailing edge region due to the passage vortex being in the opposite sense to that of blade rotation. Now this explanation will not suffice in the Eckardt compressor because both the experimental results and my computed results show the passage vortex to be in the same sense as blade rotation and the shroud does not show a low loading in the trailing edge region. In this case then I have no mechanistic explanation to offer.

I do not know in the case of Moore and Moore what efflux pattern they would have obtained for inviscid flow but it must be highly significant that the sense of their passage vortex for their viscous flow as illustrated in Figure 12 is contrary to both my own and the experimental results. The implications of this for their inviscid calculation and the effects it must have on the secondary flow in the boundary layers is profound. It suggests however in the latter case that the efflux pattern is not related to their boundary layer secondary flow.

J.W. Raily, Birmingham University, UK

Would the author confirm from his calculations that at the quasi-orthogonal corresponding with Eckardt's plane V, the relative total pressure was everywhere the same (or, more specifically, that relative total pressure minus $U^2/2$ was uniform over that plane). Also would the author confirm that the calculation was initiated with uniform absolute total pressure upstream (i.e. there was no boundary layer profile) and that the static pressure at "q-O" 25 was uniform.

Author's Reply

The upstream conditions applied to the results presented were of uniform absolute total pressure with no boundary layer profile. The applied downstream static pressure at q-O 25 was uniform. The relative total pressure at plane V is not computed as a variable and does not appear in the printed results so that its variation is not known. However the variation of this quantity is not a significant factor in the computed results as far as velocity distributions are concerned because if one refines the grid, thereby reducing all errors including the lack of constancy of relative stagnation pressure, the qualitative distributions as presented become more clearly defined and show no tendency to diminution. In particular, the jet/wake pattern tends to reduce only if the grid is made coarser and acquires more definition as the grid is refined. Like all 3-D methods the calculation contains first order errors and the acceptable coarseness of the grid has to be assessed in the light of user experience. In our experience the grid used here is on the limit of coarseness and has been dictated by available store and computer running time.

COMPUTATION OF FLOW IN RADIAL- AND MIXED-FLOW CASCADES BY AN INVISCID-VISCOUS INTERACTION METHOD

George K. Serovy
Department of Mechanical Engineering
Iowa State University
Ames, Iowa 50011

Elmer C. Hansen
Department of Mechanical Engineering
University of Florida
Gainesville, Florida 32611
United States of America

SUMMARY

In general, computation systems successfully applied to axial-flow turbomachinery have not been found satisfactory for radial- or mixed-flow compressor configurations. There is, however, a good potential for application of some of the recently developed inviscid-viscous interaction methods to stationary passages in these geometries. This paper suggests the use of these interaction methods and shows how they may be used for the specific case of radial- or mixed-flow cascade diffusers. It is expected that the methods will contribute to the increased effectiveness of future centrifugal compressor design systems.

LIST OF SYMBOLS

AVDR axial velocity-density ratio, $\rho_2 V_{x,2} / \rho_1 V_{x,1}$
 c chord length
 D diffusion parameter
 M Mach number
 m meridional distance
 R radial coordinate (Ref. 3)
 RVDR radial velocity-density ratio, $\rho_2 V_{r,2} / \rho_1 V_{r,1}$
 Re_c Reynolds number based on chord length
 r radius
 x length along chord line
 V velocity
 β fluid angle measured from axial or radial direction
 γ blade setting angle
 δ^* displacement thickness
 θ^* momentum thickness
 θ circumferential coordinate (Ref. 3)
 ρ density
 σ solidity
 Subscripts
 x axial component
 r radial component
 1 cascade inlet
 2 cascade exit

1. INTRODUCTION

In the development of design systems for both axial-flow and centrifugal compressors, realistic evaluation of the flow field on blade-to-blade stream surface approximations has been an objective for many years. In the case of axial-flow compressor blade rows, the results of linear cascade experiments continue to be useful in evaluation if the experiments are carefully controlled and correctly interpreted. These requirements and the enormous practical range of aerodynamic and geometric variable sets under consideration indicate that computational approaches to the problems should also be actively followed. Recently, computational systems have been moderately, but by no means universally successful in predicting turning angles, total-pressure losses and internal flow fields in linear cascades. These methods should now be improved and further developed.

An inviscid-viscous interaction computational method for cascade flows was reported in References 1 and 2. This method has been, like others, moderately successful in turning angle, loss and flow field prediction. From the beginning of development it was believed that the best mechanism for program improvement would be to collect the widest possible range of valid experimental test cases, to compute results corresponding to the available data from these test cases, and to try to use differences as the basis for concentration of subsequent effort.

One group of possible test case situations considered has been the class of cascade diffuser configurations sometimes used in radial- and mixed-flow centrifugal compressors. As in every other test case category studied, the quantity of useable data were found to be very limited. However, a few cases were thought to be adequately defined and documented, and a number of trial computations were made. In this paper, it is the intent of the authors to direct attention to a few interesting trends shown by the results, to recognize the limitations exposed by the trials and to demonstrate that centrifugal compressor design methods might be improved by continued effort along the lines already followed.

2. CASCADE FLOW-FIELD PREDICTION BY INVISCID-VISCOUS ITERATIVE COMPUTATION

The character of the inviscid-viscous interactive cascade flow field solution method used here was discussed in general terms in Ref. 1, and considerable detailed information was given earlier in Ref. 2. Fundamentally, the procedure is based on the old idea of iteration to convergence between an inviscid field solution assumed to be adequate in a large part of the blade-to-blade passage, and limited viscous, but highly influential regions near the cascade blade profile surfaces. The base inviscid solution was a well-known computational method developed by Katsanis and McNally (Ref. 3). The base viscous region solution was an equally well-known boundary layer procedure described by Albers and Gregg (Ref. 4). Although the referenced reports describe the essential features of the computer programs used, both programs were modified to adapt to the requirements of an iterative combined solution and to the specific demands of a generalized cascade geometry. The interaction of inviscid and viscous solutions was based on a scheme suggested by Prune, Rubbert and Nark (Ref. 5). It should be noted that the displacement effect of the viscous region in the flow field, necessary in the inviscid region iterative computations, was modeled by "injection" of fluid along the cascade airfoil surfaces. Boundary layer laminar separation occurrence was predicted by a method due to Roberts (Ref. 6) and limited regions of turbulent separation were dealt with by methods suggested by Carter and Wornom (Ref. 7). As reported in Reference 2 the combined interactive solution program could be and was run in a continuous mode to reach a converged output.

3. RADIAL- AND MIXED-FLOW CASCADE DIFFUSERS IN CENTRIFUGAL COMPRESSORS

The relationship between two-dimensional flows in radial and linear airfoil cascade configurations has been discussed frequently in the literature. A clear and concise summary exists in the Scholz-Klein text (Ref. 8). However, even in this encyclopedic reference, the total attention focused on radial- and mixed-flow cascades is quite limited.

3.1. EXAMPLE APPLICATIONS

Although it was evident that there have been a number of radial- and mixed-flow cascade diffuser configurations built and tested, not many have been discussed in the open literature. In papers describing experiments, the geometry is frequently not sufficiently defined for computational purposes. Finally, it was not possible to find in any publication the detailed row performance measurements and blade surface pressure distributions needed for test case studies.

However, References 9-14 serve as evidence that radial- and mixed-flow cascade diffusers exist and exhibit satisfactory performance. Study of these references and discussion with some designers led to selection of the multiple-row-radial-cascade diffuser tests of Reference 12 as representative in terms of both configuration and aerodynamics. Background information on the diffusers discussed in Ref. 12 was supplied by R.C. Pampreen and J.R. Switzer and released with the generous permission of the AIRESEARCH Manufacturing Company of Arizona. This information included geometric data on the cascade arrangement and selected experimental performance. The authors of this paper (Serovy and Hansen) accept responsibility for any errors made in adapting the information received and for the choice of aerodynamic conditions reported in the investigation.

3.2. DESIGN PROCEDURES

Radial cascade configuration design is, without question, an interesting aerodynamic problem. References to design frequently suggest that axial (i.e., linear) cascade methods might be used. While the suggestions are valid, it is necessary to recognize the important influences present due to the radial through-flow direction. In each row, there is an effective stream-tube area change due to the radius increase from entrance to exit, but this increase is countered by the effective area reduction due to the radial-wall boundary layers on the diffuser boundaries. There is as a result, a radial velocity-density product change (RVDR) across the cascade (corresponding to the axial velocity-density ratio (AVDR) influence in linear cascades). There is also a change in blade tangential spacing between inlet and exit of a radial cascade. Both of the effects are permitted in the program of Ref. 3, but the RVDR effect is difficult to handle in a quantitative sense.

3.3. EXPERIMENTAL PERFORMANCE

Radial, multiple-row cascade diffusers represent one of several alternatives in centrifugal compressor design. In well-documented examples, they have demonstrated good performance. There is, unquestionably, better potential for variable geometry diffuser arrangements in cascade diffusers than in other alternatives.

4. RADIAL CASCADE COMPUTATION STUDY

As reported in Reference 12, a number of multiple-row radial cascade diffuser configurations were evaluated experimentally in connection with a centrifugal research compressor with a design pressure ratio of about 5/1. Because, in the present investigation, only a limited amount of time and money were available, it was decided to concentrate on study of a single row of the diffuser. The row selected was the third (last) row; and the selection was based on the fact that a relatively clear geometric definition was possible, and the additional fact that this cascade was tested so as to point out several examples of unresolved problems in cascade aerodynamics.

4.1. CASCADE GEOMETRY

The third blade row of the test case cascade was run under several sets of aerodynamic conditions in the experiments of Reference 12. The row was designed to operate in a constant-thickness radial passage. It was tested as designed and with varied blade setting angles. The row was also tested with half of the blades removed so as to decrease the row solidity to half of the design value. Finally, the diffuser was tested with the first and second rows in the radial passage, but with the same third row blades installed as an axial diffuser cascade downstream of a 90-degree bend. This arrangement is shown in Figure 3 of Reference 12.

The test case row consisted of NACA 65-18 (A_{10}) 15 profiles (transformed to the radial-tangential plane) at a setting angle of 27 degrees. The row solidity in the radial configuration was 1.24 with 88 blades. The intended design point angle of attack was 23 degrees. This would correspond to a mean camber line incidence angle of about 0.5 degrees for an equivalent circular-arc camber line shape.

For discussion in this paper, four test computation cases are sufficient to illustrate the type of results available, some features of radial cascade flows that might be of technical interest, and some cases in which future calculations might be improved. The blade profiles were set up for computation as follows:

- Case 1 - axial arrangement, AVDR = 1.0,
- Case 2 - radial arrangement, RVDR = 0.836,
- Case 3 - axial arrangement, AVDR = 0.836.
- Case 4 - radial arrangement, half solidity, RVDR = 0.836

All computations were made for an inlet flow angle of 50 degrees, measured from the radial or axial direction. The AVDR and RVDR values of 0.836 correspond to the passage area increase between entrance and exit of the radial cascade with parallel end walls. Computation field conditions for the flow cases are shown in Figures 1, 2 and 3.

4.3. EVALUATION OF RESULTS

Case 1 simulates the third cascade row blades installed in the axial passage with parallel end walls. Computational conditions, except for the unusually thick profiles, were similar to many two-dimensional test cases used previously. Calculated suction and pressure surface boundary layers are shown in Figures 4 and 5.

Case 2 simulates the third cascade row blades installed in the radial passage with parallel walls. This case uses the capability of the Katsanis and McNally inviscid flow calculation to change radius for a stream tube between cascade entrance and exit. There does not seem to be a significant change in the boundary layer growth shown in Figures 6 and 7 from that in Figures 4 and 5.

Case 3 uses the same geometry as Case 1, but an AVDR equal to the RVDR of Case 2 is imposed by changing the stream tube thickness. This would be equivalent to the axial cascade mounted between diverging end walls (instead of parallel as in Case 1). The boundary layer calculations for the suction surface in Figure 8 show a substantial change in character near the trailing edge as compared with Figure 4. Figure 9 does not show remarkable changes from Figures 7 and 5 for the pressure surface.

Case 4 represents the half-solidity radial cascade. The suction surface boundary layer plots of Figure 10 again show the rapid growth near the trailing edge noted in Case 3.

Figure 12 shows approximate Mach number contours for Cases 1, 2 and 3. These contours give some idea about the strong variation in conditions near the suction surface trailing edge which can be predicted when stream tube areas are changed by different mechanisms.

5. CONCLUDING REMARKS

A few consequences of attempts to compute the flow field in a radial cascade arrangement of blades have been studied. It is recognized that the computation has been performed using conditions which do not correspond to the real flows in radial diffusers. However, the design of radial cascade diffusers on the basis of linear cascade data correlations requires assumptions concerning effective area variation which even this limited study calls into question. Therefore any move toward better accounting for AVDR and RVDR would have positive effects. This investigation demonstrates the strong influence of the manner in which stream tube area variation is accomplished in computing the flow through blade-to-blade channels.

A great contribution to the value of future radial cascade design and analysis could be made through benchmark experiments reporting the results of flow field measurements in a typical cascade geometry.

6. REFERENCES

1. Hansen, E.C., Serovy, G.K. and Sockol, P.M. Axial-Flow Compressor Turning Angle and Loss by Inviscid-Viscous Interaction Blade-to-Blade Computation. Jour. Engrg. For Power, Trans. ASME. 102:28-34, 1980.
2. Hansen, Elmer C. Blade-Surface Boundary Layer and Wake Computational Models for Estimation of Axial-Flow Compressor and Fan Blade-Row Fluid Turning Angles and Losses. Ph.D. Dissertation, Iowa State University, Ames, Iowa. 1978. (University Microfilms Thesis 78-13230).
3. Katsanis, T. and McNally, W.D. FORTRAN Program for Calculating Velocities and Streamlines on a Blade-to-Blade Stream Surface of a Tandem Blade Turbomachine. NASA TN D-5044, 1969.
4. Albers, J. and Gregg, J. Computer Program for Calculating Laminar, Transitional, and Turbulent Boundary Layers for a Compressible Axisymmetric Flow. NASA TN D-7521, 1974.

5. Brune, G.W., Rubbert, P.E. and Nark, T.C., Jr. A New Approach to Inviscid Flow/Boundary Layer Matching. AIAA Paper 74-601, 1974.
6. Roberts, W.B. Effect of Reynolds Number and Laminar Separation on Axial Cascade Performance. Jour. Engrg. for Power, Trans. ASME. 97:261-273, 1975.
7. Carter, J.E. and Wornom, J.F. Forward Marching Procedure for Separated Boundary-Layer Flows. AIAA Jour. 13:1101-1103, 1975.
8. Klein, A. Aerodynamics of Cascades (translated and revised from Aerodynamik der Schaufelgitter by Prof. Dr-Ing. N. Scholz). AGARD-AG-220, 1977.
9. Groh, F.G., Wood, G.M., Kulp, R.S. and Kenny, D.P. Evaluation of a High Hub/Tip Ratio Centrifugal Compressor. Jour. Basic. Engrg., Trans. ASME. 92:419-429, 1970.
10. _____. Teledyne CAE Model TS-120 Turboshift Engine Program. Final Technical Report, Vol. II, TCAE Rep. No. 1161. U.S. Army Contract DA 44-009-AMC-760(T). September 1970.
11. Kenny, D.P. Supersonic Radial Diffusers. In Advanced Compressors. AGARD-LS-39-70, Paper 7, 1970.
12. Pampreen, R.C. The Use of Cascade Technology in Centrifugal Compressor Vaned Diffuser Design. Jour. Engrg. for Power, Trans. ASME. 94:187-192, 1972.
13. Erwin, J.R. and Vitale, N.G. The Radial Outflow Compressor. In Advanced Centrifugal Compressors. New York. American Society of Mechanical Engineers, 1971. pp. 56-117.
14. Sakurai, Teruo. Flow Separation and Performance of Decelerating Channels for Centrifugal Turbo-machines. Jour. Engrg. for Power, Trans. ASME. 97:388-394, 1975.

7. ACKNOWLEDGMENTS

The initial development of the computer program and test case computation reported in this paper was funded by the National Aeronautics and Space Administration through Grant Nsg-3033. Additional analysis and program improvement was supported by the Air Force Office of Scientific Research under Grant 78-3609 and Contract F49620-79-C-0002.

The authors thank these agencies and the individuals and organizations who have supplied and suggested test cases.

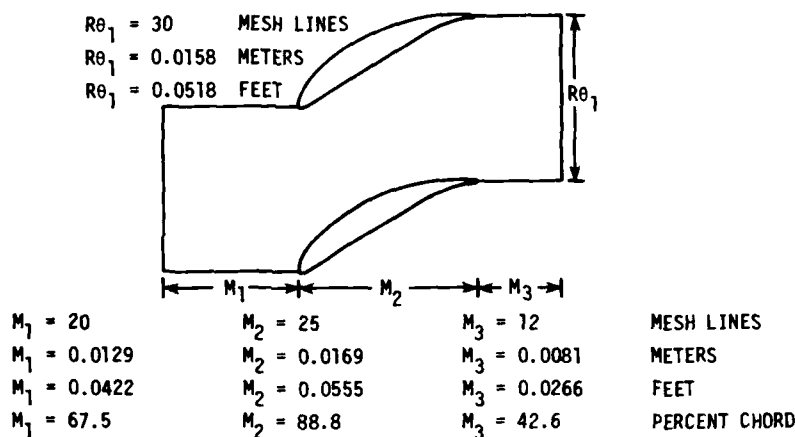


Figure 1. Geometry, calculation regions, and mesh sizes used for the 65-(18)A₁₀₋₁₅ blade cascade in axial arrangement (Cases 1 and 3), $\gamma = 27^\circ$, $\sigma = 1.24$, $c = 19.05$ mm.

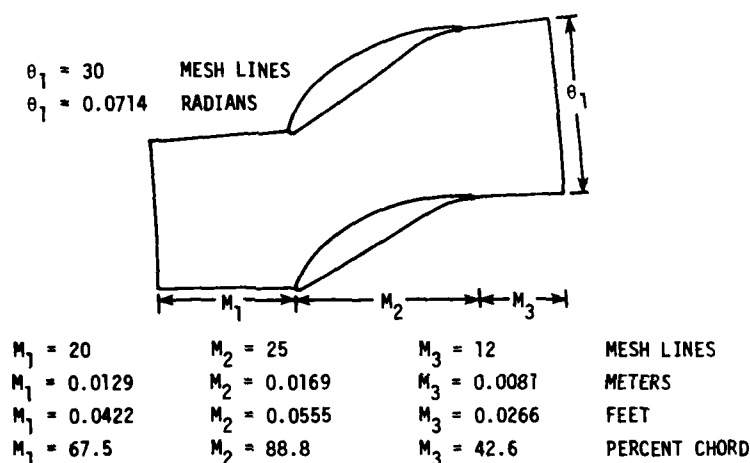


Figure 2. Geometry, calculation regions, and mesh sizes used for the 65-(18)A₁₀₋₁₅ blade cascade, in radial arrangement (Case 2), $\gamma = 27^\circ$, $\sigma = 1.24$, $c = 19.05$ mm.

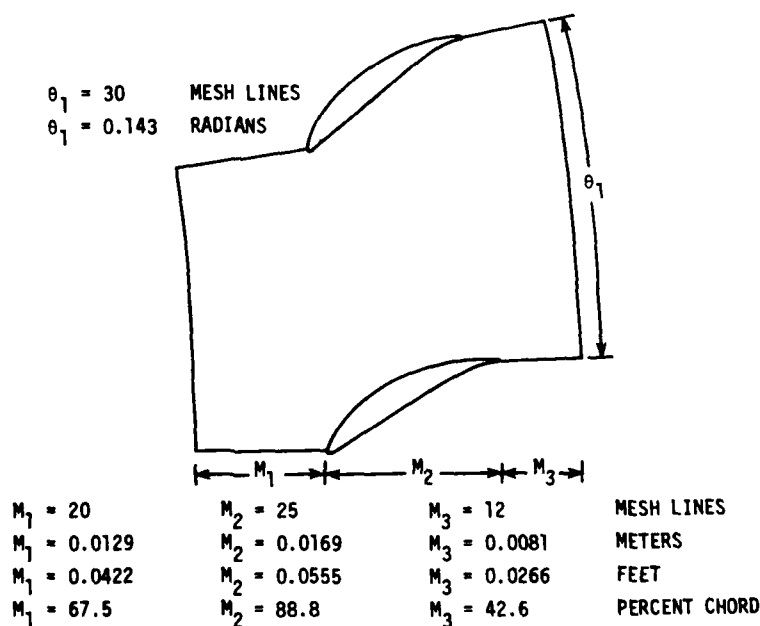


Figure 3. Geometry, calculation regions, and mesh sizes used for the 65-(18)A₁₀₋₁₅ blade cascade, in radial arrangement (Case 4), $\gamma = 27^\circ$, $\sigma = 0.62$, $c = 19.05$ mm.

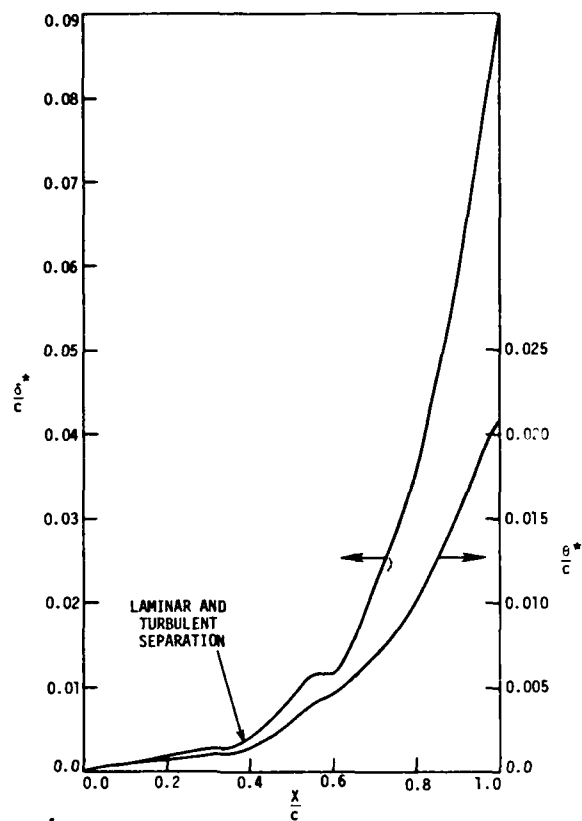


Figure 4. Calculated suction surface boundary layer for the 65-(18) A10-15 blade cascade in axial arrangement (Case 1), $M_1 = 0.43$, $Re_c = 1.7 \times 10^5$, $\beta_1 = 50^\circ$, $D = 0.540$, $\gamma = 27^\circ$, $\sigma = 1.24$, $c = 19.05$ mm, $AVDR = 1.0$.

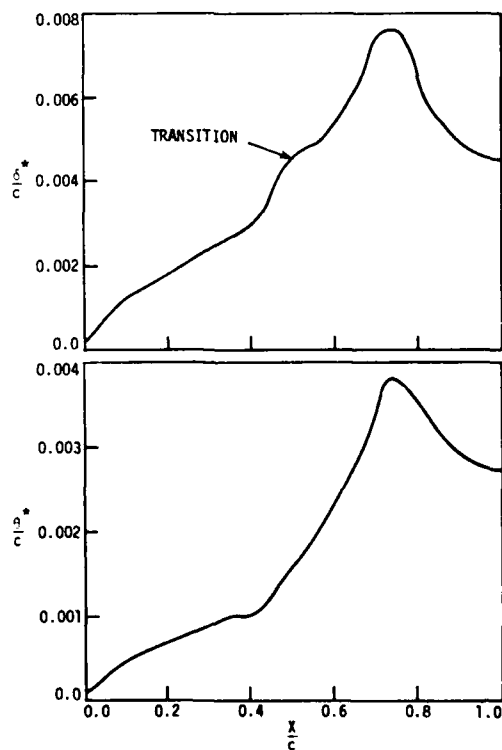


Figure 5. Calculated pressure surface boundary layer for the 65-(18) A10-15 blade cascade in axial arrangement (Case 1), $M_1 = 0.43$, $Re_c = 1.7 \times 10^5$, $\beta_1 = 50^\circ$, $D = 0.540$, $\gamma = 27^\circ$, $\sigma = 1.24$, $c = 19.05$ mm, $AVDR = 1.0$.

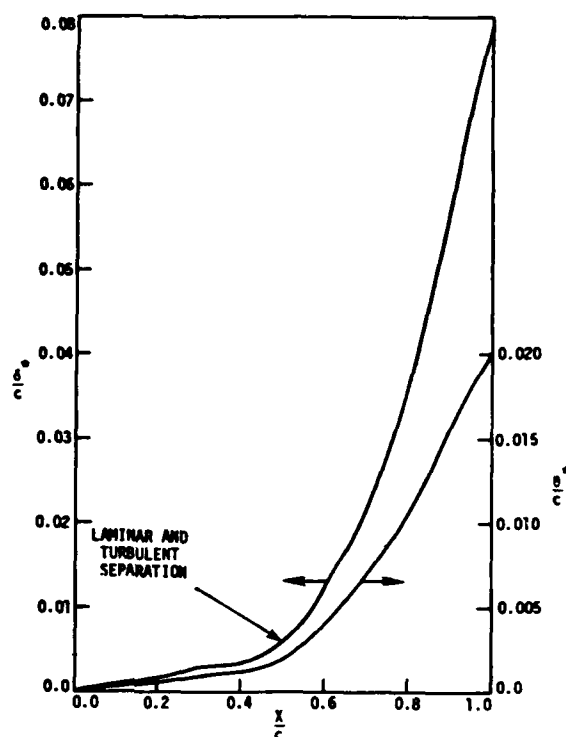


Figure 6. Calculated suction surface boundary layer for the 65-(18) A10-15 blade cascade in radial arrangement (Case 2), $M_1 = 0.43$, $Re_c = 1.7 \times 10^5$, $\beta_1 = 50^\circ$, $D = 0.687$, $\gamma = 27^\circ$, $\sigma = 1.24$, $c = 19.05$ mm, RVDR = 0.836.

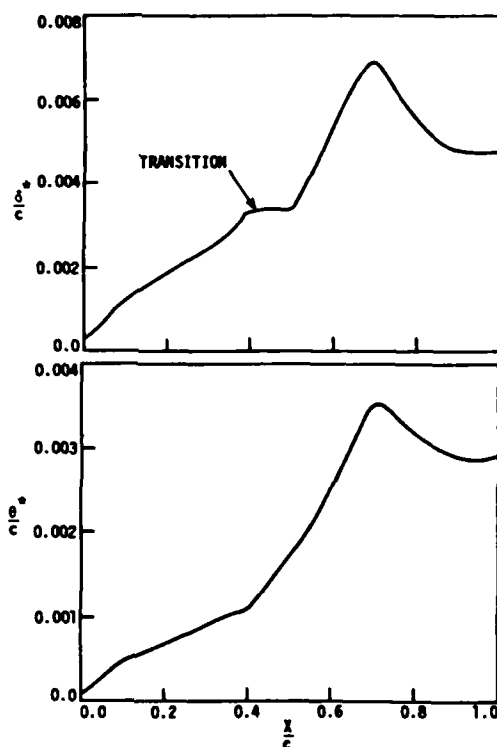


Figure 7. Calculated pressure surface boundary layer for the 65-(18) A10-15 blade cascade in radial arrangement (Case 2), $M_1 = 0.43$, $Re_c = 1.7 \times 10^5$, $\beta_1 = 50^\circ$, $D = 0.687$, $\gamma = 27^\circ$, $\sigma = 1.24$, $c = 19.05$ mm, AVDR = 0.836.

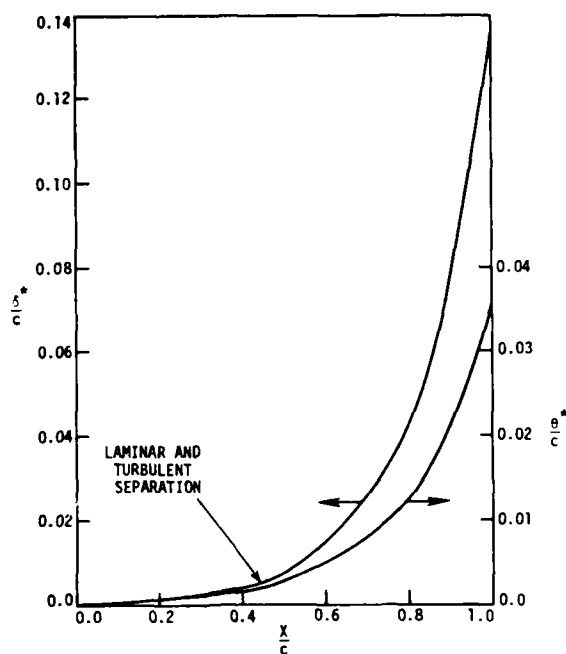


Figure 8. Calculated suction surface boundary layer for the 65-(18) A10-15 blade cascade in axial arrangement (Case 3), $M_1 = 0.43$, $Re_c = 1.7 \times 10^5$, $\beta_1 = 50^\circ$, $D = 0.630$, $\gamma = 27^\circ$, $\sigma = 1.24$, $c = 19.05$ mm, AVDR = 0.836.

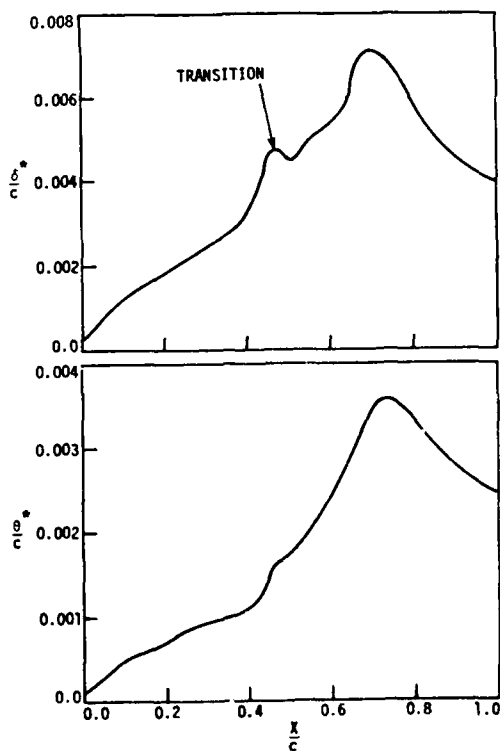


Figure 9. Calculated pressure surface boundary layer for the 65-(18) A10-15 blade cascade in axial arrangement (Case 3), $M_1 = 0.43$, $Re_c = 1.7 \times 10^5$, $\beta_1 = 50^\circ$, $D = 0.630$, $\gamma = 27^\circ$, $\sigma = 1.24$, $c = 19.05$ mm, AVDR = 0.836.

AD-A094 912

ADVISORY GROUP FOR AEROSPACE RESEARCH AND DEVELOPMENT--ETC F/G 21/5
CENTRIFUGAL COMPRESSORS, FLOW PHENOMENA AND PERFORMANCE.(U)
NOV 80

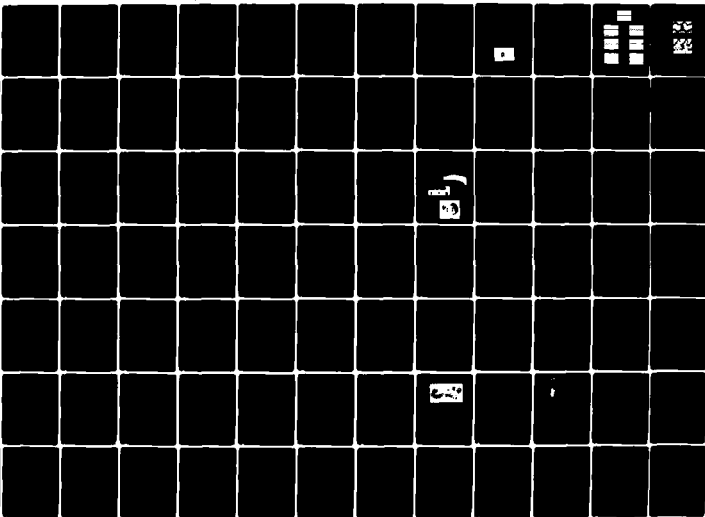
UNCLASSIFIED

AGARD-CP-282

NL

3 of 4

AG
A0949-12



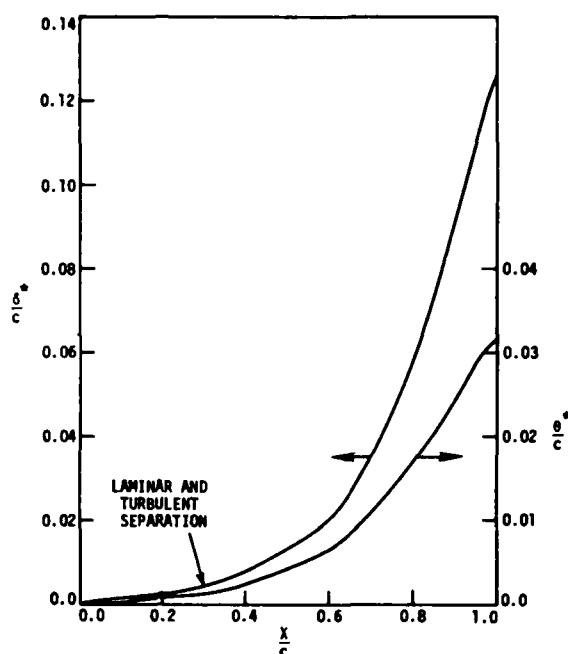


Figure 10. Calculated suction surface boundary layer for the 65-(18) A10-15 blade cascade in radial arrangement (Case 4), $M_1 = 0.19$, $Re_c = 8.6 \times 10^4$, $\beta_1 = 50^\circ$, $D = 0.766$, $\gamma = 27^\circ$, $\sigma = 0.62$, $c = 19.05$ mm, AVDR = 0.836

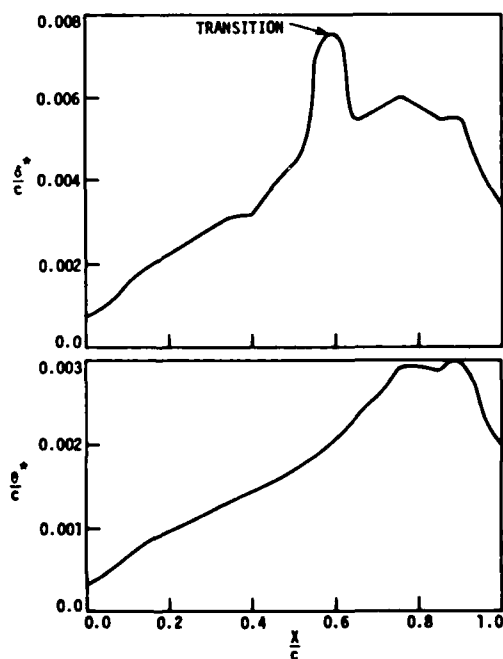


Figure 11. Calculated pressure surface boundary layer for the 65-(18) A10-15 blade cascade in radial arrangement (Case 4), $M_1 = 0.19$, $Re_c = 8.61 \times 10^4$, $\beta_1 = 50^\circ$, $D = 0.766$, $\gamma = 27^\circ$, $\sigma = 0.62$, $c = 19.05$ mm, AVDR = 0.836.

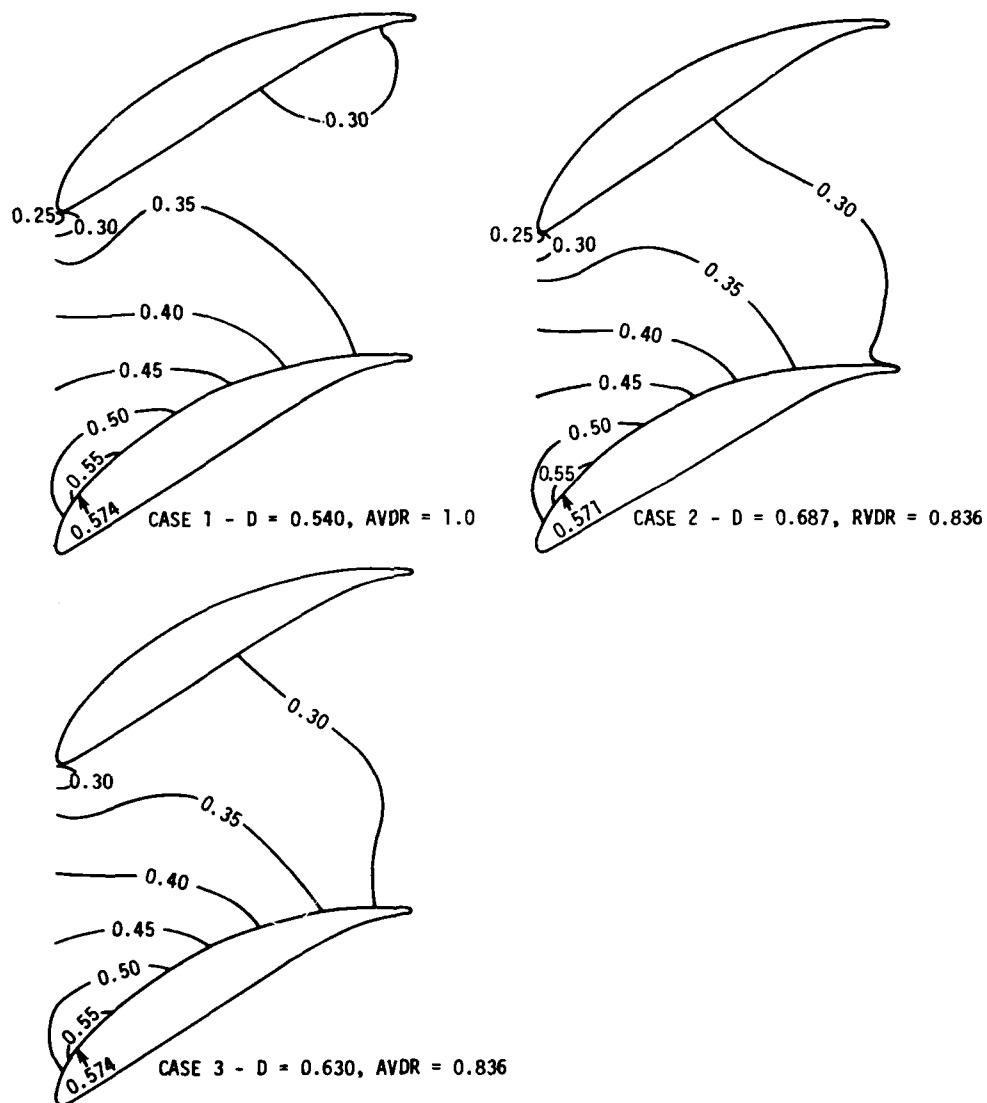


Figure 12. Lines of constant Mach number for the 65-(18) A_{10-15} blade cascade.

DISCUSSION

J.W. Raily, University of Birmingham, UK

We have carried out some calculations using a thin aerofoil theory and introducing a source distribution to allow for boundary layer growth. After separation, the free stream velocity was assumed constant and the displacement thickness determined. Subsequent loss calculations using the latter showed that mixing loss was much larger than the "profile" loss of the boundary layer. If boundary layers were allowed for by a source distribution and the inviscid calculations then repeated, the question of convergence of the process (if separation was present) occurred. A further problem (in the rotating radial impeller) arises since the source flow contains a Coriolis force which is mostly absent in the separated boundary layer, thus affecting the pressure distribution.

R.A. Novak, G.E. Company, US

Is the procedure described capable of dealing with rotation in the presence of radius change? This will certainly change the picture.

Author's Reply to both comments

The mixing loss downstream of the trailing edge is significant. If the iterative process is carried out by adding the full boundary layer thickness convergence can be a problem for separated flows.

The Katsanis program is written for a rotating blade row. The boundary layer program does not take into account rotation. We have computed no test cases involving rotating blade rows where experimental data is available for comparison.

ROTATING NON UNIFORM FLOW IN RADIAL COMPRESSORS

R.A. Van den Braembussche P. Frigne
Associate Professor Research Fellow IWONL
von Karman Institute for Fluid Dynamics
Chaussée de Waterloo, 72
B-1640 Rhode Saint Genèse, Belgium

M. Roustan
Ingénieur de Recherche et Développement
Société Creusot-Loire
BP 31 Cedex
F-71208 Le Creusot, France

SUMMARY

Rotating non uniform flow has an important impact on mechanical vibrations of compressors, especially when they are operating at high pressure level.

These rotating non uniformities have been experimentally measured by means of hot films, in centrifugal compressors of different geometry and at different Reynolds numbers. Results have been compared with other available data and theoretical predictions. These rotating instabilities can only be explained by Senoo's theory for reverse flow in radial diffusers, if a correction term in function of Reynolds number is added.

First inviscid results obtained with a time-evolutive interaction model are presented.

LIST OF SYMBOLS

b axial width of impeller or diffuser
DF diffusion factor of impeller $DF = w_2/w_1$
L impeller blade length
Leq equivalent length of impeller blade $Leq = L \frac{1+DF}{2DF}$
M absolute Mach number
m number of stall cells
N number of impeller blades
P static pressure
R radius
Reb Reynolds number with respect to diffuser width and local absolute velocity
ReR Reynolds number with respect to radius
t time
U peripheral speed
v absolute velocity
w relative velocity
X(θ) auxiliary function

 α absolute flow angle with respect to radial direction
 α_c critical absolute flow angle
 β_b impeller exit blade angle, with respect to radial direction
 ζ vorticity
 ψ stream function
 ω_{RS} rotational speed of rotating stall pattern (rad/sec)
 Ω impeller rotational speed (rad/sec)
Subscripts

1	impeller inlet	4	diffuser outlet
2	impeller outlet	R	radial direction
3	diffuser inlet	θ	tangential direction
		M	mean

1. INTRODUCTION

Flow instabilities such as rotating stall and surge are not only important because of their influence on efficiency and mass flow range, but also because they constitute a vibrational excitation, resulting in mechanical failures. The last reason becomes very important in the case of radial compressors operating at very high pressure levels (up to 300 ata) as present in reinjection or chemical processes.

Typical for these applications is the very small volume flow, resulting in low specific speed compressors and very small values of b_2/R_2 .

This study concerns mainly the prediction of rotating instabilities in vaneless diffusers with an extension to small values of b_2/R_2 .

2. PUBLISHED DATA AND THEORETICAL PREDICTIONS

Rotating instabilities in radial vaneless diffusers have been studied previously by Jansen (Refs. 1, 2), Senoo (Refs. 3, 4, 5) and Abdelhamid (Refs. 6, 7). Most of these references agree on the following conclusions:

- Instabilities occur when the absolute flow angle α reaches a critical value α_c . This value strongly depends on diffuser geometry and aerodynamic parameters.
- Generated flow instabilities extend over the whole axial width of the diffuser (Refs. 6, 7).
- Pressure fluctuations can reach about 10% of the inlet dynamic pressure (Ref. 7).
- These fluctuations can be interpreted by a stationary observer as cells of low energetic fluidum, rotating in the diffuser at a fraction of the circumferential velocity of the impeller tip (Refs. 2, 6).

In analogy to axial compressors, we shall call these rotating instabilities also rotating stall.

Comparing results of references 2 and 6 with reference 7, one observes important

- differences in
- amplitude of the pulsations,
 - number of stall cells,
 - level of propagation speed of the stall cells,
 - radial position of maximum amplitude.

It is also suggested that two different physical phenomena can be at the origin of rotating stall (Ref. 7).

Furthermore, the analytical prediction methods developed by Jansen (Ref. 2) and Senoo (Refs. 3, 4, 5) are not in agreement and lead to contradictory conclusions concerning the influence of b_3/R_3 .

A summary of geometrical parameters and flow characteristics of the published test results are listed in Table I (Test Nr 6 to 16). Because not all of these values are explicitly given in the references, some missing values had to be calculated or estimated by means of correlations or approximations (f.e., in some cases the diffuser inlet air angle α_3 was calculated by a slip factor correlation). These values are followed by an asterisk in Table I. Figure 1 shows a comparison of both analytical predictions with these experimental results.

The criterium of Senoo is confirmed by the experimental results of Senoo (Tests Nr 6, 7), of Tsurusaki (Test Nr 9) and one result of Abdelhamid (Test Nr 15).

The criterium of Jansen shows good agreement with the results of Abdelhamid if one applies a linear Mach number correction deduced from Jansen's correlation.

The discrepancy of tests 12 to 14 could be attributed to the sudden contraction at rotor exit. It is quite acceptable that this discontinuity at rotor exit could create an important flow perturbation and therefore influence the incipience of rotating stall.

Although most experimental results agree with one of the correlations, no conclusions can be drawn from this comparison. This almost suggests the existence of two distinct types of rotating stall in vaneless diffusers.

3. EXPERIMENTAL INVESTIGATION

In order to clarify this situation, and to verify also the validity of these correlations for small values of b_3/R_3 , a test program has been set up.

Four different impellers and diffusers have been designed with values of b_3/R_3 between .018 and .07 (Table I, Nr 2 to 5). The variation of channel width between rotor and diffuser is small except for compressor 5. The blade angles of the impellers are also very similar except for rotor 4.

Besides the classical measurement devices, required for overall performance and steady flow measurements, four hot film probes have also been installed in order to investigate the flow instabilities. One is placed at rotor inlet, two at diffuser inlet, at 90° on the circumference and one at diffuser exit.

These probes (Fig. 2), consisting of a platinum film diffused on a glass support, are flush mounted on the walls. The silver points on both ends connect the film to two wires inside the glass support and allow also to adjust the resistance of the platinum film. These probes are used together with a constant temperature hot wire anemometer bridge and allow to visualize the velocity fluctuations close to the wall with frequencies up to 5. kHz. The main advantage of these hot films, compared to hot wires is their resistance to shocks and dust. The output of the anemometer is connected to a dual trace oscilloscope and photographically recorded.

The overall performance curve of compressor Nr 2 is shown on figure 3 as a typical example. The dashed lines separate the zones of stable and unstable operation and the overlap indicates a zone of hysteresis. No change in pressure ratio or efficiency is observed when passing from the stable to the unstable zone.

A typical variation of the signals along a constant speed line at rotor inlet and diffuser inlet is shown on figure 4. At the diffuser inlet, the flow changes from stable, where the only oscillations are due to blade wakes (point 1) to low frequency oscillations (points 2, 3, 4) to higher frequency oscillations (points 5, 6). The amplitude of the oscillations is progressively increasing with decreasing mass flow. At this mass flow no oscillations are observed at rotor inlet, which confirms the assumption of diffuser rotating stall.

Once in surge (point 7), oscillations become irregular and appear also at rotor inlet. A phase correspondence can also be observed.

The signals of figure 5 are measured with two hot films at rotor exit. Both signals show 1/4 period phase shift at 111 Hz which indicates the presence of 3 stall cells rotating at 37 Hz or at 16% of rotor RPM (14 000).

A comparison of the instabilities at diffuser inlet and outlet is shown on figure 6. The periodic oscillations at the diffuser inlet are damped out and become quite random at diffuser outlet because the vane return channel is acting as a filter on these oscillations.

Experiments have shown two to four stall cells rotating in the diffuser at 10 to 16% of rotor RPM.

A sudden change in frequency has been observed only in compressor 5. A comparison between points 4 and 5 on figure 4 shows a jump from 45 Hz to 112 Hz. The signal frequency of 45 Hz corresponds to two cells rotating at 22.5 Hz or 9.6% of rotor RPM. The signal of 112 Hz, due to 4 stall cells, corresponds to a rotation of the cells at 28 Hz or 12% of rotor RPM.

Comparing these results with other experimental data, it turns out that in radial vaneless diffusers, the stall cells rotate at 10 to 16% of RPM.

Experimental values of the critical air angle for all the compressors of Table I are plotted against Senoo's correlation on figure 7. No attempt was made to compare our experiments with Jansen's criterium because the flow parameters of our tests are completely out of the range for which Jansen's theory has been developed.

Based on the experimental results of Senoo and the present authors, one would tend to conclude that Senoo's correlation is valid only for values of b_3/R_3 larger than .05, and

that below .05 the critical air angle slightly increases again.

However, the situation becomes much more difficult if one also includes the experimental results of Abdelhamid and the unpublished result of the University of Gent (RUG). Furthermore, compressor Nr 3 has also been tested under real conditions (multistage at 200 ata). Rotating stall has been observed at $90^\circ - \alpha_c = 6.3^\circ$ (Test Nr 1).

Based on theoretical calculations, it was stated by Senoo that for narrow diffusers, the Reynolds number has no influence on critical flow angle. However, observing the experimental results, the authors found out that Re_{B_3} must have an influence on diffuser stability.

Figure 8 shows the difference between measured critical flow angles and the one predicted by Senoo as a function of Re_{B_3} . This figure contains all the available experimental data of Table I.

At low Reynolds numbers (below 10^5) a clear tendency of Re_{B_3} influence can be seen (represented by a full line). At higher Reynolds numbers, tests Nr 17 and 19 suggest a continuous influence of Re_{B_3} on critical flow angle. However, test Nr 1 does not indicate any further decrease in critical flow angle. Although this discrepancy could be explained by a different influence of Re_{B_3} on wide or narrow diffusers or by a roughness effect, the authors feel that not enough experimental data are available to draw a definite conclusion. A possible correction is therefore shown by a dashed line.

This Re_{B_3} correction (full line and dashed line) is then applied to all experimental data (except Nr 1) to define the equivalent diffuser critical flow angle α_c^E at $Re_{B_3} = 10^5$. Results are plotted against Senoo's correlation on Fig. 9. The good agreement of most of the points confirms the validity of Senoo's correlation at $Re_{B_3} = 10^5$. Concerning the somewhat larger disagreement for tests Nr 5, 8, 12 and 13, one should keep in mind that they are obtained with an important discontinuity at rotor exit. The value for test Nr 10 is outside the figure. It should, however, be controlled if the available experimental data are correctly interpreted in this study and if the stabilities are of the diffuser rotating stall type. For test point Nr 10, the measured frequency is only 3% of rotor RPM, which is much lower than in all the other experiments.

The discrepancy observed for test point Nr 16 could be attributed to the larger radius ratio ($R_4/R_3 = 1.8$). Both Senoo and Jansen agree that an increasing radius ratio can influence the diffuser stability.

Taking into account the difficulties in measuring correctly the diffuser flow angle, one can conclude that Senoo's correlation, together with a correction for Re_{B_3} gives a good prediction of diffuser critical flow angle.

4. THEORETICAL APPROACH

Previous experimental and theoretical work gives only a limited answer to this problem because they do not give any information on speed of propagation, wave shape or number of cells. A theoretical research program has therefore been initiated, to analyze this problem in a more fundamental way. At the present state, this model is far from complete, nevertheless, some indications about some aspects of the problem can already be obtained.

The instationary and viscous behaviour of the phenomenon does not allow many simplifications of the three dimensional Navier-Stokes equations. The problem can be simplified in a drastical way by confining it to the definition of a stability criterium for the diffuser flow (Refs. 2 and 8). In this case the amplitude of the instabilities is supposed to be very small so that the equations of motion can be linearized in the vicinity of the operation point investigated. By means of the well-known stability analysis techniques for linear systems, it is then possible to deduce the critical inlet flow angle α_{c_3} , for which the main flow becomes unstable. The number of cells is then determined from the wavelength of the perturbations.

However, the prediction of the amplitude of the pulsations, the evolution of the wave form and the change in number of stall cells is beyond the scope of the linear techniques. These last parameters are nevertheless very important if one intends to determine the influence of rotating stall on the aerodynamic performances and mechanical excitation of the compressor system.

A significant approach requires the preservation of the non linear form of the equations of motion. However, to keep the problem mathematically tractable, we use the basic hypothesis that the dynamic features which allow the oscillations are associated with the inviscid diffuser main flow. The boundary layers in the impeller or along the diffuser walls are interpreted as destabilizing influences. In this way it is possible to fulfil the conditions for the generation of self-excited vibrations, namely, the presence of

- an exciting system : the impeller blade- or diffuser wall boundary layers
- a responding system : the diffuser main flow core.

This basic hypothesis allows a simplification of the problem, as well with regard to the viscosity effect as to the number of dimensions.

Attributing all viscous influences to the boundary layers, the main flow in a radial vaneless diffuser can be investigated using the incompressible, two dimensional Euler equations in cylindrical coordinates.

Introducing the vorticity ζ

$$\zeta = \frac{1}{R} \frac{\partial v_\theta}{\partial R} - \frac{v_\theta}{R} \frac{1}{R} \frac{\partial R}{\partial \theta} \quad (1)$$

and stream function ψ

$$v_r = \frac{1}{R} \frac{\partial \psi}{\partial \theta}$$

$$v_\theta = - \frac{\partial \psi}{\partial R}$$

the Euler equations reduce to a hybrid set of equations.

- The hyperbolic vorticity transport equation :

$$\frac{\partial \zeta}{\partial t} + v_R \frac{\partial \zeta}{\partial R} + \frac{v_\theta}{R} \frac{\partial \zeta}{\partial \theta} = 0 \quad (4)$$

- The elliptic Poisson equation :

$$\frac{\partial^2 \psi}{\partial R^2} + \frac{1}{R} \frac{\partial \psi}{\partial R} + \frac{1}{R^2} \frac{\partial^2 \psi}{\partial \theta^2} = - \zeta \quad (5)$$

These equations cannot be solved simultaneously as it is done with a time marching procedure for completely hyperbolic systems. These equations have to be solved alternatively and the right hand side of the Poisson equation is determined by the solution of the vorticity equation. v_R and v_θ in equation (4) are deduced from equation (5) via equations (2) and (3).

The diffuser inlet flow conditions are determined by the impeller response. An extension of the theory of Adamczyk (Ref 9) for loss free, straight bladed impellers with no exit slip allows to define following equations for the unsteady behaviour.

$$\frac{\partial v_{R_2}}{\partial t} + \frac{U_2}{R_2} \frac{\partial v_{R_2}}{\partial \theta} = X(\theta) \quad (6)$$

$$\frac{\partial X(\theta)}{\partial \theta} + R_2 \frac{\text{tg} \beta_{2b}}{L_{eq}} X(\theta) = \frac{R_2 v_{R_2} \zeta_2}{L_{eq}} \quad (7)$$

$$v_{\theta_2} = U_2 - v_{R_2} \text{tg} \beta_{2b} \quad (8)$$

The set of equations (6), (7) and (8) gives the diffuser inlet flow velocities, v_{R_2} and v_{θ_2} , as inlet boundary conditions for equations (4) and (5) while the solution of equations (4) and (5) defines the vorticity ζ_2 as an exit boundary condition for the impeller in equations (6), (7) and (8). Both systems must be solved in a coupled way.

Based on the experimental conclusion that rotating stall also occurs in vaneless diffusers with an atmospheric exit, the diffuser outlet boundary condition is defined as :

$$\left. \frac{\partial P}{\partial \theta} \right|_{R=R_L} = 0 \quad (9)$$

At the actual state of development, the program does not yet contain any boundary layer triggering system as required by the basic hypothesis. Prior to this, more basic research is necessary to find a suitable model for the dynamic behaviour of the boundary layers along the diffuser walls. However, by introducing an artificial velocity perturbation, one can already study some characteristics of the unsteady swirling flow in vaneless diffusers. This artificial velocity perturbation must satisfy the following conditions :

- the perturbation must be compatible with the boundary conditions;
- the perturbation must satisfy continuity.

The easiest way to satisfy both conditions is to perturb the streamlines in a limited zone as shown on figure 10a. The shape of the perturbation is defined by a sinusoidal shift of streamlines with respect to the free vortex flow. This locally perturbed flow field is used as initial condition for the solution of equations (4) and (5).

Figure 10b shows a computed flow field at time level 5, resulting from the single velocity perturbation of figure 11a. The streamline distribution clearly contains a zone of back flow, bounded in the tangential direction by a region of high speed radial flow. One can conclude that a single perturbation of a homogeneous diffuser flow leads to a rearrangement of the streamline pattern in high - and low speed "zones".

Furthermore, this cells are not stationary but propagate in tangential direction as indicated on figure 11. The tangential shift of the radial velocity distribution at radius $(R_4+R_3)/2$ between time level $t = 0$ and $t = 5$ allows to calculate the propagation speed relative to the rotor. The corresponding value of $\omega_{RS}/\Omega = .143$ corresponds fairly well with the experimentally observed values. Important is also that this confirms the basic hypothesis, namely that rotating stall in radial vaneless diffusers is mainly a potential core instability, triggered by viscous effects.

REFERENCES

1. JANSEN, W.: Steady fluid flow in a radial vaneless diffuser.
ASME Transact., Series D : J. Basic Engrg, Sept. 1964, pp 607-619.
2. JANSEN, W.: Rotating stall in a radial vaneless diffuser.
ASME Transact., Series D : J. Basic Engrg, Dec. 1964, pp 750-758.
3. SENOO, Y.; KINOSHITA, Y.; ISHIDA, M.: Asymmetric flow in vaneless diffusers of centrifugal blowers.
ASME Transact., Series I : Jnl Fluid Engrg, March 1977, pp 104-114.

4. SENOO, Y. & KINOSHITA, Y.: Influence of inlet flow conditions and geometries of centrifugal vaneless diffusers on critical flow angle for reverse flow. ASME Transact., Series I : J. Fluids Engrg, March 1977, pp 98-103.
5. SENOO, Y. & KINOSHITA, Y.: Limits of rotating stall and stall in vaneless diffuser of centrifugal compressors. ASME Paper 78 GT 19.
6. ABDELHAMID, A.M.; COLWILL, W.M.; BARROWS, J.F.: Experimental investigation of unsteady phenomena in vaneless radial diffusers. ASME Paper 78 GT 23.
7. ABDELHAMID, A.M. & BERTRAND, J.: Distinction between two types of self excited gas oscillations in vaneless radial diffusers. ASME Conference on Gas Turbine Power, San Diego, March 1979.
8. YERSHOV, V.N.: Unstable conditions of turbodynamic rotating stall. FTD MT 24-04-71; AD 731 355.
9. ADAMCZYK, J.J.: Unsteady fluid dynamics response of an isolated rotor with distorted inflow. AIAA Paper 74-49.

Acknowledgements

The experimental work described in this paper is part of a research project at VKI and has been sponsored by the Société Creusot-Loire.

The authors wish to express their gratitude to the Société Creusot-Loire for the permission of publishing these data.

TABLE I

TEST NR	REFERENCE	R_2 (m)	b_2/R_2	N	β_{2b}	RPM	b_1/R_1	R_1/R_2	$90-\alpha_c$	Re_{b_1}	M	$\frac{m \cdot R_s}{..}$
1	Creusot-Loire &	.1142	.0184	11	68	14000	.0175	1.55	6.4	$1.7 \cdot 10^6$.25	.138
2	von Karman	.1142	.0313	11	68	14000	.0306	1.55	9.3	$3.1 \cdot 10^6$.39	.215
3	Inst.	.1142	.0184	11	68	14000	.0175	1.55	10.4	$1.1 \cdot 10^6$.25	.428
4		.1142	.0832	19	45	14000	.0701	1.55	10.3	$7.0 \cdot 10^6$.38	.420
5		.1142	.0412	17	65	14000	.0212	1.55	10.3	$2.0 \cdot 10^6$.27	.19/.4
6	Senoo	.250	.056	18	41.5		.056	1.80	9.4	$6.7 \cdot 10^{6*}$.20	
7	Ref. 5	.250	.056	18	41.5		.076	1.80	10.5	$9.1 \cdot 10^{6*}$.20	
8		.250	.056	18	41.5		.040	1.80	9.7	$4.8 \cdot 10^{6*}$.20	
9	Tsurusaki Ref. 5				65		.130	2.25	12.2		.20	
10	Abdelhamid	.235					.063	1.51	21.1	$1.5 \cdot 10^{6*}$.035*
11	Ref. 6	.305					.130	1.52	9.6	$6.0 \cdot 10^{6*}$.098*
12	Abdelhamid	.1175	.152	10	27	5000	.076	1.55	15.5*	$3.2 \cdot 10^{6*}$.71/.98
13	Ref. 7	.1175	.152	10	27	5000	.090	1.55	15.0*	$3.7 \cdot 10^{6*}$.34/.57/.95
14		.1175	.152	10	27	5000	.108	1.55	13.9*	$4.3 \cdot 10^{6*}$.32/.65
15		.1175	.152	10	27	5000	.128	1.55	13.5*	$4.9 \cdot 10^{6*}$.135*	.31/.82/1.0
16	Abdelhamid Ref. 7	.1175	.152	10	27	5000	.128	1.83	17.4*	$4.6 \cdot 10^{6*}$.127*	.49/.65
17	U. Gent (unpubl.)	.208	.077	20	0	5600	.077	1.62	7.9	$1.4 \cdot 10^6$.37	.31

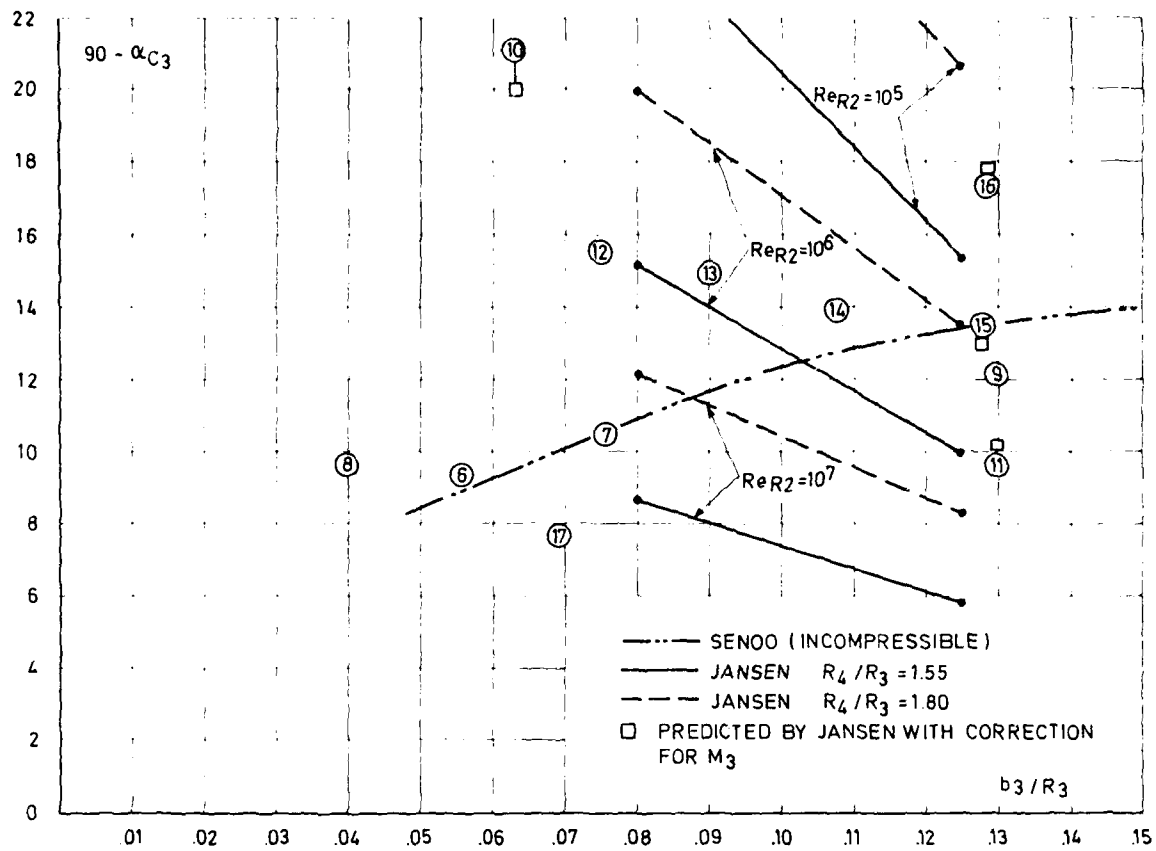


Figure 1



Figure 2

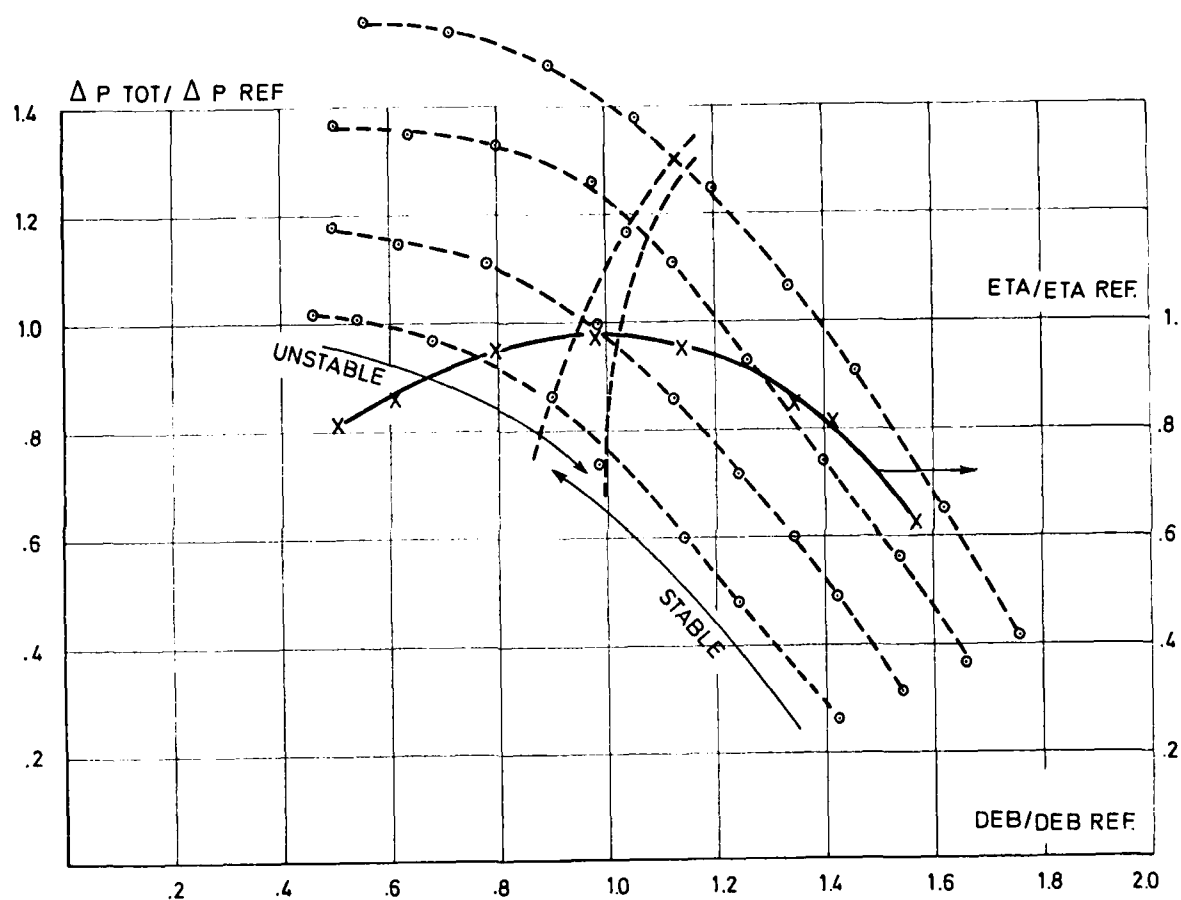


Figure 3



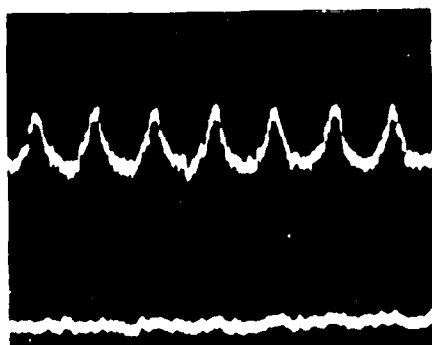
POINT 1



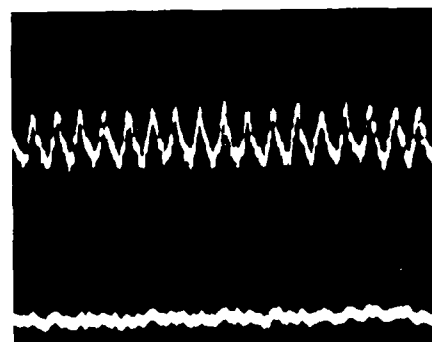
POINT 2



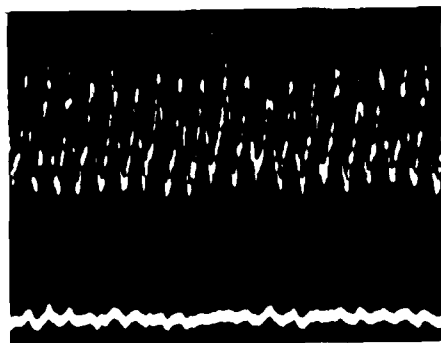
POINTS 3



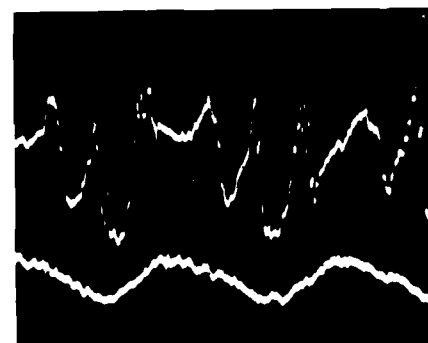
POINT 4



POINT 5



POINT 6



POINT 7

Figure 4

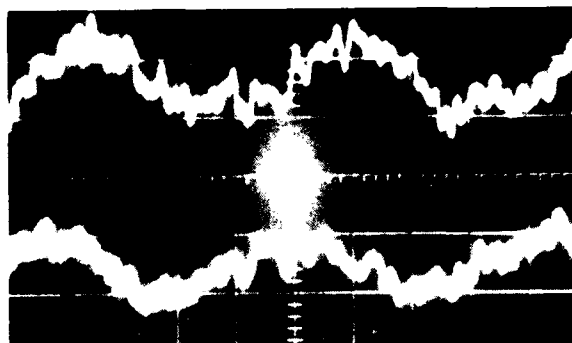


Figure 5

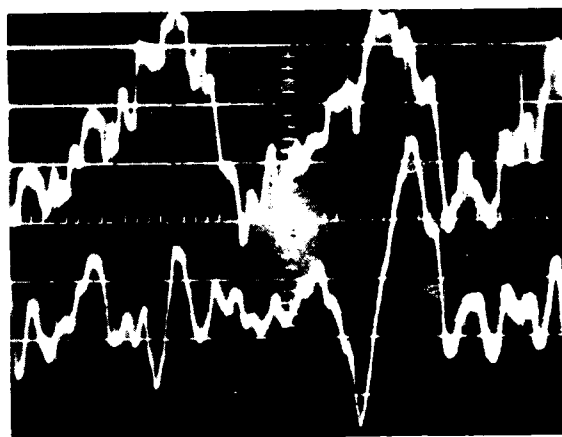


Figure 6

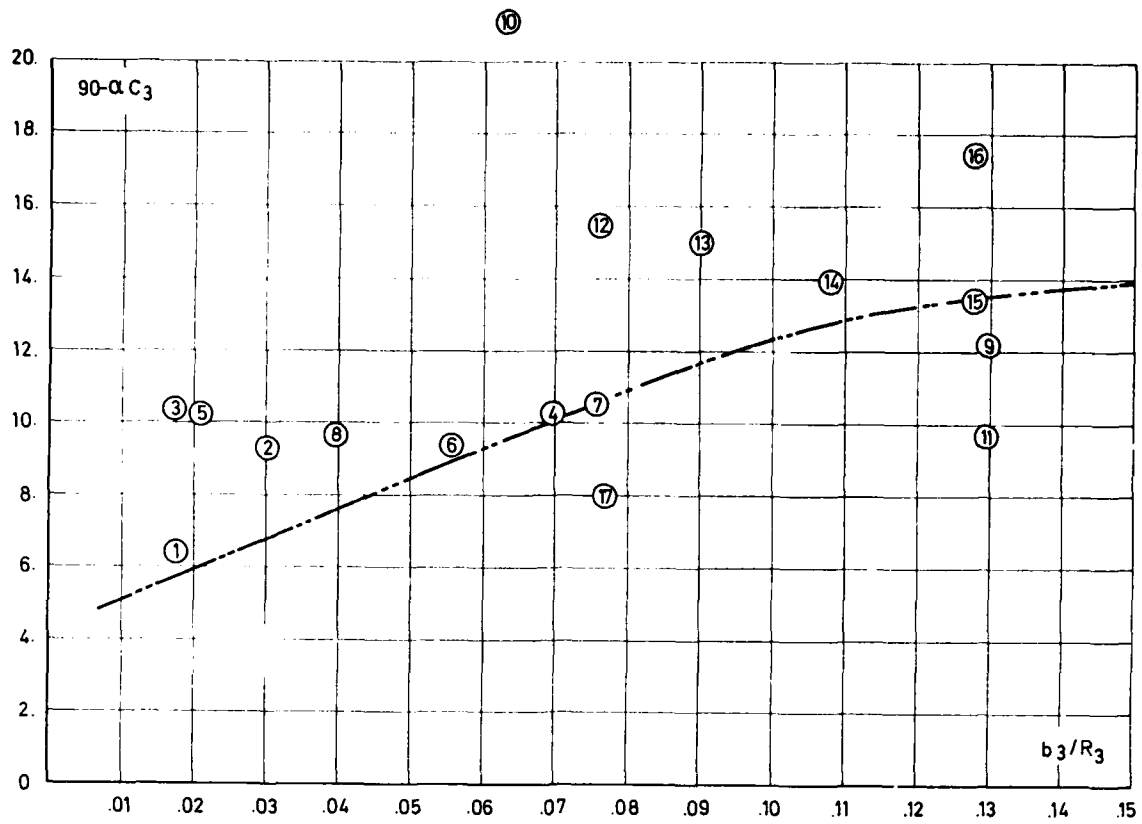


Figure 7

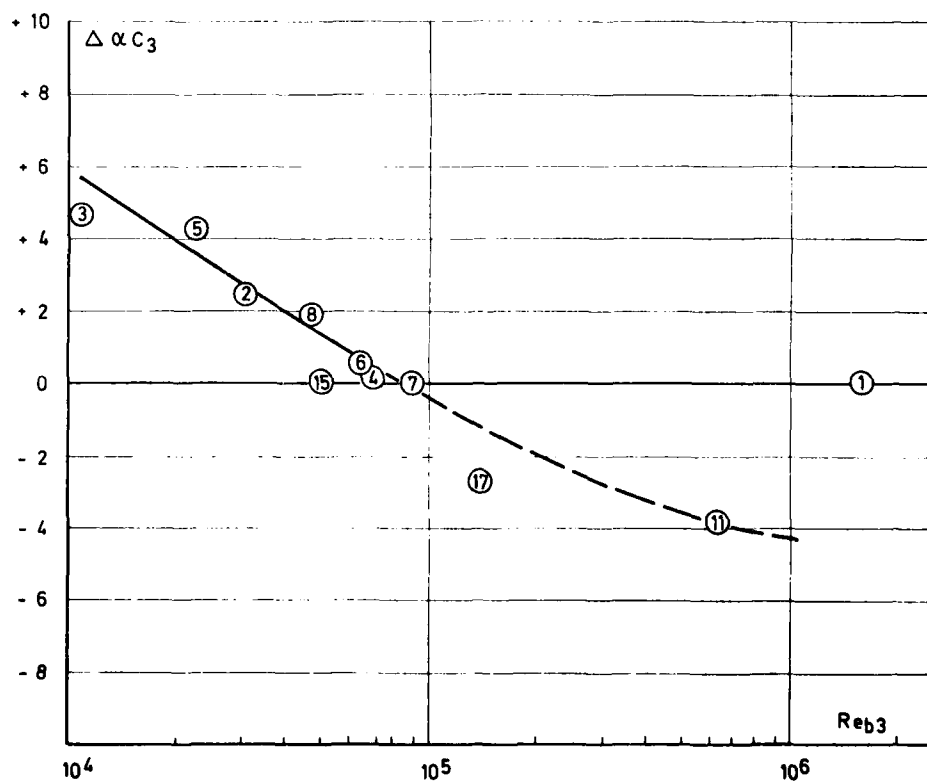


Figure 8

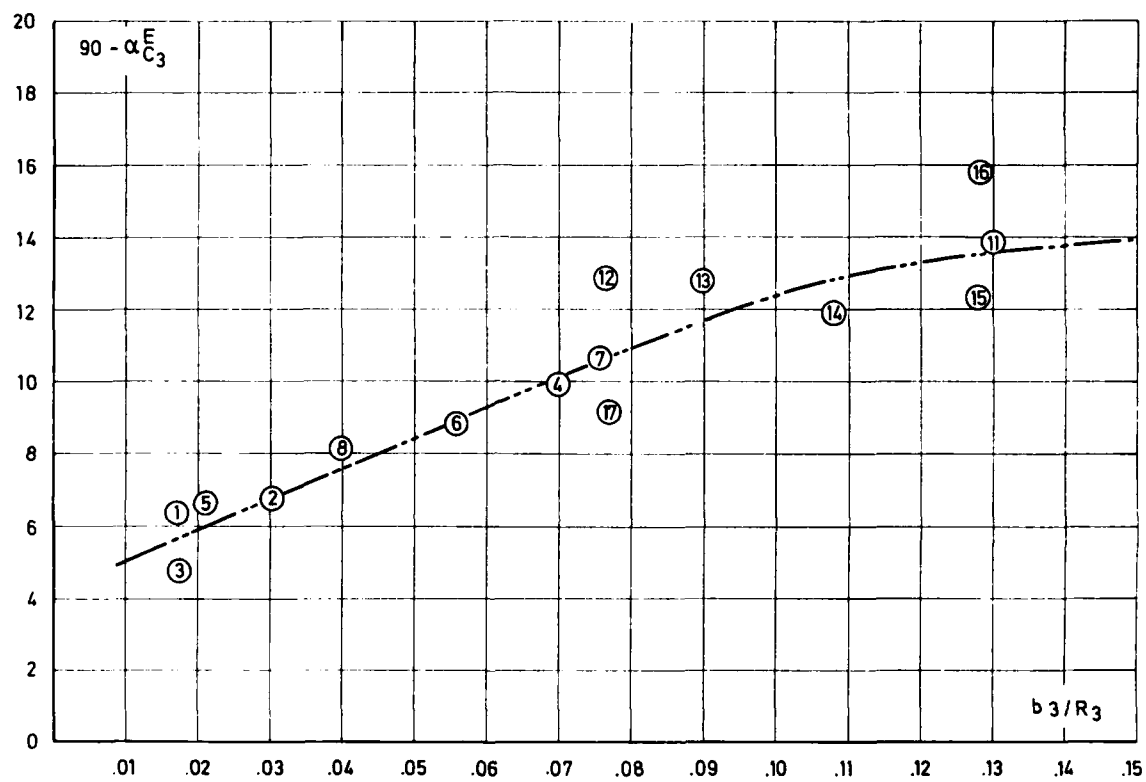
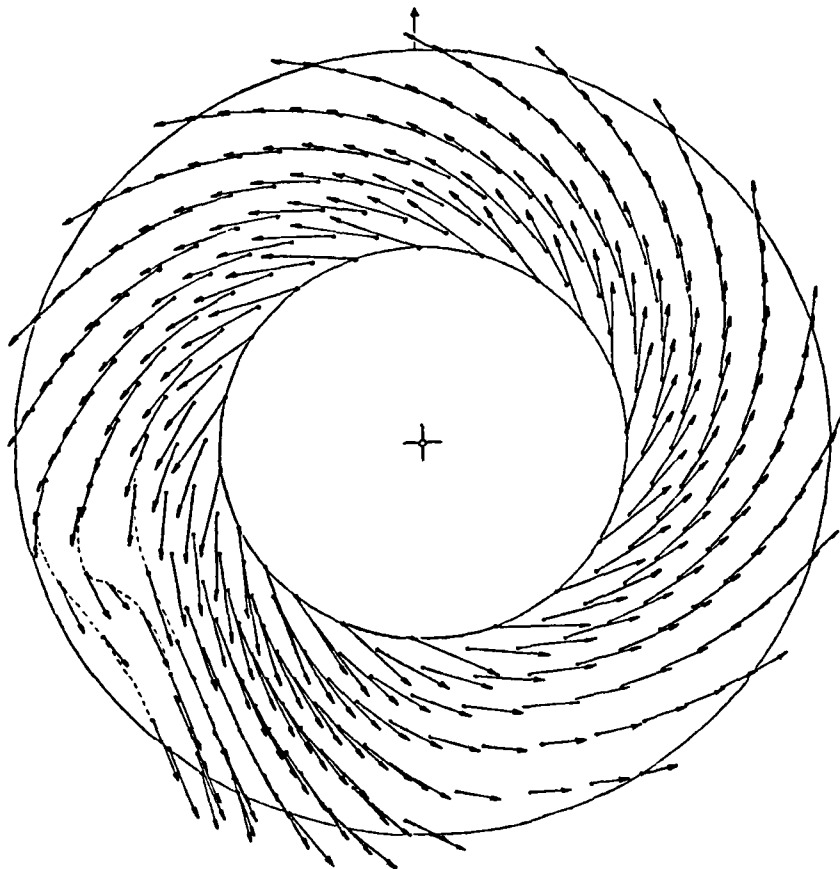
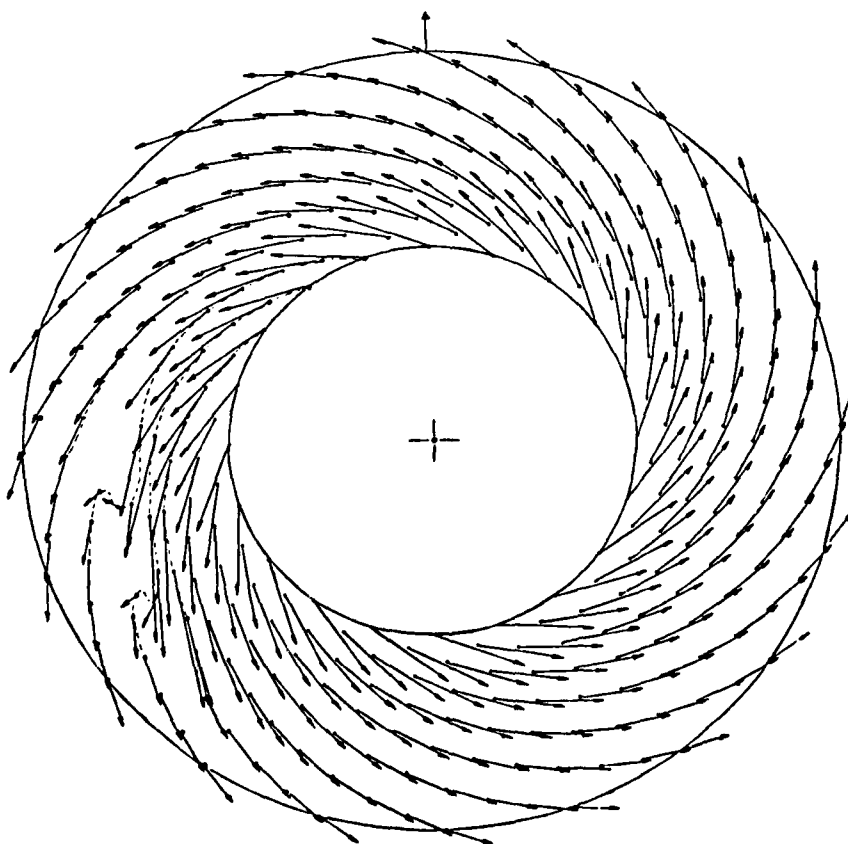


Figure 9



FLOW FIELD RESPONSE AT $t=5$

Figure 10b



INITIAL PERTURBATION ($t=0$)

Figure 10a

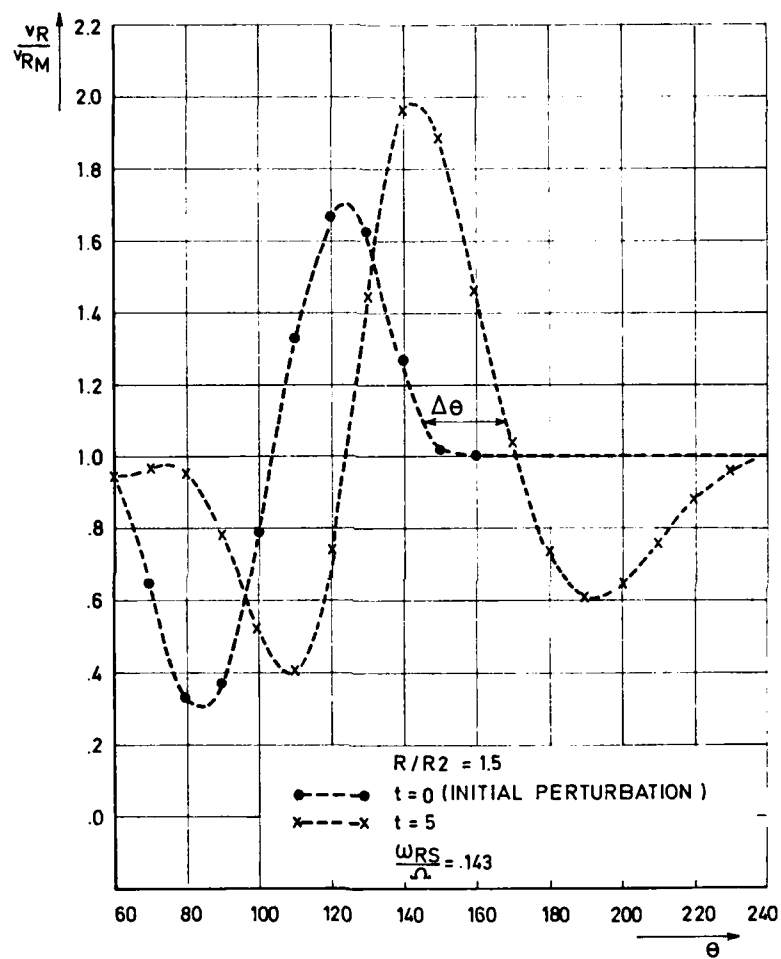


Figure 11

DISCUSSION

H.Weyer, DFVLR, Cologne, Ge

Is the prediction of rotating stall based on Senoo's correlation only valid for the design speed of the compressor or also for off-design conditions?

Author's Reply

Senoo's correlation or analytical prediction accounts for the variation in rotor speed only through the variation of parameters like diffuser inlet flow angle, Mach number, or by a change in flow non-uniformity at diffuser inlet. It does not indicate a direct influence of RPM on rotating stall.

Y.Ribaud, ONERA, Fr

When the rotating stall appears in the diffuser have the authors observed a back-flow with pre-rotation in the entry region of the impeller? Pre-rotation can easily explain the measurement of static pressure being equal to the stagnation pressure upstream of the impeller.

Author's Reply

We have measured the flow at the inlet to the impeller with the help of a hot film probe. The results are presented in Figure 4 and one can not see any perturbation at the inlet of the inducer except for point 6.

D.Japikse, CREARE, US

Could the author explain how the flow angle was measured.

Author's Reply

The flow angle was not measured. It was calculated from the temperature rise across the impeller.

C.Rodgers, Solar, US

We have observed differences between our results at Solar and Senoo's results, observing exactly opposite trends in critical flow angle. But in order to make sense of this type of measurement one should take results from more than one impeller.

Author's Reply

The experiments described in the paper were made with similar impellers but the sweep-back angles were different.

THE INFLUENCE OF DIFFUSER INLET PRESSURE FIELDS ON THE
RANGE AND DURABILITY OF CENTRIFUGAL COMPRESSOR STAGES

By
David Japikse
President, Fluid Machinery Division
Creare Incorporated
Box 71
Hanover, New Hampshire 03755
United States

SUMMARY

An anomalous range characteristic of two stages differing only in diffuser passage number has led to this study. Pressure field data in the diffuser inlet region was carefully examined and a strong shock pressure recovery system was discovered when a low diffuser number is used and a mild shock recovery process resulted when a large diffuser number was employed. When strong shocks were present, it was found that a leading shock set up a subsequent accelerating flow field which stabilized a second shock. In turn, the second shock contributed substantially to the static pressure recovery process in the diffuser inlet region. The combined effect was a highly stabilized flow field, in agreement with the Kantrowitz¹ shock stabilization criterion. By contrast, the strong shock system contributed to a loss in total pressure of up to 2% of the total pressure rise in the stage. Two different stages are discussed where mechanical failure occurred. These cases may be related to the strong shock system of the diffuser inlet region closely coupled to the impeller blade tips.

NOMENCLATURE

AR area ratio
L/D₄ length to throat diameter ratio
m referenced mass flow
M Mach number
N; N_D speed; design speed
p static pressure
p₀ stagnation pressure
p* critical pressure corresponding to p₀₂* (p*=0.526 p₀₂*, assuming perfect gas behavior)
pr stage pressure ratio
r radius
R radius ratio, r/r₂
T static temperature
T₀ stagnation temperature
u wheel speed
2θ diffuser divergence angle
Δ2θ diffuser divergence parameter differenced to show location relative to transitory stall
ρ density

Subscript
TS total-to-static
0 inlet, 2 impeller tip, 2* mixed out tip, 3 diffuser leading edge, 4 diffuser throat

Superscript
^ measured value

1 INTRODUCTION

This investigation was motivated by a careful study of the anomalous range characteristics of the two compressor stage evaluations shown in Figure 1a. The two stages were essentially identical except for a factor of two difference in the number of diffuser passages. The resulting aerodynamic difference was so astounding that it motivated a long term investigation which involved many different stages from several different Creare clients. Peculiar also to the problem was the fact that several impellers failed, possibly for causes that are interconnected with the basic range characteristics.

2 THE ANOMALOUS STAGE

The stages whose overall aerodynamic characteristics are presented in Figure 1a are typical small gas turbine stages with pr=5 and design mass flow in the range of 4 to 5 lbm/sec. They involve state-of-the-art technology impellers with a blade backsweep angle of 28°. These particular stages use conical diffusers such that the region preceding the throat is of a conical section leaving cusps on both the front cover and rear cover of the well known "swallow-tail" configuration. Past the diffuser throat the passage is a simple conical diffuser. The spacing between the diffuser leading edge (cusp) and the impeller tip is characterized by a radius ratio of 1.064 for the A1 stage and by 1.033 for the A2 stage. In other words, these stages are similar to many industrial stages. Exactly the same impeller was used for both test stages shown in Figure 1a, and, further, they have exactly the same inlet and the same collector system. Hence it is clear that a significant fluid dynamic process must be altering the performance characteristics of the stage and that this process must be a function of the diffuser number.

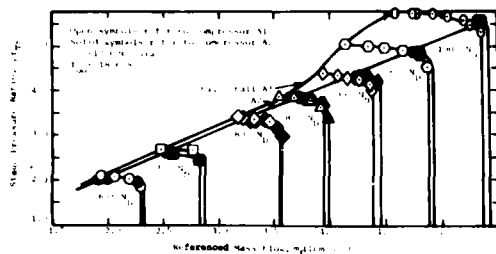


Figure 1a. Comparison of compressors A1 and A2 operating maps; same impeller for each stage except A1 has 17 diffuser pipes and A2 has 34 diffuser pipes.

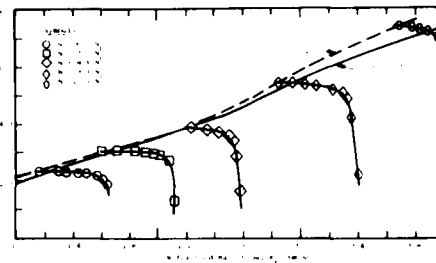


Figure 1b. Comparison of compressors B1 and B2 operating maps; same impeller for each stage except B1 has 19 diffuser vanes and B2 has 31 diffuser vanes.

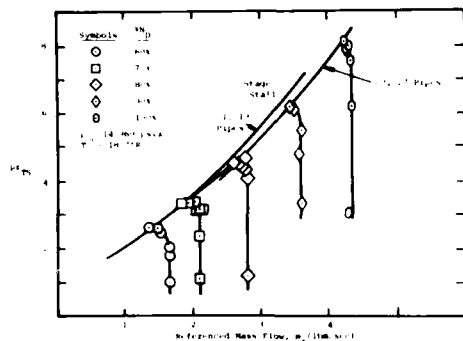


Figure 1c. Comparison of compressors C1 and C2 operating maps; same impeller for each stage except C1 has 19 diffuser pipes and C2 has 27 diffuser pipes.

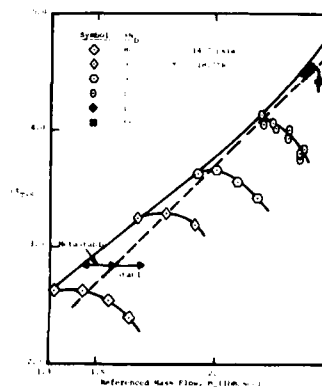


Figure 1d. Compressor D stage showing transonic surge line kink at $pr=4.2$ or 4.3 .

Table 1 Dimensional Comparison

Stage	Number of Pipes	$\frac{29}{AR}$	$\frac{L/D_4}{AR}$	$\frac{L/D_4}{AR}$
A1	17	6.01	2.5	5.6
A2	34	4.44°	2.58	7.5

The diffuser is different in that twice as many diffuser passages are employed, but there are further similarities in the diffusers as indicated in Table 1. We see that they have very nearly identical area ratio. Further they have virtually the same diffuser throat area (a small difference in throat area accounts for the different choke-lines on Figure 1a). There are, however, differences in the divergence angle of the diffuser and length-to-diameter ratio across which the area ratio is achieved. However, the biggest single difference must lie in the fact that the wedge angle of the diffuser inlet system obviously differs by a factor of two in the two configurations. Still, these differences are not sufficiently great that one can immediately appreciate the difference in the two stages shown in Figure 1a; instead, we must look carefully at the basic aerodynamic characteristics of the two stages.

3 AERODYNAMIC EVALUATION OF SHOCK ENHANCED RANGE

The general impeller tip aerodynamic characteristics are substantially the same between the two stages, A1 and A2, at least as far as can be deduced from rather simple impeller tip static pressure and diffuser throat total pressure instrumentation. The only unusual characteristic was the comparatively low value of C_{p2*-4} (static pressure recovery coefficient between the impeller mixed-out reference state and the diffuser throat). This value is comparatively low along the surge line, being 0.12 to 0.22 for speeds of $85\% N_D$ or less for both stages and about the same for higher speeds for the A2 stage. By contrast, the value of C_{p2*-4} rose to a peak of 0.48 for the A1 stage for speeds greater than $85\% N_D$, which compares quite favorably with conventional values associated with stage stall (see for example Kenny²). Thus the survey of geometric differences and aerodynamic differences has pointed to the diffuser inlet region, where the stage-stall values of C_{p2*-4} are different and where we encounter the largest single geometric difference: the diffuser inlet wedge angle differs by a factor of 2. These differences encourage us to take a careful look at the flow field characteristics in the region between the impeller tip and the diffuser throat.

For the A1 and A2 stages substantial pressure tap data is available in the vaneless and semivaneless space between the impeller tip and diffuser throat. Later, some similar data for the D stage is also presented. Much of this data was taken both from the front cover and rear cover, but only the front cover data is shown herein (the rear cover data matched rather closely the front cover information). A series of comparative pressure field surveys for the A1 and A2 stages are shown in Figures 2 through 7. In each case, the first figure refers to the A1 stage and the second figure refers to the A2 stage.

It is interesting to first consider Figures 2 and 3 showing results along the 100% speed line. Figure 2 shows the results close to surge whereas Figure 3 shows results close to choke. An approximate diffuser center streamline is sketched into the figures for reference. The configuration with the small number of diffusers (stage A1, 17 passages) shows very strong pressure field distortions and it appears that a typical fluid particle will probably pass through about two shocks before entering the diffuser throat. For the A2 stage (34 passages) it is possible that the fluid particle may pass through three shocks and the distortions are comparatively mild. For the case close to choke, distortions are still greater for the A1 stage than the A2 stage, but the shock structure which

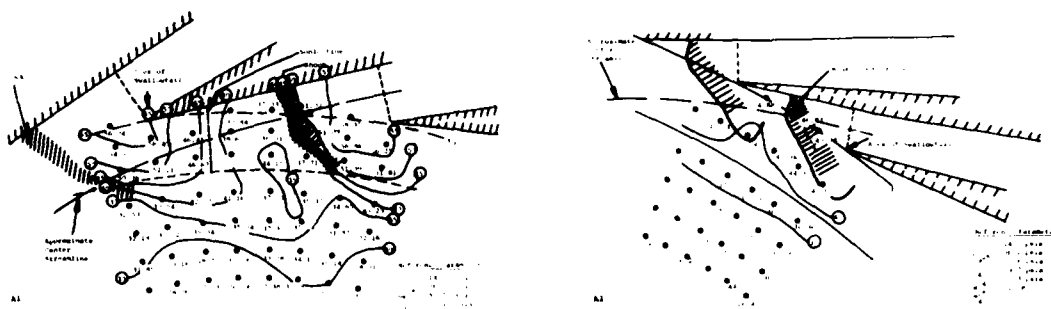


Figure 2. Pressure contour comparisons for the A1 & A2 stages at 100% N_D . Near Surge

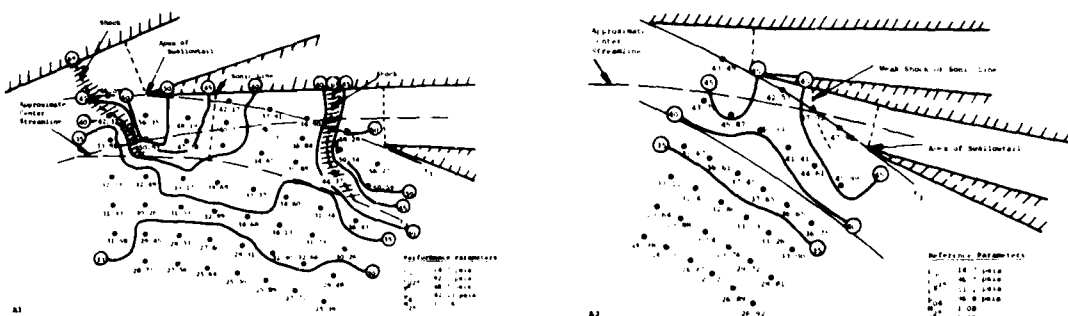


Figure 3. Pressure contour comparisons for the A1 & A2 stages at 100% N_D . Near Choke

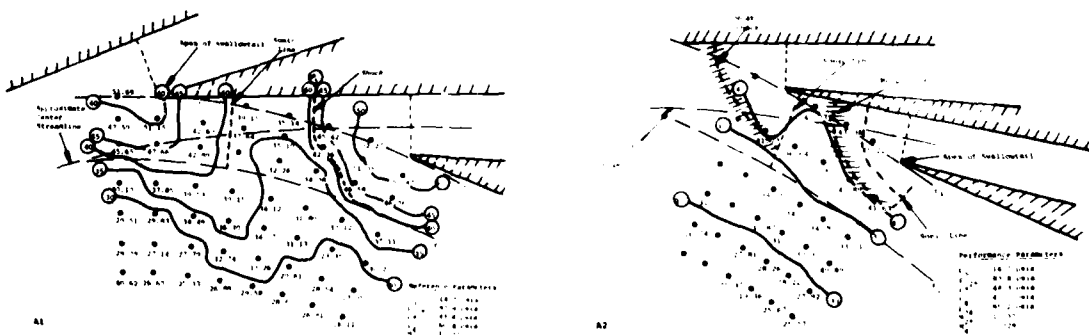


Figure 4. Pressure contour comparisons for the A1 & A2 stages at 95% N_D .

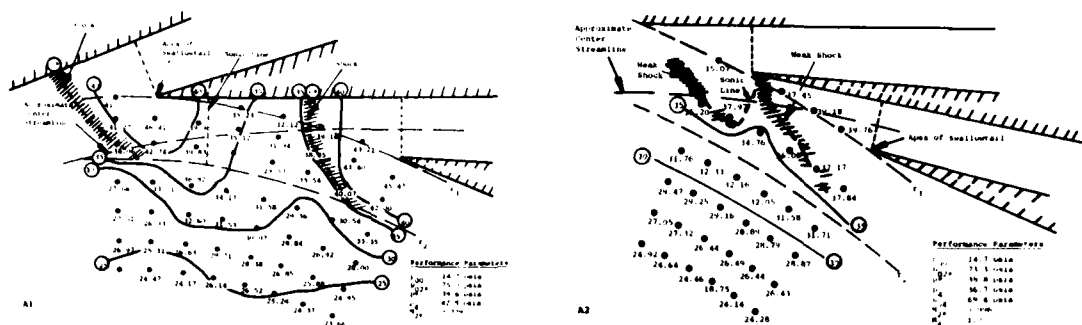


Figure 5. Pressure contour comparisons for the A1 & A2 stages at 90° N_D .

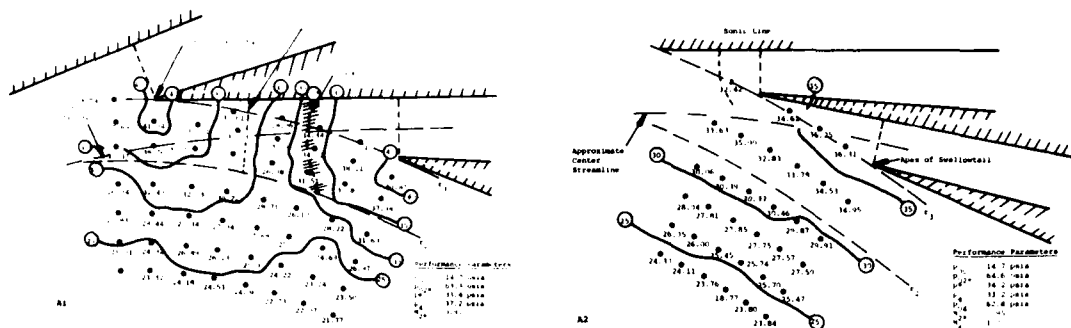


Figure 6. Pressure contour comparisons for the A1 & A2 stages at 85% N_D .

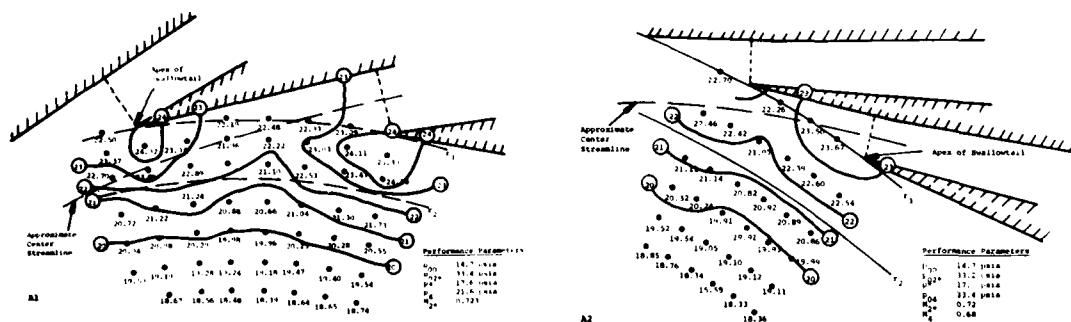


Figure 7. Pressure contour comparisons for the A1 & A2 stages at 60% N_D .

is quite pronounced for the A1 stage appears to be masked for the A2 stage. Similar general results are shown in Figure 4 for the 95% speed case and in Figure 5 for the 90% speed case. Here we see that the pressure distortions for the A2 stage are becoming very mild indeed but the A1 stage still has very strong pressure distortions. At 85% speed, a noticeable shock structure still exists for the A1 stage but only a weak sonic line is observed for the A2 stage. At 60% speed, our next lowest speed for which comparative data is available, the shock structures have disappeared completely but pressure field distortions are strongly in evidence for the A1 stage and are very very mild for the A2 stage.

It is now interesting to reconsider Figure 1a and to note the point at which the surge line diverged for the A1 and A2 stages. This is at approximately 85% speed and we observe that it is at this speed where the shock structure becomes pronounced and significant for the A1 stage (other plots, available but not shown for the A1 stage, only indicate that the shock structures are extremely weak or non-existent at speeds below 85%). In other words, when the impeller exit Mach number reaches a value of approximately 0.9, then it is possible for a shock structure to develop which may begin to participate strongly in the pressure recovery process and the flow stabilization events, if the geometry is such so as to cause a certain type of strong shock structure.

The highest local Mach numbers observed for each figure are shown in Table 2. Clearly the acceleration effects are much stronger for the A1 stage than for the A2 stage. This acceleration is sufficiently strong such that the transonic flows exiting the A1 impellerpass through a sonic line, are further accelerated, and then pass through a moderately strong shock in order to establish the flow conditions observed. It is interesting to note that the strongest shock observed is sufficient to cause a 2% loss in total pressure, which is a substantial performance penalty. This applies to the A1 stage where-

$\%N_D$	m/m _{choke}	M_{2*}^+	M_{max}^*	M_4^+
A1 Stage				
100	1.0	1.054	1.21	1.00
100	0.972	1.064	1.24	0.84
100	0.884	1.062	1.25	0.66
95	1.0	1.03	1.21	1.00
95	0.85	1.022	1.20	0.596
90	0.95	0.999	1.19	0.807
85	1.00	0.95	1.14	1.00
85	0.977	0.95	1.16	0.85
85	0.905	0.94	1.16	0.76
80	0.92	0.90	1.07	0.76
70	0.893	0.81	0.92	0.71
60	0.955	0.72	0.80	0.72
A2 Stage				
100	1.0	1.075	1.13	0.97
100	0.994	1.076	1.15	0.96
95	1.0	1.037	1.10	0.93
90	1.0	0.996	1.04	1.0
90	0.956	0.998	1.06	0.89
85	1.0	0.95	1.00	1.0
85	0.95	0.96	1.01	0.85
60	0.925	0.72	0.76	0.68

*Using β_{min} scaled to reduced conditions.

*Based on reduced conditions.

$\%N_D$	m/m _{choke}	M_x	\hat{p}_x	\hat{p}_y	$p_{y,N.S.}^+$
A1 Stage					
100	1.0	1.16	36.84	48.28	51.69
100	0.972	1.14	36.38	47.22	49.095
100	0.884	1.12	37.71	48.09	48.90
95	1.0	1.14	35.06	45.12	47.31
95	0.85	1.13	35.19	45.42	46.46
90	0.95	1.09	33.54	40.07	40.90
85	1.0	1.03	29.55	32.63	31.65
85	0.977	1.08	28.96	34.02	34.58
85	0.905	1.01	30.80	33.3	31.52
80	0.92	1.07	25.38*	30.61	29.67
70	0.983	-	-	-	-
A2 Stage					
100	1.0	1.02	45.99	49.90	48.16
100	0.994	1.01	46.83	49.74	47.93
95	1.0	1.03	40.07	43.36	42.91
90	1.0	1.01	36.05	37.17	36.89
90	0.956	1.00	36.73	38.17	36.73
85	1.0	-	-	-	-
85	0.95	-	-	-	-
60	0.925	-	-	-	-

*Note: Only tap where $M > 1.0$. Shock may not be present.

*Pressure downstream from simple normal shock of strength M_x , given by measured \hat{p}_x .

as substantially weaker shock systems are found for the A2 stage. It is of course evident in Table 2 that the flow has accelerated as it prepares to enter the diffuser and the peak Mach numbers are substantially higher than the computed impeller exit Mach numbers.

Further data is shown in Table 3. The computed values in Table 3 are bounding values that are established as follows. We have used the highest of the three static pressure measurements immediately in front of the shock to set the level of \hat{p}_x and we have taken the downstream static pressure, \hat{p}_y , to be the lowest of the three static pressures immediately after the shock. This gives us the lowest observed pressure difference (or rise) setting the lower bound to the possible shock strength. The expected static pressure after the shock ($p_{y,N.S.}$) given in Table 3 has been computed for comparison purposes from the simple normal shock relationship.

By comparing Mach numbers given in Tables 2 and 3, it is clear that the shock process does not start at the highest Mach number, but rather at a slightly lower Mach number downstream. Thus it is evident that some diffusion has occurred before the shock. Further, the shock does not occur at the tip Mach number but at a higher value. We also observe that the actual static pressure rise across the shock is distinctly less than what would have been obtained with a normal shock, except possibly at the 85% speed line. It can be noted also that the static pressure rise across the shock structure, for the A1 stage, is quite strong and clearly overpowers the static pressure drop due to the acceleration process. Further, the shock is sufficient to give a higher static pressure rise throughout the entry region than was achieved with the nearly shock free entry flow for the A2 stage.

Therefore, it is apparent that the increased range for the A1 stage vs. the A2 stage at speeds greater than 85% N_D is due to the presence of a uniquely different entry diffusion process for the A1 stage; that is, the characteristic shock structure. It is also clear, however, from the normal shock calculations, that the resulting total pressure loss will be greater for the A1 stage than for the A2 stage which is in excellent agreement with the lower observed efficiencies for the A1 stage. Further, the very strong pressure fields associated with the A1 stage diffuser inlet region give an excellent possibility for increased backflow and the data evaluation for these two stages showed approximately 2.5 times the computed backflow loss for the A1 stage than compared to the A2 stage on the 100% speed line.

In order to obtain a deeper appreciation for the stability of the flow process under consideration, we must go back and consider the path of a typical particle passing through the pressure fields of the A1 and A2 stages. If we consider figures 2 through 7, and particularly those on the high speed lines, it will become clear for the A2 stage, that the diffusion is gradual all the way from the tip of the impeller to the throat. By contrast, for the A1 stage there is almost no diffusion from the impeller tip to the front of the shock. In fact, none of the pressure rise occurs between the tip of the wheel and the face of shock, but instead, about 60% of the pressure rise occurs across the shock and 40% occurs as subsonic diffusion downstream of the shock prior to throat entry.

These differences may suggest an important characteristic of the enhanced flow stability of the A1 stage. We can speculate that the diffusion through the strong entry shock is more stable to downstream disturbances than is a weak shock system. We particularly note, in the comparison just given, that, according to the Kantrowitz¹ criterion* the shock is strongly stable to downstream disturbances. This is due to the accelerating velocity field located ahead of the shock structure. In other words, throat pulsations will not cause the shock position to diverge. Under the influence of pulsations, the entire flow structure will change, and the shock will move such that the pressures re-balance, but the shock itself will not be unstable. So long as the excursions of the shock structure do not carry it out of the stable velocity field ahead of it, the flow situation will be stable.

It is important to observe that it is the interaction of the pressure fields of the shocks from two adjacent passages that is critical to flow field stability. The reacceleration after the shock of the preceding passage stabilizes the shock of the next passage. When an entrance is not strongly shocked, reacceleration after the shock of the preceding passage is mild and, hence, the succeeding shock is not strongly stabilized. Thus the best explanation that can be offered as to the fundamentally different range characteristics of the A1 and A2 stages lies in the inherently different shock structures in the diffuser inlet region. We conclude that a stable (according to the Kantrowitz¹ criterion) shock structure has been achieved for the A1 stage.

It is now useful to return to Figure 1 and observe the characteristics of the seven different stages presented therein. The first three figures, 1a, 1b, and 1c, each reveal a pair of stages which were tested much as the A1 and A2 stage. In other words, for each configuration an impeller was used with two different diffusers having approximately the same area ratio and the same diffuser throat area. However, the number of vanes or pipes differed as shown in the figures. As with the A1 and A2 stages, we observe a substantial improvement in flow range for the B1 vs. B2 stages and also for the C1 and C2 stages. Again, it is clear that a process exists that is stabilizing the stage characteristic and providing enhanced range. Unfortunately, for the B stages and C stages, detailed pressure fields of the type shown in Figures 2 through 7 were not measured. We can only speculate that events similar to those characteristic of the A1 and A2 stages may be present. It is also clear that a rather sharp kink occurs in the surge line, particularly for the A1, B1 and C1 stages, and to a lesser extent for the B2 and C2 stages at a pressure ratio of approximately 3.7 to 4.3, depending on the particular stage. It is expected that this pressure ratio would correspond approximately to an impeller exit Mach number of approximately 0.9. Figure 1d shows the map for the seventh stage under consideration, to be discussed in greater detail later, where only one impeller is available for evaluation. Here again we see the possible beginning of a surge line kink at a pressure ratio of approximately 4.2 or 4.3.

Having described the fundamental differences between the A1 and A2 stages, we are left with the intriguing question: which condition is normal? From a traditional standpoint it may seem that the A2 stage is normal due to its comparatively straight surge line (truly accurate surge lines are never straight but may approximately fall in a nearly straight line). On the other hand, the comparatively low value of C_{p2*-4} along the stage stall line for the A1 and A2 diffusers below the 85% speed line, suggests that neither stage is "normal" at the low speeds. Instead, the stage appears to have hit an early stall limit. By contrast, the comparatively high values of C_{p2*-4} of approximately 0.45 to 0.5 for the A1 stage at speeds greater than 85% N_D are much more nearly characteristic of the stability limits of high pressure ratio stages, see for example Kenny². In as much as the stages considered by Kenny² deal with pressure ratios in the range of 6 to 10, it would appear that the A1 stage has characteristics which are more nearly normal. However, the absence of similar characteristics at the low speed end raises questions which cannot be answered here, so the question is moot.

Before closing this section, it is instructive to consider Figures 8 and 9 to further appreciate the influence of this shock structure on the stage stability characteristics. The present study was actually a mild interlude in a much more comprehensive evaluation of a series of industrial stages. One characteristic used to correlate the stage range is the measure of $\Delta\theta$. If we examine Figure 8, we observe typical channel diffuser pressure recovery maps. Such maps represent the basic geometric and aerodynamic characteristics of channel diffusers (similar maps are available for conical diffusers). The important characteristic here is the change in the relative location of pressure recovery contours as a function of inlet aerodynamic blockage. Each contour map shown in Figure 8 corresponds to a different blockage level; it will be noted that the contours shift to the right as one moves to ever increasing values of blockage. In other words, for a compressor operating along a speed line from a high flow to a low flow level, where the throat blockage is known to continuously increase, we move closer and closer to the ridge of peak recovery, which is also the region of transitory stall! Thus the hypothesis has been suggested** that a measure of resistance to stage stall is the change in $\Delta\theta$ for a point located on the choke line vs. the stage stall line for the respective diffuser maps. Thus one can obtain an estimated value of $\Delta\theta$ and plot it versus the known range characteristic, as is shown in Figures 9a and 9b. The correlation is observed to be generally good, with but a few exceptions. We note first that the A1 and A2 stages fall on the curve for the low speed correlation but that the A1 stage does not fall on the curve at the high speed

*The author appreciates the guidance from R. C. Dean, Jr., to include this approach.

**This hypothesis was put forward by R. D. Dean, Jr. at Creare in 1974.

whereas the A2 stage does. Further, we note that the B1 and C1 stages are not on the curve for the full speed correlation whereas the B2 and C2 stages are on the trend. Rather similar results are shown for the part speed correlation. Actually, this correlation should be much improved by plotting the results versus an impeller exit Mach number rather than a percent of design speed, which can imply vastly different pressure ratios and Mach numbers depending on the stages selected. It is felt that this correlation can be quite useful to guide designers but is not a fundamental stage stall theory in its own right.

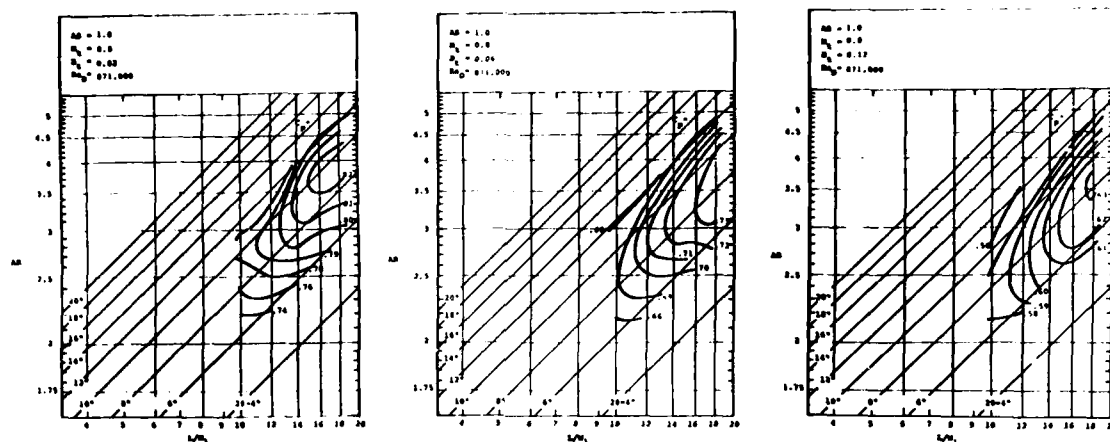


Figure 8. Channel diffuser maps showing pressure recovery as a function of inlet aerodynamic blockage.

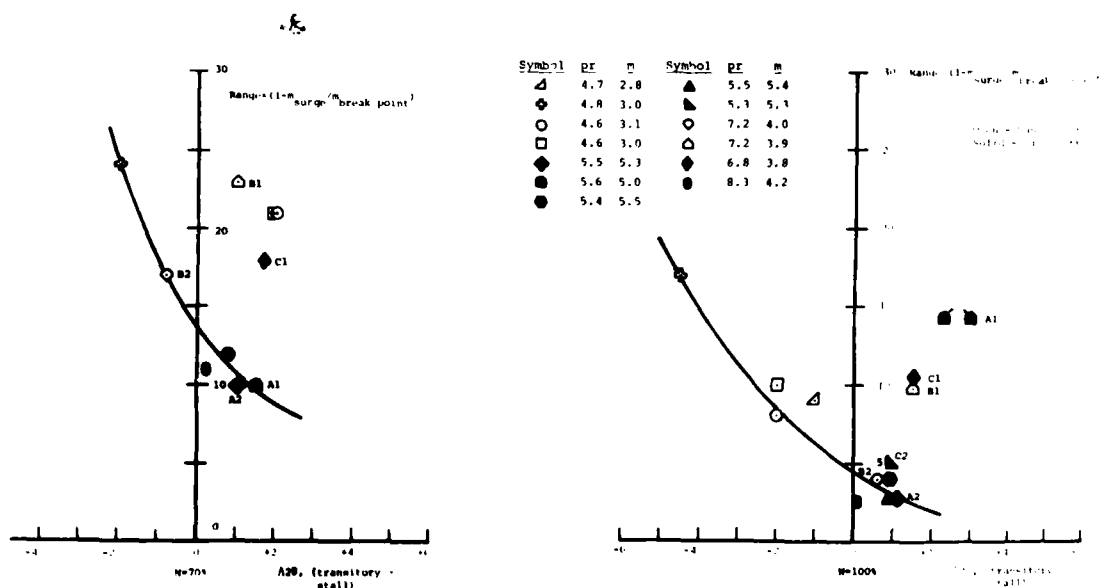


Figure 9. Stage operating range versus $\Delta 2\theta$ diffuser parameter.

4 STAGE DURABILITY

It is interesting to note that the A2 and D stages both experienced mechanical failures in the impeller discharge region. For the A1 stage, the failure was apparently catastrophic and resulted in the complete destruction of the impeller. For the D stage, various failures had been experienced which ranged from substantial cracking in the impeller exit regions to occasionally losing a section of an impeller in the knee region or exit region. Therefore, it is only natural to inquire whether the strong pressure fields observed in Figures 2 through 7 may play a role in the failure mechanism.

Figures 10 and 11 show the level of pressure field variation that the impeller tip experienced. Figure 10 shows the directly measured pressure contours as a function of tangential location for the A1 stage. Contours are shown at different radius ratio ($R = r/r_2$) where a value of 1 is exactly at the impeller tip and values greater than 1 imply radial locations greater than the tip radius. It will be observed that peak-to-peak static pressure variations at the impeller tip location are equivalent to approximately 20 psi for an impeller that gives a static pressure rise of approximately 30 psi! Similar results are shown in Figure 11 for the D stage measured exactly at the impeller tip radius. Unfortunately, only three pressure taps span a single diffuser pitch and it is strongly expected (particularly by contrast to Figure 10) that the maximum, and possibly the minimum, pressure value has not been detected and recorded in this data. Nonetheless, peak-to-peak static pressure variations of at least 10 psi are in evidence for an impeller whose static pressure rise is equivalent to approximately 22 psi! Clearly, very strong pressure fields exist for both the A1 and D impeller.

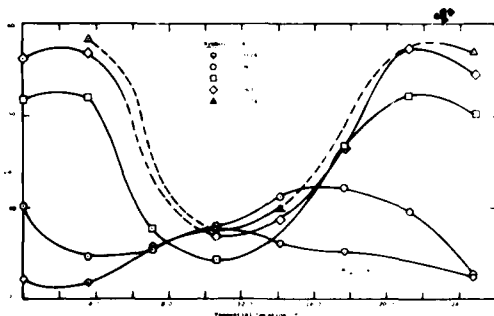


Figure 10. Characteristic impeller tip pressure distributions, A1 stage.

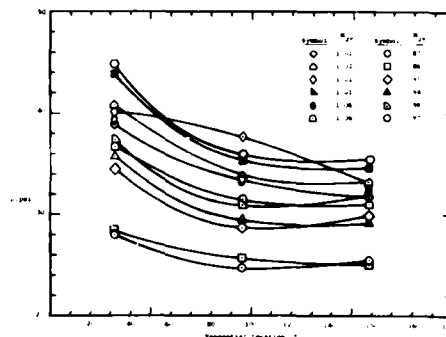


Figure 11. Characteristic impeller tip pressure distributions, D stage.

Fortunately, for the case of the D impeller comprehensive structural analyses have been carried out to determine the probable cause of failure in the impeller. It was concluded that no one single cause was responsible for the failure, but rather that a number of strong forces contributed to an over stressed impeller. The level of dynamic stresses due to the diffuser inlet pressure fields was not high, but of a sufficient magnitude that it could easily be the "straw that broke the camel's back". So the vibratory stresses brought about by the strong tip pressure field are not the sole source of excessive stress for the impeller. However, it is quite possible that this source was neglected in the basic design (due to a lack of data to quantify the effect) and that it is only a matter of time until a critical number of cycles have accrued to yield a substantial vibratory stress level. Thus it is probable that the strong pressure fields associated with a diffuser inlet shock structure is responsible for the ultimate failure of the A1 and D impellers.

The type of information shown in Figure 10 can be further modified to be of use to designers. Figures 12, 13 and 14 show data for the A1 impeller, the A2 impeller and the D impeller, respectively. In this case, the peak-to-peak pressure differential established at the impeller tip (or other specified radius) resulting from the diffuser inlet vane pressure field has been plotted against the impeller discharge Mach number. The A2 impeller, Figure 13 shows comparatively small differentials at least when compared with the A1 impeller shown in Figure 12. Similar results are shown in Figure 14 for the D impeller, but it must be emphasized that these effects are probably underestimated due to the absence of the end values shown in Figure 11. It is recommended that the results of Figure 14 be increased by approximately 50 if a safe upper limit is desired. It is interesting to note the plateau region in both Figures 12 and 14 just before a Mach number of 1.0. It is curious that this effect has been found for two different stages from two totally different manufacturers, but the reason is not at all obvious. The results of Figures 12, 13 and 14 are not applicable to other design studies due to their dimensional form. Therefore, a non-dimensional tip pressure distortion parameter has been defined as:

$$\Delta P_{ND} = \frac{\Delta P_2 / \rho_2}{U_2^2} = C \frac{\rho_2 T_2}{P_2 U_2^2} \quad (1)$$

where the dimensional constant depends on the system of units employed. This non-dimensional parameter varied as follows:

Impeller	$\frac{\Delta p_2 / \rho_2}{U_2^2}$	$R_3 = r_3 / r_2$
A1	0.13 \pm 0.03	1.064*
A2	0.03 \pm 0.01	1.033*
D	0.10 \pm 0.02	1.035

*Note: These values have not been reversed!

The non-dimensional parameter has been plotted versus M_{2*} but the trends were not as smooth as in Figures 12, 13 and 14. The peak values for the A1 and D impellers were found at $M_{2*} \approx 0.95$. It is recommended that this parameter be held below 0.05 for a safe design by choosing vane number and R_3 appropriately (Figure 12 can be used as a guide).

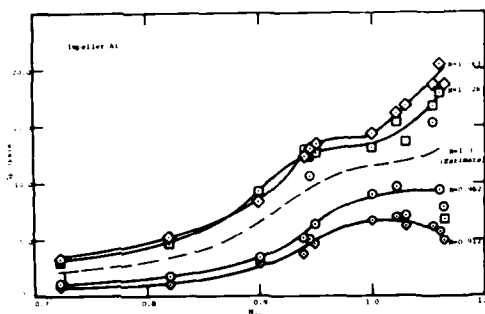


Figure 12. Impeller tip pressure distortion versus tip Mach number, A1 stage.

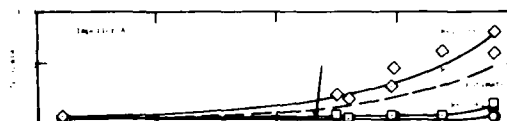


Figure 13. Impeller tip pressure distortion versus tip Mach number, A2 stage.

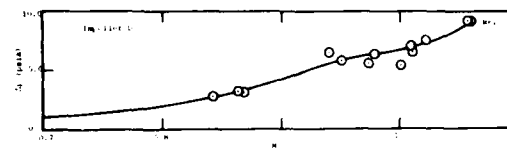


Figure 14. Impeller tip pressure distortion versus tip Mach number, D stage.

CONCLUSIONS

As a result of the work presented herein, the following conclusions were reached:

1. Evaluation of the range characteristics from two highly similar stages, differing principally in diffuser vane number, revealed a shock enhanced pressure recovery and flow stabilization process. The low diffuser number contributed to strong shocks such that a fluid particle leaving the impeller passed first through a leading shock and was then accelerated to a subsequent shock where most of the diffusion process occurred. The accelerating region between the two shocks provides a highly stabilized flow field, in agreement with the Kantrowitz shock stabilization criterion.
2. Data revealed that this process began when the impeller tip Mach number equaled or exceeded 0.9. A characteristic kink in the surge line was found at this point for the two principal stages under investigation, and similar results have been noticed with three other sets of data.
3. The efficiency degradation due to the shock stabilization process was substantial, leading to a 2% loss in the total pressure rise from the impeller.
4. Two of the seven stages reviewed herein had mechanical difficulty with the impeller. It is observed that the very strong pressure fields at the impeller tip contribute to cyclic stresses that may drive the impeller to a failure mode.

CLOSURE

The author would like to extend his appreciation to two colleagues and to two supporting organizations. Special appreciation is expressed to Dr. Robert C. Dean, Jr., who has continuously challenged the author in the search for deeper physical understanding. Appreciation is also expressed to Mr. Lawrence Young, who assisted in some of the data evaluation work. Finally, two clients, who choose to remain anonymous, are acknowledged with great appreciation. Their support of this work is a contribution to all designers.

REFERENCES

Kantrowitz, A.; ONE-DIMENSIONAL TREATMENT OF NONSTEADY GAS DYNAMICS; Section C of Fundamentals of Gas Dynamics, Princeton, New Jersey, Princeton University Press, 1958, pages 350-415.

Kenny, D.P.; A COMPARISON OF THE PREDICTED AND MEASURED PERFORMANCE OF HIGH PRESSURE RATIO CENTRIFUGAL COMPRESSOR DIFFUSERS; ASME Publication 72-GT-54.

Runstadler, P.W., Jr., Dolan, F. X. and Dean, R.C., Jr.; DIFFUSER DATA BOOK; Hanover, New Hampshire, Creare Incorporated TN-186, May 1975.

DISCUSSION

W.A.Connor, Holset Engineering, UK

I would like to congratulate the author on a very stimulating and thought-provoking paper. The compression system instability work of Greitzer and others indicates that a close-coupled throttle should reduce or even eliminate the tendency for a compressor to surge. Could the author comment on any possible analogy between this and the throttling effect of the strong shock system produced by the 17 channel diffuser?

Author's Reply

The author is grateful for the supporting compliments. Yes, an added resistance will usually help stabilise a compressor system. But one would hardly have thought that a two per cent stagnation pressure loss resistance would make such a large increase in range. Thus I must believe that, while the increased resistance for 'A1' and 'A2' may contribute to enhanced range, a much stronger process probably exists.

P.M.Came, NGTE, UK

I would like to ask the author two questions. Firstly, were values of pressure recovery coefficient for the semi-vaneless space calculated? Secondly, could the author please describe the geometry of the collector system downstream of the radial diffuser?

Author's Reply

We calculated pressure recovery for the semi-vaneless space. The values were approximately, for the 'A2' compressor 0.25 along the stage stall line, and for the 'A1' stage, 0.25 to 0.5, varying along the stage stall line. The collector used was strictly axisymmetric with exit Mach numbers equal to a small fraction (we suggest less than a quarter) of the diffuser exit Mach number.

N.A.Cumpsty, University of Cambridge, UK

Could the author please confirm which stage suffered mechanical failure; was it 'A1' or 'A2'?

Author's Reply

Impeller 'A1' suffered the mechanical failure. In the text of the report there is a misprint suggesting that it was the 'A2' compressor.

Y.Ribaud, ONERA, Fr

Do you think that the surge margin depends more on the number of vanes or on the curvature of the suction surface in the semi-vaneless space, Kenny has been carrying out for some time calculations of the supersonic flow which shows clearly acceleration of the flow before the shock, this acceleration effect being greater than the effect of the number of blades. It seems to me that if the suction surface had a spiral form the acceleration of the flow would be able to be attenuated if not nullified whatever the blade number.

Author's Reply

Thank you for your comments. In this particular case the vane number must be more important than suction side vane shape in controlling shock strength and location. This is because a straight centre line bore, with a conical cross section, is used to form the diffuser inlet. However, when one uses a vane shape (as opposed to a conical configuration), then I agree that curvature should be used to control shock strength and location.

INFLUENCE DE L'HETEROGENEITE DE L'ECOULEMENT A LA
SORTIE DU ROTOR SUR LES PERFORMANCES DU
DIFFUSEUR D'UN COMPRESSEUR CENTRIFUGE

Henri HUS
Hispano Suiza

Christian FRADIN
ONERA

SOMMAIRE

Etude des performances d'un diffuseur de compresseur centrifuge alimenté par une roue mobile délivrant un écoulement plus ou moins hétérogène. Les mesures classiques au moyen de sondes pneumatiques ne donnant que les grandeurs moyennes ne permettent pas de caractériser correctement l'intensité de la non-uniformité de l'écoulement. Les mesures instantanées par capteurs de pression et anémomètres à fil chaud donnent la structure fine de l'écoulement et conduisent à une estimation plus précise de l'effet de la non-uniformité de l'écoulement sur les performances du compresseurs. Elles montrent notamment que les pertes sont dues essentiellement à cette non-uniformité et permettent de choisir entre les diverses méthodes globales d'estimation du coefficient de récupération de pression du diffuseur celle qui est physiquement la plus plausible.

SUMMARY

Analysis of the performances of the diffuser of a centrifugal compressor. The inlet flow is deliberately more or less non-uniform. The conventional pressure probes and the corresponding mean values do not allow a correct evaluation of the performance of the diffuser. The measurement of instantaneous values of pressure and velocity by means of pressure transducers and hot-wire anemometers gives the detailed structure of the flow field. An accurate estimation of the effect of non-uniformities on the performances of the diffuser can be derived from these measurements. They show that the pressure losses are directly related to the non-uniformities. Validation of an overall estimation of diffuser performance from conventional probe measurements is derived from this experiment.

NOTATIONS

B	Coefficient de blocage, rapport de la section de passage utile à la section de passage totale
C_d	Vitesse débitante
C_θ	Vitesse tangentielle en axes absolues
h_a	Enthalpie d'arrêt
h_{a_0}	Enthalpie d'arrêt à l'entrée du compresseur
K_D	Débit masse
K_h	Flux d'enthalpie d'arrêt
K_M	Dynalpie
K_S	Flux d'entropie
K_θ	Moment cinétique
$K_{P(M,an)}$	Coefficient d'étalonnage déterminé en soufflerie
M	Nombre de Mach
P	Pression statique
P_i	Pression d'arrêt
P_{s_0}	Pression d'arrêt moyenne à la sortie du diffuseur
S	Entropie
t	Temps
T	Intervalle de temps séparant le passage de deux aubes devant la sonde
δ	Exposant isentropique
ξ	Abscisse rapportée à la profondeur du canal à la sortie de la roue mobile ($\xi = 0$ carter avant, $\xi = 1$ carter arrière)
χ	Taux de récupération de pression
ρ	Masse volumique
ωR	Vitesse périphérique de la roue mobile

- les grandeurs non surlignées correspondent aux valeurs instantanées,
- une fois surlignées aux valeurs moyennes compte tenu d'un facteur de blocage,
- deux fois surlignées à des grandeurs homogènes.

1 - INTRODUCTION

Le diffuseur d'un compresseur centrifuge est toujours alimenté par un flux hétérogène en vitesse, incidence et pression. Il est donc bien difficile de définir de quelle façon l'énergie cinétique délivrée par le rotor est transformée en énergie de pression et de ce fait d'optimiser le diffuseur.

Il a donc paru intéressant de réaliser un rotor qui délivrerait un écoulement azimutalement uniforme et que, par des artifices convenables, on rendrait hétérogène, mais avec une structure imposée. Le principe de cet essai repose sur des résultats acquis en soufflerie en montrant que l'introduction de pertes de charges importantes permet l'homogénéisation d'un écoulement hétérogène. Ce sont généralement des nids d'abeilles à faibles mailles que l'on utilise à cet effet et un montage expérimental conçu dans cet esprit a été réalisé en vue de caractériser la capacité de récupération de pression d'un diffuseur donné.

2 - DESCRIPTION DU MONTAGE EXPERIMENTAL

Le banc d'essais est constitué par une boucle fermée où circule du fréon 114. Le rotor centrifuge utilisé (Fig. 1) est classique par sa forme et comporte une avant roue et une roue radiale, cette dernière ayant un nombre d'aubes double de celui de l'avant roue. Ce rotor est directement dérivé d'un compresseur de suralimentation de moteur Diesel conçu et fabriqué par Hispano-Suiza.

Pour les essais en vue il a été modifié par adjonction de deux couronnes en nids d'abeilles en acier inoxydable dont les parois d'alvéoles avaient une épaisseur de 0,07 mm et les alvéoles hexagonales avaient 6 côtés de 1,2 mm de largeur (Fig. 2). Les nids d'abeilles étaient brasés sur deux flasques supports et la tenue mécanique du montage a été vérifiée sous des conditions d'accélération extrêmes (26 000 g).

Des caches, placés de façon périodique et obstruant une partie seulement de la section de sortie de la roue (coefficient d'obstruction réglable) pouvaient être placés sur les nids d'abeilles (Fig. 3) et afin d'assurer la sécurité de fonctionnement, la vitesse de rotation du compresseur a été limitée à 5 500 tr/mn (accélération 7 000 g) ce qui, avec le fréon 114 utilisé, donnait un Mach périphérique de l'ordre de l'unité.

Un diffuseur classique à aubes (Fig. 4) était placé à la sortie de la roue mobile, un diffuseur lisse entre le rayon de sortie de la roue et le bord d'attaque des aubes (rapport des rayons 1,08) était prévu pour l'installation d'instruments de mesure destinés à caractériser l'écoulement issu du rotor.

3 - ESSAIS GLOBAUX

Dans une première série d'essais destinés à définir la caractéristique globale débit-pression de la machine et le taux de récupération de pression du diffuseur, des méthodes classiques de mesure et de dépouillement ont été utilisées. Ces essais et dépouillements ont été effectués par Hispano-Suiza.

La figure 5 représente les résultats des estimations du taux de récupération de pression du diffuseur effectuées par diverses méthodes :

a) la figure 5a représente le taux de récupération de pression du diffuseur

$$\chi = \frac{P_3 - P}{P_1 - P}$$

où P_1 et P_3 sont les pressions d'arrêt respectivement à la sortie de la roue mobile et du diffuseur et P la pression statique à la sortie de la roue mobile obtenue à partir de :

- la mesure directe de la pression d'arrêt au moyen d'une sonde pneumatique (pitot) placée à la sortie du rotor,
- la moyenne pondérée par le débit de la pression à la sortie du diffuseur.

On observe que la présence des caches augmente le taux de récupération, ce qui semble indiquer que la méthode n'est pas correcte, elle ne s'appuie d'ailleurs sur aucune base théorique.

b) pour la figure 5b nous avons essayé de déduire la pression d'arrêt moyenne à la sortie du rotor des mesures de pression statique, de débit et d'accroissement de température. La composante tangentielle moyenne de la vitesse est déduite de l'accroissement d'enthalpie d'arrêt par application du théorème d'Euler et le composante débitante au moyen d'itérations successives sur la conservation du débit. L'inconvénient de cette méthode, qui conduit d'ailleurs à des taux de récupération exagérés (> 1), est de nécessiter une hypothèse sur le taux moyen de remplissage de la veine, que nous avons pris égal à 0,96.

c) l'attaque du diffuseur étant subsonique élevé, le col géométrique entre deux aubages adjacents est sonique au cours d'essais effectués à grand débit et, au moyen de la température d'arrêt du débit et de la valeur géométrique de ce col (affecté d'un taux de remplissage de veine de 0,97 à 0,98) il est possible de calculer la valeur moyenne de la pression d'arrêt à l'entrée du redresseur. Par comparaison avec les résultats de la méthode (b) ci-dessus il est possible d'obtenir une valeur expérimentale du taux de remplissage de la veine à la sortie du rotor et c'est cette valeur que l'on a conservée pour le tracé de la figure 5c. On notera que l'ordre de grandeur du taux de récupération est analogue à celui donné par la méthode (a) mais que la présence de caches diminue le taux de récupération (ce qui paraît plus vraisemblable).

4 - CARACTERISATION DES HETEROGENEITES

L'incertitude des analyses globales et notamment l'inversion du sens de variation des taux de récupération du diffuseur semblent montrer que l'état du fluide ne doit pas être fondamentalement différent dans les essais avec caches ou sans caches. Pour caractériser les hétérogénéités, des mesures instantanées de vitesses, en intensité et en direction ont été effectuées par l'ONERA. Le tableau I résume l'ensemble des mesures effectuées et les moyens mis en oeuvre : la figure 6 indique l'emplacement des points de mesure.

La mesure de l'angle instantané de l'écoulement est basée sur la symétrie des courbes représentant l'évolution du nombre de Nusselt en fonction de l'angle constitué par la direction de la vitesse et l'axe du fil. La mesure du module instantané de la vitesse est basée sur les travaux de Morkovin [1], Spangenberg [2] et Kovaszny [3]. La loi d'échange thermique, fonction des nombres de Reynolds et de Mach, proposée par ces auteurs a été vérifiée dans la boucle à fréon de l'ONERA. L'influence des autres paramètres, tels que l'angle entre la direction du fil et celle de l'écoulement, la température du fil chaud, son coefficient de récupération et la température de l'écoulement, a été également déterminée expérimentalement et prise en compte dans les dépouillements. Ces étalonnages ont mis en évidence une dérive dans le temps des informations délivrées par le fil chaud. Une technique de dépouillement a été développée pour pallier cette difficulté : elle consiste à associer :

- les mesures instantanées de pression $p(t)$
- les mesures instantanées de vitesse $V(t)$ desquelles on déduit le nombre de Mach $M(t)$ dans l'hypothèse d'une température d'arrêt constante et connue (hypothèse valable dans le fréon)
- les mesures moyennes de pression d'arrêt \bar{P}_i obtenues par la sonde à trois trous

au moyen de la relation :

$$\bar{P}_i = \frac{1}{T} \int_0^T \left\{ K_p(M, \Delta\alpha) \left[\left(1 + \frac{\gamma-1}{2} M^2(t) \right)^{\frac{\gamma}{\gamma-1}} - 1 \right] + 1 \right\} p(t) dt$$

où T est le temps séparant le passage de deux aubes successives et $K_p(M, \Delta\alpha)$ est un coefficient de correction, voisin de l'unité, déterminé au cours de l'étalonnage de la sonde de pression trois trous dans le fréon, à divers nombres de Mach et divers angles $\Delta\alpha$ entre la sonde et direction de l'écoulement.

5 - STRUCTURE DE L'ÉCOULEMENT ISSU DE LA ROUE MOBILE

L'analyse des résultats globaux présentés figure 5 montre que, quelle soit la méthode de dépouillement utilisée, l'efficacité maximum du diffuseur s'obtient pour sensiblement la même valeur ($\approx 8,5$) du débit volume à la sortie du rotor. Dans la comparaison de la structure de l'écoulement avec ou sans caches, nous avons donc choisi de présenter côte à côte des grandeurs relevées au cours des deux types d'essais dans les conditions d'attaque optimale du diffuseur.

5.1 - Valeurs instantanées de la vitesse débitante

La figure 7 représente la variation en fonction du temps t (rapporté au temps T séparant le passage de deux aubes) de la vitesse débitante à la sortie de la roue mobile pour quatre profondeurs relatives ξ entre carters avant et arrière.

On remarque, malgré une forte hétérogénéité axiale de la vitesse débitante, une grande similitude des répartitions de vitesse dans le demi-canal entre extradors et aube intercalaire et dans le demi-canal entre aube intercalaire et intrados.

Les mesures au fil chaud ont mis en évidence des courants de retour situés au milieu du canal et au voisinage du carter avant ($\xi = 0,27$) en l'absence de caches (Fig. 7a) et limités entre les caches et l'intrados de l'aube la plus proche, aube longue ou aube intercalaire, et près des carters ($\xi = 0,27$ et $\xi = 0,96$) en présence des caches (Fig. 7b).

Cette structure de l'écoulement se maintient sans trop de déformation au fur et à mesure que l'on se rapproche de l'entrée du diffuseur, c'est-à-dire lorsqu'on passe du rayon de mesure "21" au rayon "23" (Fig. 8).

Notons que l'exploration axiale de l'écoulement au moyen d'une sonde classique met déjà en évidence le déficit en débit côté carter externe (Fig. 9).

5.2 - Valeurs instantanées de la vitesse tangentielle

Une étude analogue a été effectuée pour la composante tangentielle de la vitesse. Nous ne présentons ici que les répartitions azimutales de cette vitesse relevée à la profondeur relative $\xi = 0,73$ aux trois rayons analysés, sans caches (Fig. 10a) et avec caches (Fig. 10b). On remarquera encore l'effet prédominant des caches sur la structure de l'écoulement qui, hétérogène par nature même en l'absence de caches, montre d'importants gradients de vitesse tangentielle dans le sillage des caches. Comme nous l'avions signalé plus haut, la comparaison s'effectuant au même débit volume à l'entrée du diffuseur, les valeurs moyennes des vitesses tangentielles ne sont pas les mêmes dans les deux configurations.

6 - ESTIMATION DES TAUX DE RÉCUPÉRATION À PARTIR DES MESURES INSTANTANÉES DE VITESSE ET DE PRESSION

Le taux de récupération de pression du diffuseur étant fonction de ses qualités aérodynamiques propres aussi bien que de l'hétérogénéité de l'écoulement incident, il importe dans une analyse fine du type de celle que nous venons de décrire, de séparer la part de ces deux paramètres sur les performances du diffuseur.

Bien que l'écoulement soit fortement hétérogène, il est possible de lui appliquer des règles de définition des écoulements moyens analogues à celles élaborées par le Groupe de Travail WG 14 de l'AGARD [4].

Le schéma qui semble donner une analyse rationnelle des résultats expérimentaux repose sur les hypothèses suivantes :

- à la sortie de la roue mobile, l'écoulement équivalent ne débite que sur une fraction B de la surface de sortie d'un canal interaube ; ce coefficient de blocage B est une des inconnues du calcul de détermination de l'écoulement équivalent ;
- aux hétérogénéités induites par la roue mobile et qui sont stationnaires en axes liés à celle-ci, donc fonctions périodiques du temps réduit t/T , se superposent des perturbations induites par les aubes du diffuseur ; ces perturbations dues en partie aux effets irrotationnels induits par les parois des aubes

et en partie aux ondes de choc attachées aux bords d'attaque dans les fonctionnements supersoniques ne devraient pas être prises en compte dans l'étude comparative des performances du redresseur, c'est pourquoi nous avons choisi pour la définition de l'écoulement équivalent les grandeurs mesurées au rayon "21" situé immédiatement à la sortie de la roue mobile et au point A, milieu de l'arc de cercle limité aux lignes de courant aboutissant aux bords d'attaque de deux aubes adjacentes, en faisant l'hypothèse qu'en ce point les perturbations induites par le diffuseur sont minimales ;

- l'écoulement équivalent à mêmes débit, dynalpie, moment cinétique et enthalpie d'arrêt que l'écoulement hétérogène qu'il représente. On écrit donc les équations de conservation

$$\begin{aligned} \text{masse} & \quad \bar{\rho} B \bar{C}_d = K_D \\ \text{dynalpie} & \quad \bar{\rho} B \bar{C}_d^2 + \bar{P} = K_M \\ \text{moment cinétique} & \quad \bar{\rho} B \bar{C}_d \bar{C}_\theta = K_\theta \\ \text{enthalpie d'arrêt} & \quad \bar{\rho} B \bar{C}_d \bar{h}_i = K_h \\ \text{entropie} & \quad \bar{\rho} B \bar{C}_d (\bar{S} - S_1) = K_s \end{aligned}$$

auxquelles s'ajoutent les deux relations de cohérence

$$\begin{aligned} \bar{h}_i &= \frac{\bar{C}_d^2 + \bar{C}_\theta^2}{2} + \frac{\gamma}{\gamma-1} \frac{\bar{P}}{\bar{\rho}} \\ \bar{h}_i &= \omega R \bar{C}_\theta + h_{i0} \end{aligned}$$

la seconde exprimant l'accroissement moyen d'enthalpie à la traversée du compresseur.

Les grandeurs K_D, K_M, K_θ et K_h sont données par les intégrales suivantes :

$$\begin{aligned} K_D &= \frac{1}{T} \int_0^T \int_0^1 \rho C_d dt d\zeta \\ K_M &= \frac{1}{T} \int_0^T \int_0^1 (\rho C_d^2 + P) dt d\zeta \\ K_\theta &= \frac{1}{T} \int_0^T \int_0^1 \rho C_d C_\theta dt d\zeta \\ K_h &= \frac{1}{T} \int_0^T \int_0^1 \rho C_d \left(\frac{C_d^2}{2} + \frac{C_\theta^2}{2} + \frac{\gamma}{\gamma-1} \frac{P}{\rho} \right) dt d\zeta \\ K_s &= \frac{1}{T} \int_0^T \int_0^1 \rho C_d (S - S_1) dt d\zeta \end{aligned}$$

On remarquera que nous n'avons pas utilisé directement la valeur de la température d'arrêt du gaz mesurée à la sortie du compresseur, cette grandeur intervient indirectement dans le calcul de la masse volumique locale

$$\rho = \frac{\gamma-1}{\gamma} \frac{P}{h_i - \frac{C_d^2 + C_\theta^2}{2}}$$

le paramètre K_h peut donc être obtenu indifféremment comme valeur moyenne pondérée par le débit de l'enthalpie d'arrêt locale ou comme l'indique la formule ci-dessus.

On dispose donc de 7 équations pour calculer les 7 inconnues $\bar{\rho}, \bar{P}, \bar{S}, \bar{C}_d, \bar{C}_\theta, \bar{h}_i, B$ et on obtient ainsi l'écoulement hétérogène équivalent, le coefficient de blocage B caractérisant de façon claire l'hétérogénéité de l'écoulement physique. Notamment la pression d'arrêt \bar{P}_i de l'écoulement hétérogène équivalent sera donné par

$$\bar{P}_i = \bar{P}_{i1} \left(\frac{\bar{h}_i}{h_{i1}} \right)^{\frac{\gamma}{\gamma-1}} e^{-\left(\frac{\bar{S} - S_1}{R} \right)}$$

Le taux de récupération de pression du diffuseur peut être défini alors par le rapport

$$\bar{\chi} = \frac{\bar{P}_{i2} - \bar{P}}{\bar{P}_{i2} - \bar{P}}$$

où \bar{P}_{i2} est la pression d'arrêt moyenne calculée à la sortie du diffuseur.

Afin de séparer dans $\bar{\chi}$ la part qui incombe à l'hétérogénéité calculée de l'écoulement de celle qui est intrinsèque au diffuseur, nous définirons un écoulement moyen uniforme remplissant la veine ($B=1$) à la sortie de la roue mobile, ayant même débit et même enthalpie d'arrêt que l'écoulement réel mais un niveau d'entropie différent.

Surplignant deux fois les grandeurs correspondantes nous obtenons les équations de définition suivantes :

$$\begin{aligned} \bar{\rho} \bar{C}_d &= K_D \\ \bar{\rho} \bar{C}_d^2 + \bar{P} &= K_M \\ \bar{\rho} \bar{C}_d \bar{C}_\theta &= K_\theta \\ \bar{\rho} \bar{C}_d \bar{h}_i &= K_h \\ \bar{h}_i &= \frac{\bar{C}_d^2 + \bar{C}_\theta^2}{2} + \frac{\gamma}{\gamma-1} \frac{\bar{P}}{\bar{\rho}} = \bar{h}_i \end{aligned}$$

On en déduit la pression d'arrêt de l'écoulement homogène

$$\bar{P}_i = \bar{P} \left(\frac{h_s}{\frac{\gamma}{\gamma-1} \frac{\bar{P}}{\bar{\rho}}} \right)^{\frac{\gamma}{\gamma-1}}$$

ainsi que le nouveau coefficient de récupération

$$\bar{\alpha} = \frac{\bar{P}_i - \bar{P}}{\bar{P}_i - \bar{P}}$$

Si on applique la méthode que nous venons de décrire au dépouillement des résultats expérimentaux obtenus sur ce compresseur muni ou non de caches à la sortie de la roue mobile, on obtient pour les fonctionnements correspondant à l'optimum du diffuseur dans chaque configuration les valeurs portées sur le tableau II.

On remarque que le coefficient de blocage calculé est très faible dans les deux cas ($B = 1$ correspond à un écoulement homogène) mais que la présence de caches diminue le taux de récupération. Il est très proche de la valeur obtenue avec la méthode globale décrite au § 3c (Fig. 5c) considérée comme la meilleure.

L'analyse des résultats obtenus par un calcul d'homogénéisation de l'écoulement montre que pratiquement toutes les pertes déterminées plus haut proviennent de l'hétérogénéité de l'écoulement.

7 - CONCLUSION

L'étude expérimentale d'un diffuseur de compresseur centrifuge alimenté par un rotor muni de nids d'abeilles destinés à uniformiser l'écoulement, puis par le même dispositif modifié par mise en place de caches obstruant partiellement la sortie des canaux interaubes a mis en évidence :

- l'insuffisance des nids d'abeilles utilisés pour donner un écoulement homogène à la sortie de la roue mobile, surtout en ce qui concerne la vitesse débitante ;
- la difficulté d'interprétation correcte des mesures globales en vue de caractériser les performances du diffuseur ;
- la présence d'importants écoulements secondaires en aval des caches, conduisant même à des courants de retour près des deux carter, tandis que l'on ne note de courants de retour que près du carter avant si la roue n'est pas munie de caches ;
- la faible atténuation des hétérogénéités dans le diffuseur lisse de rapport de rayon 1,08 placé entre la sortie de la roue mobile et le diffuseur à aubes ; il s'en suit qu'une grande partie des hétérogénéités s'amortit dans le diffuseur à aubes [5] [6].

Les mesures de vitesse et de pression instantanées dans le diffuseur lisse permettent de décrire la structure fine de l'écoulement hétérogène issu de la roue mobile. L'analyse de cet écoulement et la définition d'écoulements hétérogènes ou homogènes équivalents à l'écoulement réel donne la valeur du taux de récupération de pression du diffuseur et montre le rôle essentiel de l'homogénéisation sur les pertes.

Cette analyse fine de l'écoulement semble valider la méthode globale de calcul du taux de récupération de pression du diffuseur, utilisant un coefficient de débit déduit du blocage sonique du diffuseur.

REFERENCES

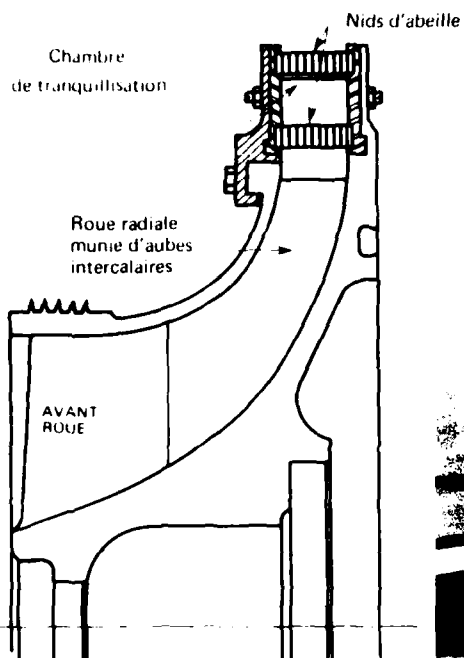
- [1] M.V. MORKOVIN
Fluctuations and hot wire anemometry in compressible flows.
AGARDGRAPH 24, November 1956.
- [2] W.G. SPANGENBERG
Heat loss characteristics of hot wire anemometers at various densities in transonic and supersonic flow.
NASA NT 3381.
- [3] KOVASNAY
The hot wire anemometer in supersonic flow.
J. Aero. Sciences. Vol. 17, n° 9 September 1950.
- [4] M. PIANKO
Écoulements moyens dans une turbomachine
in AGARD - Proceedings of WG 14 - 1980.
- [5] D. ECKARDT
Jet wake mixing in the diffuser entry region of a high speed centrifugal compressor.
ASME Paper, June 1978.
- [6] M. INOUE, N.A. CUMPSTY
Small perturbation analysis of non-uniform rotating disturbances in a vaneless diffuser.
ASME Paper 78 GT 154.

TABLEAU I
EQUIPEMENT DE MESURE DANS LE DIFFUSEUR LISSE

	Grandeur mesurée		Rayon de sondage (cf. Fig. 6)	Emplacement de la mesure	Sonde utilisée	Remarques
Grandeurs moyennes	Au sein de l'écoulement	Pression statique	"21"			- Caractérisation de l'écoulement moyen
		Pression d'arrêt	"22"	A	Sonde à trois trous	- Evolution des grandeurs moyennes le long du rayon
		Direction de la vitesse	"23"			- Etalonnage de sondes
	à la paroi	Pression statique	"21"	A B C D E	Orifice de paroi	- Détermination aux rayons 21 et 23 de la valeur moyenne de la pression statique
			"22"	A		
			"23"	A B C D E		
Grandeurs instantanées	au sein de l'écoulement	Module et direction instantanés de la vitesse	"21"		Anémomètre à fil chaud	- Nécessité de l'étalonnage préalable des fils chauds
			"22"	A		
			"23"			
	à la paroi	Fluctuation de pression	"21"		Capteur de pression piézoélectrique	- Nécessité d'un étalonnage préalable
			"22"	A		
			"23"			

TABLEAU II
EXPLOITATION DES RESULTATS EXPERIMENTAUX OBTENUS
AVEC OU SANS CACHES A LA SORTIE DE LA ROUE MOBILE
(Comparaison au régime de récupération optimum)

Configuration	Sans caches	Avec caches
(i) Avant homogénéisation		
Taux de compression statique \bar{P}/P_{t1}	0,978	0,948
Taux de compression d'arrêt \bar{P}_0/P_{t1}	1,843	1,862
Mach absolu	1,138	1,173
Mach débitant	0,689	0,742
Coefficient de blocage B	0,482	0,450
Taux de récupération du diffuseur \bar{X}	0,89	0,84
(ii) Après homogénéisation		
Taux de compression statique \bar{P}/P_{t1}	1,106	1,091
Taux de compression d'arrêt \bar{P}_0/P_{t1}	1,695	1,675
Mach absolu	0,951	0,955
Mach débitant	0,297	0,295
Taux de récupération du diffuseur \bar{X}	1	1



◀ Fig. 1 Schéma du compresseur d'essais.

Fig. 2 Vue des nids d'abeilles destinés à homogénéiser l'écoulement.

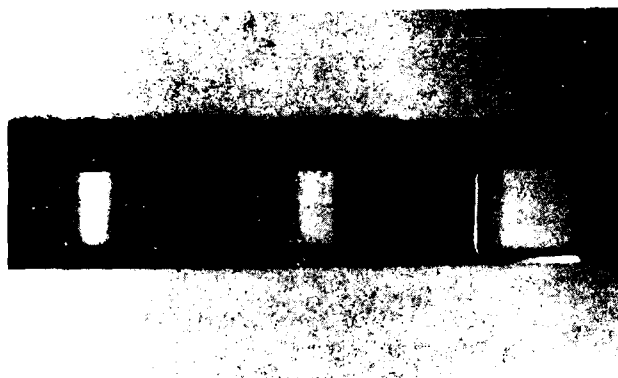
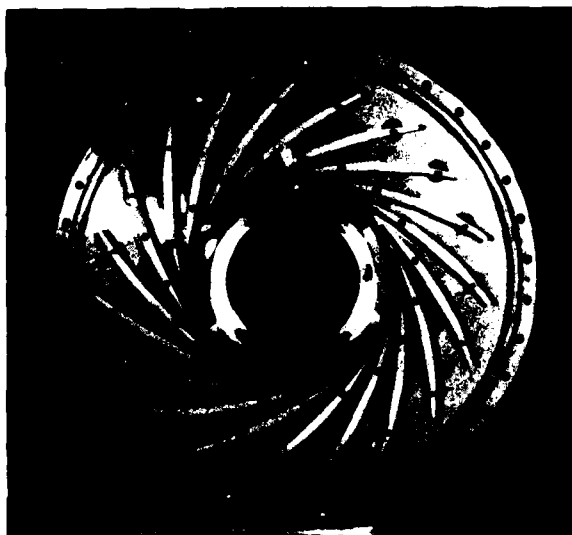


Fig. 3 - Vue des caches générateurs d'hétérogénéités.

Fig. 4 Diffuseur à aubes.



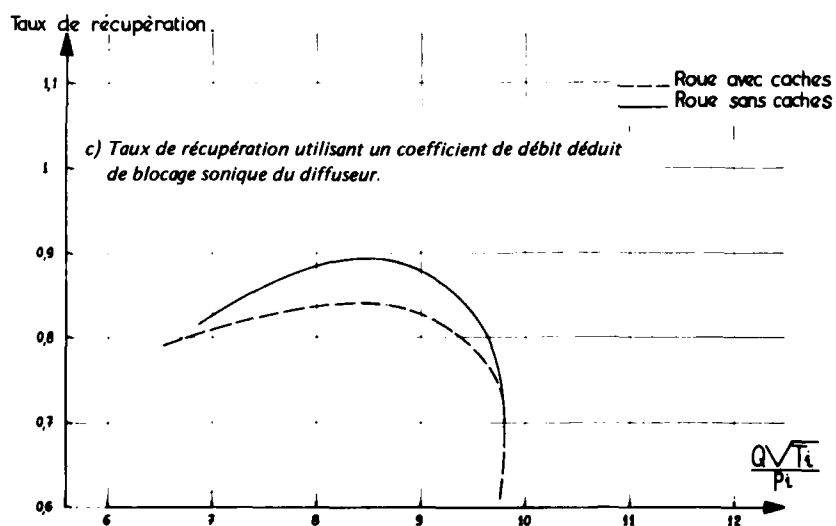
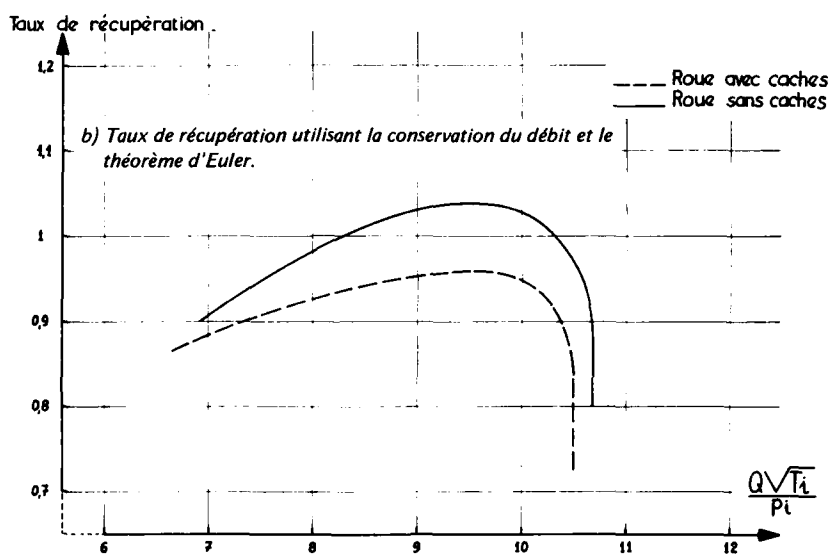
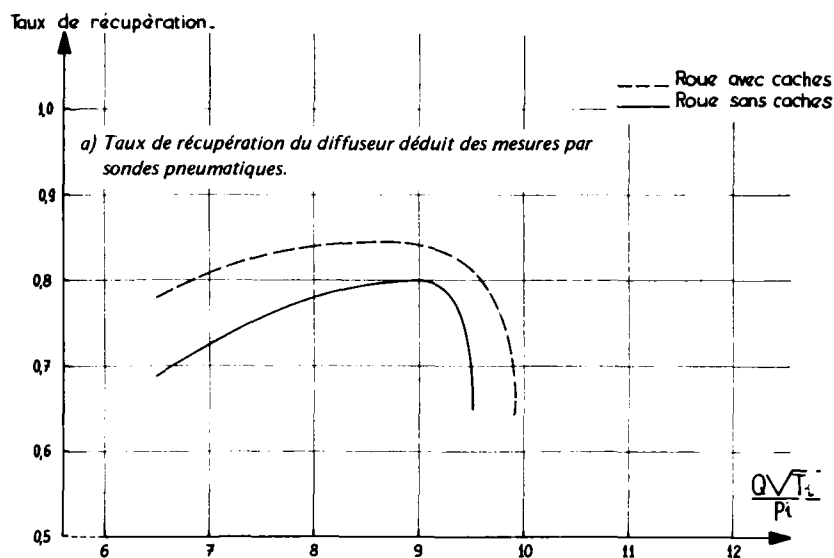


Fig. 5 – Diverses méthodes de dépouillement donnant le taux de récupération de pression du diffuseur.

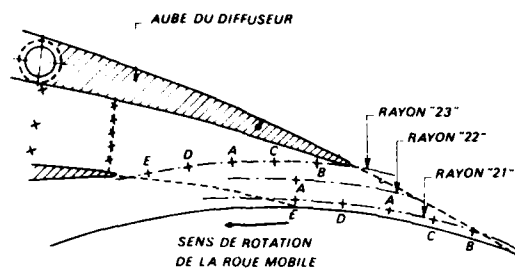


Fig. 6 – Emplacements des points de mesure dans le diffuseur lisse.

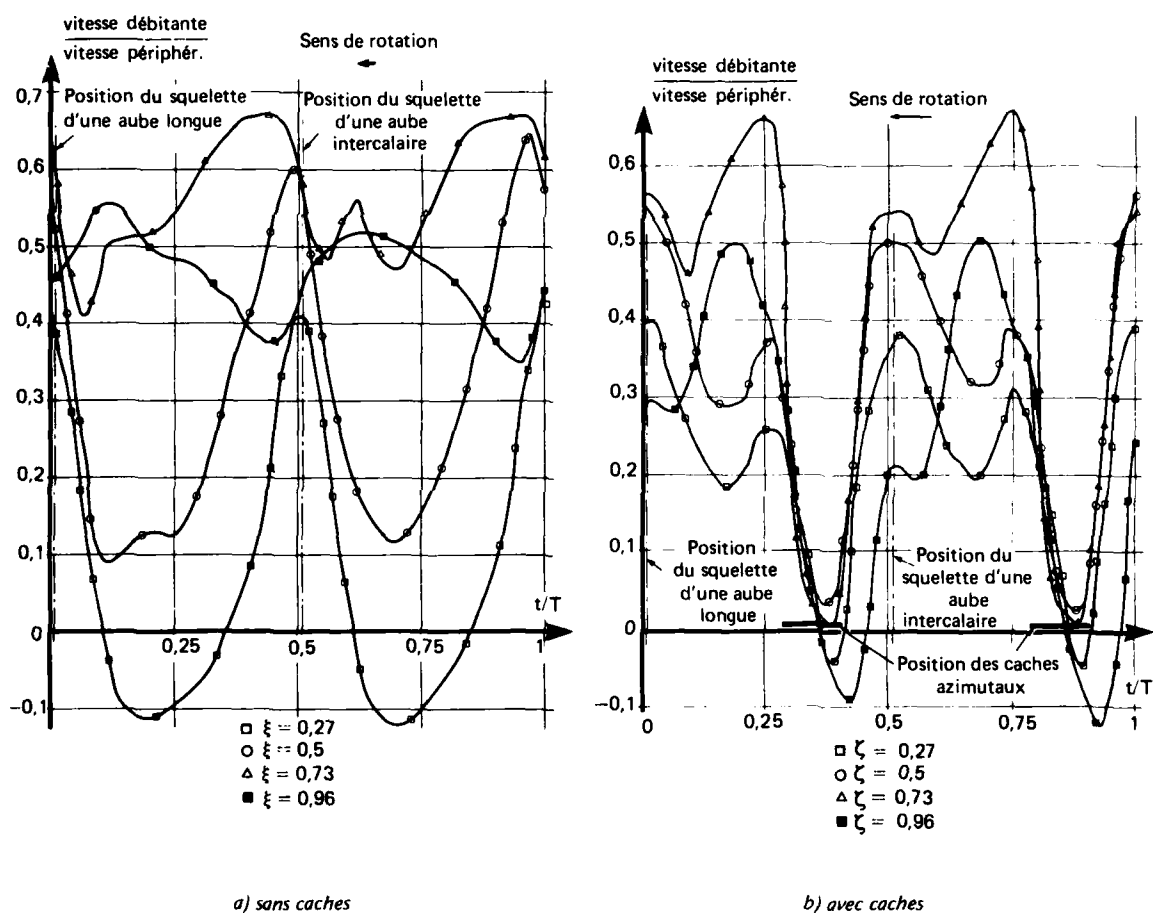


Fig. 7 – Comparaison de la répartition azimutale de la vitesse débitante à la sortie du rotor, rayon "21" avec ou sans caches (mesures effectuées au débit optimum de chaque configuration).

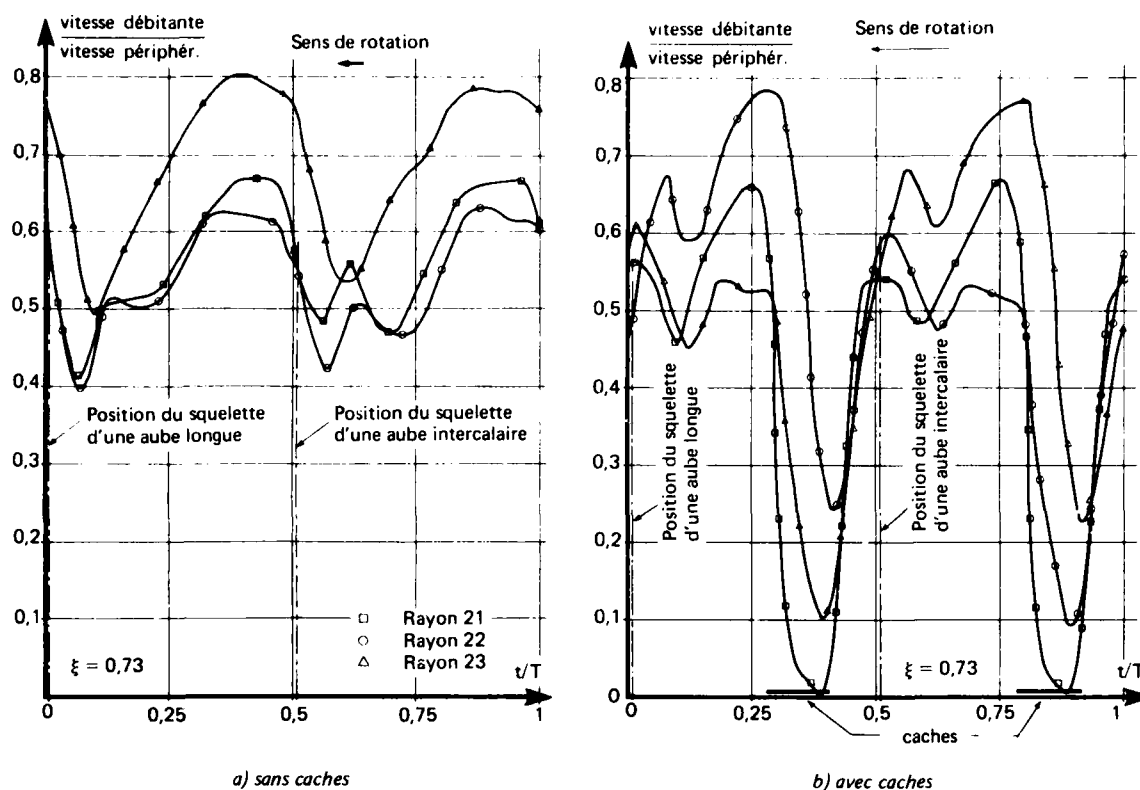


Fig. 8 — Comparaison de l'évolution entre la sortie de la roue mobile (rayon "21") l'entrée du redresseur (rayon "23") de la répartition azimuthale de vitesse débitante avec ou sans caches.

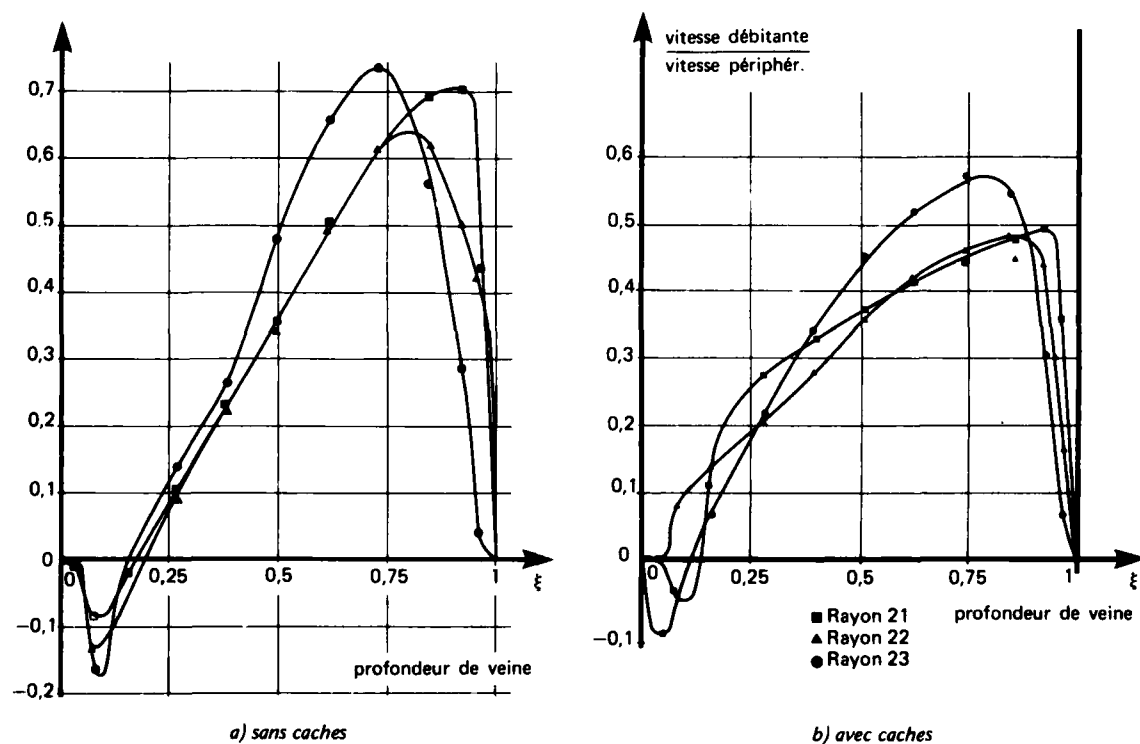
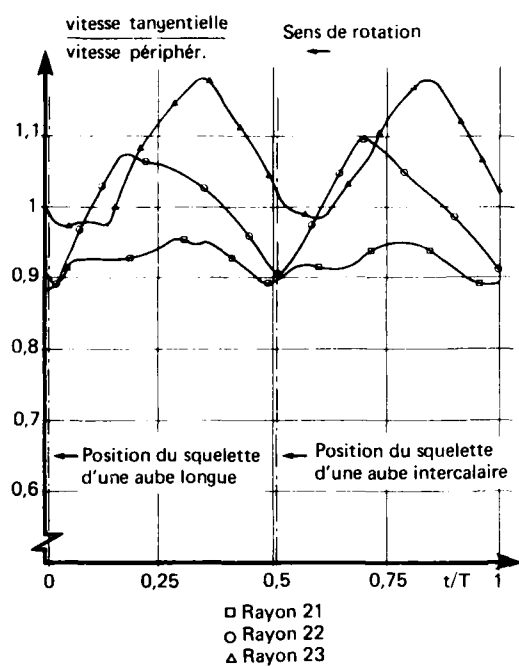
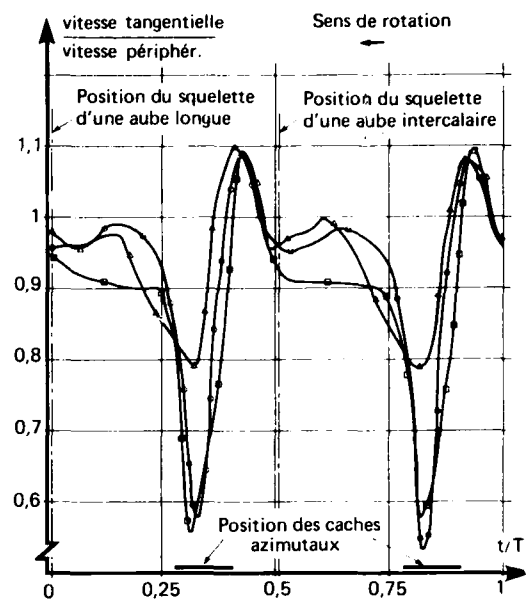


Fig. 9 — Analyse au moyen d'une sonde pneumatique à trois trous de la structure de l'écoulement à la sortie du rotor. Répartitions suivant la position axiale de la sonde de la composante débitante de la vitesse.



a) sans caches



b) avec caches

Fig. 10 — Comparaison des valeurs instantanées des composantes tangentielles de la vitesse avec ou sans caches. Mesures effectuées à la profondeur réduite $\xi = 0,73$ au débit optimum de chaque configuration.

DISCUSSION

H.Krain, DFVLR, Ge

Could the authors please expand upon their definition of blockage factor for the diffuser which was given as 0.4 or 0.45. Is this a percentage value?

Author's Reply

Two blockage factors were mentioned in the paper. The classical throat blockage was 0.8 to 0.85. At outlet of the diffuser the value of blockage factor was 0.48.

W.Jansen, Northern Research, US

Have the authors made any measurements which indicate the effects of the "caches" on the stalling characteristics of the vane diffuser (rotating stall). Are you planning to conduct such investigations?

Author's Reply

The unsteady measurements and hot wire traverses have been carried out exclusively in the stable operating regions of the system. The analysis of the flow at stall, rotating or not, has not been done. It is not intended to carry out research in this particular domain.

Y.Ribaud, ONERA, Fr

I would like to add to Fradin's reply by saying that in the region of stall there appeared in the vaneless diffuser a separation, not only in meridional velocity, but also in the absolute velocity; this occurred in both configurations.

DESIGN AND EXPERIMENTAL PERFORMANCE OF SOME HIGH PRESSURE RATIO CENTRIFUGAL COMPRESSORS

by

P. M. Came and M. V. Herbert

National Gas Turbine Establishment

Pyestock, Farnborough, Hampshire, England

Copyright © Controller HMSO London 1980

SUMMARY

A design procedure for impellers and diffusers of high pressure ratio centrifugal compressors is described. Particular emphasis is given to a philosophy of design for supersonic inlet, vaned radial diffusers. Test results are presented for several transonic diffusers operating in a 6½ pressure ratio stage. Observations of surge in this and other compressors are used as a basis for a discussion of possible surge mechanisms in centrifugal compressors.

NOTATION

A_g	total geometric throat area of channel diffuser	α	absolute flow angle	} measured from meridional direction
A_w	wetted surface area of semi-vaneless space	β	relative flow angle	
B	blockage factor (defined as 1 - blocked area/total area)	β_m	blade angle	
C_f	skin friction coefficient	γ	ratio of specific heats	
C_{pr}	pressure recovery coefficient (of vaned diffuser channel)	δ^*	boundary layer displacement thickness	
D	diameter	θ	boundary layer momentum thickness	
$f()$	a function of	Θ	diffuser channel divergence semi-angle (in radial plane)	
E	} mixing parameters defined in text	κ	included angle of diffuser channel at throat	
F		λ	included angle of diffuser vane leading edge	
G		μ	included angle of diffuser channel at outlet	
H	boundary layer shape factor ($= \delta^*/\theta$)	ϕ	diffuser channel sidewall divergence semi-angle	
h	height of blade or passage (in meridional plane)	ψ	function defined in text	
l	length of vaned diffuser channel			
M	Mach number	AR	channel diffuser geometric area ratio (outlet/throat)	
m	meridional length (measured from impeller inlet)	AS	channel diffuser throat aspect ratio ($= h_{th}/w_{th}$)	
n	number of diffuser vanes	LWR	channel diffuser length/throat width	
P	pressure	PRC	pressure recovery coefficient of semi-vaneless space	
R	gas constant	ΔH	compressor total head enthalpy rise	
r	radius			
T	temperature			
U	blade velocity (at impeller outlet if no subscript)			
V	absolute flow velocity			
W	relative flow velocity			
w	passage width			

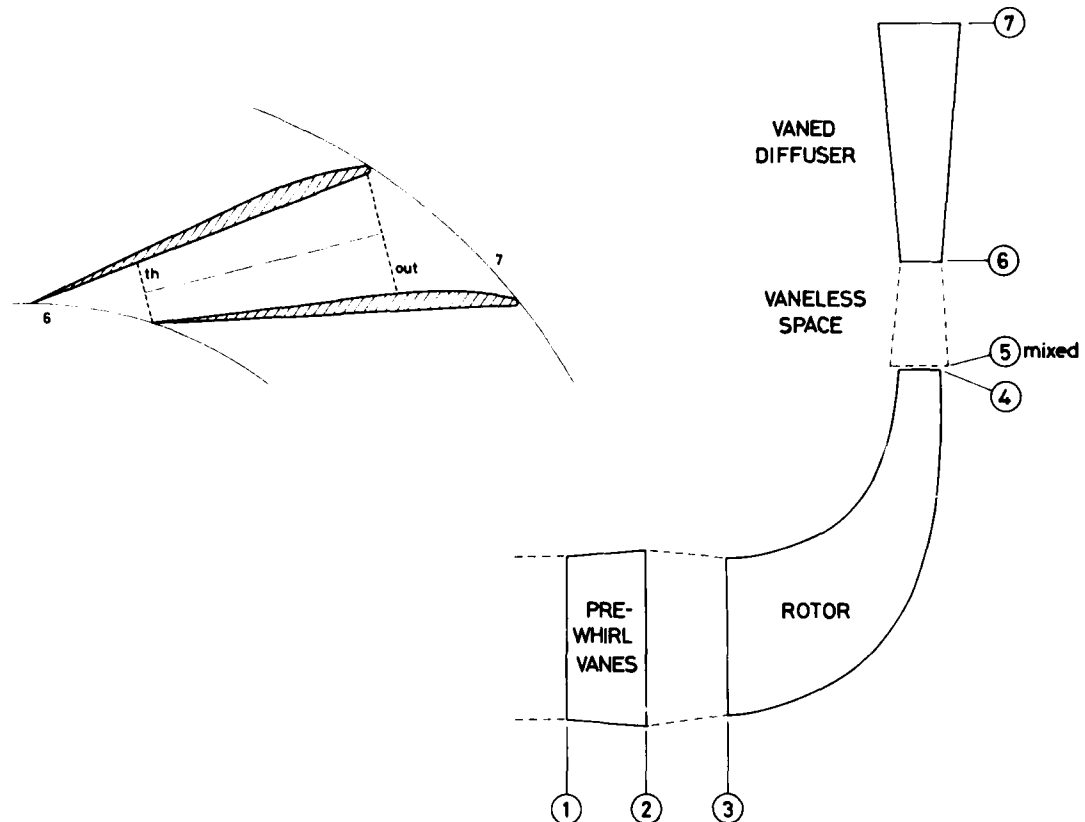
Superscripts

'	relative flow condition (no superscript means absolute flow condition)
^	core or mainstream flow quantity
-	average one-dimensional flow quantity

Subscripts

s	static condition
t	total head condition
th	diffuser channel throat
out	diffuser channel outlet
2D	two-dimensional equivalent

Numerical subscripts refer to stations in compressor as shown in diagram following



1. Introduction

In response to the evolving requirements of small engine projects, the National Gas Turbine Establishment is engaged in a programme of research on high pressure ratio centrifugal compressors. The first objective of this programme was to develop a complete procedure for the aerodynamic and mechanical design of centrifugal compressors. Emphasis was then shifted to experimental research, with the twofold intention of, firstly, assessing the effectiveness of the design procedure and, secondly, thorough analysis of both overall performance and detailed measurements, to improve understanding of compressor flow phenomena.

The initial experimental evaluation of the design procedure was described in Reference 1 which compared the performance of two compressors each with stage pressure ratio $6\frac{1}{2}$. Experimental investigations have continued, at pressure ratios of $6\frac{1}{2}$ and 8. In this paper, following a more detailed presentation of certain features of the aerodynamic design process, the design and performance of the impeller and several transonic vaned diffusers for the pressure ratio $6\frac{1}{2}$ machine are described. Observation of surge behaviour in both of the N.G.T.E. compressors, and in a number of other compressors designed and tested elsewhere, forms the basis for a discussion of the apparent connection between surge onset and the geometric features of diffuser and delivery system.

2. Compressor design procedure

A self-sufficient design procedure for centrifugal compressors must provide for the following essential requirements:

- (i) Preliminary design procedure
- (ii) Definition of impeller blade geometry
- (iii) Impeller aerodynamic analysis
- (iv) Impeller stress analysis
- (v) Vaneless space aerodynamic analysis
- (vi) Geometry definition and aerodynamic performance assessment of vaned diffuser
- (vii) Provision of manufacturing data for impeller and diffuser.

Reference 1 summarises the N.G.T.E. design procedure under these headings. Certain aspects of the techniques and methods employed have been selected for more detailed treatment in the following paragraphs, concentrating chiefly on the aerodynamic features. Figure 1 shows a summary flow chart of the entire design package.

2.1 Preliminary design

The function of the Preliminary Design Program is to compute, on an essentially "one-dimensional" flow basis, the chief parameters defining the skeletal geometry of the impeller and a rudimentary description of the flow at inlet and outlet. Taken together, these data then form sufficient basis for the subsequent detailed geometry specification and aerodynamic analysis to proceed. Usually the designer will be manipulating three types of parameter at the preliminary design stage, viz: fixed constraints (e.g. pressure ratio, rotational speed), parameters having preferred values or ranges of values (e.g. inlet relative Mach number, incidence), and parameters which are almost totally free from constraint (e.g. blade inlet angles). The Preliminary Design Program has been arranged so that the designer may, by successive trials varying the values of the "free" parameters, obtain a preliminary design within the limits of the fixed constraints and, as far as possible, with optimum values of his "preferred" parameters.

The sequence of calculations performed by the program may be broadly summarised as:

- (a) Impeller approach flow conditions
- (b) Throat conditions, for given choke margin
- (c) Impeller outlet "mixed-out" conditions
- (d) Impeller outlet unmixed "core" conditions.

Calculations (a) to (c) are performed in customary manner by solution of the equations of continuity and momentum in one-dimensional form, also invoking the perfect gas equation and Wiesner's expression for slip velocity² at the outlet "mixed-out" condition, as summarised in Reference 1 and more fully described in Reference 3. Calculation of the impeller outlet mixed-out flow conditions subsequently enables the calculation of the vaneless space flow to proceed as described later. All geometric parameters at impeller inlet and outlet are defined and may then be used as the starting-point for the full three-dimensional impeller blade description (Section 2.3.1). Calculation (d) supplies flow conditions at the outlet before the occurrence of the supposedly instantaneous mixing of boundary layers and core flow, this information being required for the subsequent detailed aerodynamic analysis of the impeller. The "reversed-mixing" calculation is, to the authors' belief, an unusual feature and is therefore described here in some detail.

Given a one-dimensional description of the impeller outlet mixed-out flow — relative velocity, Mach number, and flow angle — the object is to calculate similar parameters for the unmixed flow, together with the boundary layer blockage factor.

Ignoring the blade thickness at outlet as being small compared to the pitch, the fractional area blockage is that due to the boundary layers which can be expressed as

$$F = \delta^* f(h_u, D_u, \beta_u)$$

where the boundary layer displacement thickness, δ^* , is an average value for the four layers on hub and casing and blade pressure and suction surfaces.

An analogous momentum deficit can be written as

$$G = (\delta^* + \theta) f(h_u, D_u, \beta_u)$$

where θ is the momentum thickness of the boundary layers specified in the same way as δ^* .

Hence,

$$G = \left(\frac{1 + H}{H} \right) F$$

where H is the boundary layer shape factor.

An empirical relationship between F and overall pressure ratio is assumed as follows:

$$F = 0.4 \log_{10} (PR_{\text{overall}})$$

which may be rewritten in terms of a blockage factor,

$$B = 1 - 0.4 \log_{10} (PR_{\text{overall}})$$

Assuming $H \approx 2$, an analogous factor based on G may be written

$$\begin{aligned} E &= 1 - G \\ &= 1 - 1.5 F \\ &= 1 - 1.5 (1 - B) \end{aligned}$$

By an analysis⁴ akin to that of Stewart⁵ for axial blades, in which the governing equations of continuity and radial and tangential momenta are solved, the following "reversed-mixing" equation may be derived:

$$\psi_d \psi_c \cos^2 \beta_s + \psi_c \sin^2 \beta_s - \psi_c^{\frac{1}{2}} \cos \beta_s \left[\frac{\gamma (M_s')^2 E \psi_g + (M_s'/M_4')^2}{B \psi_g^{\frac{1}{2}}} \right] = 0$$

where

$$\begin{cases} \psi_c = \left(\frac{W_s}{W_4} \right)^2 = \left[\frac{1 + \frac{\gamma-1}{2} (M_4')^2}{1 + \frac{\gamma-1}{2} (M_s')^2} \right] \left(\frac{M_s'}{M_4'} \right)^2 \\ \psi_d = 1 + \gamma (M_s')^2 \\ \psi_g = 1 - \psi_c \left(\frac{B}{E} \sin \beta_s \right)^2 \end{cases}$$

Also,

$$M_s' = \frac{W_s}{\sqrt{\gamma R T_{ss}}}$$

Therefore, in the reversed-mixing equation, only M_4' is unknown and the equation is solved by an iterative process.

Finally,

$$\beta_4 = \sin^{-1} \left(\sqrt{1 - \psi_g} \right)$$

and

$$W_4 = \frac{W_s}{\sqrt{\psi_c}}$$

2.2 Blade geometry definition

Having obtained, by means of the Preliminary Design Program, the impeller geometry scantlings in the form of inlet and outlet diameters and blade angles, the next step is to set up an initial three-dimensional blade geometry, specifying hub and casing meridional profiles and distributions of blade camber angle and thickness. Representation of the impeller geometry is achieved by means of a system of three-dimensional analytic surfaces, for which full documentation is provided in References 1 and 6, allowing a brief summary to suffice here. An impeller blade is modelled as three surfaces (Figure 2), each of which in turn comprises four sub-surfaces or "patches". A patch may be envisaged as a surface generated by an infinite number of straight lines running from hub to casing or by an infinite number of cubic curves running along the length of the patch. These characteristics provide, on the one hand, a surface which can be formed by a straight-sided cutting tool on a numerically-controlled multi-axis milling machine and, on the other, a continuous family of shapes which are sufficiently "flexible" in lengthwise direction to afford the designer freedom of choice during the process of aerodynamic analysis and blade shape refinement.

The advantages of the "patch" system of blade specification when implemented on an interactive computer with visual display output facilities are:

- (a) Complete and unambiguous definition of the impeller shape
- (b) Rapid visual inspection of distributions of key design parameters using graphical data display
- (c) Ease of generation of geometric data in other forms, as required by aerodynamic analysis, stress analysis and manufacturing data programs
- (d) Rapid changes to geometry during the design process.

2.3 Impeller aerodynamic analysis

The full geometric description of the blade geometry previously outlined permits the generation of geometric data necessary for a process of successive aerodynamic analysis and revision of the flow path, culminating in the evolution of a satisfactory impeller design. The method of aerodynamic analysis employed in the N.G.T.E. design system will now be discussed; this is followed by an example of an impeller design, for a compressor of pressure ratio 6 $\frac{1}{2}$, the performance of which is discussed in the later Sections of this paper.

2.3.1 Method

It is widely recognised that the flow in an impeller is extremely complex, its structure being strongly influenced by three-dimensional effects and viscous forces, and so ideally some representation of these features should be included in an impeller flow model. Even at the present time, however, which is some five years after the initial development of the N.G.T.E. design procedure, three-dimensional viscous analyses for turbomachinery are only just emerging from infancy, require long periods of computer time, and are thus unsuited for compressor design. The adoption in the present design system of a conventional inviscid throughflow procedure is therefore not only inevitable but also, in all probability, to the advantage of the compressor designer.

The particular program used is the Matrix Throughflow Program of Marsh⁷, specially adapted for centrifugal impellers. Such programs are familiar to compressor designers. The analysis provides a computation of the flow conditions obtaining on a "mean-stream-surface" of the impeller through solution of a matrix form of the Laplace equation governing the stream function distribution along the mean-stream-surface. Thus the distributions through the impeller of pitchwise average values of, for example, relative velocity and static pressure may be obtained. By means of simple assumptions regarding pitchwise variation, blade-to-blade, of static pressure, an additional computation giving blade surface static pressure and relative velocity or Mach number may be made, thus providing an indication of the course of the diffusing and accelerating processes on the pressure and suction surfaces.

As used in the impeller design procedure, the throughflow program draws upon the three-dimensional "patch" definition of the impeller geometry, an interface program converting from this form to the mesh of calculating points required by the throughflow program. At this stage certain modifications to the "actual" geometry are incorporated so as to account, in an elementary manner, for the aerodynamic effects of boundary layer blockage and slip, in order that the throughflow program may calculate a mean-stream-surface representation of the inviscid core flow. Taking boundary layer effects first, the overall blockage at the impeller outlet, due to boundary layers on hub, casing, and blade surfaces, is obtained from the "reversed-mixing" calculation (Section 2.1) which yields a definition of impeller outlet core flow and boundary layer blockage. The overall blockage is divided between hub, casing, and blade surfaces by a simple, general allocation (as in Figure 3) derived from impeller boundary layer calculations by the method of Reference 8. The hub and casing boundary layer blockage thus evaluated is modelled as displacement thicknesses in the throughflow program geometric data by adjustments to hub and casing coordinates. The blade boundary layer blockage is included as an adjustment to the mean-stream-surface thickness parameter which, in unmodified form, models the effect of blade blockage alone on the mean-stream-surface. Linear distributions of boundary layer blockage between impeller leading and trailing edges are then incorporated. Blade boundary layer blockage at the leading edge is taken as zero; hub and casing displacement thicknesses each of one per cent of blade height are assumed. An alternative representation of the irreversible processes occurring within the impeller is also available. In this latter model no displacement thicknesses are added; instead a distribution of polytropic efficiency is scheduled throughout the entire (unblocked) impeller flow, following Marsh's analysis⁷.

The second adjustment is required to account for the effect of slip on the mean-stream-surface camber angle distribution. Between leading edge and about 70 per cent meridional distance the effects of slip are assumed to be negligible and the mean-stream-surface is given a camber angle variation identical to that of the blade itself (Figure 4). At the impeller outlet, the mean-stream-surface camber angle is set equal to β_4 , the relative flow angle of the isentropic core obtained from the "reversed-mixing" calculation into which is fed mixed-out conditions based on, inter alia, Wiesner's expression for slip factor² (Section 2.1). Between the 70 per cent position and impeller outlet a smooth curve joining these prescribed values is assumed.

2.4 Design of an impeller

As an illustration of the use of the aerodynamic analysis summarised ante, the design of an impeller for a pressure ratio 6.5 compressor will now be described, concentrating primarily on the means of effecting improvements to the initially selected impeller flow-path geometry. The objectives of the centrifugal compressor research project of which this impeller design formed a part are given in Reference 1.

The compressor was designed for a rotational speed of 40,000 rev/min, specific speed of 68 (Baljé's definition⁹), mass flow of 1.81 kg/s and an overall pressure ratio of 6.5. Other salient design parameters are given in Table I.

Figure 5 portrays the first, arbitrarily chosen, impeller flow-path geometry. When analysed by the Matrix Throughflow Program (with the distributed polytropic efficiency model) the mean-stream-surface relative velocity diagram appeared as in Figure 6a. The blade surface relative velocities were transformed into values of blade loading coefficient*, also given in Figure 6a. Two simple criteria were applied to the calculated results. The first criterion was adapted from the work of Dallenbach¹⁰ and Smith¹¹: for avoidance of boundary layer separation, relative velocity/peak velocity should not fall below 0.6 on any surface. The second criterion, that the blade loading coefficient must not exceed 0.7, is based on Morris & Kenny's interpretation¹² of Hill & Moon's data¹³ concerning the effects of rotation on separation at the suction surface of a rotating radial flow passage.

Inspection of Figure 6a shows that both criteria are contravened: there is an unnecessarily steep diffusion gradient at the hub between leading edge and 40 per cent meridional distance which is linked with the appearance of high loading at that point. The sharp drop following the peak loading is due to the half-blade leading edge, doubling of the blade number acting to halve (approximately) the blade-to-blade static pressure difference. The casing mid-channel velocity distribution suffers somewhat less rapid diffusion, although the steeper drop at about 20 per cent meridional distance has again caused a corresponding local peak in the loading diagram. It will be noted that the loading fails to drop to zero at the trailing edge as it naturally must in reality. This is an inevitable feature of the approximate method of obtaining the blade surface static pressures which merely bases its calculation on the mean-stream-surface conditions obtaining at each grid point inside the impeller without attempting to satisfy any kind of trailing edge closure conditions.

From this initial geometry and analysis a sequence of successive revision and further analysis was undertaken. Eleven geometries in all were examined, but for the present account comments are confined to the final outcome which is compared with the first attempt i.e. Figures 5 and 6. It may be observed that the steep hub diffusion was eliminated in the finally accepted design by a quite small adjustment to the hub meridional profile which also removed the high peak loading at 40 per cent meridional distance. By the use of some intuitive judgement, the casing camber angle distribution ahead of the throat (up to about 10 per cent meridional distance) was flattened (Figure 5) in order to avoid the possible danger of supersonic expansion on the suction surface — a feature which the throughflow program would not be able to detect — noting the fairly high value of design incidence of 7° and relative inlet Mach number of only just less than unity (Table I).

3. Diffuser design procedure

3.1 The vaneless space

As has already been explained, flow conditions at impeller outlet are assumed to be one-dimensional, i.e. blockage due to blades and boundary layers or wakes fully mixed-out, and the velocity triangle such that slip velocity conforms to the correlation of Wiesner². This means that boundary layers on the two sidewalls of the vaneless space grow from zero thickness at impeller outlet. The classic treatment given by Stanitz¹⁴ for flow development in the vaneless space fails to distinguish between displacement and momentum thicknesses, so it has been necessary to recast the analysis from first principles⁸. In other respects similar assumptions to those of Stanitz have been made, namely that static pressure and flow angle are uniform across mainstream and boundary layers; however, only configurations with their centreline in a radial plane are considered, although variation of axial dimension with radius (usually taken as linear) is allowed. Sidewall boundary layers are treated as turbulent and attached.

The spiral flow calculations in the vaneless space can fall into two phases: the first in which boundary layers develop on the two sidewalls with a central region of uniform core flow; the second in which the two boundary layers have met in the middle. In both cases the analysis is written in terms initially of h , h' ($= h - 2\delta^*$) and h'' ($= h - 2\delta^* - 2\theta$), and the simple method of Stratford & Beavers¹⁵ for a one-seventh power-law velocity profile, in which H ($= \delta^*/\theta$) is a function of Mach number only, is used to connect the boundary layer integral parameters. So long as the two boundary layers remain unjoined, h' and h'' can then be written as functions of h , θ and \hat{M} ($=$ core Mach number), and three simultaneous differential equations emerge in terms of the three variables \hat{M} , α ($=$ flow angle) and θ — one of these (Equation C) is the appropriate form of the momentum integral equation. The Stratford & Beavers relation for H is

$$*\text{blade loading coefficient is defined as } \Delta P_s / \left[\gamma P_s (M')^2 \right]_{\text{mean-stream-surface}}$$

responsible for the terms inside the square brackets in Equation A. Step-by-step solution of Equation A for \hat{M} , Equation B for α , and Equation C for θ then proceeds in a series of small increments of radius.

$$\frac{1}{\hat{M}} \frac{d\hat{M}}{dr} \left\{ \frac{h (1 - \hat{M}^2 + \epsilon \tan^2 \alpha) + 2H (1 + H) \theta}{1 + \frac{\gamma - 1}{2} \hat{M}^2} - 2H\theta \left[\frac{0.704 \hat{M}^2}{1 + 0.8 \hat{M}^2} + \frac{0.14 \hat{M}^2}{1 + 0.1 \hat{M}^2} \right] \right\}$$

$$= H C_f \zeta \sec \alpha - \frac{h \sec^2 \alpha}{r} - \frac{dh}{dr} \quad \dots (A)$$

$$\frac{1}{\tan \alpha} \frac{d\alpha}{dr} = - \frac{\epsilon}{\hat{M}} \frac{d\hat{M}}{dr} \left(\frac{1}{1 + \frac{\gamma - 1}{2} \hat{M}^2} \right) - \frac{1}{r} \quad \dots (B)$$

$$\frac{d\theta}{dr} = \frac{C_f \zeta \sec \alpha}{2} - \frac{\theta \sec^2 \alpha}{r} - \frac{\theta}{\hat{M}} \frac{d\hat{M}}{dr} \left(\frac{2 + H - \hat{M}^2 + \epsilon \tan^2 \alpha}{1 + \frac{\gamma - 1}{2} \hat{M}^2} \right) \quad \dots (C)$$

where

$$\begin{cases} \epsilon = \left[1 - \frac{2\theta}{h} (1 + H) \right]^{-1} \\ \zeta = \left[1 + \frac{1}{4} \left(\frac{dh}{dr} \right)^2 \right]^{\frac{1}{2}} \end{cases}$$

After each step a check is made as to whether the two boundary layers have met: this is only likely to occur if there is no vaned diffuser — i.e. if the vaneless space is large in extent. Thereafter it is assumed that a similar power-law velocity profile is maintained, with physical thickness of boundary layer equal to half the passage axial dimension, and the centreline total pressure is progressively reduced. In that situation h' and h'' become functions of h and \hat{M} (= centreline Mach number) only. The three variables are now \hat{M} , α and \hat{P}_t (= centreline total pressure); Stratford & Beavers relations give rise to the various Γ terms now appearing in all the three simultaneous equations (D, E and F). Step-by-step solution for increments of radius proceeds as before. (Full derivation of Equations A to F will be found in Reference 8.)

$$\frac{1}{\hat{M}} \frac{d\hat{M}}{dr} \left[\frac{\hat{M}^2 - \sec^2 \alpha - \gamma \hat{M}^2 (\Gamma_a + \Gamma_b)}{1 + \frac{\gamma - 1}{2} \hat{M}^2} + \frac{\gamma_c}{1 - \Gamma_a} + \left(\frac{\tan^2 \alpha}{\Gamma_e} - \gamma \hat{M}^2 \right) \left(\frac{\Gamma_b \Gamma_c}{1 - \Gamma_a} - \Gamma_d \right) \right]$$

$$= \frac{1}{h} \frac{dh}{dr} + \frac{\sec^2 \alpha}{r} + \left(\frac{\tan^2 \alpha}{\Gamma_e} - \gamma \hat{M}^2 \right) \frac{C_f \zeta}{h \cos \alpha} \quad \dots (D)$$

$$\frac{1}{\tan \alpha} \frac{d\alpha}{dr} (\tan^2 \alpha - \gamma \hat{M}^2 \Gamma_e) = \frac{1}{\hat{M}} \frac{d\hat{M}}{dr} \left[\frac{1 + (\gamma - 1) \hat{M}^2}{1 + \frac{\gamma - 1}{2} \hat{M}^2} - \frac{\Gamma_c}{1 - \Gamma_a} \right] + \frac{1}{h} \frac{dh}{dr} + \frac{1 + \gamma \hat{M}^2 \Gamma_e}{r} \quad \dots (E)$$

$$\frac{1}{\hat{P}_t} \frac{d\hat{P}_t}{dr} \left(\frac{\tan^2 \alpha}{\gamma \hat{M}^2 \Gamma_e} - 1 \right) = \frac{1}{\hat{M}} \frac{d\hat{M}}{dr} \left[\frac{1 - \hat{M}^2 + \frac{\tan^2 \alpha}{\Gamma_e}}{1 + \frac{\gamma - 1}{2} \hat{M}^2} - \frac{\Gamma_c}{1 - \Gamma_a} \right] + \frac{1}{h} \frac{dh}{dr} + \frac{\sec^2 \alpha}{r} \quad \dots (F)$$

where

$$\begin{cases} \Gamma_a = 0.125 (1 + 0.8 \hat{M}^2)^{0.44} \\ \Gamma_b = 0.097 (1 + 0.1 \hat{M}^2)^{-0.7} \\ \Gamma_c = 0.088 \hat{M}^2 (1 + 0.8 \hat{M}^2)^{-0.56} \\ \Gamma_d = 0.0136 \hat{M}^2 (1 + 0.1 \hat{M}^2)^{-1.7} \\ \Gamma_e = 1 - \Gamma_a - \Gamma_b \end{cases}$$

With a vaned diffuser — the case of most usual interest — this treatment[†] yields values of flow angle and mainstream Mach number at the pitch circle of the vane leading edges, these being the two properties of prime concern for vaned diffuser design.

3.2 The vaned diffuser

The first feature of any vaned diffuser design to be decided is the level of Mach number at vane leading edges. Although diffusion in the vaneless space is achieved with relatively high efficiency, it occurs relatively slowly, so that most of the burden of diffusion has to fall on the vaned diffuser. Thus there is in general a need to obtain the maximum length of channel after the throat (consistent with other factors) within a given overall engine diameter, leading to an incentive to keep the vaneless space short. Sidewall divergence of the vaneless space does not in principle alter this argument, as excessive divergence can lead to a situation in which the meridional component of velocity at the wall approaches zero and stalling results; while quantitative evidence is insufficient to lay down any hard and fast rule, 10° outward lean from radial on each or either wall of the vaneless space is felt to be about the limit of safety on present knowledge, i.e. 20° included angle of divergence, and this accomplishes relatively little extra diffusion. The design practice at N.G.T.E. has for many years been to use a parallel-sided vaneless space with radius ratio about 1.05, that figure being what is regarded as the minimum to avoid rotor blade excitation. At the end of such a vaneless space the Mach number is still supersonic, around 1.05 to 1.15 depending on impeller pressure ratio, blade sweepback and specific speed. Consequently N.G.T.E. designs of vaned diffuser are traditionally "transonic", capturing and diffusing flow from a condition of $M > 1$.

A further point to be noted in relation to this choice of Mach number level is the major influence, amply demonstrated by Runstadler¹⁶, of throat blockage on the subsequent pressure recovery achieved in a given channel geometry. Blockage grows quite rapidly in the vaneless space (typical figures of blockage factor being 0.95 at radius ratio 1.05 and 0.85 at radius ratio 1.25, with further blockage growth in the semi-vaneless space between vane leading edge and throat), so that even disregarding any geometrical limitation as to overall diameter there is a clear conflict between the effects of having on the one hand a short vaneless space, low throat blockage (certainly beneficial) and high vane leading edge Mach number (> 1 , arguably disadvantageous), and on the other hand a longer vaneless space, higher throat blockage (certainly disadvantageous) and lower leading edge Mach number (< 1 , arguably beneficial). A satisfactory resolution of this conflict, in favour of a short vaneless space, is possible if the vaned diffuser is designed for efficient transonic diffusion in the semi-vaneless space.

A prime requirement is then to ensure that the Mach number is nowhere significantly increased above the leading edge value, either by incidence or by vane surface shape. For this reason the semi-vaneless space and the channel portions of the vane surfaces in the N.G.T.E. method are designed independently; use, for instance, of single circular arc contours from leading edge to trailing edge would impose a restriction denying the designer freedom to choose an optimum combination of vane number, leading edge angle (i.e. incidence), and throat area. Once the flow has passed the throat it may fairly be regarded as constrained in direction by the channel walls, but ahead of the throat the vane surface shape must be designed in relation to the rotating frame imposed by the flow leaving the vaneless space. Considerations of geometry show that the total angle by which the vane surface between leading edge and throat can change is less than the vane pitch angle ($= 2\pi/\text{number of vanes}$) by an amount equal to the sum of the vane included angle at leading edge (λ) and the channel included angle at the throat (κ) — see Figure 7. If the vane is "unwrapped" from around the rotor, to give an effective change of surface angle relative to the rotating flow field, this difference ($\lambda + \kappa$) is seen to represent surface curvature in an expansive sense, wherefore it is desirable to keep both λ and κ to minimum values. The angle λ is usually made 4° , and a minimum of 1° taken for κ , the initial channel divergence angle, to allow for boundary layer growth immediately after the throat. A cubic contour is then used for the vane surface between leading edge and throat, the object being ideally to distribute the curvature more or less uniformly from leading edge to throat along a wholly concave profile; in practice a mathematical point of inflection in the cubic at up to about 10 per cent of the surface length from leading edge is sometimes accepted if the surface locally appears visually straight on a greatly-magnified scale of plot.

[†]The vaneless space flow calculations are performed using one part of a composite computer program having the general purpose of predicting overall performance and intermediate flow properties at various stations through the compressor over the whole compressor operating range; it is known as the Performance Prediction Program.

At all conditions below choking the channel is a subsonic diffuser. In the N.G.T.E. design method the channel is disposed about a straight centreline (see Figure 7), the two sidewalls which enclose the vanes being either parallel or slightly divergent. Some divergence of the channel sidewalls obviously enables a greater area ratio to be achieved in a given length, which is usually advantageous. It is felt that the amount of channel sidewall divergence should be limited to half the optimum divergence of a straight-sided parallel-sidewall channel diffuser: vide Runstadler¹⁶, the latter is about 8° for throat aspect ratio near unity, so the sidewall divergence limit is then about 4° - in the case of a straight-sided channel that would give symmetrical divergence in both directions, preserving minimum wetted perimeter at all stations. Mostly, however, the channels are not designed to be straight-sided (in the radial plane), partly in order to accommodate a low value of κ for reasons indicated ante. Given a value of $\kappa = 1^\circ$, for example, either there must be a rapid change in wall angle while the Mach number is still relatively high, which could cause immediate and permanent separation, or the profile must be "trumpet"-shaped. The latter has the advantage that the rate of diffusion (pressure gradient) is least where the Mach number is highest, and vice versa, so minimising the dangers of separation in the region where most recovery is to be gained, at the expense of the final region where the dynamic head has lowest value.

Against this it may be argued that, in accomplishing diffusion from given conditions through a given area ratio, the least boundary layer growth and hence the best pressure recovery corresponds to a velocity distribution in which the diffusion is greater at the start than at the end. This thesis is readily illustrated by the simple incompressible concept that, between given limits of velocity (V) and surface length (S), the boundary layer growth is a function of $\int V^2 dS$: this integral is clearly greatest for a "trumpet"-shape of passage, less for a "wedge"-shape (i.e. straight-sided), and least for a "tulip"-shape. However, the merit of such argument in this particular situation is debatable. Diffuser channels are usually designed, for reasons of maximum pressure recovery, close to incipient stall, and have thick boundary layers at their entry. In these conditions a rate of diffusion which is graduated from gentle at first and increases towards outlet may have real advantages. If separation were never a danger, then the "trumpet"-shape is certainly wrong; where that danger is imminent, the case is not proven one way or the other.

Channel designs are based on achieving given area ratio in given length, hence having a certain effective divergence angle. For example, in the case of a parallel-sidewall channel, a "trumpet"-shape might be chosen with included angle changing progressively from 1° at the throat (κ) to 14° at outlet (μ), or in the case of a channel with $2\frac{1}{2}^\circ$ sidewall divergence, from $\kappa = 1^\circ$ to $\mu = 10^\circ$. Attempts to produce comparative diffuser designs to check out experimentally the relative merits of "trumpet" versus "wedge"-shapes of channel (the latter having $\kappa = \mu$) have highlighted the difficulty of obtaining a satisfactory vane surface shape ahead of the throat when κ is high: Figure 8 illustrates two designs for the same duty - the one with straight-sided channel (Figure 8b) is clearly unacceptable. For all these reasons it is usual N.G.T.E. practice to adopt a design of channel having straight (but diverging) sidewalls and a "trumpet"-shaped passage in the radial plane.

Designing the channel for optimum pressure recovery within the available geometric limits of diameter is of course of paramount importance. Here the work of Runstadler¹⁶ on isolated channel diffusers has provided data maps of great value. Optimum pressure recovery is shown to correspond to a state of incipient stall, and the value attainable to be heavily influenced by throat blockage. Runstadler's rectangular diffusers were all straight-sided and had parallel sidewalls; the salient geometric parameters governing pressure recovery are defined as outlet/throat area ratio (AR), length/throat width ratio (LWR), and throat aspect ratio (AS). Inevitably, of course, many designs of diffuser channel do not lie on any of the Runstadler data maps. In the first place he tested only three values of AS ($\frac{1}{2}$, 1 and 5) and the great differences in pattern found between AS of $\frac{1}{2}$ and 1 (in which range most compressor diffusers lie) render accurate interpolation well-nigh impossible. Secondly, he concentrated on the range of LWR 10 to 20, whereas some compressor diffusers may be forced to have values considerably below 10. A third major difficulty is to know how to treat channels with diverging sidewalls. Tentative means have, however, been found to "extend" Runstadler's data to cater for intermediate AS, low LWR, and sidewall divergence, as described fully in Reference 8 and summarised in Reference 17. Essentially the procedure used is to reduce all channels for purposes of calculating pressure recovery to a common form of representation having parallel sidewalls and AS = 1, by the following means.

- (i) Introduce a "two-dimensional equivalent channel width" given by $w_{th,2D} = w_{th} \times \frac{h_{th}}{h_{out}}$. Then the geometric parameters defining the "two-dimensional equivalent" channel are:

$$AR; \quad LWR_{2D} = \frac{l}{w_{th,2D}}; \quad AS_{2D} = \frac{h_{out}}{w_{th,2D}}$$

$$\text{and} \quad 2\theta_{2D} = 2 \tan^{-1} \frac{AR - 1}{2 LWR_{2D}}$$

- (ii) When $AS < 1$, apply a change in 2θ [$= \Delta(2\theta)$] at the given LWR so as to produce an effective 2θ (and hence an effective AR) at that LWR, for use with data at $AS = 1$; that is to say, assume

$$C_{pr} [LWR; 2\theta; AS < 1] = C_{pr} [LWR; 2\theta - \Delta(2\theta); AS = 1]$$

$$\text{where} \quad \Delta(2\theta) = \left(\frac{1}{6 AS} + 1 \right) \left(\frac{1}{AS} - 1 \right)$$

$$\text{Then } AR_{(AS=1)} = 1 + 2 LWR \tan \frac{1}{2} [2\theta - \Delta(2\theta)]$$

When $AS > 1$, within the usual range of interest only small error is likely by treating as if $AS = 1$.

If the channel has diverging sidewalls then throughout this section (ii) AS is to be read as

$$AS_{2D}, \text{ LWR as } LWR_{2D}, \text{ and } 2\theta \text{ as } 2\theta_{2D}.$$

Reduction to a common datum of $AS = 1$ has the advantage from the design point of view that the optimum 2θ for that AS lies, according to Runstadler's data maps, close to 8° ($\pm \frac{1}{2}^\circ$ at the level of throat blockage of usual interest for compressor diffusers) irrespective of other parameters, so that one can immediately select as one of the channel design conditions

$$2 \tan^{-1} \frac{AR_{(AS=1)} - 1}{2 LWR_{2D}} \approx 8^\circ$$

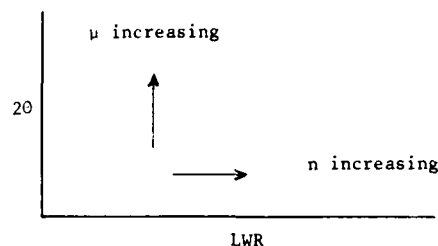
The vane diffuser design problem can be stated as, generally, given circumscribing radii at vane leading and trailing edges, and incident flow conditions at leading edge (angle, blockage and Mach number) to find, for a combination of vane number and throat dimensions giving the total effective throat area required to match the impeller flow characteristics, a vane shape which combines a satisfactory surface contour ahead of the throat with a channel having geometric properties (AR , LWR and AS) affording the best pressure recovery possible consistent with these other factors. In some circumstances other considerations may conceivably override the desire for optimum pressure recovery, if for instance it could be concluded with certainty that compressor surge was affected by diffuser vane number (a matter which is discussed later), but for the present we assume the design problem to be as just stated. It is immediately obvious (e.g. from a simple picture showing only vane chord lines) that the more vanes there are the higher LWR can potentially become. With the present design method an upper limit to vane number is usually imposed by the appearance of an undesirable inflection in the cubic contour giving a convex region of vane surface near the leading edge. Another restriction to freedom of choice of vane number may arise from the need to avoid vibrations excited by "coupling" effects between rotor blades and diffuser vanes.

At this stage we take a provisional value of geometric throat area (A_g), which is subject to future adjustment in the light of calculation of throat blockage (B_{th}) for a particular selected geometry of diffuser. For a parallel vaneless space h_6 (= axial dimension at leading edges) is known. Suitable values for the radii of circles closing the vane shape at leading and trailing edges are prescribed. The remaining variables are now

- (i) n (= number of vanes): primarily controlling LWR
- (ii) μ : primarily controlling 2θ (= mean passage divergence in the radial plane)
- (iii) h_7 (= axial dimension at trailing edges)
: primarily controlling 2ϕ (= included angle of sidewall divergence)

To a first approximation, for a given h_7 , the effects of μ and n may be represented as in the diagram following. Hence the first skirmish is made using a rough estimate for h_7 and varying μ and n systematically. When a suitable n has been found (at the desired 2θ), a second skirmish is required, at the same n , to adjust μ and h_7 together in order to bring both 2θ and 2ϕ to the chosen values. It should be

appreciated here that none of the factors affecting choice of n concerns conditions after the throat, and since the amount of sidewall divergence between leading edge and throat is small, h_7 (and hence 2ϕ) can be altered without upsetting the choice of n ; μ alone needs to change with h_7 , in order to restore 20.



The vane shapes are generated each time by a short computer program (called the Vane Design Program) which has as input the following data:

- inner and outer circumscribing radii (r_6 and r_7)
- radii of circles closing vane shape at leading and trailing edges
- leading edge tip included angle (λ)
- included angle of channel at throat (κ)
- included angle of channel at outlet (ν)
- vane leading edge angle, to match incident flow direction (α_6)
- number of vanes (n)
- axial dimensions at leading and trailing edges (h_6 and h_7)
- total geometric throat area (A_g)

and which produces a complete specification of one vane and one channel as per Figure 7, namely coordinates of the surfaces GJSPDH and EQ, and the point of inflection in the cubic describing the portion DH (the point of inflection should desirably be outside the region of the vane DH), together with a graphical display which includes a large-scale plot of the cubic portion DH, also the various channel dimensions and properties required for assessment of channel pressure recovery (w_{th} , h_{th} , w_{out} , h_{out} , l , 2θ , 2ϕ , AR , LWR_{2D} , AS_{2D}). Each design of a series with varying n is examined to determine whether a maximum limit imposed by cubic contour shape has been reached. Then, when a suitable design has been selected, the channel pressure recovery coefficient (C_{pr}) is obtained from the "extended" Runstadler data.

Finally, a check is necessary on the assumed value of B_{th} . For this purpose an additional portion of the Performance Prediction Program is used, which carries the calculation on beyond the end of the vaneless space and evaluates blockage growth along two paths: first, that on the vane surface (starting from zero thickness), and second, a mean path on each of the two sidewalls (starting from the conditions at end of the vaneless space). The "core" Mach number distribution along each path is assumed to be linear from the starting value to the (unknown) mean throat value. Iteration is required between continuity and blockage growth to determine the mean throat Mach number. (Built into this iteration, but not relevant to the design-point case, is an empirical schedule which arranges for "core" total pressure to be reduced below the leading edge value at flows towards the surge end of the flow range. This device was found a convenient way of dealing with an otherwise unrealistic situation at operating conditions towards surge in which calculated displacement thicknesses at the throat corresponded, on simple power-law velocity profile assumptions, to physical thicknesses greater than the throat dimensions.) Diffuser throat blockage factor (B_{th}) is thus determined, and, if necessary, a change to A_g is fed back into the Vane Design Program and the procedure repeated.

4. Test experience

The N.G.T.E. design procedure has been used for the designs of a number of compressors for commercial or research applications. For the N.G.T.E. internal research programme two compressors have been designed and tested, their pressure ratios being 6.5 and 8.0 respectively. This Section describes some of the observations made during a series of tests on the former compressor. The discussion of surge in Section 6 draws upon test experience with both compressors.

4.1 Tests with vaneless diffuser

The impeller for the pressure ratio 6.5 compressor has been described ante. In order to assess its performance the impeller was first installed on the test rig with a vaneless diffuser. The measuring station downstream of the impeller was chosen to be at a radial position of $1.065 \times$ impeller tip radius, rather than at the tip itself where strong pressure fluctuations due to passing "jets" and "wakes" may engender poor measurement accuracy. Eight tapings were used to measure static pressure; total head pressure was then derived on a mass-flow-continuity basis, and pressure ratio and isentropic efficiency were calculated. An estimate, by the method of Reference 8, of the efficiency loss incurred between impeller

outlet and the measuring station is $1\frac{1}{2}$ percentage points, so true impeller efficiency may be supposed to be higher than the test-derived values by about this amount.

Experimental performance characteristics are shown in Figure 9. A peak efficiency at design speed of 85.5 per cent was obtained which compares well with the design target modified to account for the vaneless diffuser loss as already explained. The peak was in fact obtained at the design mass flow, with a choke flow margin (defined as the difference between design and choke flows divided by choke flow) of 10 per cent. The combination of good efficiency and good choke flow margin is seen as a particularly satisfactory outcome of specifying high impeller casing incidence (7 degrees) at design mass flow, the intention having been to achieve high choke flow with the peak of the efficiency characteristic situated in the region of design mass flow.

The attainment of correct incidence and flow margin depended critically upon estimates of the radial variation of inlet axial velocity and incidence, required as input for the Preliminary Design Program and obtained from an exploratory computation of the inlet duct flow using the Matrix Throughflow Program (as described earlier).

In order to provide comparative measurements, therefore, a radial traverse of the impeller approach flow was carried out at a station 12.7 mm upstream of the blade leading edge plane using a simple pitot probe. Its readings were combined with wall static pressures taken at the same axial station, yielding axial velocity and hence flow parameters in the impeller rotational frame. Figure 10 shows axial velocity and relative flow angle compared to the throughflow estimates. Agreement is quite good, the only serious discrepancies arising very close to the annulus walls where the presence of local boundary layers is observed in the measured results. It is concluded that the throughflow predictions of inlet conditions allowed a satisfactory compromise between impeller incidence and choke flow margin to be achieved.

4.2 Tests with vaned diffusers

Further tests with this impeller were carried out using several different vaned diffusers. The results from three such builds will be described here. All these three vaned diffusers (details as in Table II) were designed according to the method and principles set out in Section 3.2, save that the first (that with 41 vanes) was an early design which departed from later thinking in having

- (i) $2\theta_{2D}$ appreciably below 8° , the difference being subsequently estimated as losing about $\frac{1}{2}$ percentage point in stage efficiency
- (ii) no channel sidewall divergence.

A further point to note in relation to the first (41-vane) diffuser is that it was designed before the Performance Prediction Program became available, and consequently was based on an unreliable estimate of leading edge incident flow angle (α_6); as Table II shows, subsequent calculations suggest that this diffuser suffered 3.6° expansive incidence at the compressor design flow and speed, resulting in some further penalty in stage performance. Vane shapes of all three diffusers are illustrated in Figures 11 to 13.

The second (13-vane) diffuser is a deliberate "oddity". It was designed to conform as nearly as possible to the third (37-vane) diffuser in every respect except number of vanes. The value of $2\theta_{2D}$ ($= 8.5^\circ$, c.f. 8° for the 37-vane) results from the increase in optimum value when $AS < 1$. As will be described more fully in a later Section, certain evidence has been adduced as indicating that a small number of vanes gives better choke-to-surge flow range, other things being equal. Should this prove to be the case, it is clear that to take advantage of the increased flow range will necessitate some loss of design-point efficiency due to the much reduced available area ratio of channel (Table II). In this series of tests the 13-vane diffuser was included especially to check whether it gave improved flow range.

Figures 14 to 16 present the stage performance characteristics with these three vaned diffusers. Let us first compare the 41-vane build (Figure 14) with the vaneless diffuser build (Figure 9). At the design flow ($= 1.81$ kg/s) and speed, both these two builds had the same impeller tip clearance (≈ 0.28 mm), and should thus have had the same impeller efficiency. The estimated loss in the 1.065 radius ratio vaneless space of the "vaneless" build is 1.5 percentage points, so we take a value of 0.870 for impeller efficiency. That implies 10.5 percentage points lost between impeller and outlet of that vaned diffuser — a rather poor result. But that diffuser is realised to have been an incorrectly designed one, as explained ante, and certainly capable of improvement. Figure 11 shows clear evidence of the leading edge expansion resulting from 3.6° (estimated) incidence, causing the Mach number to rise from 1.05 (estimated) to around 1.29 (c.f. 1.22 from supersonic flow tables for that amount of incidence). What deserves particular note is the quite wide choke-to-surge flow range of this vaned diffuser build (Figure 14): choke flow at design speed is nearly identical between vaneless and vaned builds (calculation suggests that impeller and diffuser

choke together at this speed, as is the usual intention for compressors designed at N.G.T.E.), so comparison of surge flows gives direct comparison of flow range.

	100 per cent design speed		
	choke flow	surge flow	$\frac{\text{surge flow}}{\text{choke flow}}$
vaneless	1.99	1.58	0.794
41-vane	1.98	1.67	0.843

Next we come to the 13-vane diffuser build. Unfortunately the no-rotation impeller tip clearance was set at too low a value so that "zero" clearance was reached and the test stopped while the compressor was still some way from surge at design speed. Nevertheless it is abundantly clear from comparison of Figures 14 and 15 for 90 and 95 per cent design speed that the choke-to-surge flow range has not been improved through this major reduction of vane number. Total-to-total efficiency, however, has risen. There is a consistent increase of about 3 to 3½ percentage points relative to the 41-vane diffuser build; at 1.9 kg/s and 100 per cent design speed the difference in efficiency is 3.4 percentage points. This efficiency gain must be apportioned among several causes, which can be classified as

- (i) effect of impeller tip clearance
- (ii) more limited diffusion to the final measuring station due to relatively higher diffuser channel outlet Mach number (a feature inherent in the design: Table II)
- (iii) potential design improvements, namely less leading edge incidence and more nearly optimum 20_{2D} .

In order to make a fair comparison of the several diffusers tested, means must be established of fixing a datum which takes into account differences of impeller tip clearance and of the extent of diffusion. Some discussion of tip clearance loss appears in the next Section of this paper: at 1.9 kg/s and design speed the clearance for the build with 13-vane diffuser was 0.05 mm as against 0.28 mm for the 41-vane build, and this difference is reckoned to be worth about 0.75 percentage point in impeller (and hence stage) efficiency. The question of what value to attach to the final dynamic head leaving the diffuser of any compressor is to some extent tied up with the type of collector arrangement following the vaned diffuser and with the application for which the compressor is intended; however, when as here a snail-shell form of collector is used, a reasonable comparison may be made by calculating in each case the effect on efficiency of losing the whole channel outlet dynamic head - this is tantamount to comparing total-to-static efficiencies. On that basis we get, at 1.9 kg/s:

	41-vane build	13-vane build
estimated outlet \bar{M}	0.259	0.334
dynamic head as % of P_t	4.56	7.43
value as %age points in efficiency	3.1	5.1
difference from datum	datum	-2.0

In sum, then, the 3.4 percentage points to the credit of the 13-vane build must be reduced by 2.75 (0.75 for impeller tip clearance and 2.0 for dynamic head), leaving a net advantage of 0.65 percentage point. This shows that useful gain has resulted from elimination of the leading edge expansion due to incidence; Figure 12 shows only very slight expansion in the transonic region, to a maximum Mach number of ≈ 1.085 .

Finally, turning to the 37-vane diffuser build, this had similar impeller tip clearance to the original 41-vane case (0.33 mm c.f. 0.28 mm), and Figure 16 indicates about 1.0 percentage point improvement in efficiency at design speed, while at the same time more diffusion has taken place. Casting up the account in the previous manner, we have:

	41-vane build	13-vane build	37-vane build
estimated outlet \bar{M}	0.259	0.334	0.158
dynamic head as % of P_t	4.56	7.43	1.73
value as %age points in efficiency	3.1	5.1	1.2
difference from datum	datum	-2.0	+1.9
tip clearance effect	datum	-0.75	+0.1
total %age points	datum	-2.75	+2.0
measured efficiency difference	datum	+3.4	+1.0
corrected efficiency difference	datum	+0.65	+3.0

This comparison indicates a satisfactory result of the diffuser redesign from the 41-vane build to the 37-vane build.

5. Effect of impeller tip clearance

According to the treatment used in Reference 8, the loss due to impeller tip clearance is assumed to increase rapidly between zero clearance and some fairly small value, and thereafter linearly with the quantity "clearance/passage height": in other words the linear relationship does not pass through the condition "zero clearance, zero loss". The form of this assumption was suggested by a survey of the rather limited amount of data available, and the treatment is not claimed to be rigorously accurate. In the foregoing Section the instance of a compressor having clearance of 0.05 mm at design speed (that with 13-vane diffuser) lies in the non-linear region, all other cases cited being in the linear region.

It is of interest to note some N.G.T.E. test experience obtained with change of impeller tip clearance on the compressor of pressure ratio 8. This impeller, although of quite large diameter (270.8 mm), had blade height at impeller outlet only 5.31 mm, i.e. relatively smaller in proportion to impeller diameter than the majority of compressors for which the available literature provides data concerning the effect of tip clearance on performance. In this respect it was quite similar to the N.G.T.E. compressor of pressure ratio 6½. Small blade height is, of course, inevitably encountered with any very small diameter compressor, and the feature which is of importance in this discussion is the relationship between blade height and what can be employed as a minimum practical operating clearance.

Two builds of this compressor of pressure ratio 8, with a vaned diffuser, differed only in the amount of impeller tip clearance. With the first of those builds clearance fell as speed was increased from 1.75 mm at zero rotation to around 1.14 mm at design speed. With the second of those builds clearance fell from 0.97 mm at zero rotation to around 0.25 mm at design speed. There was a consistent improvement of 1.3 to 1.5 percentage points in peak stage efficiency at all speeds (from 70 to 100 per cent of design) in the later build as a result of closing the clearance.

Exchange rates between clearance and efficiency are often cited which would lead one to expect a much larger change in efficiency for such a change in clearance. It is therefore worthwhile giving an explanation of the reason which, it is believed, accounts for the difference in behaviour in the case of this compressor. Essentially it amounts to the fact that the change in clearance makes a significant change to total passage height, due to the small blade height. Predictions of performance by the method of Reference 8 illustrate the point. Three cases have been calculated at design speed and the peak efficiency value of flow:

- a) datum case: blade height 5.31 mm + clearance 0.25 mm = passage height 5.56 mm;
thus clearance/passage height = 0.045
- b) clearance increased by 0.89 mm to 1.14 mm, giving passage height 6.45 mm and
clearance/passage height 0.177; loss of impeller efficiency from datum case is
0.0147, which agrees well with the experimental result
- c) clearance 1.14 mm as for case (b), but passage height left at datum value 5.56 mm;
thus clearance/passage height = 0.205; loss of impeller efficiency from datum case
is 0.0316.

It can thus be seen that if passage height remains substantially the same (as it would do if blade height is such that clearance represents only a small proportion of the total passage) then change of clearance has a much larger effect on efficiency. In the present instance, with so small a blade height, much of the effect of changing clearance/passage height has been offset by the simultaneous effect of changing passage height itself.

Reduction of tip clearance per se is of course always of benefit to efficiency, since two sources of loss are thereby reduced: first, in the case of an unshrouded impeller, the leakage of flow round blade tips from pressure side to suction side; second, the tendency for flow to recirculate from outlet to inlet along a path following the casing surface. Other things being equal, reduction of impeller outlet passage height (i.e. reducing h_u , keeping constant both h_s and clearance/ h_u) affects efficiency via the loss arising from mixing at impeller outlet — which represents a major part of the whole impeller efficiency deficit. The effect on this mixing is two-fold: in the first place the dynamic head of the flow before mixing is increased; secondly the area ratio of enlargement (area-after-mixing/area-before-mixing) is increased; the flow in other words is first accelerated and subsequently has to undergo more diffusion relative to the datum situation. There are other considerations concerning change of flow angles before and after mixing, but the net effect of reducing impeller outlet passage height in this manner can be seen to be detrimental

to efficiency. Thus a change of clearance which significantly affects passage height introduces two opposing effects.

6. Compressor surge

It is commonly the case that, for a given rotor at a given speed, surge occurs at a higher flow when the rotor is followed by a vaned diffuser than when it is followed only by a vaneless space. This is almost always true at high rotational speeds (although one known exception will be cited herein); at speeds of 70 per cent of design and lower, vaned and vaneless builds tend to surge at values of flow rather closer to one another. The compressor with pressure ratio $6\frac{1}{2}$ described in previous Sections conforms to this usual pattern. (Even if vaned and vaneless builds surge at the same flow at low speed, the choke-to-surge flow range of the vaned build will be smaller due to the lower choke flow imposed by the diffuser throat. For this reason we shall usually refer in this discussion to minimum mass flow rather than to flow range.)

The mechanisms by which surge is induced in either the vaneless or vaned diffuser case are not at all well understood. But there is clear evidence that different diffuser geometries following the same impeller can in some situations markedly affect surge of a compressor stage. Thus we can conclude that, while a variety of potential surge-producing mechanisms may exist, it is one associated in some manner with the vaned diffuser which is usually the first to come into play. This represents the case of greatest practical interest for gas turbine compressors.

Data which, in this connection, are sometimes adduced as having particular significance relate to the number of diffuser vanes. For instance, one example is known, for an impeller with 19 blades, where reducing diffuser vane number from 29 to 13 was accompanied by a marked fall in minimum mass flow, particularly at the higher rotational speeds where flow range had formerly been narrow (see Table III, from Reference 18). To this may be added the general observation that there are quite a large number of published instances in which compressors with relatively narrow flow range at design speed have had a large number of diffuser vanes (more than the number of impeller blades) while some compressors with relatively wide flow range at design speed have had a small number of diffuser vanes (e.g. that described in Reference 19, with 34 impeller blades and 13 diffuser vanes). Such evidence has been linked with the idea, put forward in Reference 20, that when the number of diffuser vanes is less than the number of blades at impeller outlet then every diffuser passage is always receiving some mixture of "jet" and "wake" flow from the impeller, whereas when the number of diffuser vanes is the greater it is possible to have some passages receiving flow consisting alternately of all low-energy "wake" fluid and all high-energy "jet" fluid, causing a rapid and large cyclical variation of mean total pressure and mean flow angle at the vane leading edge. On that argument premature onset of surge in the latter situation is ascribed to some breakdown of throughflow in the diffuser passage(s) so treated.

Given a vaneless space small in extent in relation to the rate of mixing-out between "jets" and "wakes", such a flow situation might perhaps be envisaged. But as an explanation of differences in surge limit any such reasoning seems to be negated by the work of Baghdadi and Macdonald²¹. They tested three centrifugal-compressor-type vaned diffuser systems, which were supplied through a "vortex nozzle", consisting of inwards radial flow through a ring of swirl-imparting vanes, followed by a contoured approach section which turned the flow radially outwards ahead of the diffuser. This arrangement simulated the mean outlet flow conditions from an impeller, but without the pronounced "jet-wake" pattern of a real compressor. And yet these authors obtained a surge phenomenon typical of a compressor; they also record an effect of diffuser vane number, the larger number having earlier surge (although marked differences of vane shape, in addition to number, between their three builds detract from the conclusiveness of the latter fact).

In the same context it is most noteworthy that the 41-vane diffuser build of our compressor with pressure ratio $6\frac{1}{2}$ (and 34 impeller blades at outlet) has, by comparison with other machines of comparable pressure ratio (e.g. Reference 22), very wide flow range at design speed, and that changing the diffuser to one with 13 vanes produced no improvement at all in flow range (see Section 4.2). A similarly wide flow range at design speed has been achieved with another N.G.T.E. design of compressor having pressure ratio 8, as shown in Figure 17, and in that case also the number of diffuser vanes (41) exceeded the number of blades at impeller outlet (32). Diffuser vane number as such, therefore, certainly cannot be the predominant influence on surge.

The compressor to which Figure 17 relates affords the one known instance where the minimum mass flow at high rotational speed is lower (although not much) with a vaned diffuser than with only a vaneless space.

It is also worth mentioning the question of diffuser vane incidence. Reeves²³ has proposed linking surge with a particular condition of incidence to the diffuser vane leading edges. Because of the design error in vane leading edge angle mentioned in Section 4.2, the 41-vane diffuser build of our compressor with pressure ratio 6½ had mean incidence at surge (as estimated for all speeds tested) of about +4.9°. Similar calculations by our Performance Prediction Program for the machines of Reference 22 give values of mean incidence at surge in the range +1.5° to -0.5°, and another instance is known* for which the similarly calculated mean incidence at surge is -4.8°. Since the two extremes of incidence (+4.9 and -4.8°) relate to compressors with the best flow range at design speed of all those mentioned, the evidence clearly does not support any critical value of diffuser vane incidence as a surge criterion.

The literature contains a number of suggestions relating surge to some diffusion limit in the semi-vaneless space (e.g. References 20, 21, 24, 25). This seems a more fruitful line of argument. It has been found, in a survey of available compressor data, that in almost all cases the pressure rise coefficient of the semi-vaneless space (PRC), defined as $(P_{s,th} - P_{s,e}) / (P_{t,e} - P_{s,e})$ and calculated by our Performance Prediction Program for the experimentally determined surge flows, shows a notable degree of consistency in value over the high speed range for a given compressor. There is, however, a very wide variation of the surge value of PRC among the different compressors, considerable variation appearing between different builds having the same impeller but different diffuser geometries. An attempt has been made by the present authors to correlate the variation in PRC at surge between compressor builds with the property "wetted surface area of the semi-vaneless space/geometric throat area" $[=A_w/A_g]$, where A_w can be approximated by the expression

$$n \left\{ \left[w_{th} + \frac{h_e + h_{th}}{2} \right] \sqrt{\left(D_6 \sin \frac{\pi}{n} \right)^2 - w_{th}^2} - \frac{D_6^2}{4} \left(\frac{2\pi}{n} - \sin \frac{2\pi}{n} \right) \right\}$$

The parameter A_w/A_g may be regarded as simply a form of passage 'L/D'; since wetted area = length × perimeter and A_g = cross-sectional area, it follows that A_w/A_g is proportional to length/hydraulic mean depth. Supposing there to be a diffusion pressure gradient for the semi-vaneless space at which some critical degree of stall exists, then the longer the passage (i.e. the larger is 'L/D') the greater the overall pressure rise attainable at that gradient, and so the further flow can be reduced before reaching the critical situation. Thus a large value of A_w/A_g might be expected to give wide operating range and vice versa. Such a correlation would serve to explain the reason for two effects which have been found to lower minimum mass flow, namely:

- (1) reduction of vane number at constant A_g and h_{th} ; this increases w_{th} and hence A_w
- (2) reduction of A_g by change of h_{th} at constant n ; A_g is reduced in proportion to h_{th} , but A_w is reduced less than pro rata with h_{th} , so that A_w/A_g increases.

The result of the survey is summarised in Figure 18, which for simplicity shows data for the range of speed 90 to 100 per cent only. The two parts of this Figure relate to two different types of delivery system. One is for vaned diffusers discharging into annular "dump" collectors of snail-shell form, the "tongue" of the off-take pipe from the collector being reasonably remote from the trailing edges of the diffuser vanes. (It is well known that a snail-shell collector in too close proximity to diffuser vane trailing edges can promote a considerable circumferential non-uniformity of static pressure and cause premature surge.) In the other case the diffusers discharged into radial-to-axial bends followed by one or more rows of axial cascade vanes, the latter serving to provide further diffusion and subsequent flow straightening. There is a notable difference in the pattern of data for the two cases. Four builds of our compressor with pressure ratio 6½ appear in Figure 18a, corresponding to diffusers with 13, 37, 41 and 57 vanes, in all cases tested with snail-type collector, this being the present form of the N.G.T.E. test rig.

The consistency of PRC between speeds for a given compressor affords support for the theory that surge is somehow related to a limiting value of semi-vaneless space diffusion. But evidently that limit depends upon the individual arrangement, and, although the evidence of Figure 18 is certainly not alone adequate proof, there is some indication that the type of delivery system may exert a significant influence. A test programme has been initiated to fit a bend-plus-axial-vane delivery system on the N.G.T.E. test rig in place of the snail-shell collector, in order to see whether the 13-vane and 37-vane diffuser builds of the pressure ratio 6½ compressor will then change their surge characteristics.

*This being the Rolls-Royce compressor with 13-vane diffuser mentioned in Table III.

It might be postulated that a delivery system consisting of an infinite plenum chamber could hardly impose any overriding influence upon the onset of a phenomenon which is, almost certainly, related to a stalling situation somewhere in the flow system. The snail-shell collector might be regarded as approaching that infinite plenum. A bend-plus-axial-vane delivery arrangement, on the other hand, contains further system components which could themselves be potentially capable of producing a form of stall — e.g. either the convex side of the bend passage, or the axial vanes. The latter arrangement might then be regarded as containing two stages of stall-prone diffusing elements, namely the semi-vaneless space and some part of the delivery system. In that way a joint dependence on the semi-vaneless space and on the delivery system in determining surge might be envisaged. Some analogy appears possible between such a mutual interrelationship in a centrifugal compressor stage and the situation in a high-pressure-ratio multi-stage axial compressor: there surge at high speed coincides with stall of the last stage, while at low speed surge occurs at a condition where the last stage is free from stall but the first stage is well into stall. If there is any truth in such a loose analogy, the part of a centrifugal compressor corresponding to the "last stage" of the axial would be different according to whether there is or is not a stall-prone delivery system following the vaned diffuser. Then, if a stall-prone delivery system is present (i.e. the bend-plus-axial-vane case), that component could, at least in principle, be the critical element of the whole system at high speed, and thus, conceivably, account for surge occurring at a flow above that experienced when the semi-vaneless space is the last stall-prone element.

7. Conspectus

This paper has described a procedure for the design of high pressure ratio centrifugal compressor stages and has illustrated its use with an account of the design and experimental performance of one impeller and three diffusers for a pressure ratio 6½ compressor stage. The diffusers were designed to operate with supersonic approach flow and the measurements demonstrate that, with careful attention to the vane design in the transonic region ahead of the throat, good performance can be achieved.

Observations of surge behaviour in a number of centrifugal compressor stages having vaned diffusers support a connection between surge and the diffusion taking place between diffuser vane leading edge and throat, as has been proposed by other investigators. The nature of the dependence is, however, apparently also influenced by the arrangement of the compressor delivery system. Collectors of snail-shell type seem to give a relatively better surge condition (i.e. lower minimum mass flow) compared with the collectors more typically used in aircraft gas turbines, consisting of a radial-to-axial bend followed by axial straightening vanes.

TABLE I

COMPRESSOR FOR PRESSURE RATIO 61

IMPELLER DESIGN DATA

Rotational speed	40,000 rev/min
Specific speed (Balje definition)	68
Prewirl angle (α_3)	zero
Number of full blades	17
Number of half-blades	17
Inlet hub diameter	} D_3 60.96 mm
Inlet casing diameter	
Inlet casing relative Mach number (M_3')	0.975
Inlet hub blade angle	} $\beta_{\infty 3}$ 31.36 deg
Inlet casing blade angle	
Inlet hub incidence	14.4 deg
Inlet casing incidence	7.0 deg
Inlet axial velocity at casing/inlet axial velocity at mean radius	1.1
Flow margin (= design flow/inducer choking flow)	0.91
Diameter at impeller outlet (D_4)	274.8 mm
Blade height at impeller outlet - i.e. passage height (h_4) less tip clearance	5.81 mm
Passage height at start of vaneless space (h_5)	5.48 mm
Outlet blade angle ($\beta_{\infty 4}$)	30.0 deg
Blade tip speed (U)	575.5 m/s
Outlet absolute Mach number (M_5)	1.11
Work input parameter ($\Delta H/U^2$)	0.80

TABLE II

VANED DIFFUSER DETAILS

n	radius ratio (D_4/D_1)	D_h	D_r	h_h	h_r	leading edge vane angle	A_g	w_{th}	h_{th}	w_{out}	h_{out}	λ	κ	μ	$2\theta_{2D}$	2θ	AR	LAR_{2D}	AS_{2D}	η_{est}	η_{est}	η_{out}
41	1.05	288.6	393	6.11	6.11	72.5	1613	6.44	6.11	14.19	6.11	4	1	10.5	5.74	0	2.20	11.98	0.95	76.1	1.050	0.238
12	1.05	288.6	400	5.48	10.39	74.6	1630	19.76	6.35	23.87	9.46	4	1	5.6	8.51	2.50	1.80	5.38	0.71	74.6	1.064	0.297
17	1.05	288.6	400	5.48	10.02	74.6	1613	7.51	5.81	16.27	9.44	4	1	11.0	7.98	2.49	3.52	18.10	2.05	74.6	1.064	0.145

dimensions in mm; angles in deg.

estimated flow quantities at compressor design-point

TABLE III

SURGE DATA FOR ROLLS-ROYCE COMPRESSOR(Reference 18)

Percent design speed	Mass flow at surge ÷ mass flow at intended compressor design point	
	Build with 13-vane diffuser	Build with 29-vane diffuser
100	0.957	1.052
90	0.758	0.815
80	0.600	0.658
70	0.456	0.505
60	0.358	0.384

This compressor had a bend-plus-axial-vane collector system

References

1. P. M. Came The development, application and experimental evaluation of a design procedure for centrifugal compressors
Proc. I. Mech. E. Vol 192, No. 5, 1978
2. F. J. Wiesner A review of slip factors for centrifugal impellers
J. Engineering for Power, October 1967, p.559
3. M. G. Jones Impeller computer design package Part I: A preliminary design program
N.G.T.E. internal paper, 1976
4. M. V. Herbert Some notes on loss coefficients relating to turbine blades with finite trailing edge thickness
ARC Paper 34755, 1972
5. W. L. Stewart Analysis of two-dimensional compressible-flow loss characteristics downstream of turbomachine blade rows in terms of basic boundary-layer characteristics
NACA TN3515, 1955
6. D. J. L. Smith
H. Merryweather The use of analytical surfaces for the design of centrifugal impellers
Intl. J. for Numerical Methods in Engineering, Vol 7, p.137-154, 1973
7. H. Marsh A digital computer program for the throughflow fluid mechanics in an arbitrary turbomachine using a matrix method
ARC R&M 3509, 1967
8. M. V. Herbert A method of performance prediction for centrifugal compressors
Part I - Analysis
ARC R&M 3843, 1980
9. O. E. Baljé A study on design criteria and matching of turbomachines
Part B: Compressor and pump performance and matching of turbo components
ASME Paper 60-WA-231, 1960
10. F. Dallenbach The aerodynamic design and performance of centrifugal and mixed flow compressors
SAE Tech.Prog. Series, Vol 3, 1961
11. D. J. L. Smith Turbulent boundary layer theory and its application to blade profile design
ARC CP 868, 1966
12. R. E. Morris
D. P. Kenny High pressure ratio centrifugal compressors for small gas turbine engines
From "Advanced Centrifugal Compressors", ASME, 1971
13. P. G. Hill
I. M. Moon Effects of Coriolis on the turbulent boundary layer in rotating fluid machines
MIT Gas Turbine Laboratory Report No. 69, 1962
14. J. D. Stanitz One-dimensional compressible flow in vaneless diffusers of radial- and mixed-flow centrifugal compressors, including effects of friction, heat transfer and area change
NACA TN 2610, 1952
15. B. S. Stratford
G. S. Beavers The calculation of the compressible turbulent boundary layer in an arbitrary pressure gradient - a correlation of certain previous methods
ARC R&M 3207, 1959
16. P. W. Runstadler Pressure recovery performance of straight-channel single-plane divergence diffusers at high Mach numbers
USAAVLABS Technical Report 69-56, 1969
17. M. V. Herbert A method of centrifugal compressor performance prediction
ASME Symposium on "Performance Prediction of Centrifugal Pumps and Compressors", 1980
18. - Private communication, Rolls-Royce Ltd
19. M. G. Hodskinson
P. H. Parker The turbomachinery of the British Leyland 2S/350/R engine
ASME Paper 74-GT-148, 1974
20. C. Rodgers
L. Sapiro Design considerations for high-pressure-ratio centrifugal compressors
ASME Paper 72-GT-91, 1972
21. S. Baghdadi
A. T. Macdonald Performance of three vaned radial diffusers with swirling transonic flow
J. Fluids Eng. June 1975, p.155
22. M. G. Beard
C. M. Pratt
P. H. Timmis Recent experience on centrifugal compressors for small gas turbines
ASME Paper 78-GT-193, 1978
23. G. B. Reeves Estimation of centrifugal compressor stability with diffuser loss-range system
From "Centrifugal Compressor and Pump Stability, Stall and Surge", ASME, 1976
24. D. P. Kenny Supersonic radial diffusers
AGARD Lecture Series No. 39 on Advanced Compressors, 1970
25. K. Toyama
P. W. Runstadler
R. C. Dean An experimental study of surge in centrifugal compressors
J. Fluids Eng. March 1977, p.115

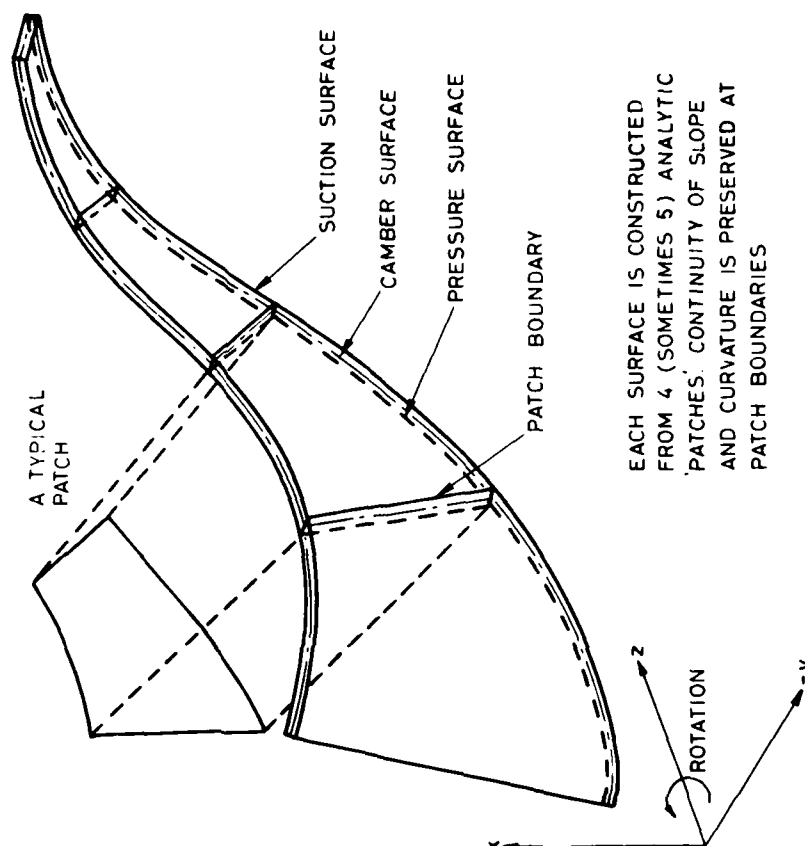


FIG. 2 ANALYTIC PATCH REPRESENTATION OF IMPELLER VANE SURFACES

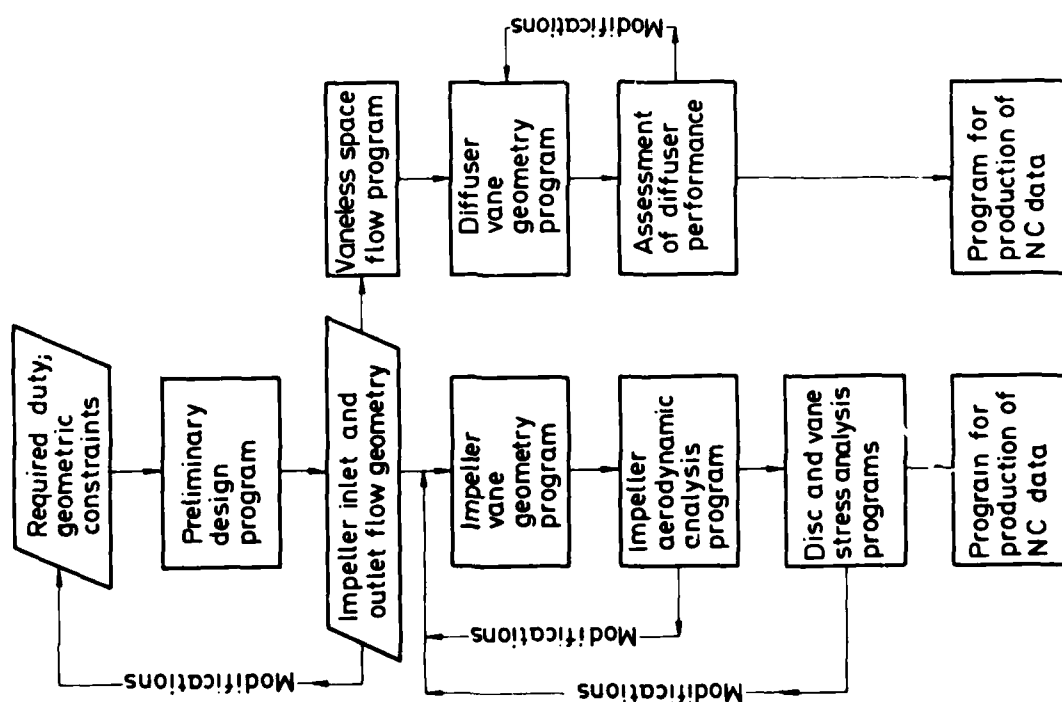
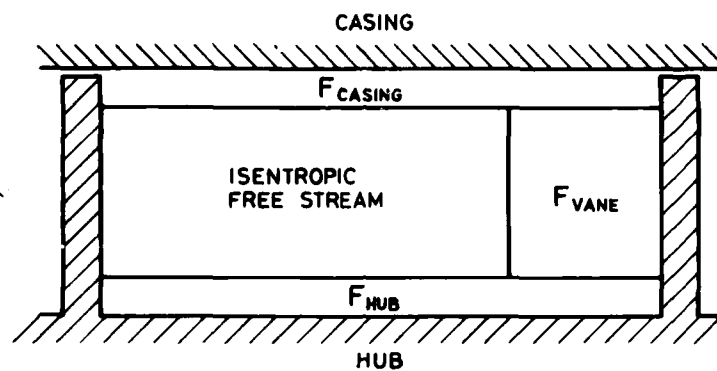


FIG. 1 CENTRIFUGAL COMPRESSOR DESIGN SEQUENCE



$$F = \frac{\text{TOTAL AREA BLOCKED BY BOUNDARY LAYERS}}{\text{CHANNEL CROSS-SECTIONAL AREA}}$$

$$= F_{\text{CASING}} + F_{\text{HUB}} + F_{\text{VANE}}$$

FIG. 3 BOUNDARY LAYER BLOCKAGE ASSUMED AT IMPELLER OUTLET

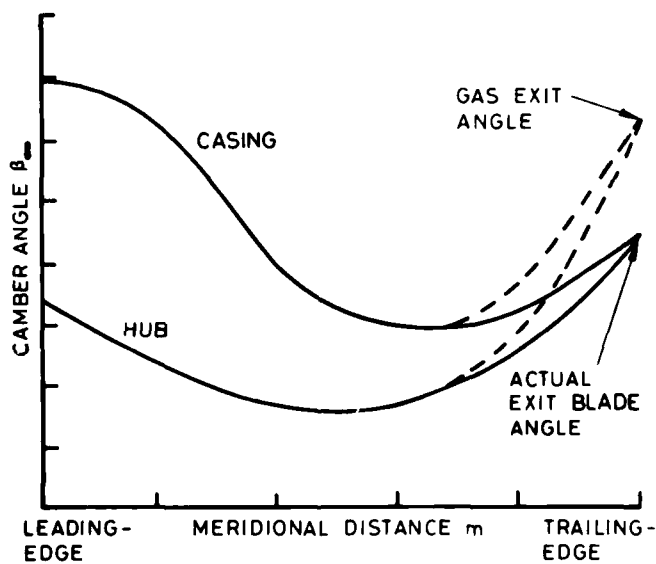


FIG. 4 ADJUSTMENT OF MEAN-STREAM-SURFACE CAMBER ANGLE DISTRIBUTION TO ALLOW FOR SLIP

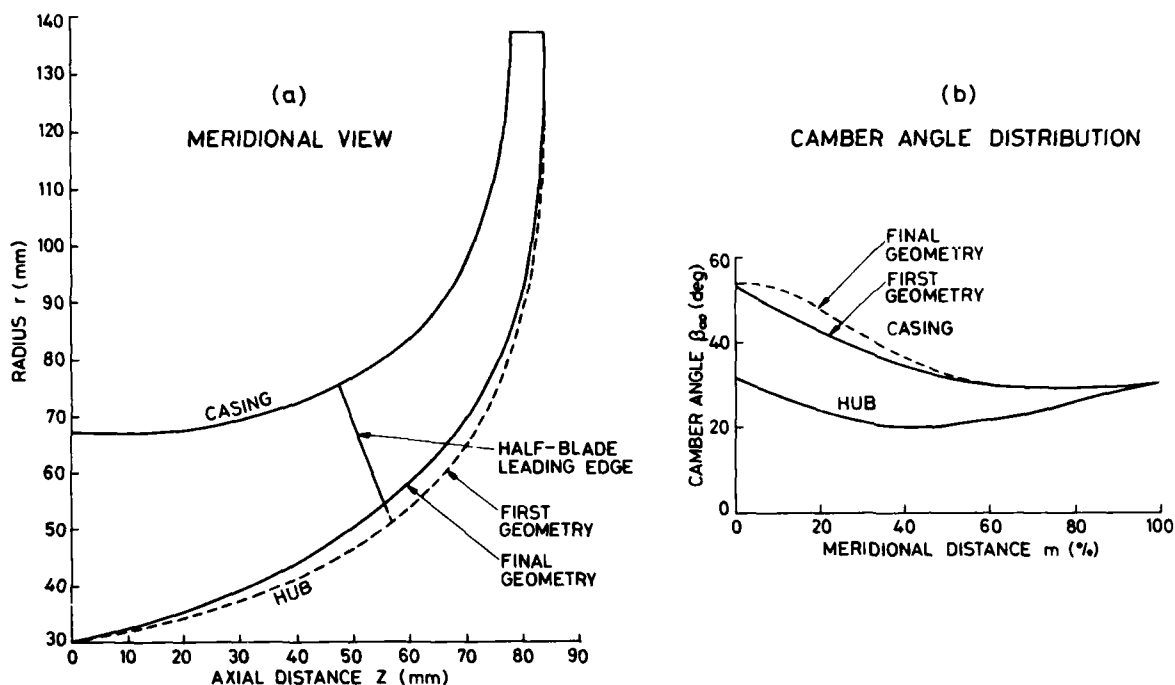


FIG. 5 IMPELLER BLADE GEOMETRY

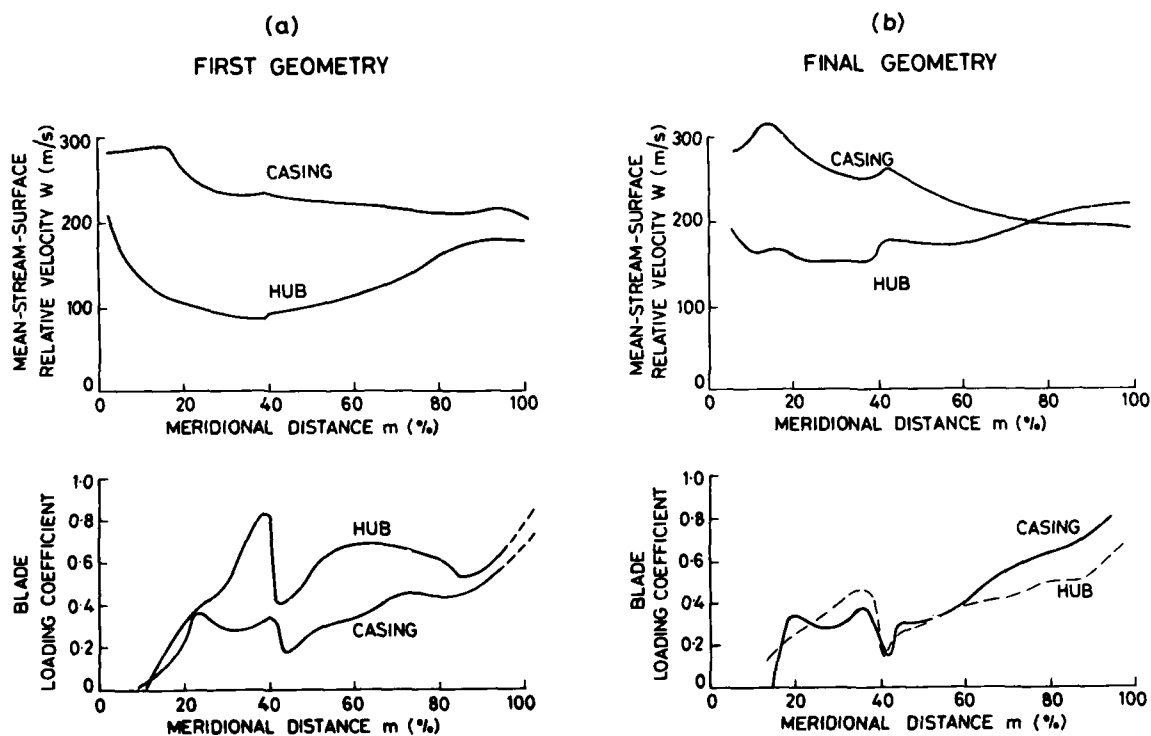


FIG. 6 IMPELLER VELOCITY AND BLADE LOADING DISTRIBUTIONS

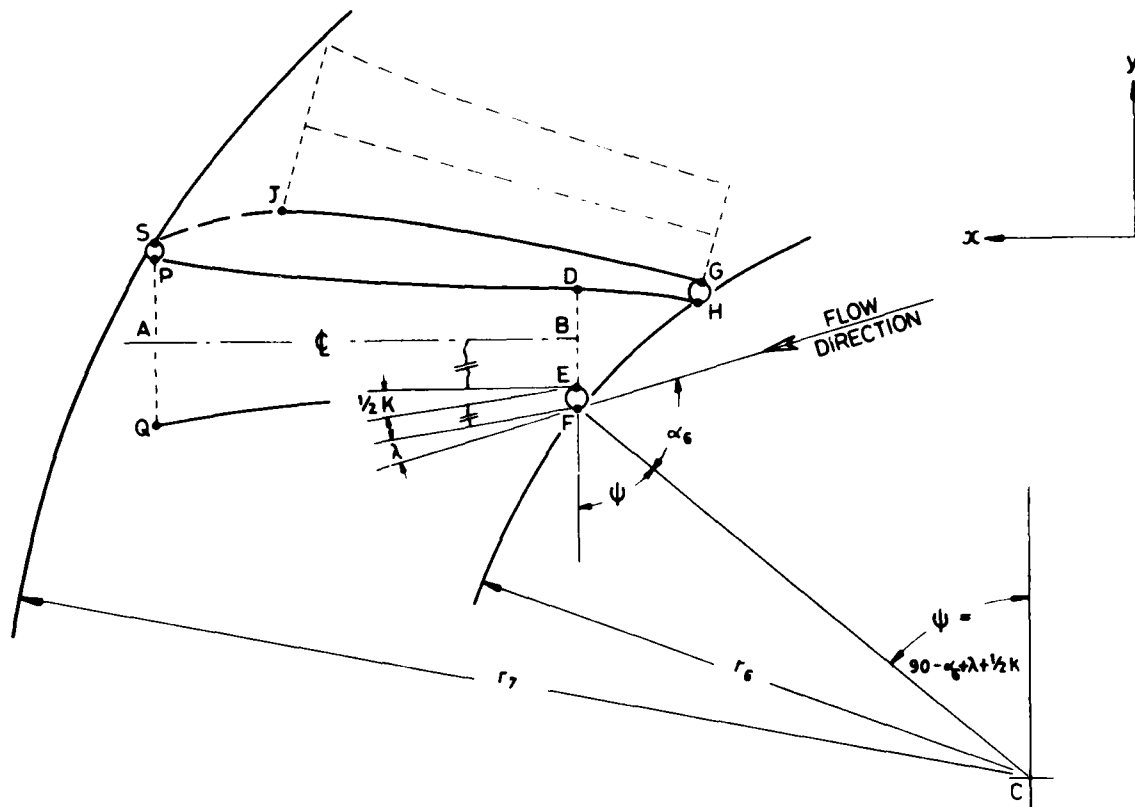


FIG. 7 VANED DIFFUSER GEOMETRICAL DESIGN

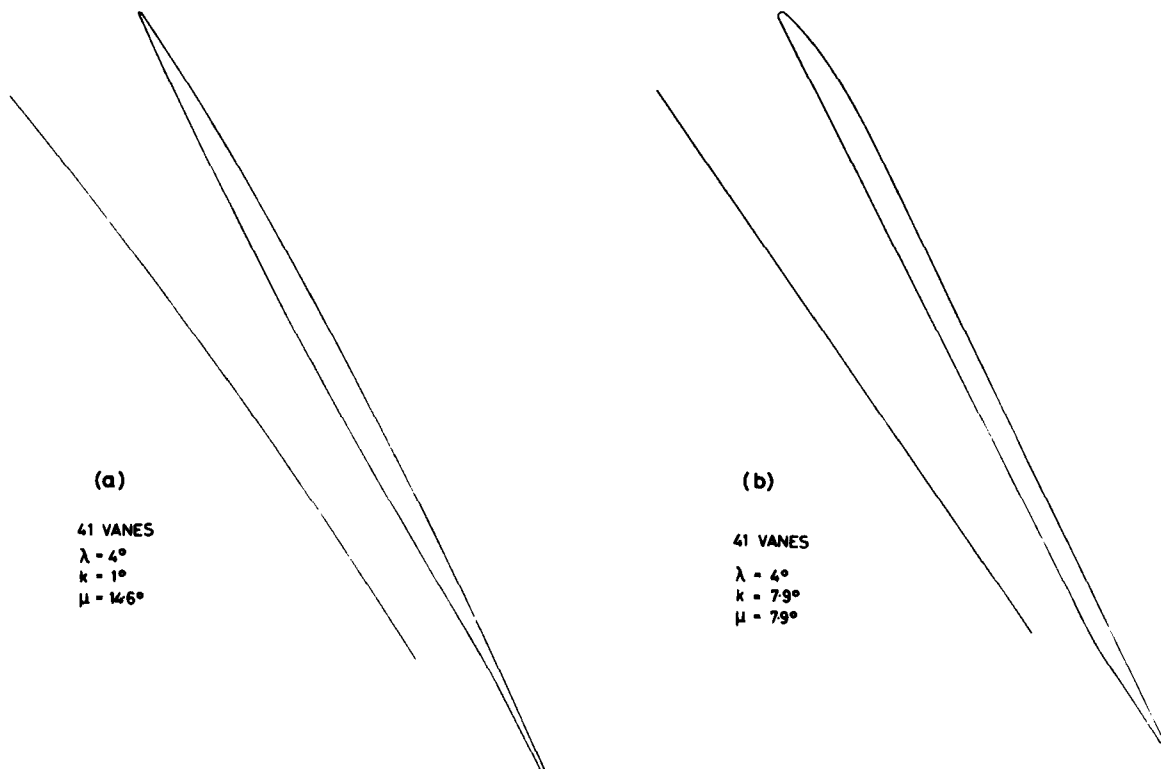


FIG. 8 COMPARISON OF VANED DIFFUSER CHANNEL SHAPES

PERFORMANCE OF IMPELLER PLUS VANELESS DIFFUSER

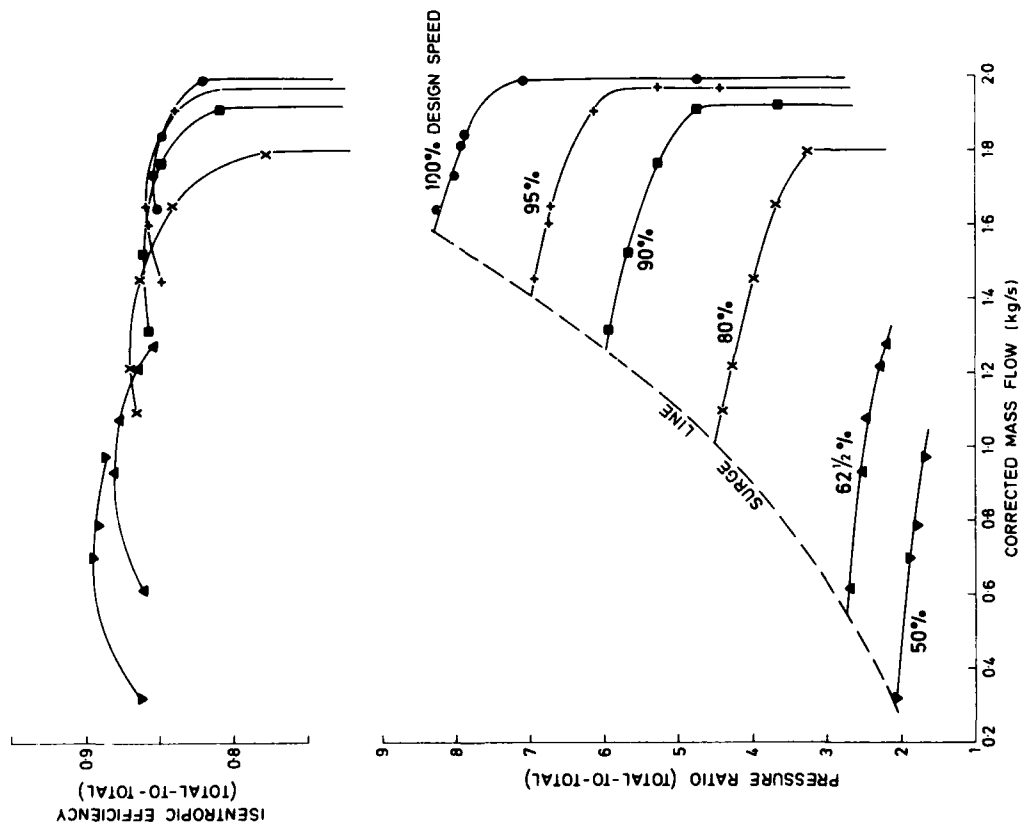


FIG. 9 TEST RESULTS FOR IMPELLER WITH SHORT VANELESS SPACE AND NO VANED DIFFUSER

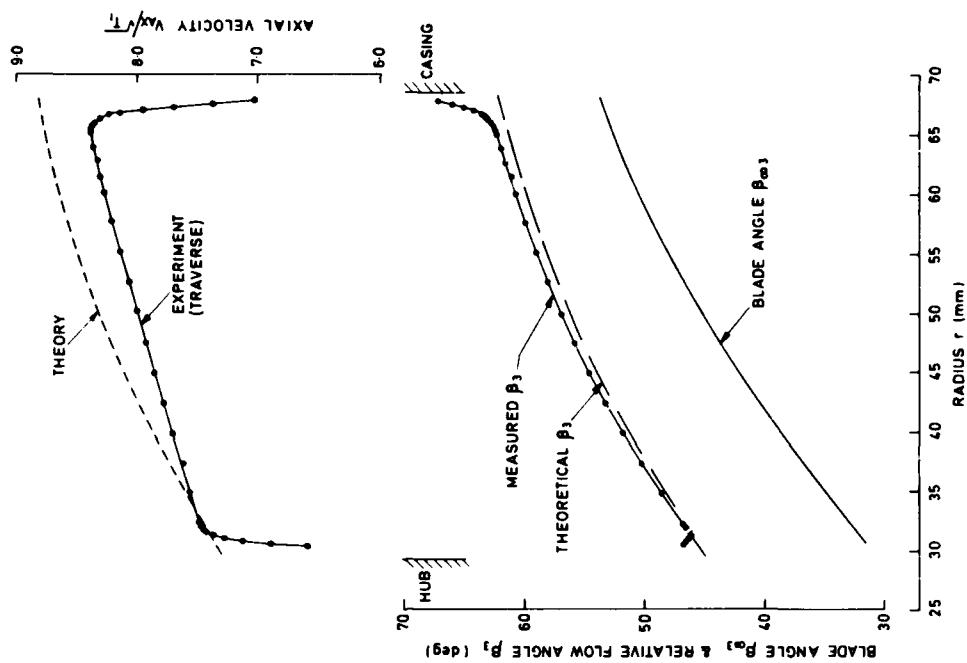
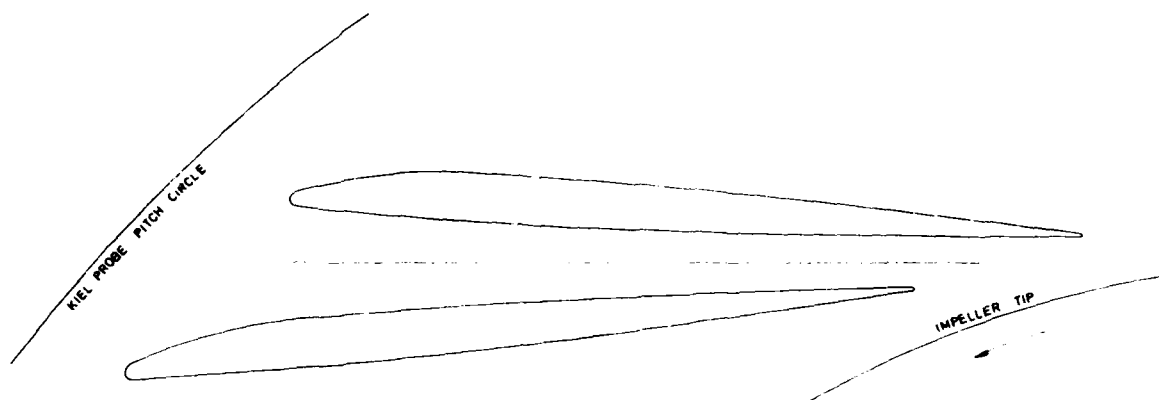


FIG. 10 INLET TRAVERSE MEASUREMENTS



41-VANE DIFFUSER

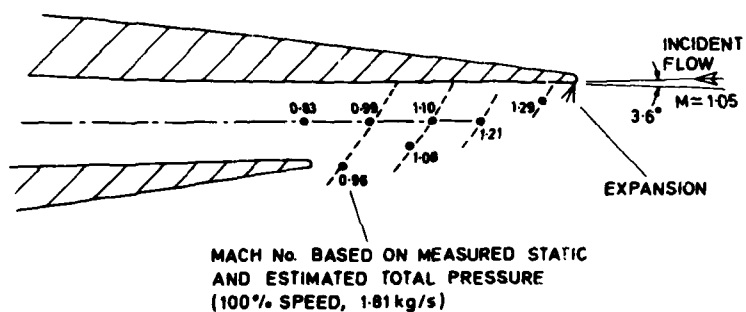
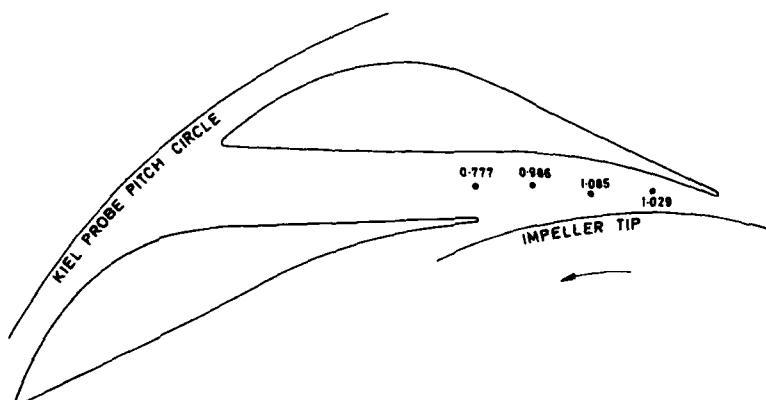


FIG. 11 GEOMETRY OF 41-VANE DIFFUSER

• STATIC PRESSURE TAPPING POSITION
NUMBERS REFER TO ESTIMATED MACH No. (100% SPEED, 1.9 kg/s)



13-VANE DIFFUSER

FIG. 12 GEOMETRY OF 13-VANE DIFFUSER

KEL PROBE PITCH CIRCLE

IMPELLER TIP

37-VANE DIFFUSER

FIG. 13 GEOMETRY OF 37-VANE DIFFUSER

PERFORMANCE OF IMPELLER PLUS 41-VANE DIFFUSER

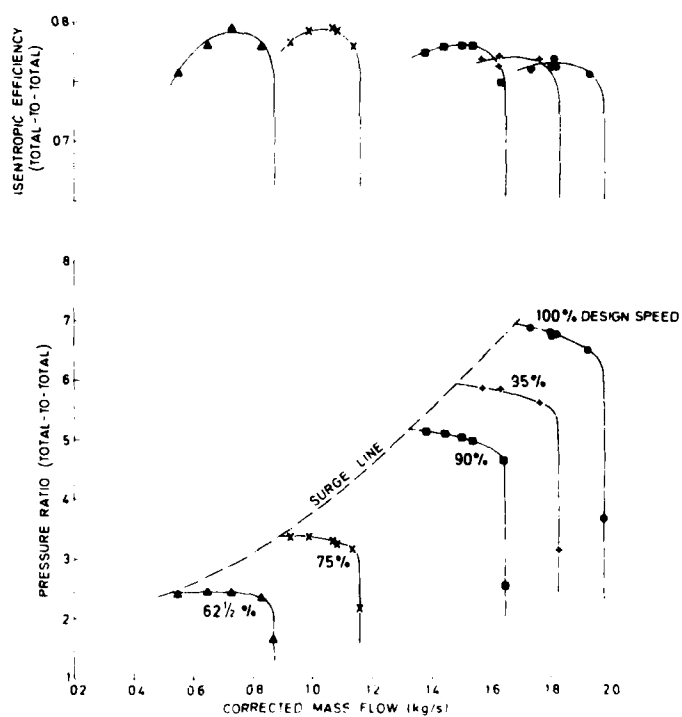


FIG. 14 TEST RESULTS FOR COMPRESSOR WITH 41-VANE DIFFUSER

PERFORMANCE OF IMPELLER PLUS 13-VANE DIFFUSER

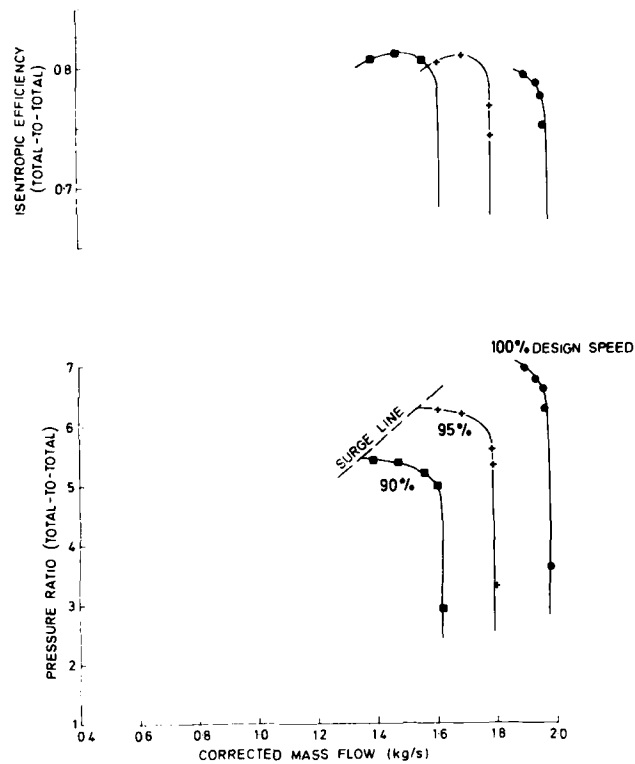


FIG. 15 TEST RESULTS FOR COMPRESSOR WITH 13-VANE DIFFUSER

PERFORMANCE OF IMPELLER PLUS 37-VANE DIFFUSER

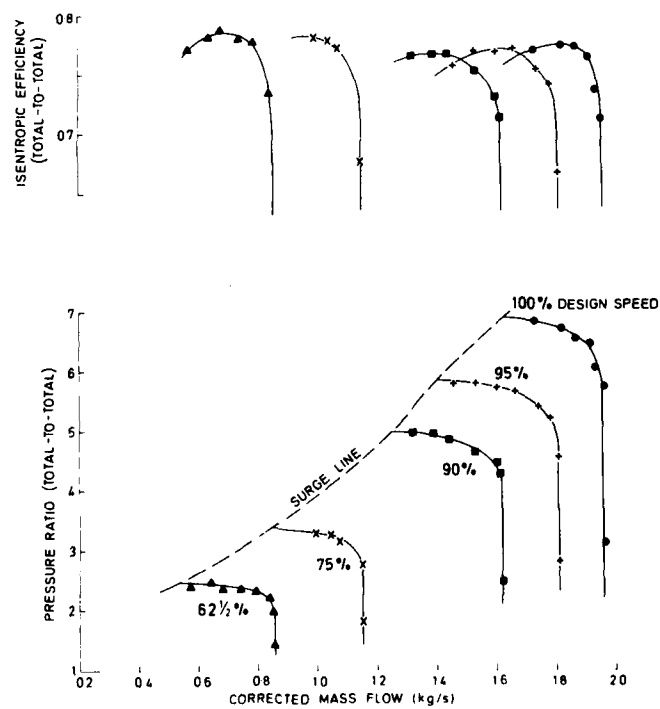


FIG. 16 TEST RESULTS FOR COMPRESSOR WITH 37-VANE DIFFUSER

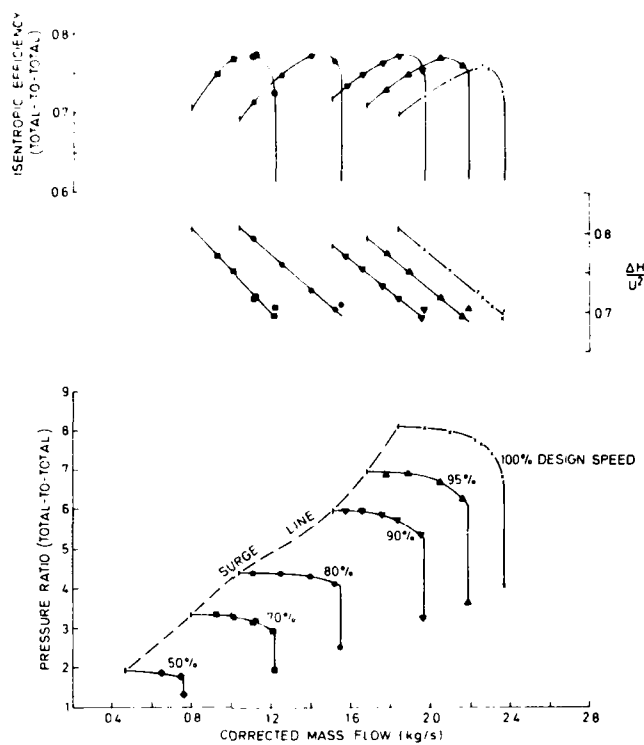


FIG. 17 TEST RESULTS FOR PRESSURE RATIO 8 COMPRESSOR

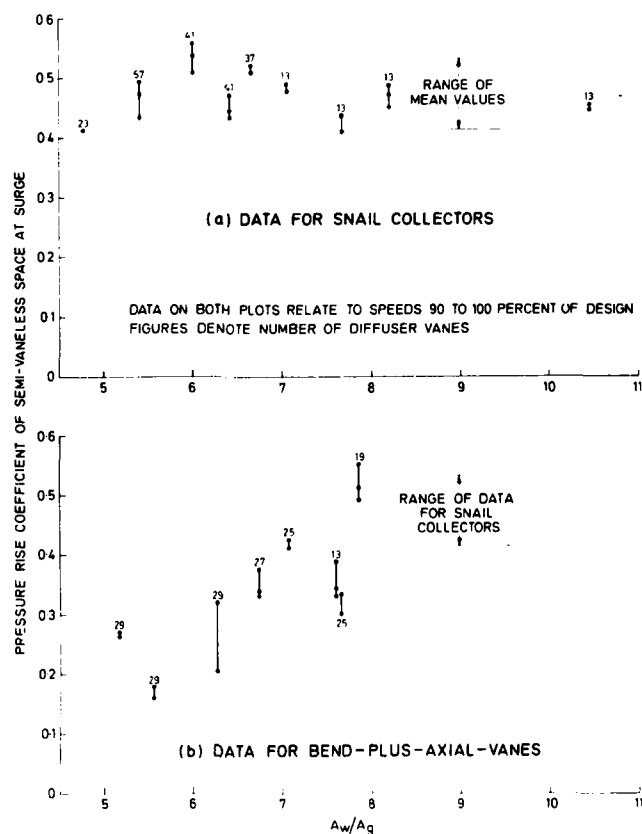


FIG. 18 SURVEY OF SURGE DATA

DISCUSSION

D.Eckardt, MTU, Munich, Ge

The correlation for A_w/A_g with the limiting surge pressure recovery between diffuser inlet and diffuser throat offer encouraging prospects for the difficult range and efficiency optimization problem. Do the authors agree that besides the mentioned incidence and blade number effects the adequate matching of the diffuser throat area in itself is of certain influence on the stage surge margin²³? Can the authors outline the matching philosophy of the investigated stages and are range data for the various matching states available?

Author's Reply

We agree that the correct matching of diffuser and impeller characteristics is very important for the achievement of optimum stage efficiency. Further, as pointed out by Jansen in his paper presented at this meeting, it is important to recognize the regimes of compressor operation in which surge is influenced either by the vane diffuser or by the impeller. All aspects, including choice of vane number (A_w/A_g) and incidence, should be taken into account in choosing the geometry of the vane diffuser in that region. The stages examined within the correlation of Figure 18 were not all designed by the same organization – three sources were in fact used – and so it is not possible to make a general reply to the last part of Dr Eckardt's question.

J.W.Railly, University of Birmingham, UK

With reference to the authors' use of the area ratio A_w/A_g , this is evidently dependent also on the impeller tip width. Would the authors please comment on this point.

Author's Reply

The parameter A_w/A_g certainly is affected by the tip width. Unfortunately among the compressors examined in our study there were no examples of compressors in which only tip width was varied. However, there were cases where the width of the vaneless space and the width of the vane diffuser throughout its length was changed by "cropping" the diffuser vane height in order to achieve a reduction of throat area, A_g . The net effect on A_w/A_g is such that A_w/A_g increases which, according to our theory, should allow a higher pressure recovery in the semi-vaneless space and hence better surge margin. This is confirmed by the experimental results, as summarised in Figure 18b of the Paper.

R.A.Novak, General Electric Company, Lynn, US

The author did not in his verbal presentation discuss the relative merits for surge and efficiency of accepting higher diffuser Mach numbers with small vaneless space or lower Mach numbers with more vaneless diffusion. Could the authors comment on this?

Author's Reply

We have not conducted a comparative test between subsonic and supersonic inlet diffusers but we have planned a quite carefully controlled comparison, to take place shortly, between one of each type of diffuser running in a compressor stage of pressure ratio 6½. We hope that this will indicate relative efficiency of the two types. In tests on transonic inlet diffusers conducted so far we have achieved surge margins which are generally as good as most published surge margins achieved with subsonic diffusers.

D.Japikse, CREARE, US

I would like to thank the authors for their contribution. Perhaps they would like to comment on the following:

- (a) The Baghdadi swirl generator gives a stalled diffuser inlet with noticeable back-flow thus requiring care in applying his results.
- (b) How did the authors traverse the impeller inlet? How does the computed mass flow agree from the traverse with the measured mass flow?
- (c) The authors correlation in Figure 18 is interesting. The use of this recovery coefficient has been employed by many authors so it should be possible to obtain substantial additional data to support the concept.

Author's Reply

The consequences of stall occurring at the inlet to the Baghdadi diffuser may or may not affect his conclusion that the jet-wake impeller exit flow has no significant effect on surge. We are interested to hear of this, however, because it could account for the rather low values of PRC achieved by his three diffusers. The impeller exit in our own experiments was not traversed. Stagnation pressure was calculated from measurements of static pressure and mass flow in the NGTE compressors which feature in the surge study. We should like to emphasise, however, that the values of PRC plotted in Figure 18 are calculated using the methods of Reference 8, and not measured.

We note with thanks your remarks concerning possibly supportive data from pressure recovery in the semi-vaneless space. We did not put the correlations of Figure 18 forward in a definitive way and clearly further evidence would be most desirable.

C. Rodgers, Solar, US

Could the authors state whether among the compressors used for their correlation of Figure 18 there were stages with both radial and back-swept impellers since the stability of the impeller characteristic and therefore the stability of the whole stage would be affected by the back-sweep of the impeller.

Author's Reply

There were impellers which were both radial and back-swept in the correlation. In fact a further correlation was attempted in which the authors tried to take account of the varying degrees of back-sweep and hence work factor on the stability of the stages. No satisfactory correlation was obtained using this simple idea, however.

A PROCEDURE FOR THE COMPUTER-AIDED CONSTRUCTION OF
RADIAL COMPRESSOR IMPELLERS WITH HIGH FLOW COEFFICIENT

Prof. Dr.-Ing. W. Fister/Dr.-Ing. J. Eikermann
Lehrstuhl für Fluidenergiemaschinen
der Ruhr-Universität Bochum
D-4630 Bochum, Universitätsstraße
Germany

SUMMARY

A computer-aided procedure for the construction of radial compressor impellers with high flow-coefficient is presented. The procedure consists of an iterative succession of constructional design, recomputation of fluid-flow-mechanical characteristics and specific geometrical correction based upon the given criteria. The significance of the computational procedures and criteria used is verified on the basis of the operating behaviour of two compressor stages.

1. INTRODUCTION

The flow-adequate construction of an impeller is an iterative process, which essentially comprises the generation of the geometrical design, the recomputation of fluid-flow-mechanical characteristics, and possibly necessary geometrical corrections based upon the given flow-criteria. The relatively complex generation and description of the geometrical design of radial compressor impellers with spatially twisted blades (fig. 1), together with an appropriate flow computation (e.g. three-dimensional or quasi-three-dimensional method) require the employment of a high-performance computer. The abovementioned flow-computational procedures require relatively long computing times, and, at the same time, high memory capacity, using presently available computers. It is therefore economically advisable to pre-optimize, as far as possible, the basic geometrical design of the impeller, as regards flow characteristics, according to simplified procedures and criteria, and to use the more sophisticated flow-computation only for the final assessment. In the following, the process of pre-optimization is described.

2. GENERATION OF THE BASIC GEOMETRICAL DESIGN

The form-determining impeller dimensions are calculated using the proven methods of one-dimensional theory and simplified formulations of potential theory. This applies basically to the rated dimension of the impeller inlet. When chaping the channel walls, attention is paid to the smoothness of the surfaces - in mathematical terms - and the lowest possible curvature.

In the respect there are virtually no problems in the design of the surfaces of revolution of hub and shroud. It is considerably more difficult to comply with the two criteria in the construction of twisted blade surfaces. A combined procedure is applied which first ensures low curvatures at the blade edges, and second leads to a smooth blade surface through appropriate surface interpolation.

To generate the blade edge curves a procedure is chosen, in which the orthogonal axisymmetric networks covering the surfaces of revolution of hub and shroud are projected conformally onto a plane quadratic network (fig. 2).

Proceeding from the predetermined geometry of the impeller inlet and outlet, the blade edge curves on the hub and shroud are designed as continuously bent curves in the projection plane (fig. 3). This is achieved in the computer-aided construction process through the assumption of elliptical, parabolic or hyperbolic functions. The plane edge curves thus produced are then conformally projected onto the surfaces of revolution of hub and shroud, according to the relevant projection rule.

Fig. 4 shows the edge contours in axially normal projection.

The blade surface between the edges is designed according to COONS' surface interpolation. To this end the generated edge curves are approximated by cubic polynomials either in total or in steps. The description of the nodal points in parametric representation results from COONS' [2] interpolation formula, according to fig. 5, the weight functions F_0 and F_1 also being assumed as cubic polynomials. Thus a bicubic blade surface is generated.

3. PRE-OPTIMIZATION OF THE BASIC GEOMETRICAL DESIGN USING SIMPLIFIED METHODS

The generated impeller channels are first evaluated according to the channel cross-section pattern between inlet and outlet. This pattern is to be as continuous as possible and to have at most one extreme value.

Taking into account the blade thickness a contour-adapted spatial network is generated from the point-by-point description of the generated channel surfaces (fig. 6). If in this difference-geometrical procedure the mesh width in normal flow direction is chosen sufficiently small, the surface elements can be treated as trapezoids. The respective channel cross section is obtained through summation over the cross section elements.

For further assessment of the geometry the approximative distribution of relative velocity on the middle stream surface of the first kind is examined. For this purpose a simplified two-dimensional approximation method of STANITZ and PRIAN [5] is used in a modified form. In contrast to the original method the calculation is not carried out in the axisymmetric coordinate system, but is based upon the contour-adapted network in the impeller channel generated for the calculation of the cross section. The calculated behaviours of relative velocity along the channel walls and in the middle of the channel are to be as continuous as possible and to have at most one extreme value. Moreover, theoretically occurring back flow areas of the impeller channel are to be avoided. Fig. 7 shows a comparison of the distributions of relative velocity according to the two-dimensional approximation method with those according to the quasi-three-dimensional difference method.

After pre-optimization the impeller geometry is finally assessed on the basis of a more significant computation of flow characteristics. To this end a quasi three-dimensional difference method is used at present. It is possible to exchange this method for a more suitable one without any problems.

The finally determined impeller geometry is prepared for the subsequent NC-manufacture of the impeller. Computer-aided construction and NC-manufacture guarantee a high degree of identity of the theoretically determined with the manufactured impeller geometry. Fig. 8 shows a flow-chart of the whole construction process.

4. TESTING THE CONSTRUCTION PROCEDURE

The construction procedure and the calculation procedures and criteria comprised are tested with two impellers which have been designed with the aid of a computer, manufactured, and experimentally examined. The impellers shown in fig. 1 are designed for different speed coefficients Ma_u and flow coefficients φ . Characteristic values are as follows:

Impeller 1: $\varphi = 0,10$; $Ma_u = 0,91$; $D_2 = 200$ mm and $\beta_2^* = 90^\circ$

Impeller 2: $\varphi = 0,17$; $ma_u = 1,05$; $D_2 = 250$ mm and $\beta_2^* = 70^\circ$

Both impellers are examined in vaneless diffusers ($D_4/D_2 = 2.0$). The design of the impeller outlet width b_2 and the appropriate meridian contours are based, among other things, on the criterion that in specified operation back flow areas on the pressure side are to be avoided. In order to check the significance of this criterion, the meridian contour of impeller 1 was first adjusted to an oversized outlet width $b_2 = 17,5$ mm. According to fig. 9 this contour was reduced on the lathe in several

steps to the calculated most advantageous outlet width $b_2 = 10$ mm, and each time examined on the test stand.

Fig. 10 shows the calculated cross section patterns of the channel and the appropriate distributions of relative velocity on the stream surface of the first kind. All patterns shown are continuous as defined by the assumption. The back flow areas at the outlet of impeller 1 with outlet widths $b_2 > 10$ mm are remarkable.

The appropriate characteristic curves of efficiency, which are found experimentally, are shown in fig. 11. In this representation the instabilities of the characteristic curves with an outlet width of $b_2 > 10$ mm under partial performance load are conspicuous.

These phenomena correspond with the occurrence of the calculated pressure side back flow areas at the appropriate outlet widths.

The measured dependence of the stage efficiency on the impeller outlet width is shown in fig. 12. According to this the maximum efficiency of impeller 1 is achieved with an outlet width $b_2 = 11.7$ mm, whereas the stability of the characteristic curve over the entire operating range is only achieved with an outlet width $b_2 = 10.0$ mm.

In the technical literature a design criterion is sometimes recommended, according to which the velocity ratio of the average relative velocity is to be $w_2/w_1 \geq 0.7$. According to this an outlet width $b_2 \leq 10.5$ mm was calculated for impeller 1.

Impeller 2 was directly manufactured with the geometry that had been found advantageous. In this case the impeller outlet width is $b_2 = 25$ mm. The calculated patterns of the channel cross section and of the relative velocities on the stream surface of the first kind are presented in fig. 13. For comparison purposes the corresponding patterns are also presented, which result from a meridian contour of the impeller with an outlet width $b_2 = 30$ mm. It can be observed that, in the latter case, back flow occurs on the pressure side, which is avoided by computation with an outlet width $b_2 = 25$ mm. In all other cases the patterns comply with the assumed criteria. The stage's characteristic curve which was measured on the test stand (fig. 14) does not show any discontinuity.

Finally it should be emphasized that the presented, computer-aided construction procedure is merely to be a means of checking calculation methods and of finding design criteria through specific studies of parameters. In this context it is of special importance that during the construction process the generated impeller geometries are

described in a numerically unambiguous way, and that in the subsequent NC-manufacture a high geometric accuracy is observed, so that the influence of particular modified geometry parameters on the behaviour of the impeller becomes recognizable.

List of Reverences

- [1] Wislicenius, G.F.: Fluid Mechanics of Turbomachinery
Mc Graw-Hill, New York (1947)
- [2] Coons, S.A.: Surface for Computer-Aided Design of Space Form
MAC-TR-41, Project MAC, MIT (1967)
- [3] Wu, D.H.: A General Theory of Three-Dimensional Flow in Subsonic and
Supersonic Turbomachines of Axial, Radial and Mixed-Flow Types
NACA TN 2604 (1952)
- [4] Schreckenber, H.: Ein Beitrag zur Berechnung der quasi-dreidimensionalen
Relativströmung radialer Verdichterräder
Diss. Ruhr-Universität Bochum (1974)
- [5] Stanitz, J.D.,
Prian, V.D.: A Rapid Approximate Method for Determing Velocity Distribution
on Impeller Blades of Centrifugal Compressors
NACA TN 2421 (1951)
- [6] Fister, W.,
Eikermann, J.: Rechnergestützte Konstruktion und Fertigung von Radialrädern
mit räumlich verwundenen Schaufeln
Preprints zur Pumpentagung Karlsruhe (1978)
- [7] Eikermann, J.: Rechnergestützte Gestaltung und Fertigung von Radialverdichter-
laufrädern mit verwundenen Schaufeln
Diss. Ruhr-Universität Bochum (1979)



Fig. 1: Radial compressor impellers with double-curved blades

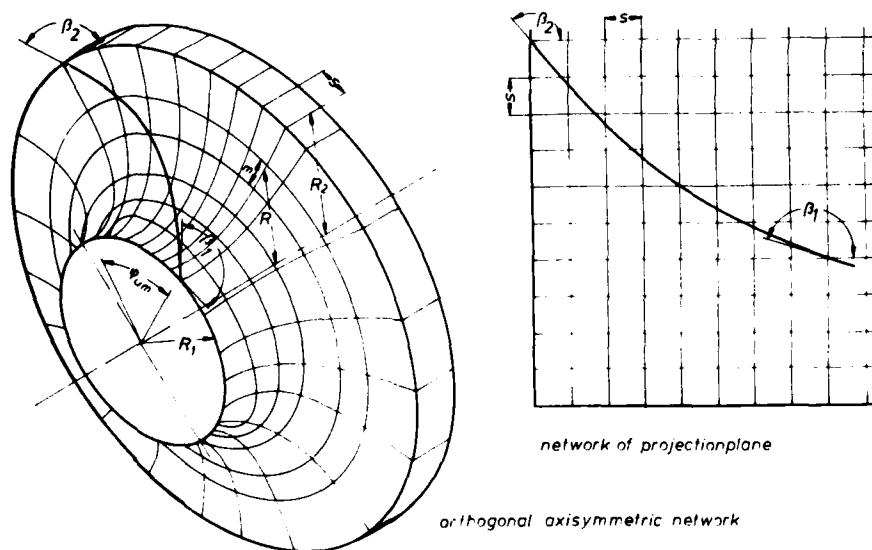


Fig. 2: Method of conformal representation

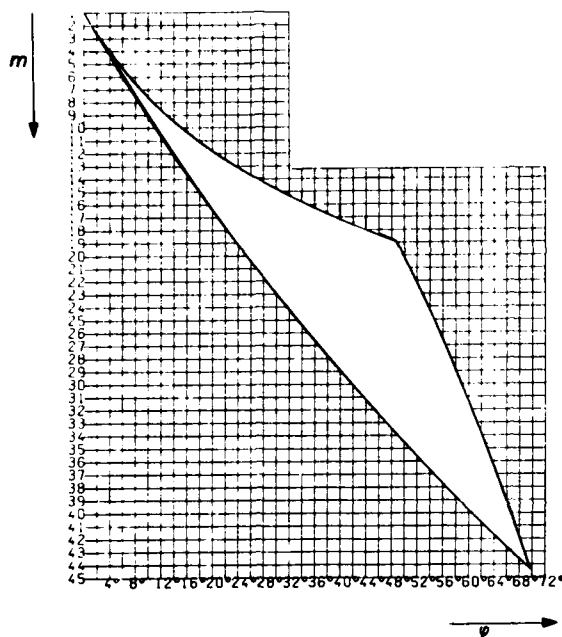
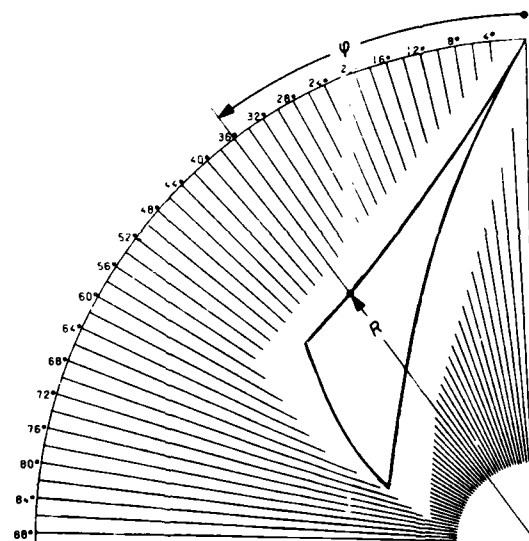


Fig. 3: Boundary curves in the plane of representation

Fig. 4: Representation in axially-normal plane



Interpolation formula by COONS:

$$\begin{aligned} \bar{R}(u,v) = & \bar{k}_1(u,0) \cdot F_0(v) + \bar{k}_2(1,v) \cdot F_1(u) + \bar{k}_3(u,1) \cdot F_1(v) + \bar{k}_4(0,v) \cdot F_0(u) \\ & - \bar{P}_1 \cdot F_0(u) \cdot F_0(v) - \bar{P}_2 \cdot F_0(v) \cdot F_1(u) - \bar{P}_3 \cdot F_1(u) \cdot F_1(v) - \bar{P}_4 \cdot F_0(u) \cdot F_1(v) \end{aligned}$$

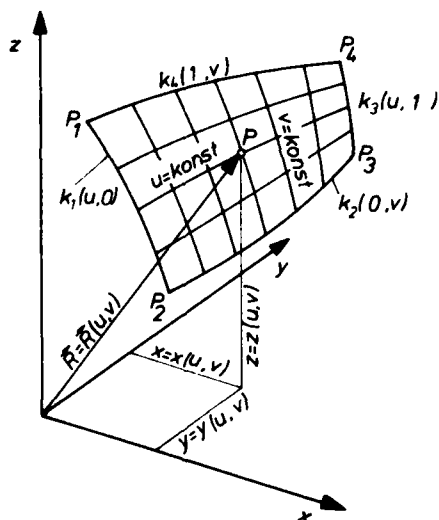


Fig. 5: Interpolation of smooth surfaces by COONS

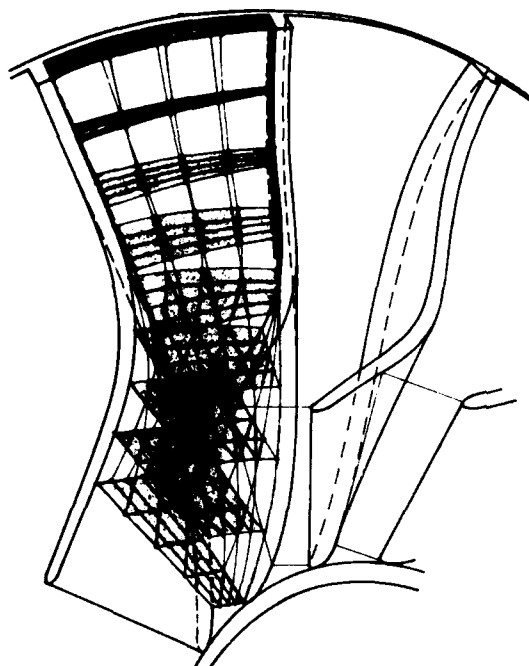


Fig. 7: Comparison of calculated
revative velocity curves

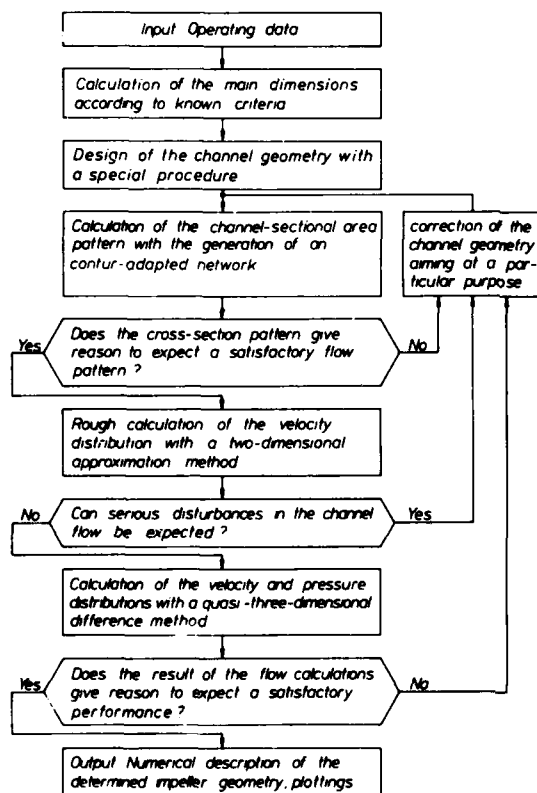


Fig. 6: Contur-adapted network

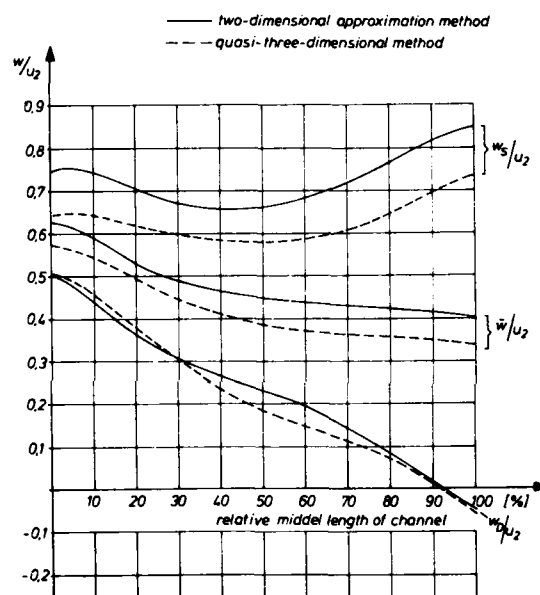


Fig. 8: Flow diagram of the impeller
design

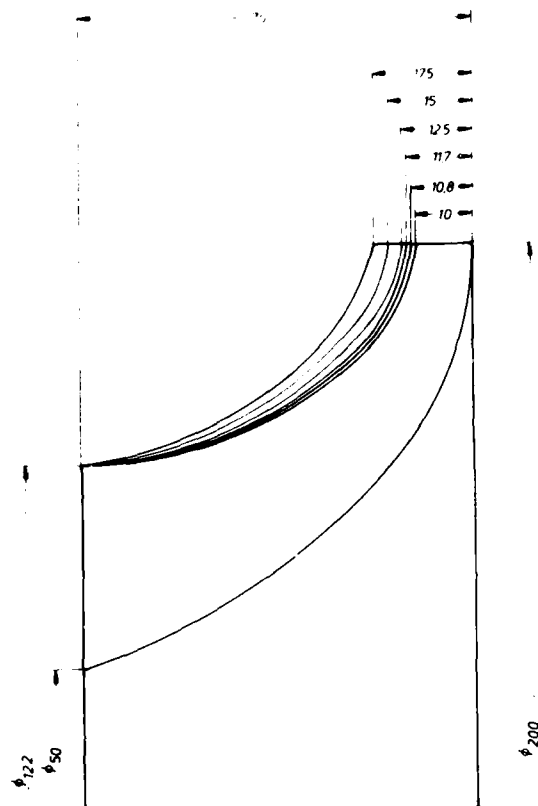
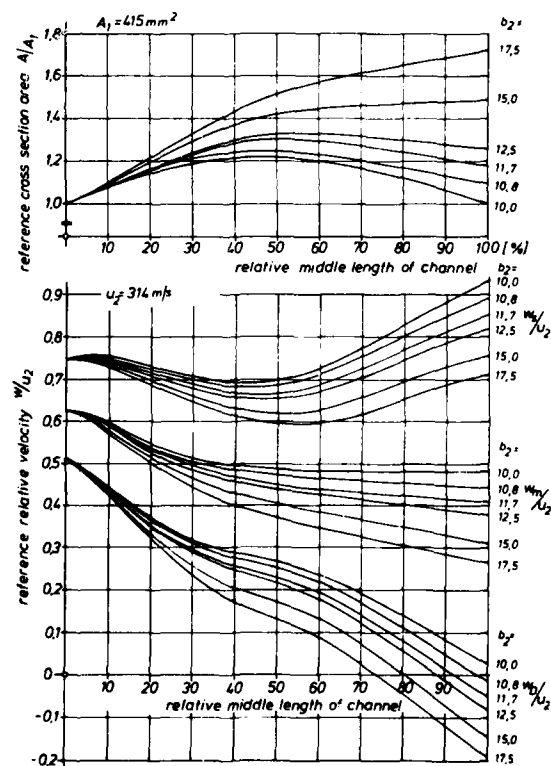


Fig. 9: Meridional sections of impeller 1
with variable outlet width

Fig. 10: Behaviour of cross section
areas and relative velocities
(impeller 1)



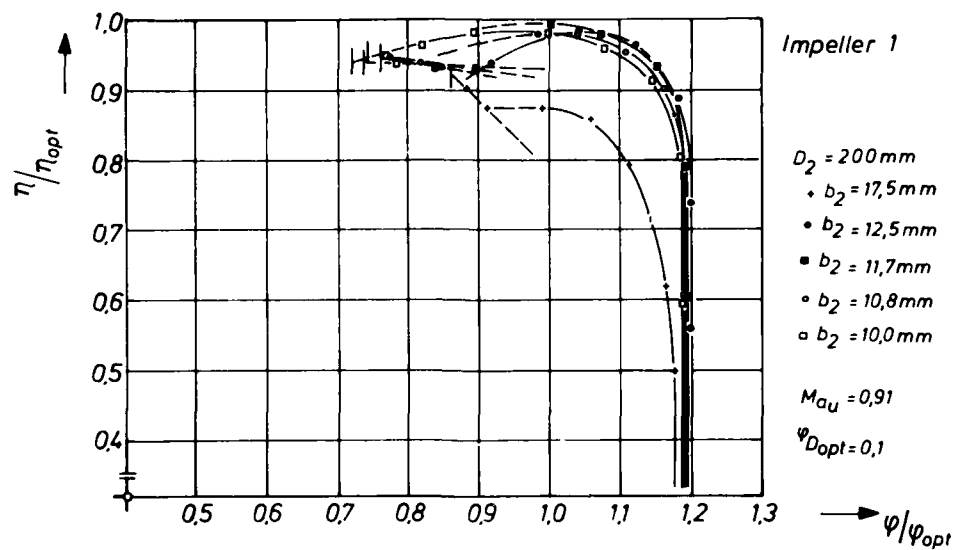
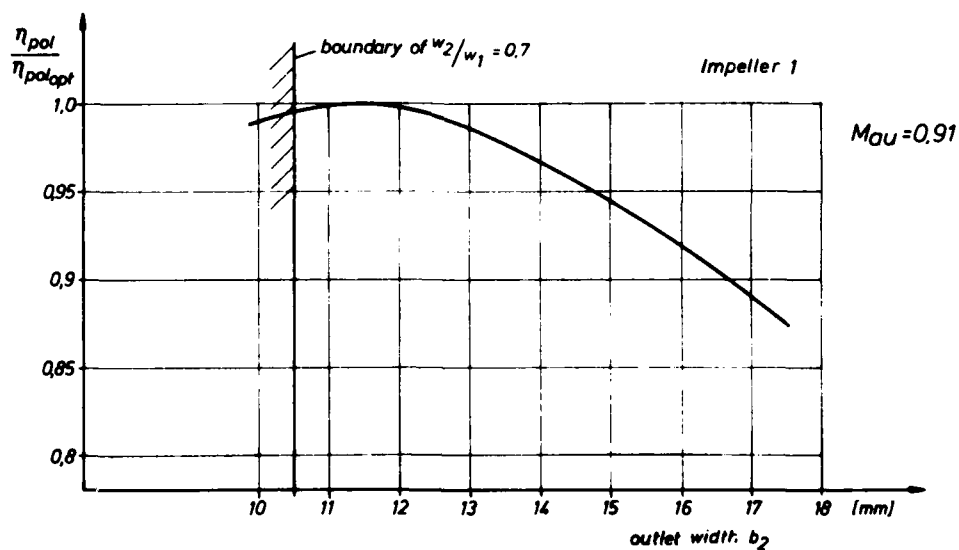


Fig. 11: Efficiency curves of impeller 1

Fig. 12: Correlation: efficiency-outlet width b_2

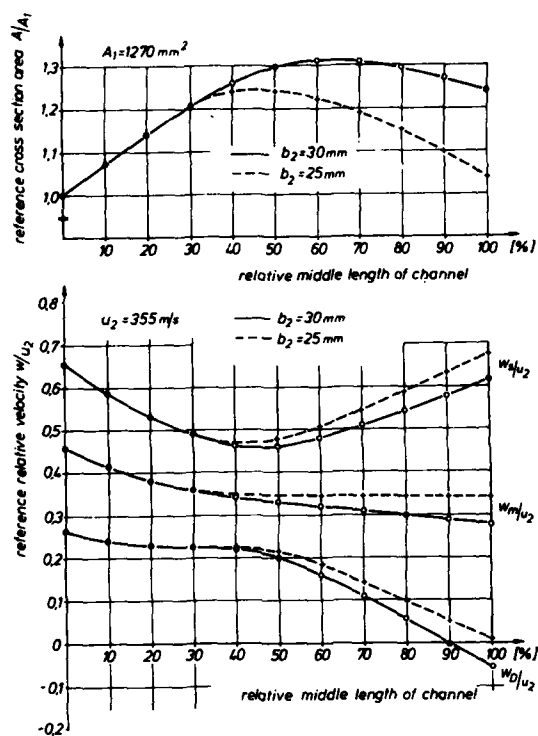


Fig. 13: Behaviour of cross section area and relative velocities (impeller 2)

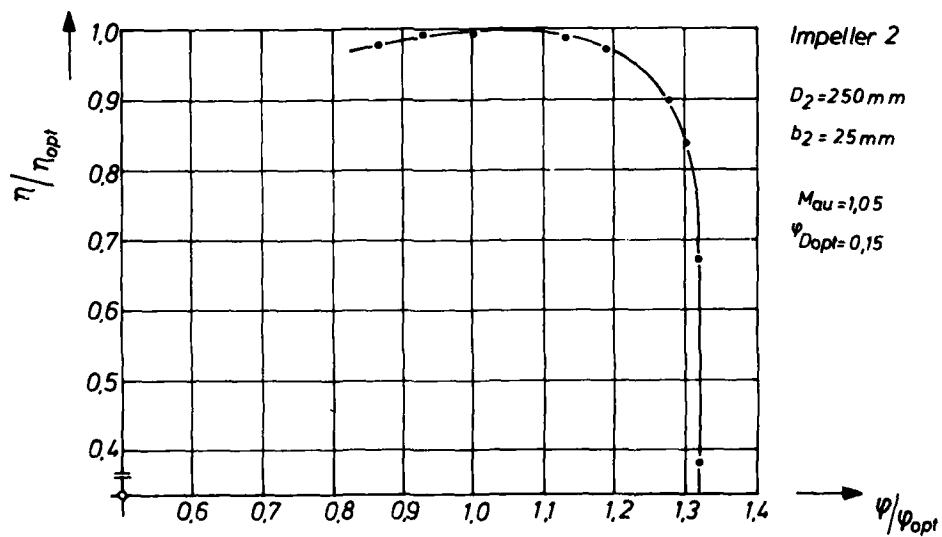


Fig. 14: Efficiency curve of impeller 2

DISCUSSION

W.Jansen, Northern Research and Engineering Corporation, US

In the analysis the authors have not included the Kutta-Joukowski condition at the trailing edge. If this were done none of the velocities near the trailing edge at the pressure surface would have been negative and much of the reasoning of the paper would be eliminated.

Author's Reply

The Kutta-Joukowski-condition is indirectly included by means of the assumption of the flow direction at the trailing edge. The represented distributions of velocities are finished at last normal-cross-section of the channel such as the trailing edges are not included.

The occurrence of theoretical back flow areas at the pressure side based primarily upon the assumption of the non-viscous channel-flow.

I.H.Skoe, Kongsberg Vaapenfabrik, No

Could the authors give absolute numbers for the efficiencies presented in Figures 11 and 17.

Author's Reply

The polytropic total efficiency of the stage 1 (Impeller 1 combined with a vaneless diffuser) was measured as 0.76 and that of the impeller was 0.84. The polytropic total efficiency of the stage 2 (Impeller 2 combined with a vaneless diffuser) was measured as 0.86 and that of the impeller was 0.91.

P.M.Came, NGTE, UK

Could the authors please explain why they selected the bi-cubic patch for the representation of the impeller surface geometry. Would not a cubic-linear patch have made the task of numerical control manufacture with a straight-sided cutter a possibility?

Author's Reply

Bi-cubic patches guarantee a sufficient approximate description of universal twisted blades. In the special case of blades with developable surfaces, the mathematical description is reduced to linear-cubic patches. This case is given at the impeller 1.

Y.Ribaud, ONERA, Fr

What was the pressure ratio of the compressor described?

Author's Reply

The pressure ratio of the stage 1 was measured as 2.0. The one of stage 2 was measured as 2.4.

ROUE DE COMPRESSEUR CENTRIFUGE SANS FLEXION DANS LES AILES

par Jean POULAIN
ALSTHOM-ATLANTIQUE
93123 La Courneuve (France)

et Gilbert JANSSENS
Office National d'Etudes et de Recherches Aérospatiales (ONERA)
92320 Châtillon (France)

SOMMAIRE

Présentation d'un compresseur centrifuge expérimental à aubes couchées en arrière dont la géométrie est conçue de façon à éliminer les contraintes de flexion dues à la force centrifuge. Ce compresseur a été expérimenté dans une boucle à fréon. Une analyse théorique des résultats expérimentaux a permis de définir une version améliorée de la machine. Ce compresseur semble bien convenir à une structure multicellulaire et donne dans cette configuration un taux de compression d'étage de 4,8 avec un rendement polytropique de 0,83. Dans une version sans canal de retour le taux de compression est de 5,3 avec un rendement de 0,85.

SUMMARY

A centrifugal compressor with backward leaned blades is presented. The geometry of the compressor is designed in such a way as to eliminate the bending stresses due to centrifugal forces. The compressor has been tested in a Freon loop. Due to a theoretical analysis of the test results, an improved version of the compressor has been designed. This compressor seems well suited for a multistage configuration and shows a pressure ratio of 4.8 with a polytropic efficiency of 0.83. In a single stage configuration, without the return duct, its pressure ratio is 5.3 with an efficiency of 0.85.

NOTATIONS

Q_0 , vitesse du son locale
 b , largeur ou hauteur de veine
 D , diamètre
 I , débit-masse
 M , nombre de Mach
 N , vitesse de rotation de la roue mobile
 p , pression statique
 p_0 , pression d'arrêt
 Q_0 , débit masse dans les conditions standard
 T , température
 u_2 , vitesse périphérique à l'extérieur de la roue
 W , puissance
 γ , rapport des chaleurs spécifiques à pression et volume constants
 η , rendement
 π , taux de compression.

INDICES

—, valeur moyenne
0, conditions génératrices amont
1, entrée roue
2, sortie roue
3, entrée diffuseur
4, sortie diffuseur
5, sortie étage
 p , polytropique

1 - INTRODUCTION1.1 - Les compresseurs à aubages radiaux caractérisés par les aspects suivants :

- Les aubages à la sortie sont radiaux ; ils donnent à l'écoulement un angle de sortie très grand, égal à 90° moins l'écart flux profil.
- La roue est généralement composée de deux parties ; une avant-roue de forme hélicoïdale qui se raccorde sur la roue radiale proprement dite.
- Il n'existe pas dans un compresseur radial de contraintes de flexion centrifuges dans les ailes ; en effet, tous les efforts se trouvent alignés sur un même rayon. Cette particularité autorise des vitesses périphériques élevées, de l'ordre de $u_2 = 550$ m/s.
- Le coefficient manométrique utile est important, de l'ordre de 0,7, ce qui signifie qu'une quantité proportionnelle à $0,7 u_2^2$ peut être effectivement transformée en pression.
- Des deux derniers caractères qui viennent d'être cités, il résulte que ce type de compresseur est capable de rapports de pression très élevés par étage, disons de l'ordre de 6 à 7 en air et 10 ou plus avec des gaz lourds.
- En contrepartie des avantages qui viennent d'être exposés, le compresseur radial présente deux gros inconvénients : d'une part, il atteint son rendement maximal à proximité immédiate du pompage, d'autre part, il se prête mal à un montage multicellulaire.

Ce travail a été effectué sous contrat DGRST.

La figure 1 représente un tel type de compresseur.

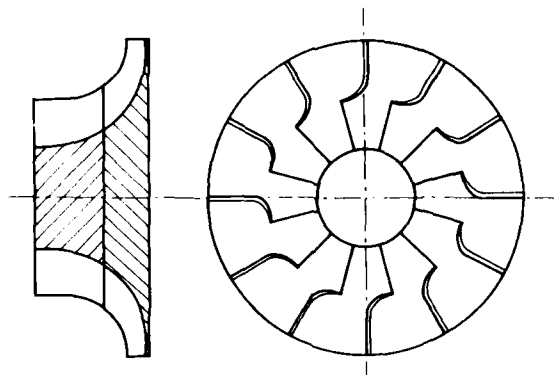


Fig. 1 - Compresseur radial.

1.2 - Les compresseurs centrifuges à aubes en arrière caractérisés par les aspects suivants :

- Les aubages à la sortie de la roue sont inclinés ; ils forment avec la direction d'entraînement un angle variant de 25 à 60° environ et la roue est ordinairement réalisée en une seule partie sans élément d'entrée.
- La roue, qu'elle soit réalisée avec ou sans frette avant, supporte des contraintes de flexion importantes dans les ailes et, pour cette raison, la vitesse périphérique est limitée à des valeurs de l'ordre de $u_2 = 320$ m/s.
- Le coefficient manométrique a une valeur moyenne de l'ordre de 0,5, ce qui signifie qu'une quantité proportionnelle à $0,5 u_2^2$ peut être effectivement transformée en pression.

Par l'influence combinée des coefficients manométriques et des vitesses périphériques une roue à ailes en arrière classique est capable de fournir approximativement le quart du travail utile délivré par une roue radiale.

- En contrepartie, le compresseur à ailes en arrière offre une courbe de fonctionnement extrêmement favorable, avec un débit au pompage qui est sensiblement 0,6 fois le débit optimum. Ce type de compresseur se prête également bien au montage multicellulaire, et cet avantage est tel qu'il est pratiquement beaucoup plus répandu et utilisé que le compresseur radial, au moins dans le domaine industriel.

La figure 2 représente un tel type de machine.

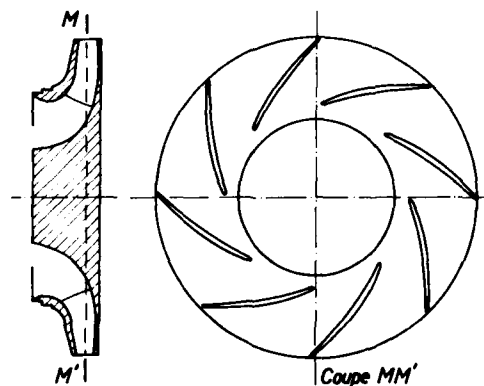


Fig. 2 - Compresseur à ailes en arrière, classique.

2 - COMPRESSEUR AYANT FAIT L'OBJET DE NOS TRAVAUX

L'objectif que nous avons poursuivi a consisté à concevoir et mettre au point un compresseur centrifuge ou légèrement hélico-centrifuge se rattachant aux compresseurs à ailes en arrière du point de vue de l'aérodynamique et aux compresseurs radiaux du point de vue des contraintes mécaniques de flexion.

Le compresseur que nous avons étudié se caractérise donc par les aspects suivants :

- C'est un compresseur exempt de flexion centrifuge dans les aubages et capable sensiblement des mêmes vitesses périphériques que le compresseur radial.
- Par suite de son dessin très particulier décrit plus loin, ce compresseur présente un angle de sortie des aubes de 66° par rapport à la direction d'entraînement.
- Les courbes de fonctionnement sont intermédiaires entre celles d'un compresseur à ailes en arrière et celles d'un compresseur radial, le niveau de rendement obtenu en fin de recherche étant cependant supérieur à celui des deux types de machines auxquels nous nous référons.

La description de notre compresseur est faite à partir des figures 3a et 3b.

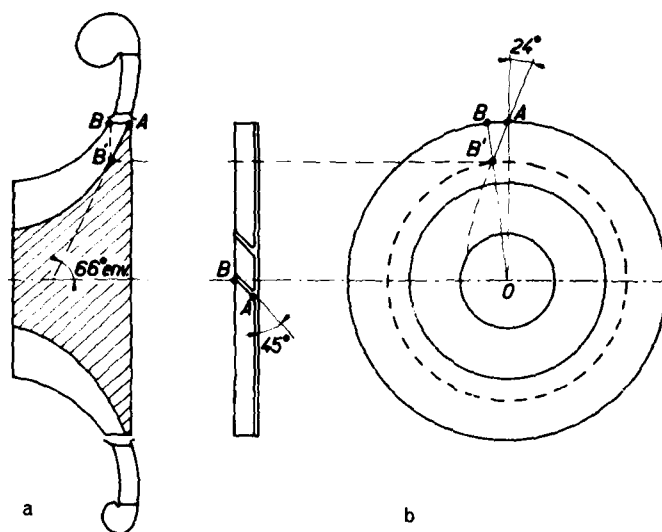


Fig. 3 - Compresseur hélico-centrifuge.

On peut voir sur la figure 3a que la veine est légèrement hélico-centrifuge puisque le fluide quitte la roue non pas dans un plan perpendiculaire à l'axe mais sur un cône de demi-angle au centre égal à 66°. D'autre part, dans la partie droite de cette même figure 3a, il apparaît que les aubages sont inclinés d'environ 45° par rapport au plan arrière de la roue.

En se reportant maintenant à la fois aux figures 3a et 3b, on peut voir que les ailes sont engendrées par des droites telles que $BB'O$ orthogonales à l'axe de rotation de la roue et assurent l'alignement sur l'axe de la matière qui constitue les ailes, éliminant ainsi les contraintes de flexion centrifuge. La direction de l'écoulement projetée sur le plan arrière de la roue est celle de l'élément $B'A$ qui fait, dans notre exemple, un angle de 24° avec la direction rayonnante.

La figure 3c présente une vue en perspective de la roue réalisée selon les principes qui viennent d'être exposés.

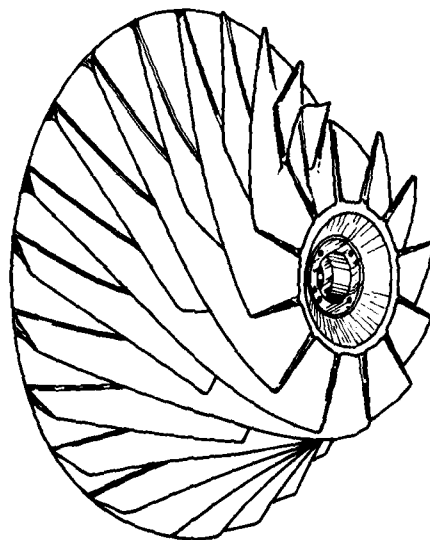


Fig. 3c - Roue mobile expérimentale.

3 - PREMIER COMPRESSEUR EXPERIMENTAL

3.1 - Description

Un premier compresseur expérimental fut dessiné pour les conditions de calcul suivantes :

- Fluide véhiculé	Air		
- Rapport de pression nominal	π	\approx	5,0
- Pression d'aspiration	P_0	\approx	1,013 bar
- Température d'aspiration	T_0	\approx	15 °C
- Débit réduit	$I \frac{\sqrt{T_0/298}}{P_0/1,013}$	\approx	6,3 kg/s
- Puissance absorbée	W	\approx	1 340 kW

- Vitesse de rotation	N	=	22 000	t/mn
- Nombre de Mach relatif à l'entrée de la roue sur diamètre supérieur	Mo	=	0,97	
- Valeur du rapport	M_2/a_0	=	1,52	
- Diamètre de sortie	D_2	=	450	mm

Les principales dimensions de la roue sont données par le schéma de la figure n° 4. La roue comporte 24 ailes dans la zone de sortie de l'écoulement et 12 ailes seulement dans la zone d'entrée. La cellule d'essai est équipée, en outre, d'un diffuseur aileté et d'un canal de retour de telle sorte que l'expérimentation puisse être représentative d'un étage de compresseur multicellulaire.

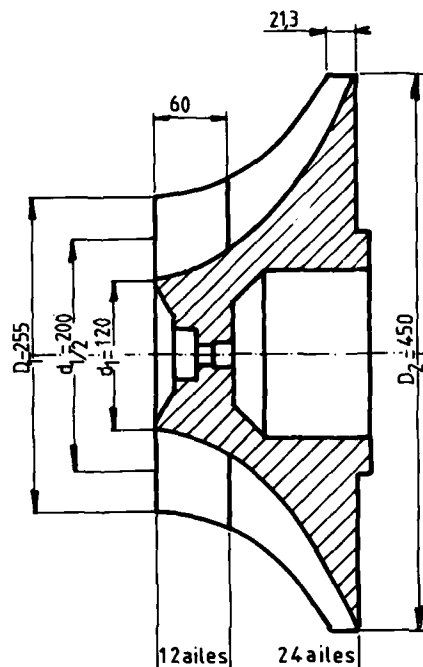


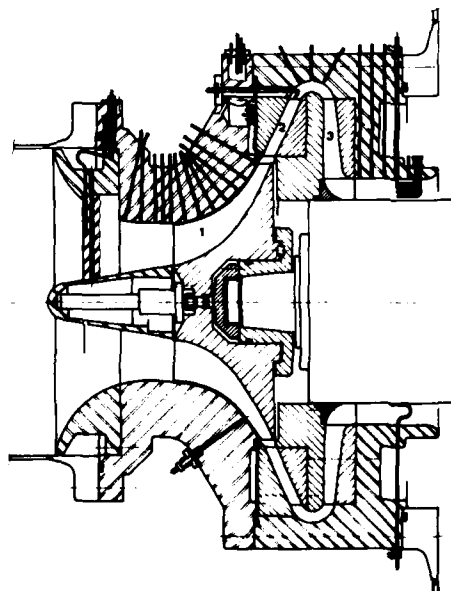
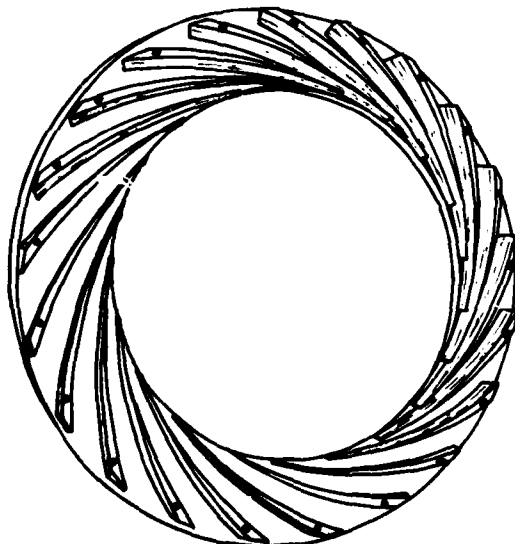
Fig. 4 - Première version de la roue mobile.

La figure n° 5 présente le diffuseur. Celui-ci est caractérisé par les grandeurs ci-après :

- Nombre de canaux	21
- Rapport hauteur sur col	1,26
- Rapport des sections entrée sortie	2,9
- Rapport des diamètres extérieur, intérieur	1,43
- Angle de divergence moyen	7°
- Rapport longueur moyenne sur col d'entrée	15,7
- Nombre de Mach à l'entrée du diffuseur (en air)	1,0

Diffuseur de hauteur constante (à faces parallèles).

Le tracé de ce diffuseur et en particulier la divergence avaient été déterminés en s'appuyant sur les travaux de Dean et Runstadler qui permettaient de prévoir un coefficient de récupération de 0,69 à 0,70. Nous ne décrivons pas le canal de retour qui est un organe classique qui ne présente aucune particularité notable. La cellule d'essais complète est présentée figure n° 6. Sur cette figure, on peut voir la roue repère 1, le diffuseur repère 2, le canal de retour repère 3.



3.2 - Essais

Pour des raisons pratiques concernant les moyens d'essais, la roue ne fut pas essayée en air mais au réfrigérant 12, sur une boucle fermée dont dispose l'ONERA à Palaiseau [1].

L'essai fut conduit dans les conditions de similitude qui conservaient le rapport u_2/c_0 à sa valeur nominale de 1,52.

On sait que lors d'un changement de gaz, si la valeur de $\gamma = Cp/Cv$ n'est pas conservée, il n'existe pas de règle de similitude qui permette de conserver en tout point les principales grandeurs aérodynamiques du compresseur.

Le tableau ci-dessous fait la comparaison des conditions de dessin et des conditions d'essai du compresseur.

Comparaison au point nominal	Air $\gamma = 1,4$	Réfrigérant 12 $\gamma \approx 1,13$
u_2/c_0	1,52	1,52
N t/mn	22 000	9 700
π rapport de pression	5,0	4,75
Mach entrée diffuseur	1,0	1,13
Invariant de débit $I \frac{\sqrt{T_0/288}}{P_0/1,013}$	6,3	12,4

On remarque que le nombre de Mach à l'entrée du diffuseur se trouve augmenté notablement dans l'essai au réfrigérant 12.

Les résultats les plus représentatifs obtenus avec ce premier compresseur expérimental sont présentés par les courbes de la figure n° 7.

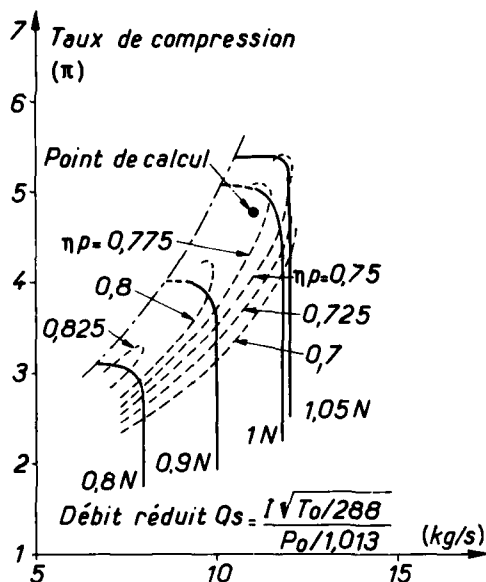


Fig. 7 - Premier compresseur expérimental.

On peut voir sur cette figure que le point nominal escompté, correspondant à un rapport de pression de 4,75, est obtenu pour une vitesse de rotation un peu inférieure à la vitesse nominale et que le rendement polytropique mesuré en ce point est de 0,785 soit une valeur déjà intéressante pour une première tentative. Néanmoins, d'assez nombreuses imperfections furent constatées sur ce premier modèle de compresseur, imperfections qui ont justifié la réalisation d'un second modèle.

3.3 - Imperfections constatées sur le premier compresseur expérimental

Ces imperfections peuvent être regroupées en quatre postes principaux :

- Evolution anormale des pressions mesurées sur le carter avant de la roue du compresseur. La figure n° 8 présente la distribution des pressions mesurées sur le flasque avant de la roue pour les points de fonctionnement optima à différentes vitesses de rotation. Sur cette figure, on peut voir qu'à la vitesse nominale, on assiste à une chute de pression sensible à l'entrée de la roue, la pression statique ne retrouvant le niveau au bord d'attaque qu'après un parcours correspondant au tiers de la longueur de la roue. Le phénomène se trouve encore accentué lorsque la vitesse de rotation augmente.

- Distribution de pression anormale à la sortie de la roue. Dans cette zone, la pression statique constatée sur le filet extérieur est plus faible que sur le filet intérieur. Au point nominal, il a été mesuré un rapport $p_{\text{extérieure}}/p_{\text{intérieure}} = 0,92$, ce qui représente une dissymétrie importante.
- En se reportant à la figure n° 9, on peut voir que l'augmentation de pression se fait totalement dans la partie d'entrée du diffuseur, les sections arrières sont inactives, la pression statique y est constante. Le relèvement du nombre de Mach à l'entrée du diffuseur, lié à l'utilisation du réfrigérant 12 comme fluide d'essai, explique au moins en partie la compression localisée que nous avons constatée.
- Facteur de glissement plus faible que celui que nous avons escompté par le calcul.

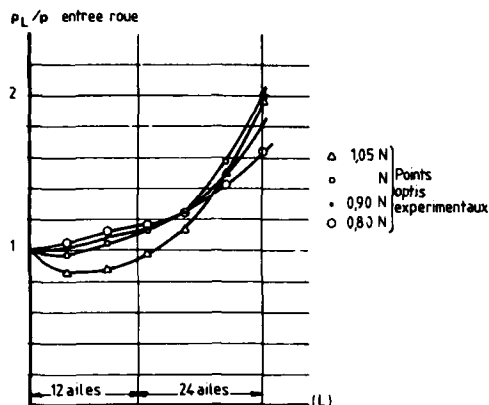


Fig. 8 - Distribution des pressions mesurées sur le flasque avant de la roue.

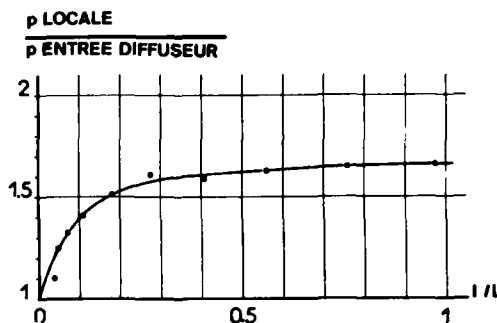


Fig. 9 - Répartition de la pression statique dans le diffuseur.

4 - SECOND COMPRESSEUR EXPERIMENTAL

4.1 - Description et différences avec le premier modèle

Nous avons cherché, pour ce second compresseur, à effacer ou du moins atténuer au maximum les défauts constatés sur le modèle précédent. Pour ce faire, les dispositions suivantes ont été prises :

- Calcul de la roue pour un fonctionnement au réfrigérant 12

Pour éviter les écarts qui séparent le fonctionnement du compresseur en air du fonctionnement au réfrigérant 12, le nouveau compresseur a été calculé directement pour un fonctionnement au R 12. De cette façon, les conditions de calcul correspondent précisément à celles que l'on rencontre en essai.

Point de calcul correspondant aux conditions de la boucle d'essai

- Fluide véhiculé
- Rapport de pression
- Pression d'aspiration
- Température d'aspiration
- Débit réduit
- Vitesse de rotation
- Nombre de Mach relatif à l'entrée de la roue à la pointe
- Valeur du rapport M_2/a_0 (au diamètre moyen de sortie)
- Diamètre de sortie moyen

Réfrigérant 12

π	=	4,75
P_0	=	1,013 bar
T_0	=	20 °C
$I \sqrt{T_0/288}$	=	13 kg/s
N	=	10 000 t/mn
M_0	=	1,022
M_2/a_0	=	1,53
D_m	=	440 mm

- Dessin de la roue profondément modifié

A l'entrée de la roue, la divergence des canaux a été augmentée pour éviter la dépression précédemment constatée à l'ouïe. Il convient de noter ici que l'écoulement à l'entrée de la roue est transsonique, voire légèrement supersonique, et qu'une modification même légère des angles et des sections conduit à une transformation importante des lois de vitesse et de pression. On s'est appuyé pour affiner le dessin de la machine, d'une part sur un programme de calcul ONERA [2] permettant de connaître l'écoulement moyen (correspondant à un nombre d'aubes infini) et, d'autre part, sur le programme de KATZANIS pour la détermination de la distribution de vitesse d'aube à aube.

Au refoulement, les ailes de la roue ont été prolongées sur le contour extérieur de telle façon que la sortie se trouve maintenant perpendiculaire à la méridienne de la veine.

La nouvelle géométrie de la roue se trouve définie par la figure n° 10. Comme précédemment, le nombre d'ailes est réduit de 24 à 12 dans la section d'entrée.

Les mesures internes au compresseur ont démontré la supériorité du nouveau tracé. La chute de pression statique à l'entrée de la roue a disparu et les pressions sont maintenant pratiquement équilibrées entre le filet intérieur et le filet extérieur à la sortie de la roue.

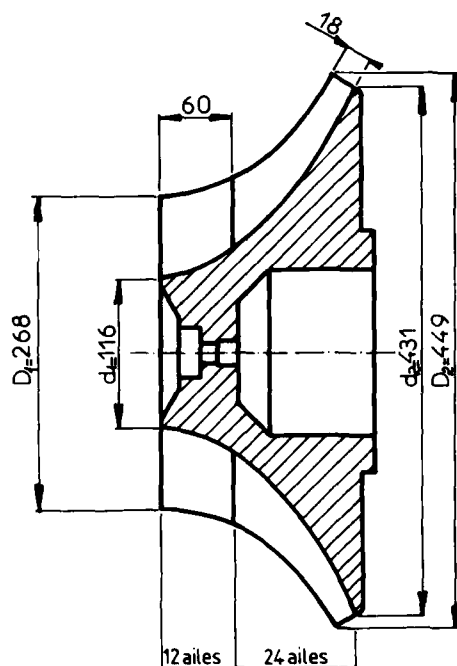


Fig. 10 - Deuxième version de la roue mobile.

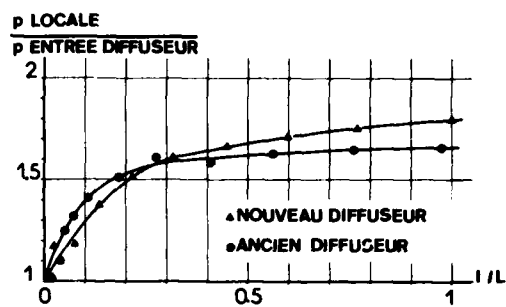


Fig. 11 - Répartition de la pression statique dans le diffuseur.

- Diffuseur de section très peu évolutive dans la région du col

Pour éviter une remontée de pression localisée comparable à celle que nous avons constatée sur le modèle précédent, une évolution de section très progressive dans la zone d'entrée a été adoptée. Les valeurs ci-après caractérisent le nouveau diffuseur :

- Nombre de canaux	21
- Rapport hauteur sur col	1,06
- Rapport des sections entrée sortie	2,54
- Rapport des diamètres extérieur intérieur	1,43
- Angle de divergence moyen	7°
- Angle de divergence local au col	2,5°
- Rapport longueur moyenne sur col d'entrée	14,25
- Mach à l'entrée du diffuseur	1,08
- Divergence sur la vue méridienne	1,085

Sur la figure n° 11, d'origine expérimentale, on peut voir les conséquences de la modification du dessin pour un fonctionnement au point nominal.

Sur le nouveau diffuseur, le gradient de pression au col est atténué avec pour conséquences une plus grande stabilité des couches limites et une remontée de pression qui s'étend à l'ensemble du diffuseur, avec des sections arrières encore actives malgré le rapport de diffusion important. On remarquera également que le rapport de pression utile dans le nouveau diffuseur est supérieur à celui du modèle précédent, bien que le Mach d'entrée ait été réduit de 1,13 à 1,080, ce qui est le signe d'une amélioration sensible du rendement et des performances.

4.2 - Variante avec diffuseur lisse

Nous avons jugé intéressant de faire un essai avec diffuseur lisse, c'est-à-dire sans aubes. On sait, en effet, qu'un compresseur équipé d'un diffuseur lisse présente à toutes les vitesses une plage d'opération plus favorable qu'avec un diffuseur aileté.

Bien qu'au point nominal de fonctionnement, la version avec diffuseur aileté bien adapté donne des rendements très élevés, un compresseur équipé de diffuseur lisse peut offrir, à vitesse réduite, des rendements égaux ou supérieurs à ceux obtenus avec un diffuseur à ailettes, et cette propriété peut être très intéressante pour une utilisation à vitesse variable.

Par ailleurs, les pertes d'un diffuseur lisse ont une forme très plate, par conséquent le point de fonctionnement optimum du compresseur avec diffuseur lisse est aussi avec une bonne approximation le point optimum de la roue seule, ce qui est une information importante pour parfaire, dans une étape ultérieure, l'adaptation simultanée de la roue avec un diffuseur aileté. Cette remarque permet de voir, à partir des essais qui sont présentés figure n° 12 que le diffuseur aileté que nous avons essayé est un peu trop fermé pour la roue et qu'une amélioration probable pourrait être obtenue en majorant légèrement sa section d'entrée.

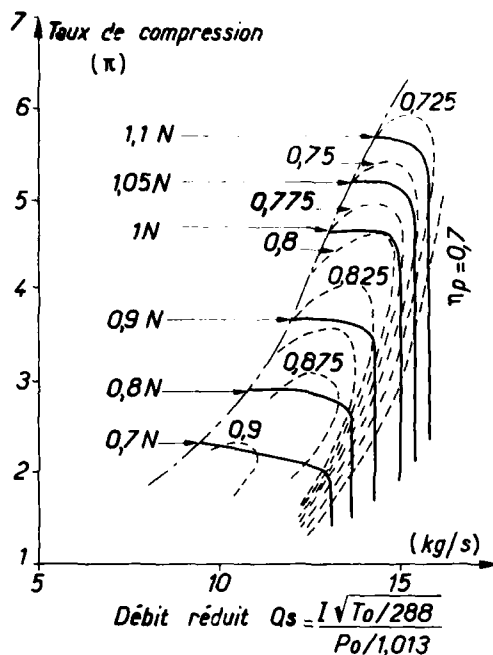


Fig. 12 — Diffuseur lisse - Sortie diffuseur.
Deuxième compresseur expérimental.

Le diffuseur lisse que nous avons expérimenté est caractérisé par :

- un rapport diamétral de 1,43
- un pincement à l'entrée (b_3/b_2) = 0,77
- un pincement sur la vue méridienne (b_4/b_3) = 0,715

4.3 - Essais avec diffuseur aileté

Les essais ont encore été effectués avec le réfrigérant 12 dans la boucle d'essais de l'ONERA.

La figure n° 13 montre les performances mesurées à la sortie du canal de retour, c'est-à-dire les caractéristiques de l'écoulement à l'entrée d'un éventuel second étage. On remarque que les conditions nominales de fonctionnement sont encore obtenues pour une vitesse de rotation inférieure à celle prévue, mais avec un rendement polytropique de 0,83 qui est très élevé pour le taux de compression recherché. On a ainsi un gain de rendement de 4 à 5 points par rapport à la première version. On remarque également que le domaine de fonctionnement à rendement élevé est très étendu et que même aux vitesses de rotation proches de la vitesse nominale une marge en débit non négligeable peut faciliter le couplage de cet étage de compression avec les autres étages.

La figure n° 14 qui représente les performances mesurées à la sortie du diffuseur aileté, met en évidence les pertes importantes en pression et en rendement dues au canal de retour. L'optimisation de ce dernier n'a pas été effectuée et des gains de performance peuvent encore être escomptés.

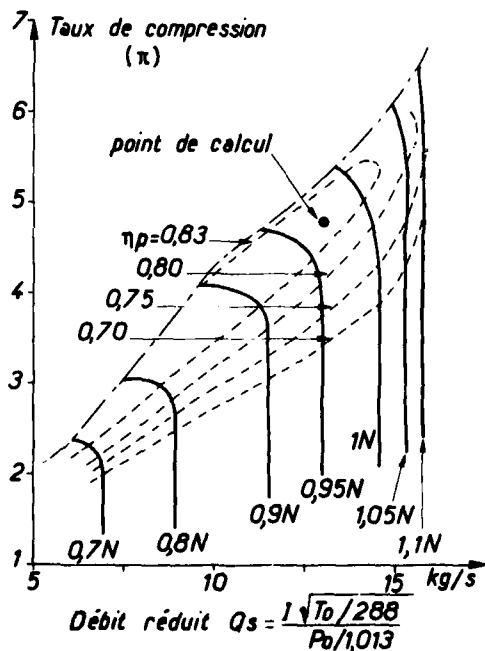


Fig. 13 — Diffuseur aileté - Sortie étage.
Deuxième compresseur expérimental.

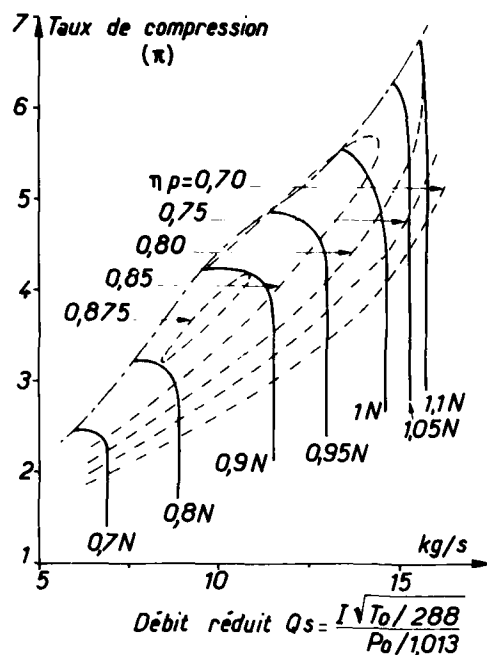


Fig. 14 — Diffuseur aileté - Sortie diffuseur.
Deuxième compresseur expérimental.

Par ailleurs, utilisé en étage isolé, sans canal de retour, ce compresseur peut fournir un taux de compression $\pi = 5,3$ au réfrigérant 12 (c'est-à-dire $\pi = 5,6$ à l'air) avec un rendement polytropique de 0,85.

5 - CONCLUSION

Les essais effectués avec un compresseur centrifuge à veine légèrement hélicoïdale et aubes couchées en arrière conçues de façon à annuler les contraintes de flexion centrifuge ont mis en évidence les performances élevées tant en taux de compression qu'en rendement que l'on peut espérer d'une telle machine. L'optimisation géométrique et aérodynamique du compresseur n'a pu être obtenue que par couplage d'une étude théorique et des résultats expérimentaux. Les difficultés rencontrées dans une première version de la machine ont pu ainsi être éliminées et la variante actuellement obtenue apparaît très prometteuse pour une version multicellulaire de compresseurs centrifuges de centrales frigorifiques industrielles. Mais même utilisé en étage isolé ou gavé par des compresseurs axiaux, ce compresseur peut trouver son emploi dans de nombreuses applications industrielles.

REFERENCES

- 1 - F. CHARRON - G. JANSSENS - J. PAULON
Banc d'essais de compresseurs supersoniques
ONERA TP.1302
- 2 - R. SOVRANO - Y. RIBAUD
Approche des écoulements compressibles dans les turbomachines par méthode de calcul axisymétrique
ATMA - Session 1979 - Paris.

DISCUSSION

I.H.Skoe, Kongsberg Vaapenfabrik, No

We have seen that total pressure deficits in the shroud region, caused by hub-to-shroud gradients in loss and work input, can be restored by rotor exit radius increase in the direction of the shroud. Have you any traverse data for the rotor exit for the two impellers?

Author's Reply

No, we have not any traverse data for the rotor exit flow for either of the two impellers

Y.Ribaud, ONERA, Fr

I would like first to say that Mr Poulain is the inventor of this type of impeller and then to ask him a question.

Does Mr Poulain think that in this type of impeller at high pressure ratio the worst stresses are in the vanes or in the disc? If they are in the vanes then perhaps they could be thickened, but what is the advantages from the mechanical viewpoint?

Author's Reply

The high stresses are in both blade and the disc. But we have designed a compressor with zero bending stresses. If it were permitted to have bending stresses in the impeller vanes then even more back-sweep would be allowed and so there would still be an advantage in this type of design. However, in this particular impeller the disc was designed in an unsatisfactory way because the back-flange was flat, but it is to be noted that we could have achieved a high rotational speed without the use of titanium; the material used for the impeller was steel.

IMPROVEMENTS IN SURGE MARGIN FOR CENTRIFUGAL COMPRESSORS

W. Jansen, Vice President and Technical Director
 A. F. Carter, Group Director
 M. C. Swarden, Project Engineer

Northern Research and Engineering Corporation
 39 Olympia Avenue
 Woburn, Massachusetts 01801

Summary

The occurrence of surge in a compressor not only limits its operating range, but it may prevent the attainment of maximum efficiency which often lies at or close to the surge line. Much work has been conducted lately to understand the phenomenon of surge with the aim to improve operating range and efficiency. This paper describes some positive aspects of the effort that has taken place at NREC. It follows the trends that were successful in previous investigations on both axial and centrifugal compressors.

Background

It is generally acknowledged that surge is initiated by compressor component stall. In a centrifugal, all three components, the impeller, vaneless diffuser, and vaned diffuser, will stall when the flow is reduced. This component stall is not a flow separation along a wall or blade surface, but a rotating stall. The phenomenon of rotating stall is often called a flow instability, but it is more correct to refer to it as an alternative mode of the flow which satisfies the complete equations of motions. Steady flow is merely the zeroth mode of the full unsteady flow equations. In rotating stall, one or more regions of severely retarded flow travel around the circumference of the compressor at a constant speed usually from twenty to seventy per cent of the rotor speed. This phenomenon has been investigated in detail over the last twenty-five years (Ref 1), and although the flow has large amplitude pressure fluctuations, linearized theories have provided reasonable understanding of the inception process. Tanaka (Ref 2) has applied non-linear theory with reasonable success.

When the steady flow suddenly changes to a rotating stall mode, the pressure rise through the component drops considerably; this shows up as a step change on the performance map (Fig 1). Surge analyses (Ref 3) show that when such a step change occurs, the compressor system consisting of inlet volume, compressor stage, and discharge volume becomes unstable and surge will take place (Fig 1).

Figure 2 shows a compressor map with the stalling lines of the different components. These stalling lines are nothing more than lines of constant angle of stalling incidence (judiciously decreased at high Mach number levels). Figure 2 shows that surge at high pressure ratios is generally caused by vaned diffuser stall, at lower speeds (and high specific speeds) impeller stall occurs first and initiates stall. When no vaned diffuser is present, it is often the vaneless diffuser that initiates surge. At low pressure ratios, even though the impeller stalls, the diffuser may generate such a pressure rise that no net loss in stage pressure occurs and, therefore, the compressor does not surge, but operates with a mild rotating stall in the impeller. In multistage centrifugals, rotating stall may exist in one stage with no compressor surge.

An alternative theory originally suggested by Stanitz (Ref 4) which maintains that the pressure surface velocity should be kept positive to prevent surge was tested by NACA (Ref 5). However, these tests did not corroborate the theory, but recent experiments (Ref 6), similar to those conducted by NACA, claim appreciable surge improvements.

Component StallGeneral

The concepts of component stall in centrifugals run parallel to those used in axial compressor technology. In fact, much of the current work on stall inhibitors finds its origin in axial compressor work (Refs 7 and 8). In centrifugals, the blades are long in chord and short in height and, since the experiments in axials have not been conclusive in the placement of component stall inhibitors such as wall treatment, we had to conduct tests with inhibitors at a number of chord lengths. For example, Ammann (Ref 9) reported success when placing wall treatment near the impeller blade trailing edges. Wiggins (Ref 10) was successful by placing circular grooves at the inlet of the impeller. Our program consisted of some thirty different treatments with configurations based on possible stall inhibiting characteristics. Most of these were unsuccessful and their (mostly negative) results are described in Reference 11. The present paper describes those stall inhibitors that give the most improvements.

Impeller Wall Treatment

There are three types of treatment used here. The case with no treatment is denoted by Item A. There are two treatments, B and C, near the impeller blade leading edge. One of the upstream treatments, B, had circular grooves as shown in Figure 3A. This would

accommodate flow communication in circumferential directions. Treatment C shows axial grooves, inclined at an angle, such that radial flow with a rotational component can easily enter the grooves and communicate in axial directions. A last wall treatment, D, is located near eighty per cent chord length. This location was selected to provide a space to alleviate flow separation along the blades.

Vaned Diffuser

When scrutinizing successful treatments in axial compressors, the conclusion is that wall treatment is successful when a rotating cascade is moving by a stationary wall treatment. However, a vaned diffuser is a stationary cascade and, in order to achieve the desired effects, the wall treatment must move with respect to the vaned diffuser. Since the impeller is the only rotating part, the configuration becomes as shown in Figure 4. Again, there is the possibility of flow movement in the meridional direction with the slots set at such an angle that they can accommodate the entering flow with a rotational component. The space in the back of the slots is provided as a settling or return channel. This is the only configuration of this type of wall treatment tried on the vaned diffuser. Its placement with respect to the vaned diffuser is similar to that of the optimum impeller configuration.

Test Compressors

General

The testing of the stall inhibitors was mainly conducted on two types of compressor stages. The impeller wall treatment was tested on stages that produce a medium pressure ratio of three-to-one at the design point. Both the impeller and diffuser treatment were applied to a stage that produces a six-to-one pressure ratio. In these high pressure ratio stages, the problem of flow range and lack of efficiency is particularly severe, with the additional problem that the high efficiency is right at the surge line and, therefore, not usable.

Medium Pressure Ratio Stage

The important flow variables for this stage are given in Table I. Its main features are a twenty-five degree backslope design impeller of medium specific speed, with bladed vaned diffusers. The impeller blade design was carefully selected to produce acceptable blade surface velocities at the hub and shroud streamtube (Fig 5), and to consist of straight line elements for ease of manufacturing (Ref 12). The physical shape of the impeller and diffuser is shown in Figure 6.

This stage is mainly used as the test vehicle for the impeller wall treatment. Since vaned diffuser stall causes surge in this stage, all testing was conducted by removing the vanes and having the remaining sidewalls function as a vaneless diffuser. This modification caused, of course, a severe drop in efficiency, but the surge line was now dictated by impeller stall and any improvement in impeller stall would clearly show up.

High Pressure Ratio Stage

The important flow variables for this stage are given in Table I. The main feature of this stage is the radial bladed impeller which has thirty-two blades, half of which are splitter blades extending over the last seventy per cent of the chord length. The impeller blade surface velocities are shown in Figure 7. The vaned diffuser consists of thin blades, rather than island diffuser blades. The physical appearance of the stage is shown in Figure 8, where the extended hub disk with the slots is clearly visible. The meridional view of the two stall inhibitors is shown in Figure 4.

Test Results

Impeller Wall Treatment

The test results are best presented when plotted on a performance map for the stage without vaned diffusers. Figure 9 shows a comparison of pressure ratio and efficiency of the smooth wall and the circular grooves, Cases A and B. The effects of the circular grooves are minimal. In fact they cause a slight reduction in efficiency.

Figure 10 shows the comparison between the smooth wall and the inclined axial grooves, Cases A and C. Here the range improvements are significant, with little to no drop in efficiency. Moreover, the area of high efficiency extends over a large flow range. The improved stage stalls due to impeller stall; vaneless diffuser stall occurs still at lower flow rates. The same effect is shown in Figure 11 for the high pressure stage.

Figure 12 shows the comparison between the smooth shroud wall and the treatment near the trailing edge of the blades, Cases A and D. Here the effects are discouraging with no improvement in the surge line but a significant drop in efficiency. Even though these results are negative, they are important because they provide guidance for future improvements, as discussed in the next section.

AD-A094 912

ADVISORY GROUP FOR AEROSPACE RESEARCH AND DEVELOPMENT--ETC F/6 21/5
CENTRIFUGAL COMPRESSORS, FLOW PHENOMENA AND PERFORMANCE.(U)

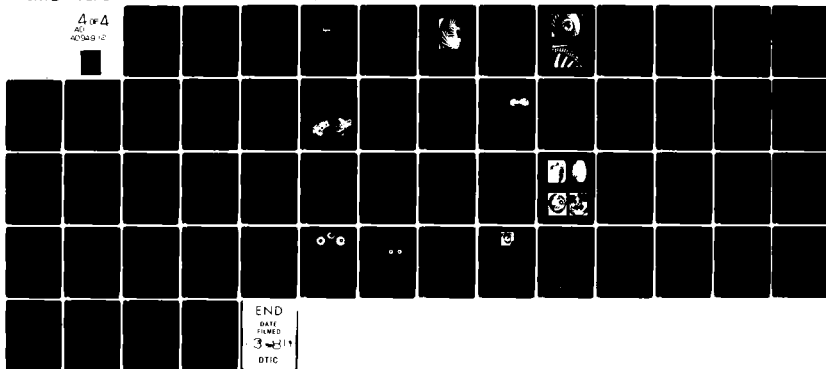
NOV 80

UNCLASSIFIED

AGARD-CP-282

NL

4 of 4
AD
40348 12



Vaned Diffuser Treatment

Since the severest lack of surge margin occurs in a high pressure ratio stage, the vaned diffuser treatment was applied to this stage. Tests were conducted with and without the treatment applied. Figure 13 shows the comparison between a conventional (untreated) and the treated vaned diffuser.

The results are quite dramatic, and not as anticipated. About half the increase in surge margin is achieved by the increase in choke flow. This can still be called a surge margin increase since an increased flow by opening up the vanes would have yielded a corresponding increase in surge flow. In the present case, both increases in low and high flow results. Nevertheless, the loss in efficiency is appreciable in this case. It is estimated that roughly seventy per cent of this loss increase is caused by the vaned diffuser treatment; the remainder is caused by the impeller treatment.

Discussion of Results

The picture that is emerging from previous investigations in References 2, 7, and 8 and the current work is that separated flows, backward flows and rotating stall are all intimately connected. When reducing flow, the corresponding positive incidence causes flow separation, back flow and restriction of the blade throat area. The restricted flow area gives rise to "spilling" of flow to the next flow passage and a rotating stall pattern is established. This pattern is very inefficient and generates pressure drops, a condition necessary for stage surge to occur. Further evidence of the existence of rotating stall was obtained from dynamic pressure measurements at the stationary shroud at the leading edge location of the impeller blades. No evidence is visible by observing the time-wise pressure. However, the frequency-analyzed results exhibit an emerging frequency peak at around 130 hz. The frequency corresponds to a system of two stall cells at a speed of 55 per cent of the wheel speeds. (It is well known that these barely observable dynamic forces generated by rotating stall can cause detrimental bearing failures in high fluid density compressors and pumps.)

The treatments provide a path for the back flow, different from the flow path. Consequently, throat blockages are reduced and the occurrence of rotating stall is delayed to lower flow rates. For this reason, circumferential grooves are not very effective since no path for back flow is provided (Refs 7, 8 and treatment B). Similarly, wall treatment beyond the blade throat section is not effective.

The drop in efficiency observed here and by others is not surprising. The wall treatment is very crude. No attempt is made to provide the treatment with an incidence-free inlet section. If blade leading edges were shaped as the wall slots, no surprise in the low efficiency would be expressed. Furthermore, the shape of the treatment flow section with its sharp corners is contrary to good fluid dynamic design practices. Finally, the location and direction of the discharge flow in the wall treatment segment is not consistent with the main flow. A Russian patent (Ref 13) by Atengoff shows a configuration that utilizes a movable concentric ring over the wall slots. At design point, this ring closes off the flow in the slots. When moving towards lower flows, the slots in the ring are tangentially aligned with the wall slots so that the flow circulation in the slots can take place. However, no results are published to indicate the design-point efficiency improvement. Current research is directed to arrive at treatment whose geometries are governed by fluid dynamic principles, and thereby reducing the losses incurred by the wall treatments.

The increased compressor cost by applying treatment should not be surprising to those familiar with modern compressors that have extensive bleed provisions, variable stators or three spool shaft systems. By demanding expanded compressor operation, the complexity and cost of the machine will increase. These increases have been small compared with the benefits of expanded operation, and the treatments presented here fall into the same categories.

Acknowledgements

The effort presented in this paper was made possible through the contribution of many American, Japanese, and West European organizations who own the patent rights on many of the treatments. The authors wish to thank Mr. Shankar Magee, who contributed throughout the analysis phase of this program and Mr. S. H. Pancygrau, who conducted most of the experiments.

TABLE I
GEOMETRIC VARIABLES FOR IMPELLERS USED IN THIS STUDY

	<u>Medium Pressure</u>	<u>High Pressure</u>
Shroud Clearance (in)	0.010	0.012
Inlet Hub Radius (in)	1.500	1.310
Inlet Shroud Radius	3.331	3.000
Exit Radius (in)	5.075	5.075
Inlet Shroud Blade Angle (deg)	-66.5	-60.0
Exit Blade Angle (deg)	-25.0	0.0
Blade Included Angle at Inlet Shroud (deg)	8.7	3.7
Average Leading Edge Normal Thickness (in)	0.015	0.014
Average Trailing Edge Normal Thickness (in)	0.0785	0.093
Throat Factor	0.519	0.606
Passage Width at Impeller Exit (in)	0.460	0.350
Impeller Axial Length (in)	2.750	3.190
Impeller Blade Length (in)	5.676	5.850
Impeller Hydraulic Diameter (in)	0.760	0.684

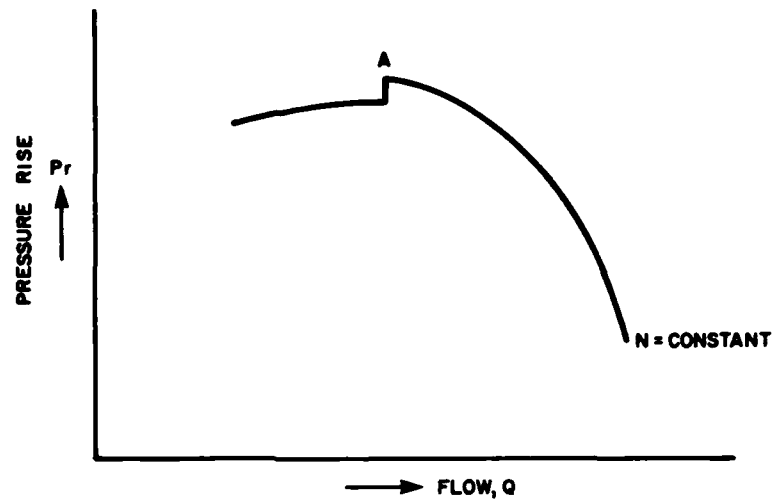


FIGURE 1 - SURGE OCCURS WHEN THERE IS A SUDDEN PRESSURE DROP IN THE PERFORMANCE CURVE AT POINT A. THIS PRESSURE DROP IS CAUSED BY THE SUDDEN CHANGE FROM STEADY FLOW TO UNSTEADY (ROTATING STALL) FLOW IN ONE OF THE COMPONENTS

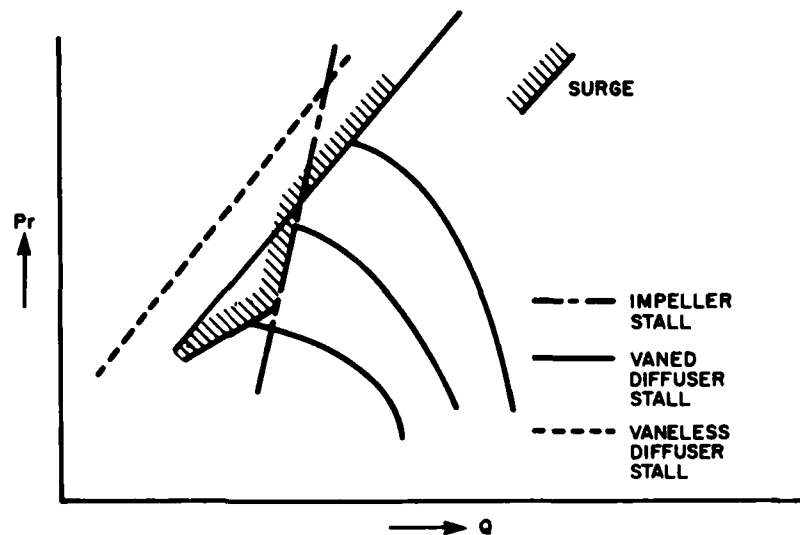


FIGURE 2 - SHAPE OF COMPONENT STALL LINES AT DIFFERENT SPEEDS. IMPELLER AND VANED DIFFUSER STALL LINES CAN BE MOVED BY BLADE ANGLE MODIFICATIONS (BUT CHOKE FLOW CONDITION WILL MOVE BY THE SAME AMOUNT). VANELESS DIFFUSER STALL LINE CAN BE MOVED BY WIDTH MODIFICATIONS

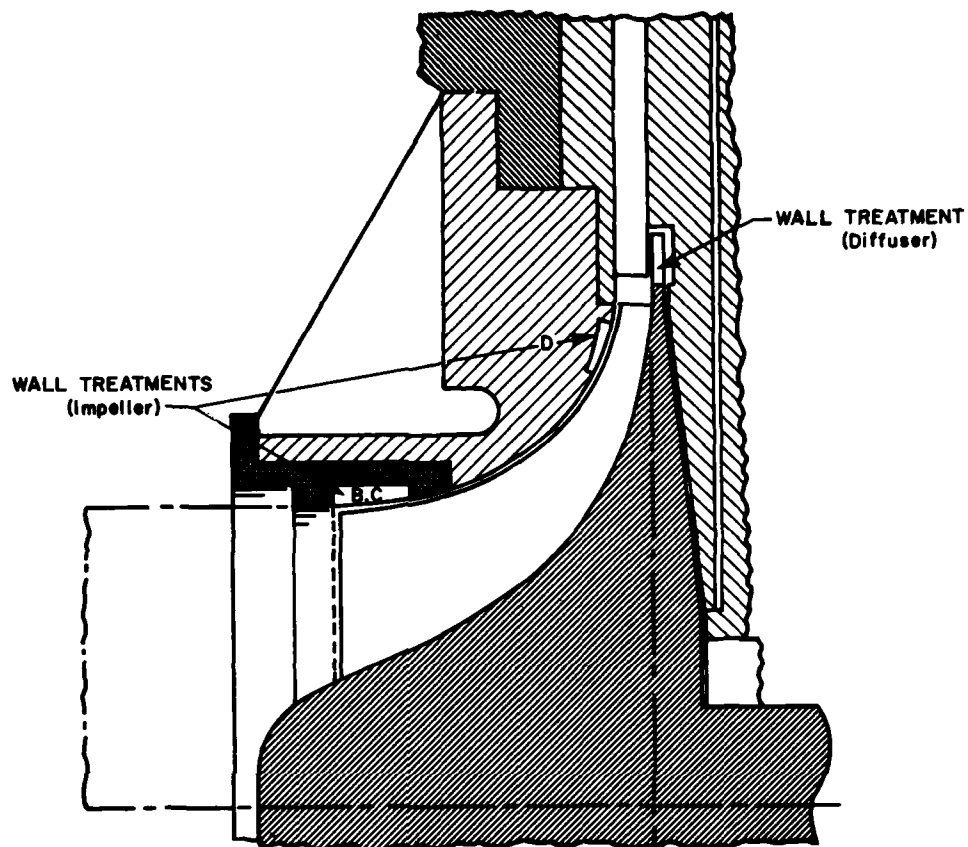


FIGURE 3A - CROSS SECTION OF COMPRESSOR STAGE WITH WALL TREATMENTS INDICATED. B DENOTES CIRCULAR GROOVES; C DENOTES AXIAL GROOVES, INCLINED. TREATMENT D HAD INCLINED GROOVES IN DIRECTION OF FLOW

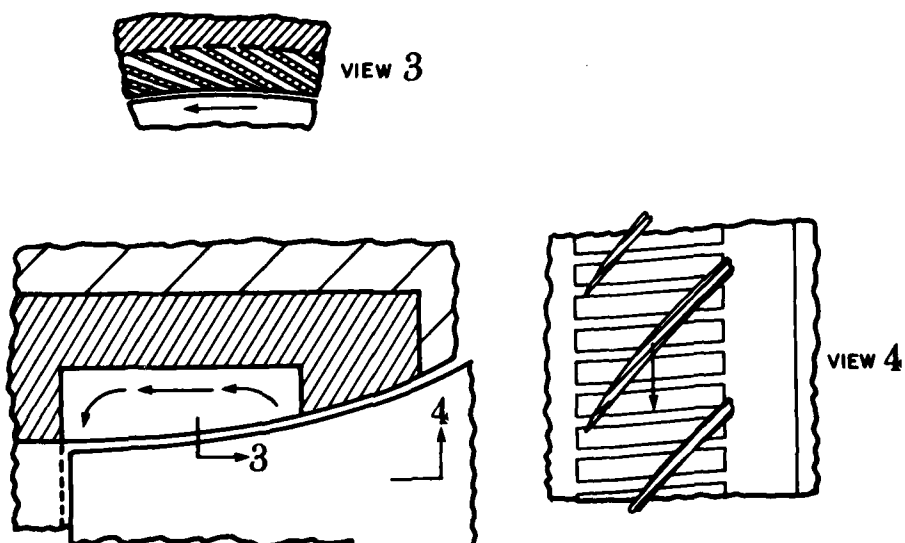


FIGURE 3B - DETAIL OF IMPELLER WALL TREATMENT FOR INCLINED AXIAL GROOVES, C

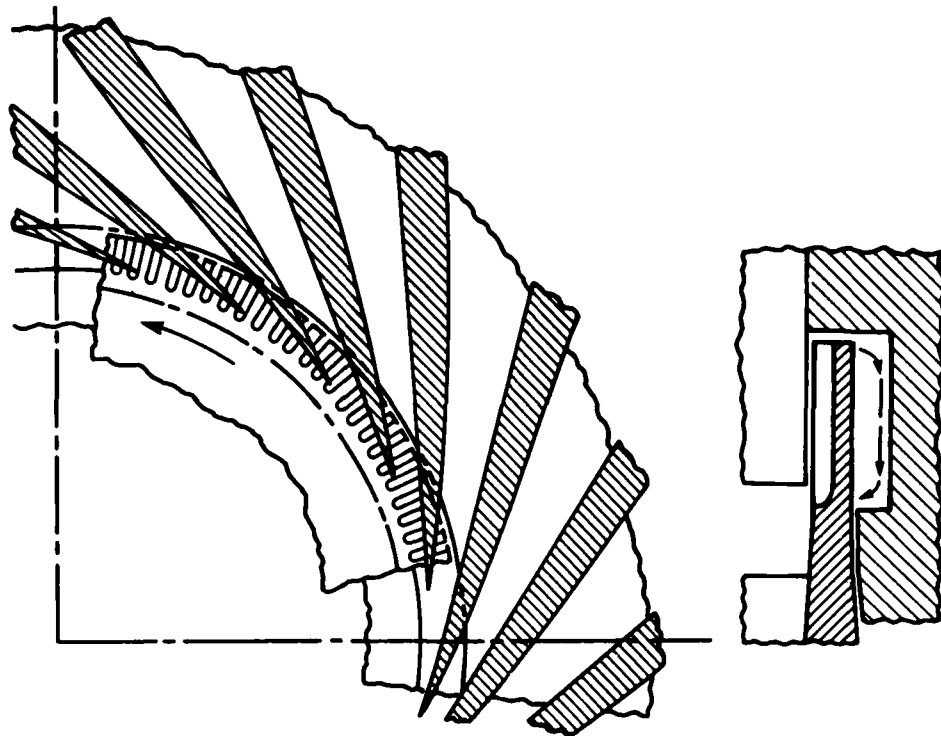


FIGURE 4 - CLOSE-UP OF DIFFUSER TREATMENT.
GROOVES ARE LOCATED AT IMPELLER RIM

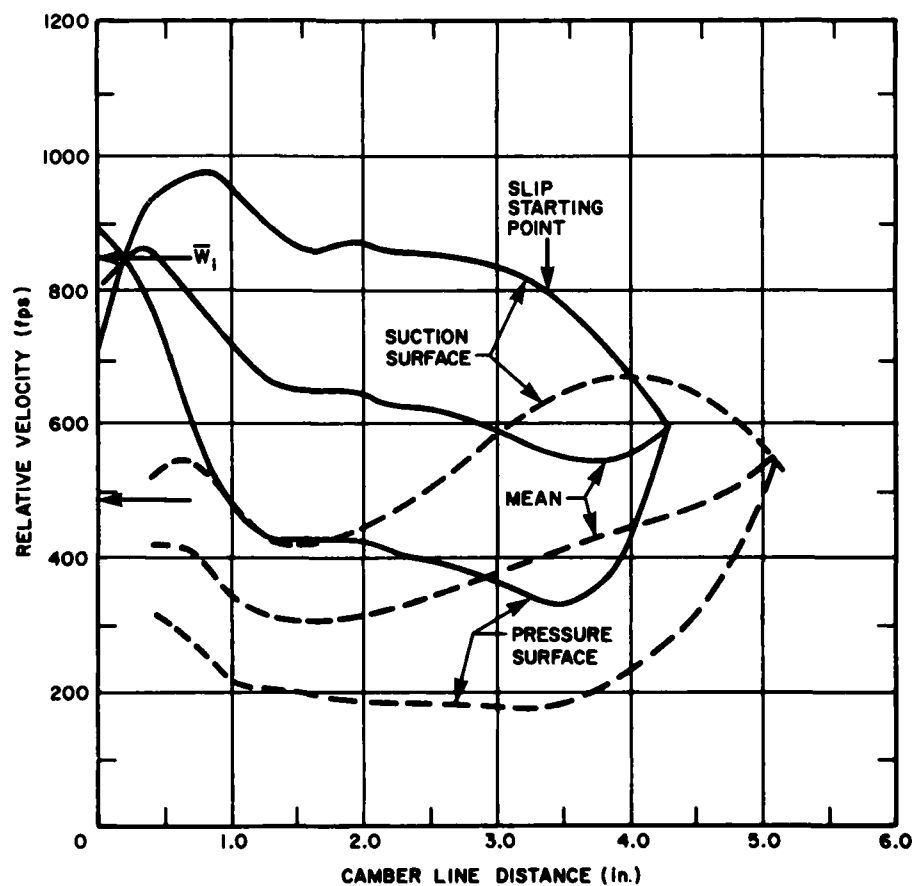


FIGURE 5 - DESIGN-POINT IMPELLER BLADE SURFACE VELOCITY DISTRIBUTIONS
FOR MEDIUM PRESSURE RATIO IMPELLER (SHROUD— AND HUB--- STREAMTUBE)



FIGURE 6 - PHOTOGRAPH OF THE MEDIUM PRESSURE COMPRESSOR STAGE

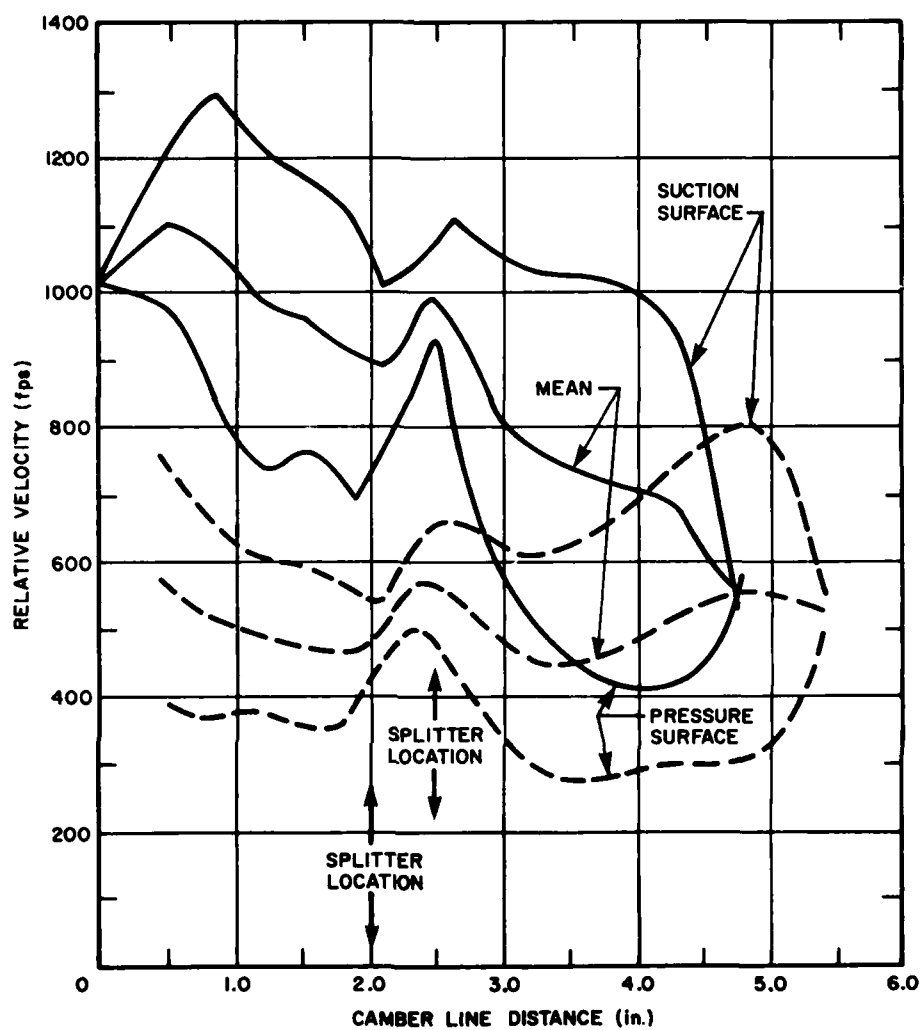


FIGURE 7 - DESIGN-POINT SURFACE VELOCITY DISTRIBUTIONS FOR
HIGH PRESSURE IMPELLER (SHROUD— AND HUB--- STREAMTUBE)

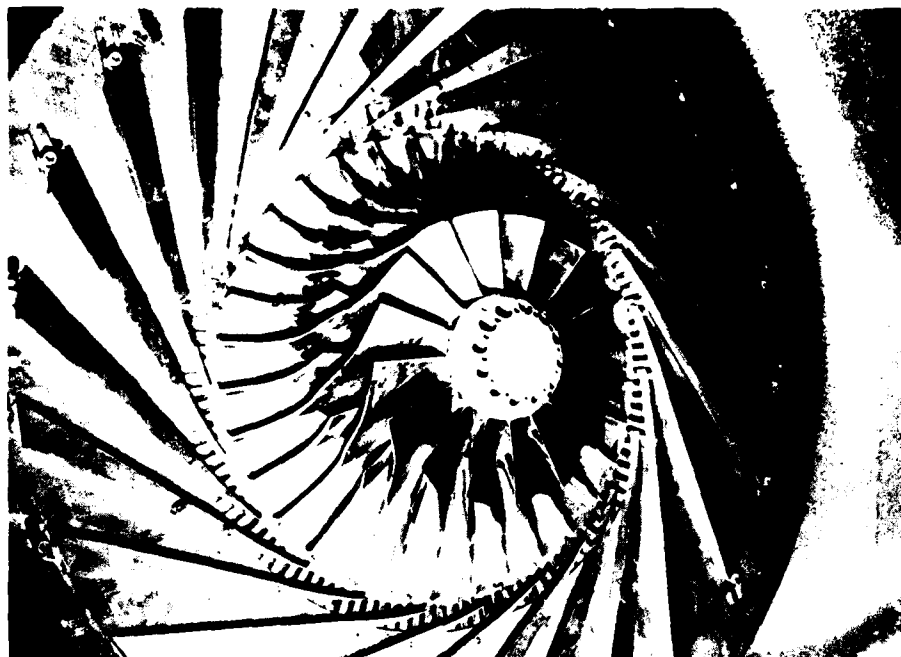


FIGURE 8A - PHOTOGRAPH OF THE HIGH PRESSURE COMPRESSOR CONFIGURATION



FIGURE 8B - CLOSE-UP PHOTOGRAPH OF VANED DIFFUSER TREATMENT

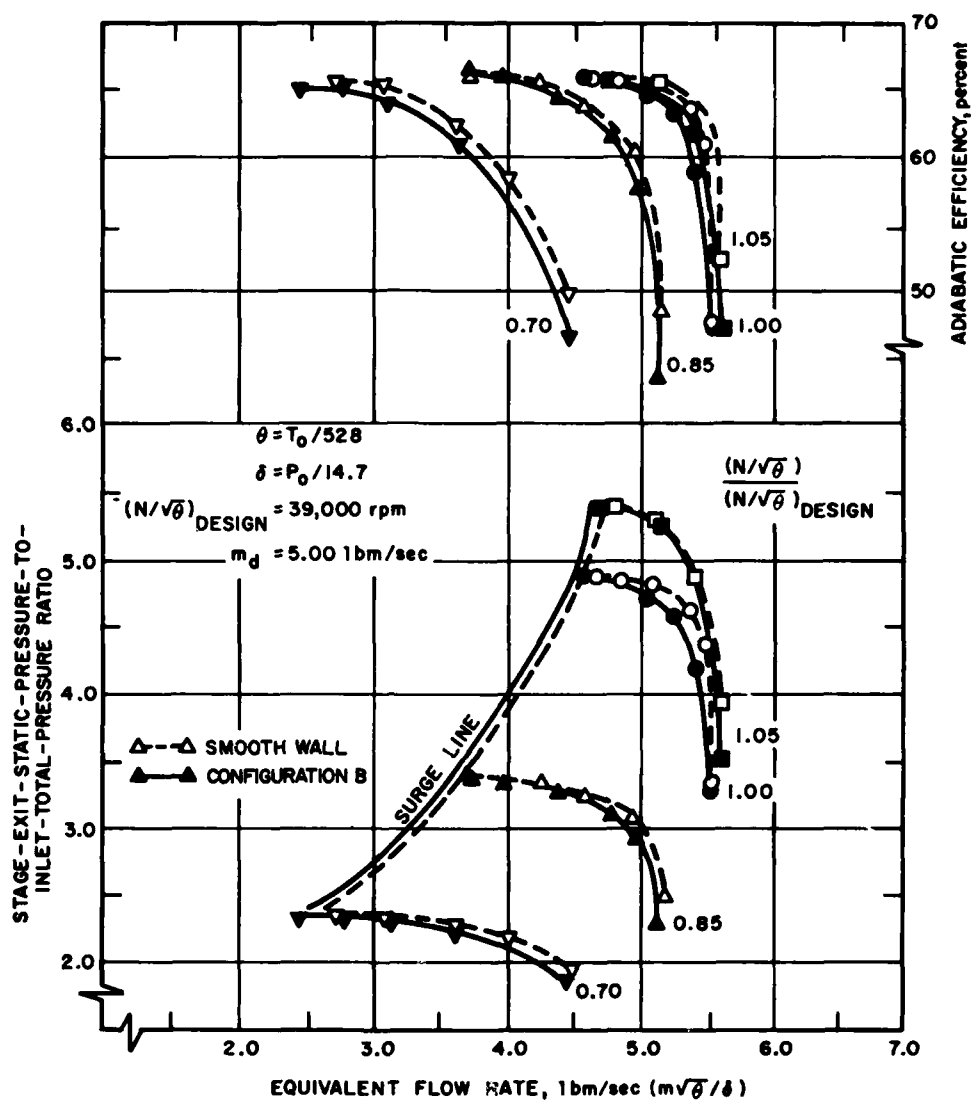


FIGURE 9 - COMPARISON OF MEASURED PERFORMANCE BETWEEN SMOOTH AND TREATED INDUCER WALL (TYPE B) FOR HIGH PRESSURE STAGE WITH VANELESS DIFFUSER

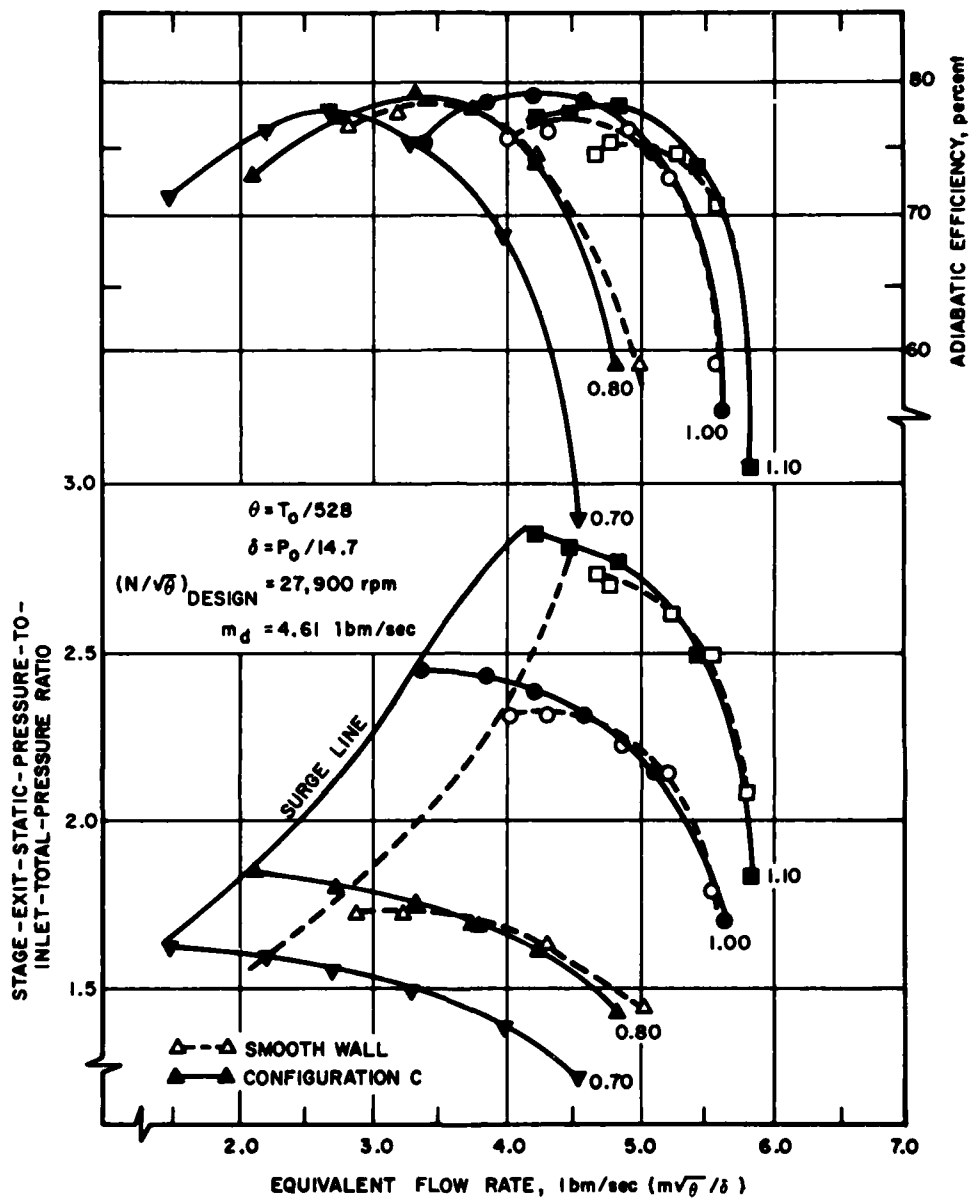


FIGURE 10 - COMPARISON OF MEASURED PERFORMANCE BETWEEN SMOOTH AND TREATED INDUCER WALL (TYPE C) FOR MEDIUM PRESSURE STAGE (VANELESS DIFFUSER)

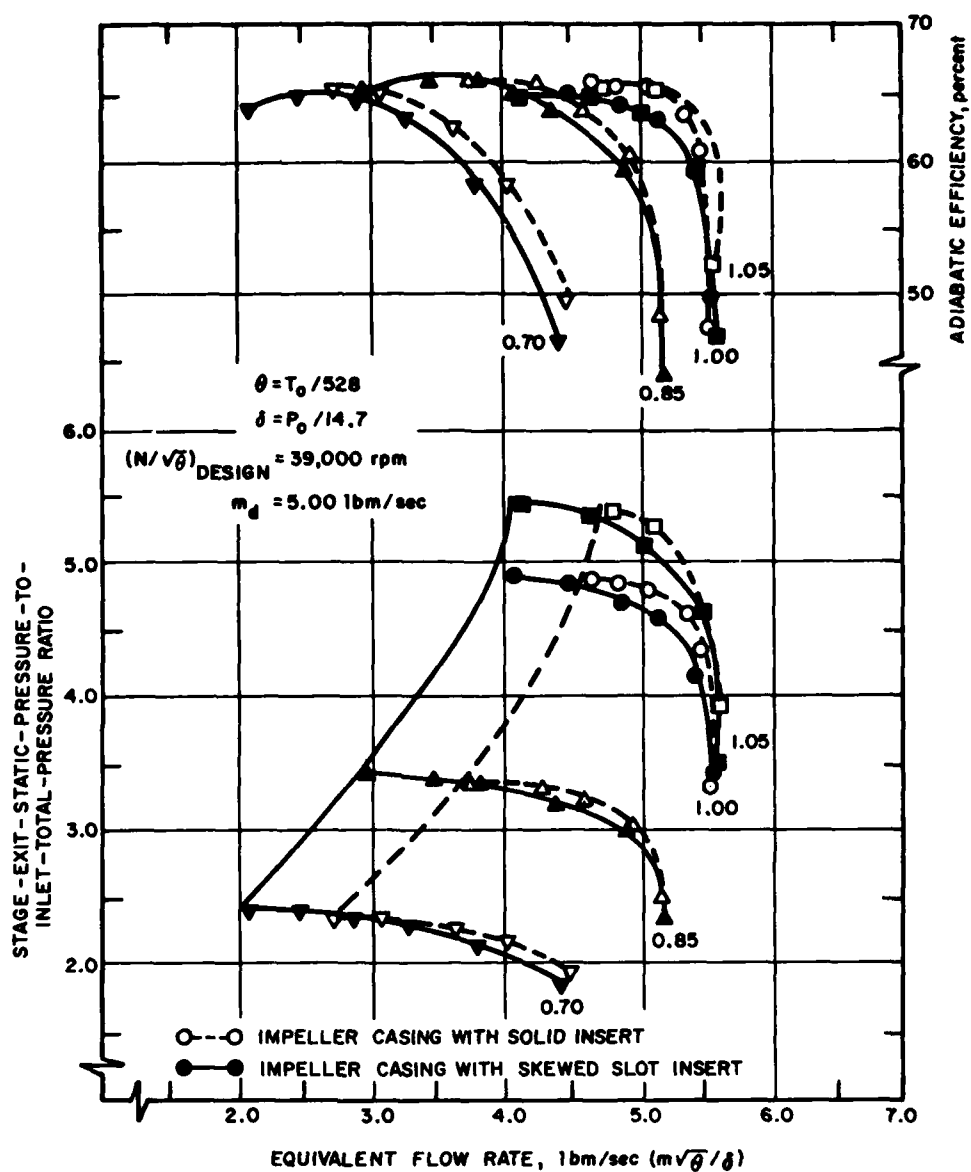


FIGURE 11 - COMPARISON OF MEASURED PERFORMANCE BETWEEN SMOOTH AND TREATED INDUCER WALL (TYPE C) FOR HIGH PRESSURE STAGE WITH VANELESS DIFFUSER

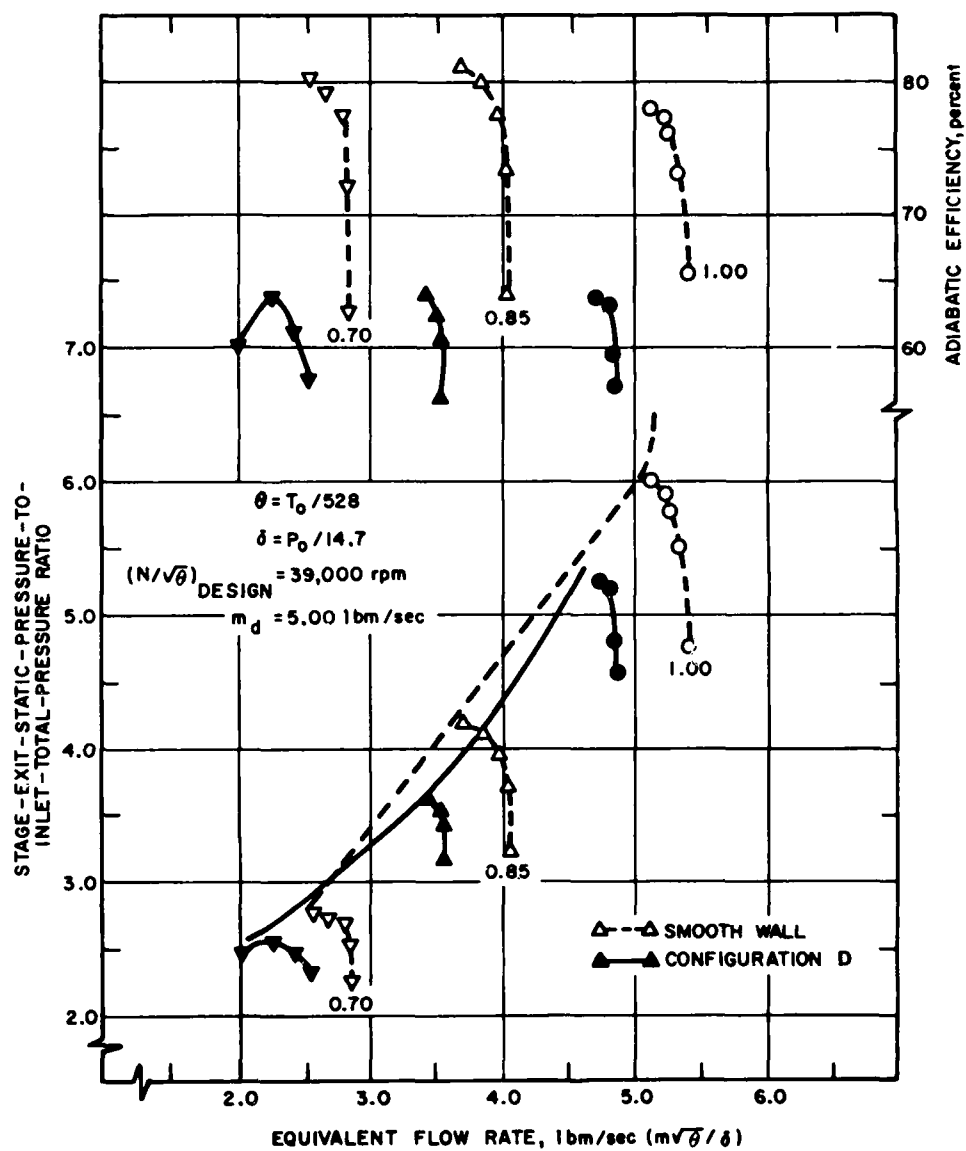


FIGURE 12 - COMPARISON OF MEASURED PERFORMANCE BETWEEN SMOOTH AND TREATED INDUCER WALL (TYPE D) FOR HIGH PRESSURE STAGE WITH VANED DIFFUSER

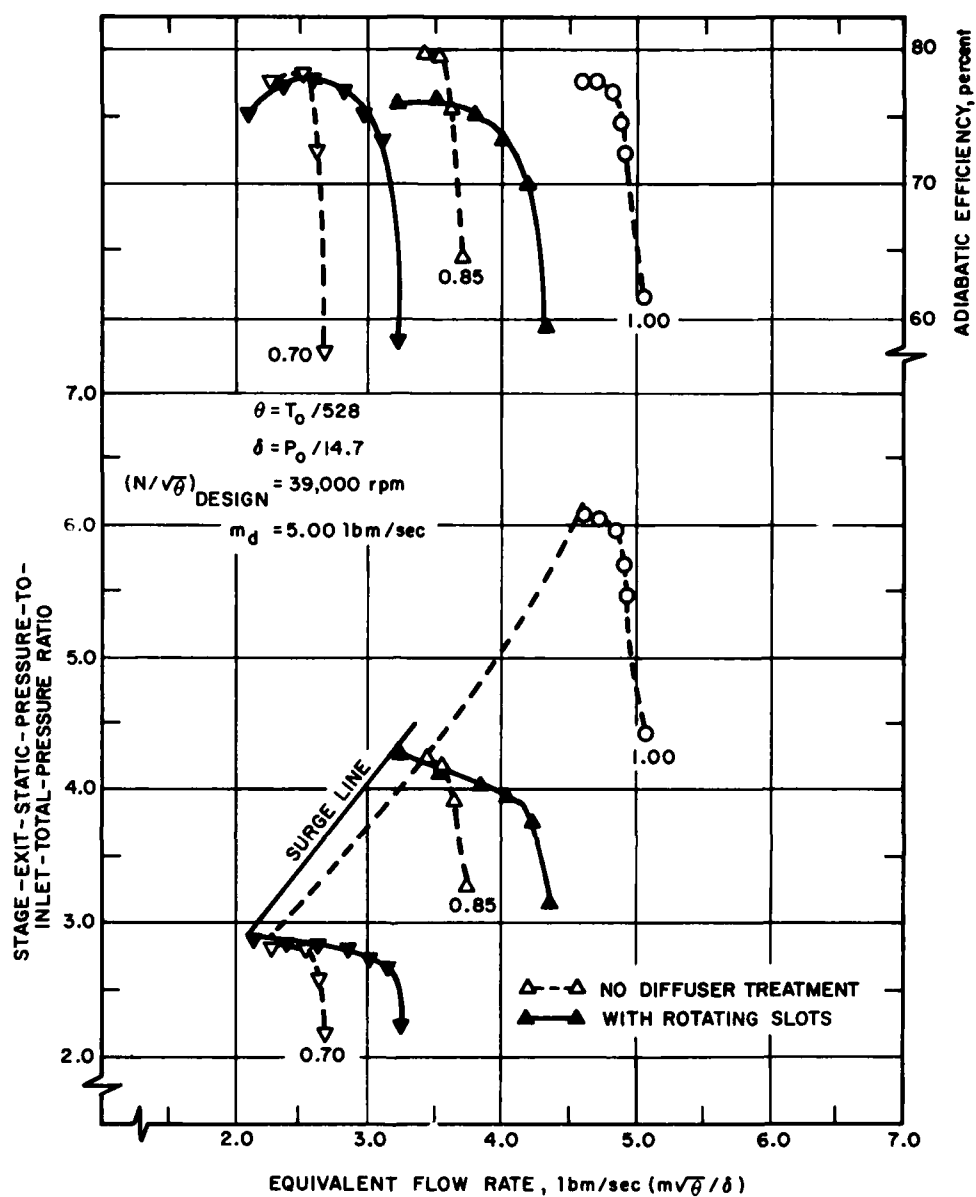


FIGURE 13 - COMPARISON OF MEASURED PERFORMANCE BETWEEN NORMAL AND ROTATING SLOTTED DIFFUSER TREATMENT FOR HIGH PRESSURE COMPRESSOR STAGE WITH VANED DIFFUSER

1. Fabri, J., "Rotating Stall in Axial Flow Compressors", Internal Aerodynamics (Turbomachinery), The Institution of Mechanical Engineers, London, England, 1970, pp. 96-110.
2. Takata, H. and Nagano, S., Nonlinear Analysis of Rotating Stall (ASME Paper No. 72-GT-3), The American Society of Mechanical Engineers.
3. Emmons, H. W., et al, "Compressor Surge and Stall Propagation", Trans. ASME, The American Society of Mechanical Engineers, vol. 77, 1955, pp. 455-469.
4. Stanitz, J. D., "Some Theoretical Aerodynamic Investigations of Impellers in Radial-and Mixed-Flow Centrifugal Compressors", Trans. ASME, The American Society of Mechanical Engineers, vol. 74, no. 4, 1952, pp. 473-497.
5. Hamrick, J. T., Osborn, W. M., and Beede, W. L., "Design and Test of Mixed-Flow Impellers, III - Design and Experimental Results for Impeller Model MFI-2A and Comparison with Impeller Model MFI-1A", NACA Research Memorandum (NACA RM E52L22a), National Advisory Committee for Aeronautics, Washington, March 10, 1953.
6. Flynn, P. F. and Weber, H. G., Design and Test of an Extremely Wide Flow Range Compressor (ASME Paper no. 79-GT-80), American Society of Mechanical Engineers.
7. Osborn, W. M., Lewis, G. W., Jr., and Heidelberg, L. J., Effect of Several Porous Casing Treatments on Stall Limit and on Overall Performance of an Axial-Flow Compressor Rotor (NASA TN D-6537), National Aeronautics and Space Administration, November, 1971 (see also NASA TN D-6538, November, 1971).
8. Takata, H. and Tsukuda, "Stall Margin Improvement by Casing Treatment-- Its Mechanism and Effectiveness", Journal of Engineering for Power, January, 1977, pp. 121-133).
9. Amann, C. A., Nordenson, G. E. and Skellenger, G. D., Casing Modification for Increasing the Surge Margin in an Automotive Turbine Engine (Research Publication GMR-1426), to be presented at the Nineteenth Annual International Gas Turbine Conference of the American Society of Mechanical Engineers, Zurich, Switzerland, March 31 - April 4, 1974.
10. Wiggins, J. O. and Waltz, G. L., "Centrifugal Compressor Vaneless Space Casing Treatment", U. S. Patent No. 4,063,848, December 20, 1977.
11. Improvements in Surge Margin and Diffuser Performance: Summary Report (NREC Report No. 1230-8), Northern Research and Engineering Corporation, Woburn, Massachusetts, 1976.
12. Jansen, W. and Kirschner, A. M., Impeller Blade Design Method for Centrifugal Compressors, Presented at a Symposium on Fluid Mechanics, Acoustics, and Design of Turbomachinery Held at the Pennsylvania State University, University Park, Pennsylvania August 31 to September 3, 1970.
13. Atengoff, M. N., "Centrifugal Compressor", Russian Patent No. 478957, October 17, 1975.

DISCUSSION

H.Krain, DFVLR, Cologne, Ge

The paper has presented experimental results showing an increased flow range if a suitable casing treatment is employed. Could the authors please supply a reasonable explanation of these results with respect to centrifugal compressor fluid dynamics. Do the authors have an idea as to which flow effects may lead to the increased flow range observed?

Author's Reply

The phenomenon of rotating stall is of course caused by the angle of incidence exceeding a certain value onto one blade leading to a separation and blockage so that the flow is deflected into the next passage. The casing treatment provides a way of redistributing the flow between adjacent vane passages and so delays the rotating stall.

R.A.Moyes, Compair Industrial Limited, UK

Were the results presented the best of a series of treatments using various dimensions, locations, and forms or was some specific non-empirical approach used in the initial selection of these features?

Author's Reply

We tried to attack our investigation on surge with a reasoned approach, where we first took all the theories that have been postulated for the initiations of surge and then try to provide means for delaying surge based on the theories. Thus, we investigated boundary layer fences (preventing low momentum flow), turbulence generators, leading edge slots, side wall settling chambers. The presented data are those that provided the best results.

D.Japikse, CREARE, US

I should like to congratulate the authors on the results obtained after years of careful investigation. Their comments would be appreciated on the following:

- (a) How have you accounted for your additional work input with the rotating slots at the impeller tip?
- (b) The authors indicated that in centrifugal compressors one invariably looks for rotating stall. Surely they must agree that cases exist where surge was not preceded by rotating stall as in the work, for example, of Toyama, Runstadler and Dean.
- (c) Similarly the authors indicated that a "compressor will surge when it reaches the first of several stalling lines". But it is well-known that one can operate with a stalled impeller and also with stalled zones in vaneless and vaned diffusers.

Author's Reply

- (a) The additional work input was measured as a slight temperature and pressure rise increase. However, the temperature rise was proportionately much larger, causing a drop in efficiency. Our current work is to devise treatment geometries where we can maintain the pressure rise increase and thus raise the efficiency.
- (b) As far as the authors are aware surge observed in their compressor stages has been initiated by rotating stall but it is not possible to be completely certain on that point.
- (c) The authors agree that a stage can operate with a stalled impeller provided that the diffuser recovery factor is good enough to maintain a characteristic with a negative slope but it is still possible to get a drop in performance under these conditions.

P.Ramette, CEPr, Saclay, Fr

The wall treatment designated type 'C' on the impeller and the rotating wall treatment on the diffuser are similar. Yet the results in the compressor maps are very different. Wall treatment type 'C' at the impeller changes the stall line but does not change the speed line very much (Figure 10) and the rotating wall treatment at the diffuser changes the speed line (Figure 13) but does not affect the stall line very much. Can the authors explain why the results are so different?

Author's Reply

The authors do not claim to understand the precise effects that are occurring here.

C.Rodgers, Solar, US

I would like to point out that although an impeller can operate in a stalled condition, this is dangerous from a mechanical point of view because of the presence of vibrations.

Author's Reply

The authors agree with this comment, particularly noting the effect of vibrations on the shaft stability performance.

DISCUSSION

H.Krain, DFVLR, Cologne, Ge

The paper has presented experimental results showing an increased flow range if a suitable casing treatment is employed. Could the authors please supply a reasonable explanation of these results with respect to centrifugal compressor fluid dynamics. Do the authors have an idea as to which flow effects may lead to the increased flow range observed?

Author's Reply

The phenomenon of rotating stall is of course caused by the angle of incidence exceeding a certain value onto one blade leading to a separation and blockage so that the flow is deflected into the next passage. The casing treatment provides a way of redistributing the flow between adjacent vane passages and so delays the rotating stall.

R.A.Moyes, Compair Industrial Limited, UK

Were the results presented the best of a series of treatments using various dimensions, locations, and forms or was some specific non-empirical approach used in the initial selection of these features?

Author's Reply

We tried to attack our investigation on surge with a reasoned approach, where we first took all the theories that have been postulated for the initiations of surge and then try to provide means for delaying surge based on the theories. Thus, we investigated boundary layer fences (preventing low momentum flow), turbulence generators, leading edge slots, side wall settling chambers. The presented data are those that provided the best results.

D.Japikse, CREARE, US

I should like to congratulate the authors on the results obtained after years of careful investigation. Their comments would be appreciated on the following:

- (a) How have you accounted for your additional work input with the rotating slots at the impeller tip?
- (b) The authors indicated that in centrifugal compressors one invariably looks for rotating stall. Surely they must agree that cases exist where surge was not preceded by rotating stall as in the work, for example, of Toyama, Runstadler and Dean.
- (c) Similarly the authors indicated that a "compressor will surge when it reaches the first of several stalling lines". But it is well-known that one can operate with a stalled impeller and also with stalled zones in vaneless and vaned diffusers.

Author's Reply

- (a) The additional work input was measured as a slight temperature and pressure rise increase. However, the temperature rise was proportionately much larger, causing a drop in efficiency. Our current work is to devise treatment geometries where we can maintain the pressure rise increase and thus raise the efficiency.
- (b) As far as the authors are aware surge observed in their compressor stages has been initiated by rotating stall but it is not possible to be completely certain on that point.
- (c) The authors agree that a stage can operate with a stalled impeller provided that the diffuser recovery factor is good enough to maintain a characteristic with a negative slope but it is still possible to get a drop in performance under these conditions.

P.Ramette, CEPr, Saclay, Fr

The wall treatment designated type 'C' on the impeller and the rotating wall treatment on the diffuser are similar. Yet the results in the compressor maps are very different. Wall treatment type 'C' at the impeller changes the stall line but does not change the speed line very much (Figure 10) and the rotating wall treatment at the diffuser changes the speed line (Figure 13) but does not affect the stall line very much. Can the authors explain why the results are so different?

Author's Reply

The authors do not claim to understand the precise effects that are occurring here.

C.Rodgers, Solar, US

I would like to point out that although an impeller can operate in a stalled condition, this is dangerous from a mechanical point of view because of the presence of vibrations.

Author's Reply

The authors agree with this comment, particularly noting the effect of vibrations on the shaft stability performance.

DISCUSSION

H.Krain, DFVLR, Cologne, Ge

The paper has presented experimental results showing an increased flow range if a suitable casing treatment is employed. Could the authors please supply a reasonable explanation of these results with respect to centrifugal compressor fluid dynamics. Do the authors have an idea as to which flow effects may lead to the increased flow range observed?

Author's Reply

The phenomenon of rotating stall is of course caused by the angle of incidence exceeding a certain value onto one blade leading to a separation and blockage so that the flow is deflected into the next passage. The casing treatment provides a way of redistributing the flow between adjacent vane passages and so delays the rotating stall.

R.A.Moyes, Compair Industrial Limited, UK

Were the results presented the best of a series of treatments using various dimensions, locations, and forms or was some specific non-empirical approach used in the initial selection of these features?

Author's Reply

We tried to attack our investigation on surge with a reasoned approach, where we first took all the theories that have been postulated for the initiations of surge and then try to provide means for delaying surge based on the theories. Thus, we investigated boundary layer fences (preventing low momentum flow), turbulence generators, leading edge slots, side wall settling chambers. The presented data are those that provided the best results.

D.Japikse, CREARE, US

I should like to congratulate the authors on the results obtained after years of careful investigation. Their comments would be appreciated on the following:

- (a) How have you accounted for your additional work input with the rotating slots at the impeller tip?
- (b) The authors indicated that in centrifugal compressors one invariably looks for rotating stall. Surely they must agree that cases exist where surge was not preceded by rotating stall as in the work, for example, of Toyama, Runstadler and Dean.
- (c) Similarly the authors indicated that a "compressor will surge when it reaches the first of several stalling lines". But it is well-known that one can operate with a stalled impeller and also with stalled zones in vaneless and vaned diffusers.

Author's Reply

- (a) The additional work input was measured as a slight temperature and pressure rise increase. However, the temperature rise was proportionately much larger, causing a drop in efficiency. Our current work is to devise treatment geometries where we can maintain the pressure rise increase and thus raise the efficiency.
- (b) As far as the authors are aware surge observed in their compressor stages has been initiated by rotating stall but it is not possible to be completely certain on that point.
- (c) The authors agree that a stage can operate with a stalled impeller provided that the diffuser recovery factor is good enough to maintain a characteristic with a negative slope but it is still possible to get a drop in performance under these conditions.

P.Ramette, CEPr, Saclay, Fr

The wall treatment designated type 'C' on the impeller and the rotating wall treatment on the diffuser are similar. Yet the results in the compressor maps are very different. Wall treatment type 'C' at the impeller changes the stall line but does not change the speed line very much (Figure 10) and the rotating wall treatment at the diffuser changes the speed line (Figure 13) but does not affect the stall line very much. Can the authors explain why the results are so different?

Author's Reply

The authors do not claim to understand the precise effects that are occurring here.

C.Rodgers, Solar, US

I would like to point out that although an impeller can operate in a stalled condition, this is dangerous from a mechanical point of view because of the presence of vibrations.

Author's Reply

The authors agree with this comment, particularly noting the effect of vibrations on the shaft stability performance.

MODEL 250-C30/C28B COMPRESSOR DEVELOPMENT

Dennis C. Chapman
 Detroit Diesel Allison Division
 General Motors Corporation
 Mail Stop U28, P. O. Box 894
 Indianapolis, IN 46206

SUMMARY

Advanced versions of the Allison Model 250 engine series are now in production for the Sikorsky S76 and Bell Long Ranger helicopters. These engines, designated 250-C30 and -C28B respectively, use a single stage centrifugal compressor matched at 8.7:1 pressure ratio at design speed. The initial design met flow, pressure ratio and efficiency requirements, but encountered both a localized deficiency in the surge line around 85% speed and excessive impeller blade vibratory stress at high speed. Several potential remedies were tried unsuccessfully and the compressor was redesigned. The redesign featured redistributed impeller blade loading, revised impeller blade thickness and increased number of diffuser vanes. These changes eliminated the vibratory stress problem. A unique inducer shroud bleed system, requiring no control, resolved the surge line problem and improved high speed flow and efficiency as well.

INTRODUCTION

The Allison Model 250 gas turbine engine (military T63) shown in Figure 1, first entered production in the early 1960s for light helicopter application. The initial engine was rated at 317 horsepower and consisted of a seven stage axial/centrifugal compressor, single can combustor, two stage gas generator turbine and two stage power turbine. This same basic configuration in the same envelope has since been grown to a 420 horsepower rating and over 14,000 such engines have been produced. Planning for additional increases in the horsepower output of this engine began shortly after production started with component technology development programs. The initial compressor effort was a three stage axial/centrifugal compressor at the same 7:1 pressure ratio as the original compressor. This compressor lacked adequate part speed surge margin and a single stage centrifugal compressor at the same pressure ratio was designed. The 7:1 centrifugal stage was quite successful and was FAA certified in a 500 horsepower engine designated 250-C28. Continuing demand for higher horsepower led to the design of a higher flow centrifugal stage at 8.5:1 pressure ratio. That compressor, in two different flow sizes, has now entered production in the 650 horsepower Model 250-C30 (shown in Figure 2) and the 500 horsepower C28B/C engines. The C30 engine currently powers the Sikorsky S76 Spirit Helicopter and the C28B/C engines power the Bell 206L-1 Long Ranger II and MBH 80-105L helicopters. This paper discusses the design and development of the compressors for these latest models of the 250 engine series.

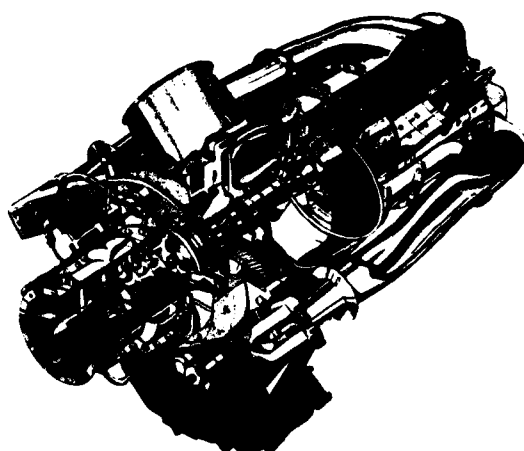


Figure 1. Allison Model 250 engine.

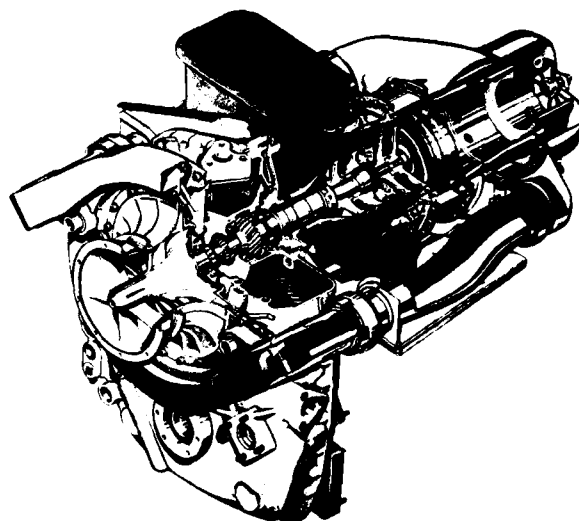


Figure 2. Model 250-C30 engine.

INITIAL DESIGN

Preliminary market and design analyses established a requirement for 5.6 lb/sec corrected flow for the C30 compressor. To minimize the sizing impact on the remainder of the engine and improve specific fuel consumption, a pressure ratio of 8.5:1 was desirable. With single stage centrifugal compressor experience at both 7:1 and 10:1 pressure ratio as background, a single stage centrifugal configuration was chosen. A goal efficiency of 78% (t-t, $M_0 = 0.17$, at design point) was established. Restrictions placed upon the design included maintaining the original engine design speed of 51,000 rpm and an engine envelope limitation/driveshaft interface requirement which established a maximum diameter for the collector at diffuser exit. The speed restriction was not a serious performance factor because a specific speed of 91 resulted. The collector diameter limitation impacted the collector/diffuser aerodynamic design by restricting diffuser area ratio, and by requiring a folded collector.

The resulting design is shown in cross-section in Figure 3. The impeller is straddle mounted between a rear thrust bearing and a ball bearing free to move axially in the front support. The front support includes five nonradial struts through which bearing lubricating oil and anti-icing air are conducted. The titanium impeller consists of 18 full blades and 18 splitter blades with 50 degrees of back curvature and an inlet radius ratio of 0.36. Corrected tip speed of the impeller is 2160 ft/sec. The diffuser consists of 31 wedge type vanes with the leading edge at a radius 8% greater than the impeller exit radius. Diffuser area ratio is 2.4. Flow from the diffuser exit enters a collector of generally rectangular cross-section which has two exits, each including a 90° turn elbow. Air is discharged from these elbows into the engine side air tubes which carry the air to the rear of the engine where it enters the combustor. Compressor pressure ratio and efficiency are based on measurements taken in the side air tubes downstream of the collector elbows.

It should be noted that this combination of high impeller tip speed and high blade backcurvature was made possible in that time frame only by application of advanced finite-element structural analysis techniques. The availability of these techniques at Allison was instrumental to the successful completion of this program.

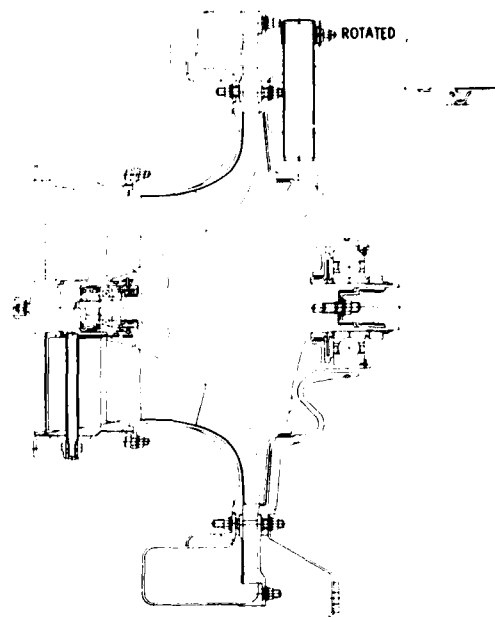


Figure 3. Model 250-C30 compressor.

Component Rig Tests

The component rig performance map for the initial configuration is shown in Figure 4. Design point objectives of 5.6 lb/sec flow, 8.5:1 pressure ratio, and 78% efficiency were met or exceeded and sufficient surge margin was demonstrated for steady state engine operation. The line of constant T_4/θ in Figure 4 is a reasonable approximation to an engine operating line during a rapid acceleration. That line is seen to be to the left or unstable side of the surge line from approximately 75% to 92% corrected speed, clearly not acceptable for engine transient operation. The diffuser throat area was reduced to 94% of the initial design value and the test map of Figure 5 resulted. Both steady-state and transient (acceleration) engine operating lines are again shown. Design flow and pressure ratio were maintained at design speed and the transient operating line now falls to the right, or stable, side of the surge line. The surge margin relative to the transient operating line in Figure 5 is adequate for in-plant development testing of engines. Experience with production engines, however, dictates that a minimum surge margin of approximately ten percent is required to account for production tolerances on compressor, turbine, fuel control, etc.

Further reduction of diffuser throat area to increase surge margin would have unacceptably compromised efficiency on the operating line. A compressor discharge bleed system which functioned by sensing compressor pressure ratio was available. Referring to Figure 5 again, increased surge margin was required up to at least a pressure ratio of 6:1 during transient operation. An engine cruise power operating condition occurred on the steady-state operating line at that same pressure ratio, precluding use of compressor discharge bleed at that pressure ratio.

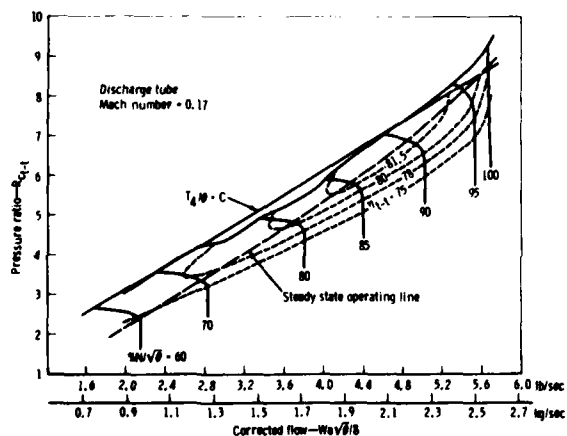


Figure 4. Initial performance map.

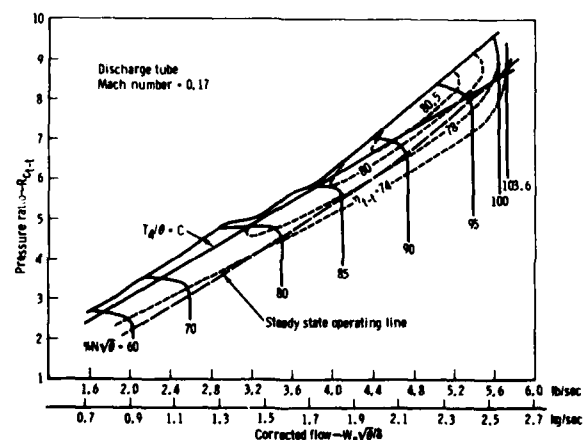


Figure 5. Rematched compressor performance.

Analysis of detailed impeller inlet instrumentation revealed that the surge line in the 80-85% speed region was greatly influenced by inducer stall, as would be expected. Referring to Figure 5, as speed is decreased from the design level along the surge line, a localized dip is encountered between 85% and 80% speed. Shroud static pressure taps over the inducer reveal a breakdown in static pressure rise in the inducer inlet corresponding to that dip in the surge line. As speed and flow are reduced even further, the static pressure rise is again established and a backward facing thermocouple in front of the impeller near the shroud records much higher temperatures than those measured in the inlet plenum. Thus the inducer has passed from unstalled flow conditions into stall and finally into a backflow regime which relieves the stall and improves the surge line.

Several alternate configurations were tried experimentally attempting to improve surge margin at intermediate speeds. Those included alternate diffuser vanes (shape and number), shroud treatment (honeycomb and grooves) and shroud bleed. None of these configurations provided an acceptable combination of surge margin and efficiency.

Impeller Blade Cracks

While the surge margin problem was being investigated, impeller blade cracks began to appear on development engines. These cracks appeared near the inducer tip leading edge and were traced to high blade vibratory mode (15 through 18) coincidence with diffuser vane passage (31 order) frequency which occurred above design speed as shown in the resonance diagram of Figure 6. Although potentially troublesome coincidences occurred throughout the operating range, only those near design speed responded with high vibratory stresses. Vibratory stress levels of $\pm 44,000$ psi were measured at around 52,000 rpm. A maximum allowable level of $\pm 18,000$ psi was established for the region of the leading edge in which the cracks were developing.

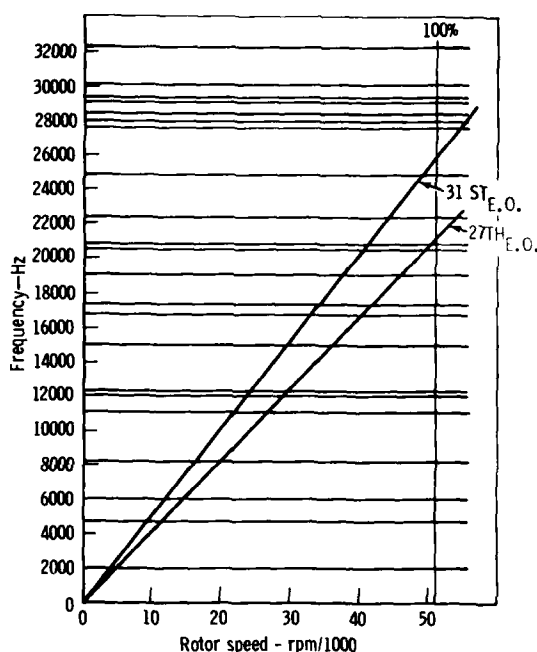


Figure 6. Impeller resonance diagram.

Several approaches to resolving the cracking problem were attempted, including both analysis and experiment. A brief overview of the results will be presented. The first modification involved a reduction of 0.100 inch in impeller tip radius to increase the radial gap between impeller and diffuser. Vibratory stress levels were reduced to approximately $\pm 16,000$ psi. This was adequate for continued developmental engine running, but surge margin was reduced to unacceptable levels. Another attempt to reduce the excitation from the diffuser vane consisted of reducing the diffuser vane inlet wedge angle to less than one-half degree. A reduction of less than 10% in vibratory stress levels resulted. A special impeller with thicker blades was tested and found to have little effect. Damping coatings applied to the blades in the inducer region reduced stresses to the $\pm 15,000$ psi range with one side coated and to $\pm 7,200$ psi with both sides coated. These coatings were ultimately judged to present excessive quality control and reliability problems and were therefore abandoned. It seemed possible that the forces exciting the inducer could be transmitted through the exducer blading although the exducer blading was "quiet" vibrationally. To simulate a separate inducer configuration, a slot 0.020 inch wide and extending from shroud to hub was cut in the full blades just forward of the splitter leading edges. Vibratory stress levels at the inducer leading edge were reduced to approximately $\pm 11,000$ psi, and a design effort to define a two piece rotor was initiated.

Referring again to the resonance diagram of Figure 6, it can be seen that the 12th through 14th modes of the impeller were coincident with 31 engine order in the high speed operating region of the engine yet did not produce high stresses. Was it therefore possible that these modes were less responsive than the higher ones? Twenty-seventh order would coincide with the 14th and 15th modes just above design speed where the high stresses were occurring. A twenty-seven vane diffuser was designed and fabricated to explore this possibility. The resulting vibratory stresses were approximately $\pm 30,000$ psi. In an attempt to determine if the excitation phenomenon was sensitive to velocity or to Mach number, the 27 vane diffuser configuration was tested at inlet temperatures of 99F and 1140F for a variation of 11% in corrected speed at a fixed mechanical speed. The stress level was essentially unaffected by the change in aerodynamic conditions.

REDESIGN

None of the aforementioned experimental approaches produced a satisfactory combination of performance and vibratory stress level. Nor was any theoretical approach forthcoming which could satisfactorily explain the phenomenon. The decision was made to design a new impeller. To minimize the impact upon the remainder of the compressor, the impeller inlet and exit dimensions were maintained. Impeller internal blade loading was redistributed in an attempt to improve performance. And finally, blade thicknesses were tailored to avoid any impeller blade modes in the frequency range which had responded in the initial design.

The high vibratory stresses of the original design were encountered in the frequency range from 26,300 to 28,000 Hz. Allowing for a blade frequency scatter of $\pm 3.5\%$ stretched the required "window" on the resonance diagram to the range from 25,400 to 29,000 Hz. The required window was identified on a theoretical basis and later confirmed experimentally as shown in Figure 7. Special care was taken with this particular impeller to control blade thicknesses and therefore blade frequency scatter. With normal manufacturing practices, the individual blade frequency scatter essentially eliminated the window and rendered that approach useless. Had it later proven to be necessary, sufficient care in manufacturing to control individual blade frequencies might have been possible.

Redistribution of the blade-to-blade loading within the impeller can be observed in Figure 8 where the original impeller design is shown on the left and the redesigned impeller on the right. The new design has much less turning in the mid-region of the impeller which reduced the loading in that region at the expense of increased loading in the exducer region. The blade "wrap" of the new impeller is also increased significantly. Both designs have the same inlet and exit dimensions, back curvature and blade numbers.

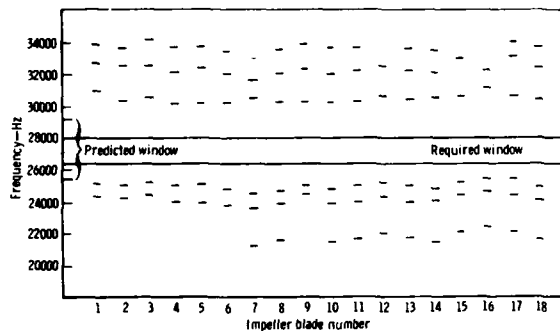


Figure 7. Measured impeller blade frequencies.

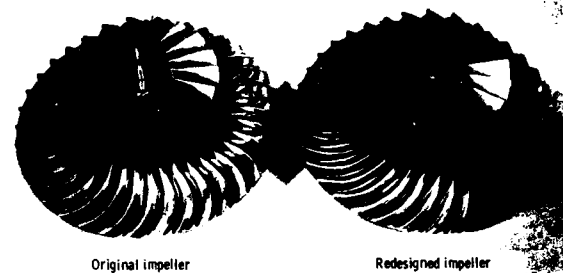


Figure 8. Original and redesigned impellers.

Redesigned Impeller Blade Vibration and Performance

Early strain gage testing of the new impeller design with the 31 vane diffuser revealed significantly reduced vibratory stress levels ($\pm 44,000$ psi to $\pm 27,000$ psi) which were still above the target. An earlier program at Allison had shown some indication of reduced impeller vibratory stresses with increased number of diffuser vanes. A 37 vane diffuser had therefore been designed and fabricated. That diffuser reduced the vibratory stress levels due to diffuser vane excitation in the new impeller to ± 9500 psi which satisfied all our objectives. It is perhaps of interest to note that the 37 vane diffuser also reduced the stress level of the original impeller, but only to $\pm 15,000$ psi. These levels were attained with the original radial gap between impeller and diffuser. So an acceptable solution to the impeller vibratory stress problem had at last been found.

Aerodynamic performance for the new impeller with 37 vane diffuser configuration is indicated by the compressor map shown in Figure 9. Compared to the compressor map of Figure 5, the surge margin is reduced. Subsequent cross-testing revealed that both the impeller and diffuser contributed to the decrease in surge margin. A reduction of 3% in diffuser throat area provided adequate surge margin except for the localized area around 85% speed.

Earlier in the program, examination of corrected shroud static pressures as a function of flow and speed revealed that, at certain locations on the shroud, the static pressures are higher than ambient at part speed and lower than ambient at high speed. This effect is illustrated in Figure 10. This suggested the possibility of a bleed slot connecting the flow path at a given shroud location to ambient as

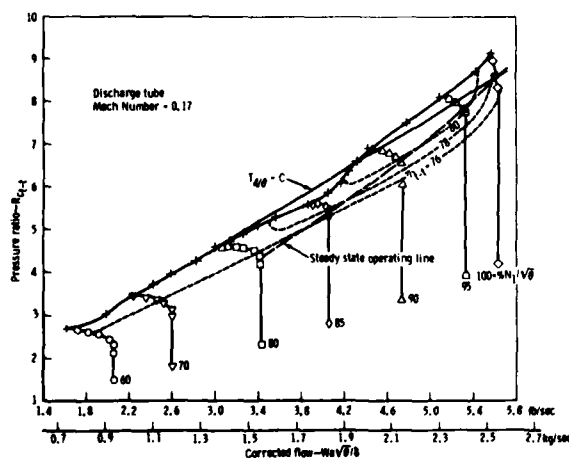


Figure 9. Performance with redesigned impeller and 37 vane diffuser.

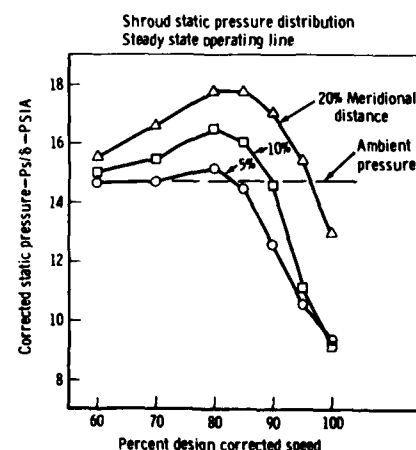


Figure 10. Shroud static pressure distribution.

shown in Figure 11. At part speed, air would bleed out from the inducer to atmosphere, increasing the airflow into the inducer, reducing blade incidence angles and also possibly reducing the boundary layer thickness on the shroud. This should improve part speed surge characteristics and perhaps efficiency as well. At high speed, where the inducer throat capacity limits flow, ambient air could flow into the inducer behind the throat. Thus inducer choking and attendant reduction in inlet static pressure could be relieved. An early attempt to use this concept with the original impeller did improve part speed surge margin and increase high speed flow capacity, but high speed efficiency was adversely affected. The second attempt was made with the new impeller and 37 vane diffuser and with a different slot location. The results were exceptional. The inducer bleed flow concept was tested on a compressor with diffuser throat area approximately 3% smaller than that which produced the performance shown in Figure 9. It should also be noted here that calculated efficiencies for a compressor with inducer shroud bleed fully account for the energy in the bleed air, i.e., the flow, pressure ratio and efficiency accurately reflect the power required to drive the compressor:

$$\eta_c = \frac{(\text{exit flow}) (\text{overall ideal enthalpy rise})}{(\text{exit flow}) (\text{overall actual enthalpy rise}) + (\text{bleed flow}) (\text{bleed enthalpy change})}$$

The compressor rig test map with inducer shroud bleed is shown in Figure 12. Compared to Figure 9, the inducer stall point has been moved down in speed and pressure ratio sufficiently to permit the use of a pressure ratio sensing bleed valve at compressor discharge. Peak compressor efficiency was increased at all speeds above 60% of design speed and by 1.5 to 3.2 percentage points in the region of principal operation between 100 and 85% of design speed.

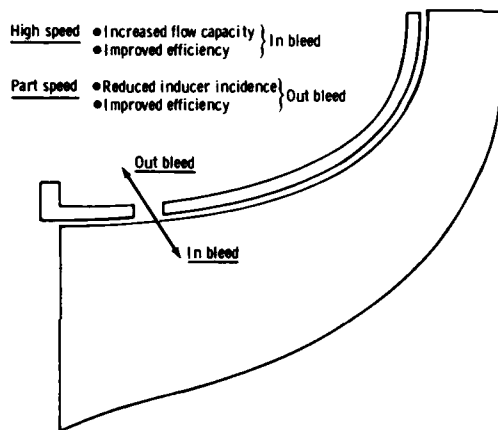


Figure 11. Inducer shroud bleed concept.

A more important indication of benefit to the engine is to compare efficiency at equal surge margin. At the steady state surge margin level of the compressor with inducer shroud bleed, the bled compressor is three percentage points higher in efficiency in the 90 to 100% speed range as shown in Figure 13. The large (7 percentage points) increase at 85% speed occurred because the baseline compressor was stalled and short on range at that speed while the bled compressor was unstalled. Inducer shroud bleed, which requires no expensive and potentially troublesome controls or valving, provided a major improvement in compressor performance. The combination of redesigned impeller with inducer shroud bleed and 37 vane diffuser provided a compressor which met all requirements of the 250-C30 engine program and is the configuration currently in production.

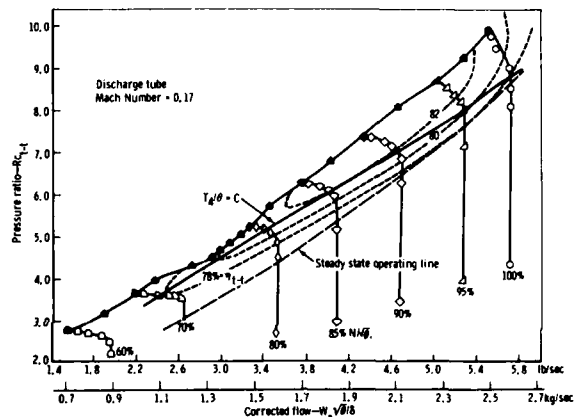


Figure 12. Compressor performance with inducer shroud bleed.

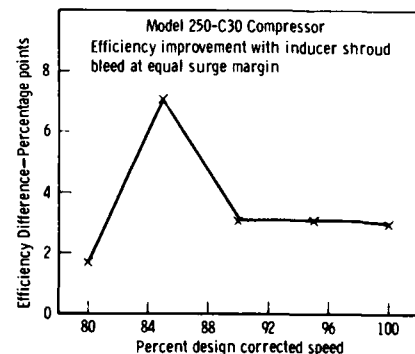


Figure 13. Performance effect of inducer shroud bleed.

250-C28B/C COMPRESSOR

The C28B/C compressor is a simple trim (both impeller and diffuser) of the C30 compressor to provide approximately 4.5 lb/sec flow at design speed, or a reduction of approximately 20 percent. That trim has been accomplished with quite similar results to those shown for the C30 compressor. Minimum surge margin of the C28B/C compressor is superior to that of the C30 compressor and some installations are operating without compressor discharge bleed for engine transients.

CONCLUSIONS

This compressor development program solved two major problems, a blade vibration and cracking problem and an intermediate speed surge line problem. Not only has the resulting compressor met all the requirements for the advanced Model 250 engines, but the technology developed in this program has proven quite beneficial to other programs as well. The inducer shroud bleed concept has demonstrated outstanding improvements in some other, but not all compressors. Future objectives for the compressors include reduction in cost of producing the impellers and improved low speed surge margin to eliminate compressor discharge bleed requirements for engine acceleration.

CENTRIFUGAL COMPRESSORS FOR SMALL AERO & AUTOMOTIVE GAS TURBINE ENGINES

R W CHEVIS MSc, C.Eng, MRAeS
Concept Manager.

R J VARLEY BA Hons (Oxon)
Research Engineer.

Noel Penny Turbines Limited, Siskin Drive, Toll Bar End, Coventry CV3 4FE, England.

SUMMARY

The development of the small gas turbine engine has been a considerable stimulus for the development of the centrifugal compressor. Compressor design requirements vary for differing engine applications and these are briefly discussed for three engine types. These types are the expendable turbojet, the low cost single shaft turbopropeller engine and the automotive truck gas turbine engine. Technical and test data are presented for representative types of compressor.

1 INTRODUCTION

During the last decade considerable progress has been made in increasing the performance bounds of centrifugal compressors. A stimulus for much of this progress has been the use of the centrifugal compressor in the small gas turbine engine. For most applications the small gas turbine has been under intense pressure for improved design and performance; a considerable portion of this pressure has been applied to centrifugal compressor development.

Given this stimulus the centrifugal compressor has advanced due to a number of factors which include:

- * the expanding technology base that enables potentially inadequate designs to be recognised and discarded early in the design analysis stage with the consequent conservation of development funds.
- * the availability of advanced computers and computational processes for aerodynamic, stress, vibration and geometric analysis.
- * the growth of experience with transonic inducers and diffusers.
- * the acquisition of rational design data not hitherto available, particularly that regarding diffuser design.
- * wider recognition of the importance of impeller vane backsweep.

The centrifugal compressor has a number of virtues which justify its use in the small gas turbine. Its blading is relatively easy to design and manufacture to cope with the low mass flows of small engines, its efficiency levels are acceptable, it is cheap and rugged.

At Noel Penny Turbines Ltd (NPT) the development of centrifugal compressors has been primarily associated with the development of advanced small gas turbine engines for aircraft, automotive and industrial purposes. The aircraft applications are simple, expendable or short life jet engines for remote piloted vehicles (RPV's) in the .45 KN to 2.0 KN (100 lbf to 450 lbf) static thrust range and a family of simple single shaft turbopropeller engines in the 225 KW to 450 KW (300 SHP to 600 SHP) range. The automotive applications have concerned truck and off-highway vehicle engines in the 335 KW to 450 KW (450 HP to 600 HP) range. Some aspects of the centrifugal compressor development associated with these engines are outlined in the following paper.

2 COMPRESSOR REQUIREMENTS

2.1 Engine Types

Three engine types are considered, by example, namely

- * the expendable or limited life RPV turbojet engine
- * the low cost single shaft turbopropeller engine
- * the automotive truck gas turbine engine.

The compressor design requirements differ considerably for each engine type. Perhaps the only common requirements are that the compressor designs and arrangements must lend themselves to low cost engine design and that surge lines are uninked. High efficiency is required for the turbopropeller and automotive engines but for many RPV missions, though desirable, it is not of first importance. Wide flow range is usually demanded for all applications but the term 'wide' is strictly relative.

2.2 RPV Jet Engine

Figure 1 illustrates the wide variety of component configuration used in small RPV turbojets. The centrifugal or axi-centrifugal compressor can be fed by an axial or radial inlet, it can exhaust to a

straight through or reverse flow combustor and it can be driven by an axial or radial turbine. Figure 2 indicates typical design point performance levels for current engines and also gives suggested targets for advanced engines using high technology turbomachinery (Ref 1). The turbomachinery of most current engines is of conservative design.

Achieving low frontal area is a most important requirement for any turbojet and is dominated by the compressor configuration. With the small RPV turbojet frontal area is, to a considerable extent, traded with cost and performance. When it is of critical importance an axi-centrifugal compressor will be used. For engines above 2KN (450 lbf) thrust an all axial compressor becomes a practical, but expensive, proposition.

For both the centrifugal and axi-centrifugal compressors low frontal area requires designing for high values of specific speed and flow-speed function, as is illustrated by Figures 8 and 9. Engine life requirements usually span 1 to 10 missions and design life 2 to 40 hours. Depending on choice of turbine material and entry temperature this lifing allows higher specific speed compressors to be used than would normally be the case. Further frontal area reduction is often achieved by severe restriction of the dimensions of the radial diffuser, to the detriment of compressor efficiency.

To keep the control system cheap and simple an unlinked compressor surge line is desired. High flow range is not needed nor use of impeller vane backsweep, thereby helping the frontal area problem.

For many applications fast engine acceleration is not necessary and rotational inertia considerations do not directly impact impeller design.

High corrosion resistance is an important consideration when the flight vehicle is designed for sea water recovery and this influences primarily choice of material and surface treatment. Engine specifications often call for the ability to withstand repeated sea recovery with immersion periods up to 24 hours.

2.3 Low Cost Single Shaft Turbopropeller Engine

The small turbopropeller engine markets directly against the turbocharged piston engine. To compete successfully, that is to achieve widespread acceptance, it must have good performance and a competitive manufacturing cost. Configurations for advanced, low cost turbopropeller engines are depicted in Figure 3 and Figure 4 shows a design point performance map applicable to these and similar configurations.

Figure 3 shows single shaft engines having a minimum of turbomachinery. All compression is achieved in a single centrifugal stage. Design pressure ratios of the order 7:1 to 9:1 are indicated from Figure 4. High compressor efficiency is needed to achieve the performance shown.

Fuel and control systems for turbopropeller engines can be very expensive and can form a large portion of the engine total price. These systems can be simplified and cheapened if wide mass flow range is available from the compressor and the surge line is unlinked. The high pressure ratio and high flow range requirements necessitate use of impeller vane backsweep.

Compressor frontal area restrictions are not usually severe since it is the main reduction gearbox that tends to dominate the maximum engine cross sectional area.

Design specific speed tends to be low and is set by stress limitations in the turbine, not by compressor aerodynamic considerations.

Restriction of engine rotational inertia is not a prime requirement since this type of engine operates with little speed variation in the flight mode. Certain inertia limits have to be met, however, to avoid the fitment of a large and therefore heavy and costly engine starter.

Target design life will be of the order 10,000 hours. This can be met by a steel or titanium impeller having a solid hub at the higher pressure ratios and machined from a forging.

2.4 Automotive Gas Turbine Engine

The automotive gas turbine has been under development for many years as an alternative powerplant to the spark and compression ignition engines used in passenger cars, trucks and off highway vehicles. These applications probably represent the most difficult design task of the gas turbine spectrum.

Although offering many real and potential advantages over piston engines the prime requirements of an automotive engine, namely low cost, good fuel economy, particularly at low power levels, and high durability are difficult for the small gas turbine to achieve. Despite this the automotive gas turbine has made substantial technical advances in recent years.

Figure 5 depicts typical one and two shaft truck gas turbine configurations and Figure 6 gives a design point performance map. Heat exchange is used in the thermodynamic cycle to give good fuel economy at both high and low power levels. The use of heat exchange limits the design pressure ratio requirements to between about 1:1 to 3:1.

The compressor needs to be of high efficiency, have an unlinked surge line and have high flow range at all operating speeds. The high flow range requirement enables the engine, in the interests of good fuel economy, to be operated at peak turbine entry temperatures at all power levels. Impeller backsweep is thus required.

To give acceptable vehicle driveability very fast engine acceleration is needed from idle to maximum power. Consequently low rotational inertia is required of the compressor and this tends to conflict with obtaining good aerodynamic design.

As with the turbopropeller engine compressor design specific speed is set by stress limitations in the driving turbine.

Life design targets for automotive compressors are usually severe, typically 10,000 hours, 30 major cycles per hour.

Table 1 summarises the compressor design requirements for the three applications discussed.

3 PERFORMANCE LEVELS OF SMALL GAS TURBINE CENTRIFUGAL COMPRESSORS

Figure 7 shows achieved rated performance for small compressors in terms of stage static - total polytropic efficiency versus specific speed. Upper bounds are tentatively shown defining 1973 and 1979 technology levels. The 1973 data has been taken from (2) and it covers design pressure ratios from 1.6:1 to 12:1; the high pressure ratio data relates to the lower efficiency levels. The 1979 data is for high pressure ratio machines in the 5:1 to 10:1 range and is taken from the literature and other sources. This type of presentation has shortcomings but nevertheless is considered to reasonably portray performance advances over the stated time interval.

A most significant advance of recent years has been the ability gained in designing impeller inducers and radial diffusers to accept transonic inlet flow with little compromise of efficiency or flow range. Attainment of high stage pressure ratio with limitation on the maximum diameter of the compressor demands the use of transonic inducers. This is evident from Figures 8, 9 and 10.

Figure 9 shows the relationship between specific speed and the flow speed function ($m N^2/\sqrt{g}$) for increasing pressure ratio. Suggested boundaries are superimposed which enclose design areas for turbojet and turboshaft-turbopropeller compressors. Good performance has been demonstrated by experimental machines at high pressure ratios and very high flow speed functions (3). However this combination produces formidable design problems with respect to the driving turbine.

Figure 10 shows the relationship between inducer tip minimum relative Mach Number, flow speed function and inducer hub-tip ratio which can be used in conjunction with Figure 9.

A stimulus for using a transonic radial diffuser rather than a subsonic one is also to reduce frontal area. Well designed transonic diffusers can be highly efficient up to incident Mach Numbers exceeding 1.3 (4).

An efficiency versus pressure ratio chart for small centrifugal and axi-centrifugal compressors is shown in Figure 11. The efficiency levels shown are appropriate targets for the design of high performance machines. Where greater latitude is allowed on the diffuser than implied in the chart higher efficiency levels would be assumed. The converse also applies. The chart is one of a number used at the authors' Company for project design purposes.

4 TECHNICAL AND TEST DATA FOR THREE SMALL TURBINE ENGINE COMPRESSORS

4.1 Compressor Types

In this section certain technical and test data are presented for three representative small gas turbine centrifugal compressors selected from the NPT range. These are

- * the NPT 'M' compressor of 8:1 pressure ratio; a generic model for a family of turboshaft-turbopropeller compressors in the 7:1 to 9:1 pressure ratio range; tested 1970.
- * the NPT 'C' compressor of 4.5:1 pressure ratio; a generic model from which derivative compressors have been developed for turbojet and other applications; tested 1972.
- * the NPT 'J' compressor of 5:1 pressure ratio; designed for an automotive truck gas turbine; tested 1975.

Pressure ratios quoted are outlet collector static pressure to inlet total pressure.

Views of the 'M', 'C' and 'J' impellers are shown in Figures 12, 13 and 14 respectively. Figure 15 shows a 'J' diffuser. Table 2 lists salient technical data.

4.2 NPT 'M' Compressor

Leading design requirements were high efficiency, wide flow range and long life. Target isentropic efficiency was 77.8% S-T at 8:1 pressure ratio. Impeller vane sweepback was deemed necessary to achieve the performance. Specific speed was set by stress limitations in the drive turbine.

The design process used was entirely computer based. Preliminary design of the impeller and the total aerodynamic design of the intake and diffuser system was carried out on a high performance desk top computer with graphic peripherals. Final impeller design was done using the National Gas Turbine Establishment (NGTE) impeller design programme package described in (5). The desk top computer programmes used were developed by NPT.

All the aerodynamic variables affecting impeller inlet and exit velocity triangles were established at the preliminary design stage. Also at this stage tentative meridional flow path and hub and shroud vane camber distributions were established, together with a first stress analysis. Final impeller design involved geometric modelling using 3 dimensional analytic surfaces, through flow analysis by a matrix method and

3 dimensional stress analysis by a finite element technique. The final output of the design process was an NC tape for the 5 axis machining of the impeller using a single straight flanked cutter.

Through flow analysis was used to design the inlet duct which was of the radial inflow type. The duct was carefully matched to the transonic inducer. 13 full and 13 splitter vanes were selected for the impeller. These allowed acceptable blade loadings to be achieved, enabled the desired inducer throat area to be obtained and satisfied cost objectives. As well as influencing aerodynamic performance vane numbers affect cost, with cost tending to be more than proportional to vane numbers.

The diffuser has radial and axial sections. Although required to diffuse and produce a static pressure rise the prime purpose of the axial section is to straighten the flow. The transonic radial diffuser is of the channel type and its design geometry was described in 3 dimensions by a mathematical method evolved from that of (6) and existing NPT methods.

This method when programmed on a desk top computer provides a very general, flexible and rapid design tool for channel diffusers; it describes the geometry by use of first, second and third order curves. Diffuser aerodynamic analysis was carried out by use of another desk top computer programme that assessed performance of a given geometry from impeller tip through to the dump at the axial straightener exit. The method accounts for shock losses and employs boundary layer calculations to determine the throat blockage of the radial diffuser; the blockage is used in the determination of the 3 dimensional diffuser channel performance. This part of the method is based on that developed in (7). Reference (7) uses 2 dimensional data with a 3 dimensional correction. The 2 dimensional data was taken from Runstadler (8) and considerably extended in terms of area ratio, blockage and aspect ratio. A through flow type of analysis is used downstream of the channels with computed pressure losses based on blockage, diffusion and dumping conditions.

The 'M' compressor was tested at the NGTE. The rig module incorporated an engine type radial inlet duct complete with support struts and the diffuser axial straightener exhausted into a constant section ring collector. Figure 16 indicates the flow path configuration. Comprehensive instrumentation was fitted as detailed in Table 3. Data acquisition was controlled by an Intercole Compulog II data logging system. This system is entirely software controlled and has routines for pre-scan transducer calibration by dead weight testers, full instrumentation scan and raw data storage, data normalising, data analysis, test point setting and holding and data validation.

Prior to a full build being run the impeller was tested at 95% and 100% of design rotational speed without the radial and axial diffuser vanes being fitted. Impeller exit total pressure was determined from mass flow rate and from the mean of 30 static pressure taps circumferentially distributed at the vaneless space radius ratio 1.035. The impeller test total-total pressure performance is shown in Figure 17. A test total-total pressure ratio of 9.2 : 1 and an isentropic efficiency of 85% were obtained at the design point. Target pressure ratio and efficiency were 9.4 : 1 and 86% respectively. The impeller test data was used for final 'tuning' of the radial diffuser throat size.

The static to total pressure ratio map for the first full build test is shown in Figure 18; at the design point a pressure ratio of 8.0 : 1 and isentropic efficiency of 78.2% were obtained ie slightly better than target. The pressure ratios quoted are for collector ring static pressure to the total pressure at the leading edge station of the radial intake duct struts. Design target efficiencies did not assume any inlet duct loss. Figure 19 gives a total-total pressure ratio map, the outlet total being measured at the radial diffuser outer radius. This map shows a design point total to total isentropic efficiency of 80.7%. The compressor achieved its overall performance targets by having its diffuser performance slightly better than and its impeller performance slightly less than design intent.

Test distributions of inlet duct wall velocities were determined from the wall static pressure data and the inlet total pressure. Figure 20 compares design point and test data and the agreement is good.

The through flow analysis method used in the impeller design incorporates two options for loss modelling. One option is the use of polytropic compression and expansion efficiency distributions along streamlines and the other a distribution of blockage along all channel walls from entry plane to exit together with the assumption of an isentropic core. The latter method was used for the 'M' impeller. Figure 21 shows test shroud static pressure distributions and the distribution at design point mass flow is seen to compare well with the design curve. The test performance of the diffuser at the design point is given in Figure 22. This shows static pressure rise from the vaneless space station at radius ratio 1.035 to the collector ring. A continuous pressure rise is maintained along the flow path including a useful increment in the axial straightener vanes. The difference between test and design performance for the bend and axial straighteners was due to a pessimistic estimate of design total pressure loss in the bend. Table 3 indicates the pressure tapping locations used to compile this figure.

During the testing excellent repeatability of data was demonstrated by the data logging system.

Further development work is being undertaken on the 'M' compressor with the view to raising the static to total isentropic efficiency to 80%. The impeller has been manufactured in both steel and titanium.

4.3 NPT 'C' COMPRESSOR

The 'C' compressor was designed as a source design for a series of compressors for small turbojet and turboshaft engines. To meet the various applications it has been scaled up and down and modified to raise or lower its specific speed and the impeller has been matched with a number of diffusers of differing design. Although designed for a pressure ratio of 4.5:1 the compressor was required to achieve good performance at pressure ratios up to 6:1 to meet certain turbojet altitude requirements. The moderate flow range, low frontal area and very low cost requirements of the RPV turbojets called for a radially vaned impeller.

The 'C' impeller and its derivatives have been produced as one piece designs in aluminium alloy or stainless steel or as two piece designs (Figure 13) with an aluminium alloy impeller section and steel inducer.

The testing of the 'C' compressor was for overall performance only and a test static-total pressure ratio map is shown in Figure 23. For this test map the impeller was matched with a 13 vane radial diffuser, channel area ratio 1.65:1. Flow range at design speed was 14%.

4.4 NPT 'J' COMPRESSOR

This compressor was designed for a two shaft recuperative heat exchanger automotive truck gas turbine. The power turbine of the engine had variable geometry nozzle guide vanes. The prime purpose of these vanes was to enable the engine to operate at high cycle temperatures at all power levels in the interest of good fuel economy. This required the compressor to have wide flow range over a large rotational speed range.

The engine was designed to produce a flat rating power at extremes of ambient temperature up to altitudes of 2750 metres. To meet this the 'J' compressor was designed for a static-total pressure ratio of 5.1:1 at the ISA SL condition. At this condition engine flat rating and idling speeds occurred at 90% and 55% of design compressor speed respectively. High efficiency was therefore required from idle up to design speed.

To obtain wide flow range the compressor featured impeller backsweep, a low inducer hub-tip ratio, and a subsonic diffuser having a low number of curved vanes. Design specific speed was set by gasifier turbine stress and total gasifier rotor inertia considerations.

The 'J' compressor was tested at the NGTE and was only instrumented to obtain overall performance. Figure 24 shows the static-total pressure ratio performance map for the second build standard. As can be seen the desired wide flow range was achieved, the hatched lines on the map indicating the regions of engine operation to achieve full flat rating and part load performance. The design pressure ratio was obtained, also the efficiency target for the build standard. For this build the area ratio of the diffuser channels was set low at 1.60:1.

The 'J' impeller, like that of the 'C' has been manufactured as a one or two piece design.

5 FINAL COMMENT

In the Introduction it was stated that the development of small gas turbine engines has been a major stimulus for the development of the centrifugal compressor. This is likely to remain so in the foreseeable future. However, the growing interest in the development of advanced piston engine turbocharger systems particularly turbocompound arrangements could well produce a stimulus of equal magnitude. To meet the advanced turbocompounding requirements we can foresee the development of very high efficiency, low cost single stage compressors of 4 to 6:1 pressure ratio having flow ranges in excess of 45%, thus giving a lead to the automotive gas turbine.

ACKNOWLEDGEMENT

The authors' wish to thank Mr Noel Penny, Managing Director, Noel Penny Turbines Limited, for his kind permission to use the technical data presented in this paper.

REFERENCES

- 1 CHEVIS, R W
Advanced Developments In Turbomachinery for Use in Small RPV Engines.
International Conference on Remotely Piloted Vehicles.
Sponsored by the Royal Aeronautical Society and the Department of Aeronautical Engineering of the University of Bristol.
September 1979.
- 2 BENSTEIN, E H
Small Flying Engines Are Different
A.I.A.A. Paper No 74-1185. 1974
- 3 KENNY, DP
A Novel Correlation of Centrifugal Compressor Performance for Off-Design Prediction.
A.I.A.A. Paper No 79-1159. 1979
- 4 WOOD, H J
Transonic Compression in Centrifugal Compressors.
Homer J Wood and Associates. Mechanical Engineering Consultants, Sherman Oaks, California.
Report HWR - 193.
- 5 CAME, P
The Development, Application and Experimental Evaluation of a Design Procedure for Centrifugal Compressors.
Proceedings I.Mech.E. 1978. Vol 192 No 5.
- 6 HERBERT, M
A Method of Designing Channel Diffusers for Centrifugal Compressors with Radial Outflow.
NGTE Note No. NT 1041. 1976
- 7 HERBERT, M
A Method of Performance Prediction for Centrifugal Compressors.
Aeronautical Research Council. R and M 3843, February 1980.
- 8 RUNSTADLER, P W
Pressure Recovery Performance of Straight Channel Single Plane Divergence Diffusers at High Mach Numbers.
USAAVLABS Technical Report 69-56, 1969.

TABLE 1. CENTRIFUGAL COMPRESSOR REQUIREMENTS FOR THREE DIFFERENT SMALL GAS TURBINE APPLICATIONS

COMPRESSOR REQUIREMENT AND DESIGN PROBLEMS	RPV TURBOJET	LOW COST SINGLE SHAFT TURBOPROP	AUTOMOTIVE GAS TURBINE
PRESSURE RATIO	4 - 6	7 - 9	4 - 8
HIGH EFFICIENCY	DESIRABLE	IMPORTANT	IMPORTANT
SPECIFIC SPEED	HIGH	LOW	MEDIUM TO LOW
DESIRED MINIMUM FLOW RANGE (DESIGN SPEED)	12%	16%	28%
LOW INERTIA	NOT IMPORTANT	NOT IMPORTANT	VERY IMPORTANT
FRONTAL AREA RESTRICTION	SEVERE	MODERATE	MODERATE
LIFE REQUIREMENT	LOW	HIGH	VERY HIGH
CONTAMINATION RESISTANCE	VERY HIGH	MODERATE	HIGH
LOW CYCLE FATIGUE RESISTANCE	LOW	HIGH	VERY HIGH

TABLE 2 SUMMARY OF LEADING COMPRESSOR DESIGN FEATURES

(i) GEOMETRIC

		COMPRESSOR DESIGNATION		
FEATURE		C	J	M
Inducer Hub diameter	mm (in)	40.4 (1.59)	61.9 (2.44)	50.8 (2.0)
Inducer Shroud diameter	mm (in)	95.00 (3.74)	145.2 (5.72)	124.5 (4.9)
Impeller Tip diameter	mm (in)	163.7 (6.45)	275.3 (10.84)	234.9 (9.25)
Number of Vanes/Splitters	-	17/17	17/17	13/13
Impeller Vane Backsweep Angle	(°)	0	35	36
Number of Diffuser Vanes	-	13	13	19
Diameter of Diffuser Leading Edge	mm (in)	180.9 (7.12)	304 (11.97)	247 (9.71)
Diameter of Diffuser Trailing Edge	mm (in)	257.1 (10.12)	432.3 (17.02)	370.8 (14.6)
Diffuser Area Ratio	-	1.65	1.6	2.1

(ii) AERODYNAMIC

Rotational Speed $N/\sqrt{\rho}$	rad (rpm)	6084 (58100)	3622 (36500)	5236 (50000)
Mass Flow $\dot{m} \sqrt{\rho}/\ell$	kg/s (lb/s)	1.03 (2.28)	2.45 (5.4)	1.95 (4.3)
Pressure Ratio Overall (S-T)	-	4.5	5.1	8.0
Inlet Swirl	(°)	0	0	0
Loading $\Delta H/U_t^2$		0.82	0.76	0.79
Impeller Tip Speed at Design, $U/\sqrt{\rho}$	m/s (ft/s)	498 (1634)	526 (1726)	615 (2017)
Inducer Tip Rel Mach No.	-	1.00	0.97	1.17
Impeller Tip Abs. Exit Mach No.	-	1.16	1.04	1.14
Diffuser LE Mach No.	-	1.0	0.90	1.06
Axial Straightener Mach No	-	-	-	0.13
Specific Speed	$-\frac{rpm(ft^3/s^{1/2})}{(ft.lbf/lb)^{1/4}}$	0.72 (92.2)	0.64 (82.7)	0.62 (79.9)
Flow Range at Design Speed % * (Test)	-	14	28	18

* $(\dot{m}_{choke} - \dot{m}_{surge})/\dot{m}_{surge}$

TABLE 3. NPT 'M' COMPRESSOR. TEMPERATURE & PRESSURE INSTRUMENTATION SUMMARY

LOCATION	TYPE	NUMBER	COMMENT
Radial Intake Inlet	PT	5	Probes set in inlet struts
Intake Duct	PS	13	Hub and shroud wall statics
Inducer Inlet	PS PT PT	5 9 1	Wall statics 3 head comb (3) Traverse yaw meter
Impeller Shroud	PS	30	Shroud statics, 2 planes
Impeller tip - vaneless space RR = 1.035 Vaneless Space at RR = 1.05	PS PS	30 1	Front and rear wall circumferential statics. Diffuser leading edge
Radial Diffuser Semi Vaneless Space	PS	8	1 diffuser vane suction surface
Diffuser Throat	PS	5	3 Channels
Diffuser Channel	PS	6	Along centre line of one channel
Diffuser Exit Throat	PS	9	Used to calculate total pressure
Diffuser Exit radius	PS PT	3 3	Keil probes
Diffuser Bend	PS	5	Wall statics, hub and shroud
Axial Vane	PS	5	Along centre line of 1 channel
Axial Vane Exit	PT PS	6 6	Keil probes In annulus shroud
Collector	PS T	6 6	On mean diameter Exit total temperature
Impeller Backplate	PS	4	

CODE

PS = Static pressure

PT = Total pressure

T = Total temperature

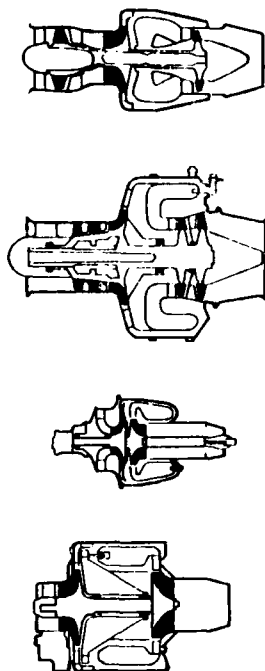


FIGURE 1. TYPICAL SMALL RPV TURBOJET CONFIGURATIONS

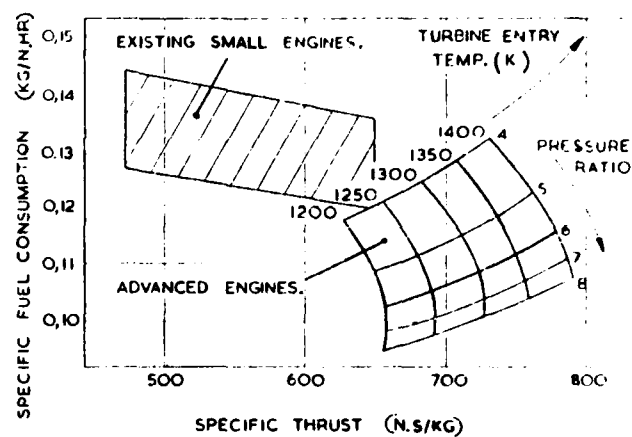


FIGURE 2. DESIGN POINT PERFORMANCE MAP FOR SMALL RPV TURBOJETS

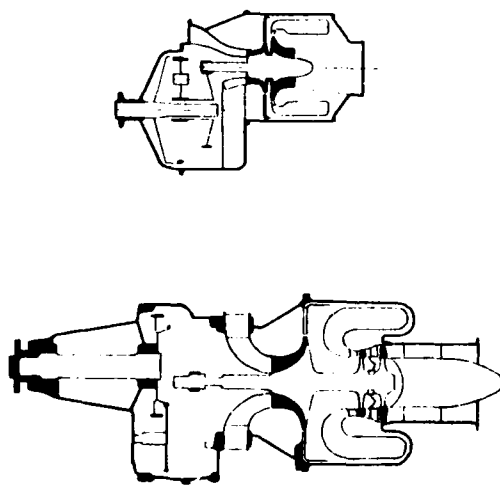


FIGURE 3. TYPICAL SMALL, LOW COST TURBOPROPELLER ENGINE CONFIGURATIONS

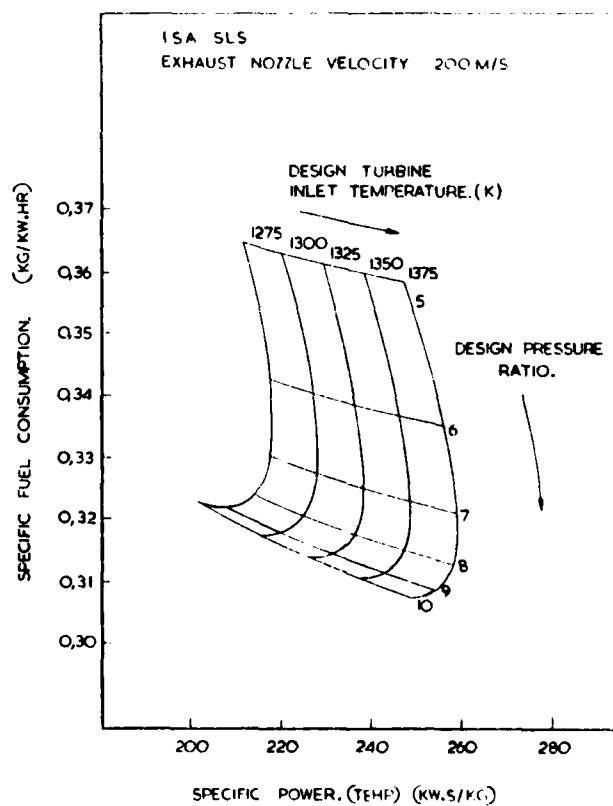


FIGURE 4. DESIGN POINT PERFORMANCE MAP FOR SMALL, LOW COST TURBOPROPELLER ENGINES

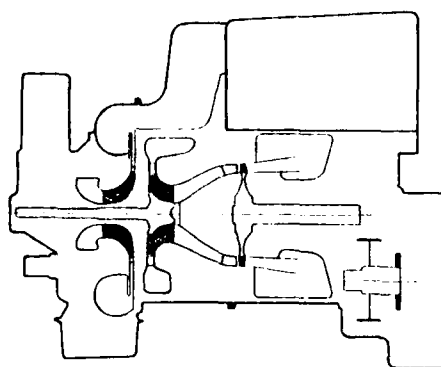


FIGURE 5. TYPICAL TRUCK GAS TURBINE CONFIGURATIONS

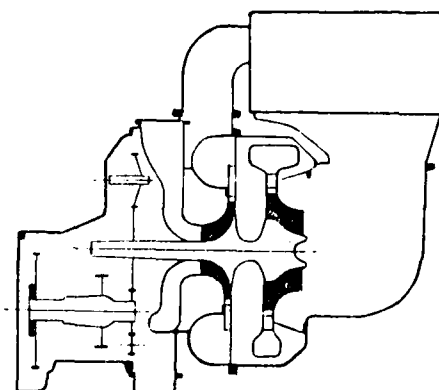


FIGURE 6. DESIGN POINT PERFORMANCE MAP FOR ADVANCED GAS TURBINE TRUCK ENGINES

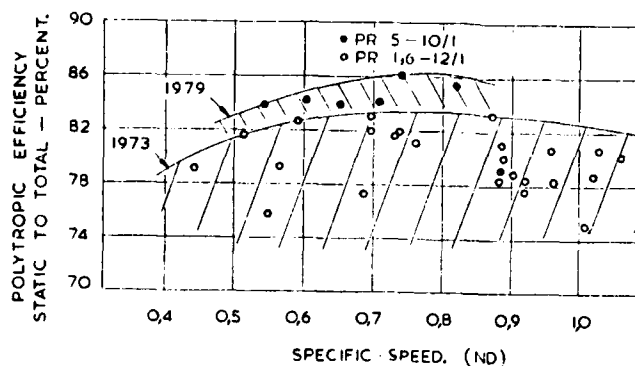
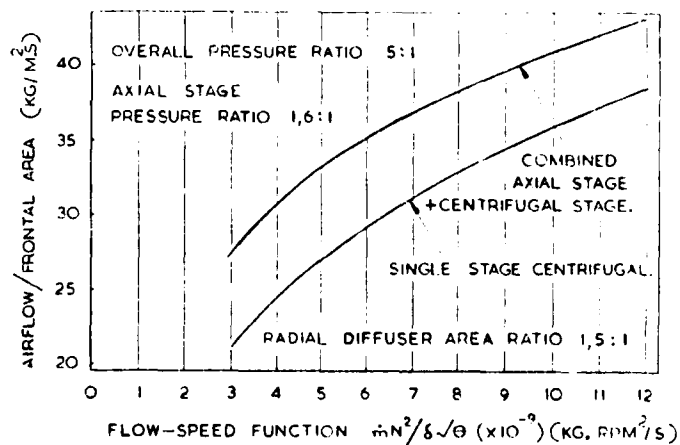


FIGURE 7. RATED PERFORMANCE POLYTROPIC EFFICIENCY FOR SMALL COMPRESSORS.
(Adapted from ref 2)

FIGURE 8. EXAMPLE OF AIRFLOW PER UNIT FRONTAL AREA v FLOW SPEED FUNCTION FOR A SMALL TURBOJET



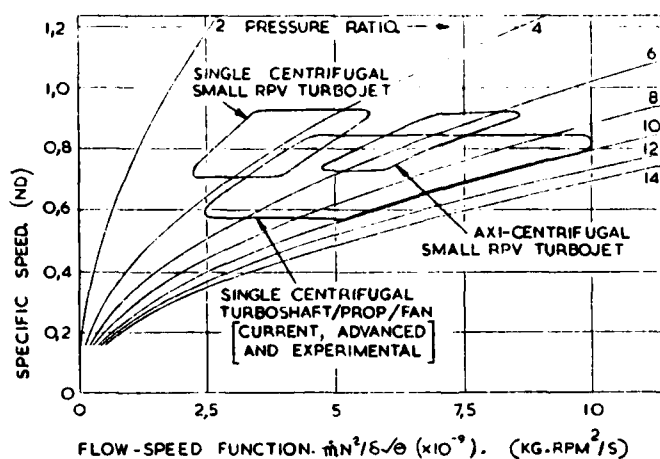


FIGURE 9. COMPRESSOR SPECIFIC SPEED v FLOW SPEED FUNCTION

FIGURE 10. INDUCER TIP RELATIVE MACH NUMBER v FLOW SPEED FUNCTION

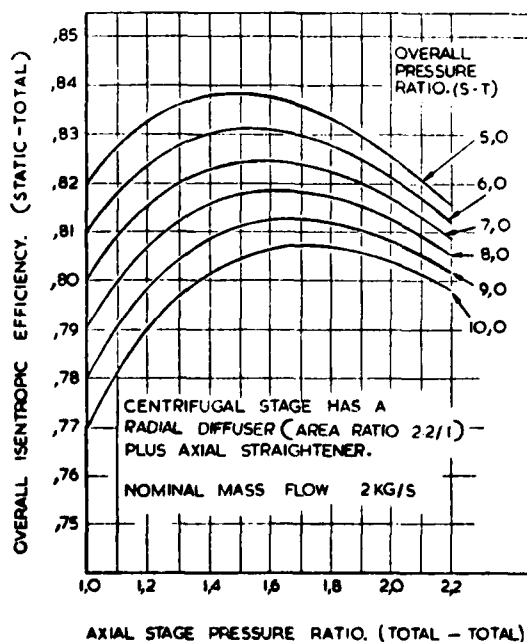
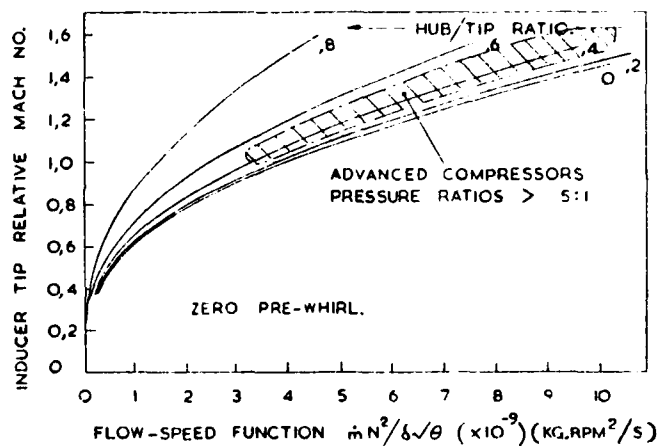


FIGURE 11. CENTRIFUGAL AND AXIAL-CENTRIFUGAL COMPRESSOR EFFICIENCY CHART



FIGURE 12. VIEW OF THE NPT 'W' COMPRESSOR
IMPELLER



FIGURE 13. VIEW OF THE NPT 'C' COMPRESSOR
IMPELLER

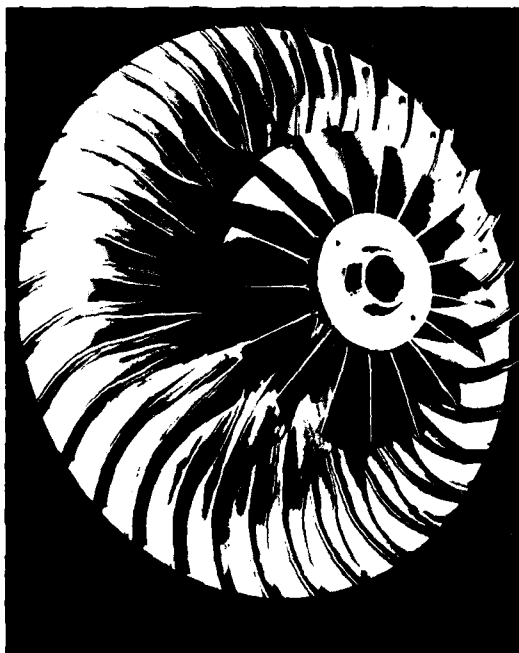


FIGURE 14. VIEW OF THE NPT 'J' COMPRESSOR
IMPELLER

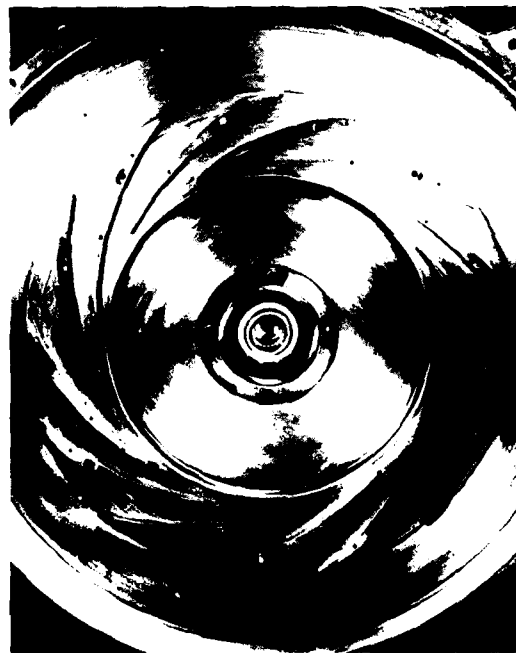
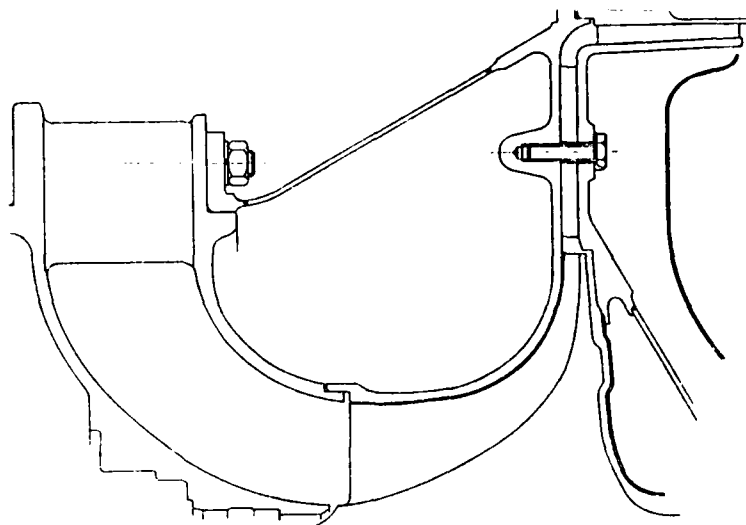
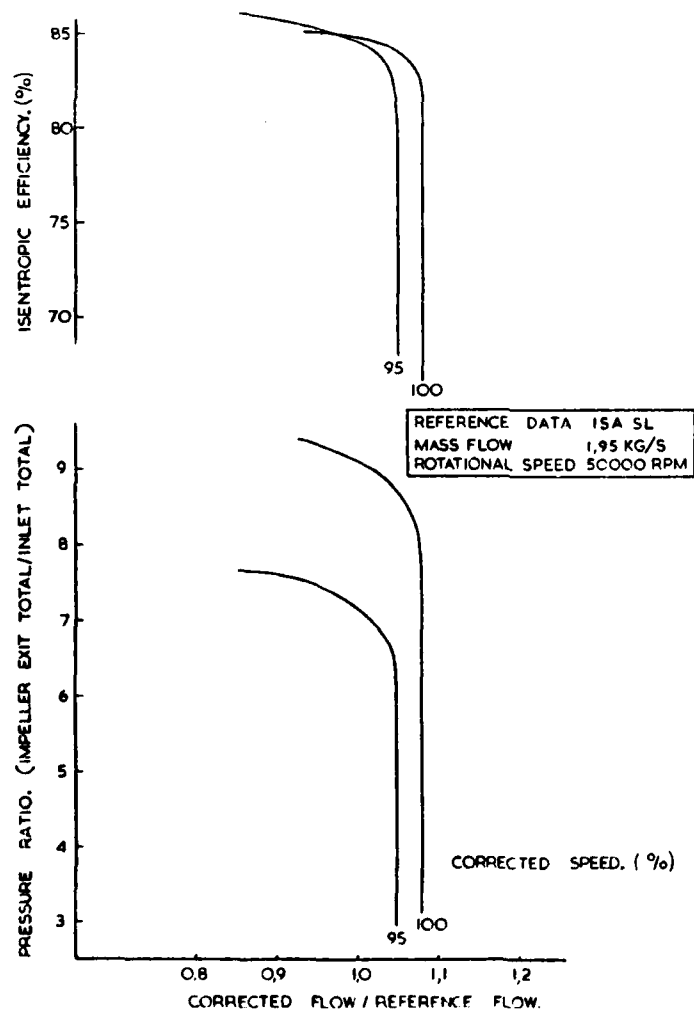


FIGURE 15. VIEW OF THE NPT 'J' COMPRESSOR
DIFFUSER

FIGURE 16. 'M' COMPRESSOR FLOW PATH SCHEMATIC



NPT 'M' COMPRESSOR IMPELLER PERFORMANCE

FIGURE 17. NPT 'M' COMPRESSOR.
IMPELLER TOTAL-TOTAL
PRESSURE RATIO PERFORMANCE

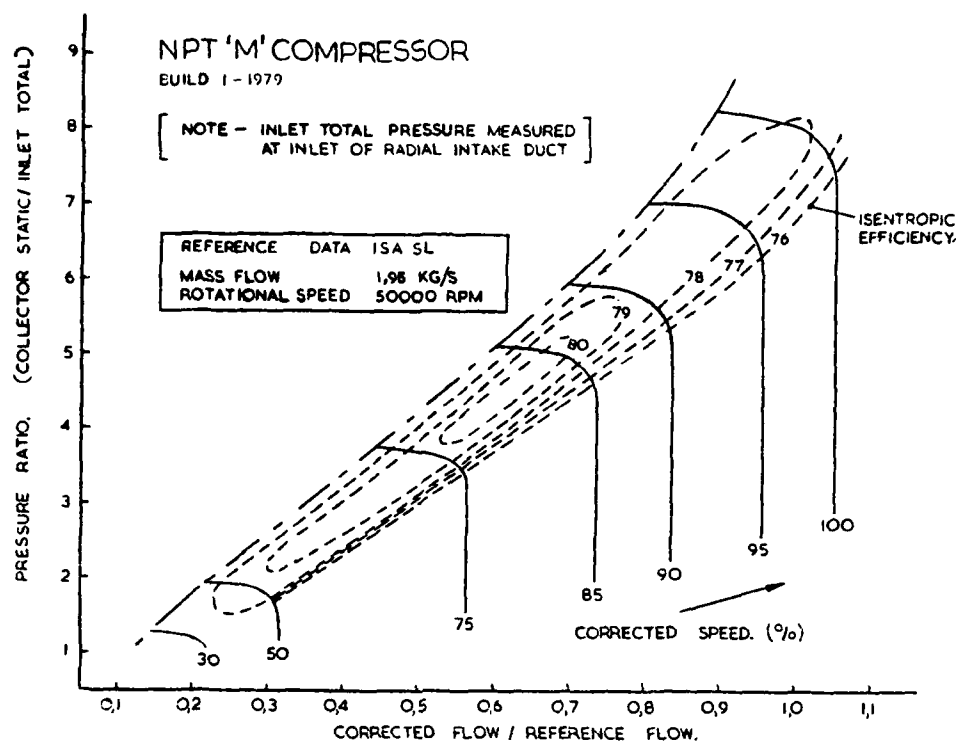


FIGURE 18. NPT 'M' COMPRESSOR. STATIC-TOTAL PRESSURE RATIO PERFORMANCE MAP

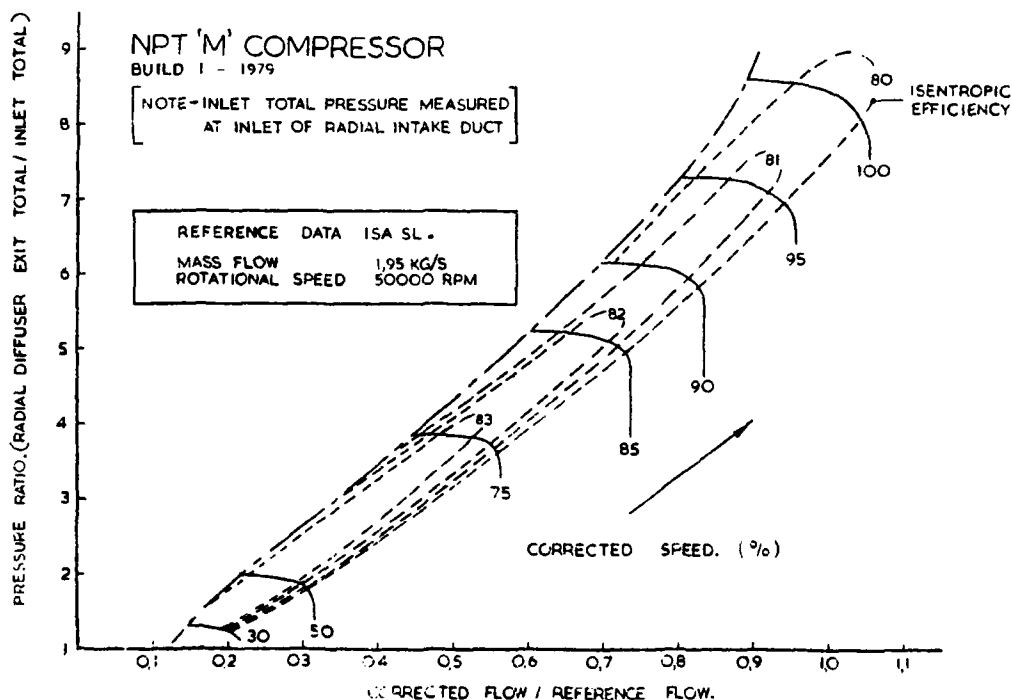


FIGURE 19. NPT 'M' COMPRESSOR. TOTAL-TOTAL PRESSURE RATIO PERFORMANCE MAP

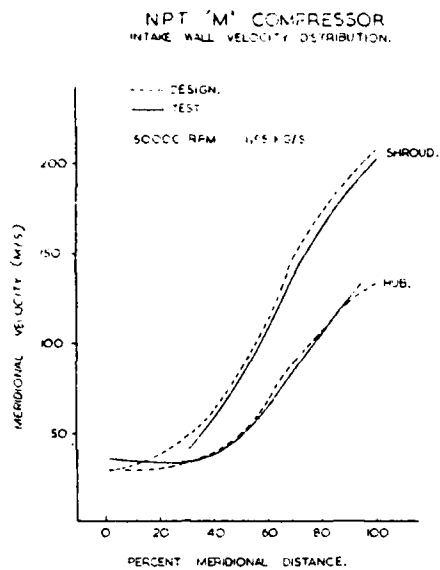


FIGURE 20. NPT 'M' COMPRESSOR. TEST AND DESIGN INTAKE WALL VELOCITY DISTRIBUTIONS

FIGURE 21. NPT 'M' COMPRESSOR. TEST AND DESIGN IMPELLER SHROUD STATIC PRESSURE DISTRIBUTIONS

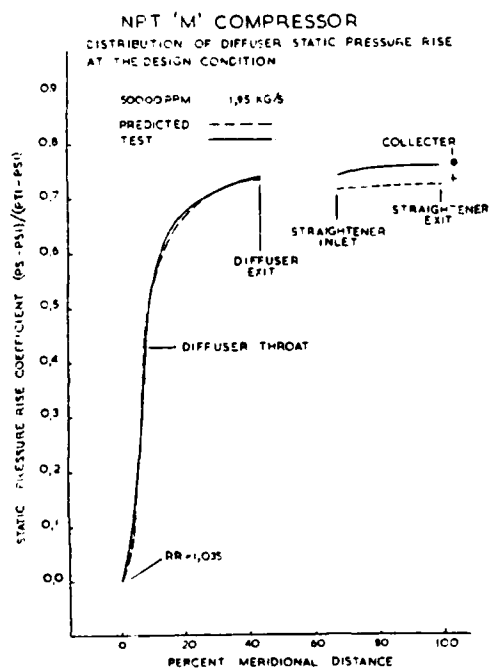
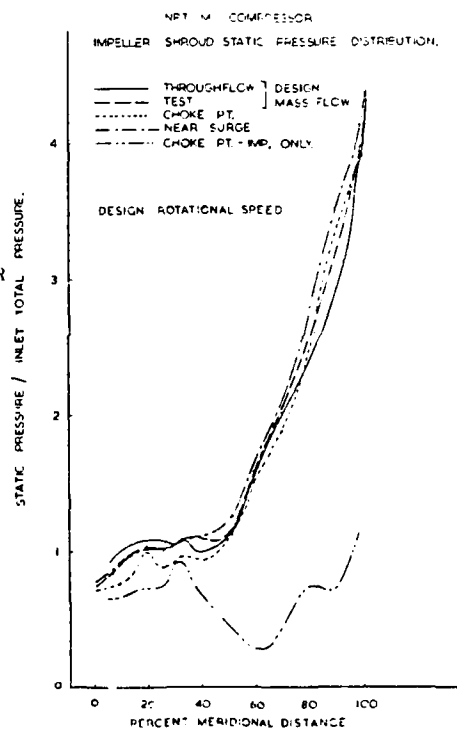


FIGURE 22. 'NPT 'M' COMPRESSOR. DISTRIBUTION OF DIFFUSER STATIC PRESSURE RISE AT THE DESIGN CONDITION

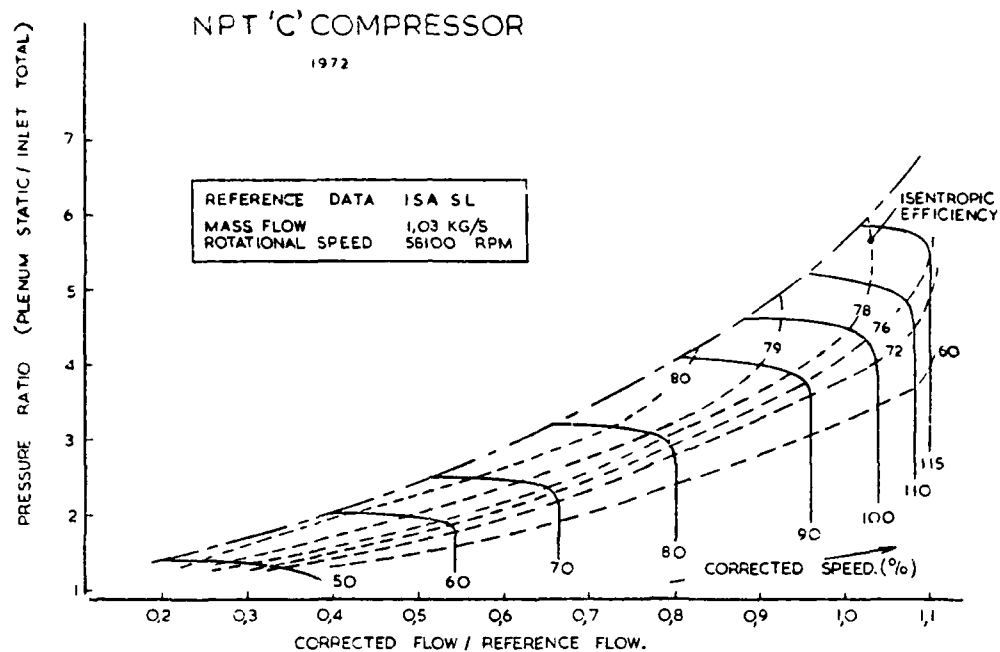


FIGURE 23 NPT 'C' COMPRESSOR. STATIC-TOTAL PRESSURE RATIO PERFORMANCE MAP

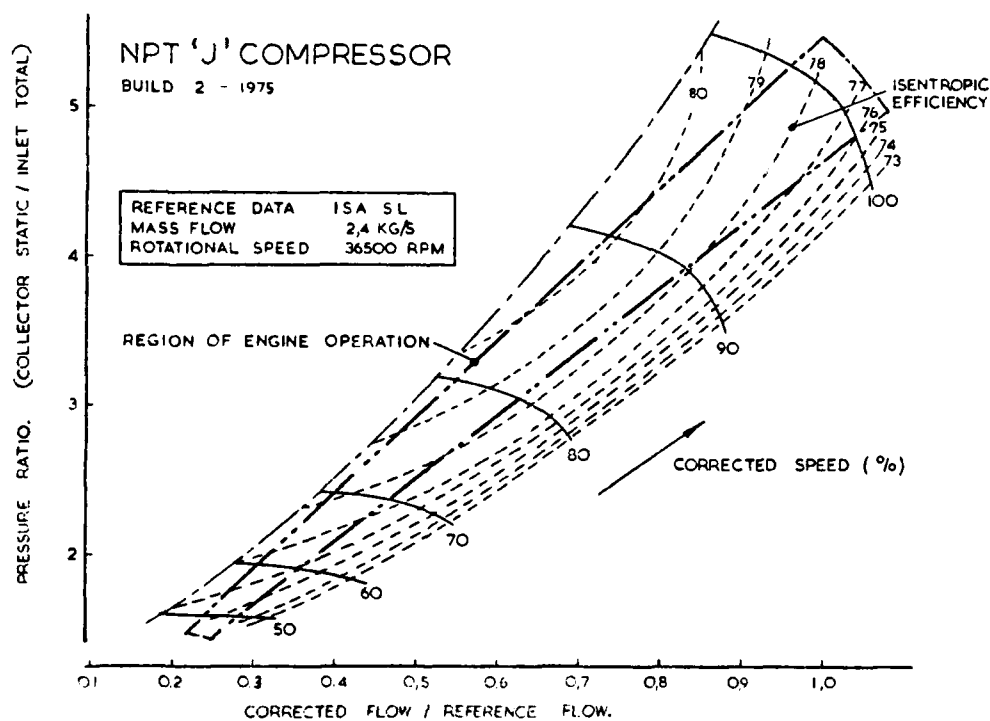


FIGURE 24. NPT 'J' COMPRESSOR. STATIC-TOTAL PRESSURE RATIO PERFORMANCE MAP

DISCUSSION

D.Japikse, CREARE, US

I was interested to observe the good surge margin of this compressor which was obtained on the first test in contrast with the Allison compressor described in Paper No.20 in which difficulty was encountered in obtaining sufficient surge margin in a compressor of 8 to 1 pressure ratio. Why was it so easy for the NPT compressor and so difficult for Allison's?

Author's Reply

We have ideas as to how we obtained such a good surge margin which were incorporated in the design but I am unable to state this information for proprietary reasons.

R.A.Novak, G.E. Company, US

Could the author please explain why the splitter-vane leading edges appear to lean forward in this compressor 'C'.

Author's Reply

The lean of the splitter-vane leading edges was somewhat arbitrary to suit manufacture and there was no particular aerodynamic reason for it.

D.Eckardt, MTU, Munich, Ge

In the case of the 'J' compressor there was only a very small diffuser area ratio of 1.6. Could the author explain if this was due to a spatial limitation.

Author's Reply

There was originally a space limitation on the design of this compressor and although that limitation was later lifted the area ratio was not changed. The design exit Mach number of the diffuser was quite high at about 0.35.

R.A.Moyes, Compair Industrial Ltd, UK

I observe that the impellers described in the paper do not have rake at the tip. Is there any aerodynamic significance?

Author's Reply

We have no experience of the aerodynamic effects of rake. Some designers claim that rake acts in a manner akin to back-sweep and also that it helps in reducing impeller tip noise or blade slap. Forward rake can be beneficial as regards reducing machining time in the tip region when cutting on a 5-axis machine. Forward rake is avoided by some designers since it could lead to extensive damage due to its natural gouging tendency should a shroud 'rub' occur.

EFFICIENCY OF CENTRIFUGAL COMPRESSOR IMPELLERS

by
Colin Rodgers
Chief Analytical Engineer
Solar Turbines International
2200 Pacific Highway
P.O. Box 80966
San Diego, CA 92138

SUMMARY

The correlation of efficiency levels of low and high pressure ratio centrifugal compressors and pumps with specific speed have produced relatively large uncertainty concerning the state of the art in maximum attainable efficiency potential. This uncertainty has arisen from the practice of extrapolating the published performances of widely differing impeller and diffuser designs, the differences in determination of efficiency measurement and computation, and basic data uncertainty and repeatability.

Improved efficiency correlation can be obtained, if the impeller and diffuser performances of centrifugal compressors and pumps can be separated. This allows the impeller performance potential to be correlated separately in terms of peak polytropic efficiency versus specific speed based upon average flowpath density. Test data are presented in this paper, to support the improved correlation, on several compressor impeller geometries at low and high Mach number and specific speed, together with design charts showing attainable state-of-the-art impeller efficiency levels as dependent upon geometry and operating conditions.

NOMENCLATURE

b	Blade Height
C	Absolute Velocity
c_f	Skin Friction Coefficient
CFS	Volume Flow
C_p	Specific Heat at Constant Pressure
D	Diameter
g	Gravitational Constant
GPM	Gallons per Minute
J	Joules Equivalent
H	Head
L	Blade Length along Mean Streamline
M_U	Machine Mach Number (Based on tip speed and inlet stagnation conditions)
N	Rotational Speed
N_s	Specific Speed
q	Work Factor or Loss Coefficient
R	Gas Constant
r_{hyd}	Hydraulic Radius
U	Impeller Tip Speed
W	Relative Velocity or Flow Rate
Z	Blade Number
β	Blade Angle (relative to axial direction)
Δ	Difference
ρ	Density
η	Efficiency
ϕ	Flow Coefficient
ψ	Head Coefficient
γ	Specific Heat Ratio
ν	Kinematic Viscosity
ω	Angular Velocity

SUBSCRIPTS

1	Impeller Inlet
2	Impeller Tip
h	Inducer Hub
d	Diffusion
f	Friction
th	Theoretical
p	Polytropic
r	Meridional
s	Shroud
w	Windage

SUPERSCRIPT

-	Average
---	---------

INTRODUCTION

The expense and duration of developing new centrifugal compressor designs to obtain higher performance levels often precludes departure from established baseline design procedures yielding satisfactory performance results. This, however, may confine and eventually stagnate compressor design technology.

With a confined technology spectrum, it is difficult to clearly establish the influence of major impeller performance parameters on impeller loss fractions and, hence, on efficiency trends. A broader centrifugal compressor technology must intrinsically be established when diversified market applications demand compressor designs to suit an ever increasing range of flow capacities for various impeller types. It is common, for example, in industrial centrifugal compressor applications to demand flow capacities for a given impeller family, varying by an order of 50:1, which pushes the extremities of the specific speed or flow coefficient curve to ever lower and higher limits.

The importance of the specific speed efficiency relationship, and the design parameters selection that enables optimum performance to be attained along the peak efficiency locus, is paramount technology for successful competitive designs. Reluctance to use the specific speed relationship in preliminary design by some designers appears to stem from:

- Insufficient published test data to clearly identify efficiency levels and trends
- Apparent diversity of specific speed curves required to cover variations in density ratio, hub diameter ratios, and Reynolds number
- Reluctance to use a "dimensional" parameter grouping with no real physical meaning other than excellence of shape, unlike true dimensionless similarity parameters such as Reynolds numbers and Mach number

The derivation and use of specific speed has been extensively treated by many authors. (Refs. 1, 2, and 3 are outstanding.) Further treatment would be superfluous, except to reiterate that specific speed combines the two most common non-dimensional turbomachinery parameters, flow and head coefficients (ϕ , ψ), with a constant, in the following relationship:

$$\text{Specific Speed} \propto \text{Constant} \times \frac{\phi^{0.5}}{\psi^{0.75}} \quad (1)$$

The three most common forms for specific speed used in the United States are:

$$N_S (\text{Pumps}) = \frac{N \cdot \text{GPM}^{0.5}}{H^{0.75}} \quad (2)$$

$$N_S (\text{Compressors}) = \frac{N \cdot \text{CFS}^{0.5}}{H^{0.75}} \quad (3)$$

$$\text{Non-Dimensional } N_S = \frac{\omega \cdot \text{CFS}^{0.5}}{(gH)^{0.75}} \quad (4)$$

Thus,

$$\text{Non-Dimensional } N_S = \frac{N_S \text{ pump}}{2736} = \frac{N_S \text{ compressor}}{129} \quad (5)$$

To aid comparison between U.S. and metric designed pumps and compressors, the non-dimensional form of specific speed is adapted herein.

Commercial pump design practice in the U.S. (Ref. 3) is to essentially rely upon a single specific speed curve, often known as "the chart," as a yardstick with which designers may judge the merit of their designs before commencing detail design, or to assess potential efficiency level. Use of the chart does not reveal the particular design features of the impeller that will produce optimum efficiency.

For this reason, it is necessary to initiate design with information relating to the corresponding optimum velocity triangles - the optimum variation of both ϕ and ψ along the optimum efficiency locus. Even with this information, good design, manufacturing, and test development practice is still necessary to attain the peak efficiency level. Thus, choosing specific speed "a-priori" is not an unconditional guarantee of maximum performance. Ref. 3 provides additional information in the form of pump impeller tip flow coefficient and exit blade angle. It will be shown later that similar optima can be derived for compressible media impellers, except that, as would be expected from dimensional considerations, both Mach number and Reynolds number variables have to be taken into account. This is a consequence of the fact that exact geometric (vector triangles) and viscous similarity cannot be maintained as both Mach and Reynolds numbers are varied.

For low Mach numbers ($M_0 < 0.6$), however, it is possible to compare centrifugal pump and compressor impellers at the same Reynolds numbers on the basis of efficiency versus inlet specific speed, since the density ratio is small. Tests on centrifugal pumps using both air and water are commonly conducted. Some of the better documented tests, described in Ref. 4, show that pump performance characteristics on air (at low speed) and water can indeed be correlated, if corrections are made for the changes in viscosity and seal

losses. The effect of using air in a water pump test is the same as using a fluid of viscosity 15 times greater than that of water, or reducing the water test speed 15 fold. Such pump and compressor comparisons for the same geometry at low speed are valid, but have been extrapolated ad infinitum, for all forms of compressors and pumps with widely different impellers, diffusers, and volutes. These extrapolations may lead to erroneous correlations of peak stage (impeller plus diffuser) efficiency.

It is established that high Mach number compressor performance is critically influenced by the matching and vane diffuser configuration, and that choking conditions result in radical discontinuities in the variation of the impeller and diffuser velocity triangles and losses. The casing losses of high specific speed pumps and compressors can also significantly influence the overall stage performance dependent upon throat area ratios and discharge treatment.

A more logical performance comparison (when specific geometries are available) ought to be possible by comparing impeller performances alone. The difficulty, however, is evaluation of impeller performance, especially for small high-pressure ratio impellers, where physical measurement of the impeller exit flow conditions is virtually impossible.

IMPELLER EFFICIENCY ASSESSMENT

Since the measurement of impeller exit momentum is problematical, it is customary to assess impeller efficiency based upon a computed exit average vector triangle. Computing methods are diverse and provide slightly different results depending upon the particular analytical model hypothesized.

Impeller performance is usually determined by testing an impeller with a short vaneless diffuser or dump section downstream of the tip. A conventional impeller efficiency calculation technique is based upon establishing a mean exit vector by using the discharge total temperatures average tip static pressure, flow and continuity equation. This technique, by no pretense an absolute measurement, provides a reliable yardstick for impeller efficiency assessment and was used to determine the performance of many impellers discussed herein.

An intrinsic weakness of the technique is the inability to rate the quality of the impeller exit flow distribution and wake mixing effects on the downstream diffusion system. It has been determined that impeller performance calculated in this manner does not always exhibit acceptable repeatability when the downstream diffusion process is changed.

With nearly uniform exit flow conditions, assumption of a mixed-out exit velocity triangle condition is meaningful and not overly sensitive to assumed blockage values and recirculation effects. At stall and lower flows, however, the flow may dichotomize into high and low momentum paths with possible recirculation of the low momentum fluid back into the impeller and/or rotating stall. The calculation of a mixed rotor tip relative velocity under such conditions may result in apparently high diffusion rates, since W_2 mixed can be substantially lower than the main core flow vector.

Representation of the impeller tip flow conditions by either blockage, jet and wake momentum deficiency, or profile corrections is a controversial subject (in both radial and axial compressor design) and becomes a matter of the taste and experience of the individual designers. All impeller geometries discussed herein were designed with the assumption of constant blockage (from five to ten percent depending upon specific speed) plus windage and recirculation losses q_w , treated as a simple external energy loss.

Albeit, analysis of impeller test data, using constant blockage and the defined windage plus recirculation allowance, tends to discredit the impeller with apparently excessive diffusion capabilities; the tip vector condition is ever elusive, in that blockage is variable and influenced by several factors amongst which are:

- Impeller Geometry - Hydraulic diameter and blade thickness
- Diffusion Factor
- Inducer Incidence - Boundary layer growth near choke and stall
- Clearance Effects

IMPELLER SIMILARITY CONSIDERATIONS

Impellers designed for the same head, inlet flow, and rotational speed with different molecular weight gases are not geometrically similar. To maintain equal diffusion ratios, the exit passage width (for a given discharge blade angle) can be shown to be proportional to:

$$\text{Exit Width} \propto \rho_1 / \rho_2 \quad (6)$$

where

$$\rho_2 / \rho_1 = \left[1 + q M_u \left(\frac{2}{\gamma-1} \right) \right]^{\frac{1}{\gamma-1}} \quad (7)$$

and

$$M_U = U_2 (g \gamma RT_1)^{-0.5} \quad (8)$$

This means that, although the inlet specific speed may be identical, the impeller geometry differs, and the larger density change design approximates a lower specific impeller exit shape with its consequent smaller exit blade height.

In Ref. 5, an alternate definition of specific speed is proposed which attempts to account for this compressibility influence and also selects polytropic efficiency instead of adiabatic efficiency. Polytropic efficiency is used as a better reference of state-of-the-art than adiabatic efficiency, since it is more indicative of the true aerodynamic (or hydraulic) losses. A constant polytropic efficiency over a density ratio range from 1.0 to 4.0 indicates that aerodynamic losses are proportional to the impeller work. A drop in polytropic efficiency over this density ratio range would, therefore, indicate proportionately higher losses as impeller work increases. Essentially, the use of polytropic efficiency and average specific speed reduces the compressor impeller flowpath to an equivalent incompressible frictional path, analogous to that of a centrifugal pump impeller, although generally at a lower Reynolds number.

Specific speed is defined with the volume flow represented by the average of the inlet and exit volume flows, namely:

$$\bar{N}_S = \frac{N [(CFS_1 + CFS_2)/2]^{0.5}}{H^{0.75}} \quad (9)$$

Note: To be consistent with the use of polytropic efficiency, polytropic head is used in this equation.

thus,

$$\bar{N}_S = N_S \left[\frac{1 + \rho_1/\rho_2}{2} \right]^{0.5} \quad (10)$$

Utilization of the average specific speed \bar{N}_S , therefore, reflects the physical geometry change of reduced exit with a higher density ratio impeller design by displacing it to a lower specific speed/lower efficiency position. All that has been changed in the dimensional similarity of specific speed derivation is really the reference density condition. It is to be anticipated that the higher density design will result in lower polytropic efficiency (apart from clearance effects) since the impeller passage frictional losses will increase with reduced hydraulic diameter.

Although the use of \bar{N}_S is empirically innovative in minimizing the number of parameters associated with efficiency correlation, the effects of impeller geometric differences, such as hub diameter ratio, blade sweep, solidity and curvatures, are not specifically delineated. Inadequate or excessive blade solidity, for example, would prevent an impeller design from reaching the peak efficiency locus. The effects of these more refined aspects of impeller design upon the efficiency of the specific speed relationship will be discussed shortly.

TEST CORRELATION

Correlation of efficiency versus specific speed for a given type of turbomachine is a common practice throughout industry. When accomplished on an overall stage basis, with relatively similar rotors and stator designs, it may provide relatively smooth data trends. This practice, however, can be abused, as mentioned previously, by extending the extrapolation to cover wider variations in geometry. As a result, data correlation can be poor, showing large scatter. Additionally, differences in measurement techniques and methods of efficiency assessment aggravate the data scatter.

In this particular correlation, the peak polytropic efficiencies of many (radial discharge) impellers manufactured at Solar were correlated against mean polytropic specific speed over their range of test speeds. At the higher specific speed stages, both peak and efficiencies at higher flows than the peak were used.

The design features of the impellers used are described in Ref. 6. Fig. 1 shows low, medium, and high impeller flow configurations to illustrate the range of specific speed covered.

Before discussing the results of the correlation, it is necessary to define its limitations in terms of those parameters influencing the viscous and non-viscous flow-path losses:

Size: Impeller tip diameters ranged from 10 to 36 cm (4 to 14 inches).

Type: All impellers were of the three dimensional inducer type with blade exit angles ranging from 0 to 50 degrees (from the radial).

Inlet: Axial accelerating (nozzle) type.

Hub Diameter: The hub-to-tip diameter ratios varied (D_{1h}/D_2) from 0.27 to 0.36.

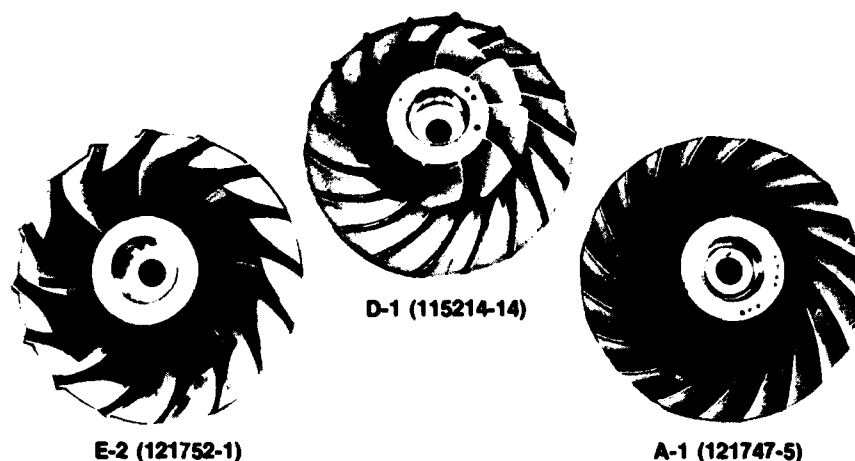


Fig. 1 Test impellers

Surface Finish: All impellers were manufactured by integral milling with a polished surface.

Blade Numbers: Blade numbers varied from 14 to 36 depending upon specific speed and Mach number.

Density: All impellers were tested at ambient suction conditions.

The influence of clearance losses is also an important performance consideration. In all test cases discussed here, the impeller casing shrouds were either manufactured from, or coated with, an abradable material so as to allow the minimum possible clearance without destructive damage. In many instances, slight rubbing did occur at maximum test speeds. Solidity and form of the impeller blade were designed to provide a relatively smooth mean-line diffusion throughout the flow path with no (calculated) zones of negative surface velocity, at the design condition. Impeller designs with higher operating inlet relative Mach numbers used modified parabolic inducer camber-line geometries from the leading edge past the throat, with low suction surface curvature. Impeller efficiency was calculated using the average of five static pressure taps at the impeller tip, the measured airflow, casing discharge temperature and a tip blockage of 5 to 10 percent, with a windage correction (subtracted from the exit momentum) according to the empirical relationship:

$$q_w \propto \frac{\bar{p} U_2 D_2^2}{2 \times 10^5 W \pi q} \quad (11)$$

Impeller tip traversing was practical for the larger impellers and revealed acceptable agreement between the measured and computed tip total pressures near the peak efficiency flow conditions.

Impeller efficiencies were examined for the various test tip speeds, which for one impeller ranged from 1080 to 2060 feet per second (fps). The correlation of impeller polytropic efficiency and mean specific speed for many impellers designed, fabricated, and tested in accordance with the previous limitations is shown in Fig. 2. Although some data scatter is inevitable, the general trend represents an improvement upon previous correlations of overall stage data. Even for this restricted range of impellers, some scatter must be anticipated due to measurement errors. Cumulative error of instruments on impeller efficiency computation was on the order of ± 2.0 percent.

Fig. 2 reveals peak impeller polytropic efficiencies of 93 to 94 percent at mean specific speeds on the order of 0.6 to 0.8, with peak radial impeller ($\beta_2 = 0$ deg) efficiencies slightly lower than those of the backswept type. Of particular interest was the data from a radial impeller (Ref. 6) run to a tip speed of 1900 fps and a backswept impeller run to 2060 fps which showed only a minor decrease of polytropic efficiency with increasing tip speed. This result will be discussed in more detail later. That peak impeller polytropic efficiencies of 93 to 94 percent are attainable (including windage) is significant in that:

- The residual inefficiency of flow path loss must be relatively small.
- Even with the relatively small size ($Re = 1 \times 10^5$), viscous losses are apparently small, no doubt due to aerodynamically smooth surfaces.

These results prompted an analytical study to investigate the residual losses in the form of a simplified mean streamline model of the impeller flow path. The presumption that such a model is indeed a valid representation of the flow process requires further deliberation of the fact that the performance level the impeller can produce, in terms of exit momentum and its distribution, is not necessarily what the downstream diffuser wants to accept. For example, the impeller tends to produce a Couette meridional flow profile, whereas the diffuser would prefer to accept a flat profile.

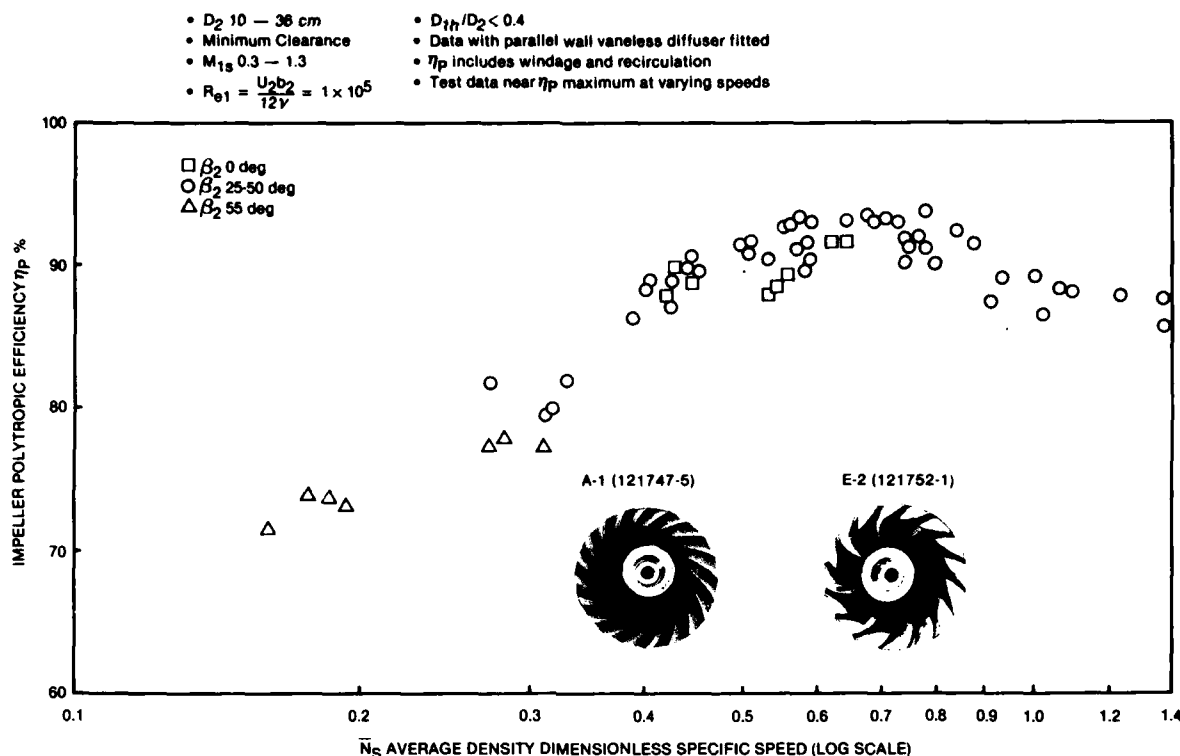


Fig. 2 Test impeller efficiencies versus average specific speed

FLOW PATH MODEL

A simple mean streamline flow path model was generated in which the ratio of the polytropic to actual work input, needed to achieve the impeller tip stagnation pressure rise, could be expressed in terms of the losses by:

$$\eta_p = \frac{q_{th} - q_f - q_d}{q_{th} + q_w} = 1 - \left(\frac{(q_f + q_d + q_w)}{q} \right) \quad (12)$$

The viscous loss coefficients q_f and q_w were associated with flow path friction and discharge windage. A "diffusion loss" was postulated encompassing all other loss sources with the exception of clearance losses, which were assumed to be negligible on the basis of the data constraints.

Both frictional loss assessments used were semi-empirical because data concerning the direct measurements of these quantities in centrifugal compressors were not available. The flow-path frictional model was based upon friction losses in 90 degree curved stationary pipes:

$$q_f = C_f \frac{L}{r_{hyd}} (\bar{W}/U_2) \left[1 + \frac{3.5 \cos \beta_2 \bar{b}}{0.5(D_2 - D_{1s})} \right] \quad (13)$$

where

$$r_{hyd} = \frac{D_1}{2} \frac{RMS}{D_1 h} + \frac{4Z}{\pi \cos \beta_1} + \frac{D_2}{2} \frac{RMS}{D_2 h} + \frac{4Z}{\pi \cos \beta_2} \quad (14)$$

The effective impeller curvature in space (for radial discharge conditions) was assumed to be proportional to the backswept angle β_2 . (Mixed-flow diagonal discharge impellers possess lower equivalent curvatures and are not covered here due to insufficient mixed-flow impeller data.) Since the frictional model is based upon stationary curved circular pipe data, its application range is limited by passage aspect ratio considerations. For example, low speed pumps conventionally use low blade numbers with higher passage aspect ratios and hydraulic radii. Rotation effects on the friction coefficient are assumed to be negligible for a turbulent flow regime at a Reynolds number of 1×10^5 . The friction and windage losses were calculated using each of the impeller geometries investigated together with the efficiency and work factor q to determine the residual loss q_d .

Fig. 3 shows the relatively small residual loss band versus the work factor q , indicating increasing "diffusion" loss with increasing work factor. This trend is expected, as Ref. 6 shows, an almost linear relationship between q and diffusion factor (DF) for a particular impeller geometry and speed. A disadvantage to the correlation q_d

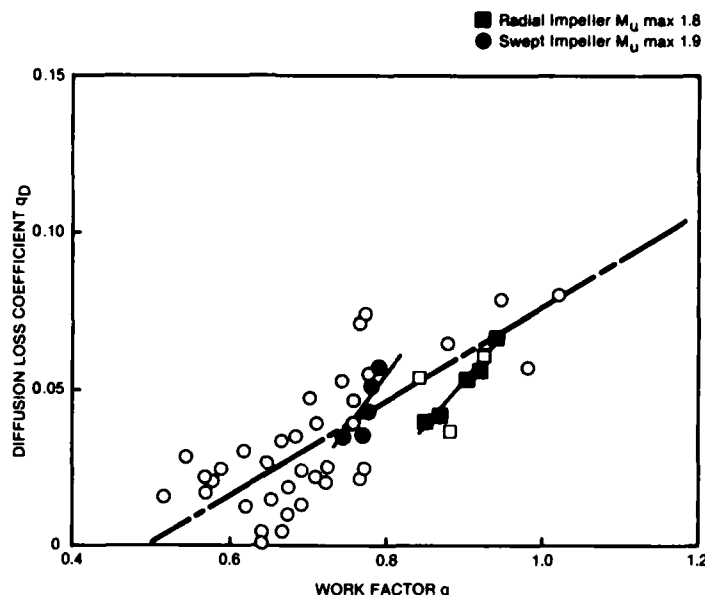


Fig. 3 Diffusion loss versus work factor

vis DF is, however, that DF must be estimated from the controversial vector conditions at the impeller exit, whereas q is obtained directly from test. The diffusion loss in Fig. 3 is expressed as:

$$q_d = 0.15 (q - 0.5) \quad (15)$$

Postulated diffusion losses, therefore, become increasingly smaller for lightly loaded impellers and appear to approach zero with a work factor of 0.5. This implies that the majority of impeller losses must be frictional, as corroborated in Ref. 4. Fig. 3 also shows the individual diffusion losses for two high-pressure ratio impellers tested over a wide range of tip speeds (identified by the shaded symbols). These data, which follow the general diffusion loss pattern trend, imply the important conclusion that the reduction in peak efficiency with increasing density ratio for a high-pressure ratio impeller of given geometry stems basically from increasing diffusion loading, providing shock boundary layer separation losses are small.

One impeller in particular (shaded circles) was operated to an inducer tip relative Mach number of 1.36 without indication of significant shock losses, both from the q_d data trend and examination of the inducer tip shroud steady-state static pressure distribution. This impeller, shown in Fig. 4, had an inducer section designed for efficient transonic operation with small curvature and blade thickness preceded by an axial inlet. Distortion of the inlet flow and departure from transonic blade design criteria would be expected to precipitate significant shock losses.

Simply labeling all residual loss as arising from internal diffusion does not preclude mixing losses downstream of the impeller. Mixing losses are also a function of internal diffusion and blade blockage. The latter was less than three percent for the impellers investigated.

Having generated the flow-path model from friction and diffusion losses using test data from a wide variety of specific speed impellers, an inverse computation procedure was conducted to compare impeller test and estimated performances. To complete such a comparison, it was necessary to calculate the work factor q from impeller geometry, flow, speed, and slippage or deviation criteria with deviation as a dependent function of diffusion factor. Such a calculation was computerized, and although not described herein, comparative analyses of the test and estimated peak impeller performances showed agreement to within ± 1.5 percentage points on efficiency and ± 5 percent on work factor.

The impeller flow-path model based on a single streamline analysis, assuming loss sources fitting the test data and polytropic compression, did, therefore, satisfactorily predict peak impeller performance for a wide variety of impeller configurations with ambient suction conditions. The application of such a model to encompass other alternate impeller configurations, operating conditions, gas or fluid properties, and suction conditions, and the interpretation of results thereby obtained is left to individual discretion.

PREDICTION OF SPECIFIC SPEED CURVES

After an improved technique was established for correlating the efficiency of radial discharge centrifugal impellers near peak efficiency conditions based upon existing impeller geometries, the incentive materialized to generate design curves for prompt identification of the efficiency potential of future or alternate designs. The computerized procedure for impeller performance prediction previously mentioned suggested an

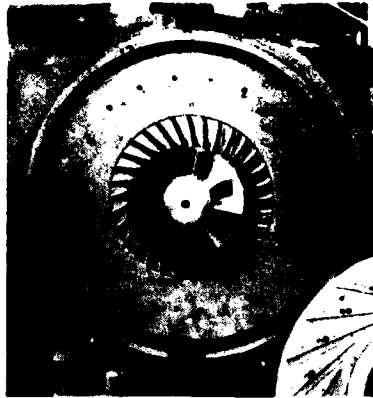


Fig. 4 Transonic impeller

immediate tool to generate such impeller peak efficiency versus mean specific speed design curves. The many parameters involved, however, have to be generalized to cover typical design configurations. Optimization for a particular design and the associated design restraints is, of course, best accomplished by successive computer iterations.

The following dependent variables were selected as an example of the capability to generate specific speed design curves.

- Impeller Tip Blade Angle (β_2) 0, 25, 50 deg
- Impeller Inlet Flow Coefficient (φ) 0.1, 0.2, 0.3, 0.4
- Impeller Mach Number (M_U) 0.77, 1.54
- Impeller Diameter Ratio (D_{1h}/D_2) 0.3
- Impeller Diffusion Ratio (W_1/W_2) 1.4
- Impeller Solidity ($\pi D_2/2ZL$) 0.25
- Impeller Tip Reynolds Number ($b_2 U_2/\nu_2$) 1×10^5

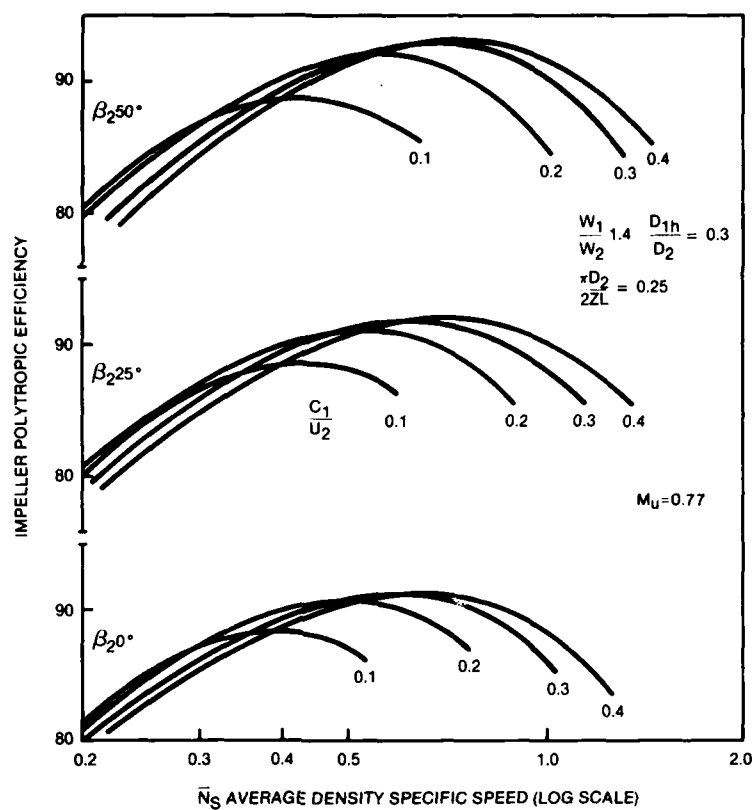
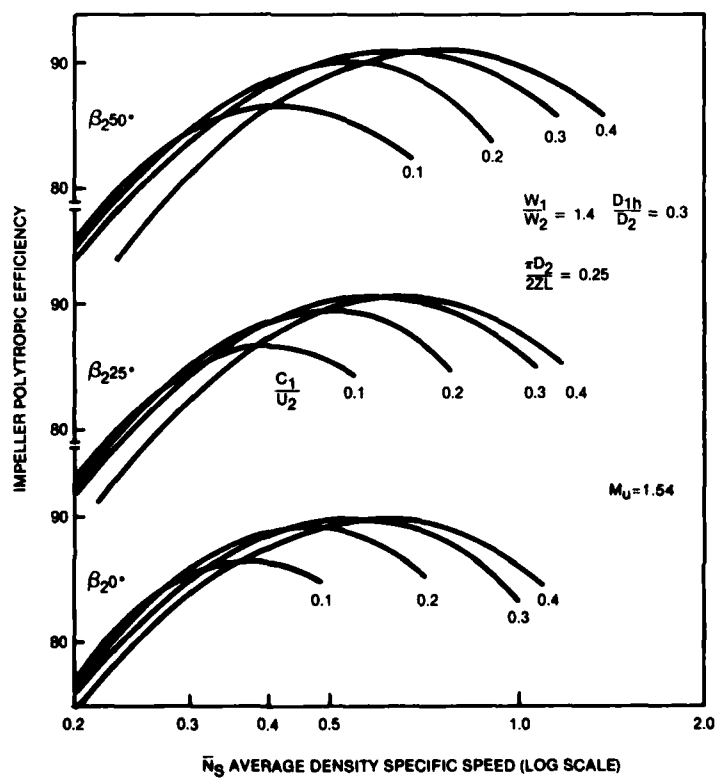
Figs. 5 and 6 show impeller specific speed design charts for Mach numbers of 0.77 and 1.54 respectively as constrained by the previous parameters and an inducer tip relative Mach number not exceeding 1.3. These specific speed charts indicate:

- Optimum mean specific speed increases as the tip blade angle increases for a given Mach number. Efficient high specific speed impellers should, therefore, be of the backswept-type, providing blade stresses are acceptable.
- Optimum specific speed for a given tip blade angle decreases slightly with increasing Mach number.
- Optimum efficiency at a given mean specific speed and Mach number is a function of the inlet flow coefficient. Low inlet flow coefficients are optimum at low specific speeds; high inlet flow coefficients are optimum at high specific speeds. This follows similar trends in established centrifugal pump practice.
- Peak impeller efficiency (for a fixed solidity) decreases by up to two percentage points, increasing the Mach number from 0.77 to 1.54 (for constant Reynolds number).
- Highly backswept impellers (50 degrees or more) are some two percentage points higher in peak efficiency than radial impellers for the constraints of Figs. 5 and 6. Straight radial impellers provide the highest efficiency at very low specific speeds.

Although not examined in this study, the data trends would support the test evidence that mixed flow impellers with tip blade angles exceeding 50 degrees would be optimum at specific speeds approaching 1.5.

These design charts provide a quick "look-see" at the optimum efficiency zones and the effects of blade sweep and inlet flow coefficient for fixed diffusion rate, diameter ratio, blade solidity, and Reynolds number.

Due to the latter constraints, the practice of referring to such charts as a design aid is rapidly becoming outmoded, since the desk computer is a far more versatile design aid and may be programmed to search for optimums without laborious, two-dimensional, chart-form, graphical determination of optima.

Fig. 5 Specific speed chart ($M_U = 0.77$)Fig. 6 Specific speed chart ($M_U = 1.54$)

DIFFUSER CONSIDERATIONS

The improved correlation of impeller efficiency may assist in more accurate definition of optimum impeller features, but its inherent shortcoming is that it does not quantitatively rate the efficiency potential of the overall stage; i.e., impeller plus stationary diffusion system (diffuser). Furthermore, the specific speed of the impeller cannot be readily calculated and requires iteration of the impeller tip vector triangle.

If it is assumed that the impeller and diffuser performances can indeed be separated and that their performances are not interdependent, it should be possible to apply the extensive data generated for two-dimensional and conical diffusers to evaluate overall stage performance potential. (See Ref. 7.)

Although component separation works reasonably well for the impeller (with undistorted inlet flow), such is not the case for the downstream diffuser. This is expected, since the single most dominant parameter affecting the performance of a particular diffuser geometry is the inlet blockage. Thus, diffuser performance with a centrifugal compressor or pump depends upon the particular impeller discharge flow conditions. (See Ref. 8.) Extensive literature, including Refs. 9, 10, and 11, is available which deals with the performance characteristics of various forms of stationary diffusion devices. The most common devices, in order of decreasing efficiency and increasing flow range, are:

- Vaned diffusers
- Volute or scroll diffusers
- Vaneless diffusers

Vaneless diffusers in themselves can, with proper design, be a source of relatively small loss, but as little diffusion other than vortex dissipation is accomplished, the exit energy is relatively high and may be lost entirely. Improved overall recovery is obtained from a vaneless diffuser by adding a volute or scroll discharge to reduce discharge losses. In effect, the scroll tongue performs as a single blade or airfoil and as such, exhibits a stalling limit, which reduces its flow range compared to a vaneless diffuser. Maximum diffuser system static pressure recovery is, of course, obtained with a cascade of diffuser vanes at the expense of reduced flow range. Typical static pressure recoveries (impeller tip to discharge static) for all three systems are given below. These recovery levels may be used, together with the impeller performance levels previously discussed, to arrive at representative overall stage efficiency levels.

Type of Diffuser	Vaned	Volute/Scroll	Vaneless
Static Pressure Recovery	0.65/0.78	0.55/0.68	0.5/0.6

Using a maximum vaned diffuser static pressure recovery of 0.78, together with the optimum impeller performance levels from Figs. 5 and 6, the representative optimum overall stage performance capabilities, shown in Fig. 7, can be plotted in the conventional form of adiabatic total-static efficiency for comparison purposes. Maximum stage adiabatic efficiency is seen to be 83.5 percent with a Mach number M_u of 1.54 and a β_2 of 50 degrees.

As the optimum impeller performances (with aerodynamically smooth surfaces) reflect essentially frictional loss sources, it is difficult to conceive how attainable centrifugal compressor performances can be raised above the stage levels shown without higher attainable diffuser static pressure recoveries or possibly increased impeller diffusion. Unfortunately, higher impeller diffusion levels precipitate reduced range and increased diffuser inlet blockage. The estimated effect of increasing the impeller diffusion ratio W_1/W_2 from 1.4 to 1.8 is also shown in Fig. 7, (assuming 0.78 recovery) and indicates only slightly higher stage efficiencies with blade angles β_2 of 25 and 0 degrees.

It would appear, therefore, that if (as postulated) the losses in high performance optimum design impellers are essentially frictional, future efforts to further raise overall stage efficiency should concentrate upon improving the flow mixing and distribution of the impeller exit and diffuser inlet. These efforts may involve investigation of the vaneless diffuser end wall profiling and of boundary layer control devices.

Various forms of diffuser entry boundary layer control and bleed have been tried throughout the industry, including end-wall plenums, diffuser vane end-wall gaps, and throat bleed. Incorporation of these features may provide small apparent improvements in compressor performance, but are often accompanied by minor parasitic performance penalties; for example, boundary layer bleed which cannot be usefully employed elsewhere. It is difficult, therefore, to conceive that ultimate stage efficiencies higher than 90 percent for small high-pressure ratio centrifugal compressors can be attained (Ref. 7).

Efficiencies greater than 90 percent are attainable for large centrifugal pumps, according to "the chart" in Fig. 8, in terms of non-dimensional specific speed. Chart efficiencies of 80 and 89 percent are indicated for flow rates of 0.028 and 0.57 m³/s. Peak efficiencies for overall compressor stage at a low Mach number, $M_u = 0.5$, are superimposed for comparison. The computed compressor efficiencies (determined in a similar manner in Fig. 7) compare qualitatively with chart efficiency trends, even with

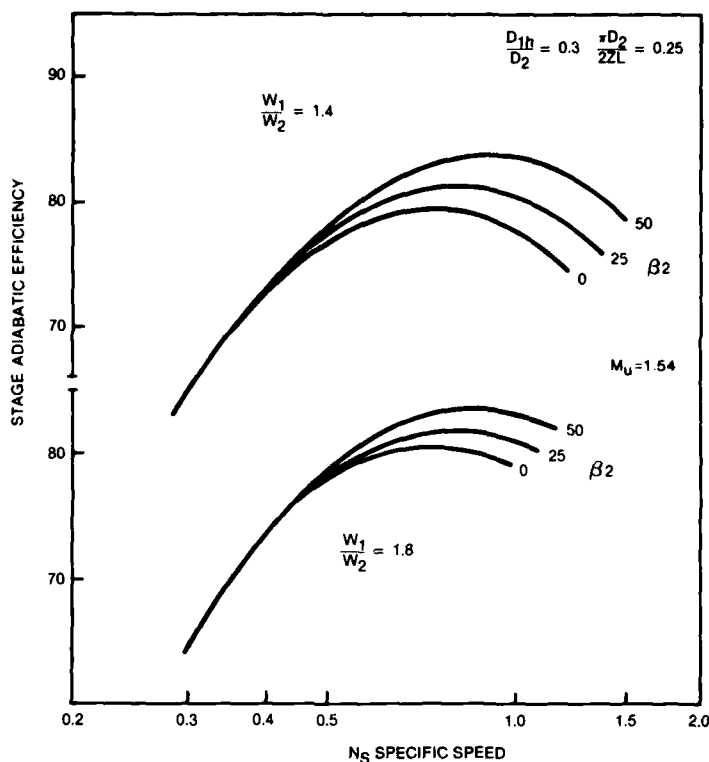


Fig. 7 Estimated stage efficiencies ($M_u = 1.54$)

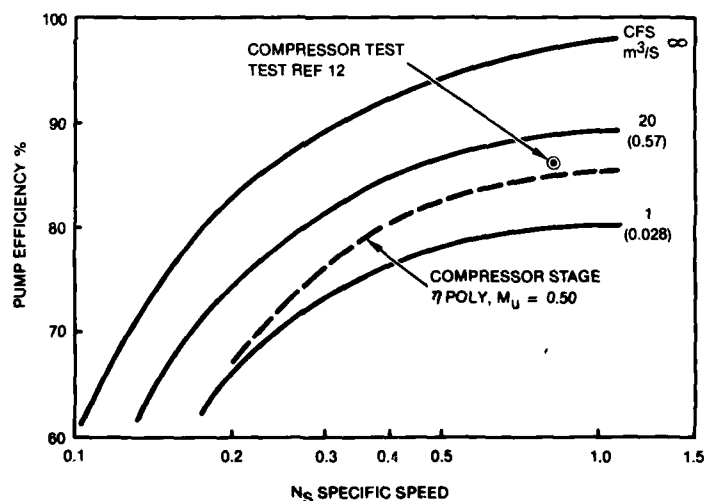


Fig. 8 Centrifugal pump and compressor efficiencies

the Reynolds number disparity. Ref. 12 offers test confirmation that adiabatic stage efficiencies of 86 percent can be attained with relatively large low pressure ratio centrifugal compressors designed near optimum specific speed.

The performance and operating range of high (air) pressure ratio centrifugal compressors suitable for aircraft gas turbine applications eventually become limited as the inducer tip relative Mach number increases beyond approximately 1.4. For aircraft applications in particular, it is desirable not only to attain high pressure ratios efficiently, but also to swallow high airflow rates per unit frontal area; i.e., to utilize high specific speed designs. Optimization was applied to the compressor performance prediction program previously described to determine the maximum specific speed and efficiency degradation for typical high pressure aircraft type centrifugal compressors as a function of pressure ratio for M_{1s} limit of 1.4. The results of optimization are shown in Fig. 9 indicating a reduction in both specific speed and efficiency as pressure ratios are increased beyond 7.0. A reduction in efficiency is also reflected at pressure ratios below 7.0 as a consequence of operating beyond the optimum Mach number and specific speed.

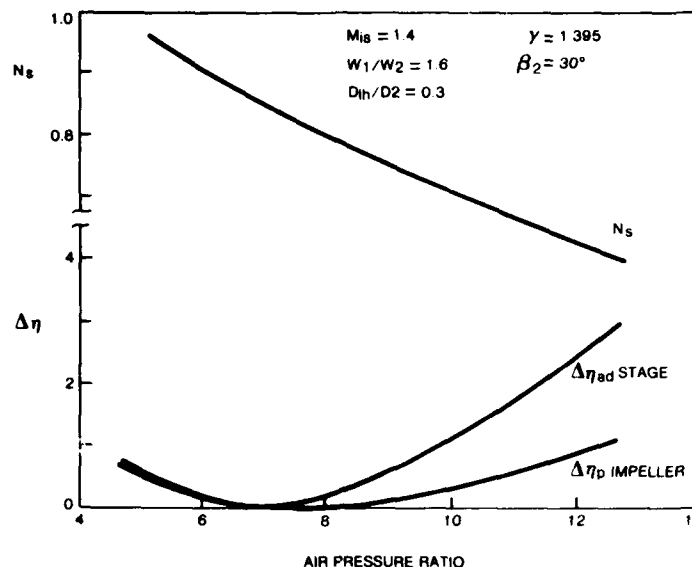


Fig. 9 Inducer tip Mach number limit on specific speed and efficiency

CONCLUSIONS

Analysis of the test performances of many high and low speed centrifugal compressors (for which the author held developmental responsibility) has shown a satisfactory correlation of impeller polytropic efficiency versus specific speed based upon average impeller density. This correlation is contingent upon the ability to assess the impeller and diffuser performances as separate components, and presumes the impeller-diffuser interaction effects are small.

The use of polytropic efficiency and average specific speed essentially reduces the impeller flow path to an equivalent incompressible frictional path, and is, thus, analogous to flow-path conditions in a centrifugal pump, although generally at a lower Reynolds number. Examination of test impeller efficiency levels and, hence, internal losses indicates that the majority of the losses is frictional from both the flow-path geometry and the windage between impeller and stationary shrouds, providing clearance losses are minimal. With friction as the major loss source, it is difficult to perceive that substantial performance improvements can be made to the impeller other than in possibly improving its discharge flow conditions and, thereby, improving the static pressure recovery of the downstream stationary diffuser.

The frictional hypothesis appears to be also characteristic of flow conditions in the channel of high-efficiency transonic impellers where shock losses may be minor if proper transonic entry design blading can be applied. An impeller mean streamline empirical frictional loss model with blade loading loss allowances satisfactorily duplicates test impeller polytropic efficiency versus average density specific speed trends. Analytical demonstration of this model assists in the generation of design specific speed charts for high performance centrifugal impellers within specific design constraints.

Although the particular correlation of impeller efficiency may assist in improved selection of optimum impeller geometries, its inherent shortcoming is that the efficiency potential of the overall stage (impeller plus stationary diffuser) cannot be determined without additional knowledge concerning the diffuser static pressure recovery, as influenced by the impeller exit flow distribution.

REFERENCES

1. Balje, O.E., "A Study on Design Criteria and Matching of Turbomachines," ASME 60-WA 230.
2. Wislicenus, G.F., "Turbomachinery Design Described by Similarity Considerations," NASA SP-304 Part I.
3. Karassik, I.J., Krutzsch, W.H., Fraser, W.H., Mess'na, J.P., "Pump Handbook," McGraw-Hill.
4. Worster, R.C., Campbell, J.M.S., Zankers, K.J., Fellerman, L., "A Comparison of Air and Water Testing of Centrifugal Pumps," Rotodynamic Pump Research, Vol. II, B.H.R.A.
5. Pampreen, R.C., Firman, P.A., Erwin, J.R., Dawson, R.W., "A Small Axial-Centrifugal Compressor Matching Study Program," AD 878040.
6. Rodgers, C., "A Diffusion Factor Correlation for Centrifugal Impeller Stalling," ASME 78-GT-61.

7. Dean, R.C., "The Fluid Dynamic Design and Advanced Centrifugal Compressors," Creare, Inc., TN-185.
8. A-Kovats, "Investigation of Volute-Impeller Interaction in Pumps," ASME 66-PE-14.
9. Senoo, Y., Kinoshita, Y., "Limits of Rotating Stall and Stall in Vaneless Diffuser of Centrifugal Compressors," ASME 78-GT-19.
10. Michina, H., Gyobu, I., "Performance Investigations of Large Capacity Centrifugal Compressors," ASME 78-GT-3.
11. Pampreen, R.C., "The Use of Cascade Technology in Centrifugal Compressor Vaned Diffuser Design," ASME 78-GT-39.
12. Wendt, P.G., Rodgers, C., Sapiro, L., "Development and Closed-Loop Testing of High Efficiency Compressors for Use with a 7000 kW Gas Turbine," ASME 78-GT-189.

ACKNOWLEDGEMENTS

The author wishes to acknowledge the efforts of the following people from Solar Gas Turbines International who were involved in the experimental test and data reduction of the impellers investigated:

- D. Lucas - Development Test Engineer
- R. Geiser - Engineering Specialist

DISCUSSION

W.Jansen, Northern Research, US

Could the author explain whether he really means that the diffusion losses are not a function of impeller relative velocity ratio. Also could the author suggest why diffusion ratios are limited to 1.7 in his impeller designs where values of 2.0 would give less frictional losses.

Author's Reply

I do not mean to imply that diffusion ratio is unimportant but nearly all of the compressors of Figure 3 have diffusion ratios lying in the relatively narrow range, from 1.4 to 1.7. They are limited to these values in order to avoid impeller stall.

Y.Ribaud, ONERA, Fr

What values will stage efficiency reach for the optimum value of specific speed?

Author's Reply

Polytropic efficiencies of about 0.85 can be obtained for machines of mass flows of around 3 lb/s.

D.Japikse, CREARE, US

What type of vaneless diffuser was used, was it a pinched type or an unpinched type and, in any case, how was backflow controlled?

Author's Reply

The choice of impeller "b" width to the vaneless diffuser "b" width was dictated by considerations of the design of the diffuser throat area, (particularly its aspect ratio) when the impeller was run with the vaned diffuser. Width ratios ranged from 0.9 to 1.1.

There would certainly be the possibility of backflow into the impeller in some cases beyond the point of stall, when running with a vaneless diffuser.

P.Langdon, Holset Engineering Ltd, UK

I have observed that in some of your impellers you feature short splitter blades near the tip. Have you found any gain from these? In our work at Holset we have sometimes obtained improvements in surge margin and slip factor but sometimes we only get an improvement in slip factor and certainly we obtain no improvement in efficiency. What methods do you use for positioning the splitter vanes and do you think that improved positioning would lead to better performance gains?

Author's Reply

We use splitter blades like everyone else to help to optimise the blade loading, but we do not have any special method of positioning them and it would be informative to conduct research in this area. However from mechanical considerations we would like really not to have to design impellers with short splitter blades at the tip at all.

REPORT DOCUMENTATION PAGE			
1. Recipient's Reference	2. Originator's Reference	3. Further Reference	4. Security Classification of Document
	AGARD-CP-282	ISBN 92-835-0271-X	UNCLASSIFIED
5. Originator	Advisory Group for Aerospace Research and Development North Atlantic Treaty Organization 7 rue Ancelle, 92200 Neuilly sur Seine, France		
6. Title	CENTRIFUGAL COMPRESSORS, FLOW PHENOMENA AND PERFORMANCE		
7. Presented at	the 55th (B) Specialists' Meeting of the Propulsion and Energetics Panel of AGARD, held at the Royal Library, Brussels, Belgium, on 7-9 May 1980.		
8. Author(s)/Editor(s)	Various		9. Date November 1980
10. Author's/Editor's Address	Various		11. Pages 352
12. Distribution Statement	This document is distributed in accordance with AGARD policies and regulations, which are outlined on the Outside Back Covers of all AGARD publications.		
13. Keywords/Descriptors			
<div style="display: flex; justify-content: space-between;"> <div> Centrifugal compressors Impellers Diffusers </div> <div> Flow distribution Fluid flow Performance </div> </div>			
14. Abstract			
<p>These Conference Proceedings contain the 21 papers presented at the AGARD Propulsion and Energetics Panel 55th (B) Specialists' Meeting on Centrifugal Compressors, Flow Phenomena and Performance, which was held in Brussels, Belgium, on 7-9 May 1980. The questions and answers after the presentation of each paper, as well as after the evaluation which was made at the end of the meeting, are included.</p> <p>The Technical Evaluation Report is included at the beginning of the Conference Proceedings.</p> <p>The meeting was divided into five sessions: Experimental Investigations on Flows in Impellers and Diffusers; Theoretical Calculations of Flows in Impellers; Interaction between Impeller and Diffuser; Design Experience and Performance of Advanced Centrifugal Compressors (Parts I and II).</p> <p>The papers were focussed on the inducer, impeller and the diffuser flow field, on interactions between impeller and diffuser, and they provided a comprehensive survey and detailed information on design experience and centrifugal compressor performance. Viscous, transonic, compressible and 3-D effects were studied. The influence of non-uniform flow at the rotor outlet on performance and surge margin, namely for high pressure ratio compressors, were discussed.</p>			

<p>AGARD Conference Proceedings No. 282 Advisory Group for Aerospace Research and Development, NATO CENTRIFUGAL COMPRESSORS, FLOW PHENOMENA AND PERFORMANCE Published November 1980 352 pages</p> <p>These Conference Proceedings contain the 21 papers presented at the AGARD Propulsion and Energetics Panel 55th (B) Specialists' Meeting on Centrifugal Compressors, Flow Phenomena and Performance, which was held in Brussels, Belgium, on 7-9 May 1980. The questions and answers after the presentation of each paper, as well as after the evaluation which was made at the end of the meeting, are included.</p> <p>P.T.O.</p>	<p>AGARD-CP-282</p> <p>Centrifugal compressors Impellers Diffusers Flow distribution Fluid flow Performance</p>	<p>AGARD Conference Proceedings No. 282 Advisory Group for Aerospace Research and Development, NATO CENTRIFUGAL COMPRESSORS, FLOW PHENOMENA AND PERFORMANCE Published November 1980 352 pages</p> <p>These Conference Proceedings contain the 21 papers presented at the AGARD Propulsion and Energetics Panel 55th (B) Specialists' Meeting on Centrifugal Compressors, Flow Phenomena and Performance, which was held in Brussels, Belgium, on 7-9 May 1980. The questions and answers after the presentation of each paper, as well as after the evaluation which was made at the end of the meeting, are included.</p> <p>P.T.O.</p>	<p>AGARD-CP-282</p> <p>Centrifugal compressors Impellers Diffusers Flow distribution Fluid flow Performance</p>
<p>AGARD Conference Proceedings No. 282 Advisory Group for Aerospace Research and Development, NATO CENTRIFUGAL COMPRESSORS, FLOW PHENOMENA AND PERFORMANCE Published November 1980 352 pages</p> <p>These Conference Proceedings contain the 21 papers presented at the AGARD Propulsion and Energetics Panel 55th (B) Specialists' Meeting on Centrifugal Compressors, Flow Phenomena and Performance, which was held in Brussels, Belgium, on 7-9 May 1980. The questions and answers after the presentation of each paper, as well as after the evaluation which was made at the end of the meeting, are included.</p> <p>P.T.O.</p>	<p>AGARD-CP-282</p> <p>Centrifugal compressors Impellers Diffusers Flow distribution Fluid flow Performance</p>	<p>AGARD Conference Proceedings No. 282 Advisory Group for Aerospace Research and Development, NATO CENTRIFUGAL COMPRESSORS, FLOW PHENOMENA AND PERFORMANCE Published November 1980 352 pages</p> <p>These Conference Proceedings contain the 21 papers presented at the AGARD Propulsion and Energetics Panel 55th (B) Specialists' Meeting on Centrifugal Compressors, Flow Phenomena and Performance, which was held in Brussels, Belgium, on 7-9 May 1980. The questions and answers after the presentation of each paper, as well as after the evaluation which was made at the end of the meeting, are included.</p> <p>P.T.O.</p>	<p>AGARD-CP-282</p> <p>Centrifugal compressors Impellers Diffusers Flow distribution Fluid flow Performance</p>

<p>The Technical Evaluation Report is included at the beginning of the Conference Proceedings.</p> <p>The meeting was divided into five sessions: Experimental Investigations on Flows in Impellers and Diffusers; Theoretical Calculations of Flows in Impellers; Interaction between Impeller and Diffuser; Design Experience and Performance of Advanced Centrifugal Compressors (Parts I and II).</p> <p>The papers were focussed on the inducer, impeller and the diffuser flow field, on interactions between impeller and diffuser, and they provided a comprehensive survey and detailed information on design experience and centrifugal compressor performance. Viscous transonic, compressible and 3-D effects were studied. The influence of non-uniform flow at the rotor outlet on performance and surge margin, namely for high pressure ratio compressors, were discussed.</p> <p>ISBN 92-835-0271-X</p>	<p>The Technical Evaluation Report is included at the beginning of the Conference Proceedings.</p> <p>The meeting was divided into five sessions: Experimental Investigations on Flows in Impellers and Diffusers; Theoretical Calculations of Flows in Impellers; Interaction between Impeller and Diffuser; Design Experience and Performance of Advanced Centrifugal Compressors (Parts I and II).</p> <p>The papers were focussed on the inducer, impeller and the diffuser flow field, on interactions between impeller and diffuser, and they provided a comprehensive survey and detailed information on design experience and centrifugal compressor performance. Viscous transonic, compressible and 3-D effects were studied. The influence of non-uniform flow at the rotor outlet on performance and surge margin, namely for high pressure ratio compressors, were discussed.</p> <p>ISBN 92-835-0271-X</p>
<p>The Technical Evaluation Report is included at the beginning of the Conference Proceedings.</p> <p>The meeting was divided into five sessions: Experimental Investigations on Flows in Impellers and Diffusers; Theoretical Calculations of Flows in Impellers; Interaction between Impeller and Diffuser; Design Experience and Performance of Advanced Centrifugal Compressors (Parts I and II).</p> <p>The papers were focussed on the inducer, impeller and the diffuser flow field, on interactions between impeller and diffuser, and they provided a comprehensive survey and detailed information on design experience and centrifugal compressor performance. Viscous transonic, compressible and 3-D effects were studied. The influence of non-uniform flow at the rotor outlet on performance and surge margin, namely for high pressure ratio compressors, were discussed.</p> <p>ISBN 92-835-0271-X</p>	<p>The Technical Evaluation Report is included at the beginning of the Conference Proceedings.</p> <p>The meeting was divided into five sessions: Experimental Investigations on Flows in Impellers and Diffusers; Theoretical Calculations of Flows in Impellers; Interaction between Impeller and Diffuser; Design Experience and Performance of Advanced Centrifugal Compressors (Parts I and II).</p> <p>The papers were focussed on the inducer, impeller and the diffuser flow field, on interactions between impeller and diffuser, and they provided a comprehensive survey and detailed information on design experience and centrifugal compressor performance. Viscous transonic, compressible and 3-D effects were studied. The influence of non-uniform flow at the rotor outlet on performance and surge margin, namely for high pressure ratio compressors, were discussed.</p> <p>ISBN 92-835-0271-X</p>

